

FINAL REPORT

AASERT GRANT NO. F49620-95-1-0398

**Shear Banding and Crack Propagation in Geomaterials:
Clays and Sands**

**Principal Investigator
Prof. Adel S. Saada
Case Western Reserve University**

²¹
July 15, 1998

DISTRIBUTION STATEMENT A

**Approved for public release;
Distribution Unlimited**

19981106 142

REPORT DOCUMENTATION

AFRL-SR-BL-TR-98-

Approved
No. 0704-0188

Public reporting burden for this collection of information is estimated to average 1 hour per record, including gathering and maintaining the data needed, and completing and reviewing the collection of information, including suggestions for reducing this burden, to Washington, Suite 1204, Arlington, VA 22202-4302, and to the Office of Management and Budget, Paperwork Project, Washington, DC 20503.

searching existing data sources, rate or any other aspect of this and Reports, 1215 Jefferson Washington, DC 20503.

1. AGENCY USE ONLY (Leave blank)		2. REPORT DATE July 21, 1998		3. REPORT TYPE AND DATES COVERED Final Technical Report 1 Jun 95 to 31 May 98	
4. TITLE AND SUBTITLE Shear Banding and Crack Propagation in Geomaterials: Clays and Sands				5. FUNDING NUMBERS F49620-95-1-0398	
6. AUTHOR(S) Professor Adel S. Saada					
7. PERFORMING ORGANIZATION NAME(S) AND ADDRESS(ES) Case Western Reserve University Department of Civil Engineering 10900 Euclid Avenue Cleveland, OH 44106-7201				8. PERFORMING ORGANIZATION REPORT NUMBER	
9. SPONSORING/MONITORING AGENCY NAME(S) AND ADDRESS(ES) AFOSR/NA 110 Duncan Avenue, Suite B115 Bolling AFB, DC 20332-8050				10. SPONSORING/MONITORING AGENCY REPORT NUMBER F49620-95-1-0398	
11. SUPPLEMENTARY NOTES					
12a. DISTRIBUTION AVAILABILITY STATEMENT Approved for Public Release; Distribution Unlimited.				12b. DISTRIBUTION CODE	
13. ABSTRACT (Maximum 200 words) Under simple and combined stresses clay and sand soils exhibit localization of deformation followed by shear banding. In clays, cracks or fissures and inclusions serve as concentrators when loads are applied to the material. The damage is in the form of one or more shear bands. It is found that for saturated clays the crack helps start shear bands but that it forms and propagates guided by the plasticity of an essentially frictional material. An inclination of $45 - \frac{\phi}{2}$ with the major principal stress is generally observed. In sands, digital image processing techniques were developed and used to observe the displacements and the development and propagation of the shear bands. Such bands are distributed along the specimens and, upon bifurcation, some coalesce and result in a major band. The inclination of the bands for three sands of different granulometry was found to follow the Arthur-Vardoulakis criterion i.e. $45 + \frac{1}{4}(\phi' + \psi)$ with major principal stress; ϕ' and ψ being the effective angle of friction and the angle of dilation respectively. Relative density and confining pressures were found to have little or no effects on this inclination. Shear and normal strain measurements were made within the shear band which was found to change in size with particles moving in and out of it.					
14. SUBJECT TERMS				15. NUMBER OF PAGES	
				16. PRICE CODE	
17. SECURITY CLASSIFICATION OF REPORT Unclassified		18. SECURITY CLASSIFICATION OF THIS PAGE Unclassified		19. SECURITY CLASSIFICATION OF ABSTRACT Unclassified	
				20. LIMITATION OF ABSTRACT UL	

ABSTRACT

1. GOALS AND SCOPE

The goal of this project is to experimentally study the initiation and propagation of shear bands in soils; and to provide the profession with the information needed to check their existing models and hopefully develop new ones. Originally two institutions, namely the University of Southern California (USC) and the University of Grenoble (France) were to work with Case Western Reserve University and use our experimentally generated data to conduct theoretical and computational analyses. This so far has not taken place because of financial and organizational reasons. However, this research stands on its own and has yielded outstanding results which have been incorporated in the Case Data Base. This Base is available to any party wishing to use it to develop constitutive relations.

At Case, shear banding and crack propagation in clays has been studied in detail and the results published in two papers, namely:

1. **"Crack, Bifurcation and Shear Bands Propagation in Saturated Clays,"** Geotechnique, 44, No. 1, 35-64

and

2. **"Fracture Mechanics and Plasticity in Saturated Clay,"** ASCE, Geotechnical Special Publication, No. 43.

Shear banding and crack propagation in sands has also been studied thoroughly with some results appearing in two papers and a thesis, namely:

3. **"The Use of Digital Image Processing in Monitoring Shear Band Development,"** Geotechnical Testing Journal, GTJODJ, Vol. 20, No. 3, 1977.

4. **"Bifurcation and Shear Banding Propagation in Sands,"** submitted for publication in Geotechnique.

5. **"Shear Banding in a Coarse Sand (Loire Sand)"**. A thesis submitted in partial fulfillment of the requirements for the degree of Master of Science, Dept. of Civil Engineering, Case Western Reserve University, May 1998.

The publications above are included in the body of this report.

2. EXECUTIVE SUMMARY

a. Research on Clays

A large number of tests were conducted on thin, long hollow cylinders of two Kaolinitic types of clays. Combinations of axial torsional and hydrostatic loadings resulted in various inclinations of the principal stresses on the axis of symmetry of the specimens. Notches were imbedded in the body of the specimen to serve as stress concentrators for the initiation of the shear bands.

It was found that for K_0 consolidated clays the response to stress was significantly influenced by the inclination of the principal stresses on the axis of symmetry of the material. Bifurcations in the form of shear bands invariably appeared near the peak stress in strength experiments. Initially well-distributed along the length of the hollow cylindrical specimens, the shear bands eventually relinquish their share of the deformation to a band along which the material fails in a catastrophic way.

The presence of a small crack (or notch) in a specimen did not substantially affect its overall strength. Stress-strain curves, for specimens with or without cracks, differed very little even though the observed pattern of displacement differed markedly. The pore-water pressures, which are measured at the specimens' ends, are affected only slightly. However, there is a lack of smoothness in the stress-strain curves related to notched specimens, especially when the crack is oriented in the direction of the forming shear bands. Here the bands start forming at about 80% of the peak value of the stress.

The presence of two cracks in close proximity to each other led to interferences which depended on their relative position and on the direction of the applied shearing stresses. These interferences affected the value of the peak stress as well as the development of the shear bands. The bands were noticed at about 80% of the peak stress.

All observations led to the conclusion that, although cracks create local stress concentrations, the behavior of the material is dictated by its plasticity, which becomes predominant at a very short distance from the tip.

The shear bands, whether they occur near the peak in an unnotched specimen, or at 80% of the peak triggered by the presence of a crack, eventually take the same direction, showing once more that the behavior is dictated by the plasticity of the material. This direction was found to be fixed with respect to the direction of the major principal stress. This indicates that a frictional model is necessary to describe the behavior of this clay. It was found that a Drucker-Prager type of model to be satisfactory during the deformation phase. However, the direction of the dominant band which is fully developed at failure is in line with the prediction of Coulomb. This direction is given by an angle of $(45-\phi'/2)$ with the major principal stress direction. If a specimen is subjected to further rotation, at or beyond the peak, an additional shear band develops in the vicinity of the crack tip. The first shear band, often hindered by the boundary, stops and

additional deformations become primarily localized in the new shear band. The second band usually starts with a flat slope but later tends to become parallel to the first one.

The inclination of the cracks was found to act in a coordinated way with the direction of anisotropy and of the applied shearing stress. The development of the shear bands seems to ignore the presence of an upstep crack (negative α) of 45° . Two bands will pass through the tips; others will form in other locations, some stopping while attempting to cross the crack. Stress concentrations at the tips of the crack have little or no influence. However, a downstep crack will become a part of the shear band, and this combination will tend to weaken the specimen.

Isotropic specimens give diffuse shear bands. It appears that the random orientation of particles and clusters inhibits the formation of the clearly defined surfaces observed when K_0 consolidated clays are tested. Also, the shear bands that develop in overconsolidated clays are thinner and more pronounced than their counterpart in normally consolidated clays; localization being more intense.

Photographs were taken at the end of the tests, showing that parts of the specimens between the shear bands suffer little or no permanent deformation. This calls into question the validity of calculated strains from measurements of deformations made on the whole specimen. However, since shear bands occur at or beyond the peak for unnotched specimens, it is only the interpretation of that part of the behavior that is in question; for notched specimens, block motions start to occur at 80% of the peak's value.

While substantial amount of rebound takes place on removal of the stresses, some rebound was observed to occur in the vicinity and on formation of the shear bands. When two cracks are present, they act independently or interact, depending on their relative position and the direction of the applied stresses. In the present study, cracks in the downstep position acted as a single unit. The space between them could suffer instabilities without affecting the overall behavior of the specimen.

In every case that was observed, the shear bands formed and propagated at an angle indicating that saturated clays, even though they were tested in an undrained condition, are essentially frictional materials. A $\phi' = 0$ analysis can be only an approximation.

b. Research on Sand

Research was conducted on three sands with different granulometries. A special procedure had to be developed to imprint indelible grids on the specimens so that the deformation and specially the initiation and propagation of the shear bands could be followed with digital cameras.

Observations backed by photographic records and the use of digital image processing indicate that, for the materials tested a dominant shear band is initiated in the vicinity of the peak

strength and fully develops as one moves towards the critical state. The inclination of the band appears to depend on both the effective angle of friction and the angle of dilation in a combination given by Arthur and Vardoulakis. Changes in confining pressure and density do not seem to have much influence on the inclination of the bands on the major principal plane.

Measurements of the deformations within the shear bands show that it is not possible to assign a fixed thickness to the dominant shear band while it is developing. It constantly varies and new particles are continuously added as it propagates as well as after its full development. The thickness also varies with the inclination of the principal stresses, i.e., with the value of b , the confining pressure and the density of the materials. The effects of grain size has also been studied and preliminary results indicate the same trends presented above.

Measurements of strains outside and within the shear bands show that the condition of no extension does not develop in the shear bands, at least up to the levels of strains reached in the experiments. Also, regardless of the stress path, the normal strains, normal to the direction of the shear bands are always negative. At large strains it is nearly impossible to express the behavior of soils with the simple mechanics of continuous media. The need to combine ϕ' and ψ (i.e., statics and kinematics) to express the inclination of the shear band is just one result of the difficulty of the problem. The constant participation of new particles in the development and propagation of the bands may necessitate the introduction of concepts of mass transport to the modeling process.

LIST OF RESEARCHERS ASSOCIATED WITH THIS PROJECT

Professor Adel S. Saada

Professor J. Ludwig Figueroa

Dr. Gary F. Bianchini

Dr. Liquan Liang

Mr. C. Tucker Cope

Mr. Thomas J. Moon, Jr.

Principal Investigator

Co-Principal Investigator

Professor J. Ludwig Figueroa was added as Co-Principal Investigator when Dr. Liquan Liang obtained his degree and left Case. C.T. Cope and T.J. Moon were partly supported by an AASERT grant.

ORGANIZATION AND CONTENT OF THE REPORT.

There are two parts to this report:

PART I - RESEARCH ON CLAYS

This part includes two papers fully describing the work conducted on clays and the results and conclusions arrived at.

PART II - RESEARCH ON SANDS

Following a short introduction, this part includes two papers and a Master's thesis describing the work conducted on sands and the conclusions drawn. The process of digitization followed by deformation and strain evaluation is slow and lengthy. Appendices contain complete results of a few of the tests.

PART I
RESEARCH ON CLAYS

PART I

RESEARCH ON CLAYS

The two following papers give in complete detail the results of our work on clays. They describe the experiments that were conducted, their results, discussions and conclusions. Each of the tests listed in the tables is fully documented in a file available on request from the principal investigator.

The first paper entitled: **"Cracks, Bifurcation and Shear Bands Propagation in Saturated Clays,"** was published in Geotechnique and was given the Telford Prize of the Institution of Civil Engineers, U.K.

The second paper entitled: **"Fracture Mechanics and Plasticity in Saturated Clay,"** was presented in conjunction with an ASCE National Convention and published in Geotechnical Special Publication No. 43.

The papers are self explanatory and, it is believed, do not require further clarifications. Should any be needed, the principal investigator would be glad to provide it to the interested reader.

PAPER 1 --- ON CLAYS

Cracks, bifurcation and shear bands propagation in saturated clays

A. S. SAADA,* G. F. BIANCHINI* and LIQUN LIANG*

Discontinuities in the form of cracks or fissures and inclusions are often present in natural clays. They serve as stress concentrators when loads are applied to the material. Such concentrations result in cracks advancing, often surrounded by and preceded by a propagating damage zone. As cracks propagate, the damage may be in the form of one or more shear bands, which may play the part of new stress concentrators and blunt the action of the original crack. This Paper examines some of the phenomena associated with cracks in over-consolidated clays and normally consolidated clays. Differences between isotropic and anisotropic materials, and the level at which serious modifications take place in the fabric of the material are noted. The influence of the cracks and the shear bands on the kinematics and strength of the test specimens is discussed.

KEYWORDS: clays; deformation; failure; laboratory tests; plasticity; shear strength.

Des discontinuités sont souvent présentes, sous forme de fractures, fissures et inclusions, dans les argiles naturelles. Elles jouent le rôle de concentrateurs de contrainte lorsque des charges sont appliquées sur le matériau. De telles concentrations se traduisent par une progression des fissures, souvent entourée et précédée par une zone d'endommagement. Lorsque les fissures se propagent, l'endommagement peut apparaître sous forme d'une ou plusieurs bandes de cisaillement qui peuvent jouer le rôle de nouveaux concentrateurs de contrainte et réduire l'action des fissures initiales. L'article étudie quelques uns des phénomènes associés à la fissuration dans des argiles sur-consolidées ou normalement consolidées. Des différences entre matériaux isotropes et anisotropes, ainsi que le niveau à partir duquel des modifications importantes apparaissent dans la texture, ont été observés. L'influence des fissures et des bandes de cisaillement sur la cinématique et la résistance des échantillons d'essai est discutée.

INTRODUCTION

The mechanical response of clays is dictated by their fabric as well as by flaws or discontinuities that may exist in the material. These flaws, often in the form of cracks (or notches) and inclusions, result in shear bands that spread from the crack and form a zone in which most of the deformation is localized. No comprehensive study of this subject has yet been conducted. The principal goal of this Paper is to observe and describe the initiation and propagation of the shear bands with and without the presence of discontinuities. This requires tests that cover a wide range of states of stress so that a reasonable set of hypotheses on which to base a behavioural model can be proposed.

The Paper is divided into four main sections. The first section briefly describes key investigations pertinent to the research: since this Paper is the first attempt to examine localization and

shear banding in clay systematically, significant literature in those areas as well as in the area of fracture applied to soils is mentioned. The second section describes the experimental programme and gives tables of the types of tests conducted. The third section discusses the mechanical behaviour in so far as it pertains to bifurcation, shear banding and crack influence. The fourth section examines the kinematics of deformation and shear band propagation.

LITERATURE REVIEW

Shear band observation

Morgenstern & Tchalenko (1967) studied the behaviour of thin sections of carbowax-impregnated clay in a direct shear device. They defined two types of discontinuities (strain and displacement), and showed that the kinematic restraint imposed by the testing configuration has a marked influence on the shear bands. Houlsby & Wroth (1980) classified kinematic discontinuities and showed that a velocity discontinuity need not be a line of zero extension; whether it is or not depends on the adopted constitutive relation. Balasubramaniam (1976) used X-rays to

Manuscript received 3 August 1992; revised manuscript accepted 19 April 1993.

Discussion on this Paper closes 1 July 1994; for further details see p. ii.

* Case Western Reserve University, Cleveland, Ohio.

study the pattern of deformation in clays. He found the strains to be uniform up to 75% of the peak value.

Arthur & Dunstan (1982) used radiography to observe granular non-cohesive material. They noticed that rupture layers, formed at failure in homogeneous samples of soil sheared slowly under homogeneous stresses with fixed principal stress directions, were oriented at a specific angle according to soil particle size between the limits $(\pi/4) - (\phi'/2)$ and $(\pi/4) - (v/2)$: the limits were determined by the plane-strain values of ϕ' , the angle of friction, and v , the angle of dilation. Scarpetti & Wood (1982) also used radiography to study the orientation of the shear bands in direct shear tests conducted on sand. They suggested that the degree of constraint experienced by the sand will influence the particular bifurcation that it adopts at a particular location. Where the sand sees freedom, it may adopt the Vardoulakis-Arthur solutions. Where the imposed constraint is greater, as in the direct shear device, the shear band will tend towards the Roscoe solution, and follow directions of zero extension.

Desrues (1983) used stereophotogrammetry to study localization in granular materials, and accurately measured the direction of shear bands due to plane-strain compression of sand samples. He provided local measurements of the dilatancy angle and showed that, under certain circumstances, the local dilatancy angle within the shear band was twice as large as the global dilatancy angle calculated from the total volume change measurements.

Bifurcation theories

Vardoulakis (1982), in his review of the theoretical and experimental work in the area of stability and bifurcation of soil samples, states that research has been influenced primarily by the work of Hill. Hill & Hutchinson (1975) based their work on Biot's (1965) pioneering studies and Ariaratnam & Dübey's (1969) studies of diffuse bifurcation modes under plane-strain conditions for elasto-plastic incompressible materials. Plane compression tests were analysed by Young (1976); Needleman (1979) extended this work to pressure-sensitive incompressible materials.

Rudnicki & Rice (1975) studied localization by comparing an isotropic hardening model with a yield vertex model for a pressure-sensitive dilatant material. They showed that the yield vertex model provides a better description and that non-normality permits non-uniqueness with positive hardening (see Mandel, 1964). Both these features are shown to be destabilizing and to influence strongly the resulting predictions for localization,

as compared to predictions based on classical plasticity idealizations involving normality and smooth yield surfaces.

Rice (1976) discusses the localization of plastic deformation into a shear band as an instability of plastic flow and a precursor to rupture. Rice & Rudnicki (1980) distinguish between continuous and discontinuous bifurcation: in the former, further plastic deformation is assumed to occur both inside and outside the zone of localization; in the latter, elastic unloading occurs outside the zone of localization while continued elastic-plastic deformation occurs within it. Vardoulakis, Goldscheider & Gudehus (1978) discussed the spontaneous formation of shear bands in sand bodies. The formation of such bands is regarded as a bifurcation problem. They demonstrated theoretically and experimentally that both Coulomb's and Roscoe's solutions for the orientation of the shear bands θ_c are possible, i.e.

$$\theta_c = \pi/4 - \phi'/2$$

$$\theta_c = \pi/4 - v/2$$

respectively. Vardoulakis (1980), in a sequel to his previous paper, gives experimental results of biaxial tests on sand which show that the inclinations of the shear bands fall between the limits of Coulomb and Roscoe.

Vardoulakis & Graf (1982) placed wooden inclusions in their biaxial testing device and studied shear band formation as an imperfection sensitivity problem. Vardoulakis (1983) studied diffuse and localized bifurcation modes in axisymmetric rectilinear deformations on rigid-granular dilatant material. He found that localizations occur in the softening regime in the compression test and in the hardening regime in the extension test. Hetter & Vardoulakis (1984) conducted an extensive investigation on sands in a large triaxial apparatus and concluded that when the platens were lubricated, bifurcation into diffuse bulging occurred in the hardening regime.

Vardoulakis (1985) examined the stability and bifurcation of water-saturated sands and normally consolidated clay. He described their behaviour by means of a two-dimensional flow theory of plasticity with a non-associated flow rule, and concluded that for dilatant materials the dominant failure mode is shear banding that occurs close to the state of maximum principal effective stress ratio. Whether or not the shear bands have a thickness is a topic that was also studied by Mühlhaus & Vardoulakis (1987), who concluded that they do, that this thickness is a small multiple of the mean grain size, and that it grows with progression in the strain hardening region.

Having shown that the difference between the true stress rate and the Jaumann stress rate could be ignored in shear band analysis, Vermeer (1982) deduced elegant and simple relations predicting the instant of initiation as well as the direction of the shear bands. His predictions are in line with Mandel's conclusions for material stability. Molenkamp (1985) studied the material behaviour under uniform deformation and the occurrence of a shear band as a coupled phenomenon. He attempted to solve the bifurcation problem for a range of popular constitutive models such as the Mohr-Coulomb and Lade-Duncan models, and found large variations between the models in the predicted directions and instants of initiation of the shear bands. Desrues & Chambon (1989) examined the implications of complex constitutive relations in the development of shear bands.

Kolymbas & Rombach (1989) used a non-linear constitutive equation for sand with fixed materials constants to express analytically a necessary criterion for shear band formation. This band is regarded as a shearing zone that may appear spontaneously in the course of a homogeneous plane deformation. Bardet (1991) discussed the scatter in the results obtained by various investigators while emphasizing the observations of Desrues. He used an extended Mohr-Coulomb model to derive an analytical expression for the average orientation of the shear bands in soils. The concept of delayed localization, together with this model, allowed the lower and upper bounds of Roscoe and Mohr-Coulomb for the orientation of shear bands to be retrieved.

Fracture mechanics applied to soils

Based on qualitative descriptions of the failure mechanisms responsible for progressive failure, it was suggested by Palmer & Rice (1973) that sliding occurs on concentrated slip surfaces. By the use of concepts from fracture mechanics (i.e. the J -integral), attempts were made to assess the propagation of a particular shear band. Saada, Chudnovsky & Kennedy (1985) applied concepts of linear fracture mechanics to overconsolidated brittle clays tested in modes I and II, and used a stability criterion to predict failure of infinite slopes. Chudnovsky, Saada & Lesser (1988) and Lesser (1989) studied the propagation of cracks and damage zones in stiff clays, in mode II, under cyclic loading. Using a plane-stress direct-shear apparatus, Vallejo (1987) tested brittle kaolinite with pre-existing opened cracks. He found that the cracks propagated from the tip in the direction normal to the direction of the maximum tensile stress. Vallejo (1988) observed marked differences between the behaviour of brittle and ductile clay when specimens with inclined cracks

were subjected to compressive loads. Vallejo (1989) examined the interference between two cracks in a specimen of brittle clay subjected to compression.

The use of fracture mechanics with clay soils is limited to very stiff materials of low water content.

EXPERIMENTAL PROGRAMME

The hollow cylinder testing cell

This cell, which had been used since 1965 to validate failure criteria and constitutive equations, was first used by Saada *et al.* (1985) to study fracture and damage propagation in clay soils. It has been discussed at length in state-of-the-art papers by Saada & Townsend (1981) and Saada (1988), and by Hight, Gens and Symes (1983). Fig. 1 shows the cell used at Case Western Reserve University. All the measurements are made both inside and outside the cell with a variety of transducers. Axial, torsional and spher-

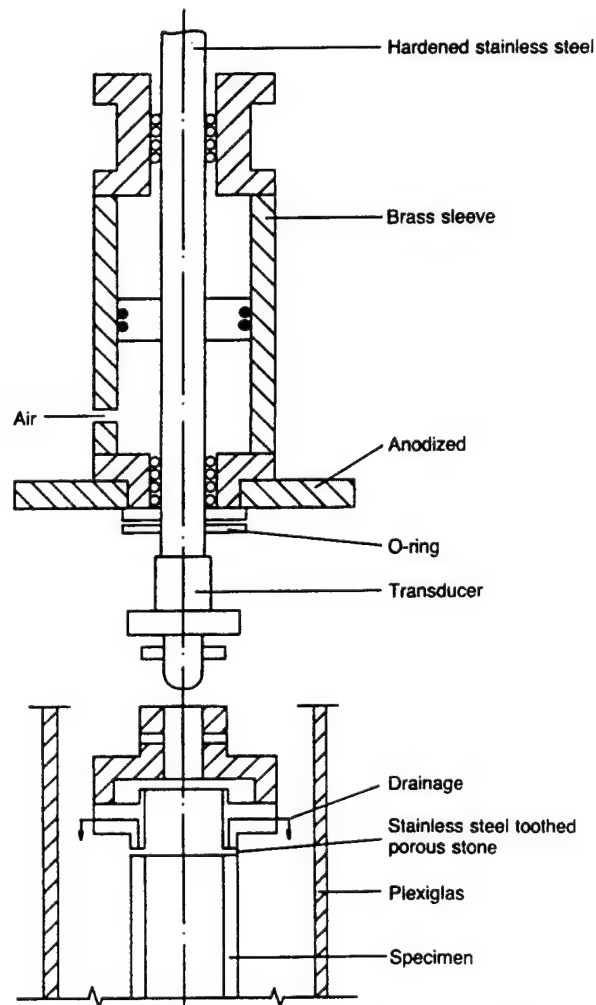


Fig. 1. Cell for axial and torsional stresses on hollow cylinders

ical stresses can be applied to the specimen through a piston and a confining fluid. To maintain uniformity of the normal stresses, the same pressure, namely the cell pressure, acts inside and outside the hollow cylinder. Expressions for the average values of the stresses and strains in terms of the measured forces and displacements are given by Saada & Townsend (1981) and Saada (1988).

Loading, observation and recording devices

Two types of loading device were used in this investigation. The first is a controlled-stress device that applies combinations of axial, torsional and spherical stresses at predetermined ratios, which result in radial paths in the deviatoric plane. It is called SPAC, and has been described by Saada & Townsend (1981). With this device one cannot go beyond the peak, and failure is catastrophic. All its controls are pneumatic and use fluidic components. The second is a controlled-rotation device that uses both mechanical and fluidic controls. A motor applies a slow rotation to the base of the hollow cylinder cell, whose piston is prevented from rotating. The resulting torque is measured with a transducer and its electrical output is converted to a pneumatic output. This output is operated on by a variety of fluidic components, and sent to an actuator which applies to the cell's piston an axial load proportional to the torque. The result is a radial path in the deviatoric plane, with the possibility of going beyond the peak when the failure is torsional. This device was used to observe the

slow development of the shear bands and the slow propagation of damaged zones and cracks.

All the tests conducted were at constant volume. If, in addition, the height of the specimen is fixed, a condition of constant cross-section applies. Fig. 2 shows the system of stresses and the sign convention adopted in this Paper.

Standard and high-speed cameras were used to keep a visual record of the crack and shear band propagation in the test specimens. A state-of-the-art data acquisition and reduction system was used to obtain, calculate and graphically present the data.

Preparation of clay specimens: macroscopic examination

Two kaolinitic types of clay were used in this investigation. The first is called Edgar Plastic Kaolin (EPK), and has been used extensively in soil mechanics research. It has a low activity, a liquid limit of 56.3% and a plastic limit of 37.3%. The second is called Hydrite 121 (H121). It has been used extensively at McGill University in Canada. Its liquid limit is 49.6% and its plastic limit is 37.9% resulting in a low plasticity index. It differs from EPK in that its particles are quite large and it crumbles easily when dried. H121 is very difficult to bring to a low water content by consolidation alone; slow drying is necessary to obtain stiff specimens. A small loss of water causes this clay to become quite stiff compared to EPK. Most of the tests were conducted on EPK.

The procedure described briefly here is presented in detail by Saada (1988). The clay powder was

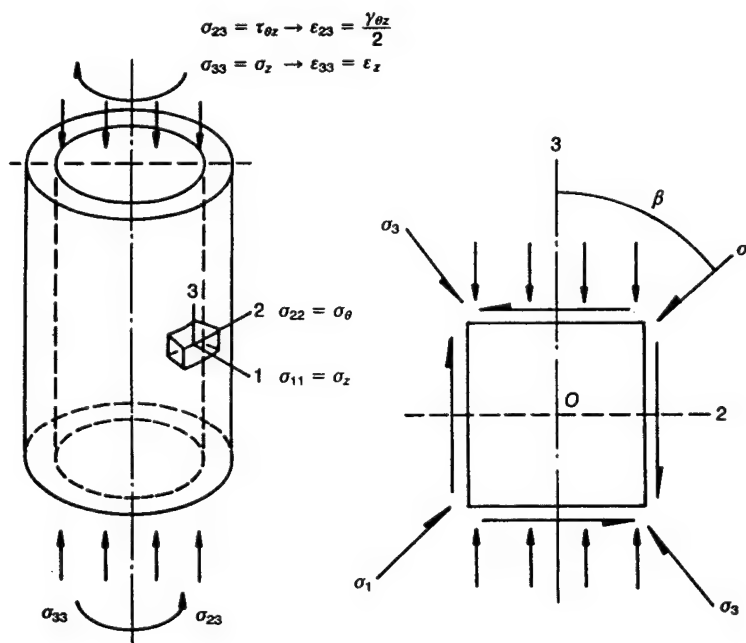


Fig. 2. Notation

mixed under vacuum with distilled water to form a slurry at approximately twice the liquid limit. The slurry was then consolidated in a large 20 cm dia. consolidometer to yield a block from which solid cylinders were cut. Cores of 5 cm diameter were removed from the centre of the cylinders to yield the specimen shown schematically in Fig. 3(a). This shape was satisfactory for routine tests not involving crack propagation studies, but another configuration had to be adopted whenever careful observation of shear band formation was required. The specimens with enlarged ends shown in Fig. 3(b) were made by pressing and coring of the configuration shown in Fig. 3(a) using special cutters and moulds. End effects were thus considerably reduced, if not totally eliminated, during testing. When isotropic clays were studied, the powder was hand mixed and specimens were consolidated isotropically.

To study crack propagation, radial notches were made in the specimens by use of a thin v-shaped brass sheet. The ratio of the circumferential length a of the notch to the mean perimeter l of the specimen varied from 0.1 to 0.4. Some of the notches were inclined to the horizontal. The reference ratio was $a/l = 0.18$ (Fig. 3(b)). To prevent the notch (or crack) from closing

during consolidation and shear, two layers of very thin polytetrafluorethene (PTFE) sheets were inserted in the artificially made notch. Such sheets transmit little or no shear, but transmit compressive normal stresses across the notch surfaces. To simplify the recording of the observation, a 0.6 cm square grid was stamped on the specimens. Photographs were taken during the tests to study the deformation patterns. Before being placed in the oven for moisture content determination, the specimens were rotated in front of a stationary camera and photographs were taken for small increments of rotation. Those photographs were then overlapped with matching grids so that deformations and slip patterns could be examined on the development of the cylinder. In the case of shear band formation, a digitizer was used to obtain a line drawing of the most important bands.

Most of the tests were conducted on K_0 consolidated specimens. This kind of consolidation is routinely performed by use of a pneumatic analog computer that measures the water expelled from the specimen as the pressure in the cell increases and imposes a vertical displacement such that the original cross-section remains constant. K_0 is given continuously by a transducer during the

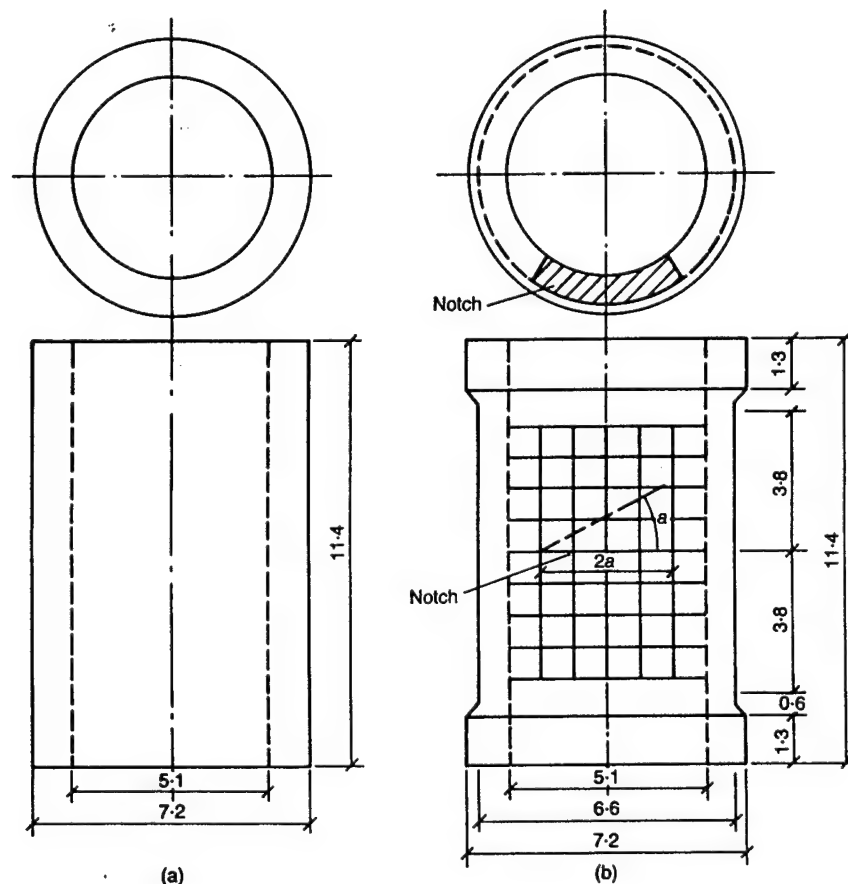


Fig. 3. Specimen geometry (dimensions in cm)

whole process. At the end of the K_0 consolidation process, K_0 was 0.44 for the EPK clay and 0.51 for the H121 clay. All the specimens were rebounded to a condition of spherical state of stress before shearing. Any K_0 consolidation test in which the piston load is removed results in a specimen that is normally consolidated in the horizontal direction and has an over-consolidation ratio OCR_v of almost 2 in the vertical direction. In terms of mean stresses, this ratio is $OCR_m = 1.3$. Because of the size of this ratio, the material is referred to as slightly over-consolidated or normally consolidated. If, as well as removing the piston load, one decreases the pressure in the cell by a factor of 3, say, the specimen is at an OCR of 3 laterally and 6 vertically. OCR_m is 4. The return to a spherical state of stress allows a radial path test to be conducted.

Scope of the experimental investigation

This experimental investigation is aimed at studying the mechanism of deformation and the development of the shear bands in a clay subjected to various systems of stresses. The influence of cracks and the way the shear bands propagate are emphasized.

Series of tests were conducted on specimens with the configurations shown in Fig. 3. Most of the cracks artificially induced in the specimens were horizontal; only a few were inclined. Some

specimens had two cracks. The specimens prepared by one-dimensional consolidation are cross-anisotropic. Some tests were conducted on isotropic materials to examine the influence of anisotropy on the direction of the shear bands. All the tests were of the consolidated undrained type, with pore pressure measurements.

The experimental investigation was extensive. Reference tests (i.e. tests without cracks) were conducted for comparison. Their number and variety are sufficient to provide a database for the validation of any constitutive model for cohesive soils. The tests conducted on specimens with cracks can be used not only to describe the kinematics of the deformation, but also to test the appropriateness of crack and bifurcation theories available at present.

A large number of back-up tests were conducted to ensure repeatability. One-dimensional as well as triaxial consolidation tests were needed to determine properties and to provide a complete description of the clays used.

Tables 1–7 list the tests conducted, with comments. The 'Designation' column entries combine a number and a date. Such labels are used to locate the file containing the data. The angle β is the inclination of the principal stresses on the vertical axis of symmetry. In all the tests for which β is given, the stress path was radial. To each β there corresponds a value for the coefficient b , where $b = (\sigma_2 - \sigma_3)/(\sigma_1 - \sigma_3)$. The tests in which

Table 1. Static tests on K_0 consolidated EPK: configuration of Fig. 3(a) without crack

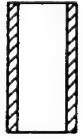

β : degrees	b	σ_c : kPa			Comments and configuration
		241.5	345	552	
		Designation			Stress controlled Radial stress path Free axial deformation 
0	0	31-1-29-91	1b-1-10-90	36-2-15-91	
30	0.25	32-1-31-91	2-11-15-89	37-2-19-91	
45	0.50	33-2-5-91	3b-12-28-89	38-2-21-91	
60	0.75	35-2-12-91	5b-11-13-91	40-3-5-91	
90	1.0	34-2-7-91	4b-12-20-89	41-3-7-91	
Average w.c.: %		36.20	34.53	32.66	

Table 2. Static tests on K_0 consolidated EPK: configuration of Fig. 3(b) without crack

β : degrees	b	σ_c : kPa	Designation	Control	Comments and configuration
30	0.25	345	62-5-16-91	Rotation	Free axial deformation 
45	0.50	345	3t-1-23-90	Stress	
60	0.75	345	61-5-14-91	Rotation	
60	0.75	345	61b-19-11-91	Stress	
Average w.c. = 34.42%					

the length of the specimen is kept constant have a variable ratio of axial to torsional stresses. The consolidation pressure in the tables is expressed in terms of effective cell pressure σ_c ; the specimen has been K_0 consolidated at a cell pressure σ_c and at whatever vertical stress is necessary to keep the cross-section constant. A sketch shows the configuration used.

Table 1 lists three series of five tests on EPK, each series corresponding to a different consolidation cell pressure σ_c , namely 241.5 kPa, 345 kPa and 552 kPa.

Table 2 lists four tests on EPK used to examine the shear bands that develop in specimens without cracks. Two tests were conducted under controlled rotation conditions and two under controlled stress conditions.

Table 3 lists tests conducted on EPK speci-

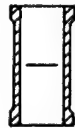
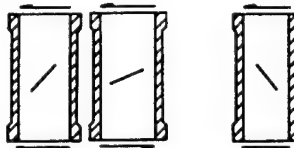
mens with horizontal cracks under various inclinations of principal stresses: five free to change length and two of fixed length. Also listed are three tests with inclined cracks.

Table 4 lists tests conducted on K_0 overconsolidated EPK where the cell pressure σ_c dropped from 621 kPa to 207 kPa, with a corresponding drop in the vertical effective stress as explained above. There were no initial cracks in these specimens. They are used for reference and to study shear band development with the inclination of the principal stresses.

Table 5 lists tests similar to the ones in Table 4, but with a horizontal crack of ratio $a/l = 0.18$. It also lists tests conducted in torsion on specimens with horizontal cracks of different a/l ratios.

Table 6 lists five tests conducted on EPK with K_0 overconsolidated specimens and two cracks.

Table 3. Static tests on K_0 consolidated EPK ($\sigma_c = 345$ kPa): configuration of Fig. 3(b) with crack

β : degrees	b	Designation	Control	Crack angle: degrees	Comments and configuration
0	0	50-4-3-91	Stress	0	Free axial deformation $a/l = 0.18$ 
30	0.25	51-4-5-91	Stress	0	
45	0.50	6v-9-26-90	Rotation	0	
60	0.75	52-4-9-91	Stress	0	
90	1.0	53-4-11-91	Stress	0	
Torsion		3f-2-6-90 6f-6-2190	Stress Rotation	0 0	Fixed length $a/l = 0.18$
45	0.50	56-4-17-91	Rotation	45	Free axial deformation Downstep inclined crack Upstep inclined crack 
45	0.50	57-4-19-91	Rotation	45	
45	0.50	58-4-23-91	Rotation	22.5	

Average w.c. = 34.60%

Table 4. Static tests on K_0 overconsolidated EPK: mean OCR = 4, configuration of Fig 3(b), no crack (one static test on EPK, 7a-9-6-90, was conducted on an isotropic overconsolidated specimen under controlled deformation conditions and fixed length under torsion; OCR = 3; w.c. = 30.2%)


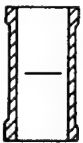
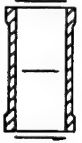
β°	b	Designation	Control	Comments and configuration
0	0	87-7-25-91	Stress	Free axial deformation 
30	0.25	89-8-1-91	Rotation	
45	0.50	86-7-23-91	Rotation	
60	0.75	90-8-13-91	Rotation	
90	1.0	88-7-30-91	Stress	
Average w.c. = 33.92%				

Table 5. Static tests on K_0 overconsolidated EPK: mean OCR = 4, configuration of Fig. 3(b) with crack

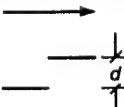
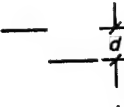
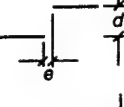
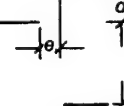
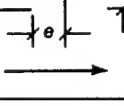
β : degrees	b	Designation	Control	a/l	Comments and configuration
0	0	67-5-31-91	Stress	0.18	Free axial deformation 
30	0.25	68-6-5-91	Rotation	0.18	
45	0.50	66-5-29-91	Rotation	0.18	
60	0.75	70-6-14-91	Rotation	0.18	
90	1.0	69-6-7-91	Stress	0.18	
Torsion		19-1-23-91	Rotation	0	Fixed length 
		16-12-13-90	Rotation	0.10	
		18-1-15-91	Rotation	0.18	
		15-11-28-90	Rotation	0.30	
		13-11-7-90	Rotation	0.35	
		14-11-20-90	Rotation	0.40	
Average w.c. = 32.97%					

The vertical distance d between the cracks is 0.63 cm; the horizontal distance e varies between 0 and 2.54 cm. Four and one of the specimens have their cracks in the downstep relative position and in the upstep relative position respectively. All were free to deform longitudinally.

Table 7 lists all the tests conducted on the H121 clay. There are five reference static tests with various inclinations of principal stresses, and two torsion tests with notched specimens.

The drawings in Tables 3 and 6 define what is meant by upstep and downstep. Both the relative

Table 6. Static tests on K_0 overconsolidated EPK: mean OCR = 4, with two cracks, free axial deformation

β : degrees	b	Designation	Control	Cracks' position*	Comments
45	0.5	81-7-3-91	Rotation		Downstep $e = 0$, $d = 0.6$ cm $a/l = 0.18$
45	0.5	82-7-9-91	Rotation		Upstep $e = 0$, $d = 0.6$ cm $a/l = 0.18$
45	0.5	83-7-11-91	Rotation		Downstep $e = 0.6$ cm, $d = 0.6$ cm $a/l = 0.18$
45	0.5	84-7-17-91	Rotation		Downstep $e = 1.3$ cm, $d = 0.6$ cm $a/l = 0.18$
45	0.5	85-7-19-91	Rotation		Downstep $e = 2.54$ cm, $d = 0.6$ cm $a/l = 0.18$
Average w.c. = 33.62%					

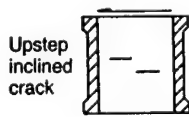
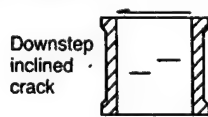

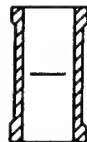


Table 7. Tests on K_0 consolidated H121: $\sigma_c = 345$ kPa

β	b	Designation	Control	Comments and configuration
0	0	1-5-1-90	Stress	Free axial deformation 
30	0.25	2-6-1-90	Stress	
45	0.50	3-5-3-90	Stress	
60	0.75	5-6-8-90	Stress	
90	1.0	4-6-5-90	Stress	
Torsion		3f-5-16-90	Stress Rotation	Fixed length Crack $a/l = 0.18$ 
Torsion		6f-9-17-90		
Average w.c. = 31.14%				

position of the cracks (or the inclination of one crack) and the direction of the applied shear are involved in these definitions.

TEST RESULTS AND OBSERVATIONS RELATED TO STRENGTH

Tests in Tables 1, 2 and 7

While the tests listed in Tables 1, 2 and 7 can be used to assess the validity of a variety of models, that is not the aim of this Paper. The relationships between stress-strain and pore-water pressure are given by Saada & Bianchini (1992). This Paper concentrates on shear bands and their directions. From the tests listed in Tables 1 and 2, the value of the angle of friction ϕ' can be obtained and the directions of the shear bands observed in the specimens subjected to various stress paths can be studied. There are five different stress paths; if the Mohr-Coulomb theory of failure were perfectly valid for the

materials tested, the plane of failure at each point would contain the intermediate principal stress, which in the present case is radial. The tests with paths corresponding to an inclination $\beta = 30^\circ$, 45° and 60° show that this is not the case: the surfaces in the three cases are slightly inclined in the radial direction across the thickness, most notably the ones corresponding to the $\beta = 30^\circ$ tests. Because of symmetry, the pure compression and extension tests give the standard conical failure surface. Fig. 4 shows the angle of friction ϕ' , as defined by $\sin^{-1}[(\sigma_1' - \sigma_3')/(\sigma_1' + \sigma_3')]$ obtained from the tests conducted on EPK, as a function of the inclination β . It is evident that ϕ' varies drastically with β and its values become unreliable as the tensile stresses become predominant. The variations in ϕ' among the various one-dimensional consolidation pressures are primarily due to changes in anisotropy as the K_0 consolidation pressures are increased. Similar results are obtained for H121, illustrating the influence of

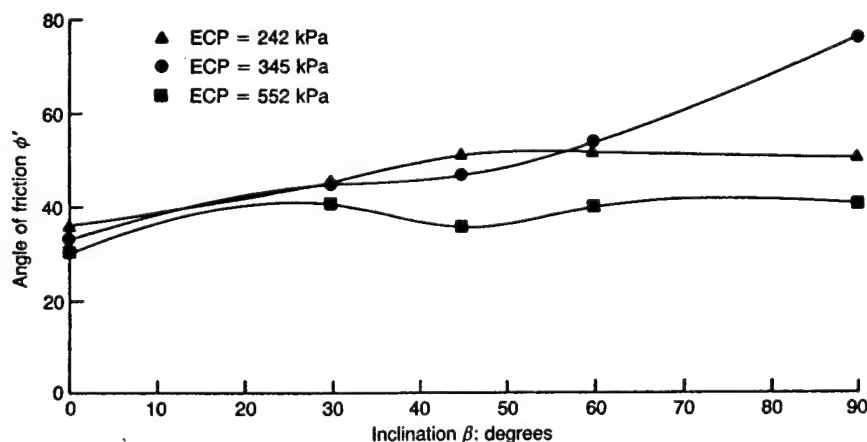


Fig. 4. Influence of inclination of the major principal stress on ϕ'

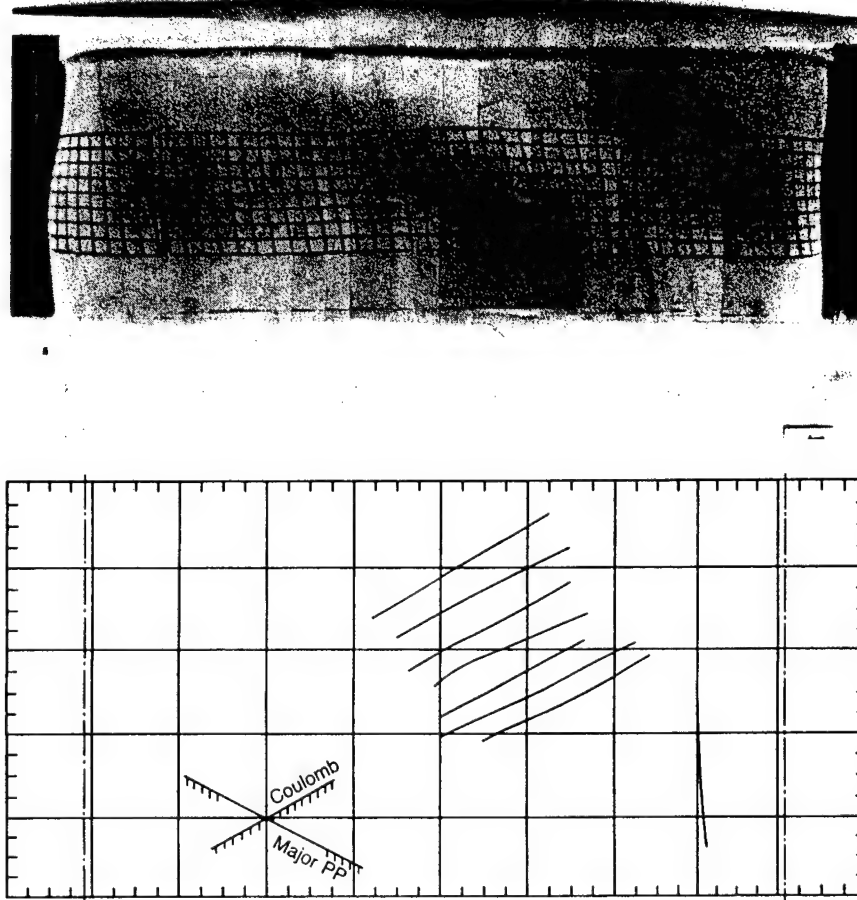


Fig. 5. Bifurcation and resulting shear bands: $\beta = 30^\circ$; specimen 62-05-16-91

both β and anisotropy on the friction angle ϕ' . Such observations have appeared in the literature, and are commented on by Saada & Bianchini (1975) and Ladd, Foott, Ishihara, Schlosser & Poulos (1977).

The inclination of the shear bands that develop near the peak of a stress-strain curve is elucidated in detail below. It is appropriate at this stage to make a few comments within the framework of the Mohr-Coulomb theory. The tests in Table 2 are ideal for this purpose, since they were conducted on specimens with enlarged ends. The photographs in Figs 5 and 6 are from a succession of single shots. (In Figs 5-11, the grid on the plot is only to locate points and to help draw the shear bands; it does not correspond to the grid on the specimen. The distance between the broken lines in the plots shown in Fig. 5, 6, 9-11 and 20-30 is equal to the perimeter of the specimen.) The digitized plots in Figs 5 and 6 show both the experimental shear bands and the direction predicted by the Mohr-Coulomb theory.

The angle $(45^\circ + \phi'/2)$ giving the inclination of the Coulomb slip planes was computed with an average angle of friction of 33° obtained from direct triaxial compression tests (Fig. 4). The results of the two tests agree very well with the Coulomb theory. The grid stamped on the specimens allows angles to be measured with reasonable accuracy, and visually enhances the shear bands and their directions.

While the above observations are important, and the first of their kind to be obtained under combined stresses, the reference ϕ' was obtained from direct compression and Fig. 4 is a reminder that the traditionally defined ϕ' is not unique.

Tests in Table 3

Seven of the ten tests listed in Table 3 were conducted on specimens with horizontal cracks and a ratio $a/l = 0.18$. The last three tests had inclined cracks 2.5 cm long. Stresses and strains were calculated from measurements taken on the whole specimen ignoring the presence of the

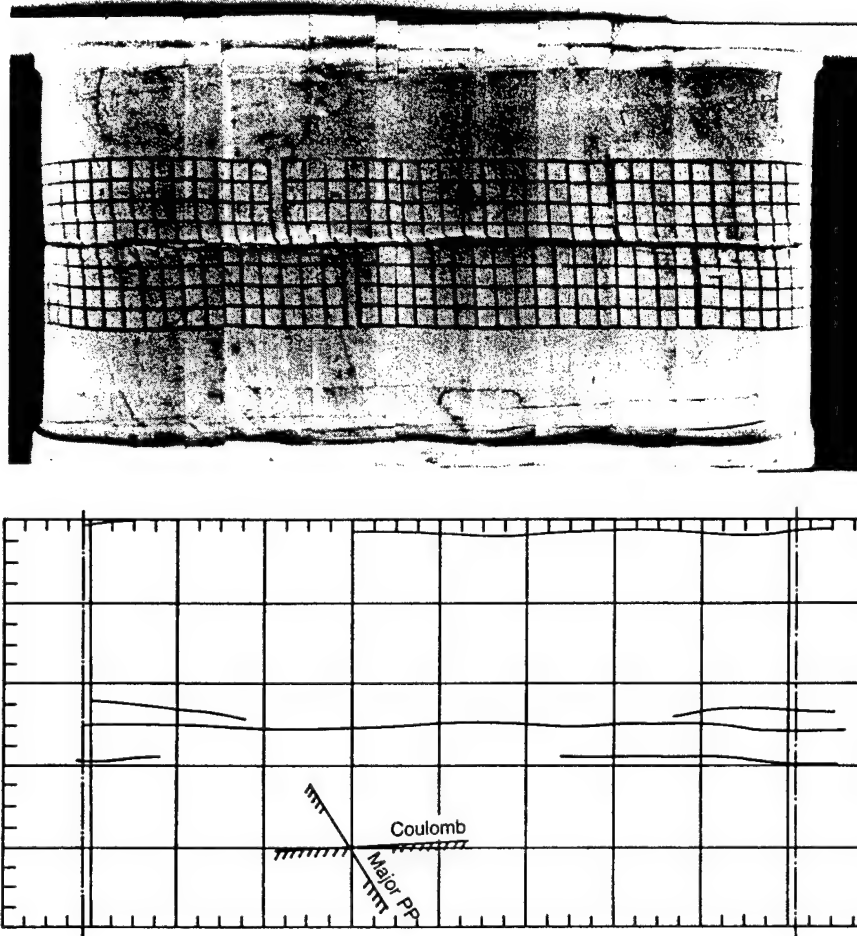


Fig. 6. Bifurcation and resulting shear bands: $\beta = 60^\circ$; specimen 61b-11-19-91

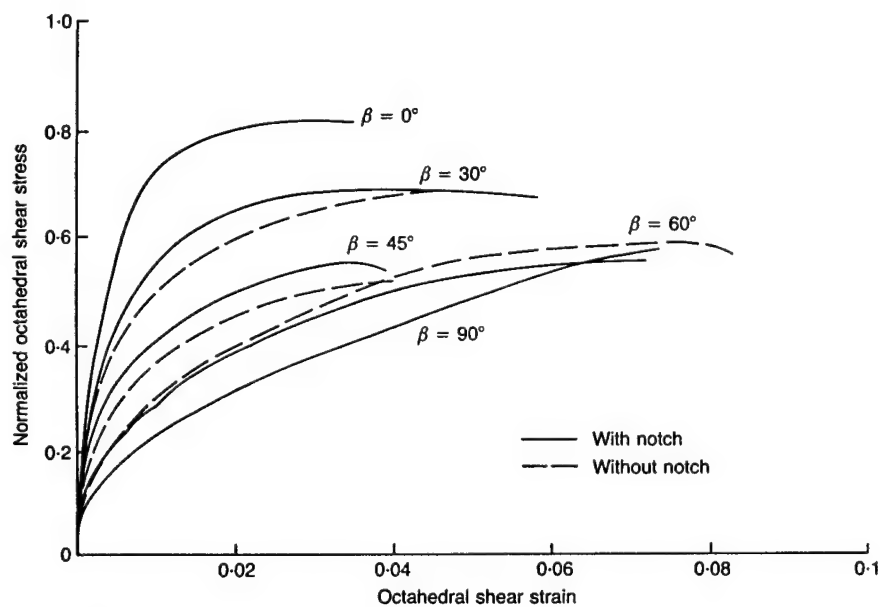


Fig. 7. Comparison of notched and unnotched specimens

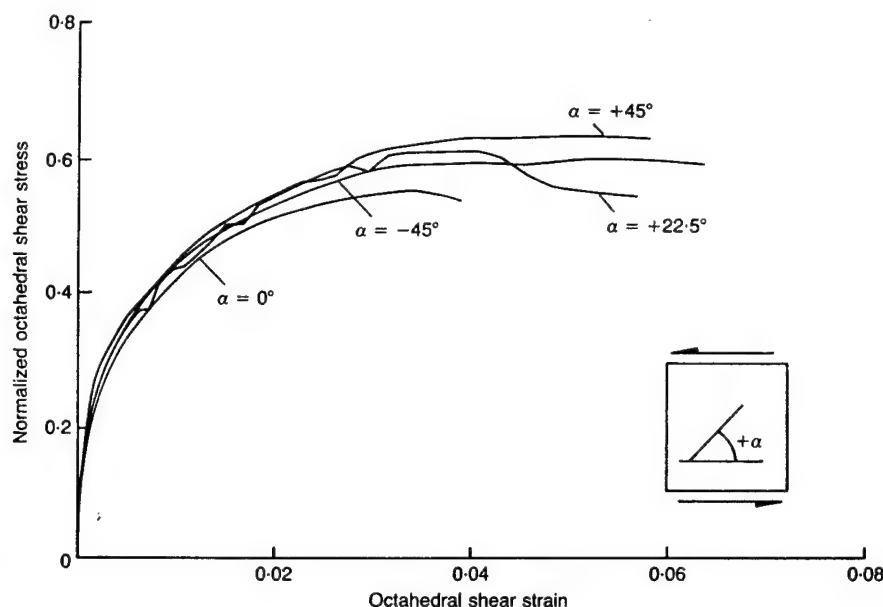


Fig. 8. Influence of crack inclination on strength

cracks. Fig. 7 shows the stress-strain curves for various inclinations of the principal stresses on the axis of symmetry obtained from identical notched and unnotched specimens. The curves correspond to the tests listed in Table 2 and the first five tests in Table 3, the normalizing stress being σ_c . They show that the influence of the crack is minimal despite its size. It is seen below that once the shear band starts in the vicinity of a crack, the deformation is completely controlled by the plastic behaviour of the material.

The influence of the inclination of the crack on the shear strength behaviour is shown in Fig. 8. The specimens are under a state of pure torsion and are free to deform axially. Whether the inclination is 45° , 22.5° or 0° , the undrained strength is nearly the same except at very large strains. The pore-water pressures were also found to be close to each other. Again, it appears that once the shear bands develop the behaviour is plastic and the influence of the crack almost vanishes. This is discussed further below.

Tests in Table 4

The tests noted in Table 4 were conducted on overconsolidated specimens of EPK clay without cracks and with a mean OCR of 4. Like their counterparts in Table 1, these tests serve as a reference: in this case for the study of strength, crack propagation and damage propagation in a more brittle material. Figs 9–11 show the pattern of slip lines that developed for $\beta = 30^\circ$, $\beta = 45^\circ$ and $\beta = 60^\circ$. In all cases the prediction of the inclinations of the slip lines by Coulomb's theory

(with $\phi' = 33^\circ$) fits the measured ones extremely well, as shown on the digitized plots in Figs 9–11. The photographs in Figs 9–11 are used for comparison when the shear bands that develop in the presence of a crack are being examined.

Tests in Table 5: influence of crack size

Table 5 gives two sets of tests: one in which the specimens of $a/l = 0.18$ were subjected to the radial stress paths as listed in Table 4, and one in which the specimens, with various crack sizes, were subjected to torsion under fixed length conditions. Fig. 12 shows the shear stress as a function of the strains: the results obtained with notched ($a/l = 0.18$) and unnotched specimens are superimposed to allow the influence of the crack to be studied. As in the case of Fig. 7, this influence is seen to be minimal even though the length of the crack is $\sim 20\%$ of the perimeter.

The above results led to a study of the influence of crack length on strength. Six specimens with various a/l values were subjected to torsion under fixed length conditions. The stress-strain relations are shown in Fig. 13. The ultimate strength drops as the size of the crack increases, as expected. However, comparison of Figs 12 and 13 shows that higher values of the stresses result when specimen length remains constant than when specimens are free to elongate.

Tests with two cracks in Table 6

Those tests were conducted in order to answer questions about coalescence of cracks and shear

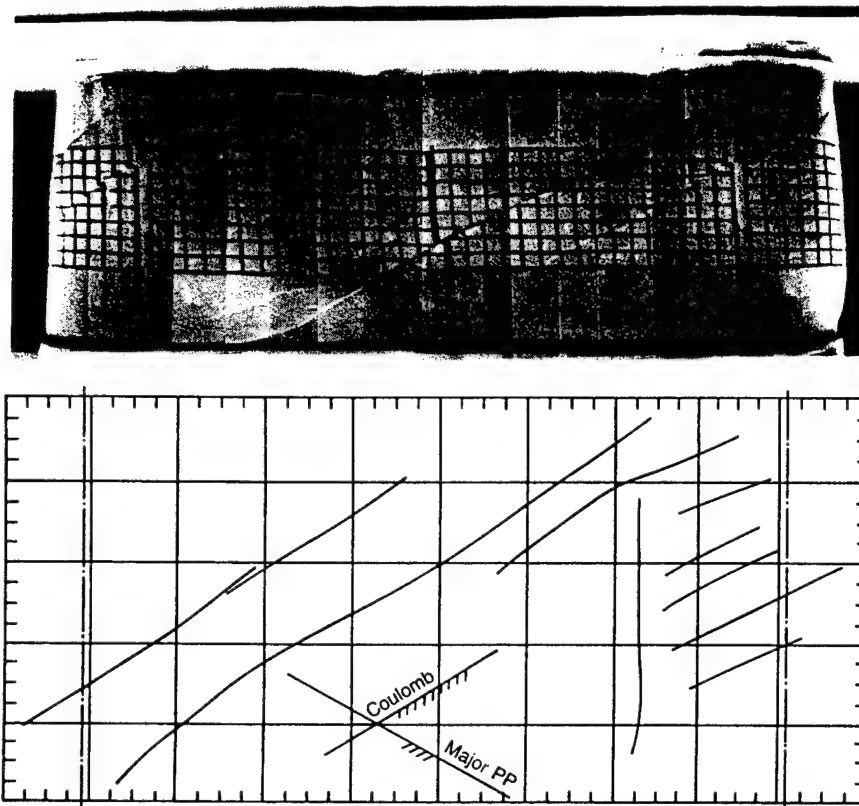


Fig. 9. Bifurcation and resulting shear bands: $\beta = 30^\circ$; specimen 89-08-01-91

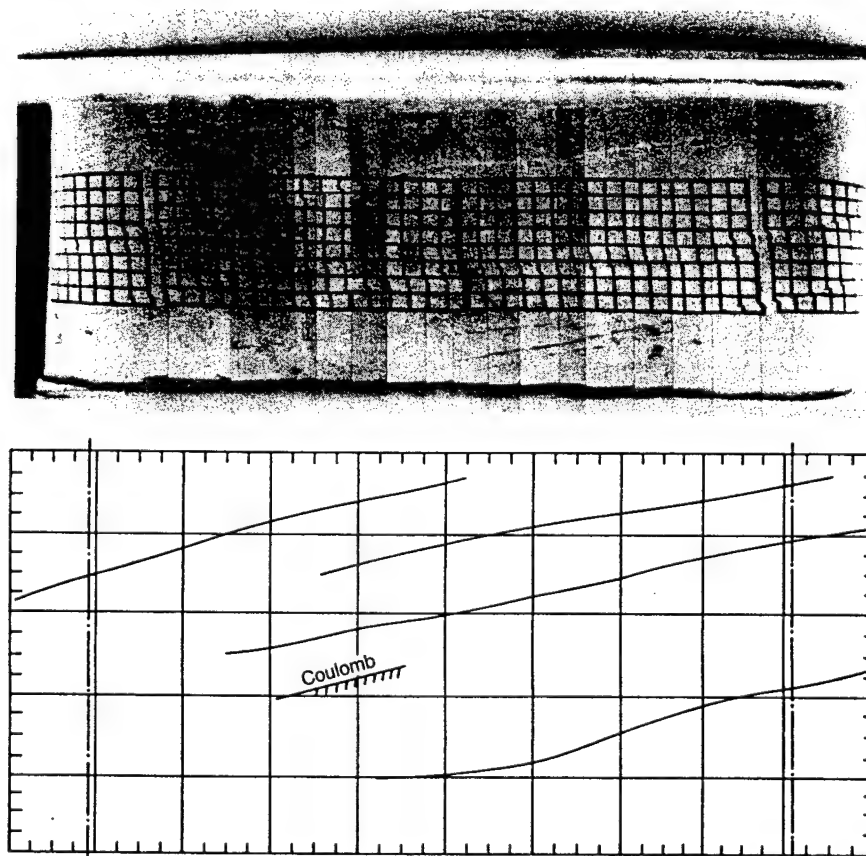


Fig. 10. Bifurcation and resulting shear bands: $\beta = 45^\circ$; specimen 86-07-23-91

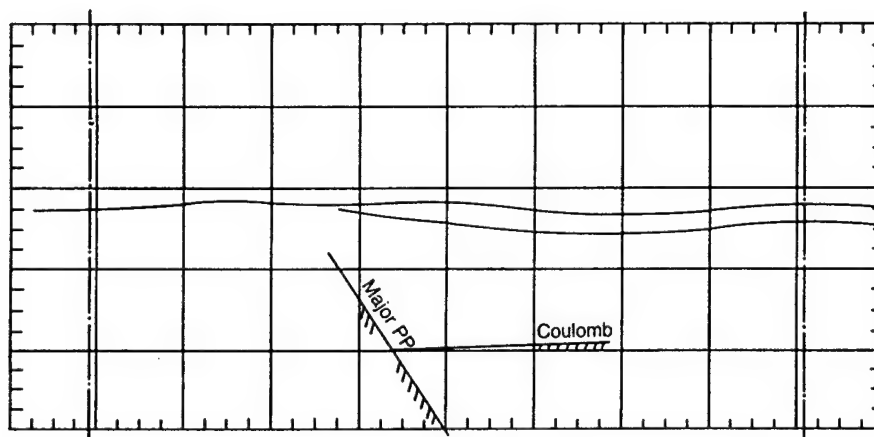
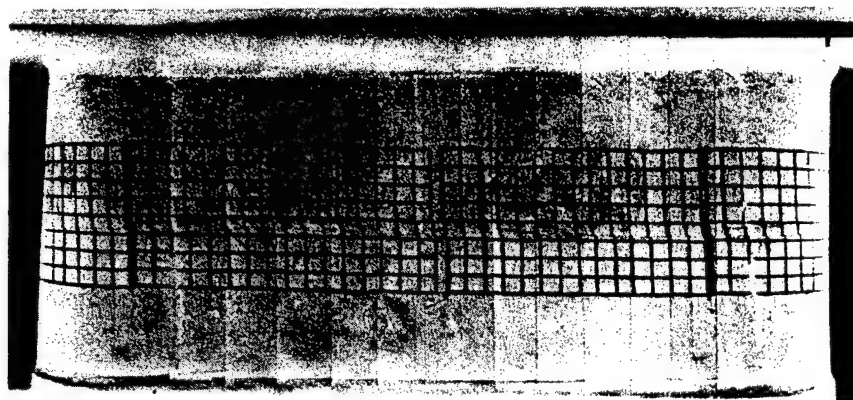


Fig. 11. Bifurcation and resulting shear bands: $\beta = 60^\circ$; specimen 90-08-13-91

bands during the shearing process. In the five tests listed in Table 6, the two cracks were separated horizontally and vertically as shown. While d was kept constant at 0.6 cm, e varied

between 0 and 2.54 cm. The direction of the torque was the same for all tests and the specimens were free to deform axially, leading to the same value of $\beta = 45^\circ$. The first two tests are

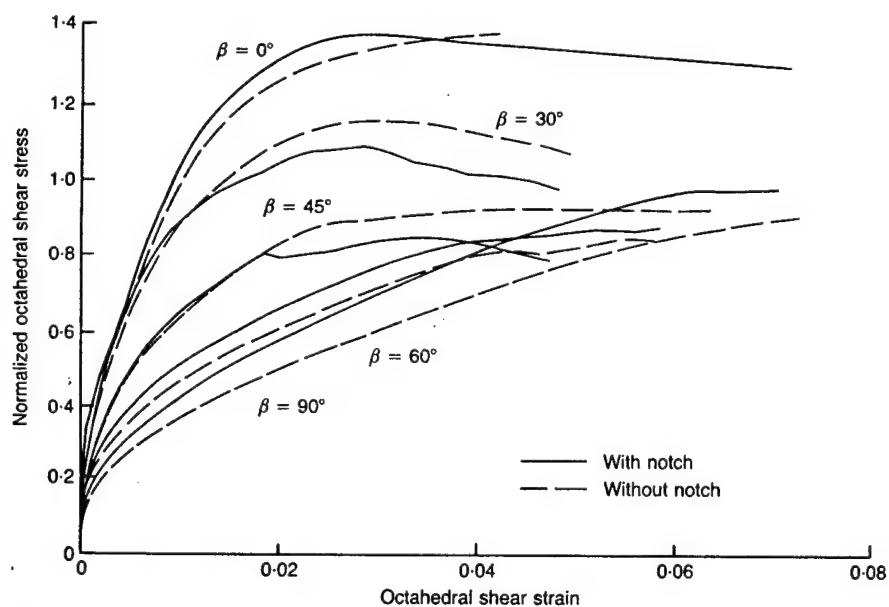


Fig. 12. Comparison of notched and unnotched specimens

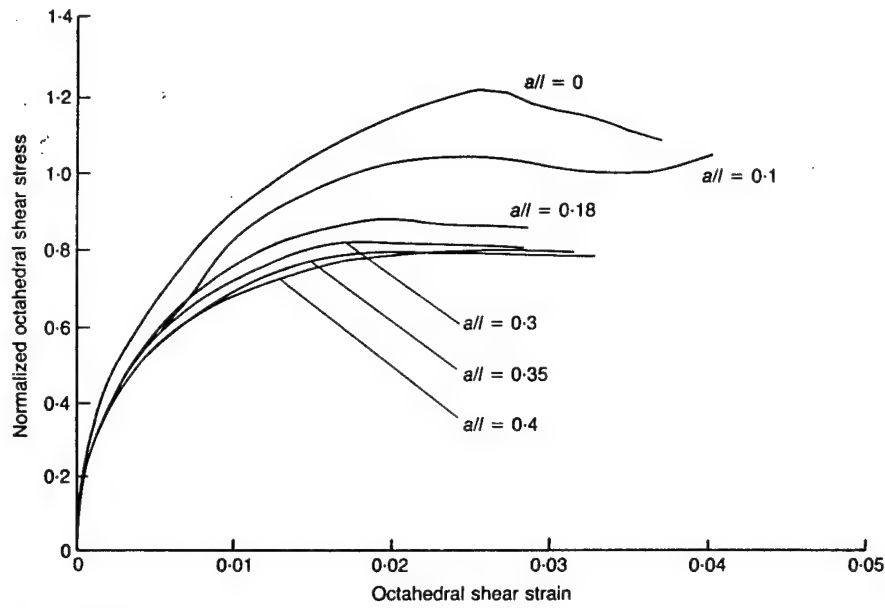


Fig. 13. Influence of crack size on strength

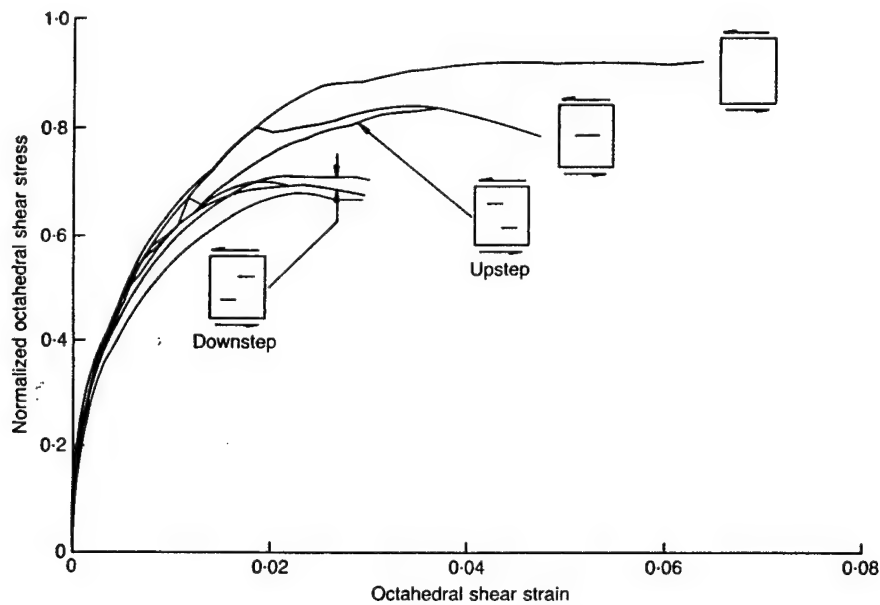


Fig. 14. Influence of number and relative positions of cracks on strength

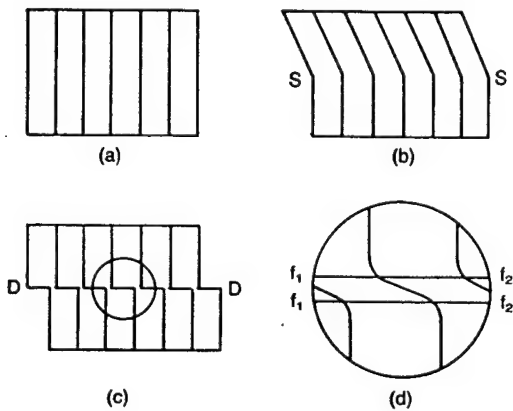


Fig. 15. Morgenstern & Tchalenko (1967) definitions: (a) unstrained state; (b) strain discontinuity SS; (c) displacement discontinuity DD; (d) magnification of central portion of DD showing two strain discontinuities, f_1f_1 and f_2f_2

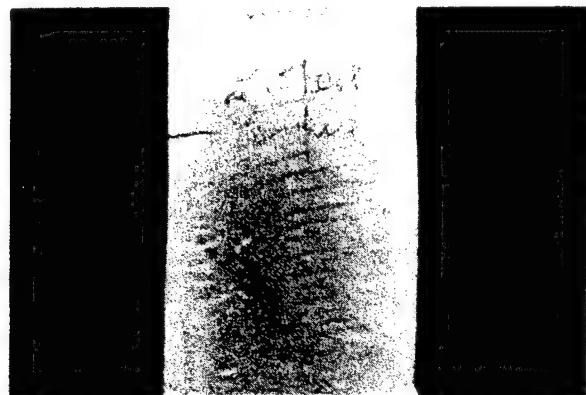


Fig. 16. Multiple shear bands in an H121 clay in torsion

identical except that the first has its cracks in the downstep position and the second has them in the upstep position.

Figure 14 shows the strength for all five tests in Table 6. For comparison, it also shows the curves for a specimen with one crack from Fig. 12, and the curve for a specimen with no cracks. As expected, the strength curves for two cracks are below the ones with one crack or no crack. Also, the position of the cracks relative to the direction of the shearing stresses is very important. For the same direction of shear stress the two notches in the upstep position give a result close to that obtained with one notch, indicating very little interaction between the two notches. However, the cracks interact when they are in the downstep position, leading to a weakening of the specimen. In such a case, for a given distance d , e plays an important role in the weakening process. It is obvious that as d increases, the behaviour tends towards that of the single-crack specimen. For all specimens, however, the cracks and their position do not seem to affect the behaviour until 50% of the stresses have been applied. Shear bands become visible to the naked eye shortly after this. The corresponding strain is $\sim 0.5\%$.

KINEMATICS OF DEFORMATION, CRACK PROPAGATION AND DAMAGE PROPAGATION

Photographs taken during and at the end of many of the tests listed in Tables 1-7 allow the pattern of crack propagation and shear band development and the relative displacement of the various parts of the specimens to be studied. One of the difficulties in the development of constitutive equations is in the measurement of strains within the soil specimens. Once a shear line or slip band is formed, whether initiated by the existence of a crack or not, different parts of the specimen under test move as blocks. Bifurcation theories and models have been developed to



Fig. 17. Influence of filter paper on the formation of shear bands

describe mathematically and to predict those phenomena in various materials. The observations described here are the first step in the development of a model suitable for clay soils.

Discontinuities that occur during deformation have been classified by Morgenstern & Tchalenko (1967) as strain discontinuities and displacement discontinuities (Fig. 15). The former generally precede the latter in front of the crack tip and in front of the propagating shear bands. The extensive photographic record made during deformation and failure allows the kinematics of the specimen to be followed while relating it to the resistance of the material. As previously stated this record was digitized and stored in a database so that a pattern of slip lines can be directly recalled and plotted without reference to the original photograph. All the observations were made on specimens with enlarged ends.

Observations on specimens without cracks under static loading

Either under axial loads or under a combination of axial and torsional loads, the

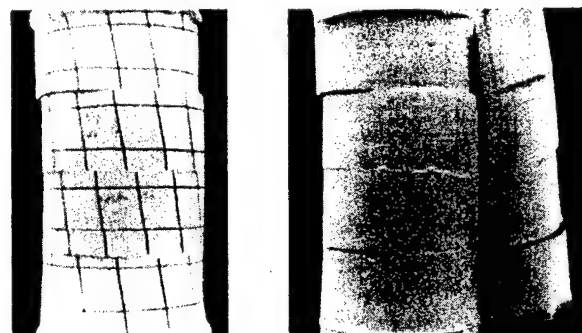


Fig. 18. Influence of filter paper on the formation of shear bands

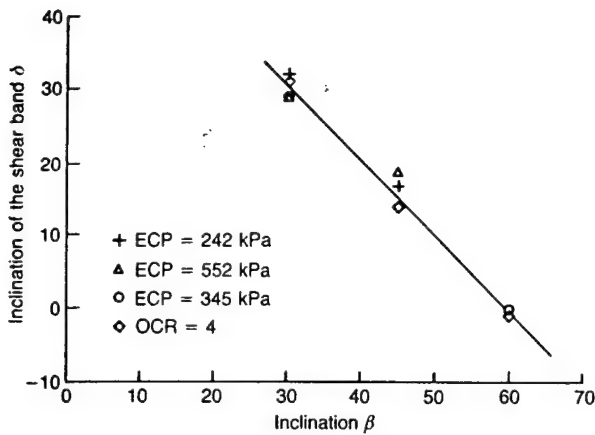


Fig. 19. Inclination of shear bands

maximum octahedral shear stress is reached before slip lines form. Close to the peak, the deformations usually occur along a large number of slip surfaces, often uniformly distributed along the length of the cylinder. In the past, such slip surfaces could not be clearly seen because of the presence of filter paper, which inhibited the formation of some while emphasizing others, especially where the paper is slit to decrease its resistance. Figs 16–18 illustrate these points.

Figure 16 shows the slip lines formed on a uniform specimen of H121 clay subjected to torsion. Fig. 17 shows the vertical shear bands after very large torsional deformations in an EPK clay specimen; the localization is along the once-vertical filter strips. Fig. 18 shows the slip bands that develop where the filter paper is slit horizontally to decrease its resistance to torsion.

Figures 5 and 6 show the slip bands for a normally consolidated clay under two different stress paths; and Figs 9–11 show the slip bands for an

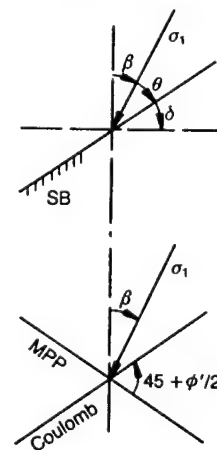
overconsolidated clay under three different stress paths. No outer filter paper was used, and the grid shows the discontinuities that occur. All stress paths used in these tests resulted in the kind of discontinuity shown in Fig. 15. The photographs in Figs 5, 6 and 9–11 were taken at the end of the test, i.e. after the release of the stresses acting on the specimens. Some rebound obviously occurred, but all parts would be expected to have suffered some permanent displacement. Figs 5 and 6, which correspond to a normally consolidated clay, support this expectation. However, Figs 9–11, which correspond to an overconsolidated clay, show regions between the slip lines where the vertical grid has little or no inclination. Also, it was noted during the tests that, at the instant of formation of the shear bands, some rebound takes place in their vicinity.

The inclination of the observed shear bands, as compared to the inclination of the principal stresses, deserved comment. Table 8 lists tests conducted on normally consolidated clays from Tables 1 and 2 and overconsolidated clays from Table 4, together with their β value, the inclination δ of the shear bands with the horizontal, and the inclination θ of the shear bands on the major principal stress. θ is seen to be nearly constant. Fig. 19 plots δ against β . Similar results were obtained by Arthur & Dunstan (1982) for non-cohesive soils. These observations show that the dilatation angle can be neglected; this is to be expected globally when the test is undrained.

The formation of the shear bands close to the peak stresses, and the subsequent occurrence of a deformation composed of relative motion of blocks along these bands, require that the validity of the displacement measurements and the subsequent calculations of the strains be questioned.

Table 8. Inclination of shear bands for various inclinations of major principal stresses: no crack

Refer to Table	σ_c	Designation	β : degrees	δ : degrees	θ : degrees
1	241.5	32-1-31-91	30	32	28
	241.5	33-2-5-91	45	17	28
	552	37-2-19-91	30	29	31
	552	38-2-21-91	45	19	26
2	345	62-5-16-91	30	29	31
	345	61-5-14-91	60	0	30
	345	61b-11-19-91	60	0	30
4	OC	89-8-1-91	30	31	29
	OC	86-7-23-91	45	14	30.5
	OC	90-8-13-91	60	-1	31



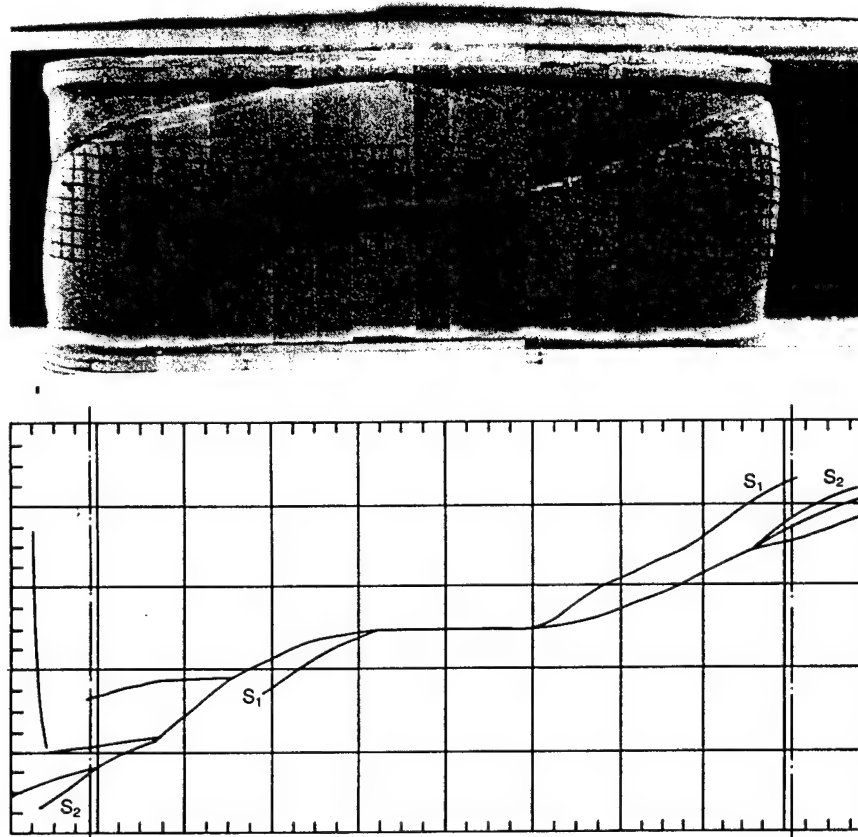


Fig. 20. Shear bands for one crack: $\beta = 30^\circ$; specimen 51-04-05-91

The jumps that are seen in the grids are clear indications of the total lack of uniformity at and beyond the peaks. Measurements during the strain softening period cannot in general be used to support or discredit many of the constitutive equations that attempt to model the behaviour of the material during this stage.

Specimens with one crack under static loadings

For an angle $\beta = 0$ (i.e. for specimens in triaxial compression) the crack affects the stress-strain behaviour only slightly. A combination of axial and torsional stresses, however, results in a shear band starting at and propagating from the tip of the crack, before the peak is reached. In the absence of cracks there are a very large number of shear lines all around the specimen, but here the number is limited to two or three, all starting at the crack or emanating from each other. The first band starts at the crack tip, with a slope that is dictated by the stress concentration and the directions of the principal stresses there. It is the steepest; the second and third start at a smaller slope. As the bands propagate, however, they tend to run parallel to each other as the influence of the crack vanishes with distance.

Figures 20-22 show the shear bands for the three K_0 normally consolidated tests in Table 3, corresponding to $\beta = 30^\circ$, 45° and 60° respectively. The displacements are large due to the nature of the stress-controlled test, where failure occurs catastrophically if left unchecked. Compare the patterns and direction of the slip lines in Figs 20-22 with those in Figs 5 and 6: while there seems to be an infinite (very large) number of shear bands in Figs 5 and 6, the presence of the crack initiates one or two main shear bands which propagate all around the specimen to cause failure. The fact that blocks of specimens move with respect to each other once the shear bands form is very striking when the crack is the initiator. In Figs 20-22, many of the vertical lines remained nearly vertical after the load was removed and do not show discontinuities. Also, away from the crack the inclination of the shear bands is nearly the same as in specimens with no crack. This is a clear indication that although the stress concentrations near the tip of the crack control the moment of initiation and the initial direction of the shear band, their influence quickly vanishes, leaving the plasticity of the material in control of the kinematics of the specimen.

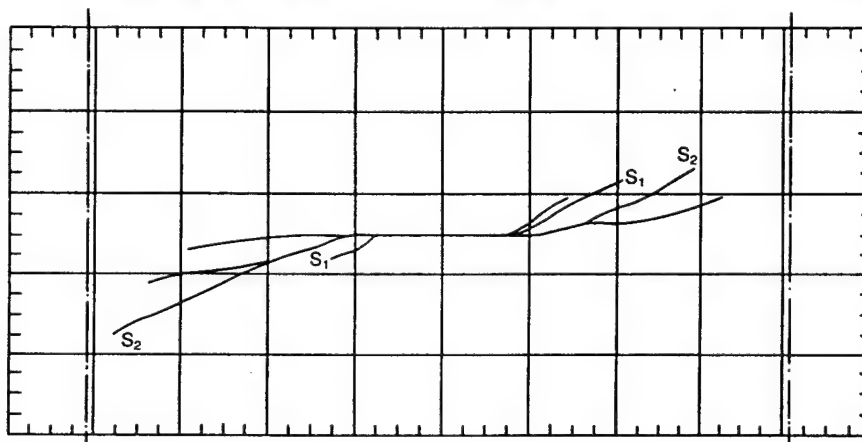
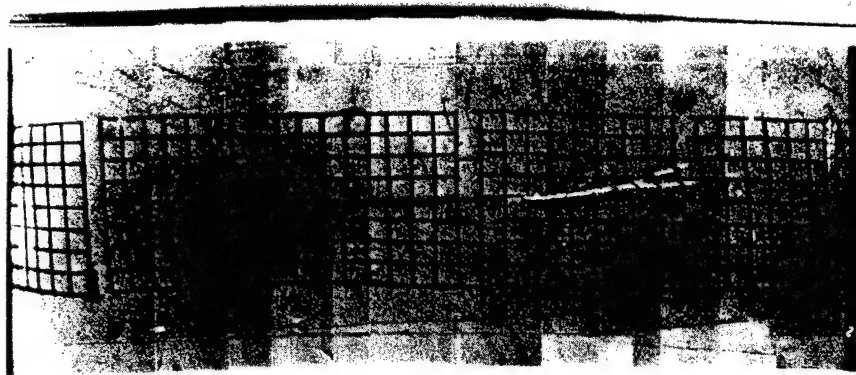


Fig. 21. Shear bands for one crack: $\beta = 45^\circ$; specimen 6v-09-26-90

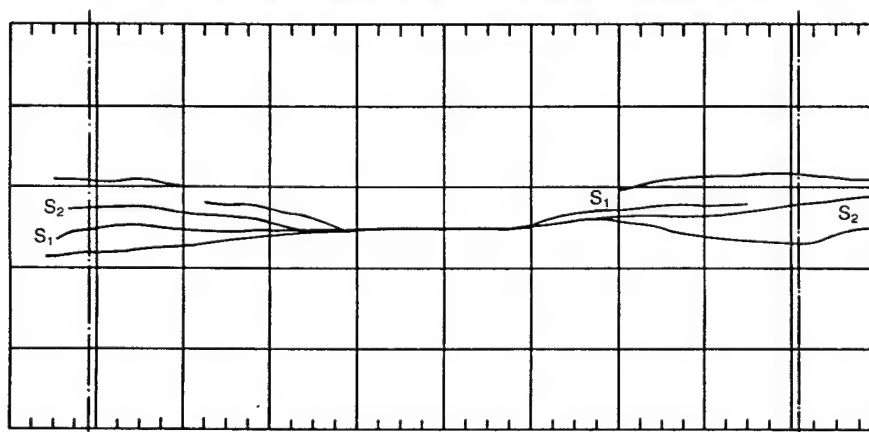
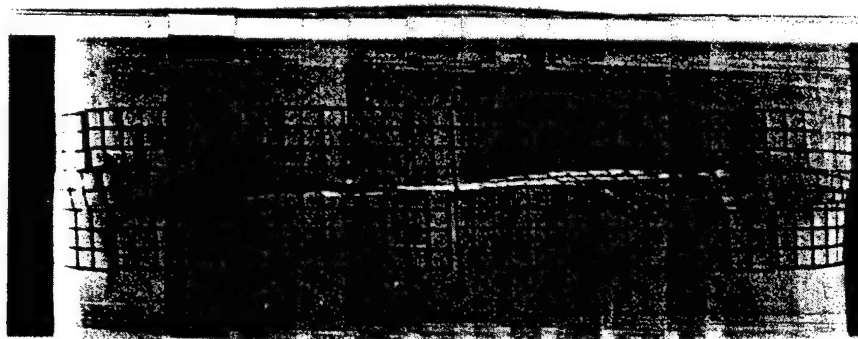


Fig. 22. Shear bands for one crack: $\beta = 60^\circ$; specimen 52-04-09-91

Table 9. Inclination of the shear bands and CSD: one crack (specimen 7a-09-06-90 is isotropic and results in a diffuse zone of shear bands; subscripts u and l refer to upper and lower bounds respectively)

Refer to Table	Designation	CSD: cm	Left side		Right side	
			Label	Angle: degrees	Label	Angle: degrees
3	51-04-5-91	2.20	S ₁	32	S ₁	30
			S ₂	35	S ₂	26
	6V-09-26-90	0.64	S ₁	30	S ₁	28
			S ₂	25	S ₂	22
	52-04-09-91	1.27	S ₁	0	S ₁	6
			S ₂	3	S ₂	5
	3f-02-06-90	1.91	S ₁	25	S ₁	35
			S ₂	22	S ₂	32
	6f-06-21-90	0.95	S ₁	28	S ₁	33
7			S ₂	20	S ₂	28
	56-04-17-91	0.16	S ₁	20	S ₂	17
			S ₂	20		
	57-04-19-91	0.8	S ₁	19	S ₁	20
			S ₂	17		
	58-04-23-91	0.89	S ₁	20	S ₁	20
	6f-09-17-90	0.64	S ₁	30	S ₁	36
			S ₂	24	S ₂	32
5	7a-09-06-90	0.64	S _{1u}	23	S _{1u}	23
			S _{1l}	8	S _{1l}	9
	68-06-05-91	0.89	S ₁	38	S ₁	39
			S ₂	33	S ₂	33
	66-05-29-91	0.95	S ₁	24	S ₁	30
			S ₂	25	S ₂	23
	70-06-14-91	0.36	S ₁	6	S ₁	4
			S ₂	-8	S ₂	-7
	16-12-13-90	0.45	S ₁	30	S ₁	28
			S ₂	21	S ₂	18
	18-01-15-91	0.43	S ₁	29	S ₁	35
			S ₂	26	S ₂	33
	15-11-28-90	0.64	S ₁	30	S ₁	34
			S ₂	29	S ₂	34
	13-11-07-90	0.71	S ₁	31	S ₁	37
			S ₂	27	S ₂	31
	14-11-20-90	0.76	S ₁	27	S ₁	33
			S ₂	27	S ₂	27

In Figs 20-22, the main system of shear bands appears to comprise a primary band which develops first, followed by secondary bands. In the digitized plots, the notation of Morgenstern & Tchalenko (1967) is used in referring to these bands. The first, or primary, are called S₁, and are followed by S₂, S₃ etc. in the order in which they were observed to form.

Table 9 gives the inclination of the shear bands emanating from the cracks, and should be read in conjunction with the digitized plots in order to see the level of approximation involved in such values. Table 9 also gives the crack sliding displacement (CSD) for the various tests.

In Figs 9 and 20 and whenever combinations of compression and torsion are present, vertical shear bands are apparent. Such shear bands are thought to materialize at large deformations as a release mechanism for excessive shearing stresses.

The photographs in Figs 20 and 22 show the magnitude of the slippage along each of the main shear bands. The slippage varies from band to band and along each band, as indicated by the grid. Often when a primary shear band could not propagate further because of boundary restrictions, secondary bands were observed to emanate from it. This is seen in Fig. 20. The case of Fig. 22 is special in that the shear bands form

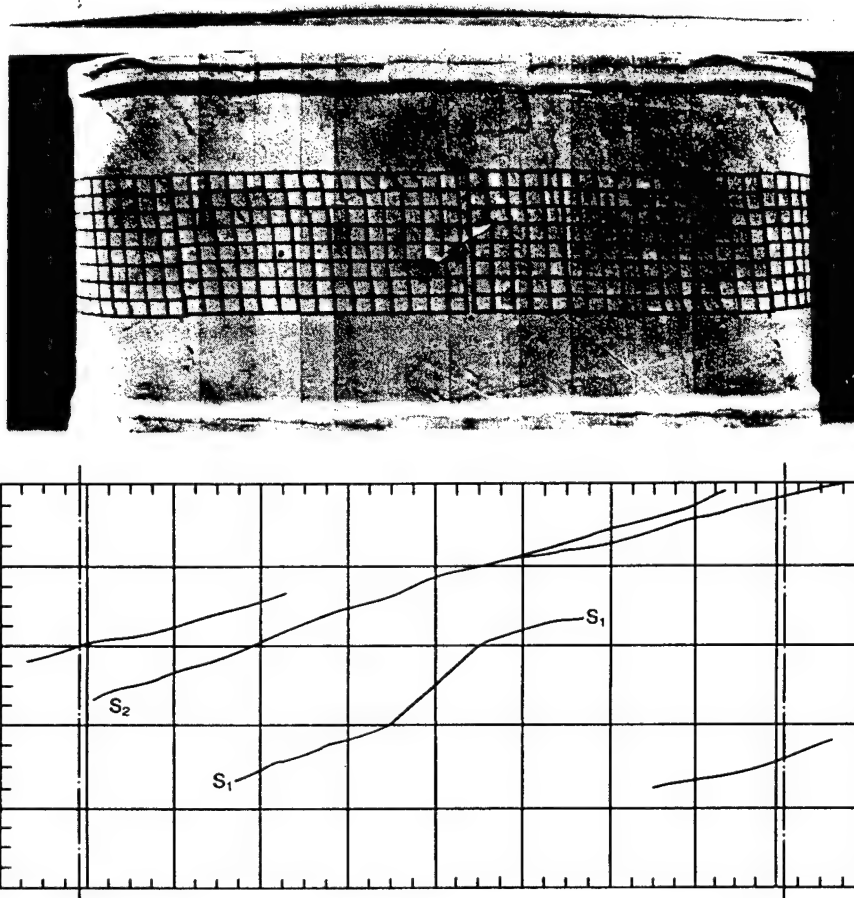


Fig. 23. Shear bands for an inclined crack in the downstep position: $\alpha = 45^\circ$; specimen 56-04-17-91

and propagate essentially along the original direction of the crack: primary and secondary bands overlap and meet.

Inclined cracks result in shear bands that also start at the tip, and again, at a short distance from the crack, take a direction dictated by the plastic behaviour of the clay. Fig. 23 shows the pattern caused by a downstep crack inclined at 45° when the specimen is subjected to torsion and free to deform axially. Additional shear bands that have no physical connection with the crack develop at the peak. This is clear in the photograph as well as in the plot.

Figure 24 shows the results of a test identical to the one described above, but with the crack in an upstep position; the slip lines at the front and tail of the cracks have the same inclinations in both cases. In the first case, however, the crack is part of the surface along which the blocks move; in the second case it is not.

Figure 25 shows a downstep crack inclined at 22.5° . Here, a shear band emanates from the tip and keeps nearly the same direction as the crack. Also, there is appreciable CSD as compared to the two previous cases. Only one shear band

passing through the crack was noticed, i.e. the specimen became two blocks moving with respect to each other.

The pattern of shear bands in Figs 23–25 is extremely instructive as regards the influence of the inclination of the principal stresses on the direction of the crack. In the case of the downstep crack (Fig. 23), torsion results in a combination of tension across the face of the crack and compression along it. This leads to a weak point at the tip of the crack, resulting in an initiation of a shear band there. In the case of the upstep crack (Fig. 24), the directions of tension and compression with respect to the crack are reversed, resulting in compression across the faces. The specimen reacts as if there was almost no crack, and the shear bands develop normally: one is seen to be passing through the tip. In both cases, the magnitude of the CSD is negligible. The crack remains closed due to hydrostatic stresses, and the shear along the faces is negligible. For all the specimens with a crack, the shear bands show up before the peak is reached. This generally causes a more or less pronounced kink in the stress–strain curves.

The shear bands observed for overconsolidated

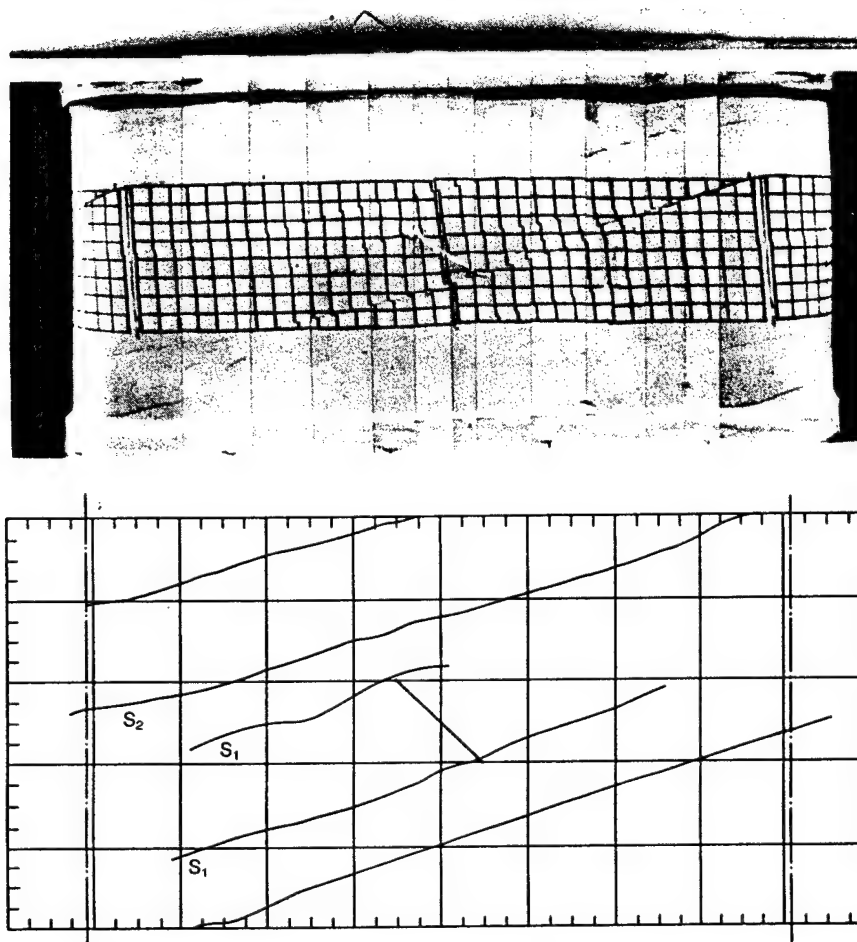


Fig. 24. Shear bands for an inclined crack in the upstep position: $\alpha = 45^\circ$; specimen 57-04-19-91

clays are in general more sharply defined than those obtained for K_0 normally consolidated clays. The tests listed in Table 5 illustrate this, especially those conducted under controlled rotation conditions; a photograph in Saada & Bianchini (1992) also illustrates this.

Isotropically overconsolidated specimens show a diffuse zone of shear bands starting at the tip of the crack, but with limited propagation. There were no displacement discontinuities similar to those that occur in the K_0 consolidated cases. Fig. 26 shows this pattern. Random orientation of clusters and particles appears to impede the formation of continuous well-defined shear bands.

Figure 27, for $a/l = 0$, shows only one shear line. Fig. 10, which corresponds to the same test but with free axial deformation, indicates the presence of a large number of slip lines. It appears that the compressive forces that are axially generated to prevent the specimen from elongating are sufficient to induce the multitude of slip lines seen in Fig. 10 to form and become active. The deformation then amounts to two blocks slipping on

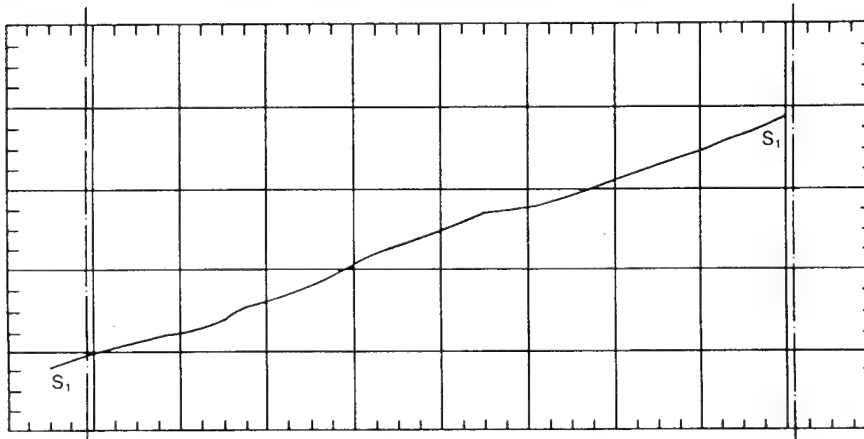
each other. The vertical lines of the grid remain continuous except where they cross the slip line.

Specimens with two cracks

Here, the relative position of the cracks plays an important role in the development of the shear bands. The interaction of the cracks depends not only on their relative position, but also on the direction of the applied torsional shear stress. In this investigation the shearing stresses were always applied in one direction, and the position of the cracks changed as given in Table 6. When placed in a downstep position, the cracks result in a tensile instability (local necking) which is quite localized and allows the specimen to resist additional loading without failing. This result of the superposition of two zones of high tensile stress was illustrated by Vallejo (1989). Actual calculations of stress distributions using the displacement continuity method are given by Bianchini, Liang & Saada (1992). Fig. 28 shows the interference of two zones of high tensile stress at the

Table 10. Inclination of the shear bands and CSD: two cracks

Refer to Table	Designation	CSD: cm	Left side		Right side	
			Label	Angle: degrees	Label	Angle: degrees
6	81-07-03-91 (downstep)	0.51	S_1	33	S_1'	27
			S_2	28	S_2'	24
	82-07-09-91 (upstep)	0.25-0.50	S_1	27	S_1	26
			S_2	14	S_2	18
			S_1	30	S_1'	22
			S_2	20	S_1'	19
	83-07-11-91 (downstep)	0.63	S_1	25	S_1'	22
			S_2	25	S_2'	20
	84-07-17-91 (downstep)	0.51	S_1	23	S_1'	26
			S_2	17	S_2'	18
	85-07-19-91 (downstep)	0.63	S_1	27	S_1'	26
			S_2	17	S_2	22

Fig. 25. Shear bands for an inclined crack in the downstep position: $\alpha = 22.5^\circ$; specimen 58-04-23-91

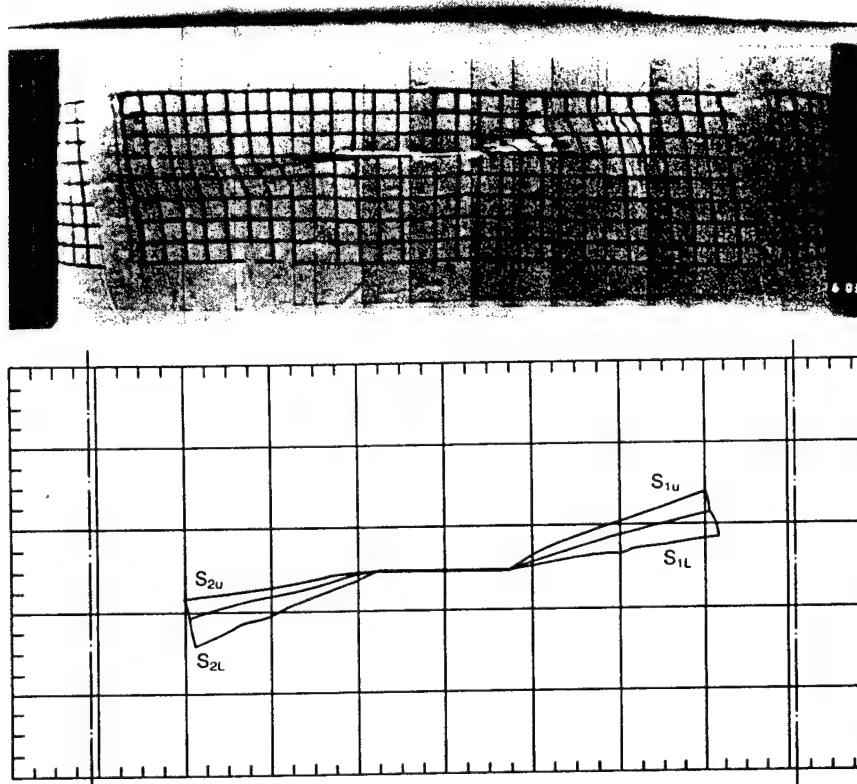


Fig. 26. Shear bands for one crack under torsion with fixed length: isotropic clay; specimen 7a-09-06-90

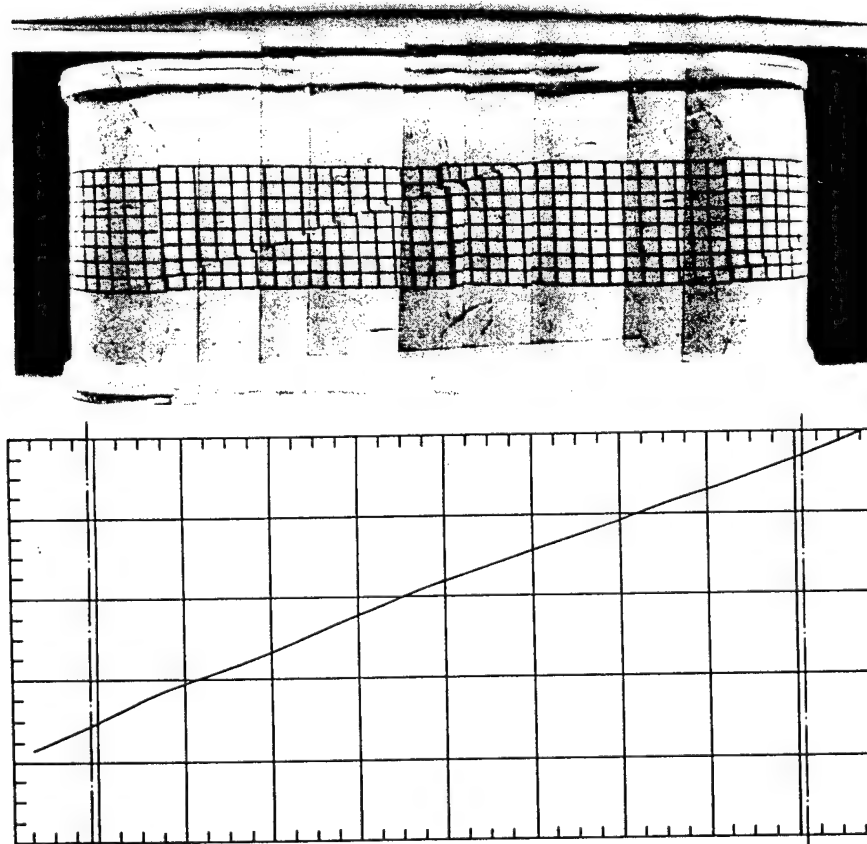


Fig. 27. Influence of crack size on shear bands: $a/l = 0.0$; specimen 19-01-23-91

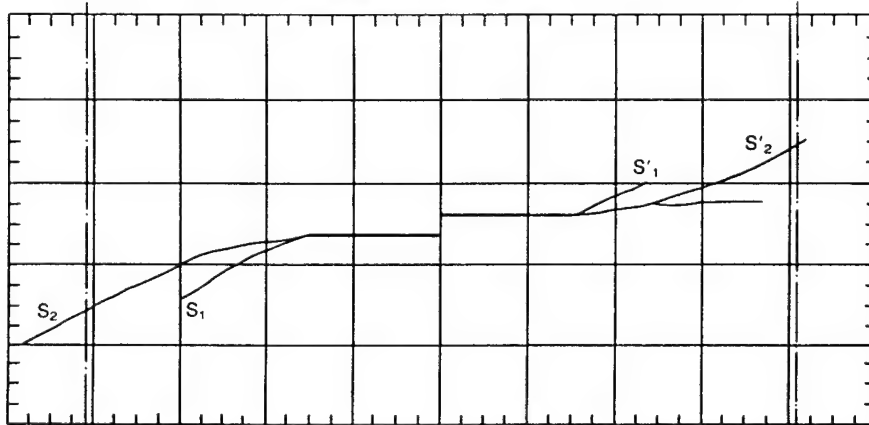
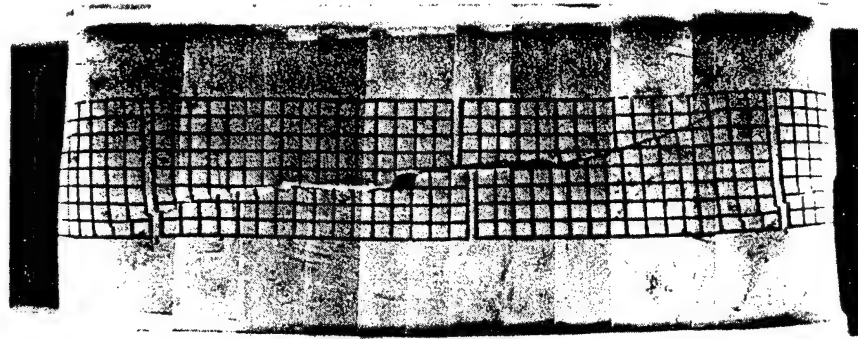


Fig. 28. Shear bands and interaction of two cracks in the downstep position: $e = 0$; specimen 81-07-03-91

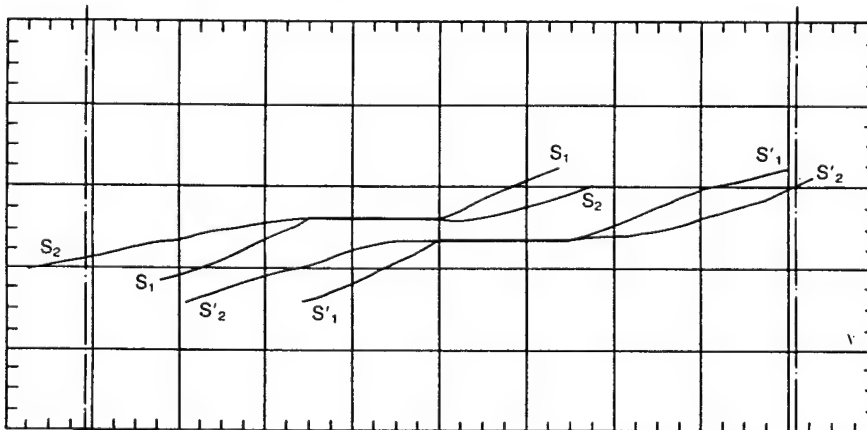
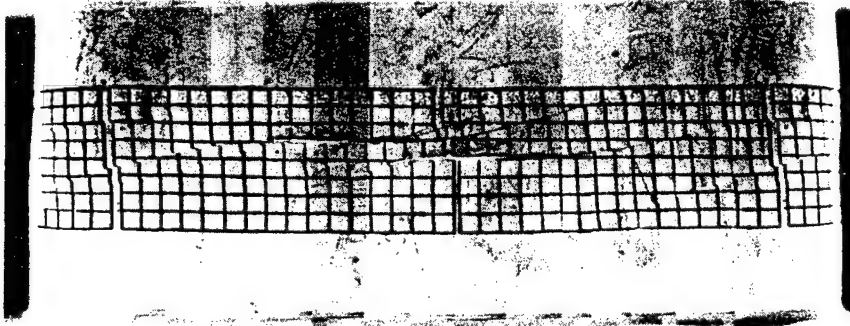


Fig. 29. Shear bands and interaction of two cracks in the upstep position: $e = 0$; specimen 82-07-09-91

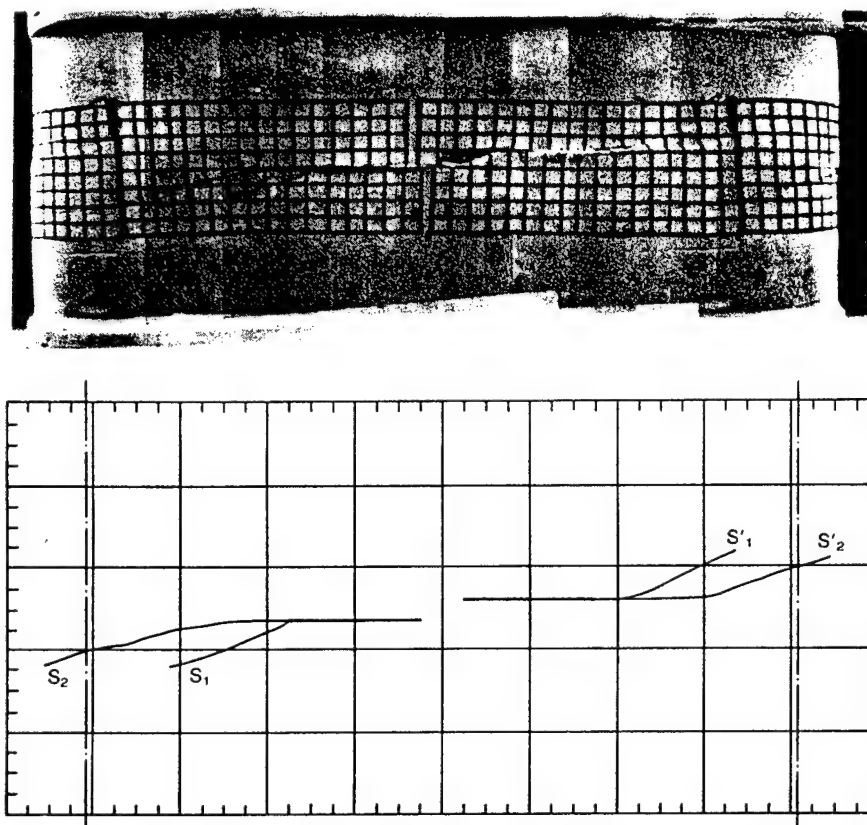


Fig. 30. Shear bands and interaction of two cracks in the upstep position: $e = 1.3$ cm; specimen 84-07-17-91

tips of two cracks. This is the first test in Table 6, for which $e = 0.0$ and $d = 0.6$ cm. The interference appears as a dark hole in Fig. 28. At this location the specimen becomes so thin locally that the inner and outer membranes touch each

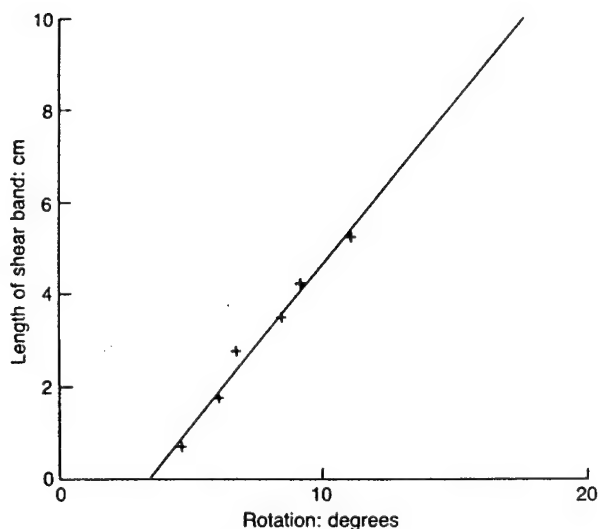


Fig. 31. Length of first shear band for various levels of rotation: specimen 18-01-15-91

other. The highly local tensile failure takes place even though the material is under general hydrostatic compression while being subjected to torsion. Fig. 29 shows two systems of shear bands, each developing and spreading on its own without visible interference effects. Here the cracks are in the upstep position.

With the cracks in the downstep position and e increasing, there comes a distance at which the superimposed tensile stresses are not sufficiently large to overcome the compressive spherical stresses. Fig. 30 shows the pattern of shear band development as e takes a value of 1.3 cm. At $e = 2.54$ cm the crack tips are far enough from each other for no tensile instability to be present. In all downstep cases, the shear bands pattern resembles quite closely that observed for large single cracks. Indeed, once the necking takes place the two cracks behave as a single large crack.

Table 10 gives the inclinations of the shear bands and the CSDs for the case of two cracks. In the photographs in Figs 28–30 the final crack shear displacement is often nearly equal to the unit size of the grid (0.6 cm). Reference grid lines on each photograph indicate the size of the displacement.

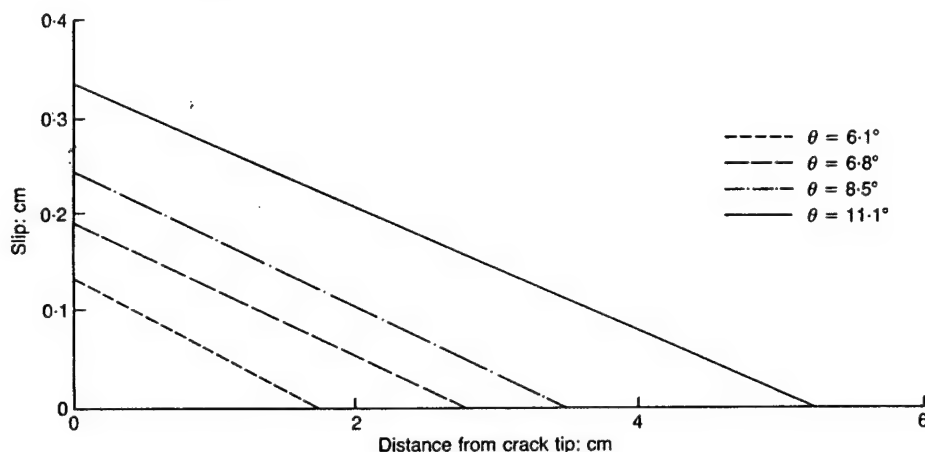


Fig. 32. Slip along the first shear band for various levels of rotation: specimen 18-01-15-91

Shear bands propagation and measurements

The series of photographs taken at the initiation of a shear band (at the tip of a crack) and during its subsequent propagation allow relations to be plotted involving the length of the band, the angle of rotation of the top of the specimen with respect to its fixed bottom, the amount of slip measured along the band, and so on. The tests for which such graphs were generated are listed in Table 5.

Figure 31 plots the length of the shear band against the angle of rotation for specimen 18-1-15-91. Fig. 32 shows the amount of slip measured along the first shear band for various angles of rotation. This is the kind of displacement discontinuity shown in Fig. 15(c). Additional graphs are shown by Saada & Bianchini (1992).

In all the cases observed, the formation and propagation of the shear bands were stable. The length of the shear band varies approximately linearly with the angle of rotation. The second shear band, after its initiation, propagated faster than the first one; it also became the dominant one.

The appearance of shear bands beyond the first depends on the amount of rotation induced in the specimen, the end effects, the presence of the inclusion formed by the PTFE strips, and the fact that the first shear band may not be propagating in the direction of the original crack. The slip that takes place along each shear band varies with the distance from the tip of the crack (Fig. 32). The appearance of secondary branches affects the magnitude of the slip and leads to a more complex relation of the two variables. At the point of branching, the magnitude of the slip along the main band is nearly equal to the sum of the magnitudes along each of the branches.

The above measurements and observations are what is needed to test the validity of the various models that have been or will be proposed for

bifurcation and shear banding resulting from localization. The level of accuracy of such measurements, although limited by the fact that observations are made from outside the cell, is more than sufficient to evaluate the suitability of a behavioural model.

SUMMARY AND CONCLUSIONS

This research has concentrated on careful observation of the behaviour of saturated clays under combined stresses. Localizations, spontaneous or induced by the presence of cracks, appear as shear bands along which most of the deformations take place.

It was found that for K_0 consolidated clays the response to stress was significantly influenced by the inclination of the principal stresses on the axis of symmetry of the material. Bifurcations in the form of shear bands invariably appeared near the peak stress in strength experiments. Initially well distributed along the length of the hollow cylindrical specimens, the shear bands eventually relinquish their share of the deformation to a band along which the material fails in a catastrophic way.

The presence of a small crack (or notch) in a specimen did not substantially affect its overall strength. Stress-strain curves, for specimens with or without cracks, differed very little even though the observed pattern of displacement differed markedly. The pore-water pressures, which are measured at the specimens' ends, are affected only slightly. However, there is a lack of smoothness in the stress-strain curves related to notched specimens, especially when the crack is oriented in the direction of the forming shear bands. Here the bands start forming at about 80% of the peak value of the stress.

The presence of two cracks in close proximity led to interferences which depended on their relative position and on the direction of the applied shearing stresses. These interferences affected the value of the peak stress as well as the development of the shear bands. The bands were observed at about 80% of the peak stress.

All the observations led to the conclusion that, although cracks create local stress concentrations, the behaviour of the material is dictated by its plasticity, which becomes predominant at a very short distance from the tip. The presence of filter paper was found to hide, inhibit and direct the formation of shear bands. At failure, the slits in the filter paper have sufficient influence to dictate the final shear band pattern.

The shear bands, whether they occur near the peak in an unnotched specimen or at 80% of the peak triggered by the presence of a crack, eventually take the same direction, showing once more that the behaviour is dictated by the plasticity of the material. This direction was found to be fixed with respect to the direction of the major principal stress. A similar result was found by Arthur & Dunstan (1982) for sand materials. This indicates that a frictional model is necessary to describe the behaviour of this clay. Bianchini *et al.* (1992) found a Drucker-Prager type of model to be satisfactory.

If a specimen is subjected to further rotation, at or beyond the peak, an additional shear band develops in the vicinity of the crack tip. The first shear band, often hindered by the boundary, stops, and additional deformations become primarily localized in the new shear band. The second band usually starts with a flat slope, but later tends to become parallel to the first one.

The inclination of the cracks was found to act in a co-ordinated way with the direction of anisotropy and of the applied shearing stress. The development of the shear bands seems to ignore the presence of an upstep crack (negative α) of 45°. Two bands will pass through the tips; others will form in other locations, some stopping while attempting to cross the crack. Stress concentrations at the tips of the crack have little or no influence. However, a downstep crack (positive α) will become a part of the shear band, and this combination will tend to weaken the specimen. In particular, the crack at 22.5° blended so well with the directions dictated by the plasticity of the material that only one band was seen to develop in this specimen to dissipate the energy.

Isotropic specimens give diffuse shear bands. It appears that the random orientation of particles and clusters inhibits formation of the clearly defined surfaces observed when K_0 consolidated clays are tested. Also, the shear bands that develop in overconsolidated clays are thinner and

more pronounced than their counterparts in normally consolidated clays, localization being more intense.

Most of the photographs shown in this Paper were taken at the end of the tests, showing that parts of the specimens between the shear bands suffer little or no permanent deformation. This calls into question the validity of calculated strains from measurements of deformations made on the whole specimen. However, since shear bands occur at or beyond the peak for unnotched specimens, it is only the interpretation of that part of the behaviour that is in question; for notched specimens, block motions start to occur at 80% of the peak's value.

While a substantial amount of rebound takes place on removal of the stresses, some rebound was observed to occur in the vicinity and on formation of the shear bands. The model of Rice & Rudnicki (1980) takes account of this possibility. When two cracks are present, they act independently or interact, depending on their relative position and the direction of the applied stresses. In the present study, cracks in the downstep position acted as a single unit. The space between them could suffer instabilities without affecting the overall behaviour of the specimen.

Since shear bands were found to propagate in a stable manner, measurements can be (and have been) made along the crack and along the shear bands. By extrapolation, the point at which banding begins in the vicinity of a crack can be found with reasonable accuracy; its evolution can thus be studied. Such measurements are indispensable in the formulation of a bifurcation and localization model.

In every case that was observed, the shear bands formed and propagated at an angle indicating that saturated clays, even though they were tested in an undrained condition, are essentially frictional materials. A $\phi' = 0$ analysis can be only an approximation.

ACKNOWLEDGEMENTS

The research reported in this Paper was conducted under the sponsorship of the Air Force Office of Scientific Research. The Authors wish to thank Dr S. C. Boyce and Dr M. D. Lewis, Program Managers, for their encouragement during the project.

NOTATION

- a length of crack
- b $(\sigma_2 - \sigma_3)/(\sigma_1 - \sigma_3)$
- d vertical distance between cracks
- e horizontal distance between cracks
- K_0 coefficient of earth pressure at rest

- α inclination of the crack to the horizontal
- β inclination of the major principal stress to the vertical
- δ inclination of the shear band to the horizontal
- ε_{ij} ($i, j = 1, 2, 3$) components of the strain tensor
- θ_c inclination of the shear band with respect to the major principal stress
- ν dilatancy angle
- $\sigma_1, \sigma_2, \sigma_3$ principal stresses
- σ_c effective cell pressure (initial cell pressure – back pressure)
- σ_{ij} components of the stress tensor in Cartesian co-ordinates ($i, j = 1, 2, 3$)
- $\sigma_z, \sigma_\theta, \sigma_r, \sigma_{\theta z}$ components of the stress tensor in cylindrical co-ordinates
- ϕ' angle of friction in terms of effective stresses

REFERENCES

- Ariaratnam, S. T. & Dubey, R. N. (1969). Some cases of bifurcation in elastic-plastic solids in plane strain. *Q. Appl. Math.* **27**, 349–358.
- Arthur, J. R. F. & Dunstan, T. (1982). Rupture layers in granular media. *Proc. IUTAM Conf. Deformation and Failure of Granular Materials, Delft*, 453–459.
- Balasubramaniam, A. S. (1976). Local strains and displacement patterns in triaxial specimens of a saturated clay. *Soils Fdns* **16**, No. 1, 101–114.
- Bardet, J. P. (1991). Orientation of shear bands in frictional soils. *J. Engng Mech. Div. Am. Soc. Civ. Engrs* **117**, No. 7, July, 1466–1484.
- Bianchini, G. F., Liang, L. & Saada, A. S. (1992). *Numerical studies of the influence of cracks on the stress field in saturated clays*. Internal Report, Department of Civil Engineering, Case Western Reserve University.
- Biot, M. A. (1965). *Mechanics of incremental deformations*. New York: Wiley.
- Chudnovsky, A., Saada, A. S. & Lesser, A. J. (1988). Micromechanisms of deformation in fracture of overconsolidated clays. *Can. Geotech. J.* **25**, 213–221.
- Desrues, J. (1983). *Localisation de la deformation dans les milieux granulaires*. DPhil thesis, University of Grenoble.
- Desrues, J. & Chambon, R. (1989). Shear band analysis for granular materials: the question of incremental non-linearity. *Ingenieur-Archiv* **59**, 187–196.
- Hetter, A. & Vardoulakis, I. (1984). Behaviour of dry sand tested in a large triaxial apparatus. *Géotechnique* **34**, No. 2, 183–198.
- Hight, D. W., Gens, A. & Symes, M. J. (1983). The development of a new hollow cylinder apparatus for investigating the effects of principal stress rotation in soils. *Géotechnique* **33**, No. 4, 355–383.
- Hill, R. & Hutchinson, J. W. (1975). Bifurcation phenomena in the plane tension. *J. Mech. Phys. Solids* **23**, 239–264.
- Houlsby, G. T. & Wroth, C. P. (1980). Strain and displacement discontinuities in soils. *J. Engng Mech. Div. Am. Soc. Civ. Engrs* **117**, EMA, Aug., 753–772.
- Kolymbas, D. & Rombach, G. (1989). Shear band formation in generalized hypoelasticity. *Ingenieur-Archiv* **59**, 177–186.
- Ladd, C. C., Foott, R., Ishihara, K., Schlosser, F. & Poulos, H. G. (1977). Stress-deformation and strength characteristics. *Proc. 9th Int. Conf. Soil Mech., Tokyo*, **2**, 421–494.
- Lesser, A. J. (1989). *Theoretical and experimental studies of cooperative fracture in overconsolidated clays*. DPhil thesis, Case Western Reserve University.
- Mandel, J. (1964). Conditions de stabilité et postulat de Drucker. *Proc. IUTAM Symp. Rheology and Soil Mechanics, Grenoble*, 58–68.
- Molenkamp, F. (1985). Comparison of frictional material models with respect to shear band initiation. *Géotechnique* **35**, No. 2, 127–143.
- Morgenstern, N. R. & Tchalenko, J. S. (1967). Microscopic structures in kaolin subjected to direct shear. *Géotechnique* **17**, 309–327.
- Mühlhaus, H. B. & Vardoulakis, I. (1987). The thickness of shear bands in granular materials. *Géotechnique* **37**, No. 3, 271–283.
- Needleman, A. (1979). Non-normality and bifurcation in plane strain tension and compression. *J. Mech. Phys. Solids* **27**, 231–254.
- Palmer, A. C. & Rice, J. R. (1973). The growth of slip surfaces in the progressive failure of overconsolidated clay. *Proc. R. Soc. Lond. A* **332**, 527–548.
- Rice, J. R. (1976). The localization of plastic deformation. *Proc. 14th Int. Cong. Theor. Appl. Mech., Delft* (ed. W. T. Koiter) **1**, 207–220.
- Rice, J. R. & Rudnicki, J. W. (1980). A note on some features of the theory of localization of deformation. *Int. J. Solids Struct.* **16**, 597–605.
- Rudnicki, J. W. & Rice, J. R. (1975). Conditions for the localization of deformation in pressure sensitive dilatant materials. *J. Mech. Phys. Solids* **23**, 371–394.
- Saada, A. S. (1988). State of the art. Hollow cylinder torsional devices: their advantages and limitations. *Advanced triaxial testing of soil and rock* (eds R. T. Donaghe, R. C. Chaney & M. L. Silver), STP 977, pp. 766–795. Philadelphia: American Society for Testing and Materials.
- Saada, A. S. & Bianchini, G. F. (1975). The strength of one-dimensionally consolidated clay. *J. Geotech. Engrg Div. Am. Soc. Civ. Engrs* **101**, GT11, 1151–1164.
- Saada, A. S. & Bianchini, G. F. (1992). *Crack propagation and fabric control on the static and dynamic strength of cohesive soils*. Final report submitted to the Air Force Office of Scientific Research, Bolling Air Force Base, Washington, D.C.
- Saada, A. S., Chudnovsky, A. & Kennedy, M. R. (1985). A fracture mechanics study of stiff clays. *Proc. 11th Int. Conf. Soil Mech., San Francisco*, **2**, 637–640.
- Saada, A. S. & Townsend, F. C. (1981). State of the art: laboratory strength testing of soils. *Laboratory shear strength of soils* (eds R. N. Yong & F. C. Townsend), STP 740, pp. 7–77. Philadelphia: American Society for Testing and Materials.
- Scarpelli, G. & Wood, D. M. (1982). Experimental observations of shear band pattern in direct shear tests. *Proc. IUTAM Conf. Deformation and Failure of Granular Materials, Delft*, 473–484.

- Vallejo, L. E. (1987). The influence of fissures in a stiff clay subjected to direct shear. *Géotechnique* **37**, No. 1, 69-82.
- Vallejo, L. E. (1988). The brittle and ductile behavior of clay samples containing a crack under mixed mode loading. *Theor. Appl. Fract. Mech.* **10**, 73-78.
- Vallejo, L. E. (1989). Fissure parameters in stiff clays under compression. *J. Geotech. Engng Div. Am. Soc. Civ. Engrs* **115**, No. 9, 1303-1317.
- Vardoulakis, I. (1980). Shear band inclination and shear modulus of sand in biaxial tests. *Int. J. Numer. Anal. Meth. Geomech.* **4**, 103-119.
- Vardoulakis, I. (1982). Stability and Bifurcation of soil samples. *Results Int. Workshop on Constitutive Relations for Soils, Grenoble*, 1982, 477-483.
- Vardoulakis, I. (1983). Rigid granular plasticity model and bifurcation in the triaxial test. *Acta Mech.* **49**, 57-79.
- Vardoulakis, I. (1985). Stability and bifurcation of undrained, plane rectilinear deformations on water-saturated granular soils. *Int. J. Numer. Anal. Meth. Geomech.* **9**, 399-414.
- Vardoulakis, I., Goldscheider, M. & Gudehus, G. (1978). Formation of shear bands in sand bodies as a bifurcation problem. *Int. J. Numer. Anal. Meth. Geomech.* **2**, 99-128.
- Vardoulakis, I. & Graf, B. (1982). Imperfection sensitivity of the biaxial test on dry sand. *Proc. IUTAM Conf. Deformation and Failure of Granular Materials, Delft*, 485-491.
- Vermeer, P. A. (1982). A simple shear band analysis. *Proc. IUTAM Conf. Deformation and Failure of Granular Materials, Delft*, 493-499.
- Young, N. J. B. (1976). Bifurcation phenomena in the plane compression test. *J. Mech. Phys. Solids* **24**, 77-91.

PAPER 2 --- ON CLAYS

Fracture Mechanics and Plasticity in Saturated Clay

Adel S. Saada¹, F. ASCE, Liqun Liang² and Gary F. Bianchini³, M. ASCE

Abstract

An experimental investigation and numerical simulations are conducted in an effort to gain an insight into the mechanism of crack and shear band formation and propagation in saturated clays. Observations indicate that, for this type of clay fracture mechanics is helpful but that the plasticity of the material dominates the behavior. The finite elements method (FEM) is used to examine the stress field and the spreading of the plasticity zone in thin hollow cylindrical specimens with one crack; the displacement discontinuity method is used to examine the elastic stress field in the case of two cracks. Elastic as well as elasto-plastic analyses are conducted in order to find a suitable model that could describe the extensive observations of shear bands. Even though all the observations were made on saturated undrained clay specimens tested under combined stresses, the conclusion is that the material is a frictional one; and that the plasticity component of any model should be in terms of effective stresses and involve an effective angle of internal friction to represent the behavior in an adequate fashion.

Introduction and General Comments

Discontinuities in the form of cracks or fissures, and in the form of inclusions are often present in natural clays. They serve as stress concentrators and are the center of origin of shear bands. Saada and Bianchini (1992) conducted an extensive series of experiments using thin long hollow cylinders of saturated clay with one and two notches, horizontal and inclined; and in the upstep and downstep positions.

¹Frank H. Neff Professor and Chairman, Department of Civil Engineering, Case School of Engineering, Case Western Reserve University, Cleveland, Ohio.

²Graduate Student, Department of Civil Engineering, Case School of Engineering, Case Western Reserve University, Cleveland, Ohio.

³Formerly Research Engineer, Department of Civil Engineering, Case School of Engineering, Case Western Reserve University, Cleveland, Ohio.

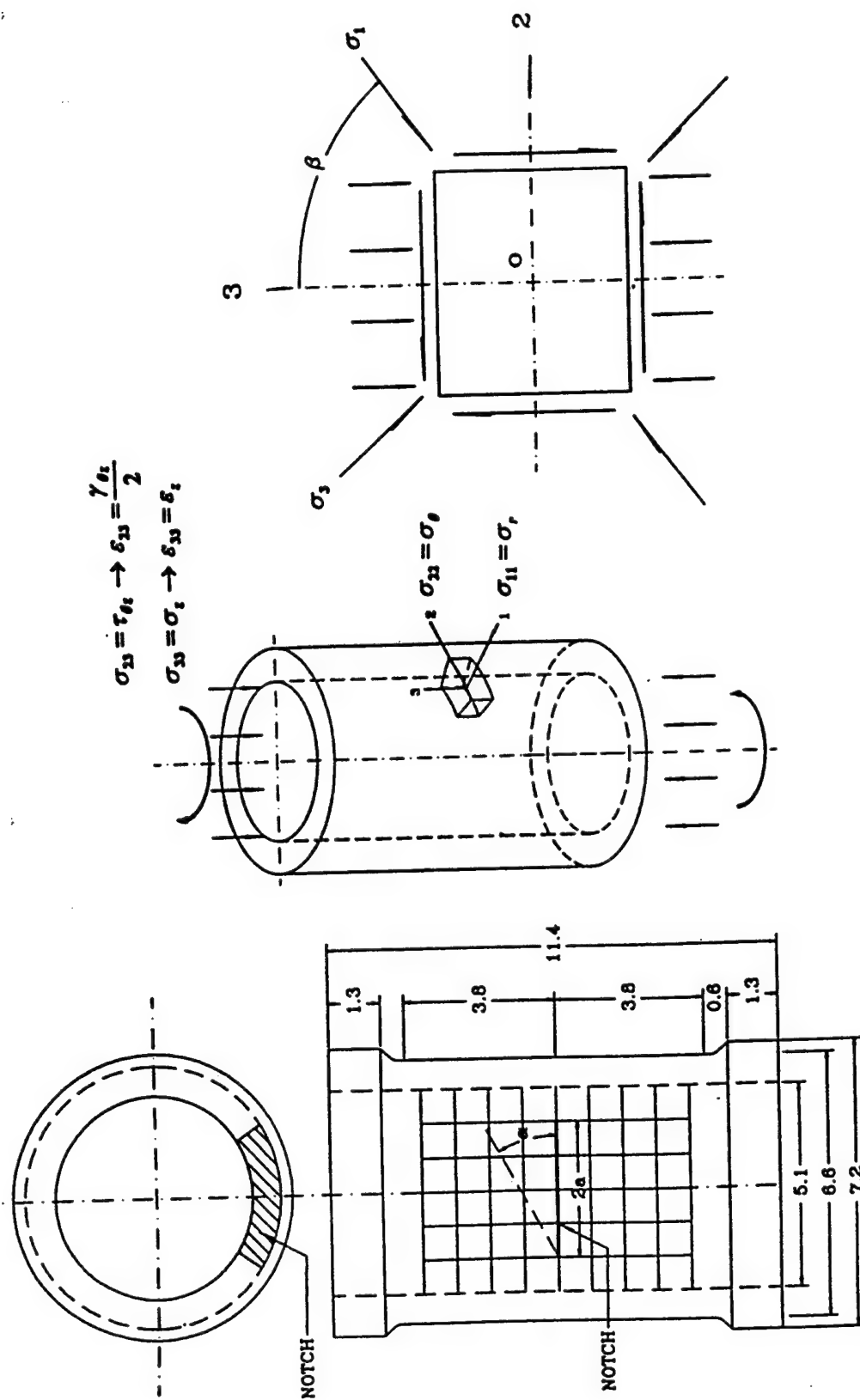


Figure 1 Specimen Geometry and Stress System

They observed and recorded the initiation and propagation of shear bands as systems of combined stresses were applied to the cylinders. The tests were undrained in nature and are completely described in their report. We give here a brief summary of the samples preparation and the conduct of the tests.

Figure 1 shows the geometry of the specimens used in the investigation. The enlarged ends help avoid end effects in the zone of observation. The grid was imprinted on the clay with indelible ink in order to help show the formation and propagation of shear bands. The radial notches were made in the specimen using a thin vee-shaped brass blade. Two layers of very thin Teflon sheets were inserted in the notches to prevent them from closing during consolidation and subsequent shear. Photographs were taken during and at the end of tests; while moving the camera around the stationary specimen or vice versa. These photographs were overlapped with matching grids so that deformations and slip patterns could be examined on the development of the cylinder.

The clay used in the investigation is known as Edgar Plastic Kaolin (EPK). It has a liquid limit of 56.3% and a plastic limit of 37.3%. Preparation of specimens from slurry is described by Saada (1988).

Two types of loading devices were used to obtain radial stress paths and both static and dynamic loadings. One is the controlled stress type and the other of the controlled deformation type. Both devices, called SPAC, have been described by Saada and Townsend (1981).

Saturated clay tested under various combinations of stresses has traditionally been looked upon as a purely cohesive material; as long as no changes in the water content are allowed. This indeed, forms the basis of the so called total stress analysis for saturated clay in which the angle of friction is assumed to be equal to zero. It is well known that the strength and mechanical behavior of clays depend on effective stresses. If the material is frictional in nature, the presence of this friction should manifest itself through the inclination of its shear bands; when such bands appear and propagate and whether drainage is allowed or not. This is what the observations made and described by Saada et al (1992) indicate.

The present paper uses the finite elements method and the displacement discontinuity method to examine stress and strain fields in the vicinity of the cracks, and interprets the formation and direction of the shear bands. Calculations are made in terms of stresses acting on the material's boundaries. No particular input is made regarding pore water pressures generated in the vicinity of the cracks or shear bands. Such pressures are unknown and cannot be measured with present experiment capabilities.

Constitutive Laws

Elasticity

Linear elasticity has been extensively used to study stress distribution in the vicinity of cracks in brittle materials. Linear elastic fracture mechanics (LEFM) was

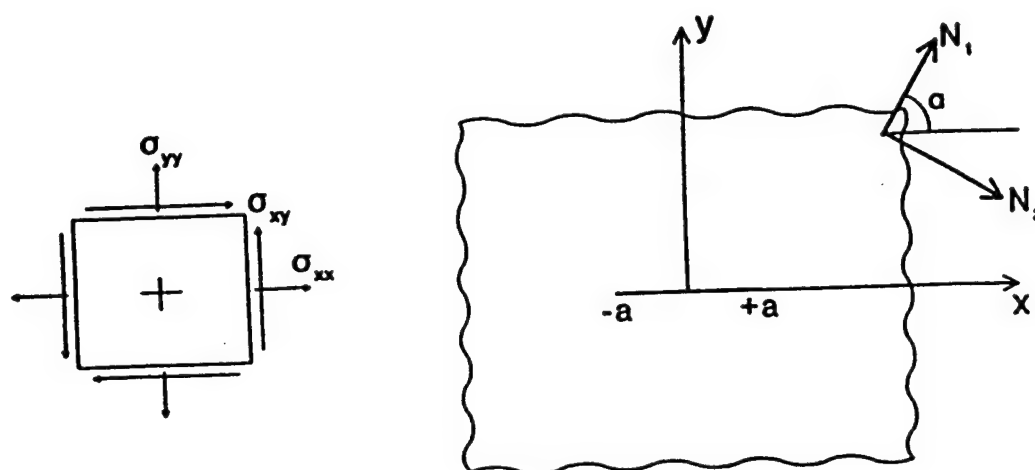


Figure 2 Muskhelishvili's Problem

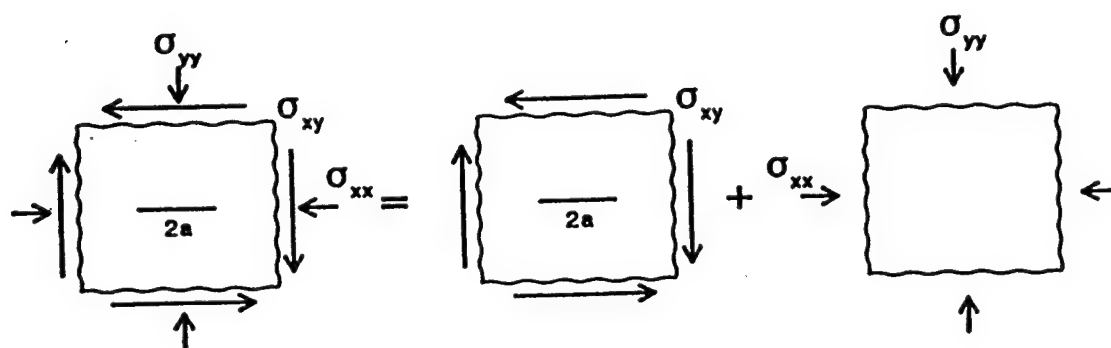


Figure 3 Superposition in Elastic Analysis

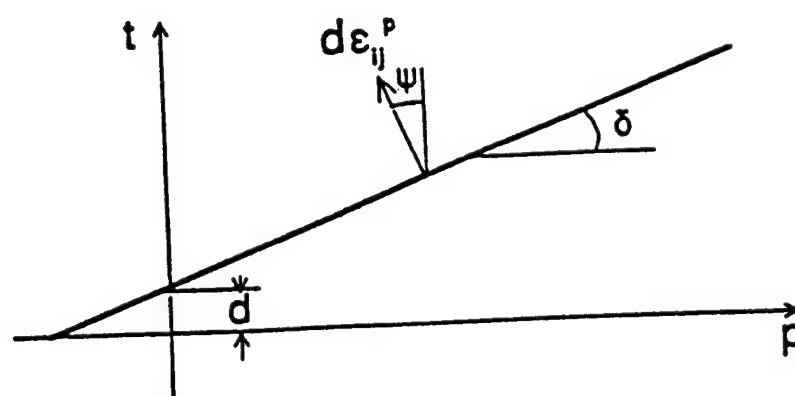


Figure 4 The Drucker-Prager Plasticity Criterion

used by Vallejo (1987, 1988, 1989), Saada et al. (1985) and Chudnovski et al. (1988) to interpret results obtained testing unsaturated brittle clay and saturated overconsolidated stiff clay respectively. However, for ductile saturated clay, it was noticed that, while LEFM can give an idea about the stress concentration in the close vicinity of the crack tip, the plasticity of the material quickly dominated the behavior. Elasticity will be used to locate the areas of concentration of the high stresses at which plastic behavior and consequently shear banding would start. If those stresses are tensile in nature, localized necking would result.

While the tests have been conducted on thin hollow cylinders, expressions established for plane conditions will be used in the next section. The cylinder is assumed to be developed into a plate with the length equal to the perimeter and a width equal to the height. Muskhelishvili (1953) has given the general expressions for the stress distribution in an infinite plate with a crack subjected to boundary forces N_1 and N_2 at infinity. Using the standard notation of elasticity theory with tension being positive, we have (Fig. 2),

$$\begin{aligned}\sigma_{xx} + \sigma_{yy} &= 2 \left(\phi(z) + \overline{\phi(\bar{z})} \right) \\ \sigma_{yy} - i\sigma_{xy} &= \phi(z) + \Omega(\bar{z}) + (z - \bar{z}) \overline{\phi'(z)}\end{aligned}$$

where the complex potentials $\phi(z)$ and $\Omega(z)$ are given by:

$$\begin{aligned}\phi(z) &= \frac{(2\Gamma + \bar{\Gamma}')z}{2\sqrt{z^2 - a^2}} - \frac{1}{2}\bar{\Gamma}' \\ \Omega(z) &= \frac{(2\Gamma + \bar{\Gamma}')z}{2\sqrt{z^2 - a^2}} + \frac{1}{2}\bar{\Gamma}' \\ \Gamma &= \frac{1}{4}(N_1 + N_2) \\ \Gamma' &= -\frac{1}{2}(N_1 - N_2)e^{-2a}\end{aligned}$$

Thus,

$$\begin{aligned}\sigma_{xx} + \sigma_{yy} &= \frac{(2\Gamma + \bar{\Gamma}')z}{2\sqrt{z^2 - a^2}} + \frac{(2\bar{\Gamma} + \Gamma')\bar{z}}{2\sqrt{\bar{z}^2 - a^2}} \\ \sigma_{yy} - i\sigma_{xy} &= \frac{(2\Gamma + \bar{\Gamma}')z}{2\sqrt{z^2 - a^2}} + \frac{(2\Gamma + \bar{\Gamma}')\bar{z}}{2\sqrt{\bar{z}^2 - a^2}} + \\ &\quad (z - \bar{z})\frac{2\bar{\Gamma} + \Gamma'}{2} \left[\frac{1}{\sqrt{\bar{z}^2 - a^2}} - \frac{\bar{z}^2}{(\bar{z}^2 - a^2)^{3/2}} \right]\end{aligned}$$

For pure shear conditions we have,

$$N_1 = \tau, N_2 = -\tau, \alpha = \frac{\pi}{4}$$

$$\Gamma = 0, \Gamma' = i\tau, \bar{\Gamma}' = -i\tau$$

Thus,

$$\sigma_{xx} + \sigma_{yy} = -2\tau \operatorname{Re} \left[\frac{iz}{\sqrt{z^2 - a^2}} \right]$$

$$\sigma_{yy} - \sigma_{xx} + 2i\sigma_{xy} = \tau \frac{ia^2 \bar{z} + iz(2z^2 - 3a^2)}{(z^2 - a^2)^{3/2}}$$

When used in soil mechanics the signs obtained from these equations must be reversed.

For a combination of axial lateral and shearing stresses, superposition is used. The crack is assumed to transfer normal compression stresses, and stress distributions due to applied compression are not affected by the presence of the crack. Figure 3 illustrates the superposition used in the calculations. The third dimension is ignored. An appropriate software is used to calculate the distribution of stresses and plot contour lines for the various components of the stress tensor.

Linear elasticity is also be used in conjunction with the finite element method to examine the influence of the boundaries on Muskhelishvili's solution and in conjunction with the displacement discontinuity method to obtain stress distributions for the case of two adjacent cracks.

Plasticity

The appearance of shear bands is intimately connected to materials in the plastic state. While there exist many elasto-plastic models capable of describing the behavior of the clay over a wide range of stress, such models are not needed here; at least initially. We are primarily interested in the state at which slipping is occurring on the shear bands and relatively simple elasto-plastic models can be used to study the directions of such bands. Two plasticity models, a non-frictional one and a frictional one, are needed. The Von Mises model and the extended Drucker-Prager model were chosen.

As mentioned in the introduction the presence of internal friction should influence the direction of the shear bands. The FEM code ABAQUS (1989) which is utilized to study the spreading of the plastic zone requires that the Drucker-Prager plasticity criterion be written as:

$$t = d + p \tan \delta$$

Where:

$$t = \frac{q}{2} \left[1 + \frac{1}{K} - \left(1 - \frac{1}{K} \right) \left(\frac{r}{q} \right)^3 \right]$$

$$r = \left(\frac{9}{2} S_y S_{\beta} S_{\alpha} \right)^{1/3}$$

$$q = \sqrt{\frac{3}{2} S_y S_y}$$

$$S_y = \sigma_y + p \delta_y$$

$$p = -\frac{1}{3} (\sigma_{11} + \sigma_{22} + \sigma_{33})$$

K , δ and d are material constants defined as follows:

$$\tan \delta = \frac{6 \sin \phi'}{3 - \sin \phi'}$$

$$d = c \left(\frac{6 \cos \phi'}{3 - \sin \phi'} \right)$$

$$K = \frac{3 - \sin \phi'}{3 + \sin \phi'}$$

and

$$\delta_y = \begin{cases} = 0, & i \neq j \\ = 1, & i = j \end{cases}$$

σ_y = components of the stress tensor

S_y = components of the deviator stress tensor

ϕ' = effective angle of internal friction

c = cohesion

This yield function is also shown in Fig. 4. If a fully associated flow rule is used to determine the strains $d\epsilon_{ij}^p$, ψ is taken equal to δ in Fig. 4.

Materials Constants and Loading Conditions.

The calculations are made for a material whose Poisson ratio is 0.49, Young's Modulus is 60000 kPa, cohesion c is 10 kPa and angle of friction ϕ' is 33 degrees. The hollow cylinder is unfolded to the plate shape shown in Fig. 5. The bottom boundary is fixed and the upper one is always horizontal during loading. There is no slip between the upper and lower boundaries and the specimen.

All the simulations requiring one loading stage are made assuming a hydrostatic stress of 345 kPa and a torsional shearing stress of 199 kPa. When simulating combinations of axial and torsional stresses, both are increased proportionally to provide the needed inclination of the principal stresses on the axis of symmetry.

The closed form elastic solution given by Muskhelishvili (1953) corresponds to a crack with sharp ends and stresses at infinity. It will be compared to a FEM solution for a crack with sharp ends but with the peripheral boundary conditions of Fig. 5. All the other numerical calculations are made for the geometry and boundary conditions shown in Fig. 5, and with the crack replaced by an inclusion 1.5mm thick. This inclusion transmits normal stresses but no shear. Such conditions are very close to the experimental ones where thin Teflon sheets were used to prevent the closing of the notch.

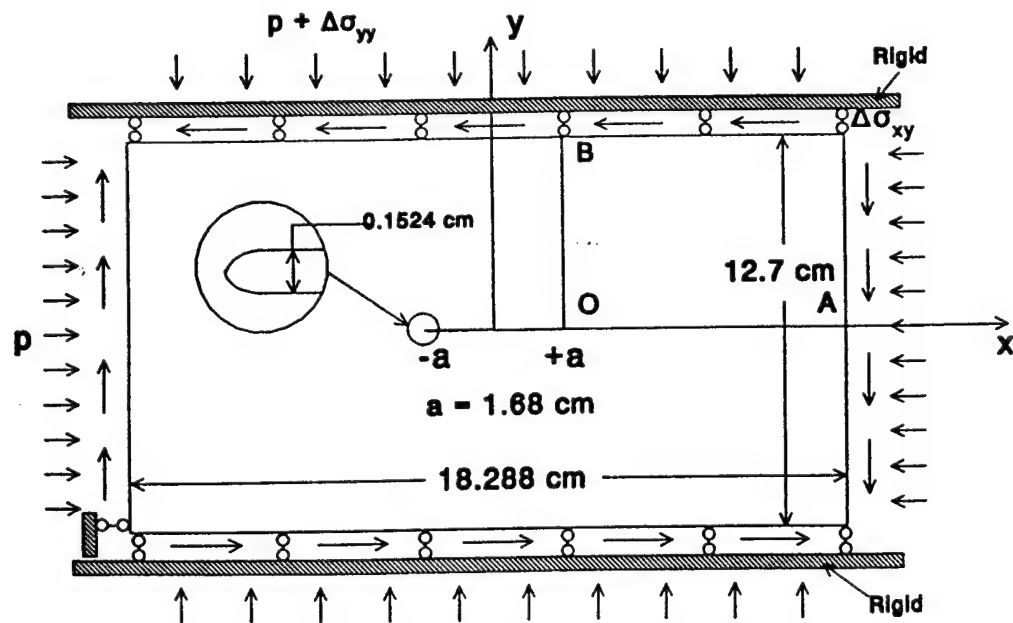


Figure 5 Boundary Conditions for Numerical Solutions

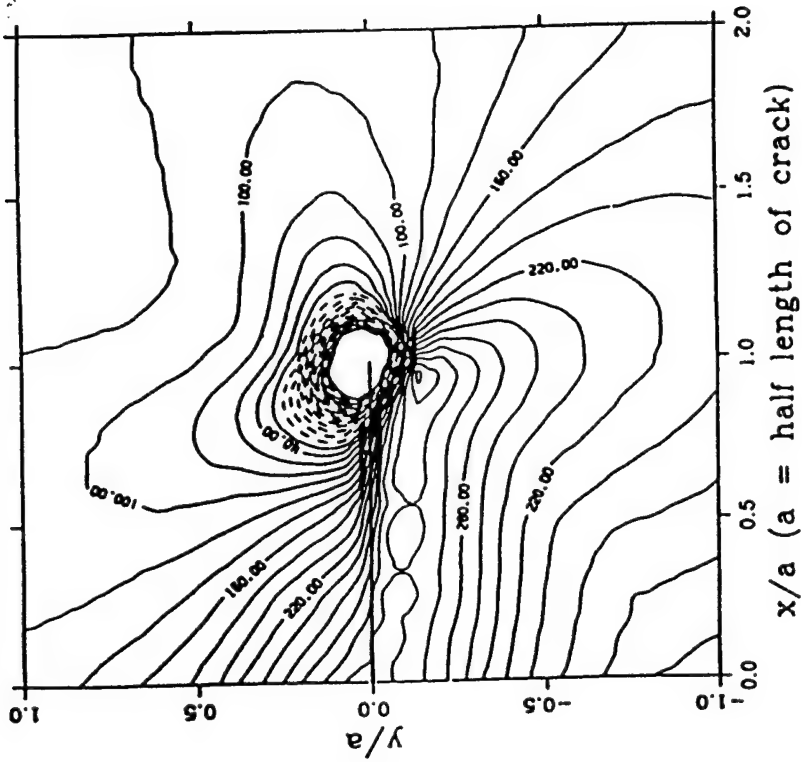


Figure 6 Lines of Equal Minimum Principal Stress from Muskhelishvili's Solution

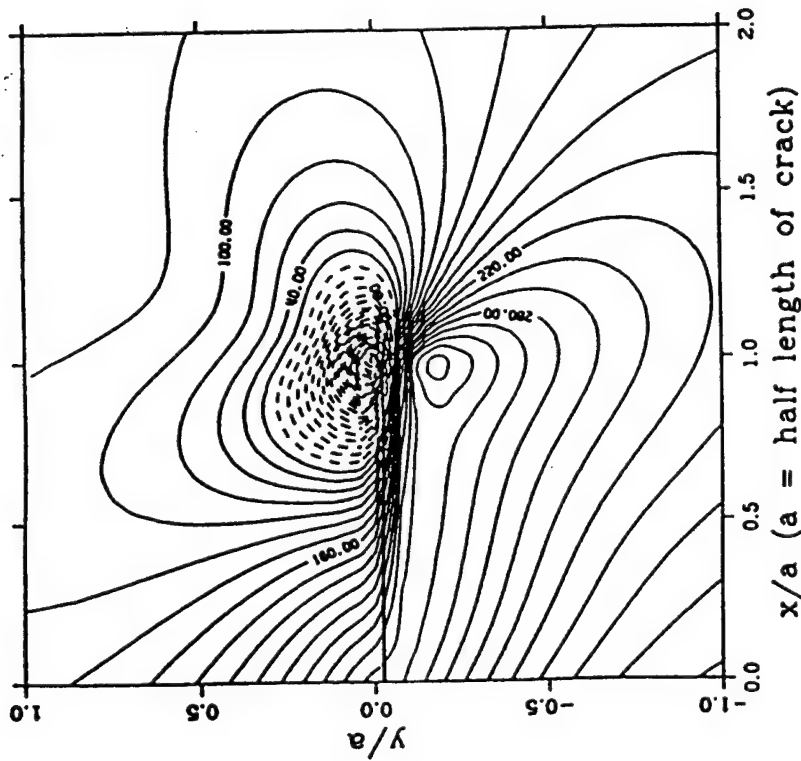


Figure 7 Lines of Equal Minimum Principal Stress from Finite Elements Elastic Solution

Numerical Analysis

Elastic and Elasto-Plastic Analysis for One Crack.

The closed form elastic solution can be used to check the finite elements solution in the vicinity of the crack. Figure 6 shows the lines of equal minimum principal stress given by such a solution. Notice that the dotted lines represent tension which occurs in spite of the high hydrostatic stress applied to the specimen. Figure 7 shows the finite element elastic solution. It is seen that the patterns are the same with the magnitudes quite similar in the vicinity of the crack. The important point is the high level of tensile stresses near the tips. The mesh used involved 8-node isoparametric elements with four reduced integration points. The number of nodes was 1626 with 480 elements.

For the elasto-plastic solution the finite elements code ABAQUS (1989) was used to investigate the spreading of the plastic zone in specimens subjected to combinations of compression and torsion, pure torsion and tension plus torsion. Referring to the report by Saada and Bianchini (1992), those tests are listed in Table 2.3 of this report and are numbered as 51-4-5-91, 6V-9-26-90 and 52-4-9-91. The mesh used involves 2618 nodes and 800 elements. The spreading of the plastic zone can be seen on a plot of lines of equal equivalent plastic strain defined as:

$$\epsilon_{eq}^p = \int \sqrt{\frac{2}{3} d\epsilon_{ij}^p d\epsilon_{ij}^p}$$

The shape of such lines allows one to envision the direction of the shear bands, should such bands form.

The Von Mises plasticity criterion, when used, results in the lines shown in Fig. 8a for the pure torsion test 6V-9-26-90. In this case, the shear bands would be horizontal. This, in reality, is not the case as seen on the photograph in Fig. 8b; the material being a frictional one. In Fig. 8b one notices that the shear bands emanating from the tips of the crack are at a marked angle to the horizontal. Looking at the grid in the middle of the photograph one notices that the crack shear displacement is about one half of a centimeter.

On the other hand when the Drucker-Prager plasticity criterion is used the results are quite different. Figures 9, 10a, and 11a show the lines of equal equivalent plastic strain as the plastic zone spreads in specimens 6V-9-26-90, 51-4-5-91, and 52-4-9-91, respectively. The first specimen was tested under pure torsion; the second specimen under a combination of compression and torsion and the third specimen under a combination of extension and torsion. The predicted directions of the shear bands as shown by the arrows are very close to what has been observed and recorded in the photographs of Figs. 8b, 10b and 11b.

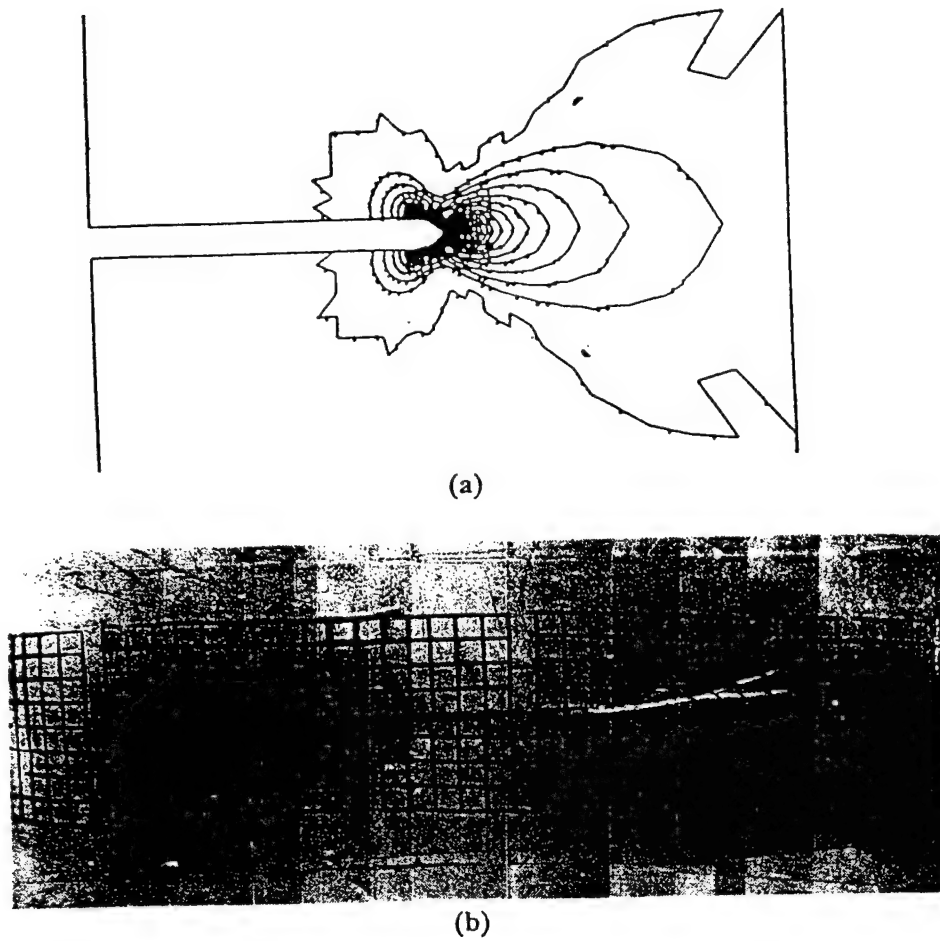


Figure 8 a) Lines of Equal Equivalent Plastic Strain using the Von Mises Model and Pure Torsion. b) Result of Pure Torsion Test

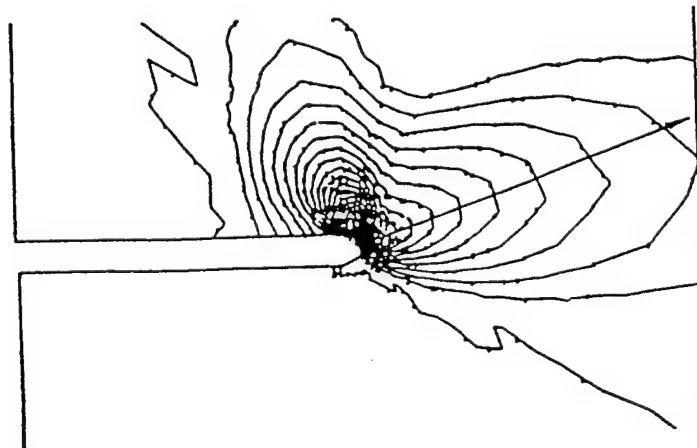


Figure 9 Lines of Equal Equivalent Plastic Strain using the Drucker-Prager Model and Pure Torsion

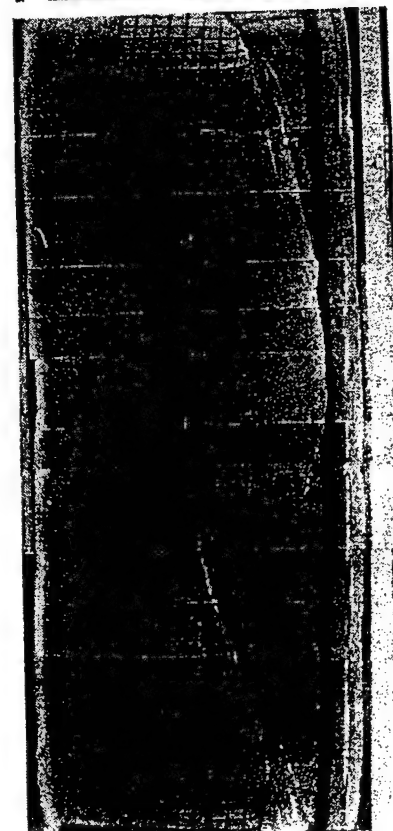
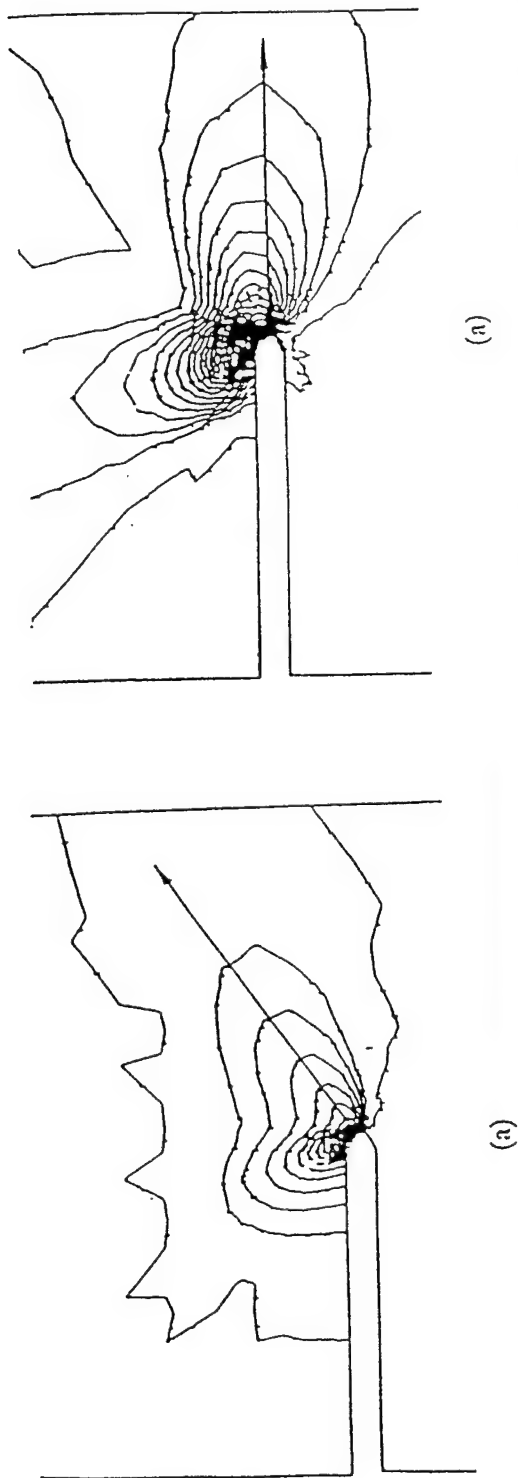


Figure 10 a) Lines of Equal Equivalent Plastic Strain using the Drucker-Prager Model and a Combination of Compression and Torsion. b) Test Results

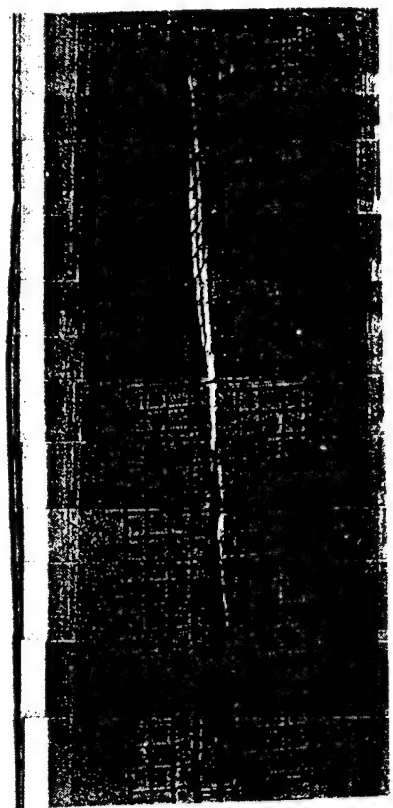
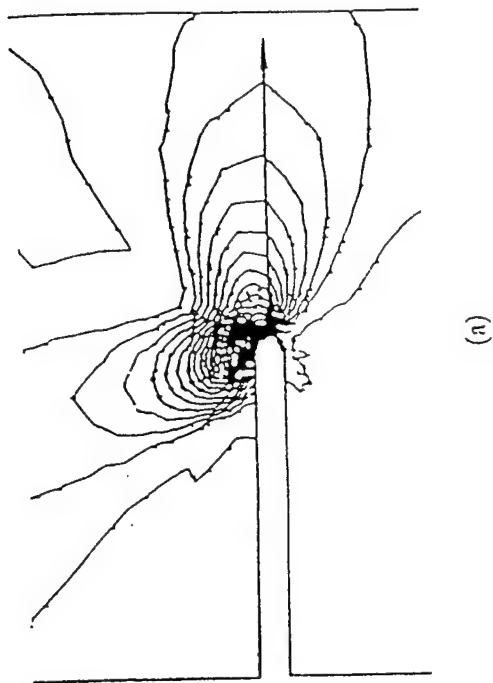


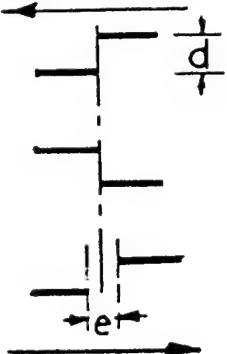
Figure 11 a) Lines of Equal Equivalent Plastic Strain using the Drucker-Prager Model and a Combination of Extension and Torsion. b) Test Results

Curves similar to the ones shown in Figs. 9 were generated for two other angles of friction besides 33° , namely 15° and 50° . They lead to smaller and larger inclinations of the shear bands respectively. Thus, for a pure torsion test, the direction of the shear bands is better predicted using the angle of friction obtained from a direct compression test.

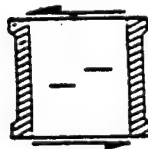
A better appreciation of the use of an elasto-plastic analysis can be gained by looking at the stress distributions along lines OA and OB of Fig. 5. Figures 12a and 12b show the magnitudes of the principal stresses and of the quantity $\left(\frac{3}{2}S_y S_z\right)^{1/2}$ along OA for the elastic and the elasto-plastic analyses respectively in the case of test 6V-9-26-90. Figures 13a and 13b show the same quantities along OB. In both Figures 12 and 13 notice the changes in σ_3 as one approaches the crack tip, and as one goes from an elastic analysis allowing tension in the material to an elasto-plastic one where tension is limited by the magnitude of the cohesion.

An important conclusion to be drawn from the above is that the development of the shear bands is reasonably well represented by an elasto-plastic model of the Drucker Prager type involving internal friction; the angle of internal friction being best predicted by direct triaxial compression.

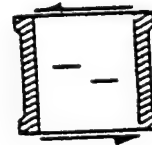
TABLE 1

DESIGNATION	CONTROL	CRACKS POSITION	COMMENTS
81-7-3-91	ROTATION		.Downstep e = 0 d = .6cm a/l = .18
82-7-9-91	ROTATION		.Upstep e = 0 d = .6cm a/l = .18
84-7-17-91	ROTATION		.Downstep e = 1.3cm d = .6cm
Average w% = 33.62			

Downstep

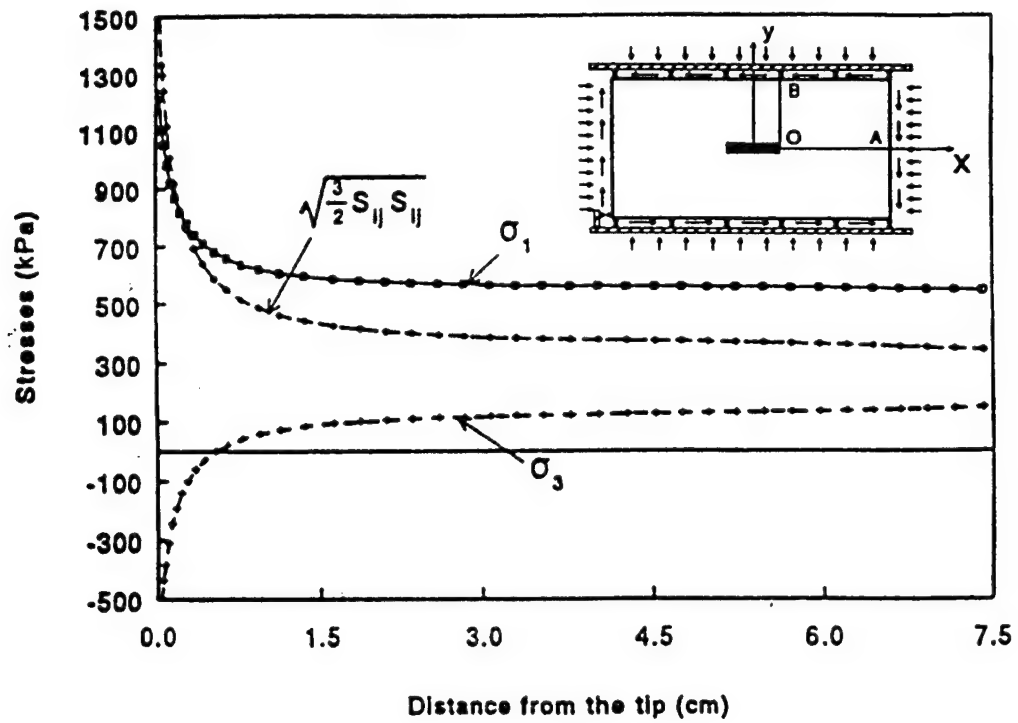


Upstep

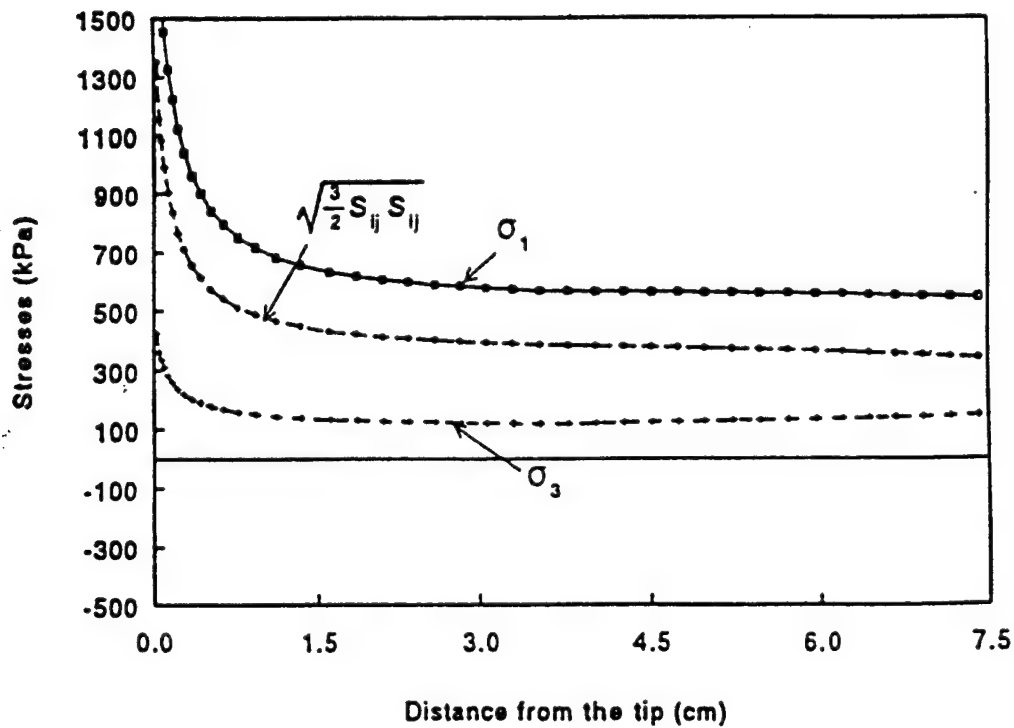


Elastic Analysis for Two Cracks

The Displacement Discontinuity Method was used to study the elastic stress field in the vicinity of two cracks in the downstep and upstep positions. The three



(a)



(b)

Figure 12 Stress Distribution along OA. a) Elastic Analysis;
b) Elasto-Plastic Analysis

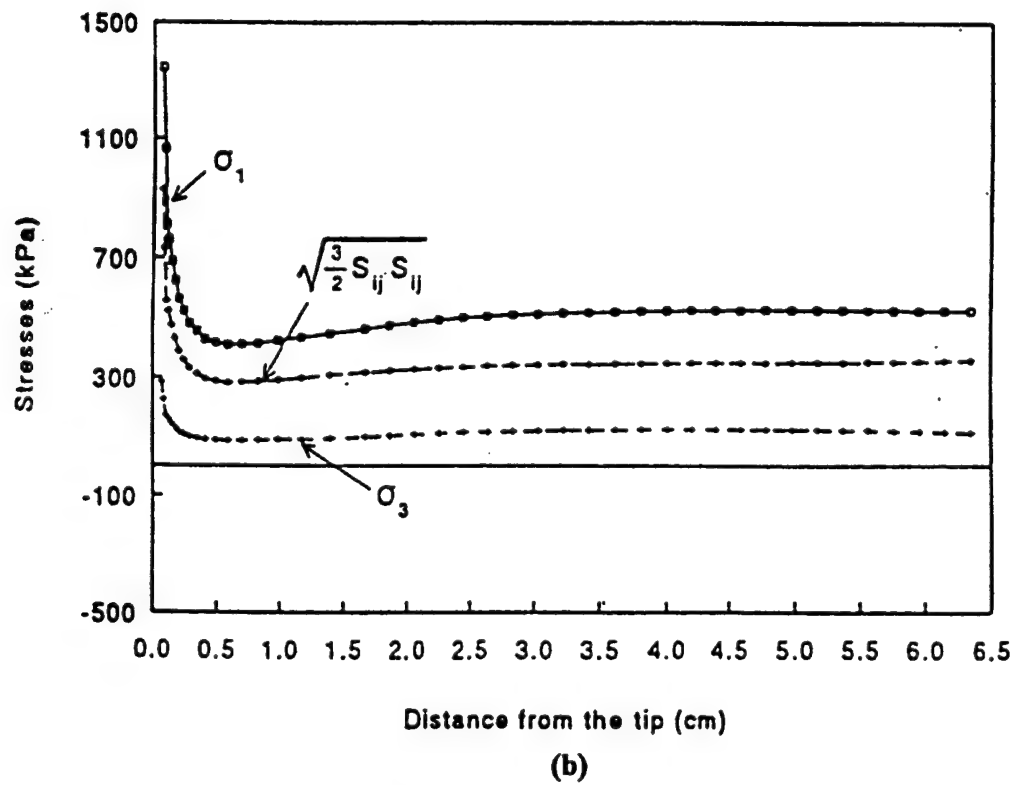
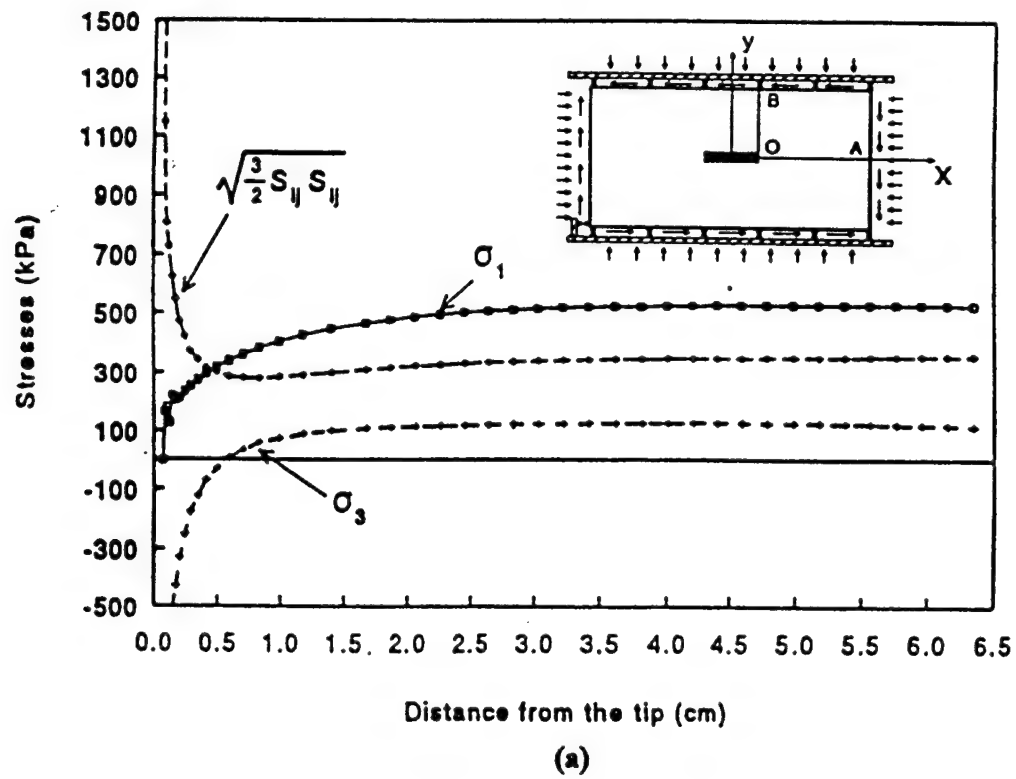


Figure 13 Stress Distribution along OB. a) Elastic Analysis; b) Elasto-Plastic Analysis

tests listed in Table 1 were chosen for analysis. They were all pure torsion tests on overconsolidated EPK clay. Notice the cracks position and the distance between them. Figures 14a, 15a and 16a show the lines of equal minor principal stress in those three cases. Notice the tensile zones between the two cracks in Figs. 14a and 16a. These are the stresses that caused the local instabilities in Figs. 14b and 16b. On the other hand, notice the lack of tension between the cracks in Fig. 15a describing the upstep case. Indeed, there was no local instability to be seen in Fig. 15b. The stress distribution depends, not only on the relative positions of the cracks but also on the direction of the shearing stress.

The above observations indicate that, even though the plasticity of the material blunts the high tensile stress concentrations that take place between the cracks in the downstep position, enough is left to overcome quite a high hydrostatic stress and cause localized necking. The elastic analysis only gives an indication of the magnitude of those stresses. Experimental support for the previous statements has been given by Saada and Bianchini (1992).

Conclusions

The numerical calculations made in this paper give some theoretical bases to the observations made in the report by Saada and Bianchini (1992). While elastic analyses are always a good first step to indicate the zones of high stress, elastoplastic analyses are needed to adequately describe the observed behavior. A frictional model was found to be necessary to describe yielding even though the tests were undrained and the clay saturated. The Drucker-Prager plasticity criterion, when used, helps predict in a very satisfactory way the direction of the shear bands.

The phenomenon of bifurcation that results in the formation of shear bands in clays deserves much scrutiny. As shown in the report, bifurcation also takes place with or without the presence of discontinuities. Future studies should take into account the pore water pressures that develop in the vicinity of the discontinuities, and their influence on the propagation of the shear bands. Numerically, special elements that reproduce emerging localized deformation patterns offer a promising approach in capturing the effects of crack and shear band propagation.

References

- ABAQUS (1989). Hibbitt, Karlsson and Sorensen, Inc.
- Chudnovsky, A., Saada, A.S. and Lesser, A.J. (1988). Micromechanisms of Deformation in Fracture of Overconsolidated Clays. *Can. Geotech. J.* 25, 213-221.
- Muskhelishvili, N. I. (1953). *Some Basic Problems of the Mathematical Theory of Elasticity*. Translated by J.R.M. Radok, P. Noordhoff Ltd., Holland.

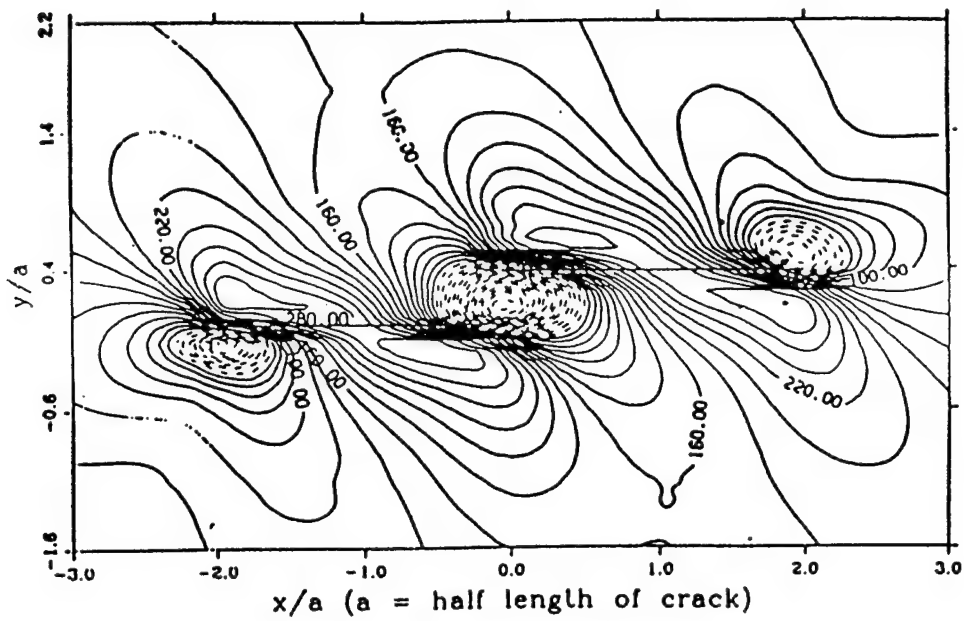


Figure 14a Lines of Equal Minimum Principal Stress for Two Cracks Pure Torsion; Downstep

Figure 14b See Figure 28 in Paper 1

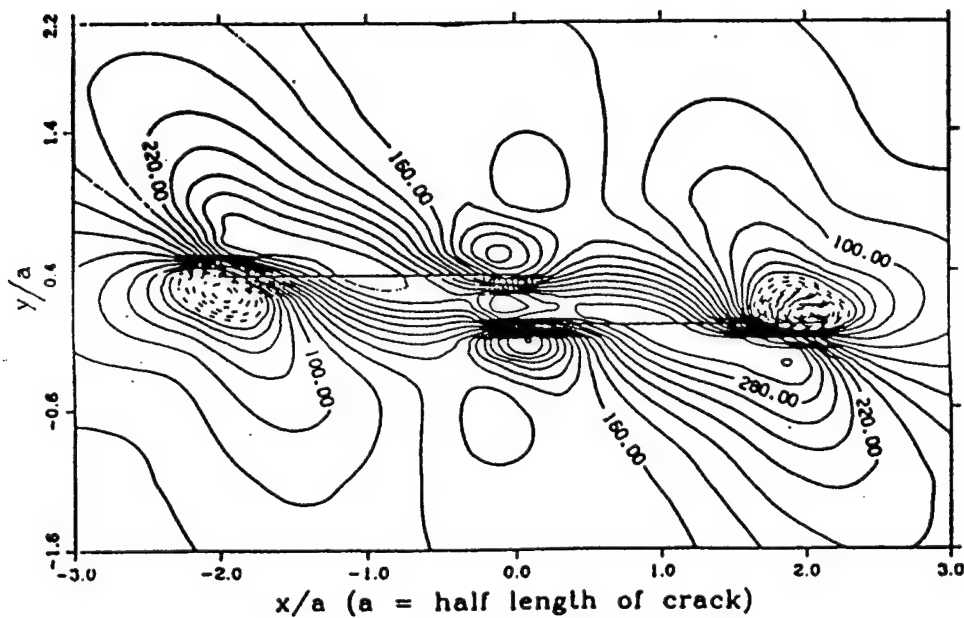


Figure 15a Lines of Equal Minimum Principal Stress for Two Cracks Pure Torsion; Upstep

Figure 15b See Figure 29 in Paper 1

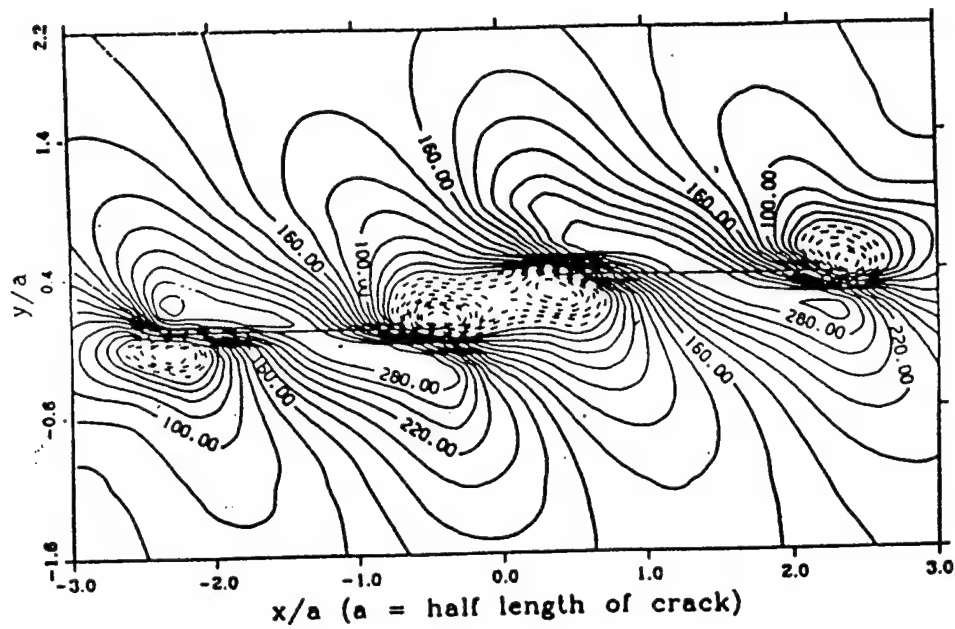


Figure 16a Lines of Equal Minimum Principal Stress for Two Cracks Pure Torsion; Downstep

Figure 16b See Figure 30 in Paper 1

Saada, A.S. and Townsend, F.C. (1981). "State of the Art. Laboratory Strength Testing of Soils." Laboratory Shear Strength of Soils, ASTM, STP 740, R.N. Yong and F.C. Townsend, Eds., pp. 7-77.

Saada, A.S., Chudnovsky, A. and Kennedy, M.R. (1985). "A Fracture Mechanics Study of Stiff Clays." Proc. 11th ICSMFE, Vol. 2, pp. 637-640, San Francisco.

Saada, A.S. (1988). "State of the Art. Hollow Cylinder Torsional Devices: Their Advantages and Limitations." Advanced Triaxial Testing of Soil and Rock, ASTM, STP 977, R.T. Donaghe, R.C. Chaney, and M.L. Silver, Eds., pp. 766-795.

Saada, A.S. and Bianchini, G.F. (1992). "Crack Propagation and Fabric Control on the Static and Dynamic Strength of Cohesive Soils." Final Report submitted to the Air Force Office of Scientific Research, Bolling Air Force Base, Washington, D.C. See also "Cracks, Bifurcation and Shear Bands Propagation in Saturated Clays," by Saada et al., to be published in Geotechnique. → See Paper 1

Vallejo, L.E. (1987). The Influence of Fissures in a Stiff Clay Subjected to Direct Shear. Geotechnique, 37, No. 1, 69-82.

Vallejo, L.E., (1988). The Brittle and Ductile Behavior of Clay Samples Containing a Crack Under Mixed Mode Loading. Theoretical and Applied Fracture Mechanics, 10, 73-78.

Vallejo, L.E. (1989). Fissure Parameters in Stiff Clays Under Compression. Proc., ASCE, Journal of Geotechnical Engineering, Vol. 115, No. 9, 1303-1317.

Acknowledgment

This research has been conducted under the sponsorship of the Air Force Office of Scientific Research. The authors wish to thank Drs. S.C. Boyce and M.D. Lewis, Program Managers, for their encouragement during the various phases of this project.

Part II

RESEARCH ON SANDS

Part II

RESEARCH ON SANDS

When studying localization and shear band formation in sands, a method had to be devised to measure deformation and strain within and in the vicinity of the shear bands in a non invasive way. Imprinting a grid on hollow cylinders of clay could be done without much difficulty since such cylinders are free standing during their cutting and shaping. For sands, specimens had to be made, moistened then frozen to allow for direct imprinting of a square grid on the sand particles using indelible ink. Once this was done the deformation of the squares could be followed with four digital cameras surrounding the cell.

Three different sands were investigated to find the influence of the granulometry on the formation and direction of propagation of the shear bands. For each sand the relative densities and the mean stresses were changed; and for each of these two variables, five different radial stress paths were examined.

It was proposed by Koenders et al. that the shear bands formed such that their inclination followed Coulomb's theory for fine sands, Roscoe's theory for coarse sands and the Arthur-Vardoulakis theory for intermediate sands. The sands were tested to check this proposition and/or choose among the three possibilities.

The three following publications give in complete detail the results of our work on sands. They describe the experiments that were conducted, their results, discussions and conclusions. Here, as in the case of clays, each of the tests listed in the tables is fully documented in a file available on request from the principal investigator. The appendices give the full digitization and evaluation of a number of tests. In all, twelve tests were fully digitized.

The first paper entitled "**The Use of Digital Image Processing in Monitoring Shear Band Development,**" was published in the Geotechnical Testing Journal and gives some preliminary results involving the use of a notch in sand hollow cylinder. The sand involved is a fine sand known as Reid Bedford Sand.

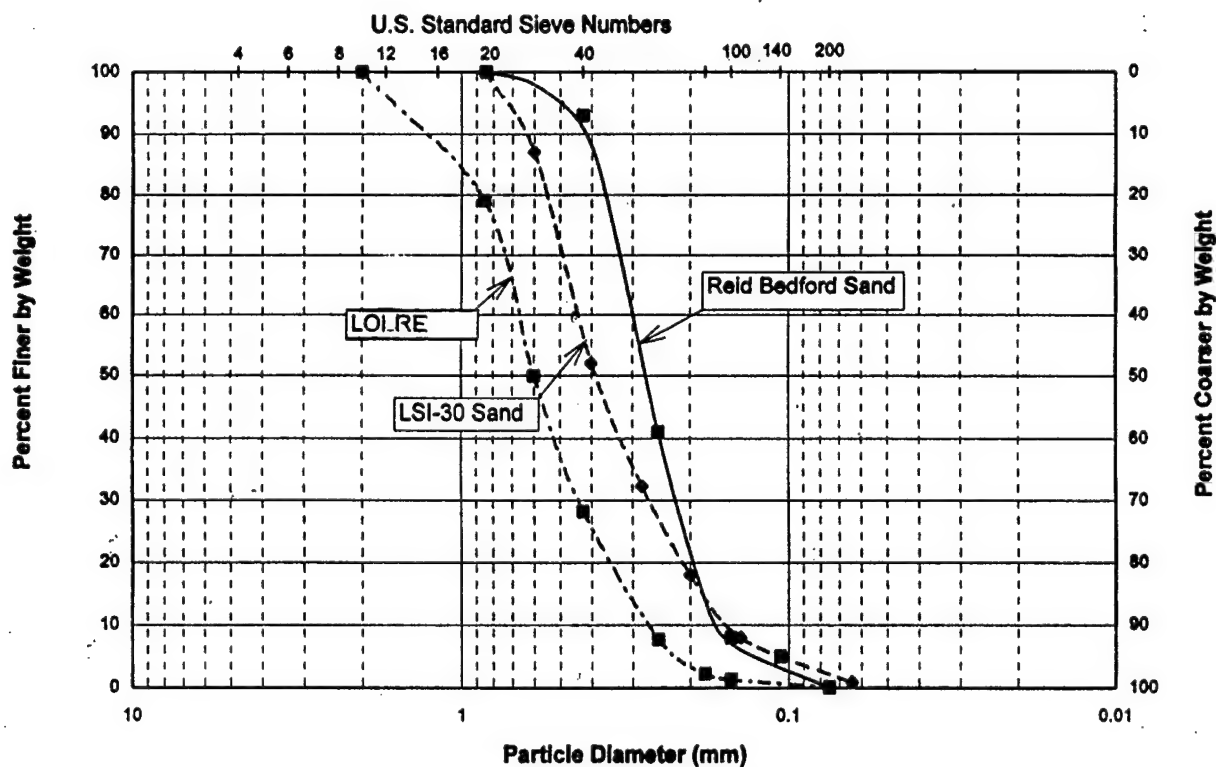
The second paper entitled "**Bifurcation and Shear Band Propagation in Sands,**" is presently going through evaluation by Geotechnique. This paper gives a most complete description of our research on sands. The sand involved here is a coarser sand known as LSI-30.

The third paper is a **thesis**. It deals primarily with the **behavior of even a coarser sand**, known as the Loire Sand.

The granulometric distributions and properties of the three sands mentioned above are shown on the following table and graphs.

Sand Name	Loire	LSI 30	Reid Bedford
USCS Group	SP	SP	SP
Specific Gravity	2.64	2.66	2.65
Maximum Void Ratio	0.76	0.83	0.85
Minimum Void Ratio	0.49	0.52	0.58
D_{50}	0.60 mm, 0.023 in	0.39 mm, 0.015 in	0.26 mm, 0.010 in

Index Properties and Classification



PAPER 1 --- ON SANDS

(Reid Bedford Sand)

Liqun Liang,¹ Adel Saada,² J. Ludwig Figueroa,³ and C. T. Cope⁴

The Use of Digital Image Processing in Monitoring Shear Band Development

REFERENCE: Liang, L., Saada, A., Figueroa, J. L., and Cope, C. T., "The Use of Digital Image Processing in Monitoring Shear Band Development," *Geotechnical Testing Journal*, GTJODJ, Vol. 20, No. 3, September 1997, pp. 324-339.

ABSTRACT: A new technique involving sample preparation, video imaging, and image analysis has been developed to observe the kinematics of shear bands when geomaterials are subjected to a general state of combined stress. The technique provides an effective, low-cost, and non-invasive way to monitor the development and measure the deformations inside and outside the shear bands. Its capabilities are demonstrated through a series of drained tests in which thin hollow cylinders of sand are subjected to combinations of hydrostatic, axial, and torsional stresses. It is shown that the deformation within the shear band is different from the global one and the one in its vicinity. For sand specimens with the same configuration, density, and confining pressure, the initiation, orientation, and thickness of shear bands depend on the loading path.

KEYWORDS: image analysis, shear band, bifurcation, sand, dilation, local deformation, laboratory tests, hollow cylinder specimen

The failure process of geomaterials such as sands, clays, and rock often involves the formation of shear bands. This bifurcation phenomenon needs to be fully understood before a realistic and complete model for soil behavior is successfully developed. Laboratory experiments conducted under controlled conditions have resulted mostly in description of rates and directions of propagation of the bands, with very little, if any, actual measurements of the changes that occur within and in their vicinity.

It is appropriate to mention that Scarpelli and Wood (1982) and Arthur and Dunstan (1982) used radiography to observe the rupture layers formed in direct shear and in triaxial tests conducted on sands; Desrues (1983), Yoshida et al. (1994), and Harris et al. (1995) used stereophotogrammetry; and Tatsuoka et al. (1990) used laser techniques to record the deformation of laboratory specimens. Papamichos and Vardoulakis (1995) provide a list of references of important theoretical and experimental research aimed at understanding the phenomena of bifurcation and localization in geomaterials.

Digital video image analysis techniques are relatively new in

geotechnical engineering. Acosta et al. (1992) used them to evaluate pavement surface distress and Gustafsson and Knutsson (1994) to study the motion of granular materials.

This paper presents and describes a technique based on video imaging to observe information about the kinematics of shear bands when geomaterials are subjected to a general state of combined stress. Such states are obtained through the use of thin hollow cylinders subjected to combinations of hydrostatic, axial, and torsional stresses. The emphasis here is on shear bands and on measurements in their vicinity and not on strength characteristics under general stress or strain systems. This work is part of a larger investigation studying the formation and modeling of shear bands in soils.

Experimental Program

Loading Device and Data Acquisition Systems

The use of the hollow cylinder test in geotechnical engineering has been discussed at length in papers by Saada and Townsend (1981), Hight et al. (1983), and Saada (1988). In order to observe the initiation and development of shear bands, a controlled strain (rotation) device is needed. In such a device, a motor applies a slow rotation to the base of the hollow cylinder cell whose piston is prevented from rotating. The resulting torque is measured with a transducer and its electrical output is read by a computer and used to control axial force and cell pressure. Maximum stress uniformity is obtained by having the cell pressure act equally inside and outside the cylinder. The references mentioned above give all the necessary equations to compute the stresses and strains from the measured forces and deformations.

Forces, deformations, and pressures were measured with a wide variety of transducers and collected by PCs. Figure 1 shows the system of stresses acting on the hollow cylinders as well as an element indicating the direction β of the major principal stress on the axis of symmetry of the material.

The axial displacements, the axial force (inside and outside the cell), the angular rotation, the torque (inside and outside the cell), and the cell pressure were measured during testing using a state-of-the-art data acquisition and reduction system. Figure 2 shows a schematic of the test monitoring setup. The solid lines in this figure are related to the data acquisition and the loading control paths, while the dashed lines are related to the image recording circuits. The control panel monitors the conversions of electrical signals (from the D/A converters of the computers) to pneumatic

¹Research associate, Department of Civil Engineering, Case Western Reserve University, Cleveland, OH 44106.

²Frank H. Neff Professor and chairman, Department of Civil Engineering, Case Western Reserve University, Cleveland, OH 44106.

³Professor, Department of Civil Engineering, Case Western Reserve University, Cleveland, OH 44106.

⁴Graduate student, Department of Civil Engineering, Case Western Reserve University, Cleveland, OH 44106.

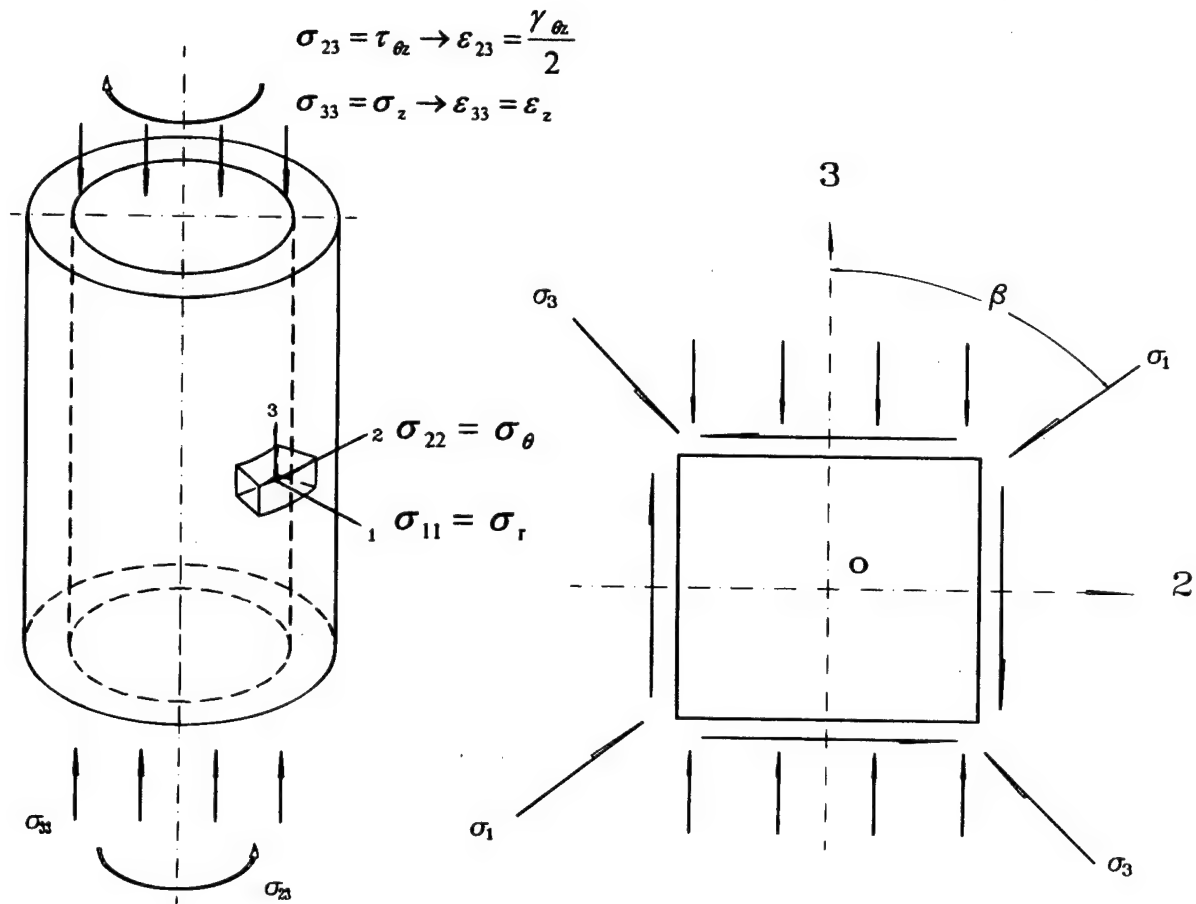


FIG. 1—Notation and stress state.

signals. These signals are sent to the force actuators and to the confining cell.

Preparation of Sand Specimens

Reid Bedford sand was used in this investigation. This sand is clean and fairly uniform and was obtained from the Reid Bedford Bend, located south of Vicksburg, Mississippi. Classification tests were conducted according to ASTM specifications to determine its properties, which are shown in Table 1. Figure 3 shows its grain-size distribution.

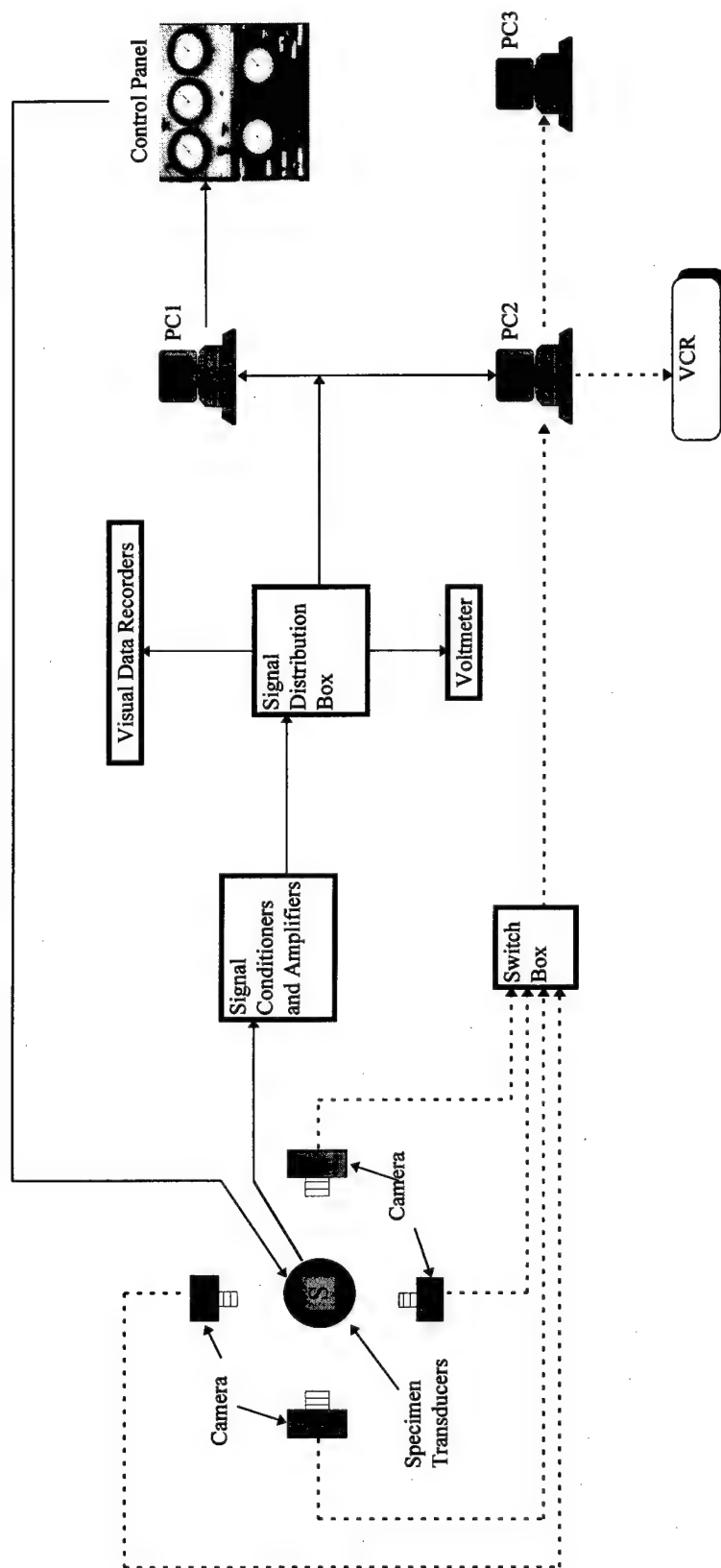
The local deformations of a soil specimen subjected to stress in a triaxial cell can be followed by taking a series of photographs during the various steps of the test. To recognize the path of specific points in a succession of photographs, a grid can be imprinted on the surface of the specimen as done by Saada et al. (1994) for clays. However, because of the difficulty in imprinting a grid on sand, Yoshida et al. (1994) imprinted it on the membrane. The authors tried this technique, which seemed to work well as long as the specimen was pressurized. However, no meaningful photographic recording could be made of the unloaded specimen due to the partial loss of contact between the soil and the membrane. A special technique had to be found to place a permanent grid on the sand.

The two specimen configurations used in this investigation are schematically shown in Fig. 4. While the shape shown in Fig. 4a with a uniform cross section was most satisfactory for routine tests, it was found necessary to adopt another configuration when-

ever careful observations of shear bands formations were needed. The specimens with enlarged ends shown Fig. 4b were made by using special moulds. End effects were thus considerably reduced, if not totally eliminated, during testing. To study shear band propagation, two layers of very thin flexible Teflon sheets, 0.38 mm thick, were placed in the middle of the specimen to form a discontinuity. The ratio of the circumferential length, a , of the discontinuity to the mean perimeter, l , of the specimen was $a/l = 0.18$. Such a discontinuity transmits very little shear, but transmits compressive normal stresses across the discontinuity surfaces. Saada et al. (1994) successfully used this technique to start shear bands at specific locations in clay soils. The expectation was that it would help initiate the bands in sands, too. It will be illustrated later that this is, indeed, what has happened, with a band starting at each tip of the Teflon sheets.

Once the amount of sand corresponding to a specific relative density was placed between the moulds, the specimen was sealed with the membranes and top and bottom caps. Water was drawn into it before it was placed in a cold room at -10°C . The water generally froze after 4 h. The moulds were removed and the outer membrane could then be rolled down. The quarter-inch ink grid (6.35 mm) was imprinted directly on the sand using an ink stamp. The ink grid was allowed to dry for 1 h before the outer membrane was rolled up. The specimen was then placed in the testing cell, pressurized, and allowed to thaw and consolidate overnight.

Photographs and video images were taken during the tests. As shown in Fig. 2, four video cameras were arranged such that the full specimen surface could be covered. The images from each



- Solid lines show the path of data acquisition and test control; Dashed lines show the path of image recording.
- PC1 records signals from transducers through a A/D board as voltages, calculates and sends out voltages to control panel through a D/A board.
- Control panel changes the voltages from PC1 to air pressure and supplies air pressure to increase/decrease axial forces and cell pressures.
- PC2 merges the voltage reading and the image, then sends the results to a VCR and PC3.
- Images are continuously recorded by a VCR and selectively by PC3.

TABLE 1—Index properties and classification of Reid Bedford sand.

Index Properties	Value
USCS group	SP
Specific gravity	2.65
Max void ratio	0.85
Min void ratio	0.58
D_{50}	0.26 mm


video camera were sent in turn to PC2 and merged with other data with the aid of a video-VCR (video cassette recorder) board. The resulting images were continuously recorded by a Super VCR and selectively captured by PC3, which is equipped with a high-resolution video image capturing board. As a backup, a photographic camera was also used to capture the deformation patterns for small increments of rotation.

Soil Tests

Tests were conducted on specimens with the configurations shown in Fig. 4. All specimens were normally consolidated under an effective confining pressure of 172.4 kPa (25 psi). Two series of tests were conducted under a drained condition with fixed and variable cell pressures. The purpose of changing the cell pressure is to keep the mean stress constant and thus the stress path in the Π -plane. To follow radial paths in the Π -plane, the axial loads and the cell pressure were controlled by the shearing stress resulting from the torsional rotation. The loading rate was about $0.5^\circ/\text{min}$ in rotation, which resulted in a rate of shear strain of $\dot{\gamma} = 0.23\%$ per min.

Table 2 lists the tests conducted using the specimen configuration shown in Fig. 4a with a discontinuity. Table 3 lists the tests conducted using the specimen configuration shown in Fig. 4b with a discontinuity. Table 4 lists the tests conducted without a discontinuity.

TABLE 2—Static test series 1: configuration of Fig. 4a with discontinuity.

Test No.	β (Fig. 1): Degree	$b = \frac{\sigma_2 - \sigma_3}{\sigma_1 - \sigma_3}$	Cell Pressure Change	Comments and Configuration
6	0	0.0	Yes	$D_r \approx 70\%$; $a/l = 0.18$ 
4	0	0.0	No	
5	30	0.25	Yes	
2	30	0.25	No	
1	45	0.5	No	
3	60	0.75	No	

ity to judge the influence of the Teflon sheets on the level of stress at which the bands are initiated, as well as on their direction.

Digital Image Processing and Deformation Measurements

Selected images were captured at different loading increments by PC3 while being recorded on tape. Those images were projected on a high-resolution screen and the coordinates of the points of the grid, in pixels, digitized and saved. To increase accuracy, areas of interest were divided into subareas and the process repeated. The digitized grids were then plotted, superimposed on the original images, and printed using a 600 by 600 dpi laser printer to check the accuracy of the digitizing process. This operation was repeated until a perfect match was reached. Software developed with a mathematical package was used for this purpose. Presently, all the previous steps are manual.

The distances are measured in terms of pixels, with 130 pixels per inch in the horizontal direction and 110 pixels per inch in the vertical direction. An error of one pixel in the count corresponds to an error of 0.23 mm in real coordinate distance. This is very close to D_{50} of the material tested (0.26 mm).

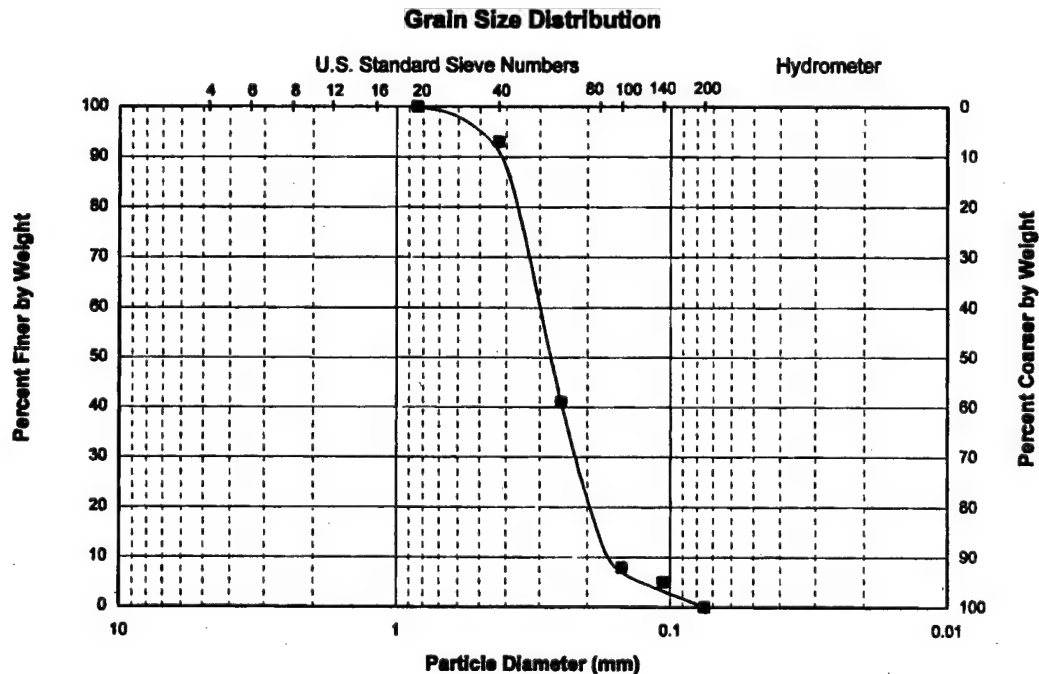


FIG. 3—Grain-size distribution of Reid Bedford sand.

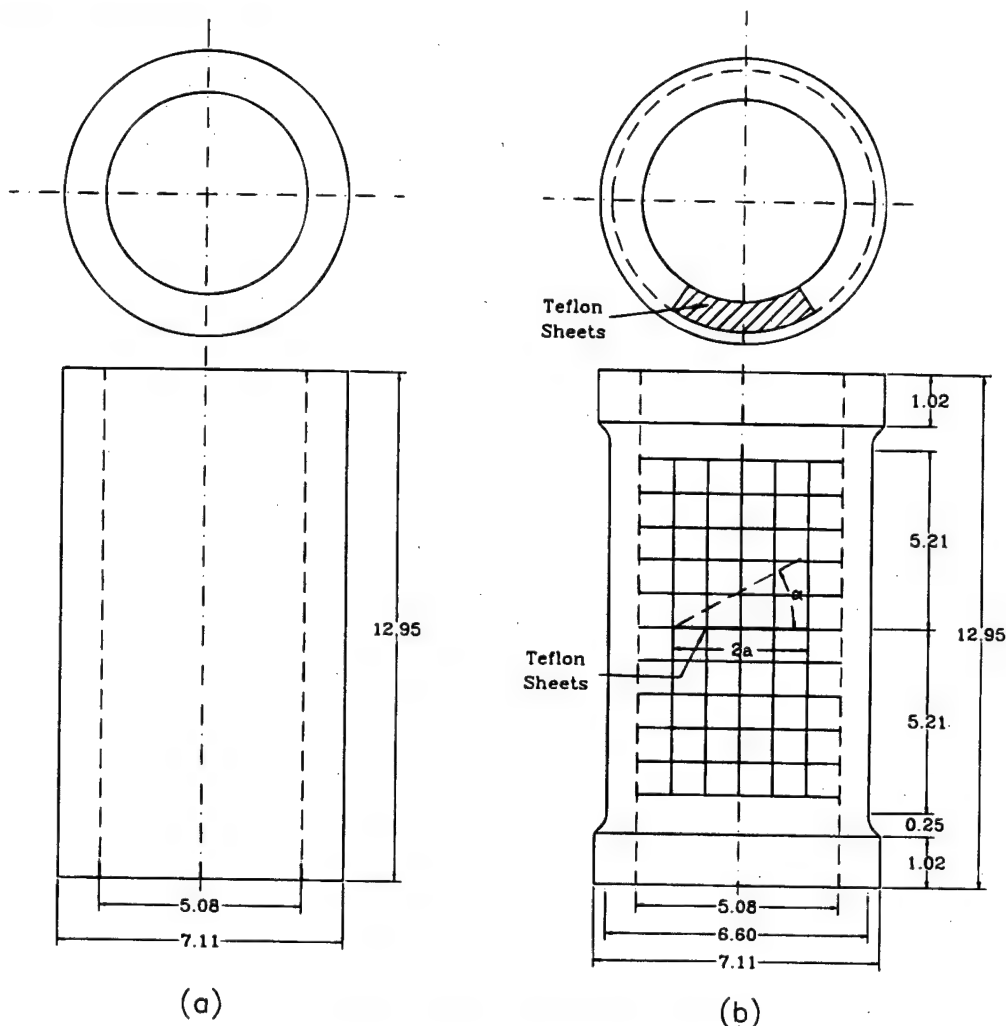


FIG. 4—Specimen geometry (all dimensions are in cm).

TABLE 3—Static test series 2: configuration of Fig. 4b with discontinuity.

Test No.	β (Fig. 1): Degree	$b = \frac{\sigma_2 - \sigma_3}{\sigma_1 - \sigma_3}$	Cell Pressure Change	Comments and Configuration
11	30	0.25	Yes	$D_r \approx 70\%$; $all = 0.18$
15	45	0.5	No	
7	60	0.75	No	
8	60	0.75	Yes	
12	60	0.75	Yes	
9a	90	1.0	No	
10	90	1.0	Yes	

Figure 5a shows an image captured during Test 11 at 2304 s after test initiation. It can be seen that this image contains both the specimen and the information that identifies this test and the time when this image was recorded, which includes: test ID number, date, rotation (RVDT in voltage), torque (in voltage), number of data points, time elapsed from the beginning of the test, video camera number, and the way to switch between cameras. The area of interest within the image was selected and is shown in Fig. 5b.

TABLE 4—Static test series 3: configuration of Fig. 4b without discontinuity.

Test No.	β (Fig. 1): Degree	$b = \frac{\sigma_2 - \sigma_3}{\sigma_1 - \sigma_3}$	Cell Pressure Change	Comments and Configuration
14	30	0.25	Yes	$D_r \approx 70\%$
13	45	0.5	No	

After digitization, the resulting grids were plotted on the image as shown in Fig. 5c. Figure 5d shows the digitized grids alone. To find the real dimension, scaling in pixels per inch in both horizontal and vertical directions had to be determined. This was done during testing by monitoring several marked points on the specimen surface using a telescopic device.

It is clear that the equally spaced vertical grid lines appear nonuniformly distributed due to the circular surface of the specimen. A correction of the horizontal dimension is needed. The real horizontal dimension can be determined using the following relationship (Fig. 6):

$$S = R \sin^{-1} \frac{L}{R} \quad (1)$$

where

- R = the outer radius of the specimen,
- L = the horizontal length measured from the image, and
- S = the real horizontal length on the specimen surface.

Figure 7 shows the grids corresponding to Fig. 5d after corrections are made.

The displacements of the various points on the specimen's surface were obtained by comparing the grid digitized from the image at selected times with the grid digitized from the image just before the test started. Figure 8 shows both deformed and original grids and displays the deformation pattern clearly. The elements of the grid were numbered as shown in Fig. 9 and the displacements of the nodes noted. The displacements of points at the top and bottom of the shear band were also noted. Displacements of points falling between the digitized ones were obtained by linear interpolation. Such displacements were used to calculate the strains both inside and outside the band.

Test Results and Discussion

The operations performed on Test 11, Test 12, Test 15 (refer to Table 3), and Test 6v-9-26-90 (refer to Saada et al. 1994: K_0 consolidated EPK clay, $\beta = 45^\circ$, with discontinuity) will now be discussed with the aim of bringing out the power of digital image processing as a tool for observing and measuring the development, propagation, and geometry of shear bands in soils. While test

results are briefly analyzed, they are to be looked upon as primarily a vehicle for illustrating the use of this technique.

For each of Tests 11, 12, and 15, six of the images captured at different times were selected to show the deformation patterns. Figure 10 shows the selected points on the stress strain curves. Those points are also listed in Table 5. The corresponding deformation stages can be clearly seen in Figs. 11, 12, and 13, respectively. Table 6 summarizes the observations made during the development of the shear bands.

A shear band was observed to start at and propagate from the tips of the Teflon discontinuity when the octahedral shear stress reached 87 to 90% of its peak value. Slippage appeared first on the discontinuity between the two teflon strips at a time t_1 followed by the appearance of the shear band at a time t_2 . The inclination of the bands to the horizontal depends on the direction of the principal stresses and is shown in Fig. 14.

At every interval of time, the thickness of the shear band in the soil as well as the thickness of the band around the Teflon strips were recorded. Two such sets of measurements are shown in Fig. 15. Thicknesses were averaged over the length of the shear band developed in the soil up to that time and plotted in Fig. 16. As expected, the thickness changed with the type of test. The combination of compression and torsion yielded the smallest increase (Test 11). Pure torsion (Test 15) and the combination of extension and torsion (Test 12) resulted in much larger ones. It was also noticed (and measured) that the change in thickness of the sands is not only due to a dilation phenomenon associated with a finite volume of soil, but also due to additional soil particles that become part of the bands as they develop and spread.

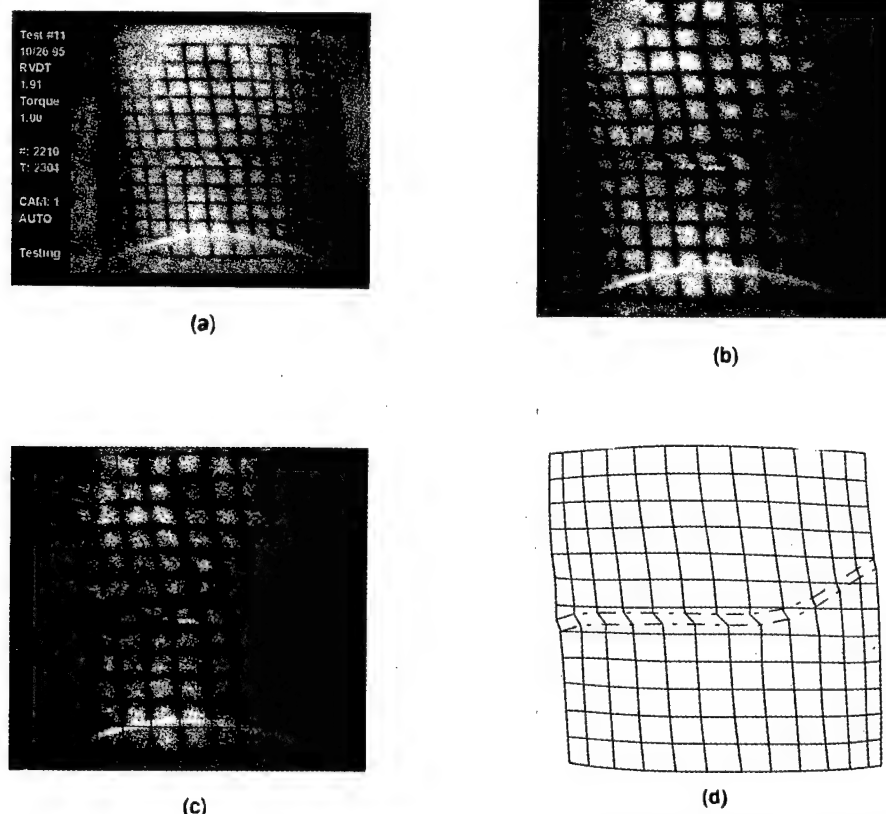


FIG. 5—(a) Image from Test 11 at 2304 s; (b) area of interest within the image; (c) superposition of image and digitized grid lines; (d) digitized grid lines.

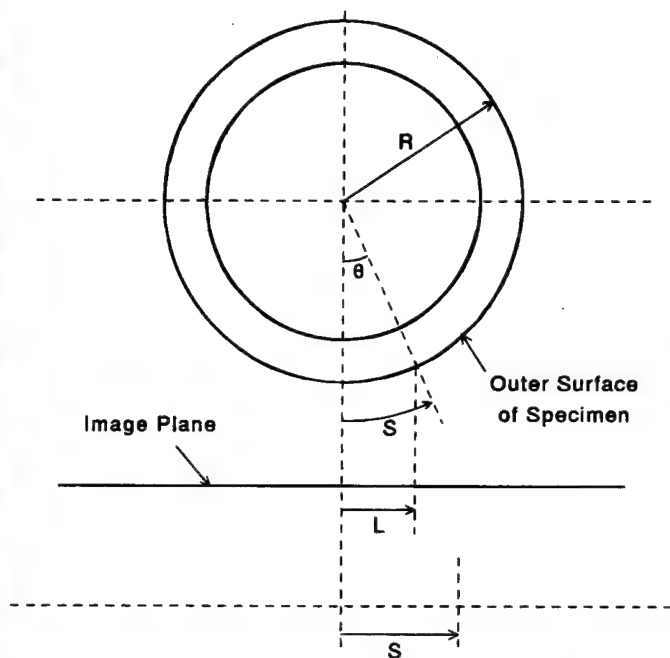


FIG. 6—Sketch showing the relationship between lengths in the image and on the specimen's surface.

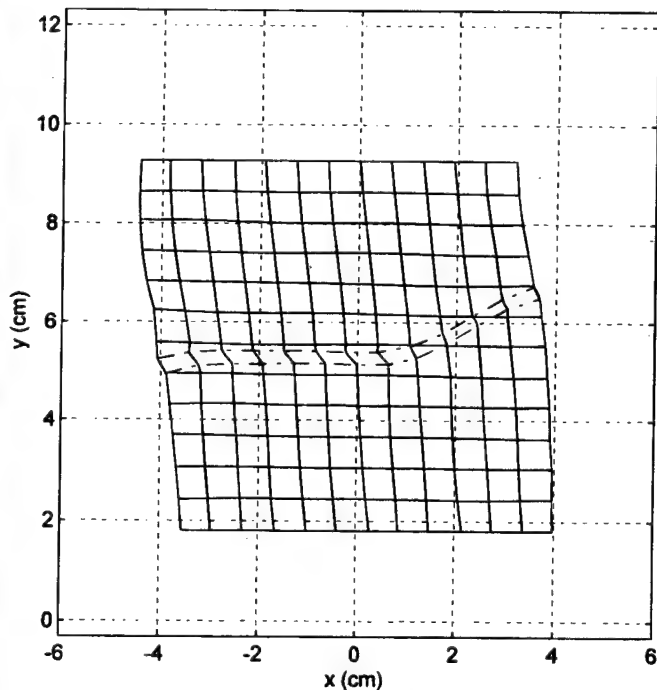


FIG. 7—Unfolded grid lines.

The average thickness of the shear band at the end of each test is listed in Table 6. It can be seen that it is 13 to 21 times D_{50} (0.26 mm) for the Reid Bedford sand used in this investigation. Three strains were calculated from:

1. Measurements made globally outside the cell.
2. The average of six rows of grid, three counted from the top and three counted from the bottom of the specimen, outside and away from the shear band.
3. Measurements made inside the shear band itself.

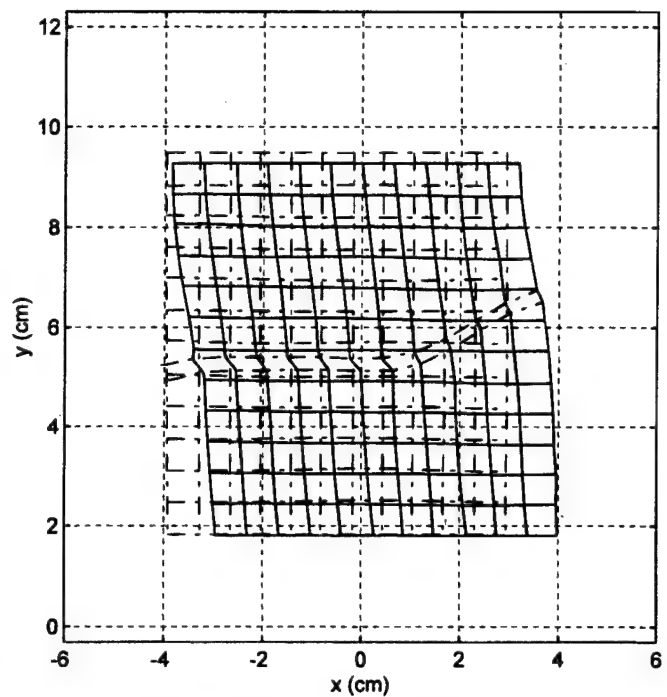
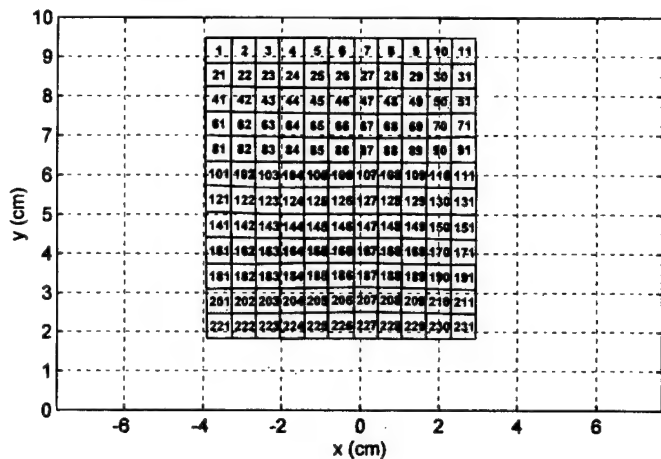
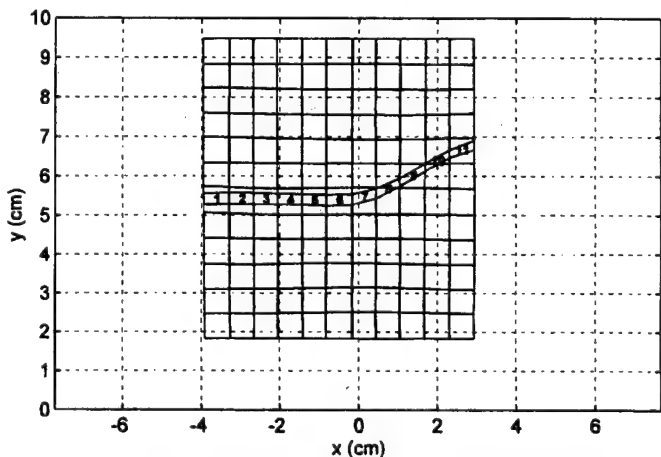


FIG. 8—Deformed mesh and original mesh.



(a)



(b)

FIG. 9—(a) Elements outside the shear band; (b) elements inside the shear band.

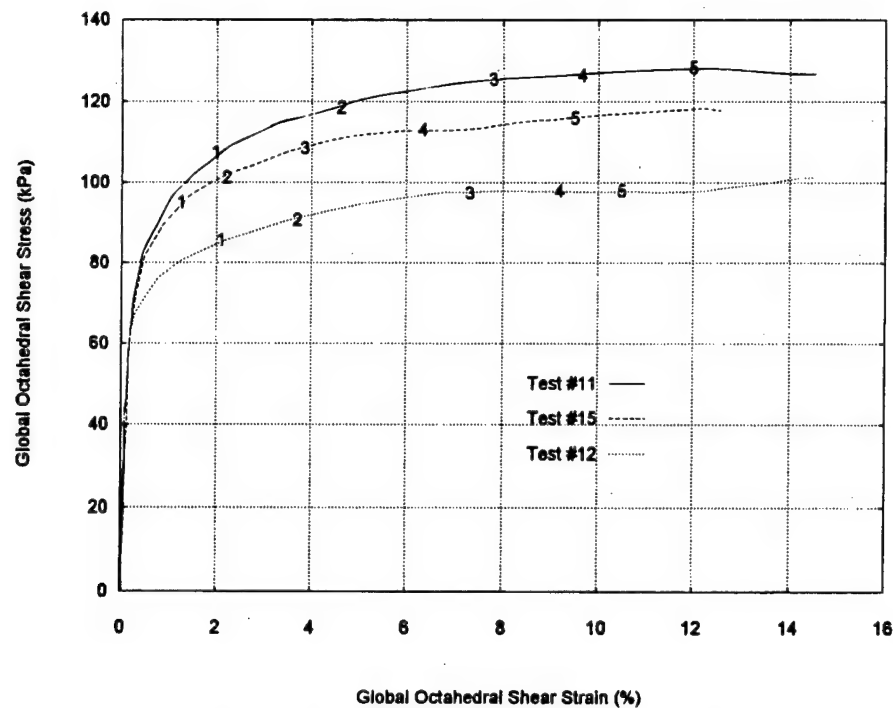


FIG. 10—Image locations on octahedral shear stress–shear strain curve.

TABLE 5—Summary of images selected for tests 11, 12, and 15.

Test No.	Image No.	Time, s	Global variables			Comments
			γ (%)	γ_{oct} (%)	τ_{oct} (kPa)	
11 $\beta = 30^\circ$	0	0	0.00	0.00	0.00	Start
	1	585	2.21	1.89	105.49	SB appears on Disc.
	2	1365	5.62	4.52	118.59	SB appears at Disc. tip
	3	2304	8.92	7.70	125.49	
	4	2805	11.06	9.56	126.39	
15 $\beta = 45^\circ$	5	3389	13.74	11.90	128.25	
	0	0	0.00	0.00	0.00	Start
	1	400	1.42	1.16	93.08	
	2	700	2.56	2.11	101.22	SB appears at Disc. tip
	3	1200	4.53	3.76	108.39	
12 $\beta = 60^\circ$	4	2000	7.53	6.24	113.08	
	5	3000	11.41	9.40	115.84	
	0	0	0.00	0.00	0.00	Start
	1	570	2.06	1.99	84.67	SB appears on Disc.
	2	1000	3.70	3.60	90.67	SB appears at Disc. tip
	3	2000	7.37	7.21	97.22	
	4	2600	9.35	9.09	97.91	
	5	3000	10.83	10.40	97.91	

Where: γ = shear strain; γ_{oct} = octahedral shear strain; τ_{oct} = octahedral shear stress; SB = Shear Band; Disc. = discontinuity.

An engineering definition of strain is used and is referred to the original undeformed shape of the specimen and grid. Such a definition is acceptable for small strains but needs serious modifications in any of the advanced constitutive models. It is used here for comparison purposes when applied to the shear band zone. Knowing the size of the grid, the reader can back-compute vertical and horizontal displacements at each point and use those values in whichever theory he chooses.

Figure 17 shows the shear strain at two instants in time, in the soil, and in the Teflon zone. Figures 18, 19, and 20 show the shear strains and vertical strains for the three tests, 11, 15, and 12, respectively. Here, too, the values corresponding to the strains in

the shear bands have been averaged over their length up to that time. As expected, global strains and those obtained from the grid away from the bands nearly coincide. On the other hand, the strains inside the shear bands become extremely large as those bands propagate, leading to a failure in the form of two blocks sliding with respect to one another. A comparison of Graphs *a* and *b* in Figs. 18, 19, and 20 indicates that large vertical strains start after a substantial amount of shearing strains take place. It is also noticed that for equal time periods combinations of extension and torsion result in the largest shear strains within the shear band (Test 12); the combinations of compression and torsion result in the smallest (Test 11), while pure torsion falls in between (Test 15).

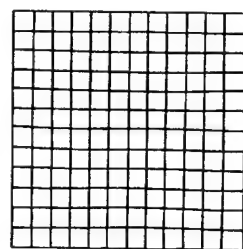
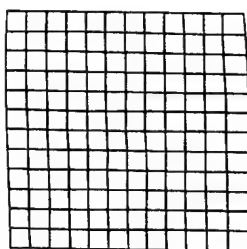
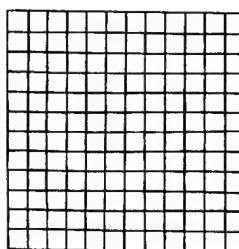
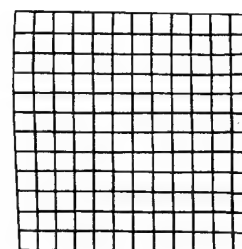
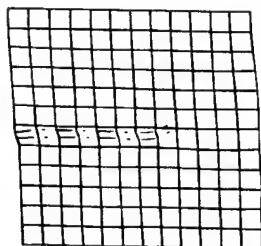
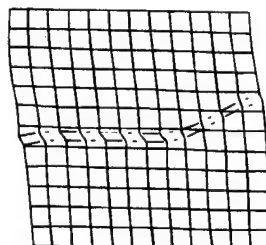
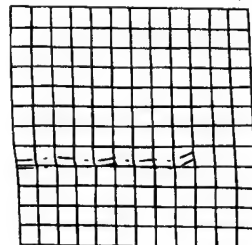
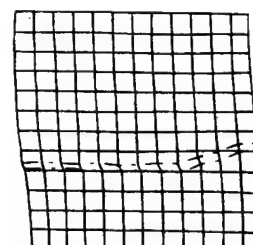
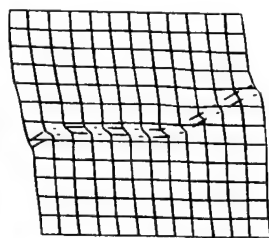
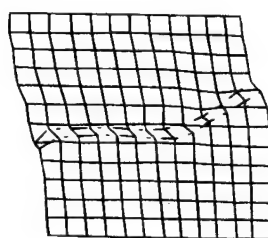
(a) $t = 0$ sec.(b) $t = 585$ sec.(a) $t = 0$ sec.(b) $t = 400$ sec.(c) $t = 1365$ sec.(d) $t = 2304$ sec.(c) $t = 700$ sec.(d) $t = 1200$ sec.(e) $t = 2805$ sec.(f) $t = 3389$ sec.

FIG. 11—A set of meshes for the torsion-compression Test 11.

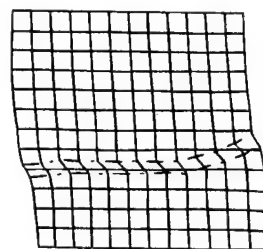
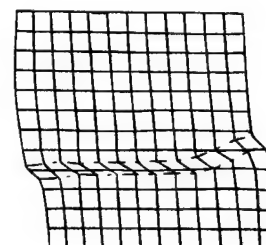
(e) $t = 2000$ sec.(f) $t = 3000$ sec.

FIG. 12—A set of meshes for the pure torsion Test 15.

The tests listed in Table 4 were conducted without a Teflon discontinuity. They showed that the shear band appeared in the vicinity of the peak stress and that once formed it had the same direction and properties as the one initiated due to the presence of the discontinuity. As a result of these observations, the rest of the experimental program is now being conducted without the Teflon insert.

It is interesting to compare the measurements made on sand and clay specimens. Test 15 on sand (Table 3) and Test 6v-9-26-90 (refer to Saada et al. 1994a) on EPK clay were chosen for comparison. Both tests have the same specimen configuration and loading path, i.e., β is the same. However, the initial consolidation pressure is different, the former being 172.4 kPa (25 psi) while the latter is 344.8 kPa (50 psi). The digitized grids after the development of the shear bands are plotted in Fig. 21 for both tests. Notice that there is only one shear band in the sand specimen. This is true for all the tests conducted on sand materials. The clay, on the other hand, has one main band and others that spring from it before it is fully developed. The shear bands in sand are also thicker than their counterpart in clay. This is due to the grain size and the mechanism of dilation involved in both materials.

Summary and Conclusions

A new technique has been developed to measure deformations in the vicinity of and within shear bands. It involves sample prepa-

ration, video imaging, and image analysis. The technique was applied to sand materials. It has the following advantages:

1. It provides an effective, low-cost and non-invasive way to monitor the development of shear bands and measure their characteristics, such as orientation, rate of propagation, and size.
2. It allows researchers to separate local deformation from global deformation in a specimen subjected to a strength test.
3. The information, which includes images and digitized grids, is saved in digital form. This makes it easy to manipulate and use for any purpose including the validation of constitutive laws.
4. With the present setup, the maximum error in measuring length is 0.23 mm. This is close to D_{50} of the material used (0.26 mm). Under the present circumstances, such accuracy is considered excellent and can still be improved with better equipment.

When a shear band appears in a sand specimen, the deformation within the shear band is different from the global one. For sand specimens with the same configuration, density, and confining pressure, the initiation, orientation, and thickness of the shear bands depend on the loading path, i.e., on β . The change in thickness results from both a dilation phenomenon and the spreading of the plastic deformation zone associated with the bands.

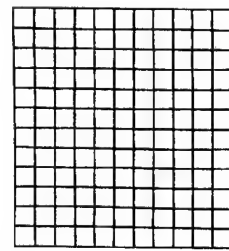
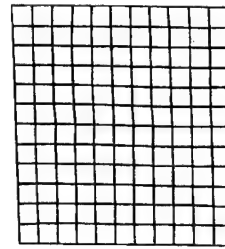
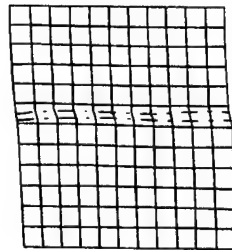
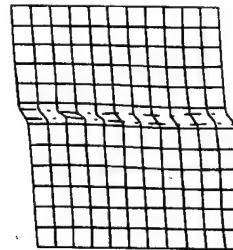
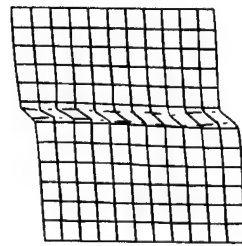
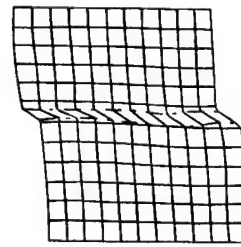
(a) $t = 0$ sec.(b) $t = 570$ sec.(c) $t = 1000$ sec.(d) $t = 2000$ sec.(e) $t = 2600$ sec.(f) $t = 3000$ sec.

FIG. 13—A set of meshes for the torsion-extension Test 12.

TABLE 6—Summary of the observations made during the shear bands development.

Test	t_1 (s)	t_2 (s)	τ_{oct} (kPa)	$\tau_{oct}/\text{final } \tau_{oct}$ (%)	Orientation (degree)	Averaged Thickness (mm)	
						h_1	h_2
11	585	1365	118.6	90%	28	2.66	3.33
15	400	700	101.2	87%	19	4.02	5.17
12	300	570	84.7	87%	1.4	3.82	5.43

Where: t_1 = the time when slippage starts to show at the discontinuity (Teflon).
 t_2 = the time when the shear band starts to propagate from the tips of the discontinuity.
 h_1 = average thickness of the band formed around the Teflon discontinuity at the end of test.
 h_2 = average thickness of the shear band in the soil at the end of test.

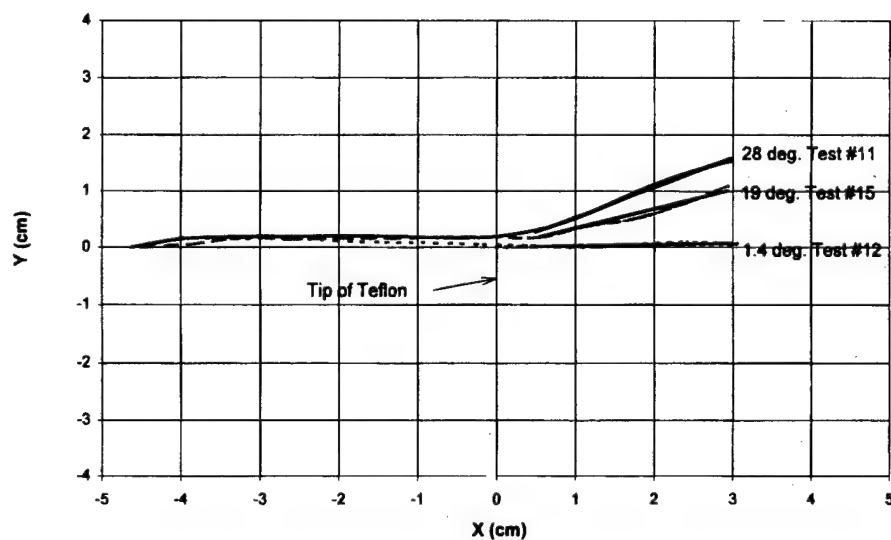


FIG. 14—Center lines of the discontinuity and the shear bands for three different tests.

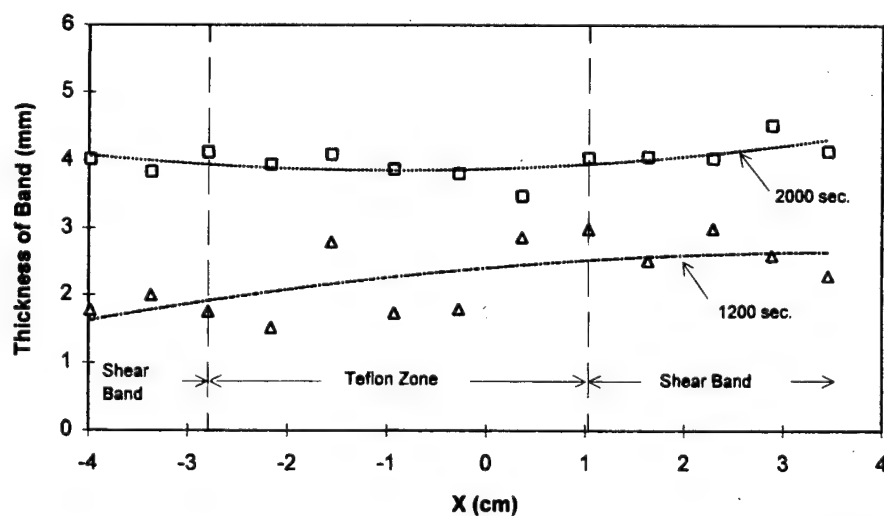


FIG. 15—Thickness of the shear band in the soil and the band around the Teflon at 1200 and 2000 s (Test 15).

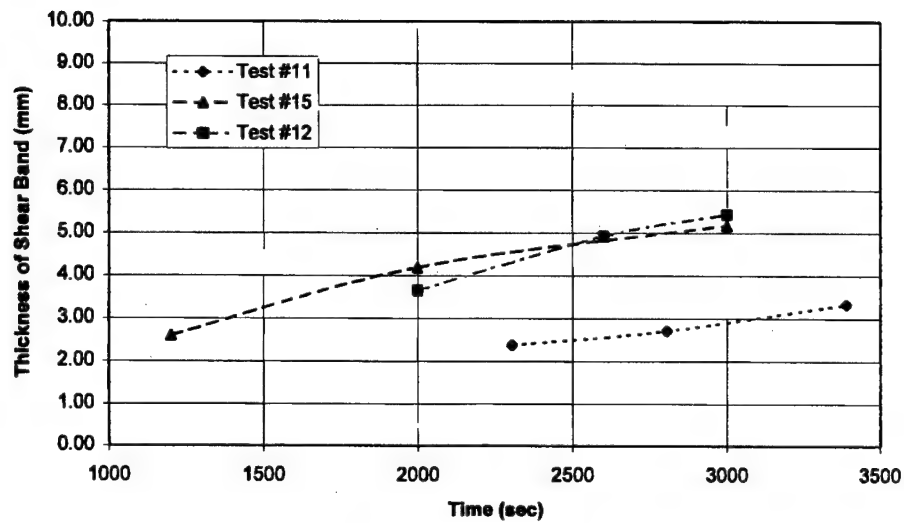


FIG. 16—Variation of thickness of the shear band in the soil.

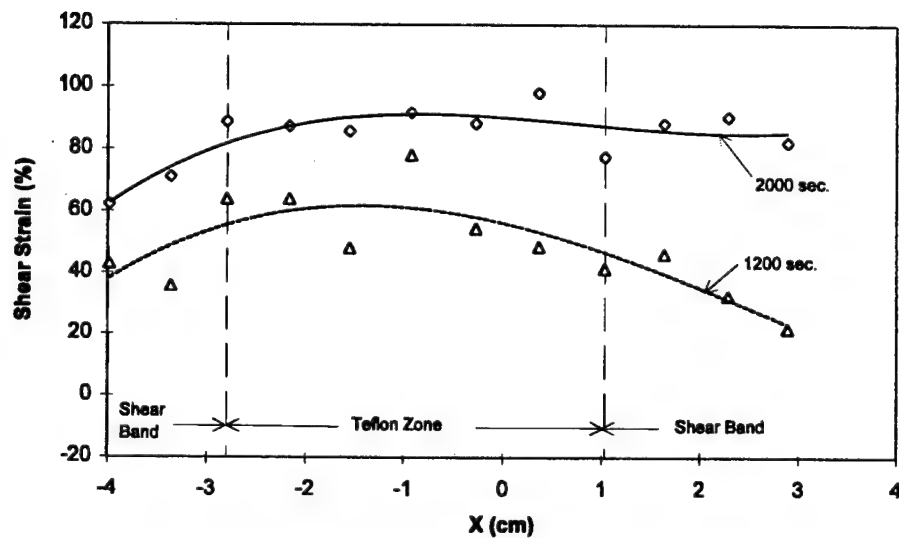


FIG. 17—Shear strain inside the shear band and Teflon zone at 1200 and 2000 s (Test 15).

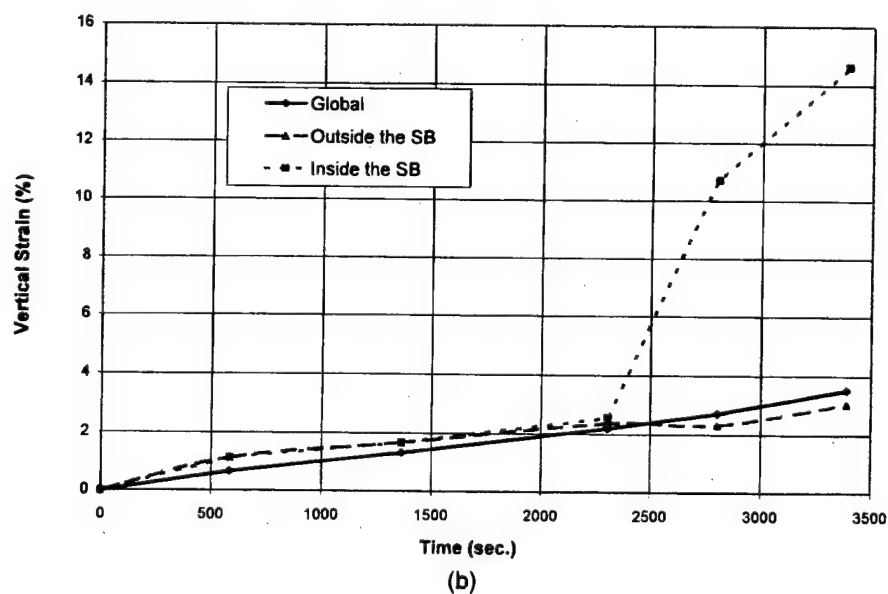
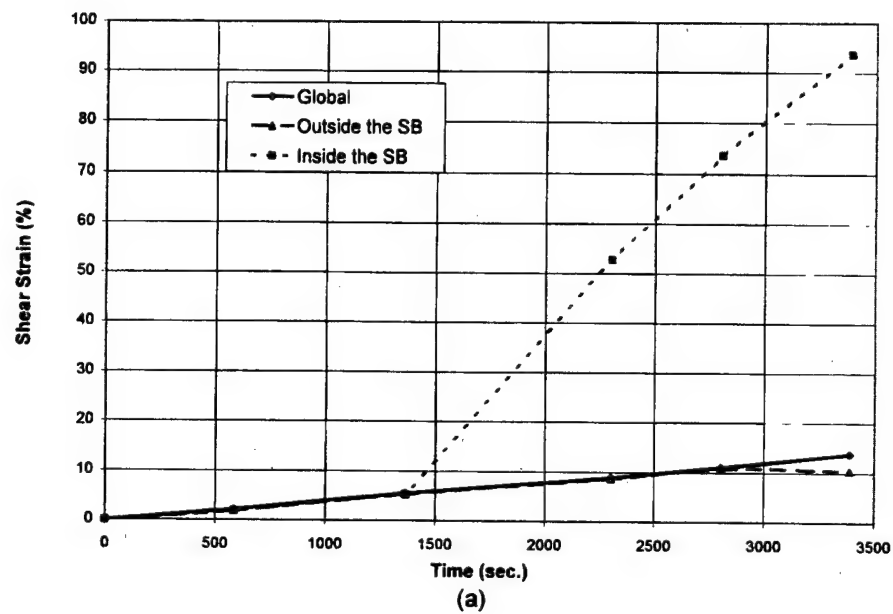


FIG. 18—Strains for the torsion-compression Test 11: (a) shear strains; (b) vertical strains.

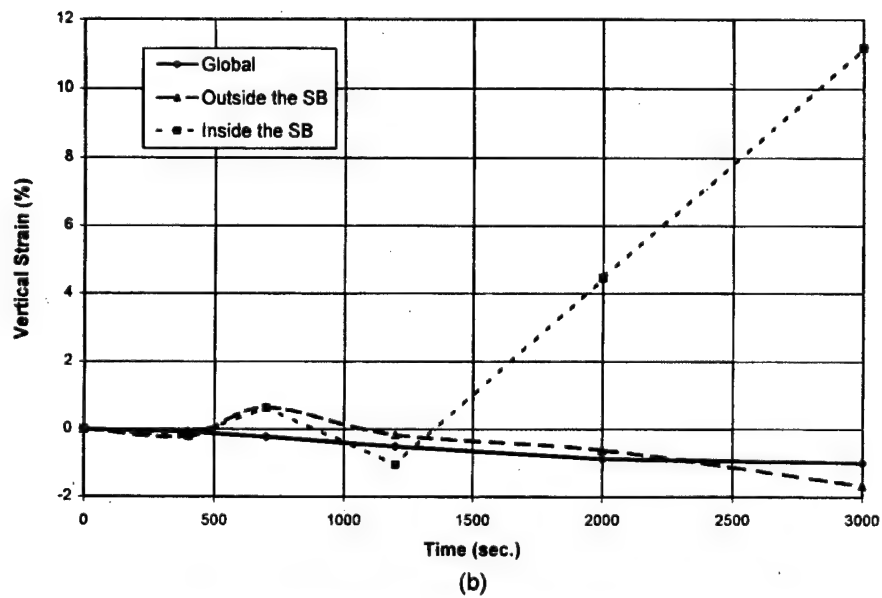
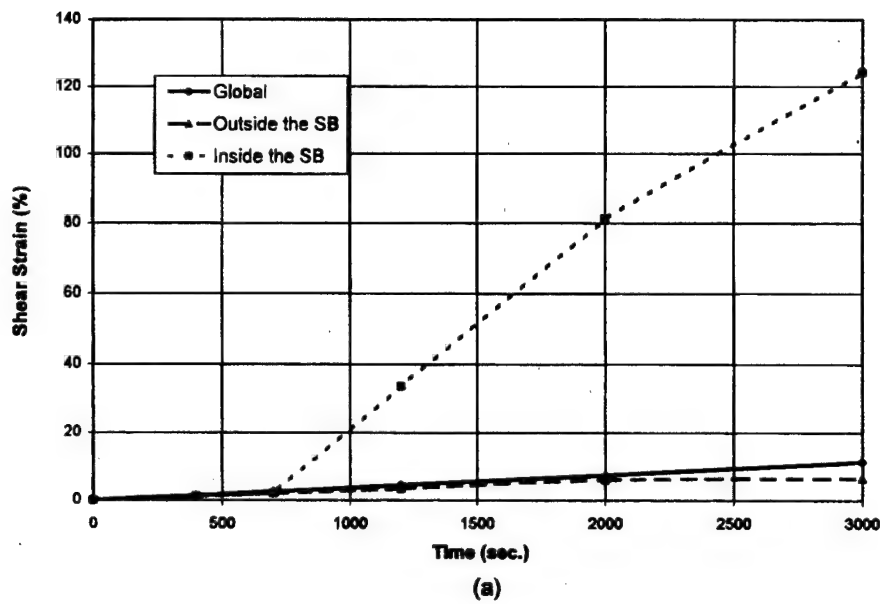


FIG. 19—Strains for the pure-torsion test 15: (a) shear strains; (b) vertical strains.

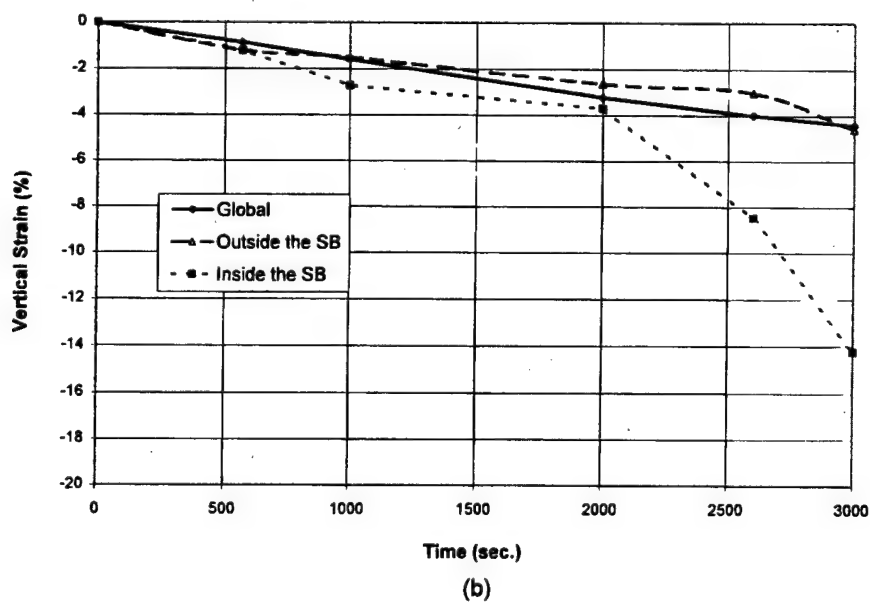
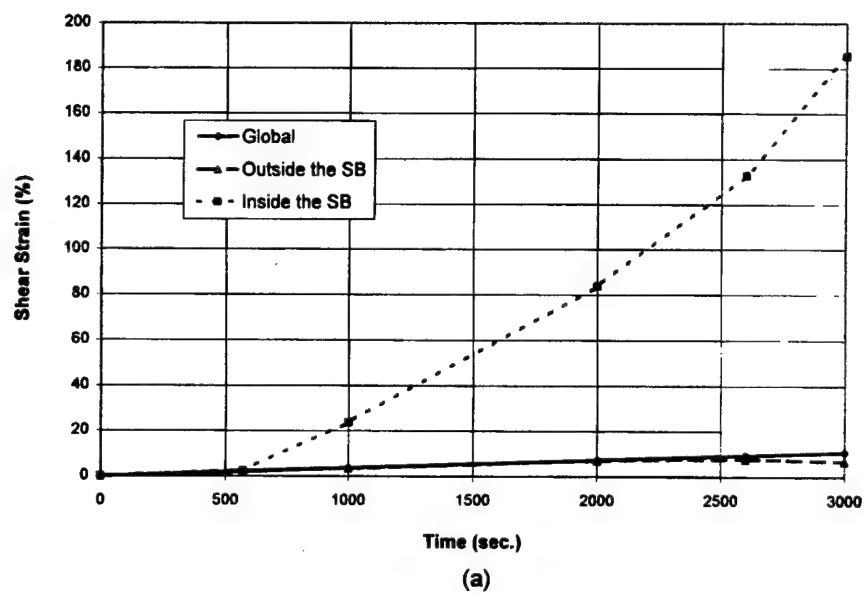
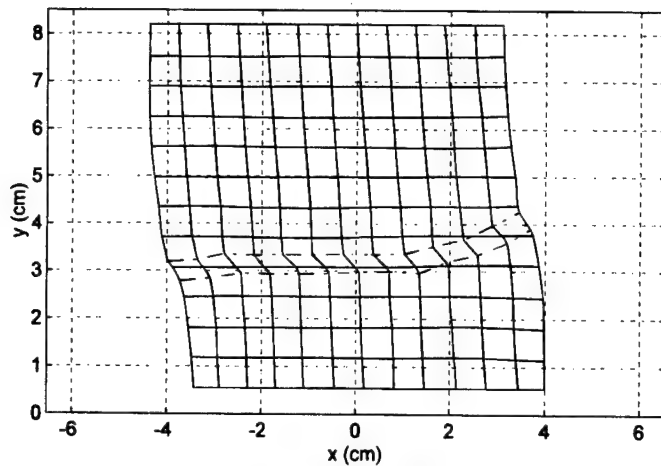
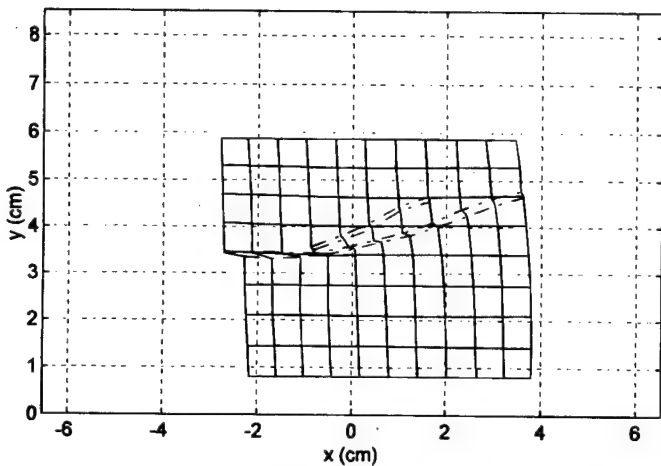


FIG. 20—Strains for the torsion-extension test 12: (a) shear strains; (b) vertical strains.



(a) Test #15, Sand



(b) 6v_9_26_90, Clay

FIG. 21—Shear bands for the pure torsion tests on (a) sand and (b) clay.

Acknowledgments

The research reported in this paper is part of a larger project on shear bands formation and propagation under the sponsorship

of the Air Force Office of Scientific Research. The authors wish to thank the Air Force and Dr. M. D. Lewis, the program manager responsible for starting this project.

References

- Acosta, J. A., Figueroa, J. L., and Mullen, R. L., 1992, "A Low Cost Video Image Processing System for Evaluating Pavement Surface Distress," Transportation Research Record 1348, Transportation Research Board, National Academy of Sciences, Washington, DC, pp. 63–72.
- Arthur, J. R. F. and Dunstan, T., 1982, "Rupture Layers in Granular Media," *Proceedings, IUTAM Conference on Deformation and Failure of Granular Materials*, Delft, Netherlands, P. A. Vermeer and H. L. Luger, published by A. A. Balkema, pp. 453–459.
- Desrues, J., 1983, "Localization de la Deformation Dans Les Milieux Granulaires," thesis presented to the University of Grenoble in partial fulfillment of the requirements for the degree of Doctor of Philosophy.
- Gustafsson, L. and Knutsson, S., 1994, "An Image Analysis Method for Studying Movements in Granular and Solid Bodies," *Geotechnical Testing Journal*, GTJODJ, Vol. 17, No. 1, March, pp. 95–100.
- Harris, W. W., Viggiani, G., Mooney, M., and Finno, R. J., 1995, "Use of Stereophotogrammetry to Analyze the Development of Shear Bands in Sand," *Geotechnical Testing Journal*, GTJODJ, Vol. 18, No. 4, December, pp. 405–420.
- Hight, D. W., Gens, A., and Symes, M. J., 1983, "The Development of a New Hollow Cylinder Apparatus for Investigating the Effects of Principal Stress Rotation in Soils," *Geotechnique*, Vol. 33, No. 4, pp. 355–383.
- Papamichos, E. and Vardoulakis, I., 1995, "Shear Band Formation in Sand According to Non-coaxial Plasticity Model," *Géotechnique*, Vol. 45, No. 4, pp. 649–661.
- Saada, A. S., 1988, "State of the Art—Hollow Cylinder Torsional Devices: Their Advantages and Limitations," *Advanced Triaxial Testing of Soil and Rock*, ASTM STP 977, R. T. Donaghe, R. C. Chaney, and M. L. Silver, Eds., ASTM, West Conshohocken, PA, pp. 766–795.
- Saada, A. S. and Townsend, F. C., 1981, "State of the Art: Laboratory Strength Testing of Soils," *Laboratory Shear Strength of Soil*, ASTM STP 740, ASTM, West Conshohocken, PA.
- Saada, A. S., Bianchini, G. F., and Liang, L., 1994, "Cracks, Bifurcation and Shear Bands Propagation in Saturated Clays," *Géotechnique*, Vol. 44, No. 1, pp. 35–64.
- Scarpelli, G. and Wood, D. M., 1982, "Experimental Observations of Shear Band Pattern in Direct Shear Tests," *Proceedings, IUTAM Conference on Deformation and Failure of Granular Materials*, Delft, published by A. A. Balkema, pp. 473–484.
- Tatsuoka, F., Nakamura, S., Huang, C.-C., and Tani, K., 1990, "Strength Anisotropy and Shear Band Direction in Plane Strain Tests of Sand," *Soils and Foundations*, Vol. 30, No. 1, pp. 35–54.
- Yoshida, T., Tatsuoka, F., Siddiquee, M. S. A., Kamegai, Y., and Park, C.-S., 1994, "Shear Banding in Sands Observed in Plane Strain Compression," *Localisation and Bifurcation Theory for Soils and Rocks*, R. Chambon, J. Desrues, and I. Vardoulakis, Eds., Balkema, Rotterdam, pp. 165–179.

PAPER 2 --- ON SANDS

(LSI - 30 Sand)

BIFURCATION AND SHEAR BAND PROPAGATION IN SANDS

by

A.S. Saada¹, L. Liang², J.L. Figueroa³ and C.T. Cope⁴

¹Frank H. Neff Professor and Chairman, Department of Civil Engineering, Case School of Engineering, Case Western Reserve University, Cleveland, Ohio.

²Research Associate, Department of Civil Engineering, Case School of Engineering, Case Western Reserve University, Cleveland, Ohio.

³Professor of Civil Engineering, Department of Civil Engineering, Case School of Engineering, Case Western Reserve University, Cleveland, Ohio.

⁴Graduate Student, Department of Civil Engineering, Case School of Engineering, Case Western Reserve University, Cleveland, Ohio.

ABSTRACT

Under simple or combined stresses homogeneous sand specimens exhibit localization of deformation followed by shear band formation. This phenomenon has been extensively studied under plane strain loading conditions. This paper studies the initiation and propagation of the shear bands that develop in thin long hollow cylinders of sand subjected to a combination of axial torsional and spherical stresses. Digital image processing techniques are used to observe and measure the displacements and the initiation and development of the shear bands. The effects of the inclination of the principal stresses on the axis of symmetry, the relative density, the confining pressure and granulometry are examined. Strain measurements within the shear bands open the door to a more complete description of the mechanical behavior of the material, in particular beyond the peak, in the so called strain softening zone.

NOTATION

b	=	$(\sigma_2 - \sigma_3) / (\sigma_1 - \sigma_3)$
D_r	=	Relative density
α_{ob}	=	Observed inclination of the shear band
α_C	=	Inclination of the shear band (Coulomb)
α_R	=	Inclination of the shear band (Roscoe)
α_{AV}	=	Inclination of the shear band (Arthur-Vardoulakis)
β	=	Inclination of the major principal stress on the vertice
$\delta_C, \delta_R, \delta_{ob}$	=	Inclination of the shear band with the horizontal direction
$\dot{\epsilon}_1, \dot{\epsilon}_2, \dot{\epsilon}_3$	=	Principal strains increments
ϵ_v	=	Volumetric strain
ϕ'	=	Angle of friction in terms of effective stresses
σ'_C	=	Initial consolidation effective stress
σ'_m	=	Mean effective stress
$\sigma_1, \sigma_2, \sigma_3$	=	Principal Stress
τ_{oct}	=	Octahedral shearing stress
ψ	=	Angle of dilation

INTRODUCTION

The interest in the phenomenon of bifurcation and shear banding in granular soils, started with Coulomb. Hansen (1958) introduced the angle of dilation v (or dilatancy ψ) and Roscoe (1970) using a plastic flow rule implying the coaxiality of principal stresses and strain rates concluded that one should think of the failure surfaces (in other words of the shear bands) as being formed of zero extension lines rather than planes of maximum stress ratio. Thus the shear bands would make an angle $(45 - \psi/2)$ with the major principal stress σ_1 , rather than the $(45 - \phi'/2)$ of Coulomb; ϕ' being the angle of internal friction. Arthur et al. (1977) using directional shear tests later found that the shear bands had an inclination that fell between the values suggested by Coulomb and Roscoe.

Shear band initiation and propagation have been theoretically and experimentally investigated by a number of researchers with the main thrust provided by J. Desrues and his colleagues at the University of Grenoble and I. Vardoulakis and his colleagues, first at the University of Minnesota and then at the University of Athens. Researchers from other institutions have made contributions just as important, but the groups above have shown remarkable continuity in their focus on this subject. Let us mention at this point four recent publications that contain extensive lists of references dealing with shear banding. The interested reader can look such lists up for a complete coverage of this topic:

- 1) "Cracks, bifurcation and shear bands propagation in saturated clay" by A.

Saada, G. Bianchini and L. Liang (1994). This paper has a comprehensive literature review.

- 2) "Shear band formation in sand according to non-coaxial plasticity model" by E. Papamichou and I. Vardoulakis (1995).
- 3) "Strain localization and undrained steady state of sand" by R. Finno, W. Harris, M. Mooney and G. Viggiani (1996).
- 4) "Effect of shear band formation in triaxial extension tests" by P. Lade, J. Yamamuro and B. Skyers (1996).

In addition, the IUTAM proceedings of the Conference on Deformation and Failure of Granular Materials (1982) have a section on shear band formation with papers by J. Arthur and T. Dunstan (1982), G. Scarpelli and D. Wood (1982) and P. Vermeer (1982); all related to the present work. T. Schanz and P. Vermeer (1996) related the angle of dilatancy to triaxial strain conditions. More reference will be given as we proceed with this study; and again, each has its own list of publications that could be of direct interest to the reader.

Most, if not all the studies conducted on sands used plane strain devices to observe the initiation and direction of propagation of the shear bands. A few tests were conducted in a classical triaxial apparatus as well as in cubical ones; each having its own advantages and drawbacks. Stereophotogrammetry, whose use was pioneered by Desrues and his team, was also used by Finno and his coworkers to measure the displacements within the shear bands in the plane strain device of Vardoulakis.

In this study, thin, long hollow cylinders of sand are subjected to combinations of axial, torsional and spherical stresses, and the initiation and propagation of shear bands are observed. Relative displacements and strains around and within the dominant shear band are measured and calculated. The influence of density, confining stresses, direction of principal stresses and granulometry are noted. This study is a continuation of the

investigation conducted on clay within the frame work of the particulate mechanics program of the Air Force Office of Scientific Research. It seems to be the first in which torsion was used to observe in detail shear banding in sands.

EXPERIMENTAL PROGRAM

Some experimental techniques developed for studying shear banding in thin hollow cylinders are presented by Liang et al. (1997). They are detailed and expanded on in the following sections.

a) Loading and Data Acquisition Systems

In order to observe the initiation and propagation of shear bands the tests on hollow cylinders had to be conducted in a controlled deformation mode. The loading system was such that the axial stresses were applied by a piston that could only move in the vertical direction in a cell attached to a rotating base. The resulting torque was measured by a transducer inside the cell and multiplied by the proper coefficient to yield the axial force which must be applied to maintain a constant inclination β of the major principal stress on the axis of symmetry. The intermediate principal stress is the cell pressure which could be changed at will to obtain the desired mean stress. A number of values of

$$b = \frac{\sigma_2 - \sigma_3}{\sigma_1 - \sigma_3} = \sin^2 \beta$$
 were thus obtained and observations made for each of them. The

whole operation which was computer controlled and electro-pneumatically driven was smoothly accomplished with excellent accuracy.

Photographs and video images were taken during the tests. Fig. 1 shows the schematic of the test monitoring setup. The solid lines are related to the data acquisition and loading control paths, while the dashed lines represent the image recording circuits. The control panel monitors the conversions of electrical signals to pneumatic signals. These signals are sent to the force actuators and the confining cell. The four video cameras

are arranged so as to cover the full specimen surface. They are pointed towards the axis of the specimen with the center of their lenses at the same horizontal level as its midheight.

b) Preparation of Sand Specimens and Testing Program

The sand selected for this investigation is known as LSI-30. It is sold by Lonestar Industries of Oakland, California under the name Lapis Lustre Dried Sand-LSI-30. Previous research conducted at Case Western Reserve University used Reid Bedford sand whose properties have been extensively studied (Saada and Bianchini, 1987). Indeed Liang et al. (1997) used it to do the preliminary work for the present investigation. It is however no longer available. LSI-30 does not differ much from Reid Bedford sand. It is clean, poorly graded, angular grained and has a specific gravity of 2.66. Its maximum and minimum void ratios are 0.83 and 0.52 respectively and its $D_{50} = 0.039$ cm. Fig. 2 shows its grain size distribution. The specimen configuration is shown in Fig. 3a. The dogbone shape helped minimize the end effects.

Specimens were prepared at two relative densities; namely 50 and 80 percent and tested at three different values of mean stress, namely 207, 345, and 483 kPa. The tests in which the mean stress is kept constant are referred to as "Generalized" and necessitate that the axial and lateral stresses be changed during the test. If on the other hand the cell pressure remains constant, the mean stress will change as the specimen is stressed in the axial direction. Such tests are called "Direct". The tests reported in this paper are mostly of the generalized type with the stress paths remaining on the π plane. The tests were relatively slow with torsional strains applied at the rate of 0.23% per minute with the appropriate axial stress and cell pressure automatically applied to maintain a constant b or β .

Some remarks have to be made regarding the chronology of the tests: At the outset of this experimental program it was thought that a discontinuity (Saada et al. 1994) would be needed to initiate bifurcation. After a number of tests, it was noticed that this was not the case (Liang et al. 1997) and that a dominant shear band would develop on its own at a certain stress level provided the influence of the boundaries was reduced to a minimum through the adoption of a dogbone shape. A first series of tests was conducted with the aim of observing initiation and propagation of shear bands but in which no volume changes were measured. This was followed by a second series using similar specimens and stress paths but in which volume changes were measured.

Table 1 lists all the tests conducted in this program. σ'_c is the initial cell pressure minus the initial back pressure, often referred to as the effective cell pressure ECP. Since all the tests were drained this value remains constant in direct tests, but changes in generalized tests to maintain the mean effective stress constant. The column labeled "volume change" identifies the test in which such measurements were made; in other words the tests for which a dilation angle can be calculated.

c) Digital Image Processing and Deformation Measurements

The local deformations of the sand can be followed by taking a series of photographs at various stages of the experiment. However to recognize the path of specific points, a grid was imprinted on the surface of the specimen as done by Saada et al. (1994) for clays. A freezing technique described by Liang et al. (1997) had to be developed to imprint 0.63 cm squares on the soil particles; a grid on the membrane having proven to be unsatisfactory.

Selected images were taken by the four digital cameras with the switch box (Fig. 1) controlling the sequence of shots at time intervals of about 30 seconds between series of four shots. In addition a VCR was used to continuously record various stages of the tests and a photographic camera was used as a back up in case of malfunction or when specific views were needed.

The digital images were displayed on a high resolution monitor and the coordinates of the grid were digitized and saved. Distances measured on the images involve the distortions caused by refractions through a number of media as well as those caused by the projection of lines drawn on a circular surface.

Fig. 3b shows the relation between a length S measured on the specimen and the distance L measured on a plane, ignoring refraction effects:

$$S = R \sin^{-1} \frac{L}{R} \quad (1)$$

To include the effects of refraction a photograph of the specimen is taken after it has been placed inside the cell and pressurized; the confining liquid being silicon oil. This is the reference photograph prior to the application of any deviation to the specimen. The true length S along the grid is known to be 0.635 cm and the length L is measured on the image. The distances are measured in pixels and transformed to inches or centimeters. The grid has 13 horizontal lines intersecting with a number of vertical lines (say 7 for the example used) forming squares of 0.635 x 0.635 cm. A 13 x 7 matrix can thus be generated giving the x and y coordinates of the nodes as they appear on the screen; the true distance between the nodes being 0.635 cm. A calibration curve giving S as a function of L can be drawn for each camera. For example the calibration curve for test 43 (camera 2) which is a pure

torsion test with $\sigma'_c = 345$ kPa and a relative density of 80 percent is shown in Fig. 4. This curve is approximated by a polynomial of the second to the fourth degree which is then used to obtain real lengths from lengths measured on the image. In this case the polynomial is

$$S = -0.011156 + 0.977054L + 0.125584L^2 - 0.085549L^3 + 0.023024L^4 \quad (2)$$

Because of the smallness of the angles of incidence, the relative radii of the plexiglas cell and the specimen, as well as the refractive properties of the plexiglas and the confining silicon oil, it was found that for reasonably small values of S the results of equations (1) and (2) were nearly identical. The polynomial was used in all cases.

Because of the distortion caused by refraction, the horizontal lines of the grid, when viewed on the screen, are convex or concave depending on whether they are above or below the center of the camera lens. Thus, adjustments must be made in the vertical direction to eliminate their curvature. Fig. 5 shows this correction. All the nodes are moved proportionally downwards or upwards. Indeed the configuration of the specimen and the rigidity of the end platens forces those lines that are initially horizontal to remain horizontal. The calibration is quite satisfactory. An accuracy check is continuously conducted on each specimen during each test by comparing the displacements measured optically by this procedure and those measured by various transducers. For example, Fig. 6 compares the shear strain measured electrically with an RVDT and that measured through image processing. The agreement is excellent up to about 4 to 5 percent of global octahedral shear strain. It is believed that the shear band started forming at that point.

As a shear band forms, points on both its sides are digitized and their displacements are determined. The points between grid lines are obtained by interpolation.

It was mentioned above that the distances are measured in terms of pixels. There are 28 pixels per 0.635 cm. Thus each pixel corresponds to 0.023 cm and the thickness of each line of the grid is about 4 pixels. Referring to Fig. 7, pixels 1 and 4 have a lower gray level index value than pixels 2 and 3 (lighter in color). Since the operation is manual one picks either pixel 2 or 3 and the possibility of an error of 1 pixel is present; leading to an error of 3.6 percent. Using a polynomial curve fitting one can easily show that this error can be reduced to 2 percent. When shear bands appear, measurements are separately made above and below the shear band.

By placing the images of the four cameras side by side one can observe the deformation, the bifurcation into a dominant shear band and the propagation pattern of the band (Fig. 8). The digital nature of the data allows one to calculate relative deformations and strains in the vicinity as well as within the dominant shear band by comparing (superimposing) the images taken at various time intervals to that taken at a time $t = 0$. Constitutive equations can be developed to predict the onset of the dominant shear band, the global behavior as well as the local behavior of the soil. Such equations would be able to take into account the influence of the granulometric distribution, the mean or confining stress, the relative density, the stress paths, as well as other variables that influence the response of the sand.

Shear bands start at a point and propagate with varying strains along their length. Digitization allows one to obtain the average strain along the band up to that point in time. Once the band extends all around the specimen and failure is incipient, the thickness of the band becomes uniform; and within the band one is approaching the critical state.

DIRECTION OF THE SHEAR BANDS AND DETERMINATION OF THE ANGLE OF DILATION

a) Shearing Surfaces and Shearing Bands

It is appropriate at this point to identify what is meant by shear or slip surfaces and by shear bands. In a granular material such as sand irreversible plastic deformations take place even under very small stresses. The particles move with respect to each other along thin surfaces that appear as lines on the body of the specimen. The placement of a grid on the particles themselves allow one to see such lines early in the experiment. In Fig. 9 black lines have been drawn along slip planes clearly seen during the experiment and easily identified by the slight kink that develop on the grid lines. Their number and distribution is an indication of the homogeneity of the specimen. Localization will take place when the deformation bifurcates from a homogeneous mode to a mode localized on one or several close groups of surfaces that coalesce and result in what is referred to as dominant shear bands. The word band is used because of the thickness of the zones involved and their change in size as the specimen deforms. Localization starts at a point from which a dominant shear band will propagate. In the absence of a boundary to hinder its advance, it will travel all around the hollow cylinder. As will be shown later, this complete localization occurs around the peak stress as one moves toward the critical state. Beyond this point most of the deformation occurs through near rigid body motion of one part of the specimen with respect to the other. The band may increase or decrease in thickness as new sand particles are incorporated into it or migrate out. There may be a small elastic rebound within the moving blocks during stress relaxation as all the deformation takes place within

the bands. Because of this kind of motion, lines within the shear bands were considered as lines of zero extension and their direction identified as directions of propagation of the shear bands. Bolton (1986) gives a clear illustration of the geometry involved under conditions of direct shear.

b) Direction of the Shear Bands

As stated by Zitouni (1988) the direction of a dominant shear band, or just of a shear band can be arrived at either through considerations based on the state of stress (statics) or considerations based on the state of deformation (kinematics).

Traditionally the approach based on statics assumes that the Coulomb plasticity criterion is valid and that the bands would develop in a direction making the angle $\alpha_C = 45 - \phi/2$ with that of the major principal stress. It is assumed that the intermediate principal stress has no influence on the plastic behavior of the material. Fig. 10a shows the Mohr representation used in this approach. The point M gives the magnitude of the normal and shearing stress on planes along the shear bands. The fact that σ_2 is ignored does not necessarily mean that we have a plane stress or a plane strain behavior.

The approach based on kinematics assumes that the shear bands fall in a principal plane along lines where the rate of extension is equal to zero. On Mohr's circle the direction of no extension is given by the angle α_R (Fig. 10b). Thus the bands would develop in a direction making an angle $\alpha_R = 45 - \psi/2$ with that of the major principal strain increment.

The angle ψ is given by

$$\sin \psi = - \frac{\left(\frac{\dot{\epsilon}_1}{\dot{\epsilon}_3} \right)_{max} + 1}{\left(\frac{\dot{\epsilon}_1}{\dot{\epsilon}_3} \right)_{max} - 1} = - \frac{\dot{\epsilon}_1 + \dot{\epsilon}_3}{\dot{\epsilon}_1 - \dot{\epsilon}_3} \quad (3)$$

This angle is used to characterize the orientation of the shear band in the plane of $d\epsilon_1, d\epsilon_3$. Notice that when $\dot{\epsilon}_1 + \dot{\epsilon}_3$ is positive ψ is negative and vice versa.

The angle ψ is often called angle of dilation. This name, which implies a change in volume, is only justified under conditions of plane strain. Indeed, in Fig. 10b, the distance OA does not represent $\dot{\epsilon}_v/2$ (Bolton, 1986) unless $\dot{\epsilon}_2 = 0$. Another approach resulting from the work of Arthur et al. (1977,1982) and supported by Vardoulakis (1980) is to use a combination of the two previous ones. In this case

$$\alpha_{AV} = \pi/4 - 1/4(\phi' + \psi) \quad (4)$$

Koender et al. (1990) introduced the effect of the grain size and suggest that for coarse sands Roscoe's expression is the one to use while Coulomb's one was more appropriate for fine sands. Houlsby (1991) suggests a generalized equation for the calculation of ψ , namely:

$$1/2 \sin^2 \psi = \frac{(\dot{\epsilon}_1 + \dot{\epsilon}_2 + \dot{\epsilon}_3)^2}{(\dot{\epsilon}_1 - \dot{\epsilon}_2)^2 + (\dot{\epsilon}_2 - \dot{\epsilon}_3)^2 + (\dot{\epsilon}_3 - \dot{\epsilon}_1)^2} \quad (5)$$

The value of ψ obtained from these equations could be used by itself or in combination with ϕ' in any of the values of α_R or α_{AV} . The angle of dilation was calculated using measurements that led to the values of ϵ_1 and ϵ_3 . Values of ψ were obtained when the initiation of the dominant shear band was first observed as well as at the peaks of the strength curves when this band completely surrounded the specimen. Notice that the peak occurs at the point of inflexion of the curve giving the volume change versus ϵ_1 . The two

points were close to each other. The angle ψ was also calculated by the method used by Zitouni (1988). This method is based on the formula

$$\sin \psi = - \frac{1 + \frac{\dot{\epsilon}_3}{\dot{\epsilon}_1}}{1 - \frac{\dot{\epsilon}_3}{\dot{\epsilon}_1}} = - \frac{1 - \tan \theta}{1 + \tan \theta} = \tan \left(\theta - \frac{\pi}{4} \right) \quad (6)$$

and θ given by the slope of the line AB in a plot of ϵ_1 versus ϵ_3 (Fig. 11). Localization is supposed to take place where the linear part of the curve stops. In our case this is close to the peaks. Figs. 12a, b, c show such plots for three of the tests listed in Table II. Also plotted on the same figure is a curve showing τ_{oct} versus ϵ_1 . Notice that there are no sharp breaks to pinpoint exactly the instant at which the dominant shear band surrounds the specimen. One can chose the maximum of the $\dot{\epsilon}_1/\dot{\epsilon}_3$ curve to determine this point. Such graphical representations were used to cross check the accuracy of the calculations.

c) Experimental Observations

In the tests for which no volume changes were measured, the directions of the shear bands could only be compared to the predictions of Coulomb, $\alpha_c = \frac{\pi}{4} - \frac{\phi'}{2}$.

Fig. 8 shows a typical appearance of a dominant shear band and its propagation around the specimen in a pure torsion test. In all the tests the band appeared slightly before the peak of the stress strain curve and completed its propagation at the peak or slightly beyond it. It is well known that the angle ϕ' changes with the direction of the principal stresses so that one can use various values of ϕ' in the expression of Coulomb. The angle ϕ' obtained from axially symmetric compression tests gives results that are the closest to the observed ones. Figs. 13 show a comparison of observed and predicted directions for tests 37 to 39 with a

mean stress of 207 kPa, tests 42 to 44 with a mean stress of 345 kPa, 47 to 49 with a mean stress of 483 kPa and 52 to 54 with a mean stress of 207 kPa. Each of the graphs has predictions based on ϕ' obtained from both compression and torsion tests.

The tests in which volume changes were measured allow one to obtain values of the dilatancy angle ψ and thus test the validity of the other approaches leading to α . One could chose the angle of friction obtained from compression or the one obtained from pure torsion; the latter being the closest to plain strain. ψ could be determined in a similar way ignoring the intermediate principal strain without necessarily being in plane strain. This would be consistent with the use of Mohr's Circle for stress. The best correlation was obtained using in all cases an angle of friction obtained from pure torsion tests and $\psi = \psi_{\max}$ obtained from Eq. 3; the two values being averaged as suggested by Arthur et al. (1977,1982) and Vardoulakis (1980) in the expression $\alpha_{AV} = \pi/4 - 1/4(\phi' + \psi)$.

Table II shows the value of the observed inclination with the horizontal δ_{ob} as well as the one predicted in the manner suggested above, i.e. with $\phi' = \phi'_{tor}$ and $\psi = \psi_{\max}$. No values of δ are given for compression and extension tests, i.e. for tests with $\beta = 0$ and 90° . Those tests did not exhibit clear shear bands whose directions could be followed in an accurate fashion. Notice that α is related to δ according to $\delta = \frac{\pi}{2} - (\beta + \alpha)$. In Fig. 14 the results of 12 tests all of the generalized type are presented together for a global view of which of the theories fits best the observed inclinations of the shear bands. Lines showing the best linear fit indicate that the Arthur Vardoulakis prediction is the closest to the observed values.

d) Influence of the Mean Stress

The influence of the mean stress on the observed inclination of the shear bands can also be seen on Fig. 15. where the results of tests conducted on sets of specimens without measurements of volume change are shown. This influence seems to be quite small. A comparison was made between generalized and direct tests yielding similar results.

e) Influence of the Density

Fig. 16 shows the observed inclination of the shear bands for two densities and three different mean stresses. Here again, the influence seems to be reasonably small.

RELATIVE NORMAL AND SHEARING DISPLACEMENTS - STRAINS

The grid printed on the specimens and the photographs taken at various stages of the deformation allow one to measure displacements at the nodes of the grid and interpolate in between them. In addition, as a dominant shear band is formed, its width and the relative displacement of its boundaries are measured. This allows one to obtain strains in whatever measure one wants to express them. Large deformations are involved and an engineering definition of strains would not be the ideal one in the development of constitutive relations. However, for the sake of presentation and comparison, this measure of strain in which the relative displacements are referred to the original distance between the points will be used in the various graphs.

Three strains have been calculated based on where the measurements were made, i.e., globally at both ends of the specimen, on the specimen itself (using the grid) on both sides of the dominant shear band, and within the shear band. Figs. 17a, 17b and 17c show the stress strain relations in terms of octahedral variables for three series of three tests each. One series at an effective initial consolidation pressure of 207 kPa and a relative density of 50 percent; one at an effective initial consolidation pressure of 345 kPa and a relative density of 50 percent; one at an effective initial consolidation pressure of 345 kPa and a relative density of 80 percent. Each of the figures has 3 curves corresponding to 3 values of b (or β). The small squares on the curves show the instants at which the photographs were digitized. The process is extremely lengthy and four pictures per test were judged sufficient. As expected, the strength in all cases decreases with the increase of value of b .

Figs. 18 show the change in thickness of the dominant shear band for the three cases above. Notice that the width varies with the value of b and reaches a near constant value as one approaches the critical state. All the tests showed this tendency.

Figs. 19a, 19b and 19c show the near block motion that took place for tests 22, 23 and 24 for values of $b = 0.25, 0.5$ and 0.75 respectively. Such motion occurred between the two times shown on the figures and correspond to the two last little squares shown on the strength curves of Figs. 17. Notice the difference in the inclination of the shear bands and in their width. From a succession of such digitized photographs and figures one can compute the strains in a system of axes along and normal to the dominant shear bands.

Figures 20a, 20b, and 20c show the normal and shearing strains in a system of axes along and normal to the dominant shear band. The global strains refer to measurements made at both ends of the specimen; strains outside the shear band refer to measurements made photographically on the grids, on both sides of the shear band; strains inside the shear band were also obtained photographically. The reference horizontal axis in all those figures is the global octahedral shear strain. The graph in the upper left hand corner of each of those figures is the same as that in Figs. 17 and is repeated here for ease of reference.

It is interesting to examine each of Figs. 20 keeping in mind that the vertical scales are very different from graph to graph. The use of the hollow thin cylinder allows for very large torsional strains that extend close or within the critical state. The strains referred to as global and those measured photographically on both sides of the shear band are extremely close as expected. On the other hand the strains within the dominant shear band start diverging around a value of the global octahedral shearing strain of 5 percent. At this stage one is close to, or beyond the peak, steadily moving towards the critical state.

For all three values of b one notices that the normal strains, normal to the direction of the shear band, decrease (tension is negative). It is appropriate to mention again here that a value of $b = 0.25$ results from a combination of "compression" and torsion, while a value of $b = 0.75$ results from a combination of "extension" and torsion. Such a behavior can also be seen in Figs. 18.

The normal strain, along the direction of the shear band also increases for all three values of b , even though it is more pronounced for $b = 0.25$ and $b = 0.5$ than it is for $b = 0.75$. Thus, the combination of extension and torsion creates a condition closer to the "no extension hypothesis" presumed to take place along the shear band. However, such a hypothesis cannot be supported by the present results up to a global octahedral shear strain of about 15 percent. Similar results were obtained for the rest of the tests conducted at the other effective mean stresses and at the higher density.

SUMMARY AND CONCLUSIONS

A technique based on digital image processing was developed and used to study initiation and propagation of shear bands in sand soils. Observations backed by photographic records indicate that, for the materials tested a dominant shear band is initiated in the vicinity of the peak strength and fully develops as one moves towards the critical state. The inclination of the band appears to depend on both the effective angle of friction and the angle of dilation in a combination given by Arthur and Vardoulakis. Changes in confining pressure and density do not seem to have much influence on the inclination of the bands on the major principal plane.

It is not possible to assign a fixed thickness to the dominant shear band while it is developing. It constantly varies and new particles are continuously added as it propagates as well as after its full development. The thickness also varies with the inclination of the principal stresses, i.e., with the value of b , the confining pressure and the density of the materials. The effects of grain size distribution is presently being studied and preliminary results indicate the same trends presented above.

Measurements of strains outside and within the shear bands show that the condition of no extension does not develop in the shear bands, at least up to the levels of strains reached in the experiments. Also, regardless of the stress path, the normal strains, normal to the direction of the shear bands are always negative. At large strains it is nearly impossible to express the behavior of soils with the simple mechanics of continuous media. The need to combine ϕ' and ψ (i.e., statics and kinematics) to express the inclination of the shear band is just one result of the difficulty of the problem. The constant participation of

new particles in the development and propagation of the bands may necessitate the introduction of concepts of mass transport to the modeling process.

ACKNOWLEDGMENTS

The research reported in this paper is part of a larger project on shear bands formation and propagation under the sponsorship of the Air Force Office of Scientific Research. The author wishes to thank the Air Force and program managers Dr. M. D. Lewis and Dr. M. Chipley for starting and supervising this project.

REFERENCES

- Arthur, J.R.F., Dunstan T., Al-Ani, Q.A.J.L. and Assadi, A. (1977). Plastic deformation and failure in granular media. *Geotechnique* 27, No. 1, 53-74.
- Arthur, J.R.F. and Dunstan, T. (1982). Rupture layers in granular media. *Proc. IUTAM Symposium on Deformation and Failure of Granular Materials*, Delft (Edited by P.A. Vermeer and H.J. Luger), Rotterdam: Balkema, 453-459.
- Bolton, M.D. (1986). The strength and dilatancy of sands. *Geotechnique* 36, No. 1, 65-78.
- Finno, R.J., Harris, W.W., Mooney, M.A. and Viggiani, G. (1996). Strain localization and undrained steady state of sand. *J. Geotech. Engng. ASCE*, 122, No. 6, 462-473.
- Hansen, B. (1958). Line ruptures regarded as narrow rupture zones. Basic equations based on kinematic considerations. *Proc. Conf. Earth Pressure Probl.*, Brussels 1, 39-48.
- Houlsby, G.T. (1991). How the dilatancy of soils affects their behavior. *Proc. Tenth European Conf. on Soil Mech. and Found. Engng.*, Florence 4, Balkema, Rotterdam, 1189-1202.
- IUTAM (1982). *Proc. Symposium on Deformation and Failure of Granular Materials*, Delft (Edited by P.A. Vermeer and H.J. Luger) Rotterdam; Balkema, pp. 453-499.
- Koenders, M.A., Arthur, J.R.F. and Dunstan, T. (1990). The behavior of granular materials at peak stress. *Yielding, Damage and Failure of Anisotropic Solids*, M.P. Boehler, Ed., London, Mechanical Engineering Publications, pp. 805-818.
- Lade, P.V., Yamamuro, J.A.C. Skyers, B.D. (1996). Effect of shear band formation in triaxial extension tests. *Geotech. Testing Journal, GTJODJ*, 19, No. 4, 398-410.
- Liang, L., Saada, A.S., Figueroa, J.L. and Cope, C.T. (1997). The use of digital image processing in monitoring shear band development. *Geotech. Testing Journal, GTJODJ*, 20, No. 3.
- Papamichos, E. and Vardoulakis, I. (1995). Shear band formation in sand according to non-coaxial plasticity model. *Geotechnique* 45, No. 4, 649-661.
- Roscoe, K.H. (1970). The influence of strains in soil mechanics. *Geotechnique* 20, No. 2, 129-170.
- Saada, A.S. and Bianchini, G.F. (1987). *Proc. of the Intern. Workshop on Constitutive Equations for Granular Non-Cohesive Soils*, Cleveland, Ohio. Balkema, Rotterdam, 727 pp.

Saada, A.S., Bianchini, G.F., and Liang, L. (1994). Cracks, bifurcation and shear bands propagation in saturated clays. *Geotechnique* 44, No. 1, 35-64.

Scarpelli, G. and Wood, D.M. (1982). Experimental observations of shear band patterns in direct shear tests. *Proc. IUTAM Symp. Deformation and Failure of Granular Materials*, Delft, (Edited by P.A. Vermeer and H.L. Luger), Rotterdam: Balkema, 473-484.

Schanz, T and Vermeer, P.A. (1996). Angles of friction and dilatancy of sand. *Geotechnique* 46, No. 1, 145-151.

Vardoulakis, I. (1980). Shear band inclination and shear modulus of sand in biaxial tests. *Int. J. Numer. Anal. Meth. Geomech.* 4, 103-119.

Vermeer, P.A. (1982). A simple shear band analysis using compliances. *Proc. IUTAM Symp. Deformation and Failure of Granular Materials*, Delft, (Edited by P.A. Vermeer and H.L. Luger) Rotterdam: Balkema, 493-499.

Zitouni, Z.E.A. (1988). Comportement tridimensional des Sables. Doctoral Thesis, Université Joseph Fourier-Grenoble I.

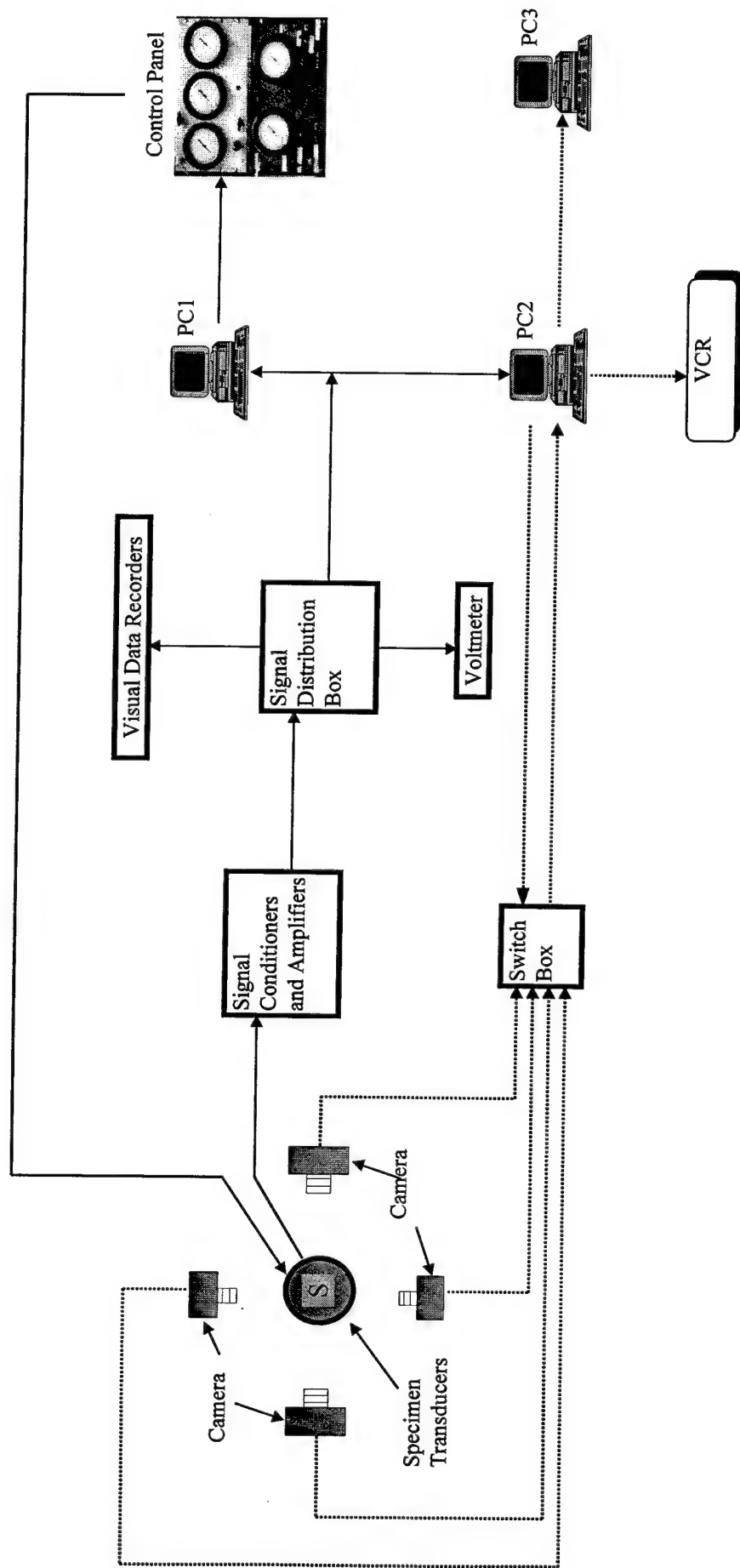
Table I. Triaxial Hollow Cylinder Tests (LSI-30 Sand)

Test #	β/b	σ'_c (kPa)	D_r (%)	Volume Change	Test Type
21	0°/0.00	207	50	Measured	Generalized
22	30°/0.25	207	50	Measured	Generalized
23	45°/0.50	207	50	Measured	Generalized
24	60°/0.75	207	50	Measured	Generalized
25	90°/1.00	207	50	Measured	Generalized
26	0°/0.00	345	50	Measured	Generalized
27	30°/0.25	345	50	Measured	Generalized
28	45°/0.50	345	50	Measured	Generalized
29a	60°/0.75	345	50	Measured	Generalized
30	90°/1.00	345	50	Measured	Generalized
31	0°/0.00	483	50	Measured	Generalized
32	30°/0.25	483	50	Measured	Generalized
33	45°/0.50	483	50	Measured	Generalized
34	60°/0.75	483	50	Measured	Generalized
35	90°/1.00	483	50	Measured	Direct
36	0°/0.00	207	80		Generalized
37	30°/0.25	207	80		Generalized
38	45°/0.50	207	80		Generalized
39	60°/0.75	207	80		Generalized
40	90°/1.00	207	80		Generalized
41	0°/0.00	345	80		Generalized
42	30°/0.25	345	80		Generalized
43	45°/0.50	345	80		Generalized
44	60°/0.75	345	80		Generalized
45	90°/1.00	345	80		Generalized
46	0°/0.00	483	80		Generalized
47	30°/0.25	483	80		Generalized
48	45°/0.50	483	80		Generalized
49	60°/0.75	483	80		Generalized
50a	90°/1.00	483	80		Generalized
51	0°/0.00	207	80		Direct
52	30°/0.25	207	80		Direct
53	45°/0.50	207	80		Direct
54	60°/0.75	207	80		Direct
55	90°/1.00	207	80		Direct
56	0°/0.00	207	80	Measured	Generalized
57	30°/0.25	207	80	Measured	Generalized
58	45°/0.50	207	80	Measured	Generalized
59	60°/0.75	207	80	Measured	Generalized
60	90°/1.00	207	80	Measured	Generalized

Table II. Predicted and Observed Inclination of the Dominant Shear Band

Test No.	D_r (%)	σ'_c (kPa)	Mean Stress	β/b	ϕ'_{pk}	ψ_{max}	δ_C	δ_R	δ_{AV}	δ_{OB}
21	50	207	constant	0°/0.00	38.6	-----	-----	-----	-----	-----
22	50	207	constant	30°/0.25	50.1	1.12	40.1	15.6	27.1	26.0
23	50	207	constant	45°/0.50	47.1	9.36	23.6	4.7	14.1	15.8
24	50	207	constant	60°/0.75	44.6	14.49	7.3	-7.8	0.4	0.7
25	50	207	constant	90°/1.00	42.8	-----	-----	-----	-----	-----
26	50	345	constant	0°/0.00	38.9	-----	-----	-----	-----	-----
27	50	345	constant	30°/0.25	45.4	-0.26	37.7	14.9	26.7	29.6
28	50	345	constant	45°/0.50	47.0	7.92	23.5	4.0	13.7	15.5
29a	50	345	constant	60°/0.75	42.9	17.05	6.5	-6.5	1.0	4.7
30	50	345	constant	90°/1.00	41.7	-----	-----	-----	-----	-----
31	50	483	constant	0°/0.00	37.9	-----	-----	-----	-----	-----
32	50	483	constant	30°/0.25	44.4	-1.23	37.2	14.4	26.9	29.4
33	50	483	constant	45°/0.50	48.9	7.24	24.5	3.6	14.0	15.3
34	50	483	constant	60°/0.75	43.0	14.66	6.5	-7.7	0.9	0.9
35	50	483	constant	90°/1.00	42.0	-----	-----	-----	-----	-----
56	80	207	constant	0°/0.00	42.8	-----	-----	-----	-----	-----
57	80	207	constant	30°/0.25	53.5	6.02	41.8	18.0	30.4	25.4
58	80	207	constant	45°/0.50	55.7	12.37	27.9	6.2	17.0	18.8
59	80	207	constant	60°/0.75	-----	22.44	-----	-3.8	4.5	0.0
60	80	207	constant	90°/1.00	-----	-----	-----	-----	-----	-----

* δ_C , δ_R , δ_{AV} , δ_{OB} are angles measured w.r.t. the horizontal



- Solid lines show the path of data acquisition and test control; Dashed lines show the path of image recording.
- PC1 records signals from transducers through a A/D board as voltages, calculates and sends out voltages to control panel through a D/A board.
- Control panel changes the voltages from PC1 to air pressure and supplies air pressure to increase/decrease axial forces and cell pressures.
- PC2 merges the voltage reading and the image, then sends the results to a VCR and PC3.
- Images are continuously recorded by a VCR and selectively by PC3.

Fig.1. Schematic of Testing Set-up

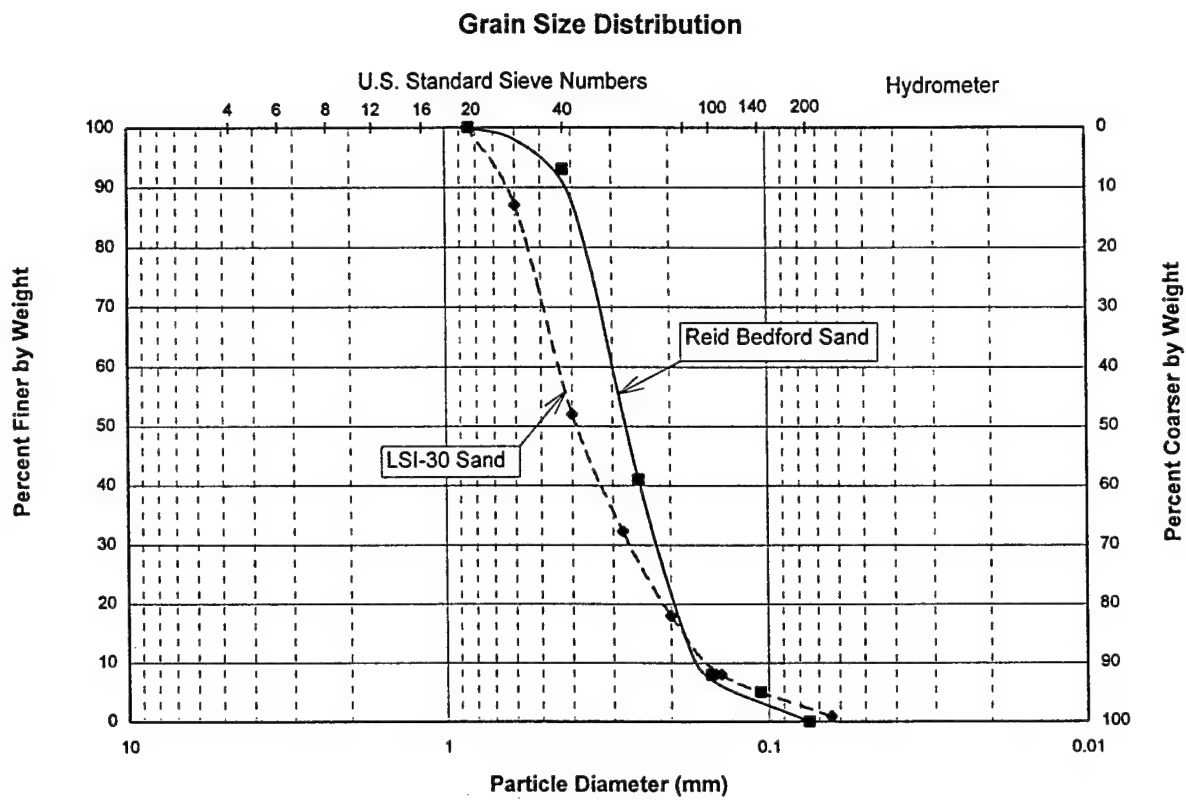


Fig. 2. Grain Size Distribution for LSI-30 and Reid Bedford Sands

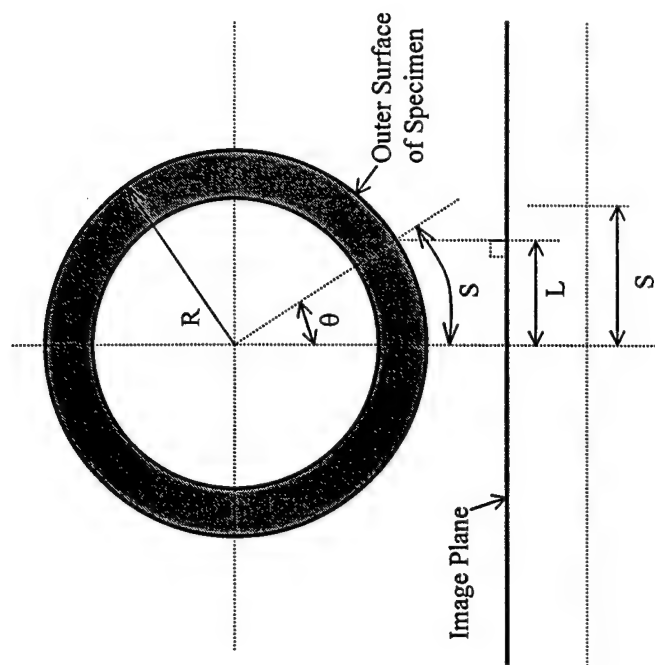


Fig.3b. Relationship between the Length on the Image and the Length on the Specimen's Surface

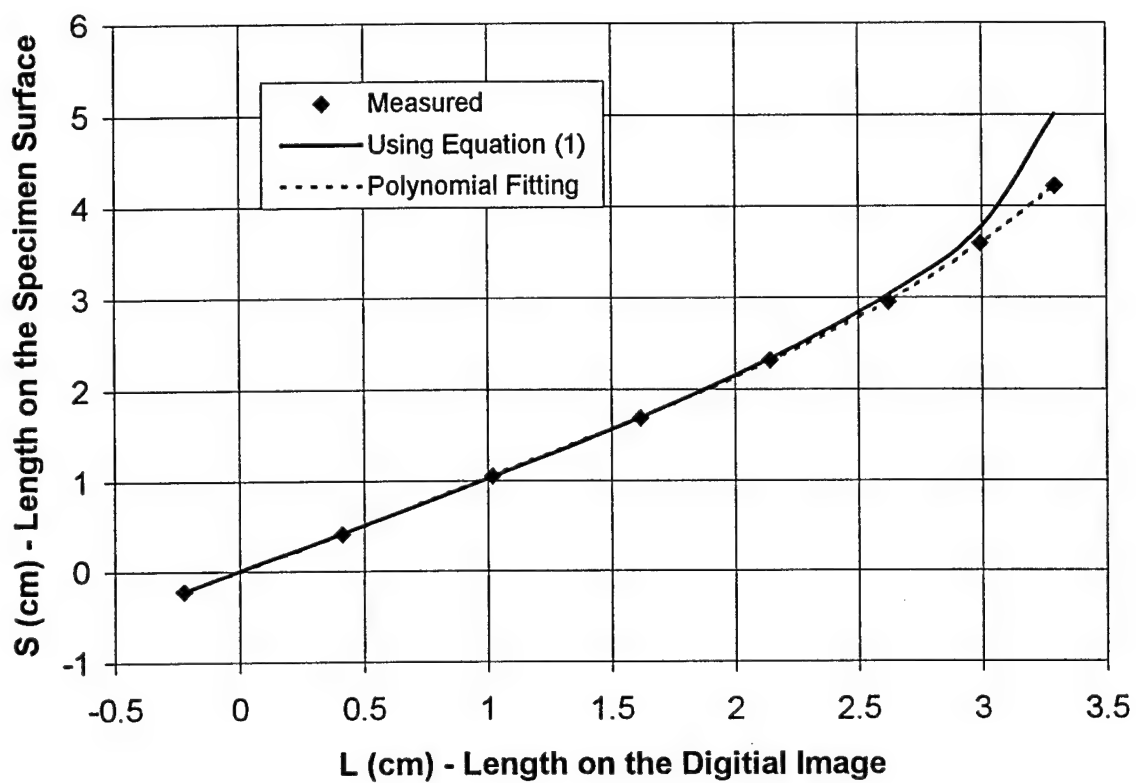


Fig.4. Relationship between S and L
(Test #43, Pure-torsion, ECP=345 kPa, LSI_30 sand, Camera #2)

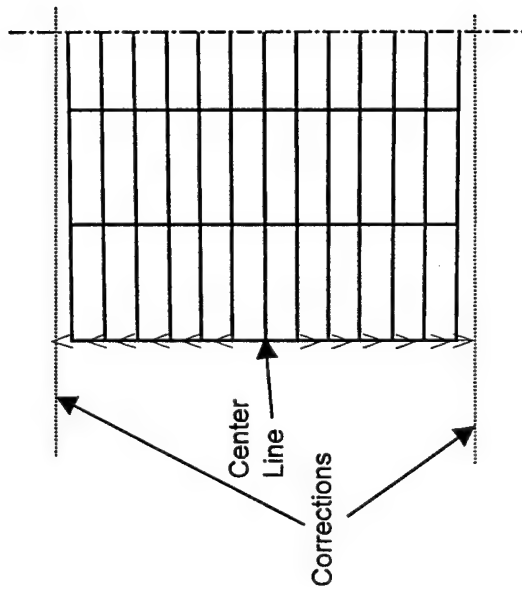


Fig. 5 Vertical Corrections

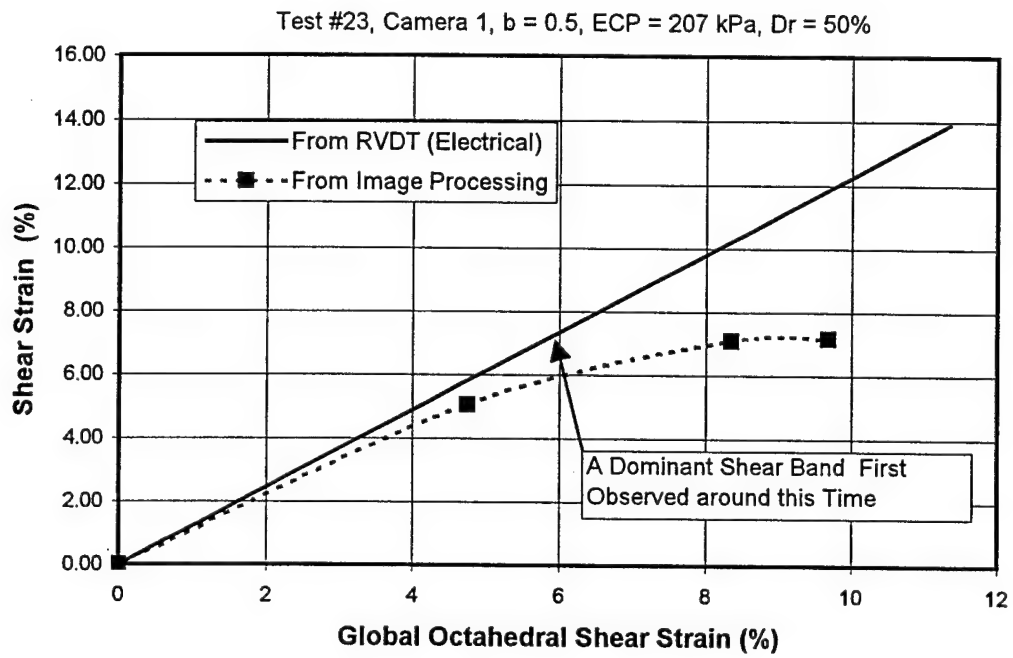


Fig. 6. Comparison between the Shear Strain Measured Electrically and through Image Processing

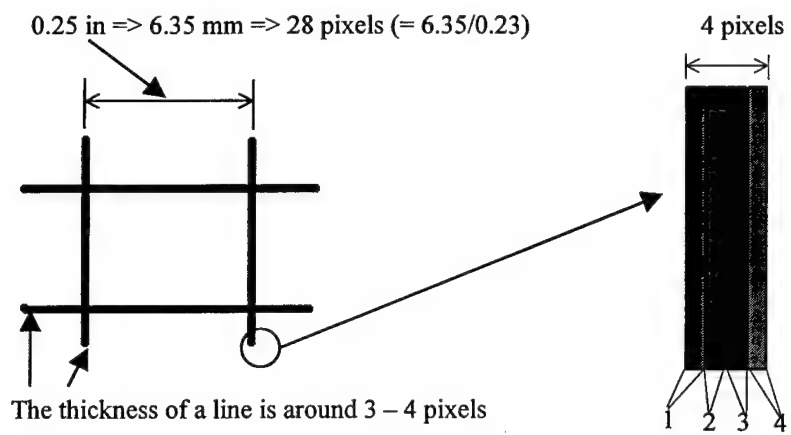


Fig. 7. Estimate of the Error Involved in the Digitizing Process

Test #43, 7/3/96, Pure-torsion, ECP=50 psi, LSI-30

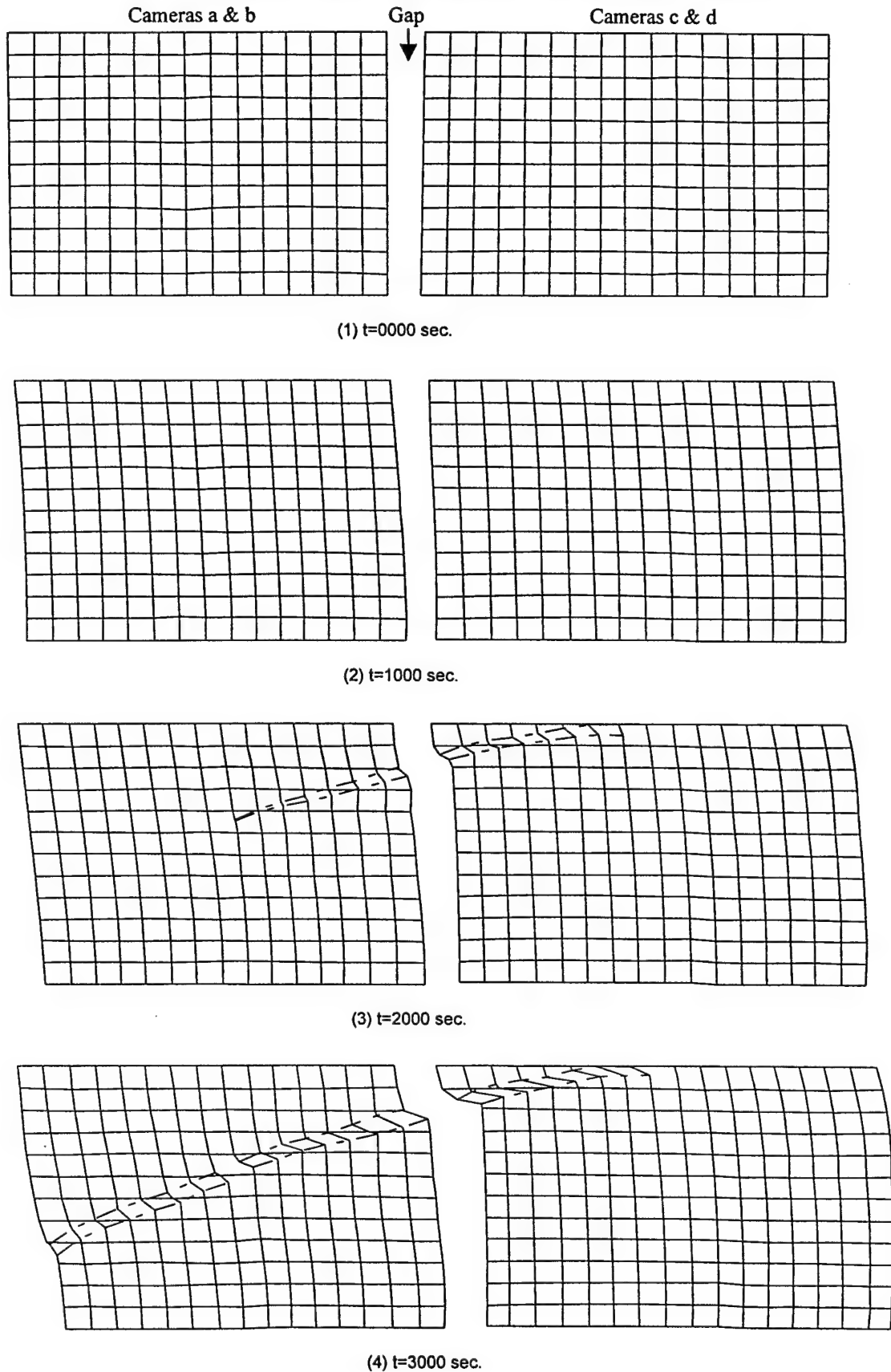


Fig.8. Digitized Grids at Various Time Increments

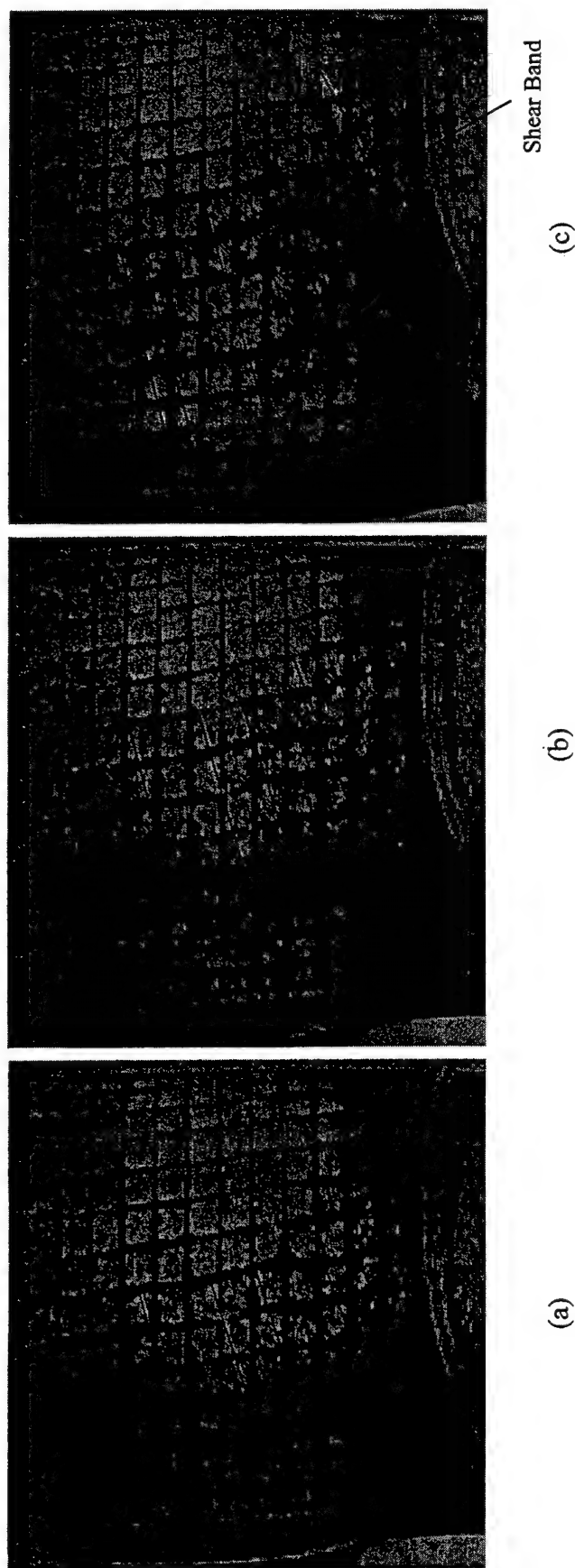


Fig. 9. From Slip Planes to a Dominant Shear Band (Test #32): a) Multiple Slip Surfaces (time = 2209 sec.); b) Propagation of Slip Surfaces (time = 3705 sec.); c) Formation of a Dominant Shear Band (time = 3705 sec.)

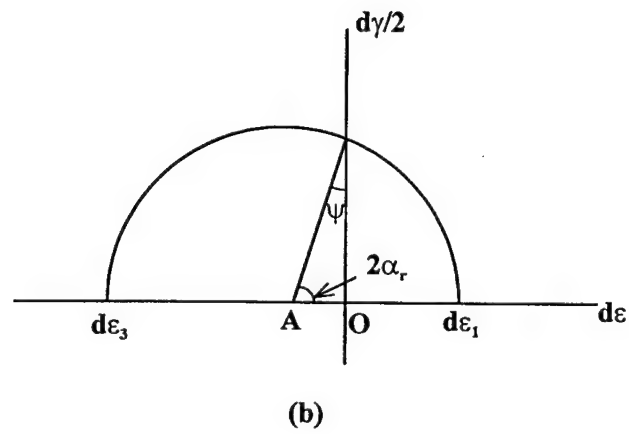
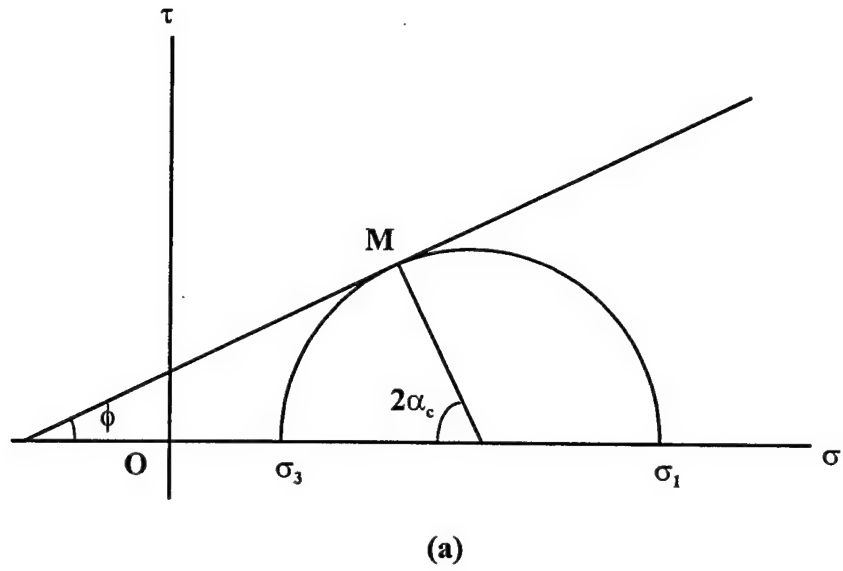


Fig. 10. Mohr Circles: a) Stress; b) Strain Increments

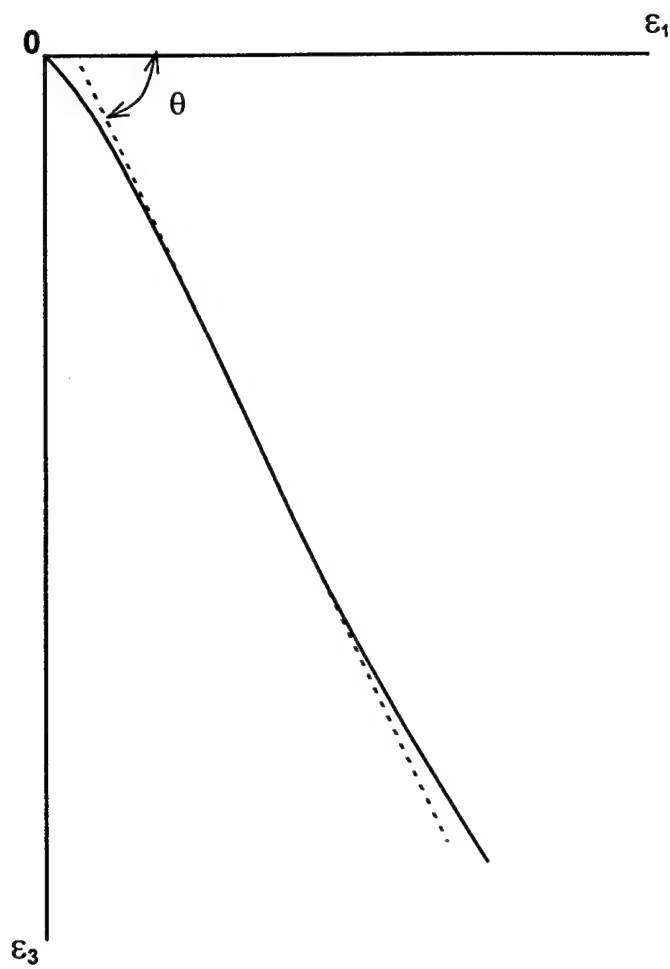


Fig. 11. Zitouni's Method for Obtaining ψ

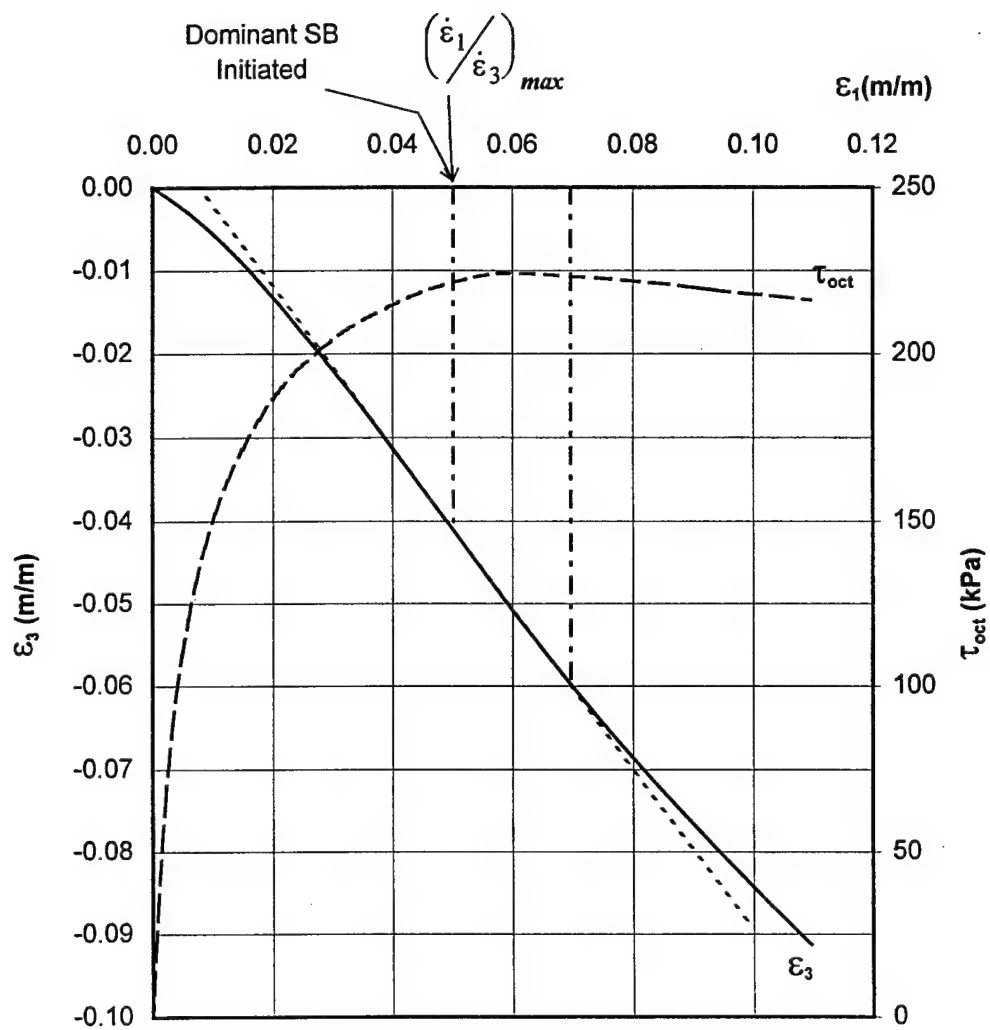


Fig. 12a. Initiation and Propagation of Shear Bands
(Test #27, $\beta=30^\circ$, $D_r=50\%$, $\sigma'_c=345$ kPa)

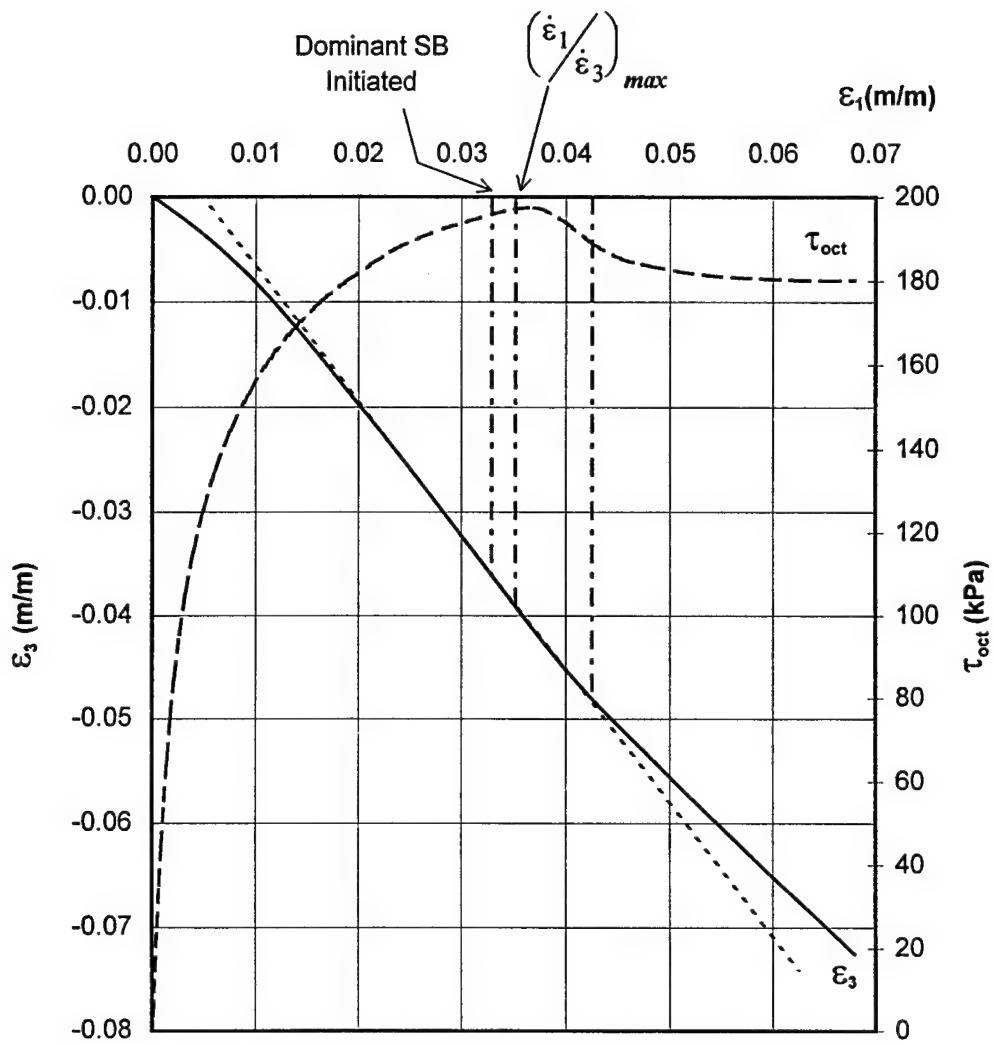


Fig. 12b. Initiation and Propagation of Shear Bands
(Test #28, $\beta=45^\circ$, $D_r=50\%$, $\sigma'_c=345$ kPa)

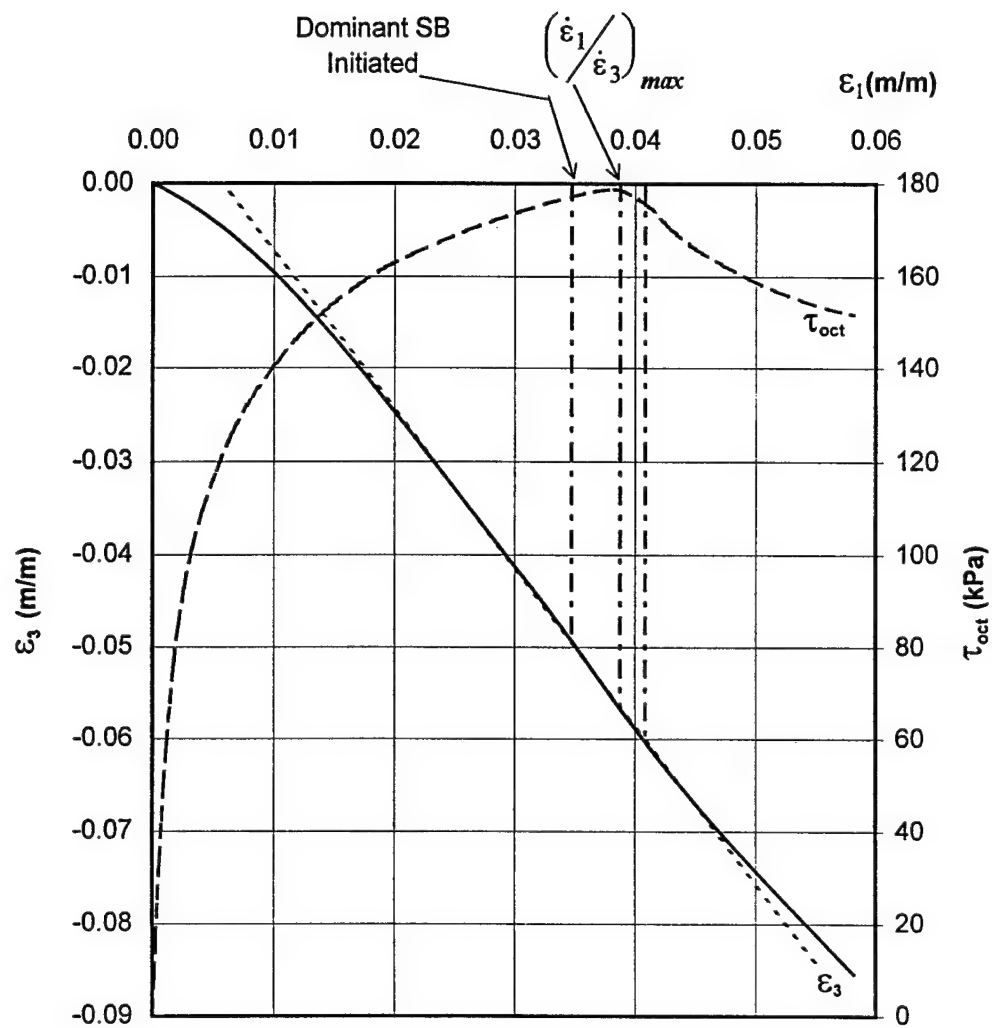


Fig. 12c. Initiation and Propagation of Shear Bands
(Test #29a, $\beta=60^\circ$, $D_r=50\%$, $\sigma'_c=345$ kPa)

Angle of the Shear Band with the Major Principal Plane (Angle with the Horizontal + β)

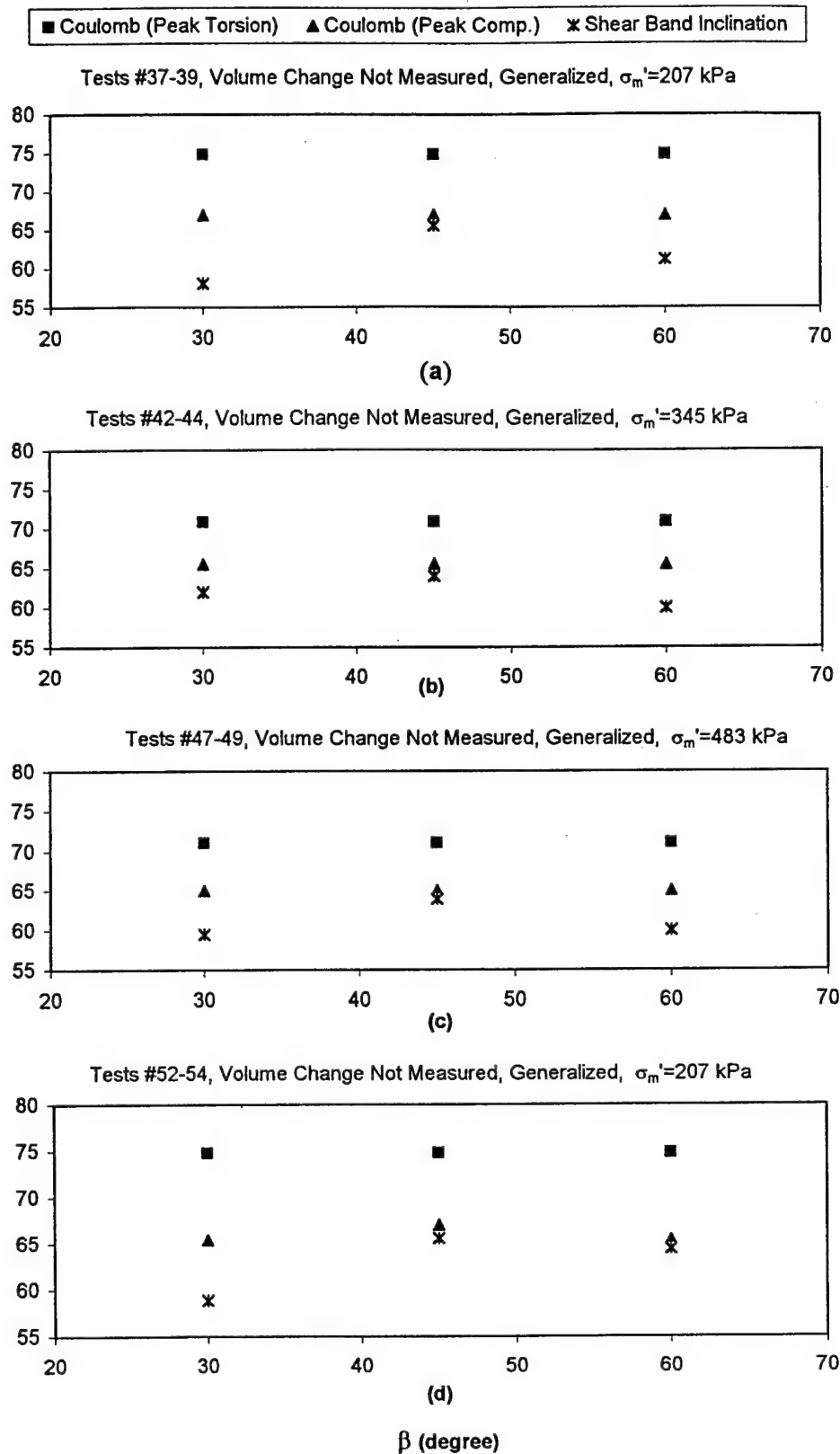


Fig. 13. Predicted and Observed Inclinations with Respect to the Major Principal Plane

Tests #22-24, 27-29a, 32-34, 57-59, Volume Change Measured

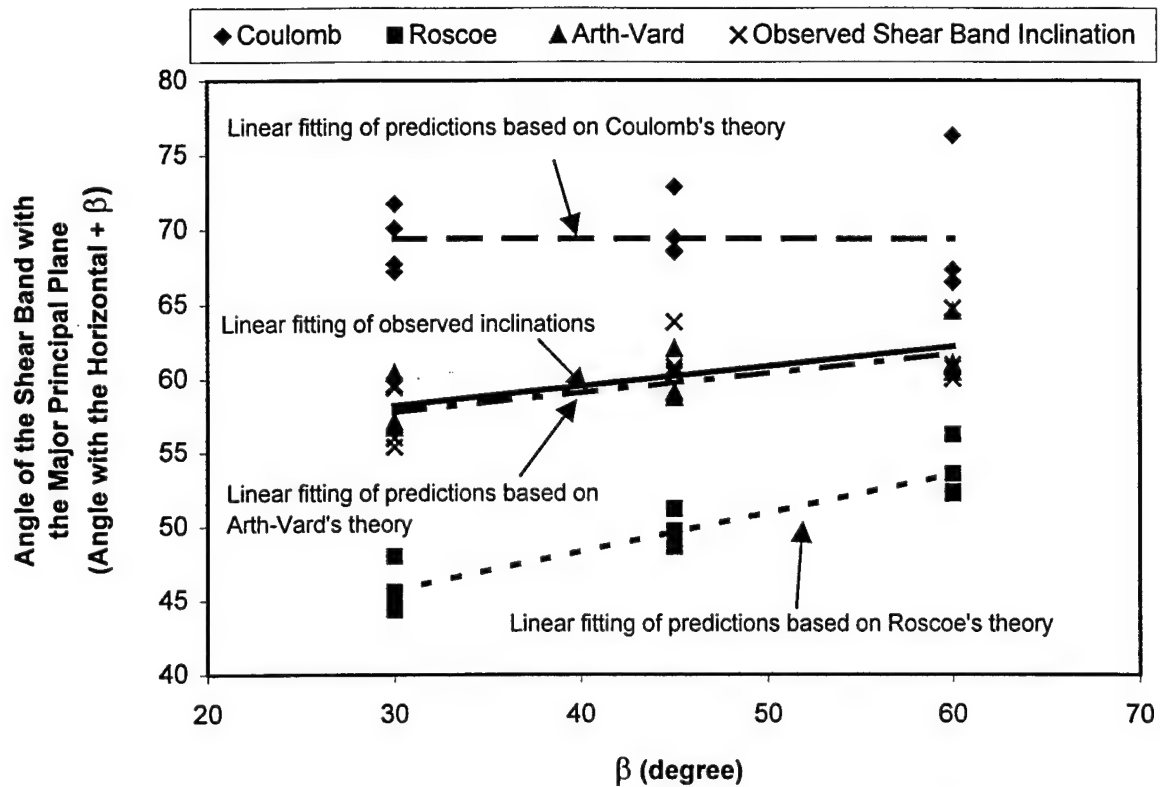


Fig. 14. Predicted and Observed Inclinations of the Shear Bands with Respect to the Major Principal Plane for Various σ_m' and D_r

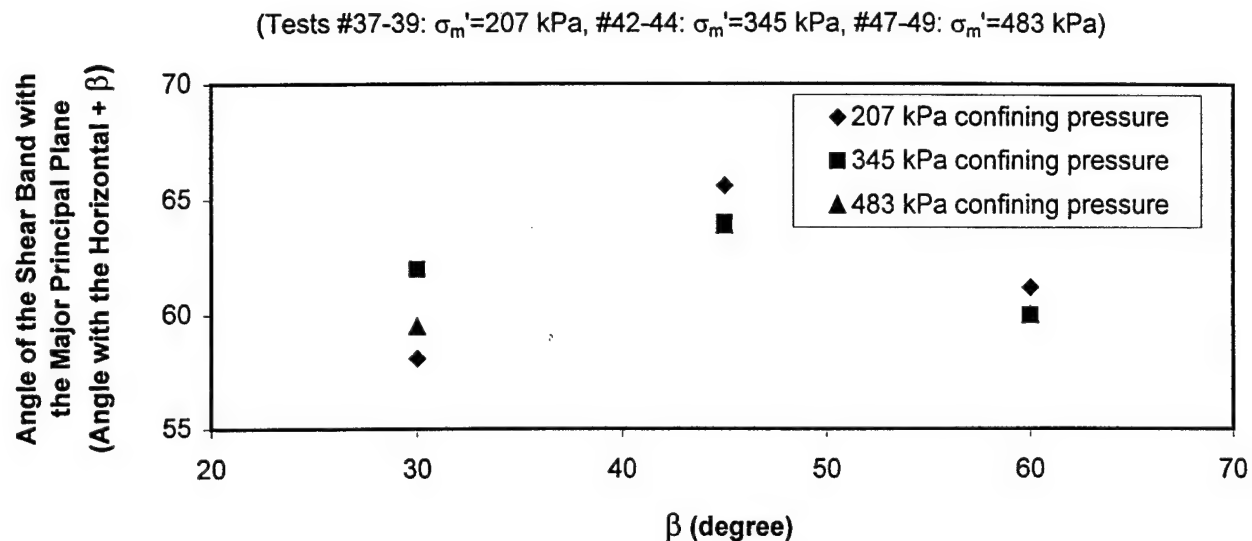


Fig. 15 Effect of Confining Pressure on Observed Shear Band Inclination

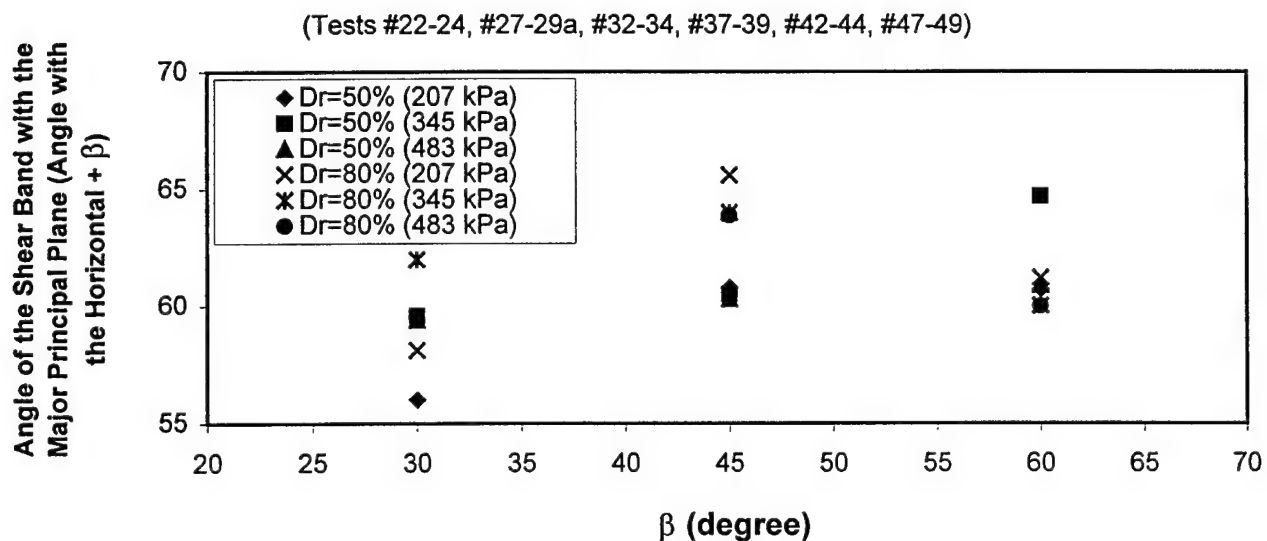


Fig.16. Effect of Density on Observed Shear Band Inclination

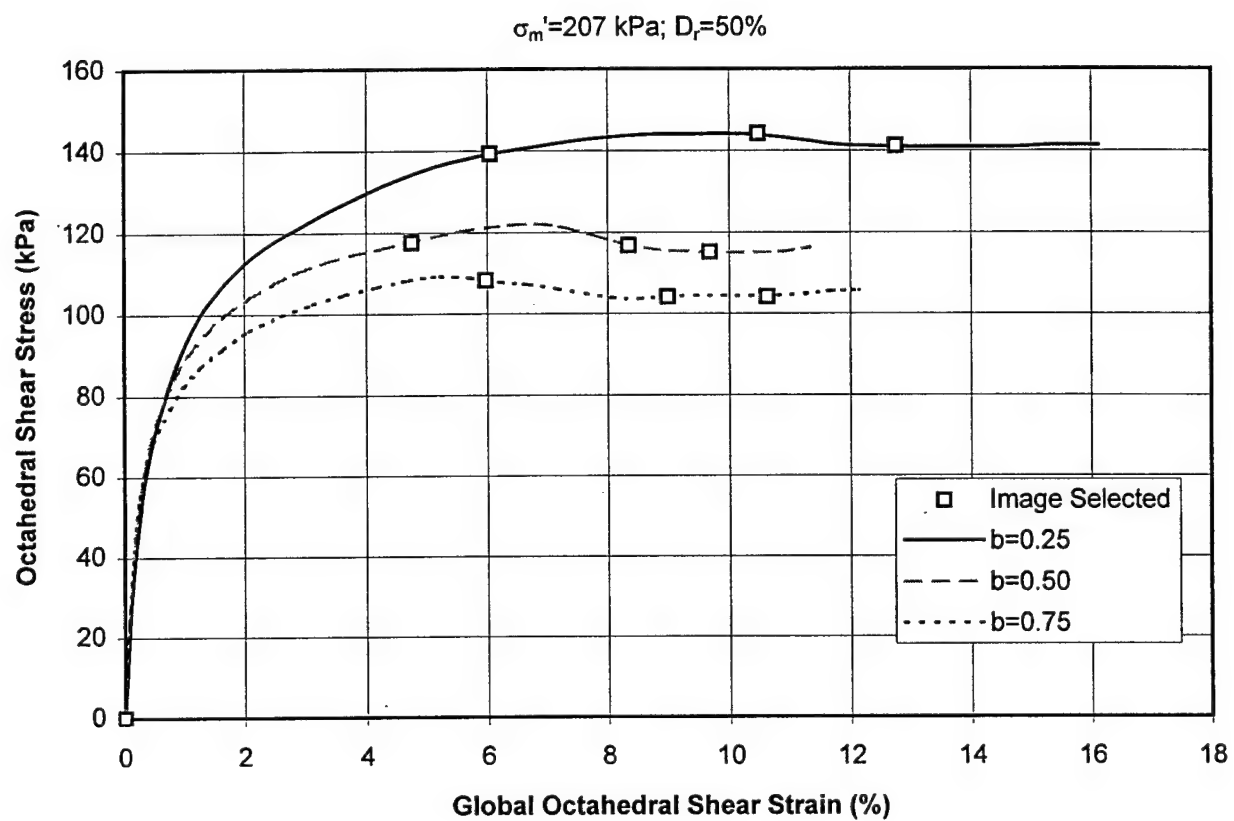


Fig. 17a. Stress vs. Strain (Test #22, #23 and #24)

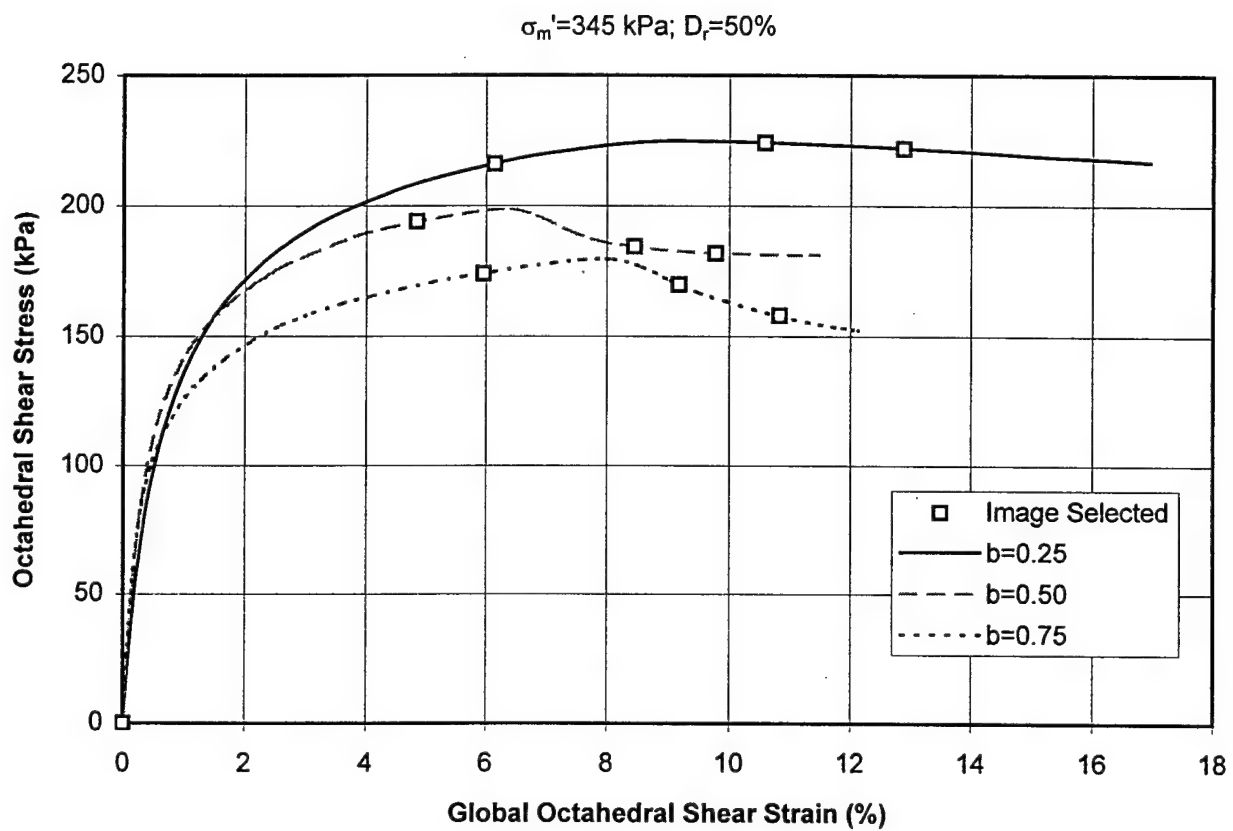


Fig. 17b. Stress vs. Strain (Test #27, #28 and #29a)

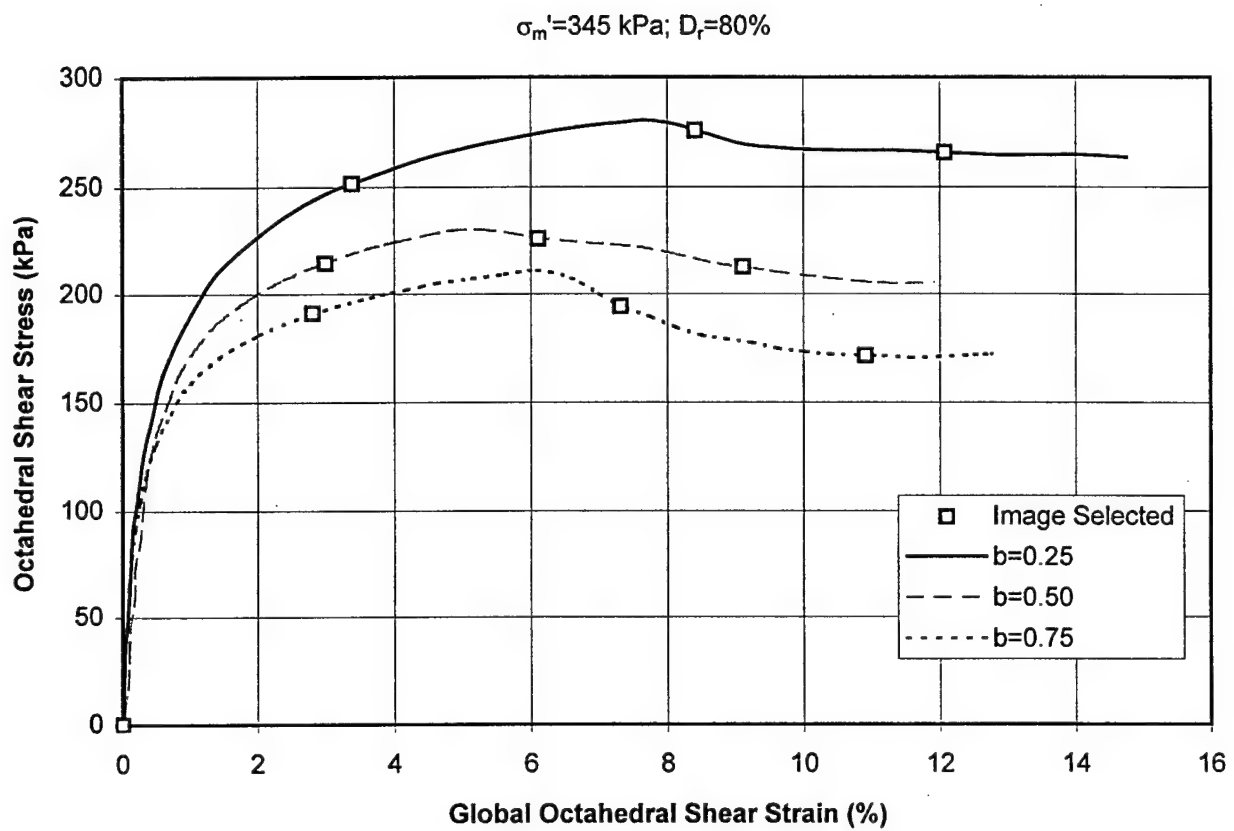
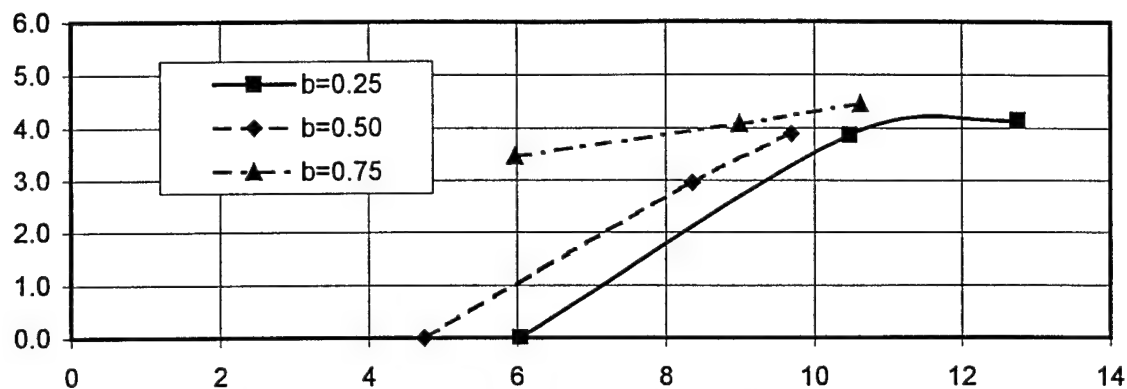
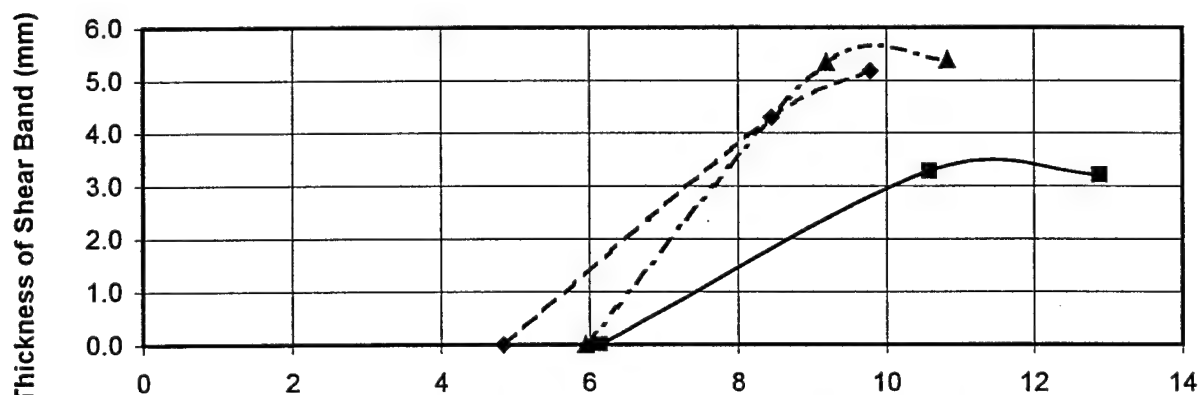


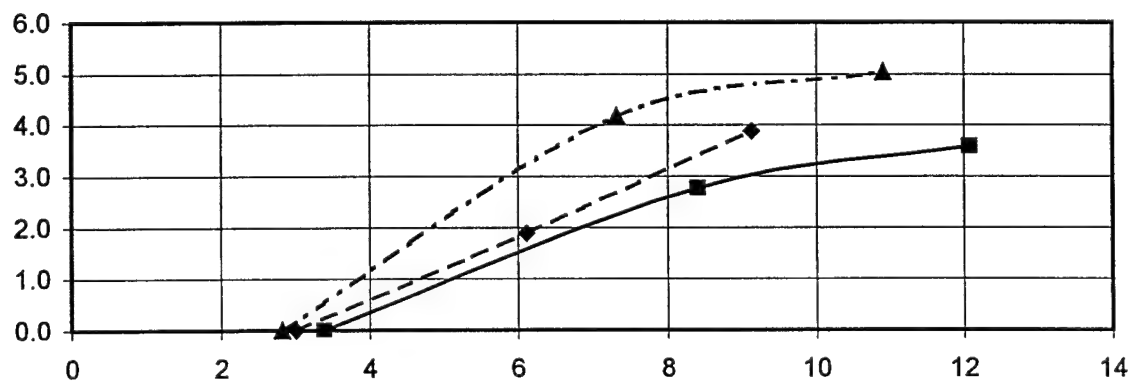
Fig. 17c. Stress vs. Strain (Test #42, #43 and #44)



(a). Test #22-24: ECP = 207 kPa, Dr = 50%, Fully Saturated



(b). Test #27-29a: ECP = 345 kPa, Dr = 50%, Fully Saturated



(c). Test #42-44: ECP = 345 kPa, Dr = 80%

Global Octahedral Shear Strain (%)

Fig. 18. Variation in Thickness of the Shear Band

Test #22; 11/1/96; Torsion-compression; ECP=30 psi; LSI_30

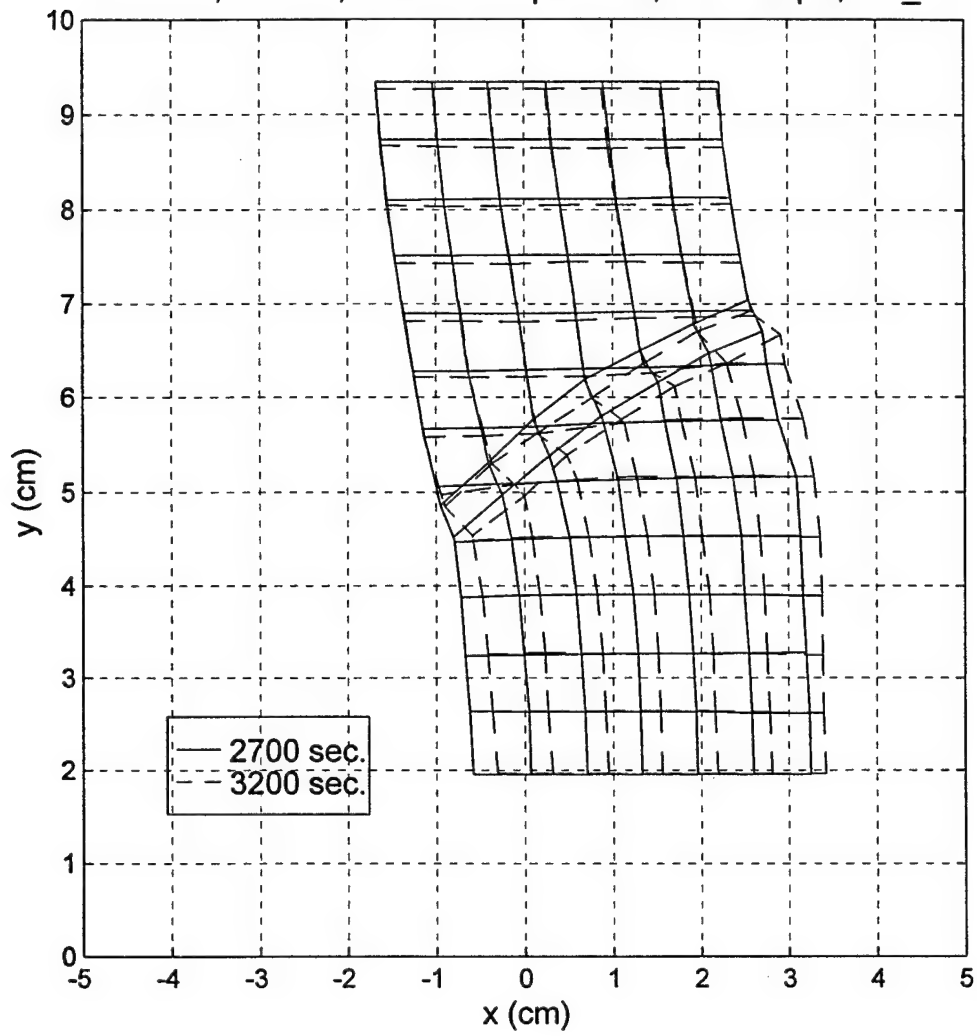


Fig. 19a. Relative Displacements within and around the Shear Band

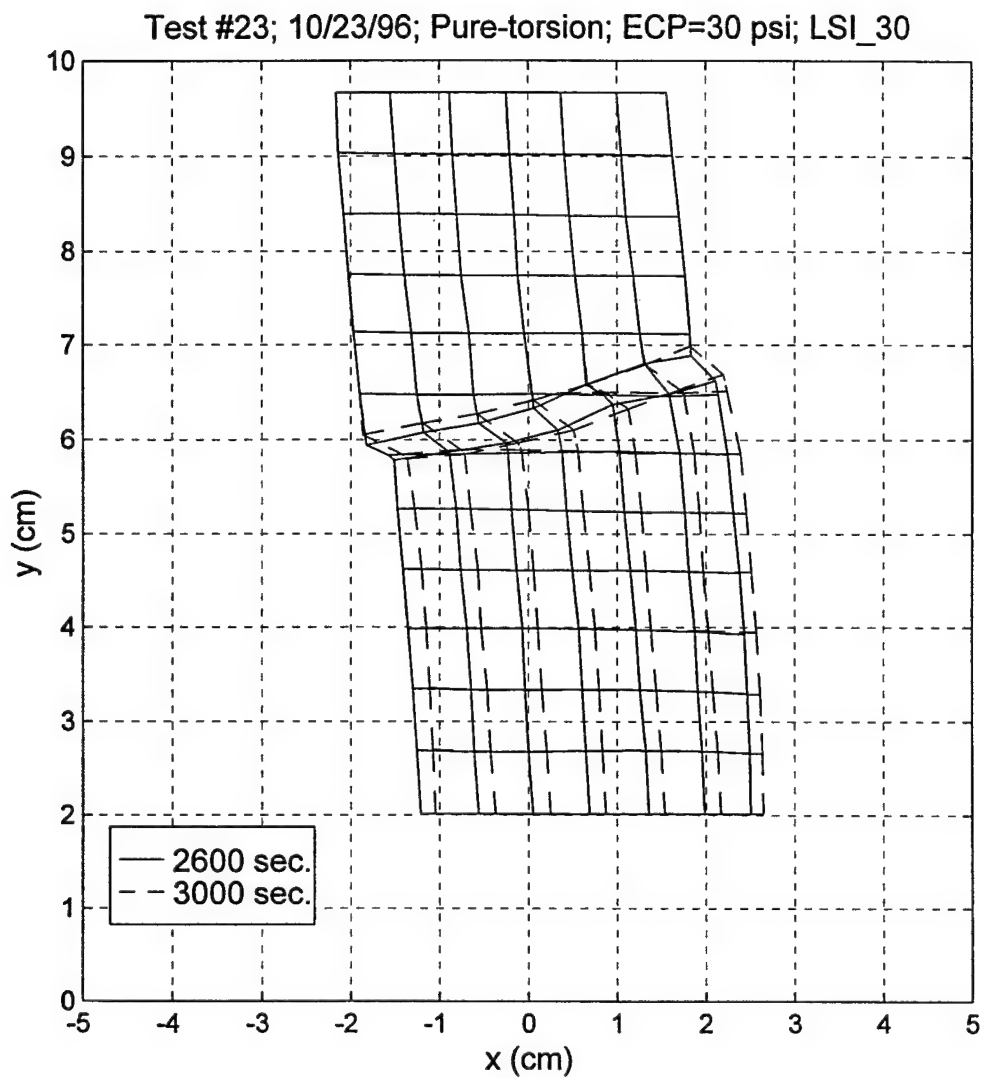


Fig. 19b. Relative Displacements within and around the Shear Band

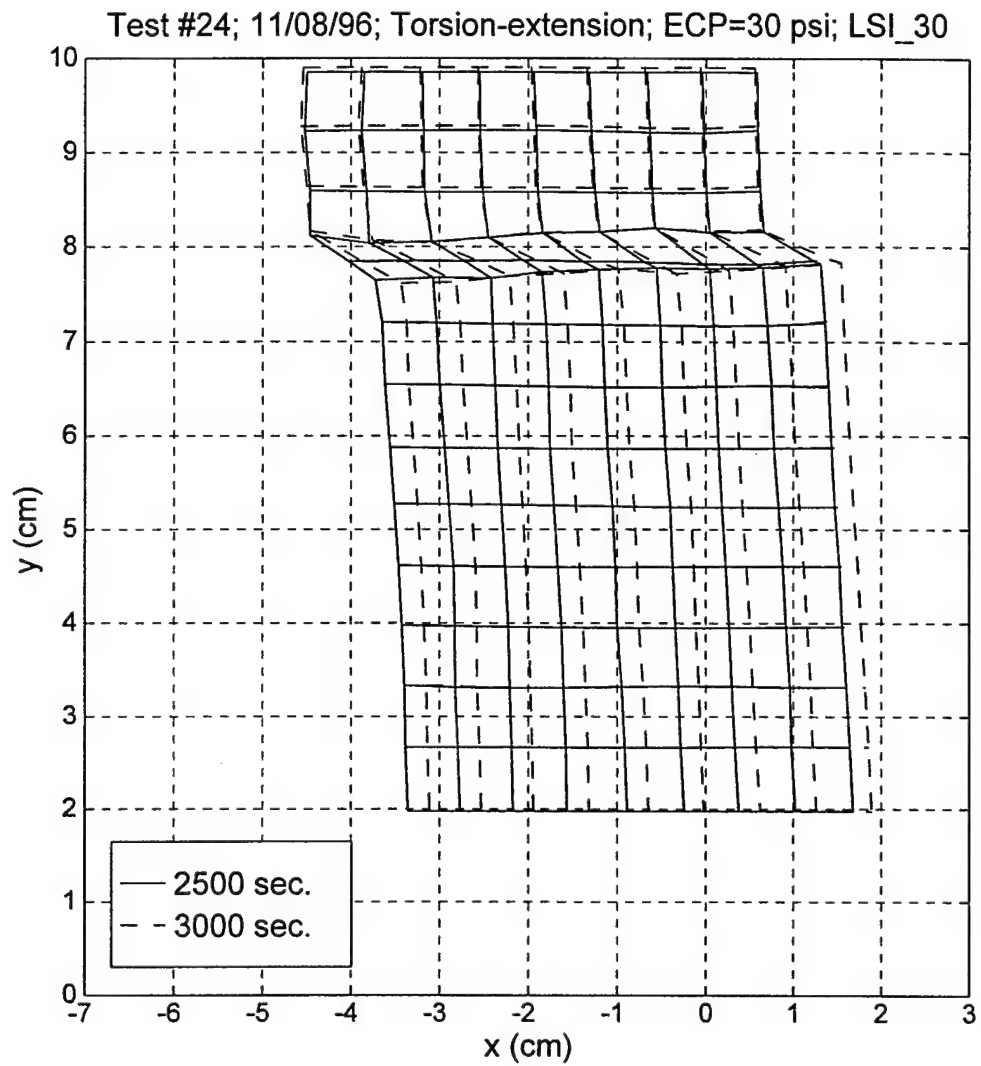


Fig. 19c. Relative Displacements within and around the Shear Band

b=0.25; ECP=207 kPa; Dr=50%; Saturated

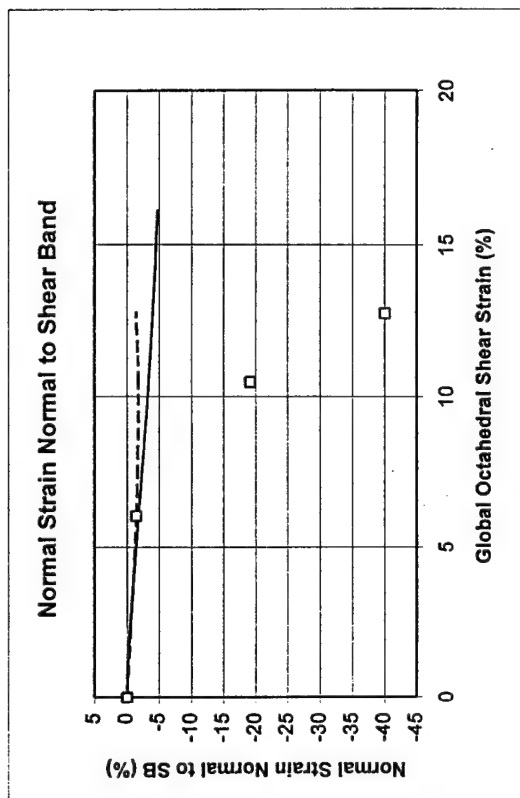
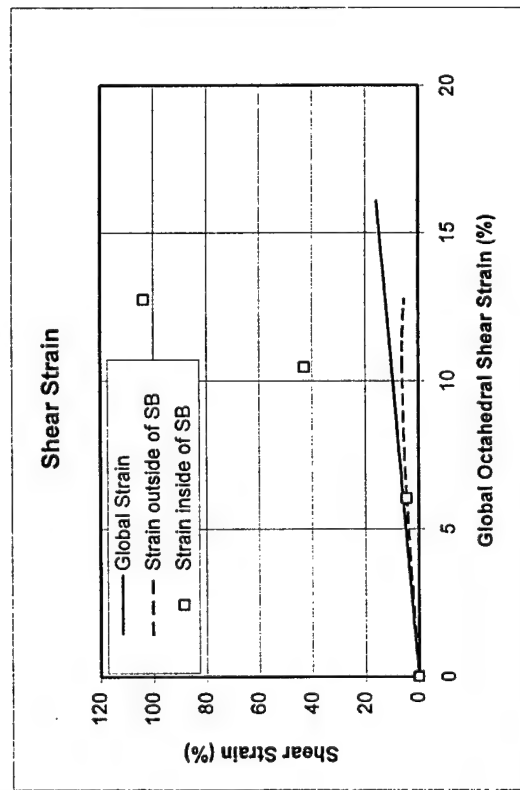
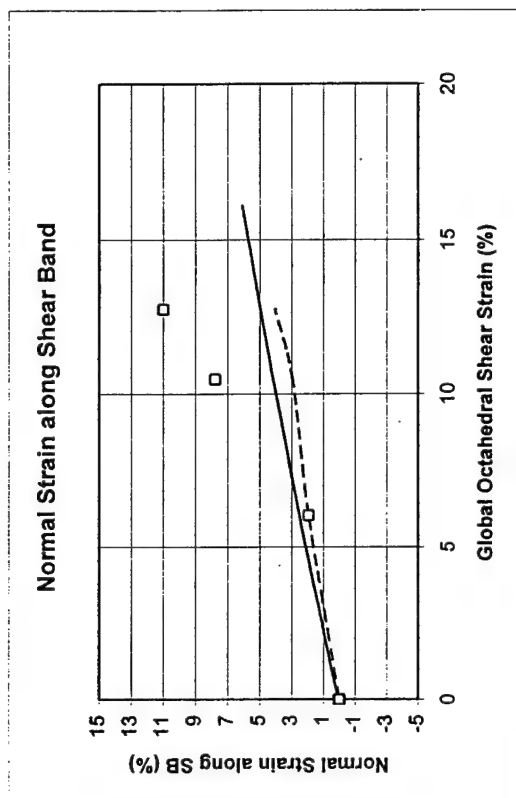
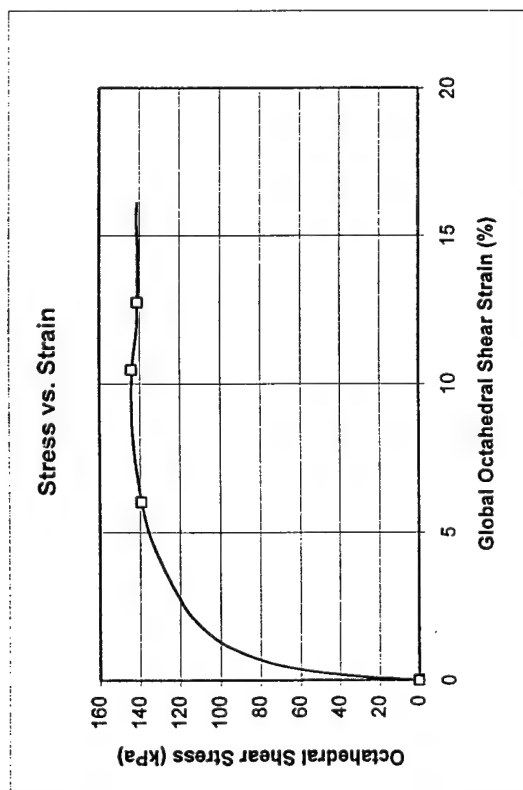


Fig.20a Strains in a System of Axes Along and Normal to the Shear Band (SB) for Test #22

$b=0.50$; $ECP=207$ kPa; $Dr=50\%$; Saturated

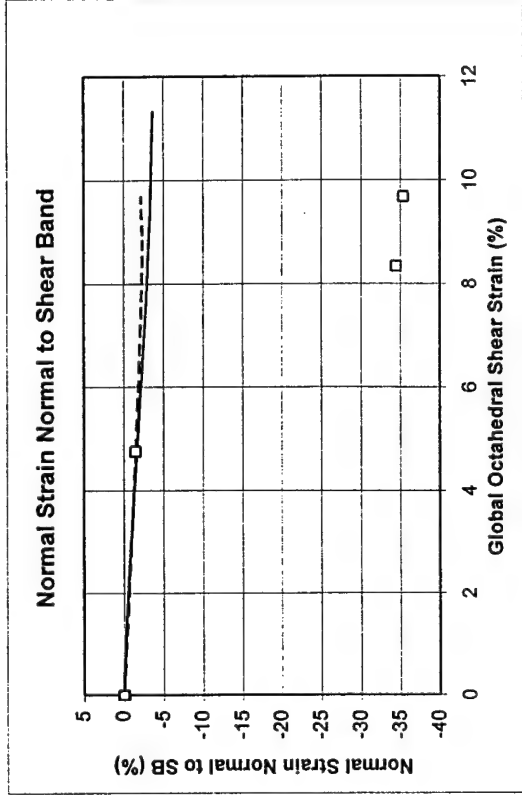
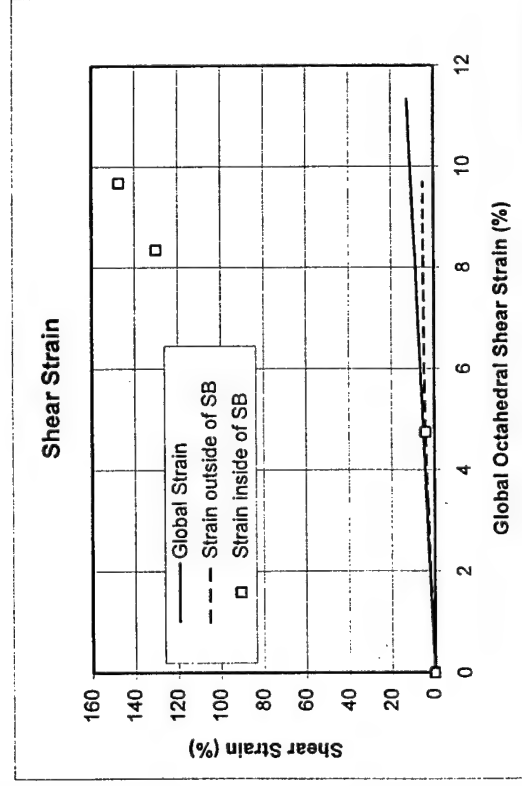
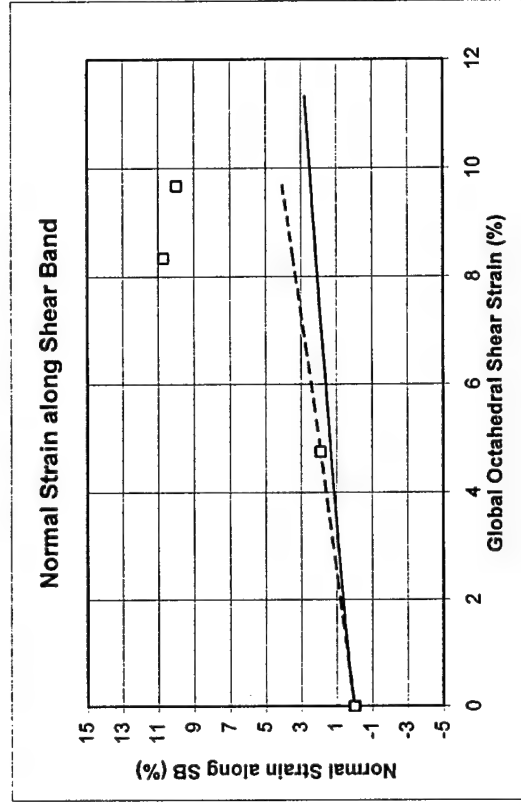
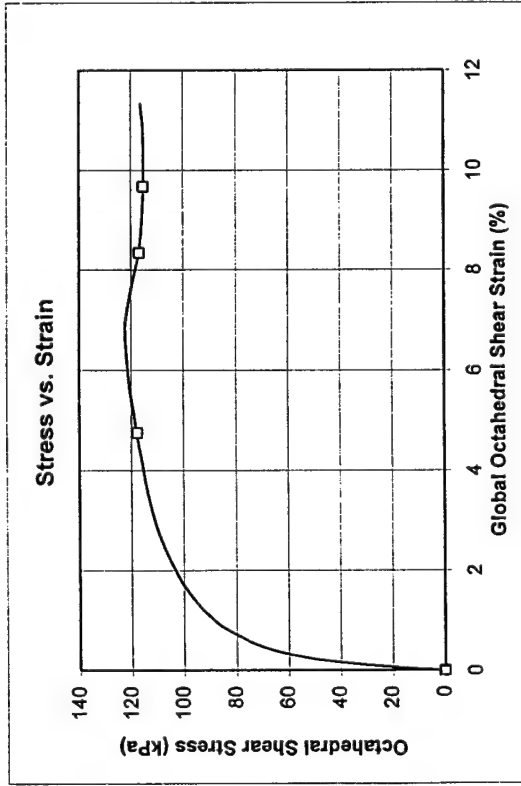


Fig. 20b Strains in a System of Axes Along and Normal to the Shear Band (SB) for Test #23

$b=0.75$; $ECP=207$ kPa; $D_r=50\%$; Saturated

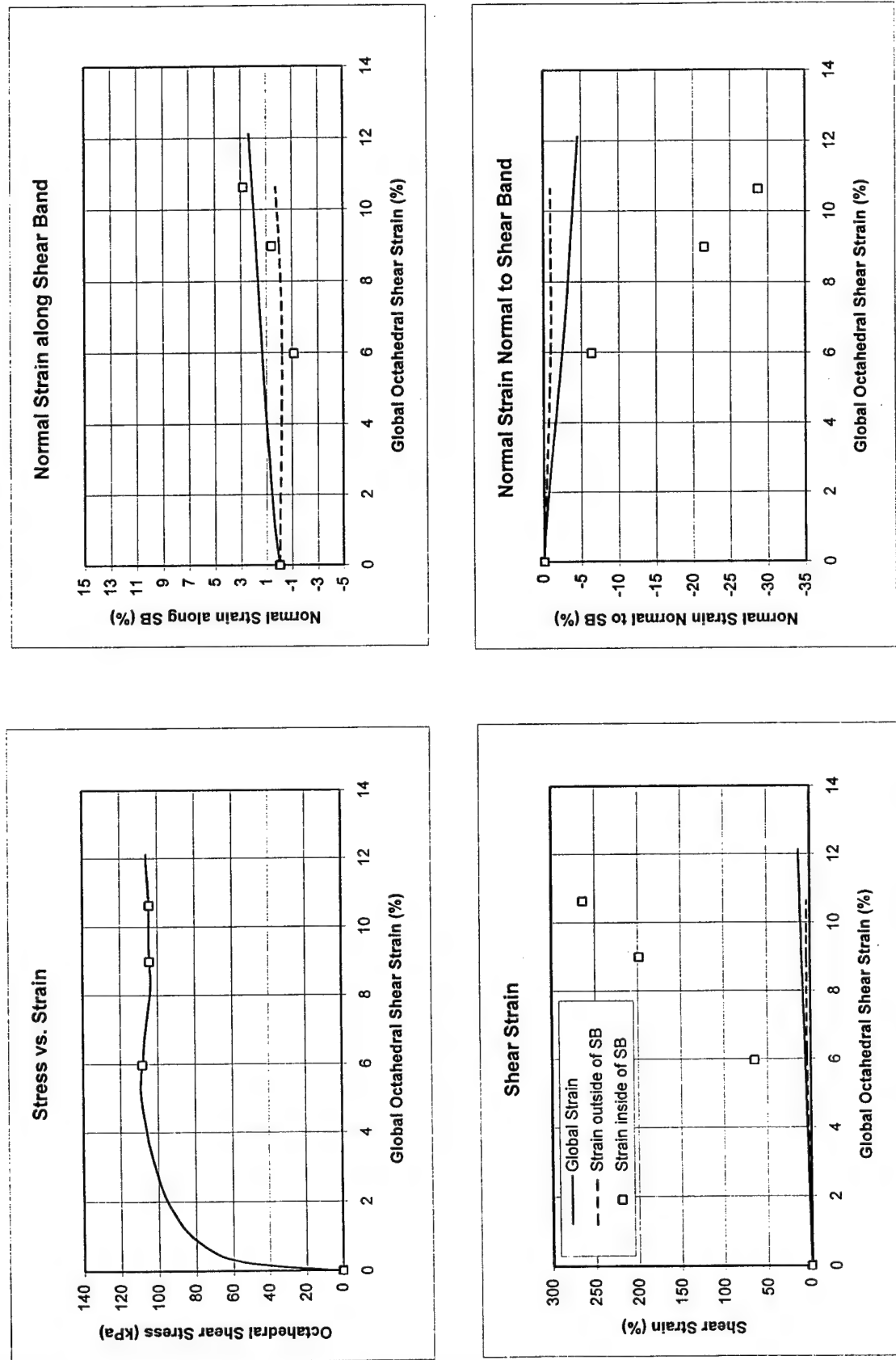
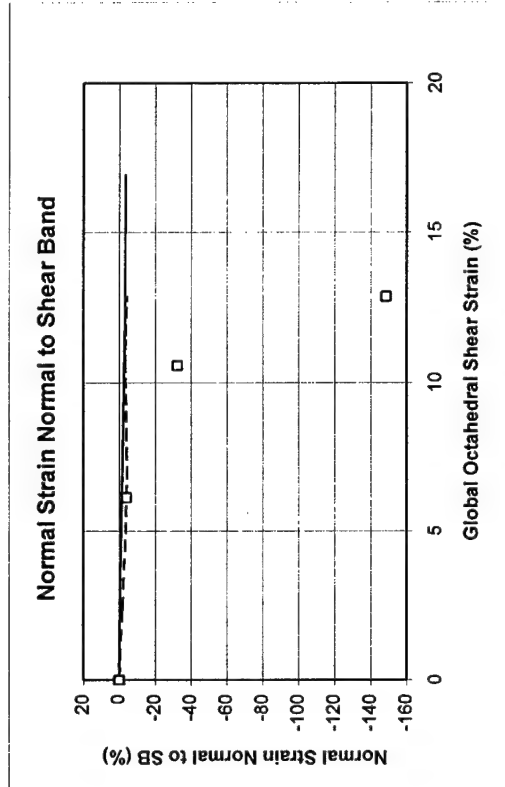
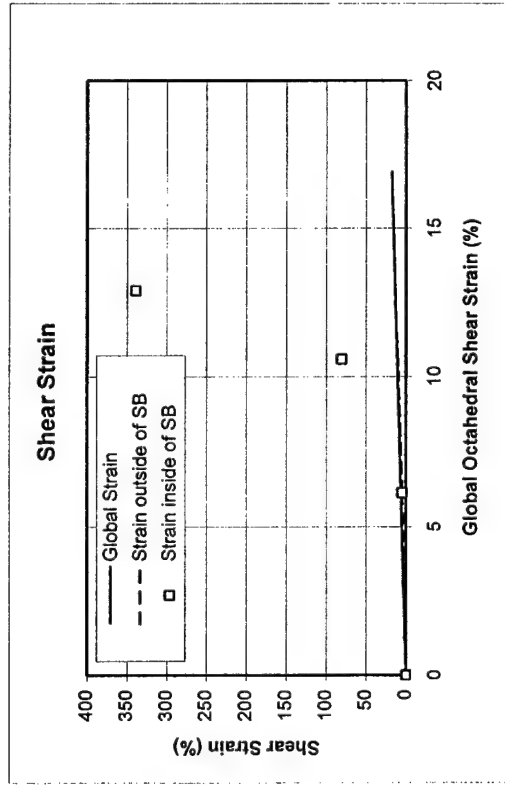
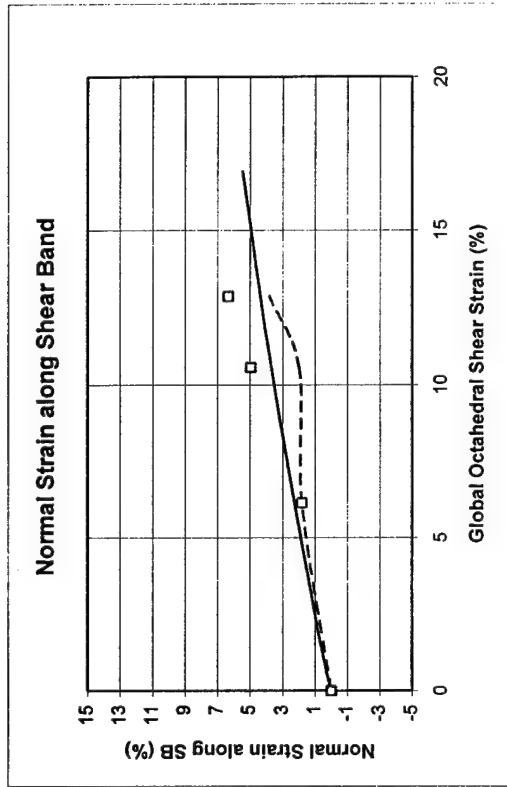
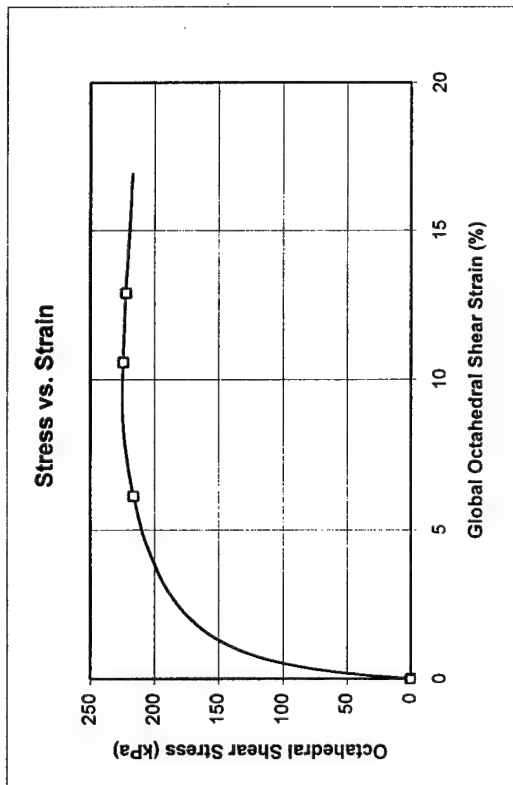


Fig. 20c Strains in a System of Axes Along and Normal to the Shear Band (SB) for Test #24

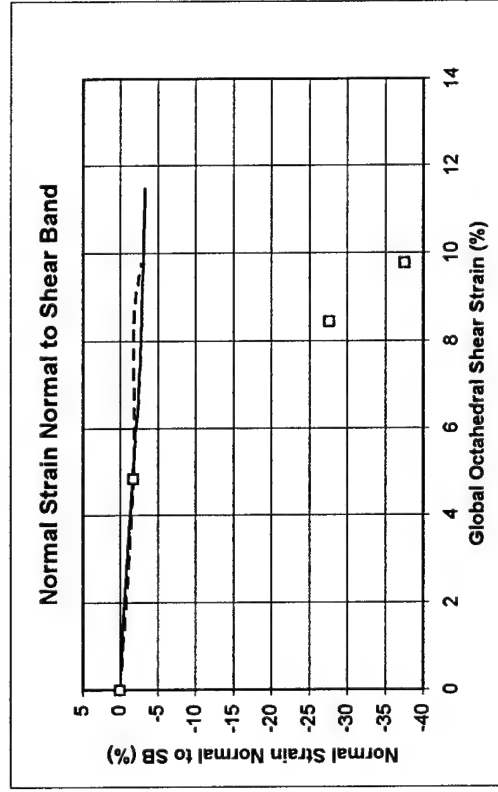
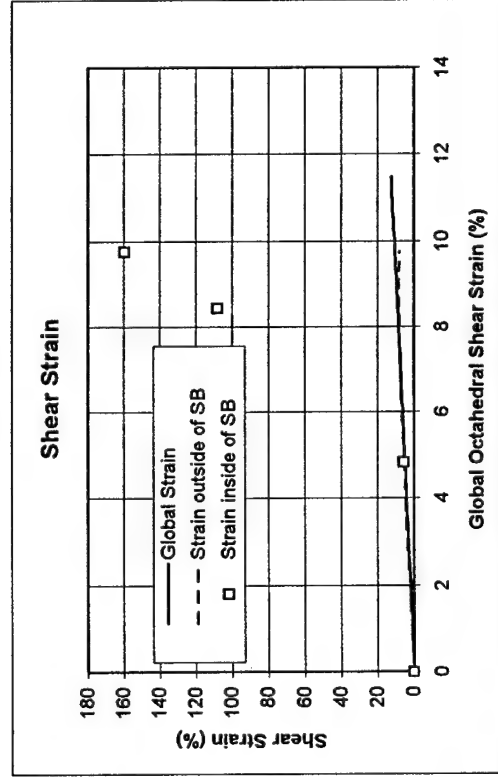
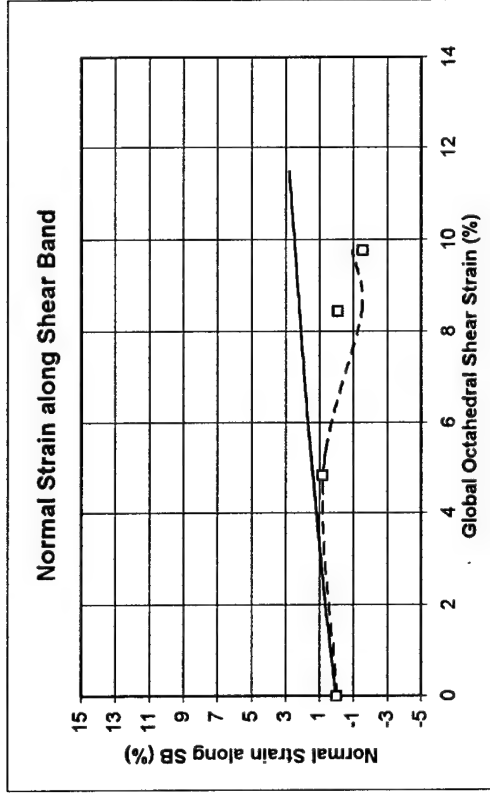
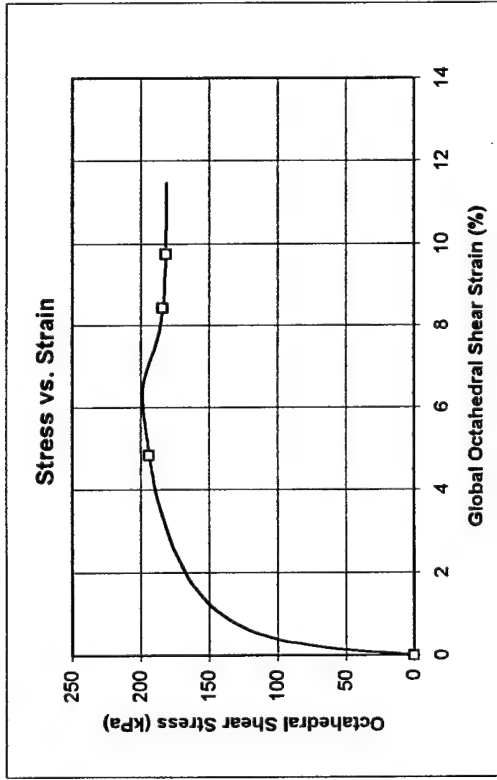
APPENDIX TO PAPER 2

b=0.25; ECP=345 kPa; Dr=50%; Saturated



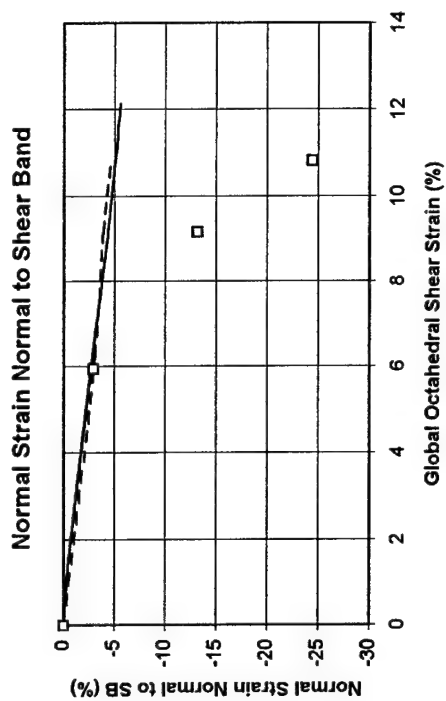
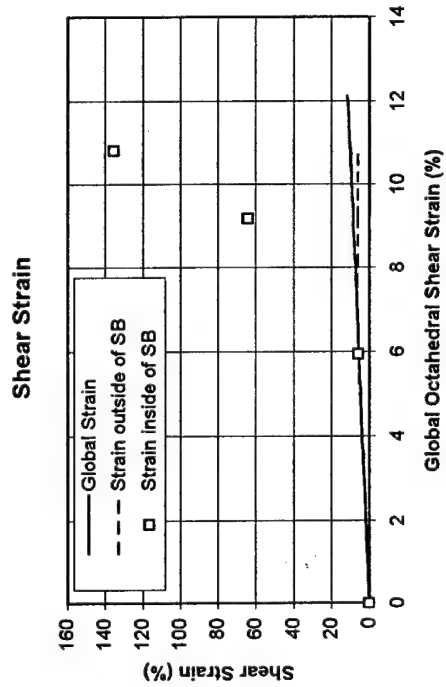
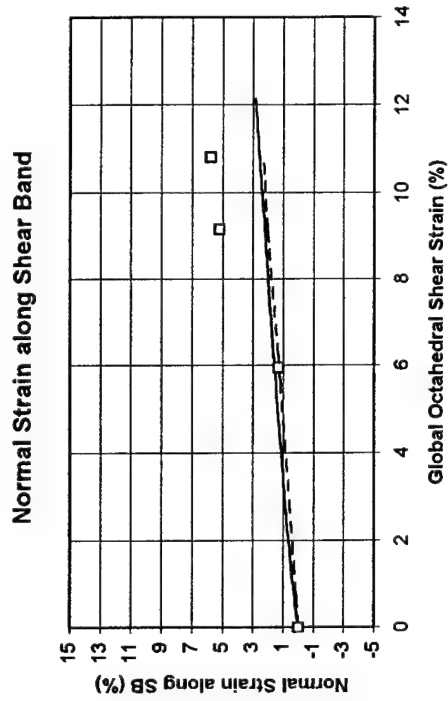
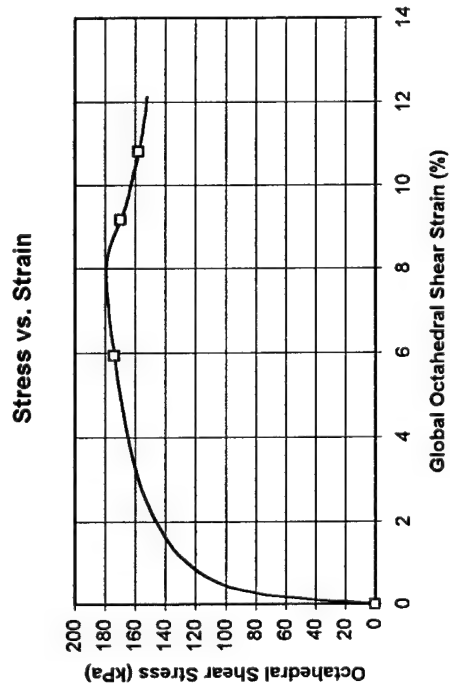
A1. Strains in a System of Axes Along and Normal to the Shear Band (SB) for Test #27

b=0.50; ECP=345 kPa; Dr=50%; Saturated



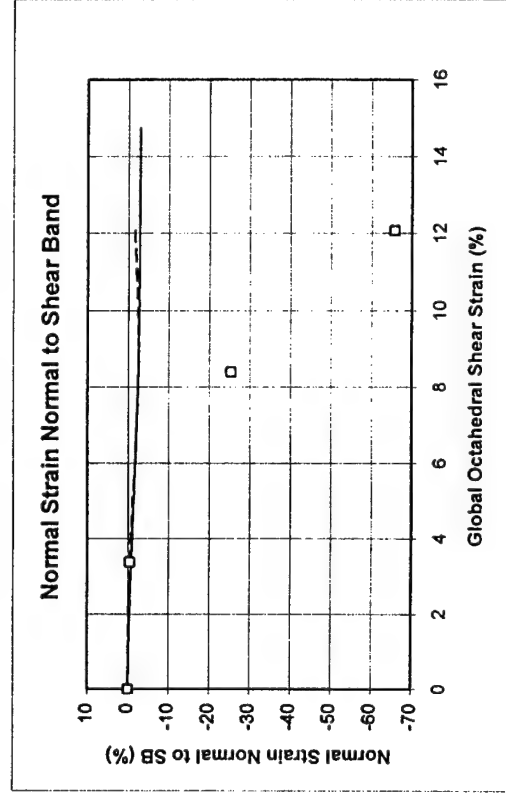
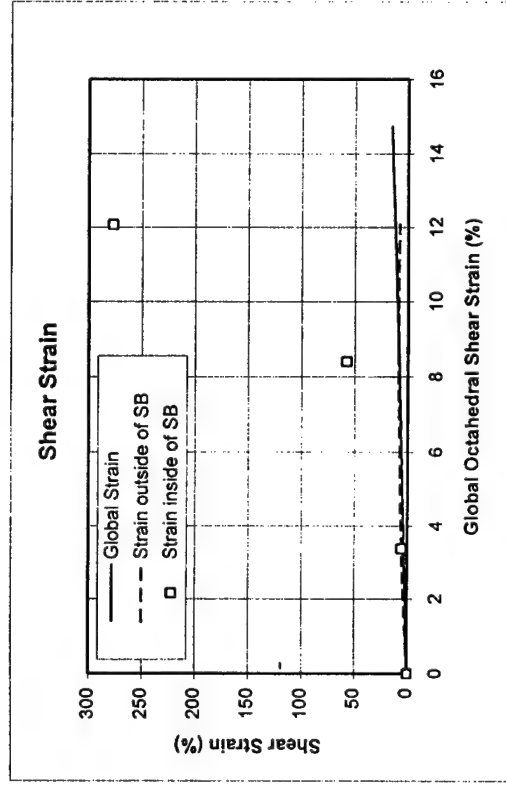
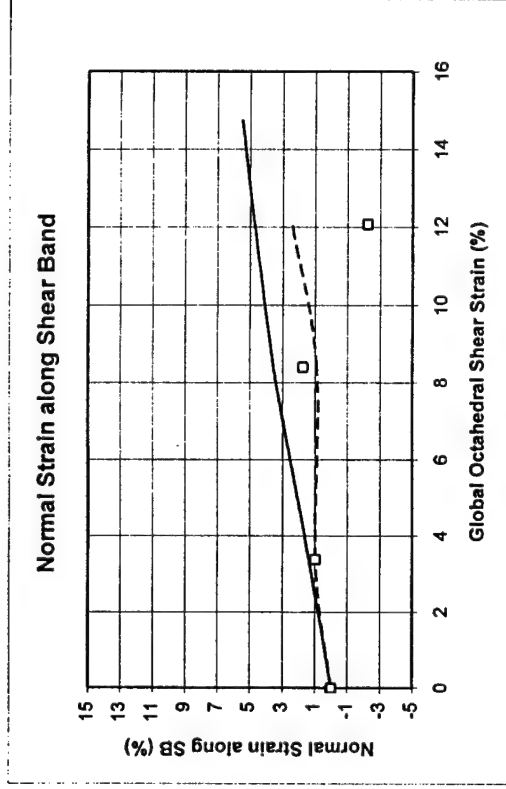
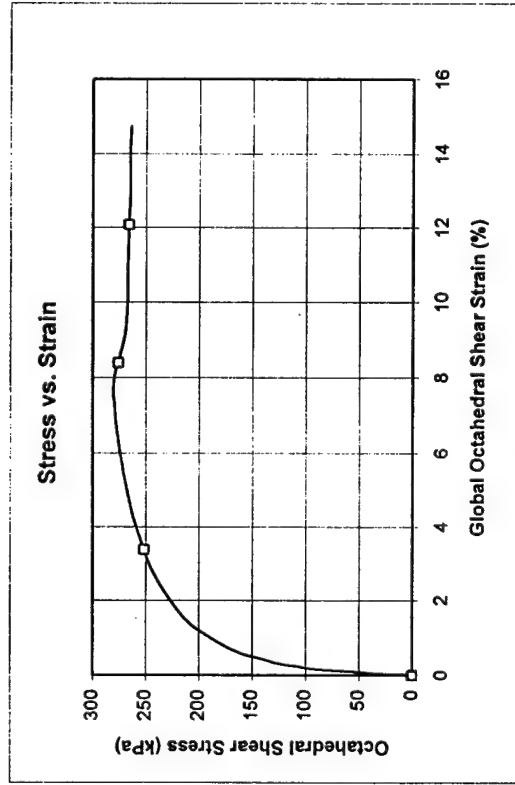
A2. Strains in a System of Axes Along and Normal to the Shear Band (SB) for Test #28

b=0.75; ECP=345 kPa; Dr=50%; Saturated



A3. Strains in a System of Axes Along and Normal to the Shear Band (SB) for Test #29a

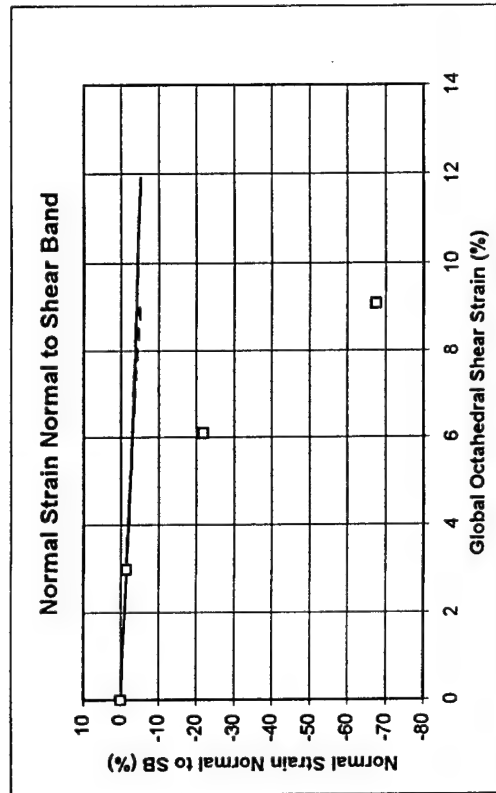
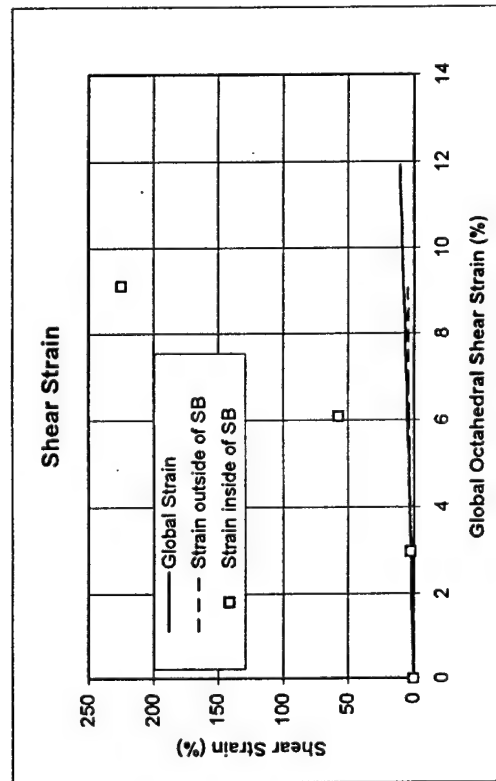
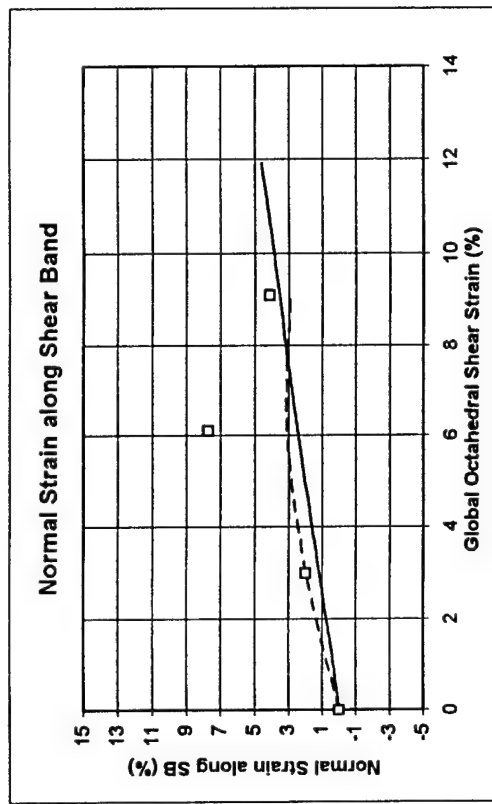
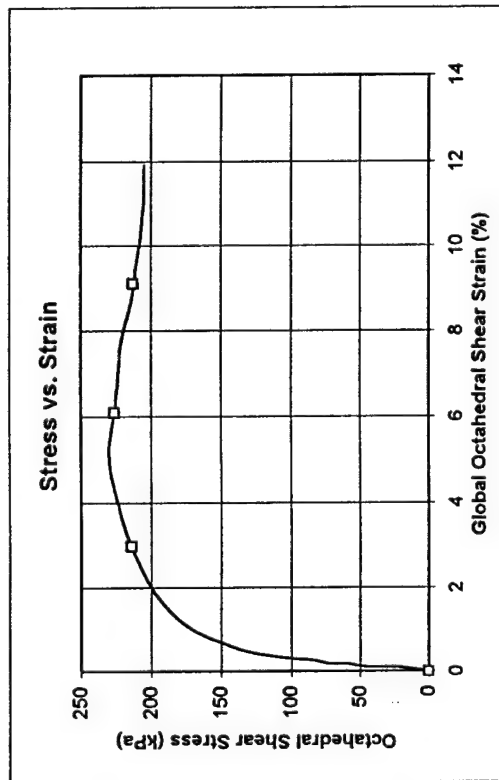
b=0.25; ECP=345 kPa; Df=80%



A4. Strains in a System of Axes Along and Normal to the Shear Band (SB) for Test #42

(Calculations for this test were made assuming no volume change)

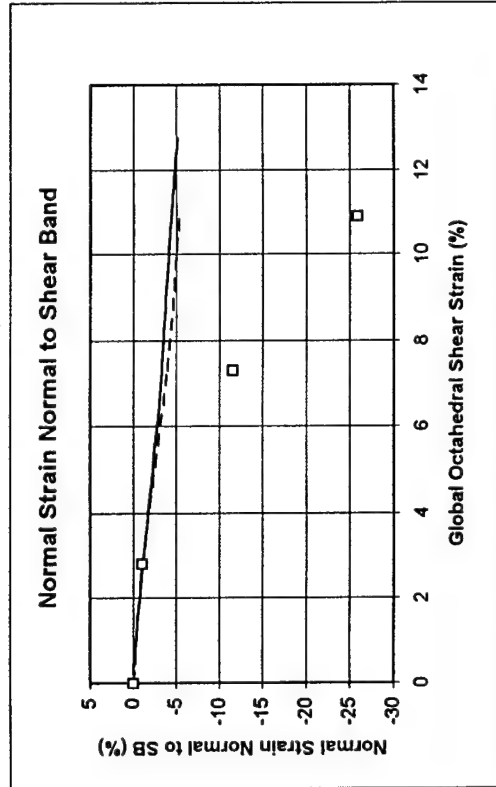
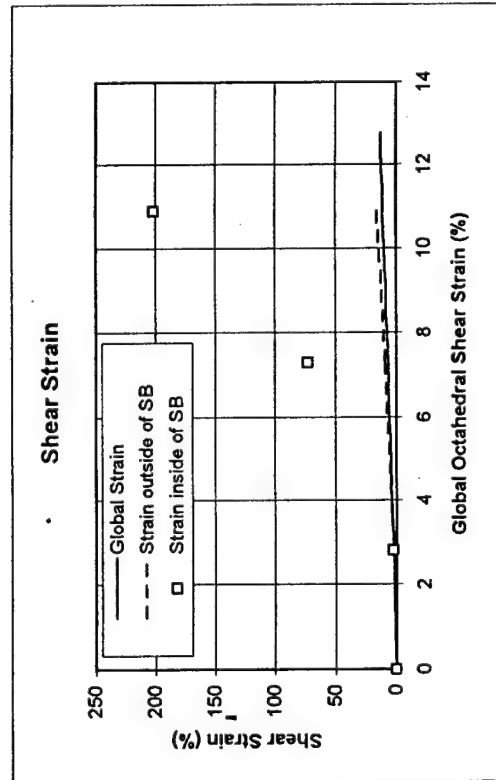
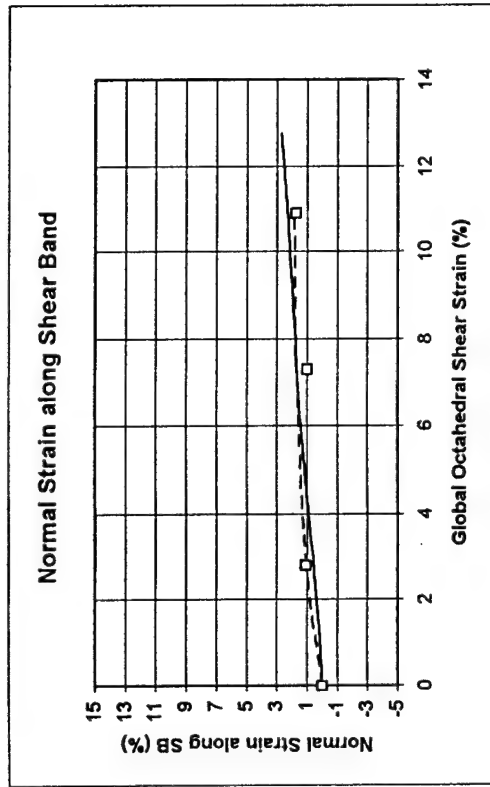
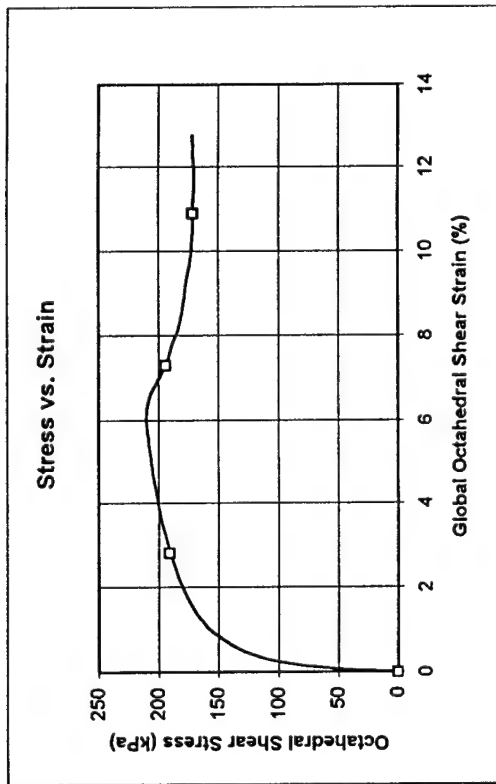
b=0.50; ECP=345 kPa; Dr=80%



A5. Strains in a System of Axes Along and Normal to the Shear Band (SB) for Test #43

(Calculations for this test were made assuming no volume change)

b=0.75; ECP=345 kPa; D=80%



A6. Strains in a System of Axes Along and Normal to the Shear Band (SB) for Test #44

(Calculations for this test were made assuming no volume change)

PAPER 3 --- ON SANDS

A Thesis

(Loire Sand)

**SHEAR BANDING IN COARSE SANDS
UNDER COMBINED STRESSES**

by

THOMAS J. MOON JR.

Submitted in partial fulfillment of the requirements
for the degree of Master of Science

Thesis Advisor: Dr. Adel S. Saada

Department of Civil Engineering
CASE WESTERN RESERVE UNIVERSITY

May, 1998

Shear Banding in Coarse Sands Under Combined Stresses

Abstract
by
Thomas Moon

The phenomenon of shear banding in soils has been studied over the last few years at Case Western Reserve University. Prior research was performed on cohesive and fine-grain, angular soils. To complete the study, a coarse-grain sand was used to determine the effect grain size has on the propagation of shear bands. Many state-of-the-art techniques were used to collect the necessary data; these include digital imaging programs and constant mean stress testing devices.

Several different variables were examined to determine the effect they have on the development and propagation of the shear band. Some of these parameters include relative density, stress path, and confining pressure. The genesis of the slip plane and the eventual direction of the shear band was monitored using video cameras. At regular times during the testing process, "snapshots" from these cameras were taken and stored as VGA images on a computer. The images were then digitally traced using specifically designed software packages. With the images digitally recorded, a great deal of information could then be calculated; such as the angle of the slip plane and the strains in and around the shear band.

With the final phase of this ongoing project now completed, a comparative analysis between the different types of media was performed. This information is summarized and several theories attempting to predict the angle of failure are evaluated in this report.

Acknowledgments

The author wishes to, first and foremost, thank his advisor and mentor, Dr. Adel S. Saada, for his patience and guidance on this thesis. His knowledge on the subject of Soil Mechanics has been a tremendous asset to myself and to Case Western Reserve University. This project was sponsored by a research grant provided by the United States Air Force Office of Scientific Research and their support is appreciated.

The author wishes to acknowledge the countless hours of work contributed by Dr. Liqun Liang. Much of the new technology used on this project was conceived by Dr. Liang and his support was invaluable. Dr. J. Ludwig Figueroa, C. Tucker Cope, and Carol Dietz provided much appreciated advice throughout the duration of this research.

On a more personal note, the author would like to thank his family and friends for their unwavering support over the past two years. My parents, Thomas and Judy Moon, and my sister, Nancy Tofil, have always stood beside me and encouraged me to better myself as a student and person. Finally, the author would like to extend his gratitude to Scott Castelli for being an excellent colleague, roommate, and friend.

Table of Contents

Abstract	ii
Acknowledgments	iii
Table of Contents	iv
List of Figures	vi
List of Tables	x
Notation	xi
Chapter One: Introduction	1
1.1 History of Research on Shear Banding	1
1.2 Phenomenon of Shear Banding	3
1.2.1 The Definition and Mechanism of Shear Banding	3
1.2.2 Parameters Thought to Affect Shear Banding	4
1.2.3 Initial Formation of Shear Bands	4
1.3 Previous Theories Predicting Angle of Shear Banding	8
1.4 Extent of Research	14
1.4.1 Selected Method of Study	14
1.4.2 Research Objectives	15
1.5 Thesis Outline	15
Chapter Two: Experimental Program	17
2.1 Introduction	17
2.2 Testing Material	17
2.3 Experimental Investigation	19
2.3.1 Variation of Parameters	19
2.3.2 Case Data Base Adopted Nomenclature	21
2.4 Specimen Preparation	23
2.4.1 Specimen Shape	23
2.4.2 Specimen Preparation	24
2.4.3 Sample Saturation Procedure	28
2.4.4 Consolidation of Specimen	29
2.5 Testing Procedure	29
2.5.1 Testing Equipment	29
2.5.2 Data Acquisition	30
2.6 Data Analysis and Parameter Calculation	31
Chapter Three: Digital Image Process and Measurements	35
3.1 Introduction	35
3.2 Image Acquisition and Camera Setup	35
3.3 Transferral of Grid on Specimen to Digital Coordinates	38

3.3.1 Initial Tracing	38
3.3.2 Inclusion of Shear Bands in Digitized Images	39
3.3.3 Horizontal Corrections for Surface Curvatures	41
3.3.4 Vertical Corrections for Surface Curvatures	47
3.4 Analysis of Shear Bands	48
3.5 Accuracy of Digitization Method	51
Chapter Four: Results	52
4.1 Introduction	52
4.2 Evaluation of Acquired Data	52
4.2.1 Explanation of Tests Evaluated	52
4.2.2 Description of Plotted Data	53
4.3 Calculation of Effective Angles of Friction (ϕ')	65
4.4 Determination of the Angle of Dilation (Ψ)	66
4.5 Summary and Conclusions	72
Chapter Five: Analysis	73
5.1 Introduction	73
5.2 Analysis of Shear Band Equations	73
5.3 Test Results	82
5.4 Influence of Testing Parameters	85
5.4.1 Confining Pressure	85
5.4.2 Generalized Versus Direct Testing	87
5.4.3 Relative Density	88
5.5 Comparison Between LSI-30 and Loire Sand	90
5.5.1 Overview	90
5.5.2 Physical Properties	90
5.5.3 Angles of Friction and Dilation Comparison	91
5.6 Summary and Conclusions	93
Chapter Six: Conclusions	95
6.1 Summary	95
6.2 Results and Conclusions	95
6.3 Suggestions for Future Research	96
Appendix A: References	98
Appendix B: Digitization Results	101
B.1 Explanation of Appendix Graphs	101
B.2 Test #77	105
B.3 Test #78a	134
B.4 Test #79	163

List of Figures

Figure 1.1	Multiple Slip Lines (Cope: Test #32, Time 2209 sec.)	5
Figure 1.2	Multiple Slip Lines (Cope: Test #32, Time 2709 sec.)	6
Figure 1.3	Dominant Shear Band (Cope: Test #32, Time 3705 sec.)	6
Figure 1.4	Multiple Slip Lines (Moon: Test #77, Time 2094 sec.)	7
Figure 1.5	Multiple Slip Lines (Moon: Test #77, Time 2498 sec.)	7
Figure 1.6	Dominant Shear Band (Moon: Test #77, Time 3192 sec.)	8
Figure 1.7	Coulomb's Theory	9
Figure 1.8	Roscoe's Theory	9
Figure 1.9	Angle of Dilation (Ψ) - Direct Shear (Bolton, 1986)	10
Figure 1.10	Stress - Strain Behavior of Dense Sand (Bolton, 1986)	11
Figure 1.11	Angle of Dilation (Ψ) - Mohr Circle (Bolton, 1986)	11
Figure 1.12	Zitouni's Method for Determining Ψ	13
Figure 1.13	Arthur - Vardoulakis Theory	13
Figure 2.1	Grain Size Distribution of Loire vs. LSI-30 Sand (Liang, 1995)	18
Figure 2.2	"Dog Bone" Shaped Specimen	25
Figure 2.3	Profile of Specimen and Preparation Mold Configuration	27
Figure 2.4	Typical Output from VOID.EXE Program (Test #77)	33
Figure 2.5	Example of Print Out from DATCNV3.EXE (Test #77)	34
Figure 3.1	Schematic of Testing Setup (Saada et. al., 1998)	36
Figure 3.2	Digital Image Combined with Test Information	37

Figure 3.3	a) Initial Digitization of Grid ($t=2500$ sec) b) Shear Band Overlaid on Deformed Grid c) Shear Band Interlaced with Deformed Grid d) Combination Image After Corrections	40
Figure 3.4	Correlation Between Perceived Length on Image and Actual Length on Surface of Specimen	42
Figure 3.5	Snell's Law	43
Figure 3.6	Plot Used to Determine Center of Image	45
Figure 3.7	Theoretical and Regression Correction Curves	46
Figure 3.8	Digitized Grid in Horizontal Direction	46
Figure 3.9	Horizontal Line Correction	48
Figure 3.10	Initial Grid and Deformed Grid After Horizontal Correction	49
Figure 3.11	Digitized Images at Various Time Intervals After Corrections	50
Figure 3.12	Estimation of the Error Associated with the Digitization Process (Saada, 1998)	51
Figure 4.1a	Torque, Axial Load and Cell Pressure (Test #77)	55
Figure 4.1b	Torque, Axial Load and Cell Pressure (Test #78a)	55
Figure 4.1c	Torque, Axial Load and Cell Pressure (Test #79)	56
Figure 4.2a	Axial Load and Displacement (Test #77)	57
Figure 4.2b	Axial Load and Displacement (Test #78a)	57
Figure 4.2c	Axial Load and Displacement (Test #79)	58
Figure 4.3a	Effective Principal Stresses (Test #77)	59
Figure 4.3b	Effective Principal Stresses (Test #78a)	59
Figure 4.3c	Effective Principal Stresses (Test #79)	60
Figure 4.4a	Volume of Specimen (Test #77)	61

Figure 5.5b	Predicted Inclination (Arthur-Vardoulakis) (Tests #92 - 94d)	80
Figure 5.6a	Predicted Inclination (Coulomb & Roscoe) (Tests #97a - 99c)	81
Figure 5.6b	Predicted Inclination (Arthur-Vardoulakis) (Tests #97a - 99c)	81
Figure 5.7a	Effect of Confining Pressure on Shear Band Inclination (Loose Samples)	86
Figure 5.7b	Effect of Confining Pressure on Shear Band Inclination (Dense Samples)	86
Figure 5.8	Effect of Generalized Versus Direct Tests on Shear Band Inclination	87
Figure 5.9a	Effect of Relative Density on Shear Band Inclination	88
Figure 5.9b	Effect of Relative Density on Shear Band Inclination (Averaged Values)	89

List of Tables

Table 1.1	Shear Band Equations as a Function of Average Grain Size (Koenders et. al., 1990)	14
Table 2.1	Index Properties and Classification of Loire vs. LSI-30 Sand (Liang, 1995)	18
Table 2.2	Inclination of Principal Stresses (Cope, 1997)	20
Table 2.3	Test Nomenclature (Saada et. al., 1993)	22
Table 2.4	Complete List of Testing Program	22-23
Table 2.5	Typical Specimen Dimensions	24
Table 4.1	Summary of the Angles of Friction and Dilation	71-72
Table 5.1a	Predicted Shear Band Inclinations with the Horizontal (Coulomb & Roscoe)	83
Table 5.1b	Predicted Shear Band Inclinations with the Horizontal (Arthur-Vardoulakis)	84
Table 5.2	Summary of the Angles of Friction and Dilation (LSI-30)	91-92
Table 5.3	Summary of the Actual Shear Band Inclinations (LSI-30 & Loire)	92-93

Chapter One

Introduction

1.1 History of Research On Shear Banding

The shear banding phenomenon has been studied for well over two centuries. Coulomb first reported his findings on the subject back in 18th century. His famous equation predicting the angle of shear banding was the recognized standard for many decades. Roscoe attempted to improve upon this classical solution by substituting the angle of dilation for the angle of friction. In the last 25 years, since these two theories were presented, there has been a concerted effort to further understand the onset and propagation of shear bands. The following section will highlight some of the major discoveries and their importance.

In 1967, Morgenstern and Tchalenko noticed shear bands were influenced by boundary conditions. They used a direct shear device to study cohesive materials. In this study, clay was infused with carbowax to instigate the onset of a shear band. Nearly a decade later in 1976, Balasubramaniam used X-rays to investigate the deformation of clays. He noticed that the local and global strains were in excellent agreement up to approximately 75% of the peak value. In 1977, Arthur et al. introduced the idea that the angle of shear banding could be more accurately predicted by taking an average of the theories presented by Coulomb and Roscoe. In this theory, both the angles of friction and dilation were taken into account. Vardoulakis (1980) further supported this claim of a geometrical average of the two classical solutions. Houlsby and Wroth (1980) stated that for the case of plastic deformation in plane strain, it was not necessary that a velocity discontinuity be a line of zero extension, contrary to prior beliefs. They also separated

kinematic discontinuities into multiple categories. In 1982, Arthur & Dunstan used radiography to study granular non-cohesive sands. They noted that the previously determined average of the Coulomb and Roscoe theories still gave the best prediction of the rupture zone angle, but the particle size of a particular media would effect this inclination. It was also found that shear bands tended to fully form at failure. This was true when the sample was under conditions of homogeneous stresses with fixed principal stress directions. Radiography was also used by Scarpelli & Wood in 1982. They investigated the inclination of shear bands found in simple shear devices. The findings from that study showed that the degree of constraint imposed on the sample effected the shear band angle. For highly restrained samples, the angle would approach the Coulomb solution and the line of zero extension. Otherwise, the angle would be more consistent with the inclination predicted by the Arthur-Vardoulakis theory.

In 1990, Koenders et al. came upon the same conclusion as Arthur & Dunstan. It was suggested that the shear band inclination was dependent upon the average grain size of the sand used. Vermeer (1990) tended to agree with the notion that the particle size effected the shear band inclination but attributed this, in part, to the width of the shear band. Fine-grained sands typically have thinner shear bands and thus have a smaller influence. Coarse-grained sands have thicker bands and these tend to be more affected by boundary conditions. For this reason, the finer sands have a tendency to yield shear band angles consistent with the Coulomb solution. The general findings from this study, Vermeer contended, showed that most sands would exhibit Coulomb-type inclinations if there were small effects from boundary conditions.

Saada, Bianchini & Liang (1994) performed numerous tests on clay using a hollow cylinder testing device. These tests indicated that clays, when tested under undrained conditions, acted like a frictional material to which Coulomb's theory applied. Cope (1997) used the same hollow cylinder device to analyze fine-grained soils. By using a new visual/digital analysis method, he determined that the Arthur-Vardoulakis theory gave the most accurate predictions of shear band angles.

With all the research on shear bands, much debate still exists on several issues. This thesis attempts to clarify some of those questions. Additional information on the subject is presented by analyzing a coarse-grained sand in a hollow cylinder device using the same testing regiment used by Cope. In this manner, definitive conclusions can be drawn about the effect of grain size.

1.2 Phenomenon of Shear Bands

1.2.1 The Definition and Mechanism of Shear Banding

Shear bands are defined as the localization of plastic deformation at areas of discontinuity in soil. A shear band can be compared to a tear in a piece of paper. Once a fissure forms, it will continue to propagate along a given path but the rest of the paper will remain relatively unaffected. In a soil specimen, a shear band starts at an area of high local stress, typically at a weakness or discontinuity. Sand behaves as an elastoplastic material and slip surfaces are generated as soon as nonrecoverable deformations take place. At a stress level close to the peak, slip surfaces coalesce in areas of high stress concentrations giving birth to a shear band that propagates until total failure is reached. Shear banding is associated with a high local deformation and only regions

relatively near the shear band are affected. Therefore, after a shear band has fully developed, the two halves of a specimen, separated by the band, will act as two independent blocks. The only permanent deformation that will take place after shear banding has occurred will be along the shear band itself. It is important to note that, after failure, the majority of the sample will be relatively unaffected by continued loading.

1.2.2 Parameters Thought to Affect Shear Banding

Several factors have been thought to affect the formation and propagation of shear bands; they include:

- confining pressure
- relative density
- applied stress path
- type of soil (sands vs. clays)
- grain size distribution
- boundary conditions

Several of these factors will be analyzed to determine their effect on shear banding. With so many parameters to study, this research will attempt to determine the most significant. The effect of grain size distribution is of particular interest in this investigation.

1.2.3 Initial Formation of Shear Bands

Slip lines, as previously mentioned, begin to form the instant plastic deformations occur in sand. To further explore the onset and propagation of shear bands, a plain strain model will be examined. This will be achieved by using a hollow cylinder testing apparatus. A paper entitled "Shear Banding in Sands Observed in Plain Strain

Compression" (T. Yoshida et al., 1994) suggests that slip lines form early on when a soil is subjected to stress. (Cope) and current studies tend to agree with this notion. Proof of this can be seen in figures 1.1 to 1.6. A shear band cannot be seen at it's initiation, however. This is because shear banding is an observation and only after sufficient deformation has occurred can one be perceived. In general, the term shear band is used to describe the rupture surface that has developed at approximately the same time as the maximum shear stress, hence the term "slip line" is used to define the smaller lines which may or may not evolve into the main shear band.

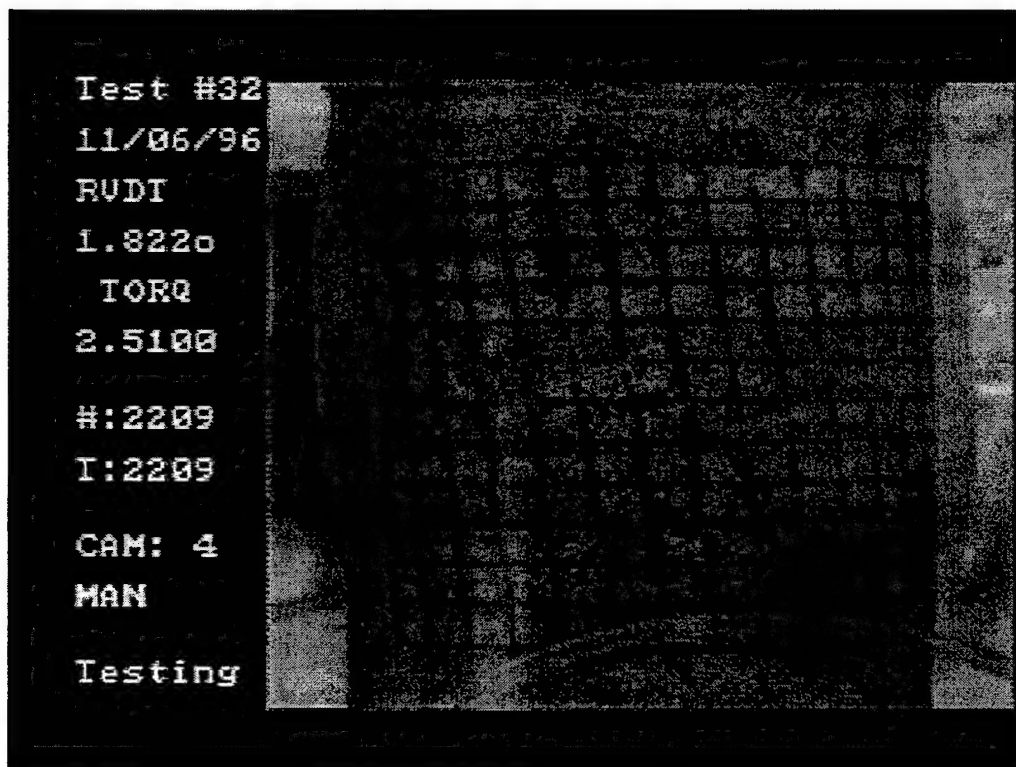


Figure 1.1 Multiple Slip Lines (Cope: Test #32, Time 2209 sec.)

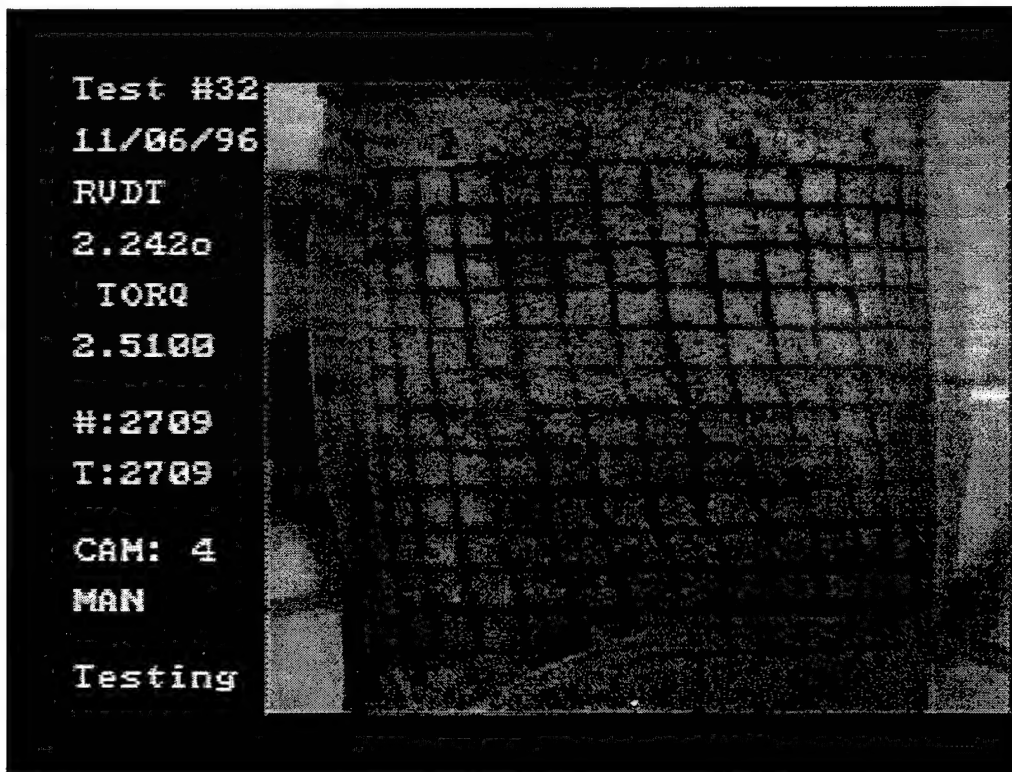


Figure 1.2 Multiple Slip Lines (Cope: Test #32, Time 2709 sec.)

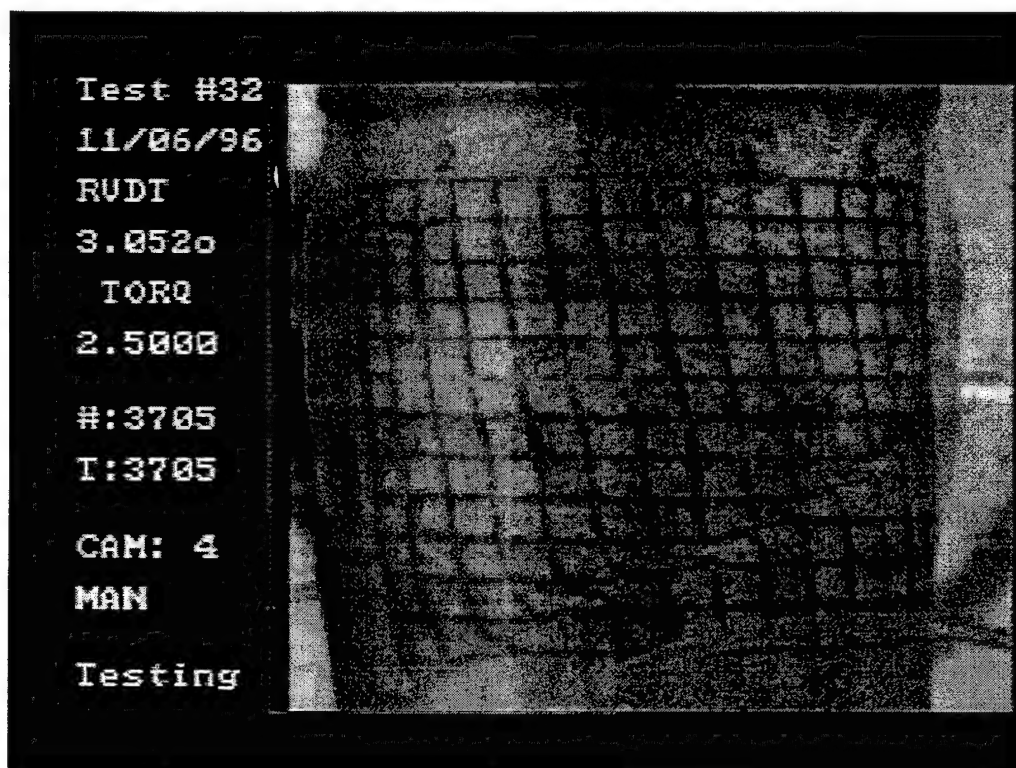


Figure 1.3 Dominant Shear Band (Cope: Test #32, Time 3705 sec)

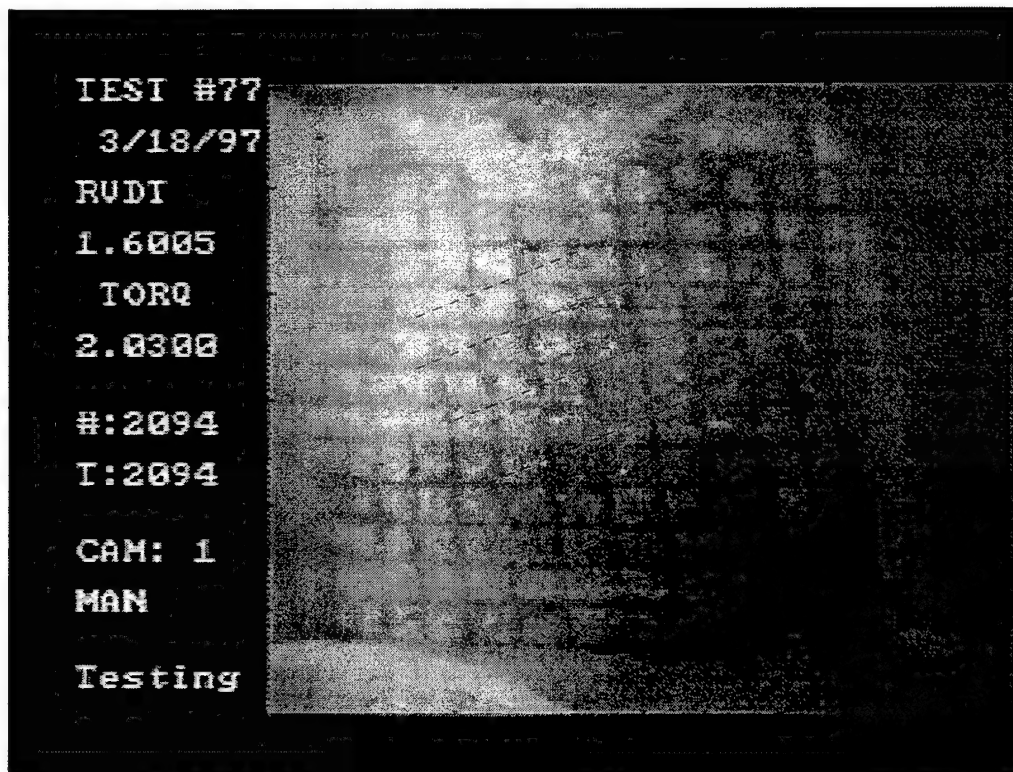


Figure 1.4 Multiple Slip Lines (Moon: Test #77, Time 2094 sec.)

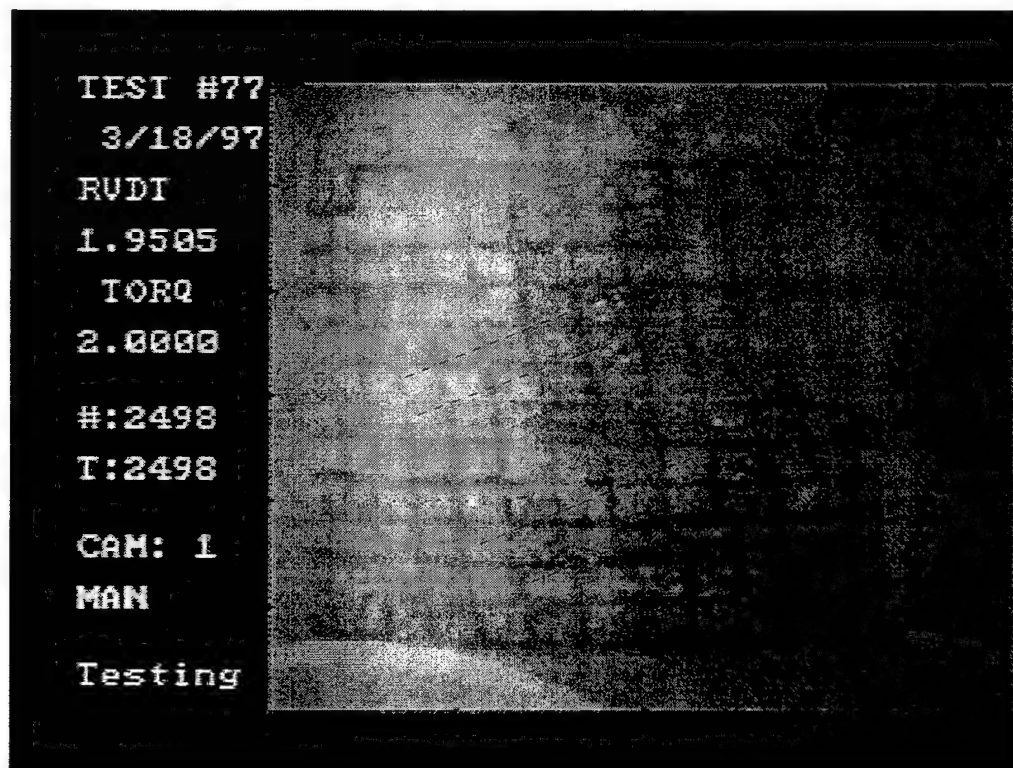


Figure 1.5 Multiple Slip Lines (Moon: Test #77, Time 2498 sec.)

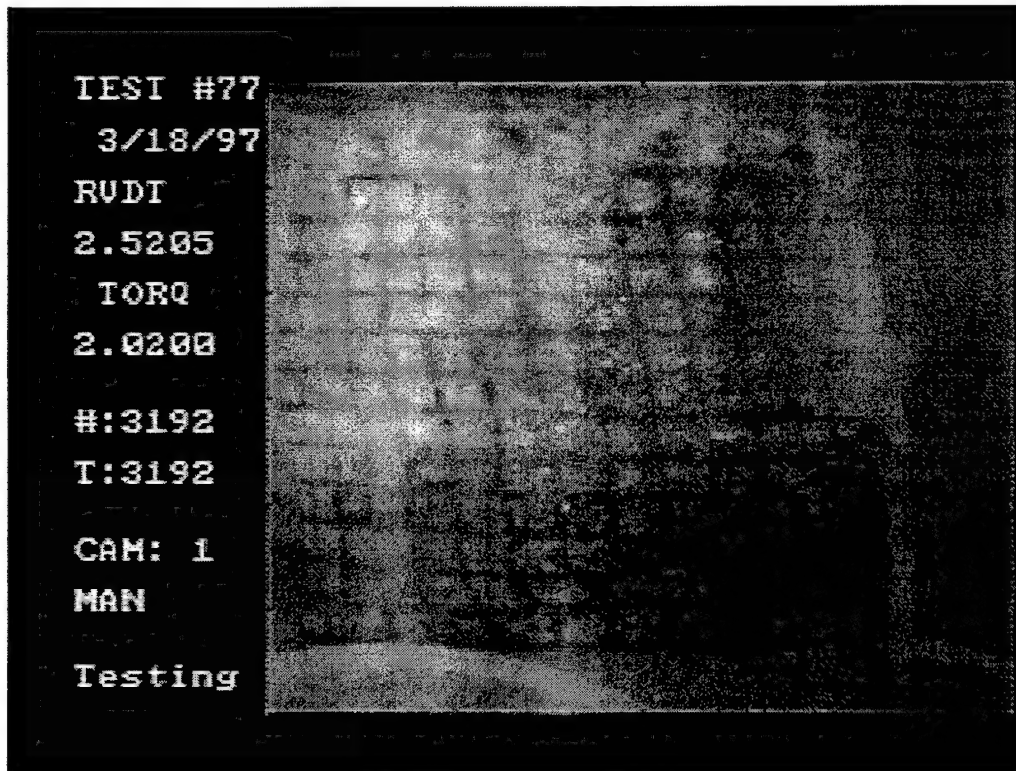


Figure 1.6 Dominant Shear Band (Moon: Test #77, Time 3192 sec.)

Since sand behaves as an elasto-plastic material, a small degree of rebounding will occur with the formation of a shear band. The smaller slip lines may become less noticeable as a result. Examples of this can be seen in figures 1.1 to 1.6 also.

1.3 Previous Theories Predicting Angle of Shear Banding

Coulomb predicted that failure in sands would form at an angle of $(\pi/4 - \phi'/2)$ from the principal stress direction. In this theory, ϕ' represents the effective angle of friction.

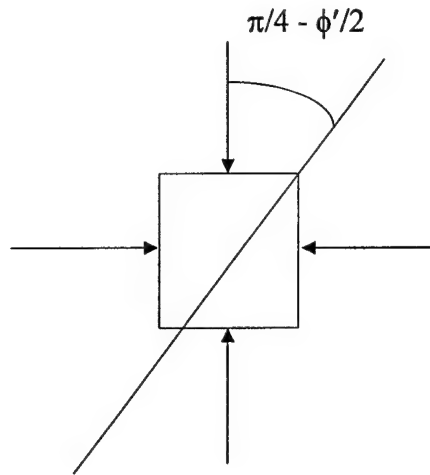


Figure 1.7 Coulomb's Theory

In 1970, Roscoe published a paper entitled "The Influence of Strains in Soil Mechanics". In this paper, Roscoe noticed that Coulomb's theory tended to overestimate the angle of shear banding. For this reason, he suggested that the angle of dilation (Ψ) be used instead of the angle of friction (ϕ'). The angle of dilation is consistently smaller than the angle of friction. Thus, Roscoe's theory states that the shear band will form at an angle of $(\pi/4 - \Psi/2)$ from the principal stress direction.

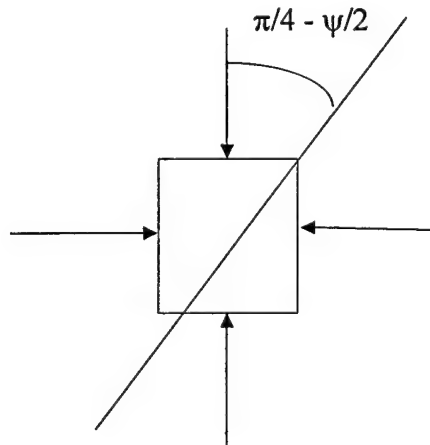
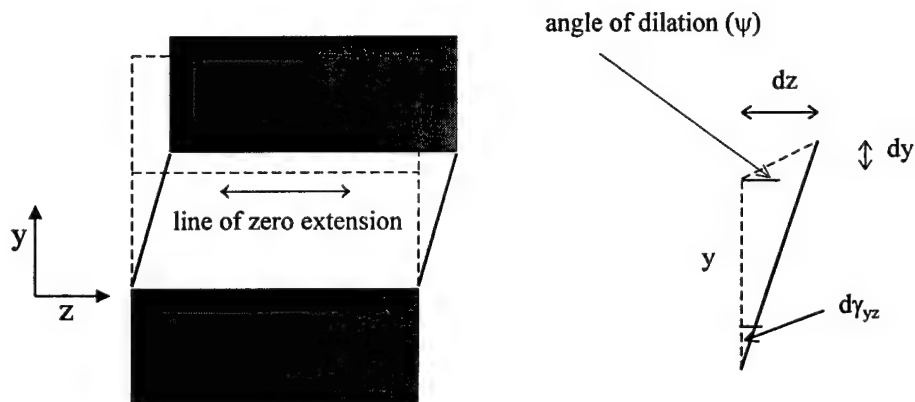


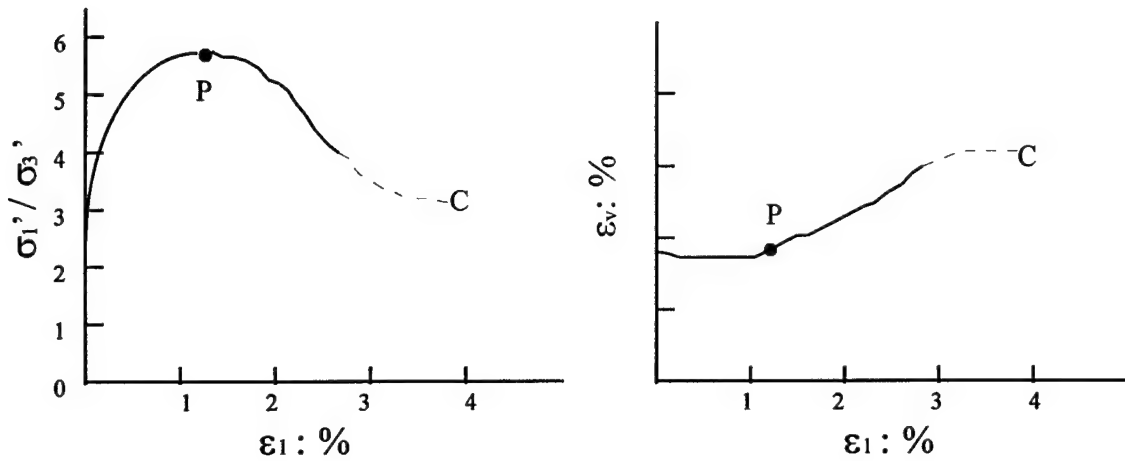
Figure 1.8 Roscoe's Theory

The angle of dilation is a quantity used to describe the expansion of a sand when subjected to shearing. A direct shear test can best be used to explain this idea. In this test, a sample is sheared but a line of zero extension is maintained. As the sand is sheared, it will tend to expand. Figure 1.9 shows how the angle of dilation is determined.



**Figure 1.9 Angle of Dilation (ψ) -Direct Shear
(Bolton, 1986)**

It is generally recognized that the maximum rate of dilation $(-d\epsilon_v / d\epsilon_1)_{\max}$ occurs simultaneously with the maximum stress. Figure 1.10 demonstrates this point. It is necessary to note that σ_1 and σ_3 are the two principal stress values of concern (σ_1 being the major principal stress), ϵ_v is the volumetric strain and ϵ_1 is the major principal strain. Both the stresses and strains are positive in compression.



**Figure 1.10 Stress-Strain Behavior of Dense Sand
(Bolton, 1986)**

Mohr's circle is used to determine the value of Ψ . Figure 1.11 shows Mohr's circle with the principal strain differences needed to calculate Ψ . This assumes a plain strain condition. There are several equations that can be used to compute Ψ from Mohr's circle (see equations 1.1 a,b,c). However, equation 1.1c is used most often for this research. This formula requires only one quantity $(d\epsilon_1/d\epsilon_3)_{\max}$.

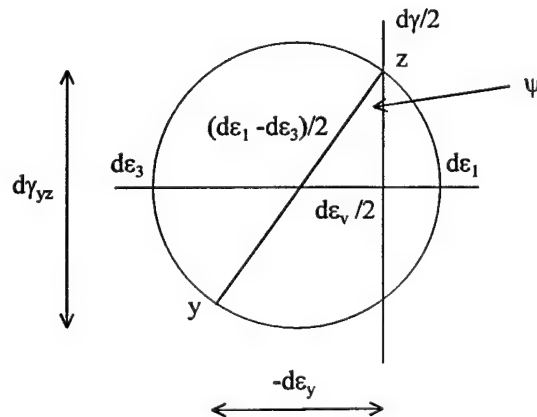


Figure 1.11 Angle of Dilation (Ψ) -Mohr Circle

(Bolton, 1986)

$$\sin \psi_{\max} = \left[-\frac{d\varepsilon_v / 2}{(d\varepsilon_1 - d\varepsilon_3) / 2} \right] \quad (1.1a)$$

$$\sin \psi_{\max} = \left[-\frac{(d\varepsilon_1 + d\varepsilon_3) / 2}{(d\varepsilon_1 - d\varepsilon_3) / 2} \right] \quad (1.1b)$$

$$\sin \psi_{\max} = \left[-\frac{(d\varepsilon_1 / d\varepsilon_3)_{\max} + 1}{(d\varepsilon_1 / d\varepsilon_3)_{\max} - 1} \right] \quad (1.1c)$$

Schantz and Vermeer (1996) noticed that the angle of dilation can be computed from a standard triaxial compression test by using equation 1.2.

$$\sin \psi_{\max} = \left[-\frac{(d\varepsilon_v / d\varepsilon_1)_{\min}}{2 - (d\varepsilon_v / d\varepsilon_1)_{\min}} \right] \quad (1.2)$$

This equation reduces to equation 1.1c when replacing the volumetric strain term (ε_v) with the equivalent term of $\varepsilon_1 + \varepsilon_3$. This is true since ε_2 drops out of the equation for a plain strain case, as is the condition of this testing. Zitouni (1988) introduced a third method for computing the angle of dilation. In this method, he uses the formula

$$\sin \psi = \left[-\frac{1 + (d\varepsilon_3 / d\varepsilon_1)}{1 - (d\varepsilon_3 / d\varepsilon_1)} \right] = \left[-\frac{1 - \tan \theta}{1 + \tan \theta} \right] = \tan [\theta - \Pi / 4] \quad (1.3)$$

Where θ is the angle found from a plot of ε_1 versus ε_3 (figure 1.12)

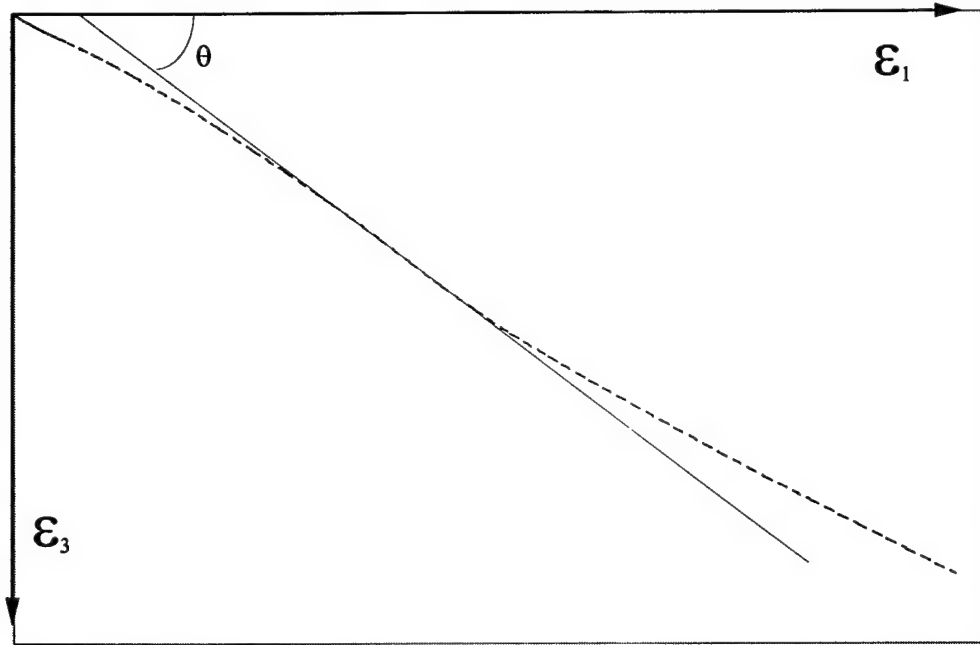


Figure 1.12 Zitouni's Method for Determining Ψ

Arthur et al. (1977) and Vardoulakis (1980) suggested that since Coulomb's theory overestimated the shear band angle and Roscoe's theory underestimated it, that a combination of these two theories should result in greater accuracy. This hypothesis stated that the angle of failure will occur at an angle of $(\pi/4 - (\psi + \phi')/4)$ with the major principal direction.

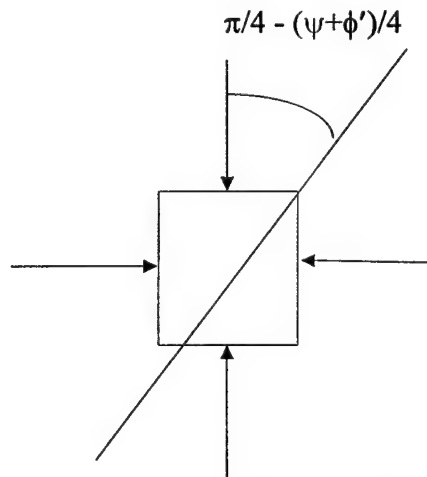


Figure 1.13 Arthur-Vardoulakis Theory

Still further research proposed that Coulomb's, Roscoe's, and Arthur-Vardoulakis' formulas were each valid depending on the particle sizes of the soil. Koenders, Arthur & Dunstan (1990) stated that the average grain size (D_{50}) was the determining factor when deciding on the most applicable formula. It was proposed that for sands with "small" grain sizes ($D_{50} \leq 0.65$ mm), Coulomb's theory would prove to be the most accurate. Conversely, for "large" grained sands ($D_{50} \geq 0.77$ mm), Roscoe's theory would give the best prediction. For the intermediate range, Arthur-Vardoulakis' theory should be used. Table 1.1 demonstrates this principle.

**Table 1.1 Shear Band Equations as a Function of Average Grain Size
(Koender et. al., 1990)**

	Shear Band Inclination		
Coulomb	$(\pi/4 - \phi'/2)$		
Arth.-Vard.		$(\pi/4 - (\psi + \phi')/4)$	
Roscoe			$(\pi/4 - \psi/2)$
	$D_{50} \leq 0.65$	$0.65 > D_{50} > 0.77$	$D_{50} \geq 0.77$
	Average Grain Size (mm) (D_{50})		

1.4 Extent of Research

1.4.1 Selected Method of Study

The goal of this thesis is to expand the current understanding of the shear banding phenomenon. Recent research at Case Western Reserve used a fine-grained sand (Cope, 1997). The results from that study would not be complete without a comparable study

using a coarse-grained sand. This paper presents the findings of the testing done on that sand and compares the results with the previous studies.

A wide variety of tests were conducted to monitor the onset and propagation of the bifurcation process. A torsional hollow cylinder device was chosen to investigate the influence of a wide array of stress combinations and loading conditions. These tests exactly match the conditions selected for Cope's research. The methods of monitoring the shear band formation remain the same. These procedures are discussed in greater detail in subsequent chapters.

1.4.2 Research Objectives

The systematic approach of this research makes it possible to determine:

- The effect of various testing conditions on shear banding including: stress path, confining pressure, relative density, and direct vs. generalized testing.
- The angle of dilation (Ψ) for each test.
- The theory that best predicts the shear band inclination.
- The effect of grain size on shear banding.

1.5 Thesis Outline

- **Chapter 2** gives an explicit description of the specific testing schedule. It also gives a detailed summary on how a test is set up and conducted.
- **Chapter 3** presents the method by which the shear bands are monitored and analyzed, including specific information on the digitization process.

- **Chapter 4** summarizes the results obtained from the testing program. In this chapter, the angles of dilation from each test are listed.
- **Chapter 5** tabulates the failure angles as well as lists the angles predicted by each of the theories mentioned. The effect of each parameter on the shear band angle are also discussed.
- **Chapter 6** gives the results and conclusions of this program of study. This section presents suggestions for any future studies which might extend this research.
- **Appendix B** presents the results from the digital image analysis. This information includes data on the shear band inclination, strains in and around the shear band, and the width of the shear band.

Chapter Two

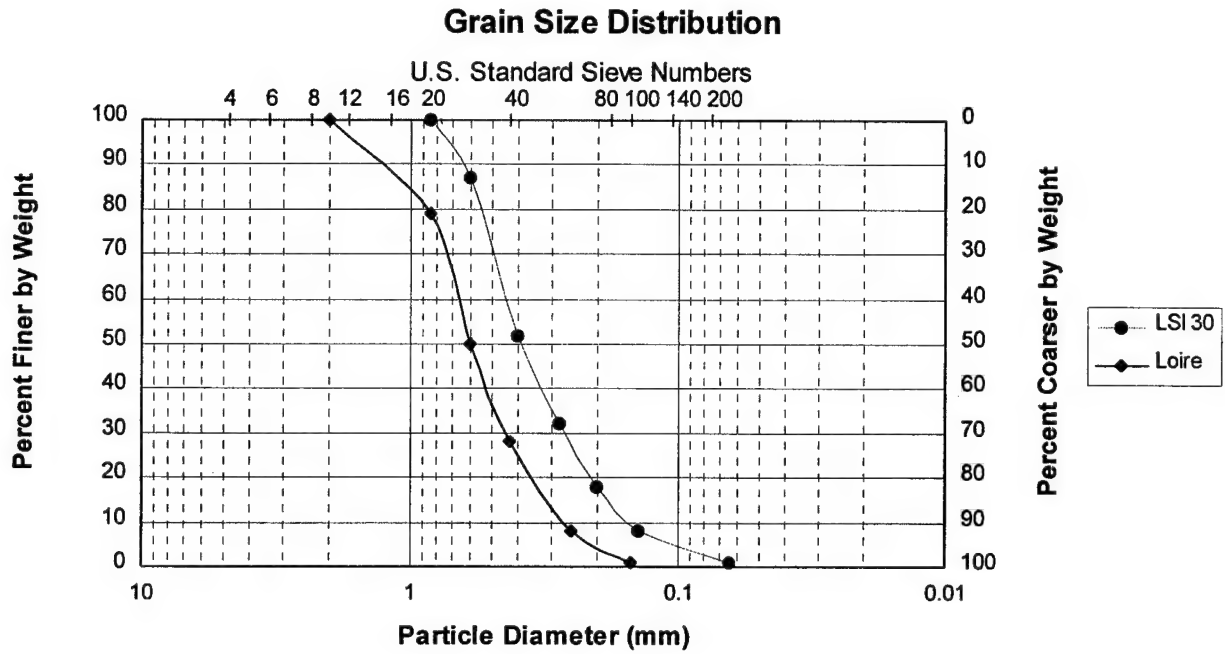
Experimental Program

2.1 Introduction

To complete our research on shear banding, the previously established testing method used for the last phase of the project was implemented for this stage (Cope,1997). While the method remained the same, the particular sand used was varied. For this section, as in the previous one, a non-cohesive, angular sand was tested. The major difference between the two media was the grain size distribution. Loire sand was chosen for this phase due to its average grain size in comparison to the previous LSI 30 sand. The Loire sand had significantly larger particle diameters versus the LSI 30, which could be described as a fine-grain sand. Figure 2.1 gives the grain size distribution curves for both sands. With the medium and the testing process determined, all the same parameters involved were researched. These include variations in the stress paths, relative density, effective confining pressure and the type of loading control (generalized versus direct testing). Each of the mentioned parameters are explained thoroughly in the following sections.

2.2 Testing Material

The sand used for this research was named Loire sand after the region in France from where it was collected. This sand was selected due to the desired particle sizes it possessed. To thoroughly complete the testing process, several ASTM standard tests were conducted on the Loire sand. These tests were needed to accurately describe and classify the sand. The tests performed included the determination of the void ratio



**Figure 2.1 Grain Size Distribution of Loire versus LSI 30 Sand
(Liang, 1995)**

**Table 2.1 Index Properties and Classification of Loire versus LSI 30 Sand
(Liang, 1995)**

Sand Name	Loire	LSI 30
USCS Group	SP	SP
Specific Gravity	2.64	2.66
Maximum Void Ratio	0.76	0.83
Minimum Void Ratio	0.49	0.52
D_{50}	0.60 mm, 0.023 in	0.39 mm, 0.015 in

(maximum and minimum), the relative density, and the particle size distribution. The information collected from these tests is summarized and compared to the corresponding data from the LSI 30 sand in Table 2.1

2.3 Experimental Investigation

2.3.1 Variation of Parameters

The variables thought to influence the propagation of the shear band were the confining pressure, the relative density, the mean stress, and the inclination of the major principal stress with respect to the vertical axis. These parameters were systematically varied to determine their individual influence on the angle of the shear band. As a result, a total of 35 separate tests were conducted. These tests were broken down into sets of five. Each set was subjected to the same conditions with the exception of the inclination of the principal stress.

Of the seven sets of tests run, three were on loose samples and four were on dense samples. The initial relative density of these samples were chosen to be 50% and 80%, respectively. The relative density of a sand is typically one of the most influential variables in the behavior of sand. For this reason, the accuracy of the initial density was carefully calculated for each test. Only samples showing an actual density within plus or minus three percent of the desired density were kept; and therefore, repeatable accuracy was extremely important. Table 2.4 lists the averaged initial relative densities.

Two types of tests were conducted; generalized and direct. In a generalized test, both the axial and cell pressures were changed throughout the test such that the mean stress remained constant. In a direct test, the axial stress was changed but the cell

pressure remained constant. Torsional stresses have no effect on the mean stress. Only one set of direct tests was run to see if the variation in the mean stress during a given test affected the angle of shear banding. The other six sets were all generalized.

There were three different initial confining pressures chosen, namely 40 psi (276 kPa), 60 psi (414 kPa), and 80 psi (552 kPa). However, since a backpressure of 10 psi (69 kPa) was used on all tests, the effective confining pressures were reduced to 30 psi (207 kPa), 50 psi (345 kPa), and 70 psi (483 kPa). Since strength depends on effective stresses, these values were the ones worthy of note. These values were chosen to maintain consistency with the previous tests conducted on fine sand.

**Table 2.2 Inclination of Principal Stresses
(Cope, 1997)**

Inclination of Principal Stresses (β)	0°	30°	45°	60°	90°
Description	Pure Compression	Compression Torsion	Pure Torsion	Extension Torsion	Pure Extension

Finally, the last parameter studied was the inclination of the principal stress with respect to the vertical axis of symmetry. This was the most important parameter studied because each of the three theories predicts the shear band inclination from this reference angle. Five different angles were chosen. Table 2.2 shows these angles and the type of test needed to produce such an inclination. Most, if not all, theories predicting the angle of shear banding include a term describing the stress path. This was the reason why all of the seven sets of tests were grouped into subsets of five.

By systematically varying the type of test conducted and analyzing the resultant

shear band angle produced, all the proposed variables and their effects were studied. In addition to this, several theories predicting the angle of the shear band were analyzed to determine the most accurate. Many of these theories incorporate the angle of dilation in their prediction. For this reason, all the tests conducted were drained since the volume change was an essential component in the dilation angle's computation.

2.3.2 Case Data Base Adopted Nomenclature

Several years ago at Case Western Reserve University, a data base was developed to systematically catalog all testing done on soil samples (Saada, 1993). The results of many years of research and testing were recorded using this program. To maintain consistency, the same system of notation was adopted to uniquely identify each test. The test identifier code is a string of six characters to describe the type of test, the relative density, the initial confining pressure... etc. The first character is either a G or D to denote a general or direct test. The second space is to describe the relative density of the specimen. Here, an L represents a loose sample of 50% while an N is for the dense sample of 80%. The next two characters are used to indicate the initial confining pressure and the inclination of the of the principal stress, respectively. The fifth space is used to describe the shape of the sample. Some possible shapes include the standard triaxial form or cube. However, since all of the conducted for this project were of the hollow cylinder, dog-bone form, every test uses the character T. Finally, the last space refers to the level of saturation for each test. A P indicates partial saturation while an F denotes complete or full saturation. Table 2.3 demonstrates this nomenclature while Table 2.4 lists the entire array of tests.

Table 2.3 Test Nomenclature
(Saada et. al., 1993)

Test Identification Format : ABXYCD	
A = Type of Test	A = G \Rightarrow Generalized A = D \Rightarrow Direct
B = Relative Density	B = L \Rightarrow $D_r = 50\%$ (Initial) B = N \Rightarrow $D_r = 80\%$ (Initial)
X = Initial Confining Pressure	X = 1 \Rightarrow $\sigma'_c = 30$ psi
	X = 2 \Rightarrow $\sigma'_c = 50$ psi
	X = 3 \Rightarrow $\sigma'_c = 70$ psi
Y = Inclination of Principle Stress	Y = 0 \Rightarrow $\beta = 0^\circ$
	Y = 2 \Rightarrow $\beta = 30^\circ$
	Y = 4 \Rightarrow $\beta = 45^\circ$
	Y = 6 \Rightarrow $\beta = 60^\circ$
	Y = 8 \Rightarrow $\beta = 90^\circ$
C = Shape of Specimen	C = T \Rightarrow Dog Bone
D = Amount of Saturation	D = P \Rightarrow Partial
	D = F \Rightarrow Full

Table 2.4 Complete List of Testing Program

Hollow Cylinder Tests (Dogbone) 1/50 motor speed or 0.012 in/min, static Drained specimen						
Test #	Name	β/b	σ'_c (psi)	D_r Target	D_r Avg. Actual	Test Type
71	GL10TF	0°/0.00	30	50	53.2	Generalized
72	GL12TF	30°/0.25	30	50	53.2	Generalized
73	GL14TF	45°/0.50	30	50	53.2	Generalized
74b	GL16TF	60°/0.75	30	50	53.2	Generalized
75	GL18TF	90°/1.00	30	50	53.2	Generalized
76a	GL20TF	0°/0.00	50	50	53.2	Generalized
77	GL22TF	30°/0.25	50	50	53.2	Generalized
78a	GL24TF	45°/0.50	50	50	53.2	Generalized
79	GL26aTF	60°/0.75	50	50	53.2	Generalized
80	GL28TF	90°/1.00	50	50	53.2	Generalized

81b	GL30TF	0°/0.00	70	50	53.2	Generalized
82	GL32TF	30°/0.25	70	50	53.2	Generalized
83a	GL34TF	45°/0.50	70	50	53.2	Generalized
84a	GL36TF	60°/0.75	70	50	53.2	Generalized
85	DL38TF	90°/1.00	70	50	53.2	Direct
86a	GN10TP	0°/0.00	30	80	79.4	Generalized
87a	GN12TP	30°/0.25	30	80	79.4	Generalized
88	GN14TP	45°/0.50	30	80	79.4	Generalized
89	GN16TP	60°/0.75	30	80	79.4	Generalized
90	GN18TP	90°/1.00	30	80	79.4	Generalized
91a	GN20TP	0°/0.00	50	80	79.4	Generalized
92	GN22TP	30°/0.25	50	80	79.4	Generalized
93a	GN24TP	45°/0.50	50	80	79.4	Generalized
94d	GN26TP	60°/0.75	50	80	79.4	Generalized
95	GN28TP	90°/1.00	50	80	79.4	Generalized
96	GN30TP	0°/0.00	70	80	79.4	Generalized
97a	GN32TP	30°/0.25	70	80	79.4	Generalized
98	GN34TP	45°/0.50	70	80	79.4	Generalized
99c	GN36TP	60°/0.75	70	80	79.4	Generalized
100a	DN38TP	90°/1.00	70	80	79.4	Direct
101a	DN10TP	0°/0.00	30	80	79.4	Direct
102	DN12TP	30°/0.25	30	80	79.4	Direct
103	DN14TP	45°/0.50	30	80	79.4	Direct
104	DN16TP	60°/0.75	30	80	79.4	Direct
105	DN18TP	90°/1.00	30	80	79.4	Direct

2.4 Specimen Preparation

2.4.1 Specimen Shape

For this particular study, a “dog-bone”, hollow cylinder specimen shape was selected. There were several reasons for this decision. This shape leads to the formation of the shear band in the middle of the sample due to its thicker ends, as well as minimizes complications due to boundary constraints. In addition, the thin wall shape helps to obtain a more uniform torsional stress. It allows for easy determination of torsional and

axial stresses, which were crucial in providing feedback to maintain constant mean stresses. The paper "Hollow Cylinder Torsional Devices: Their Advantages and Limitations" (Saada, 1988), further illustrates the rationale behind the selection of this shape. Every effort was made to prepare identical samples. Table 2.5 gives typical dimensions:

Table 2.5 Typical Specimen Dimensions

Outside Diameter (ends)	2.77 in	7.03 cm
Outside Diameter (middle)	2.60 in	6.60 cm
Inside Diameter	2.0 in	5.08 cm
Height of Middle Section	4.1 in	10.41 cm
Height of Overall Specimen	5.1 in	12.95 cm
Volume	11.80 in ³	193.40 cm ³

2.4.2 Specimen Preparation

Since the approximate volume of the sample and the properties of the soil being used were known, the weight of the soil to be used could be measured. For these experiments, two different soil sample weights were used. These corresponded to the 50% and 80% relative densities. After the soil weight was determined, the following steps were taken to build the specimen:

1. Select two membranes (outer and inner) and check each for any leaks. Each membrane must be intact. Trim the ends off to obtain the desired length and measure the thickness of each membrane.
2. Affix both membranes to the bottom cap using two concentric rubber bands and

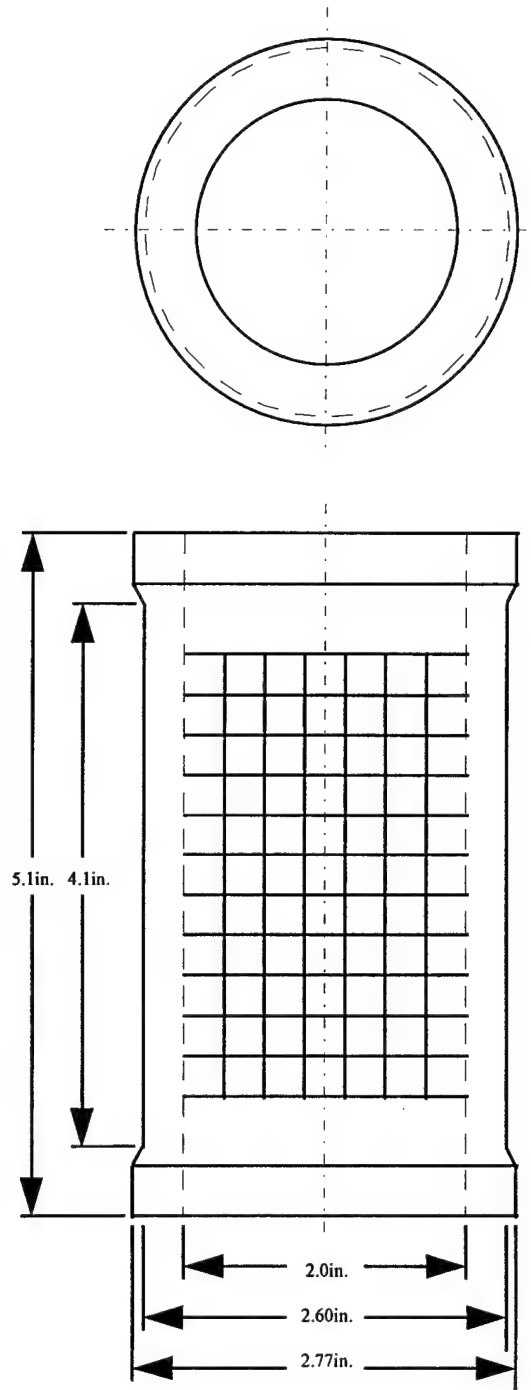


Figure 2.2 "Dog Bone" Shaped Specimen

a hose clamp. Place the outer mold on the bottom cap and around the outer membrane.

3. Apply a vacuum to the outer mold to pull the membrane taut. Slide the inner mold inside the smaller membrane and tighten the fastener to fix it into place.

4. Place the sand between the two membranes and tamp the sides to obtain the pre-selected relative density.

5. Affix the top cap over the existing specimen and fasten it to the sample, again using rubber bands and a ring clamp. Figure 2.3 gives a profile view of the sample as it look at this point.

6. Draw water into the sample to roughly fill the void spaces using a vacuum.

Place the specimen sample in the freezer for at least two hours to freeze the water.

7. Take the outer mold off the sample and roll down the membrane down, exposing the surface of the sample. Thaw the outer layer of ice off the sample to create a dry surface onto which an ink grid is stamped.

8. Pull the membrane up over the sample and apply a vacuum to the specimen to adhere both membranes to their respected surfaces. Measure the dimensions of the sample by taking several measurements and finding their average. For instance, four height measurements are taken for each sample and their values are averaged to obtain the best value. The same procedure is used for both the outside and inside diameters. All of the measurements are then used to determine the sample's actual volume and the corresponding relative density.

9. Secure the specimen to the cell and place a capped plexiglass cylinder over the

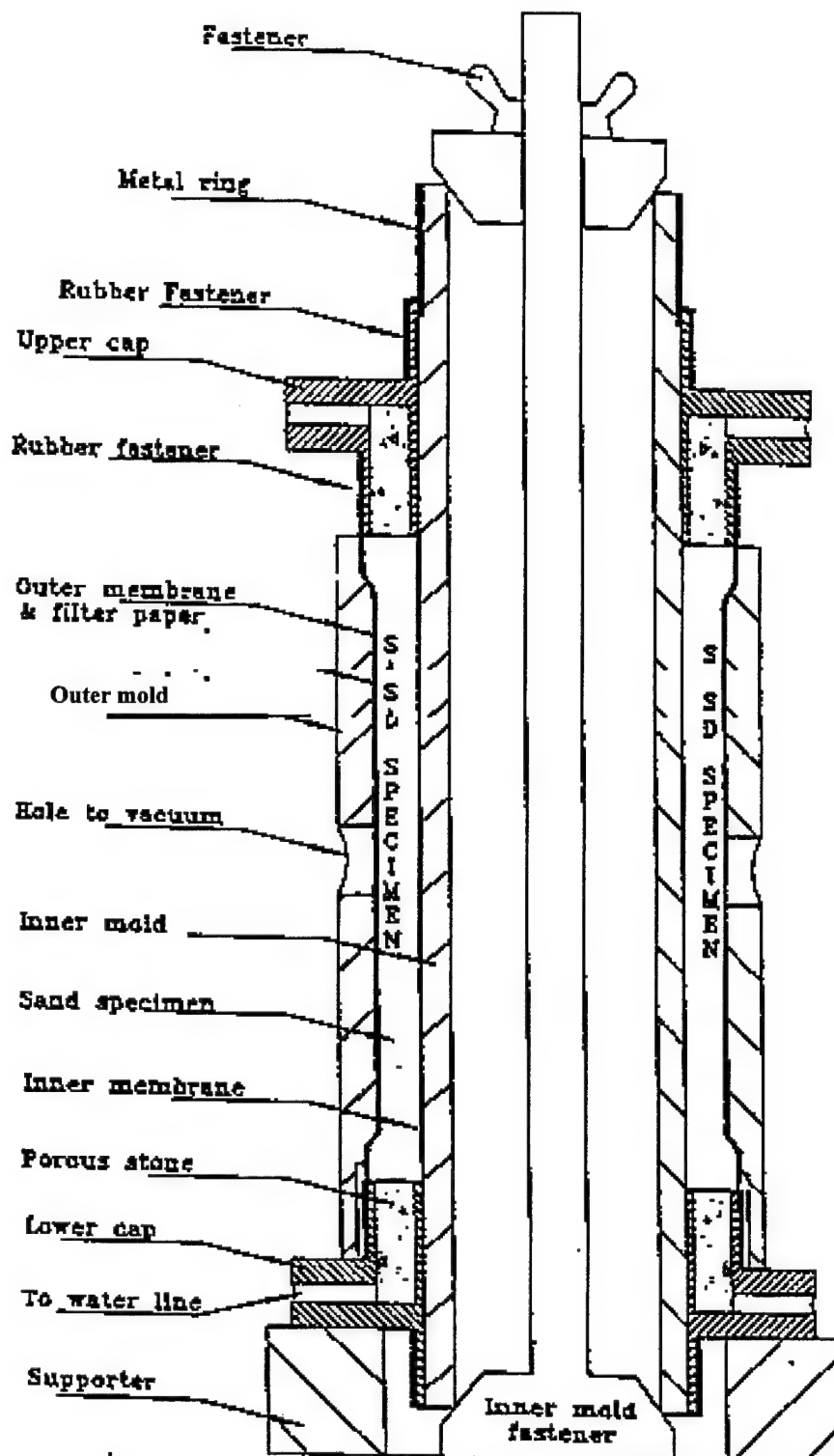


Figure 2.3 Profile of Specimen and Preparation Mold Configuration

entire setup to seal the sample inside.

10. Pressurize the cell slightly to support the now thawed sample and flood the cylinder with silicon oil. The oil will magnify the grid on the specimen, making it easier for the cameras to capture images. The sample is now ready for saturation.

2.4.3 Sample Saturation Procedure

For the volume change of the sample to be accurately measured, the specimen needed to be completely saturated with distilled water. The following procedure was used to fulfill this requirement.

1. Connect a line to the sample to supply carbon dioxide. The source of the gas was at a pressure of just over atmospheric, namely 1 psi gauge. Carbon dioxide was used to force all the air from the specimen.
2. The carbon dioxide was fed to sample via the same inlet hose but the outlet was varied between the other three hoses. Each of the three outlets were open for at least 10 minutes to allow for sufficient gaseous saturation.
3. The gas line was then replaced with a deaired water line. Again, as with the carbon dioxide, the inlet hose remained the same but the outlet varied. For the water line, at least 40 milliliters of water was passed through each hose. This cycle was repeated twice with the water pressure at 1 psi.
4. After the water was fed into the specimen with the initial cell pressure at 5 psi, the cell pressure was increased to 15 psi and a back pressure on the water line was brought up to 10 psi. This was done in small increments to keep the sample at the

same approximate effective pressure (cell pressure minus back pressure).

5. As with the previous step, water was passed through each hose. This time, however, only 20 milliliters of water was passed through each outlet hose but the cycle was still repeated twice.

6. The specimen then sat under these conditions to allow for all of the remaining carbon dioxide to dissolve into the water. Usually this was done overnight but at least for three hours.

7. Just before the application of the deviator stress, water was passed through each line again to remove any remaining gas.

8. Finally, one of the drainage lines was connected to a pressure transducer to measure the volume change by reading the water level in a vertical pipette.

2.4.4 Consolidation of Specimen

At this stage of preparation, the cell pressure was 15 psi (103.43 kPa) above atmospheric. This pressure was raised to reach the 30 psi (207 kPa), 50 psi (345 kPa), or 70 psi (483 kPa) effective initial confining pressure, depending on the test specifications. The effect of this increase tended to consolidate the specimen. Since the volume change was measured, the influence of the effective mean stress on relative density and strength can be determined.

2.5 Testing Procedure

2.5.1 Testing Equipment

The capabilities of the testing device made it possible to accurately measure seven channels of information. These included axial displacement both inside and outside the

cell, axial force and torque, rotational displacement, cell pressure and volume change. By incorporating the use of LVDT's, RVDT's, strain gages...etc., all of this information was converted to corresponding voltages and fed into a control computer. The computer was also connected to a pneumatic control panel that regulated the axial force and cell pressure accordingly to maintain a constant mean stress.

2.5.2 Data Acquisition

For the specific purposes of these experiments, a program entitled ACQ_MENU.EXE was developed. The capabilities of this program are as follows:

- To print specific experimentation information including: test date, conductor, effective initial confining pressure, back pressure, and loading control.
- To list material properties including: sample name and type (I.E. Loire sand), USCS classification, maximum and minimum void ratios, and specific gravity.
- To print the measured sample dimensions including: height, inner and outer diameters, and post-consolidation height and volume changes.
- To give input control information including: data input rate and duration, scan upper and lower bound limits, channel names, calibration coefficients, and maximum and minimum voltage limits.
- To give visual data information including: real time plot of all seven channels as they are received from the testing device.

The testing process produced a data file containing somewhere between 1200 and 3600 data points for each channel, depending on the type of test run. This data file contained all the information needed to analyze the test. However, back up acquisition

recorders were used to collect redundant data to ensure that the testing information was still gathered in the event of a computer malfunction. There were four separate graphic plotters to collect all seven channels of data.

In addition to digital and plotter data, video images were recorded as well. For all torsion tests, digital cameras were set up to capture the sample from four different views. When spliced together, these images gave a complete depiction of the sample. At predetermined times during the testing procedure, "snapshots" of the camera images were taken. These pictures were the ones that would later be digitized to complete the analysis process. In addition to the captured images, a VCR was used to record the slow progression of shear banding in case a picture turned out poorly.

2.6 Data Analysis and Parameter Calculation

Several computer programs aided in the processing of raw test data and determination of key parameters. Since testing was done on samples with two different relative densities, namely 50% and 80%, the weight of the sand used in each case needed to be known. This was calculated by the same program used to determine the relative density. Also, the raw data received from testing often contained small variations commonly referred to as "noise". In order to compensate for this unavoidable occurrence, a program was developed to perform polynomial regression to filter out the background "noise" and greatly reduce the number of necessary data points.

The dimensions of each sample varied little from test to test. Therefore the volume of each sample was relatively constant. By knowing significant properties of the sand being tested as well as the volume, a weight of sand could then be determined.

Obviously, there were two separate weights used to get the different desired relative densities. A program named VOID.EXE was helpful in performing the necessary calculations. An input data file was created for each test with all the pertinent data including measured specimen dimensions, weight of sand used, and specific material properties such as the void ratios. From this data file, the program could perform the necessary calculations and give the particular sample's relative density. When first determining the weight of soil to use, a trial and error approach was required. Typical sample dimensions were entered in the program along with a trial weight. This trial weight was varied until the relative density matched the required one.

To analyze the raw data from testing, a program was created to first filter out any unwanted noise and then compress the information into a standard form. This program, FILTER.EXE, used polynomial regression to accurately model the acquired data. From these trend lines, forty points were chosen which effectively compressed the information into the standard format. This served two useful purposes. First, it cut down on the size of the acquired data file and, second, it standardized the information into a form where it could be easily analyzed.

The program, DATCNV3.EXE, was used to take the filtered data file and summarize the information. Settings in the program enabled the output to contain data in both English and SI units. This program also modified the data into the standard format used by the Case Western Reserve University data base. This allowed for easy additions to the data base. Each test was processed by the above programs to completely record the testing results. Figures 2.4 and 2.5 show typical outputs from these programs.

This program determines:

- 1) the expected void ratio and the needed weight of sand,
after giving the volume of the mold, minimum and maximum
void ratio, expected relative density and specific gravity;
- 2) the actual void ratio and relative density obtained,
after measuring the actual volume of sample.

***** Liqun Liang (03/21/96) *****

The thickness of inner membrane	=	0.0121 (in)
The thickness of outer membrane	=	0.0119 (in)
 The relative density	=	 50.0082 (percentage)
The minimum void ratio	=	0.4900
The maximum void ratio	=	0.7600
The specific gravity	=	2.6400
The volume between two molds	=	12.2000 (in ³)
The volume between two molds	=	12.2519 (in ³)
The weight (g)	=	324.8000 (g)
The weight (lb)	=	0.7161 (lb)
The expected void ratio	=	0.6250
 The inner diameter with membrane	=	 1.9525 (in)
The outer diameter with membrane	=	2.6370 (in)
The height measured /w caps	=	8.4575 (in)
 The inner diameter of specimen	=	 1.9768 (in)
The outer diameter of specimen	=	2.6133 (in)
The height of specimen	=	5.0475 (in)
The height of middle specimen	=	4.1000 (in)
The volume of specimen	=	12.2036 (in ³)
The volume of middle specimen	=	9.4077 (in ³)
The actual Gamma _d	=	1.6250 (g/cm ³)
The actual void ratio	=	0.6255
The actual relative density	=	49.8290 (percentage)

**Figure 2.4 Typical Output From VOID.EXE Program
(Test #77)**

---- Test ID ----

Test #77; Torsion-Compression; Drained w/ Vol. Measured

Test Date = 03/18/97
 Consolidation = Normal
 Back pressure (psi) = 10.000
 Eff. Con. Press (psi) = 50.000
 Add. Axial Stress (psi) = 0.000
 Loading design = Static
 Loading control = Rotation
 Loading rate = Motor 1/50
 Height control = Free

---- Material ID ----

Name = LOIRE
 Type = Sand
 Group symbol = SP
 Specific gravity = 2.640
 Relative density = 0.670
 Minimum void ratio = 0.4900
 Maximum void ratio = 0.7600

---- Record Information ----

Ch 0 Torque (in) (50.00 inlb/V)
 Ch 1 Axial Force (in) (100.00 lb/V)
 Ch 2 RVDT (10.00 °/V)
 Ch 3 LVDT (IN) (0.05 in/V)
 Ch 4 LVDT (Out) (0.10 in/V)
 Ch 5 Cell Pressure (20.00 psi/V)
 Ch 6 Volume Change (2.50 ml/V)
 Total record point number = 41
 Scan rate (number/sec) = 1.0
 Scan duration (sec) = 3407.0
 Elapsed time (sec) = 3407.7

---- Specimen Dimension ----

Height (in) = 4.100
 Height change (in) = 0.005
 Inner diameter (in) = 1.950
 Outer diameter (in) = 2.577
 Initial volume (in³) = 9.408
 Volume change (in³) = 0.269

---- Others ----

Beta (deg.) = 30.18
 b_value = 0.25
 Angle of Friction (deg.) = 51.17

Figure 2.5 Example of Print Out From DATCNV3.EXE (Test #77)

Chapter Three

Digital Image Process and Measurements

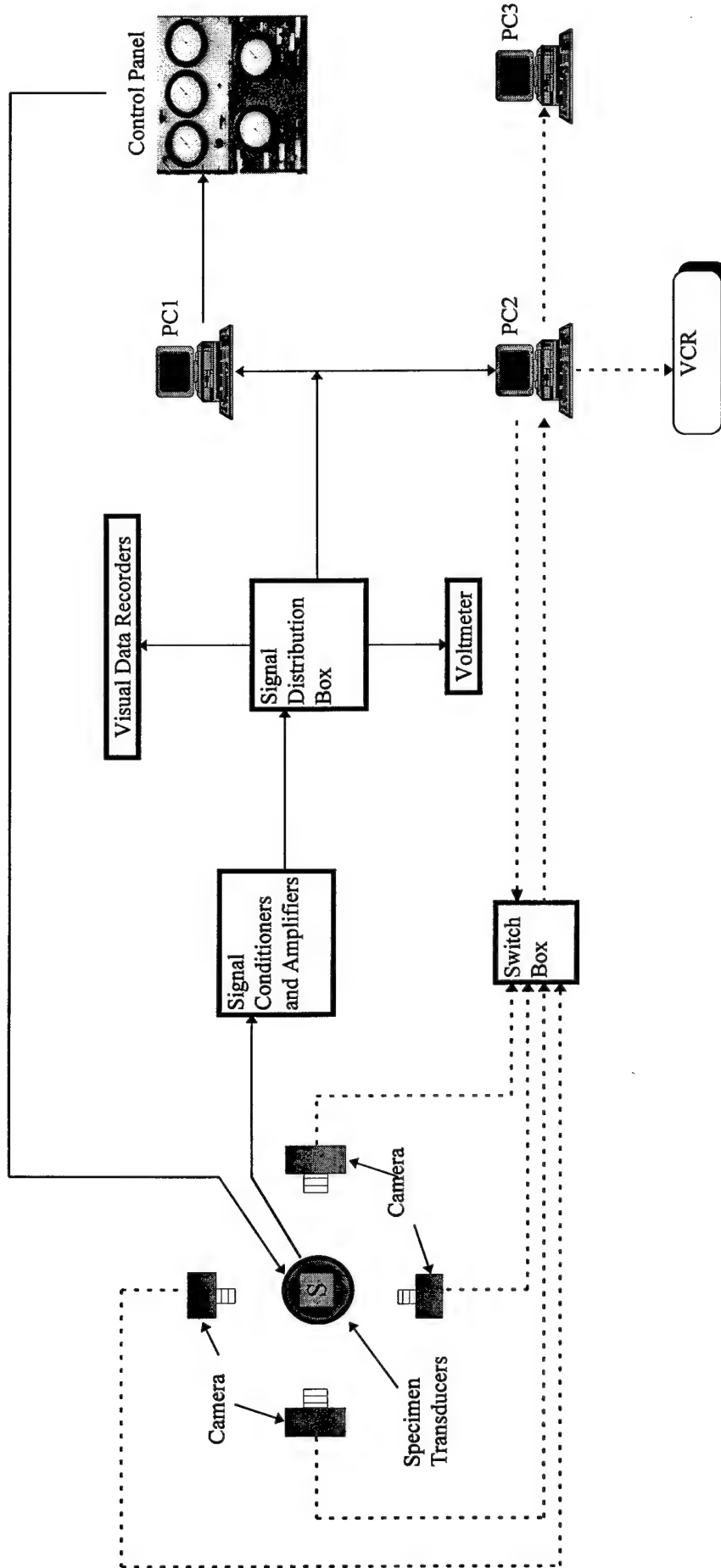
3.1 Introduction

To assist in the accuracy of analysis, a new digital imaging process was developed. This procedure involves capturing pictures of the specimen during testing with the use of digital cameras. The images obtained from this process were then, with the aid of a mathematical computer program, analyzed to determine the angle of shear banding. By using this new procedure, a great deal of information was obtained.

3.2 Image Acquisition and Camera Setup

Each hollow cylinder specimen had two grids stamped on the surface. Those two grids covered nearly the entire surface area of the sample. To ensure completeness, four separate cameras were used to view the two grids; two per side. The four cameras were mounted on brackets which were fixed in place. For this reason, the cameras did not move during the test despite the fact that the sample was subjected to rotational displacements. This did not impose a problem, however, since the top of the specimen was fixed as well and therefore a constant reference was maintained.

Figure 3.1 schematically represents the image acquisition system. Here, the dashed lines represent the pathways along which images were transferred and the solid lines show the path that data and feedback control follow. Before the images were received by the first computer (PC2), a switch box was used. This device was needed to take the four separate images and send them along a common circuit. Only one image



- Solid lines show the path of data acquisition and test control.
- Dashed lines show the path of image recording.
- PC1 records signals from transducers through a A/D board as voltages, calculates and sends out voltages to control panel through a D/A board.
- Control panel changes the voltages from PC1 to air pressure and supplies air pressure to increase/decrease axial forces and cell pressures.
- PC2 merges the voltage reading and the image, then sends the results to a VCR and PC3.
- Images are continuously recorded by a VCR and selectively by PC3.

Figure 3.1 Schematic of Testing Setup
(Saada et. al., 1998)

could be transferred at a time. For this reason, the acquisition program from PC2 had a timer programmed in to toggle the image's order. This allowed a complete set of images to be sent every 20 to 40 seconds depending on the delay between successive images. Once the pictures were received by PC2, they were assimilated with a template. This effectively combined the image with information pertinent to the test in process such as test number, date, time elapsed... etc. Figure 3.2 demonstrates a typical image collected during a test.

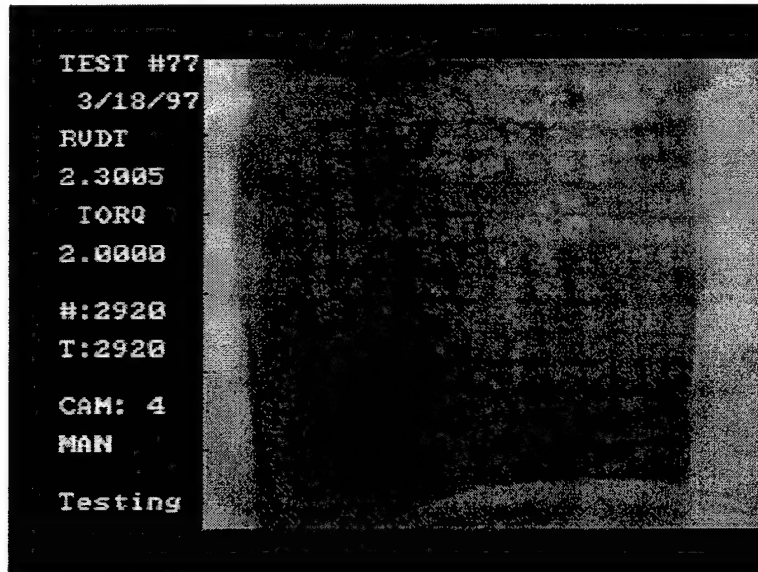


Figure 3.2 Digital Image Combined With Test Information

The images, after being merged with the template at PC2, were then sent to two separate locations where they were recorded. First, the images were transferred to a video cassette recorder where they were collected throughout the testing process. Typically, the images would change every five seconds. Second, the pictures were transferred to PC3

where they were stored as "snapshots". It was these images that were later digitized. For a normal test, "snapshots" were taken at seven pre-selected times. Therefore, a total of 28 images were collected, seven images for each of the four cameras. As a precautionary measure, a standard photographic camera was also used to collect images at the same seven times. This was used only as a back-up in the event of a computer failure.

3.3 Transferral of Grid on Specimen to Digital Coordinates

3.3.1 Initial Tracing

Dr. Liqun Liang created a series of programs using the MATLAB™ software package. This process was discussed in greater detail in the paper "The Use of Digital Image Processing in Monitoring Shear Band Development" (Liang, 1996). Essentially, the digitization procedure involves bringing up the digital snapshot of the sample on a computer and tracing the grid as it appeared on the specimen. In this manner, the deformation of the sample was followed and since each grid point then had a known coordinate, the strains could then be calculated. By using a high resolution monitor, the tracing operation was done with moderate accuracy. However, when the digitized grids were checked with a 600 dots per inch (dpi) printer, the accuracy became significantly greater. In addition to this visual cross checking, a sub-program was developed with MATLAB™ to aid in the fine tuning adjustments. The digitization process is currently very time consuming since the majority of the work still needs to be done manually.

The digital cameras used for capturing images in these experiments covered an area of 3.37 inches (8.56 cm) in the horizontal direction and 3.0 inches (7.62 cm) in the vertical direction. Each camera had a resolution of 512 pixels horizontally and 492 pixels

vertically. This yielded a resultant of 154 pixels per inch (60 pixels/cm) in the horizontal direction and 164 pixels per inch (64 pixels/cm) in the vertical direction. Once an image was captured on the computer, the resolution of the image was changed to 640 pixels (H) by 480 pixels (V). This modification reduced the size of the file and saved time when recording the image. To get an idea of the accuracy of this process, one pixel is equal to roughly 0.008 inches (0.23 mm) and the average grain size of Loire sand (see table 2.1) is 0.023 inches (0.60 mm). Therefore, there are approximately 3 pixels for every grain of Loire sand giving remarkable precision.

3.3.2 Inclusion of Shear Bands in Digitized Images

The digitizing process was performed by manually tracing the intersection points of the grid stamped on the sample. This procedure worked well for initial images and images that did not have a shear band, but a problem arose when trying to digitize pictures that contained a shear band. The issue was that a shear band produces high strains along the slip plane. Bends or kinks in the otherwise smooth grid lines appeared. Those bends occurred at places other than at grid intersections. For this reason, an extra step was included for images that contained a shear band. Those images were digitized like any other image where the grid intersection points were traced, but then another separate digitizing process was performed. The shear band was traced separately

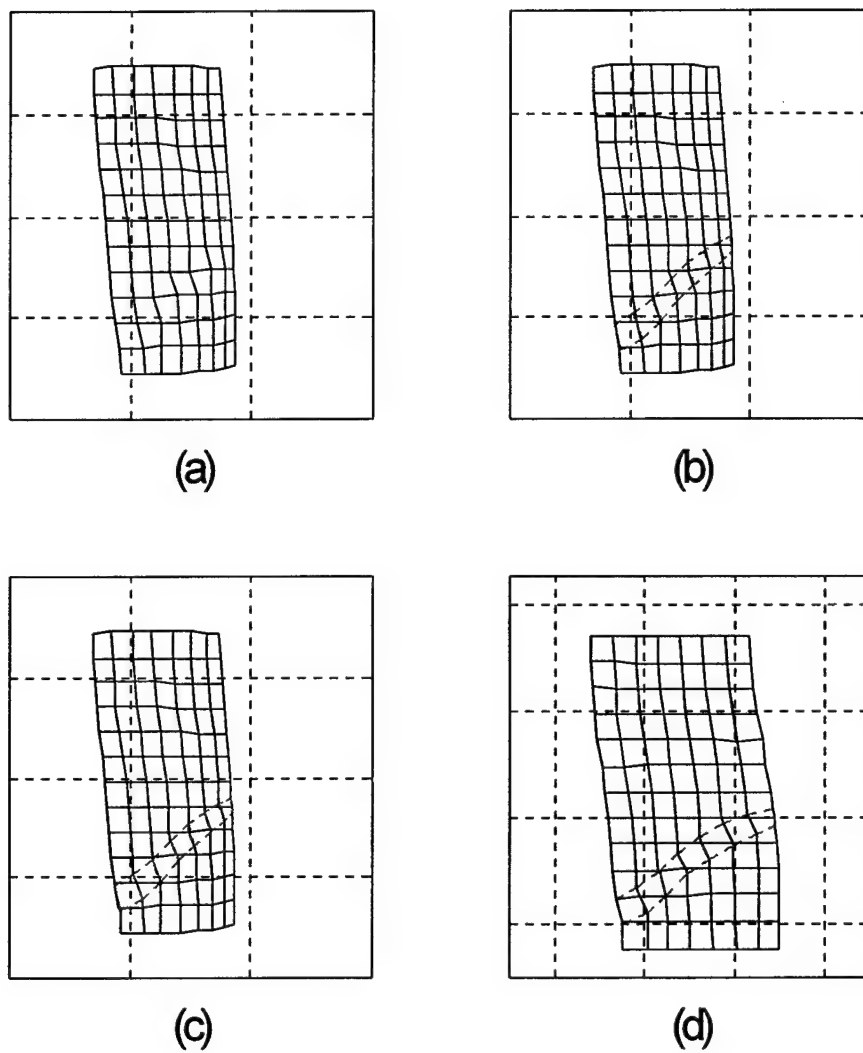


Figure 3.3 **a) Initial Digitization of Grid ($t=2500$ sec)**
b) Shear Band Overlaid on Initial Grid
c) Shear Band Interlaced with Deformed Grid
d) Combined Image After Corrections

from the overall image. The bends along the vertical lines were traced. Once the two steps were completed and modified to the desired accuracy, the two images were superimposed to give a complete representation of the shear band. Figure 3.3 shows this process. Figure 3.3a is the image with only the grid intersection points, Figure 3.3b is the images where only the shear band is digitized and, finally, Figure 3.3c is the final digitized image including both necessary parts. The fourth image, Figure 3.3d, is the same as Figure 3.3c except the modifications correcting for surface curvature and refraction are implemented. These corrections are discussed in the next two sections.

3.3.3 Horizontal Corrections for Surface Curvature

Since a two dimensional picture represents a three dimensional object, a correction needed to be incorporated in the calculations for the surface curvature. Each camera recorded approximately one quarter of the samples surface. However, since the sample was cylindrical in shape, the vertical lines appeared to converge together the further they were from the center. Theoretically, the correction could be determined mathematically. This relationship was resolved by consulting Figure 3.4. and is seen below (Equation 3.1):

$$S = R \sin^{-1} \frac{L}{R} \quad (3.1)$$

R = outer radius of the specimen

L = horizontal length from centerline of the image

S = corrected horizontal length

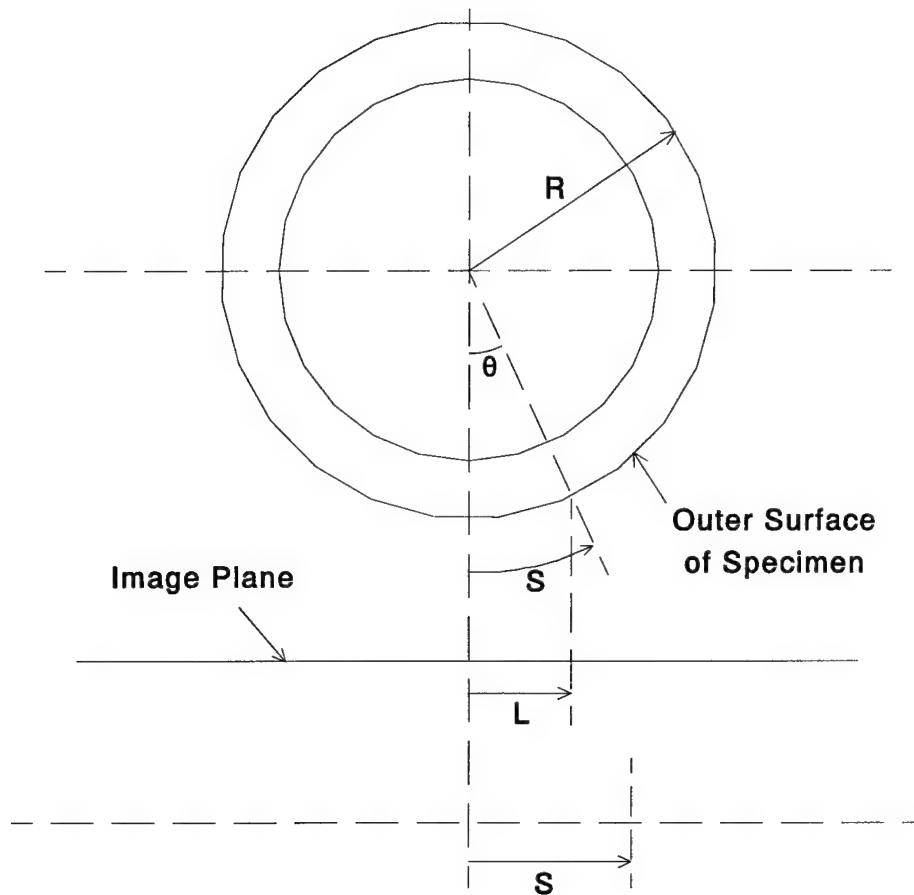


Figure 3.4 Correlation Between Perceived Length on Image and Actual Length on Surface of Specimen

Equation 3.1 would be the correction factor used to find the true length between vertical lines if the curvature of the sample was the only parameter that needed to be considered. This, however, was not the case. One more variable needed to be examined. The phenomenon of refraction was also considered. As Snell's Law (equation 3.2) points

out, the angle at which the image is being viewed from and the coefficients of refraction of both the oil and the air needed to be considered.

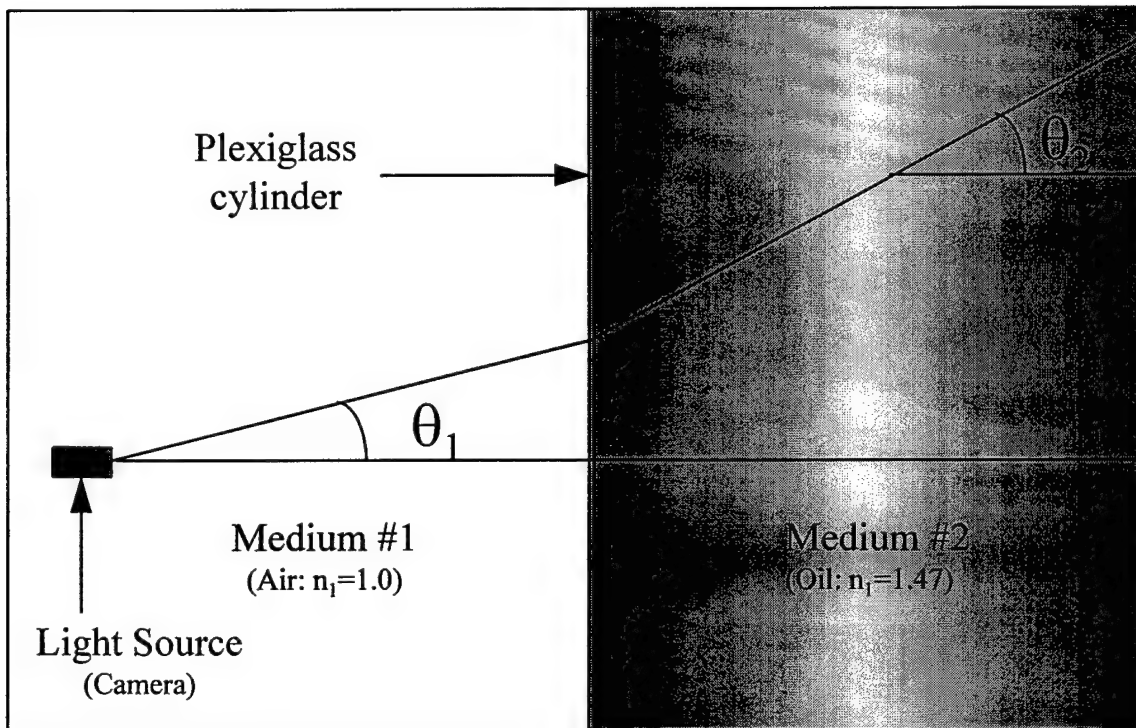


Figure 3.5 Snell's Law

$$n_1 \cdot \sin(\theta_1) = n_2 \cdot \sin(\theta_2) \quad (3.2)$$

n_1 = Index of Refraction of First Medium (Air)

θ_1 = Angle of Site Upon Object

n_2 = Index of Refraction of Second Medium (Oil)

θ_2 = Angle of Refraction

Obviously, when the camera was aimed directly at the sample (i.e. when $\theta_1 = 0$), there was no refraction. However, once a deviation from the center line was made, the problem of refraction needed to be considered. In addition to the oil, the plexiglass cylinder and the membrane should be considered as having contributions to the overall refraction results. A correction formula was therefore devised by using the fact that the initial grid had known horizontal dimensions. Specifically, the difference between each vertical line was 0.25 inches (0.64 cm). This gave a correlation between L (perceived length) and S (actual length) based upon the distance from the center of the specimen. To determine the center line, a curve plotting the average horizontal coordinates of each vertical line on the x-axis and the difference between the highest and lowest point of each vertical line on the y-axis was created. By finding the peak of this curve, the center line was established. The reasoning behind this was that the farther from the center a vertical line is the closer the upper and lower most points appeared. Figure 3.6 shows an example of how the center of a given image was found. With the center determined, the correction equation was found. This correction was automatically found by the MATLABTM software for each initial image based upon the principal that each vertical line should be the same distance apart. Figure 3.7 graphically depicts the theoretical correction with the one found using the known grid spacing. The subsequent images from each camera were subjected to this same correction as the initial image from the same camera. The assumption was that the center of the image remained at the same place. This was true since every test was a combination of torsional and axial loading but never translational

Test #77; 3/18/97; Torsion-compression; ECP=50 psi; Loire; Video #3; t=0000 sec.

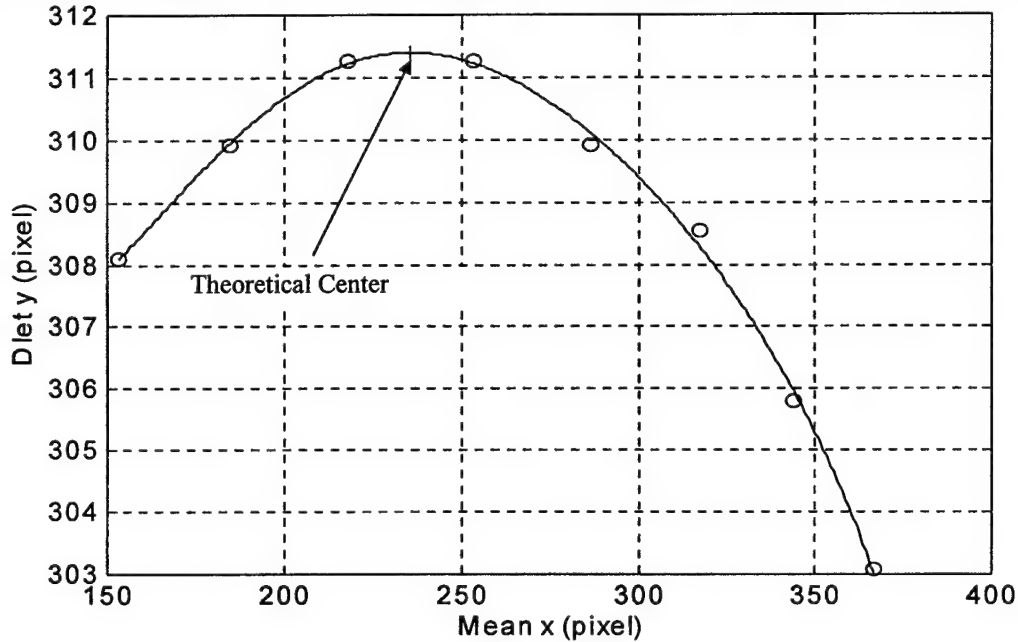


Figure 3.6 Plot Used to Determine Center of Image

movement, guaranteeing a constant center. For example, the center of the initial image from camera #1 was found and a correction curve was found for this camera. Each image digitized from camera #1 thereafter was subjected to this same correction. This correction gave the most accurate information after considering the effects of refraction and surface curvature. Figure 3.8 shows Figure 3.3d without the horizontal line correction. In this image, the difference between vertical lines appears to be relatively constant unlike an image without this correction (Figure 3.3c).

Test #77; 3/18/97; Torsion-compression; ECP=50 psi; Loire; Video #3; t=0000 sec.

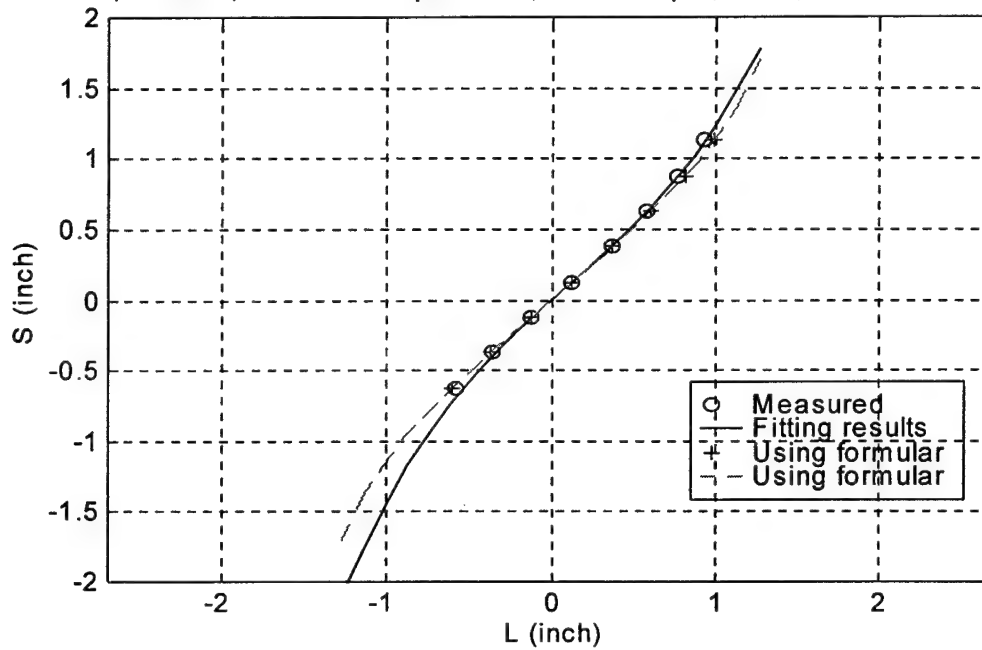


Figure 3.7 Theoretical and Regression Correction Curves

Test #77; 3/18/97; Torsion-compression; ECP=50 psi; Loire; Video #1; t=2500 sec.

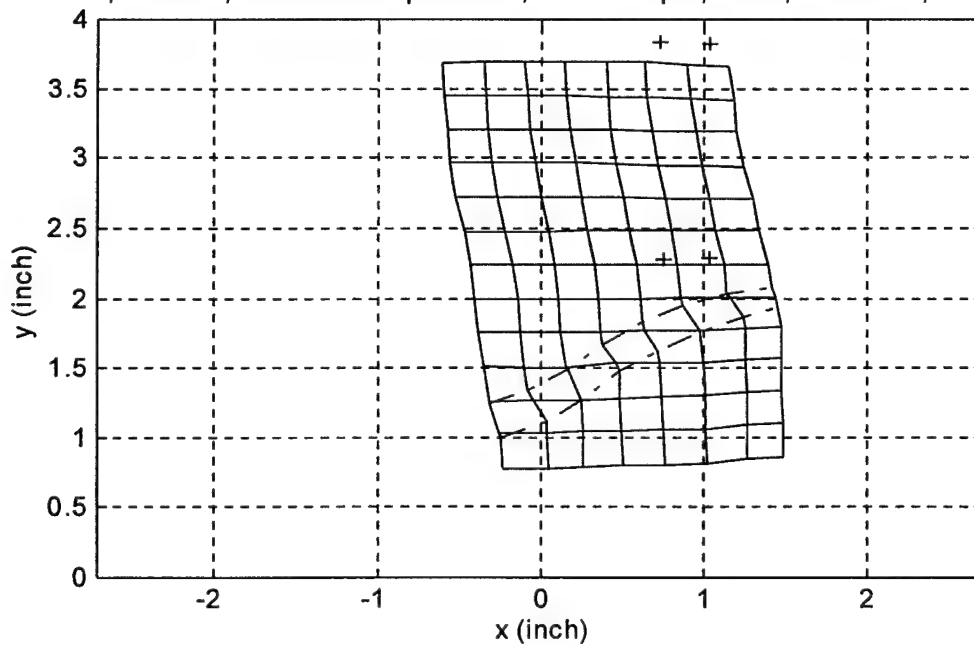


Figure 3.8 Digitized Grid Corrected in Horizontal Direction

3.3.4 Vertical Corrections for Surface Curvature

The need to correct the vertical lines to obtain their true position was a consideration as well. The horizontal lines appear to curve slightly on the digitized images. Part of this was due to the refraction of the light as it passed through the different media and another part was due to camera orientation. The upper lines appeared to curve downward while the lower lines curved upward. Since the actual grid was initially comprised of only straight lines with known spacing differentials, a correction was developed to account for this problem.

Each grid had thirteen horizontal lines. The seventh, or middle, line appeared to remain a straight line. On the other hand, the top and bottom lines seem to be curved the most. The correction used to account for this phenomenon was implemented at the last stage of the digitizing process just prior to calculating an output. At that stage, the center of the image was already determined using the method mentioned in the previous section. With the center established, the coordinates of the uppermost and lowermost horizontal lines were changed. Since the grid was known to be 3.0 inches (7.62 cm) tall, and the middle horizontal line was equidistant from the top and bottom lines, the vertical line nearest the calculated center was assigned coordinates corresponding to this information. Next, the top and bottom lines were given the same y-coordinates as this center line. The intermediate lines were then proportionally stretched to make them truly horizontal according to their relative distance from the center line. Figure 3.9 demonstrates the need for the horizontal line correction and how the upper and lower lines were modified.

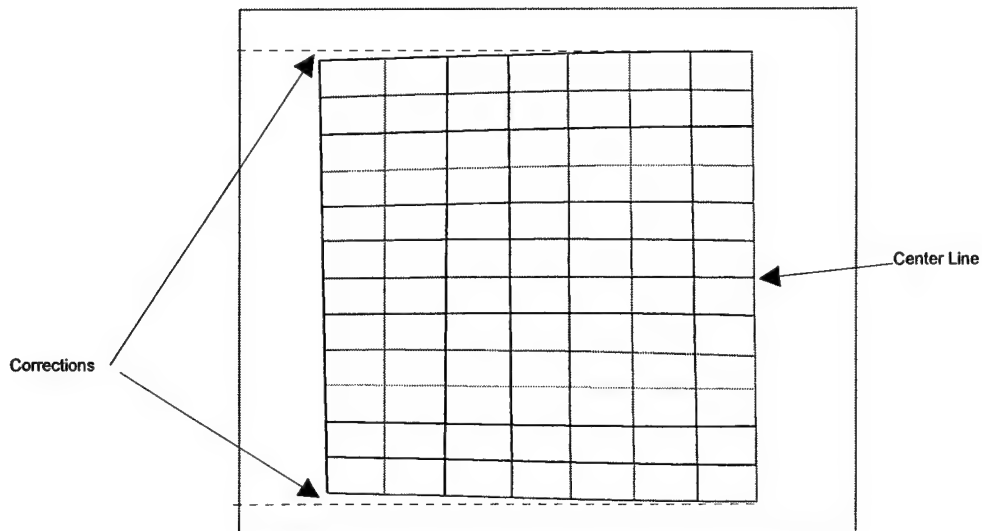


Figure 3.9 Horizontal Line Correction

3.4 Analysis of Shear Bands

To determine the angle of the shear band, each image first needed to be digitized and corrected for curvature. The displacements, strains, and many other components were then determined by a direct comparison to their respective initial images. Figure 3.10 shows an initial image overlaid upon a later image with a shear band. The MATLAB[™] software package then performed the necessary calculations to find the inclination of the shear band, the thickness of the shear band, and the strains in and around the shear band. The appendix of this thesis contains many printouts and charts to expand upon the digitizing process.

Test #77; 3/18/97; Torsion-compression; ECP=50 psi; Loire; Video #1; t=3200 sec.

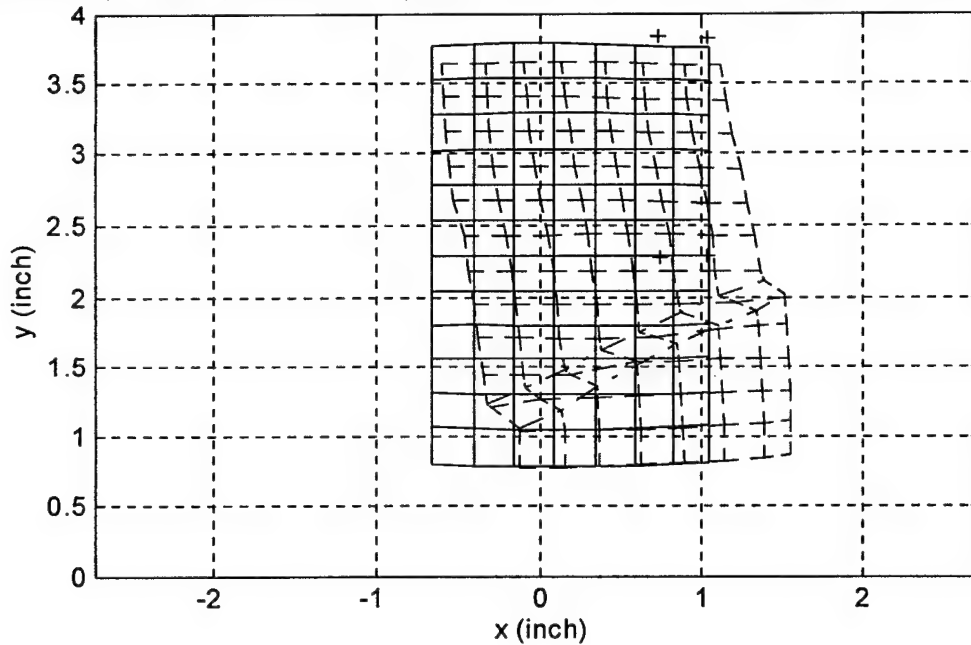
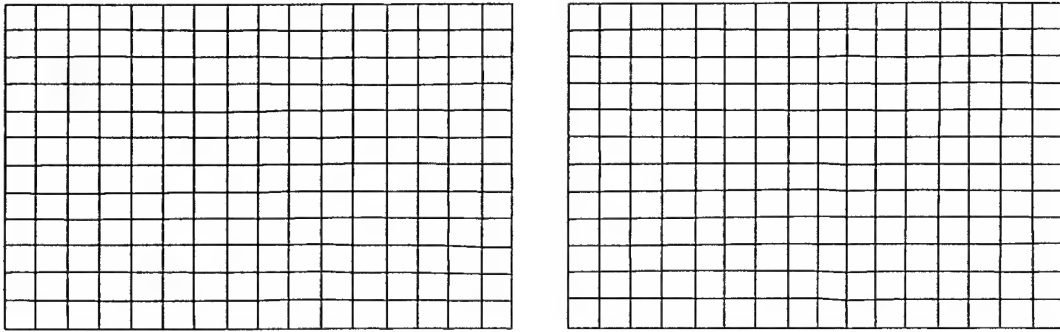
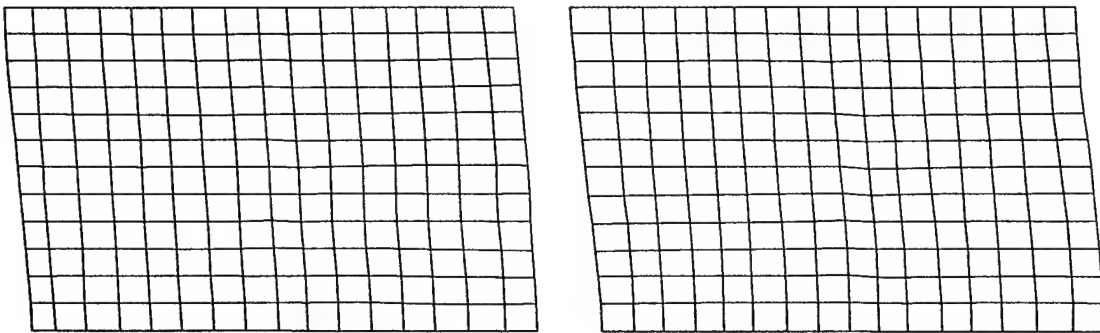
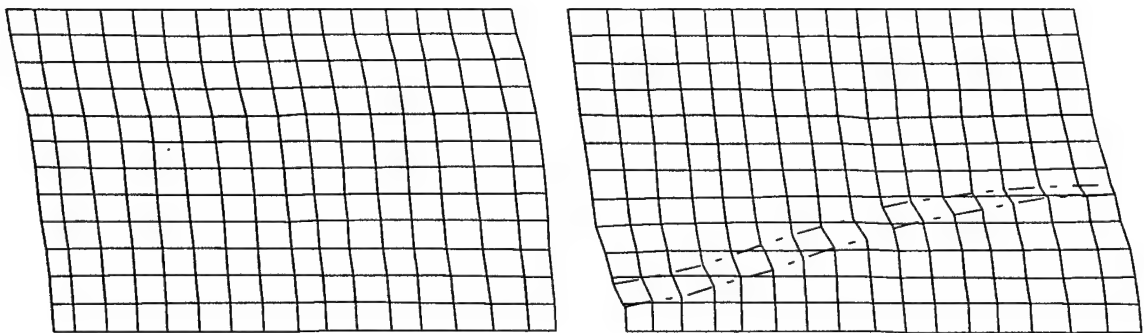
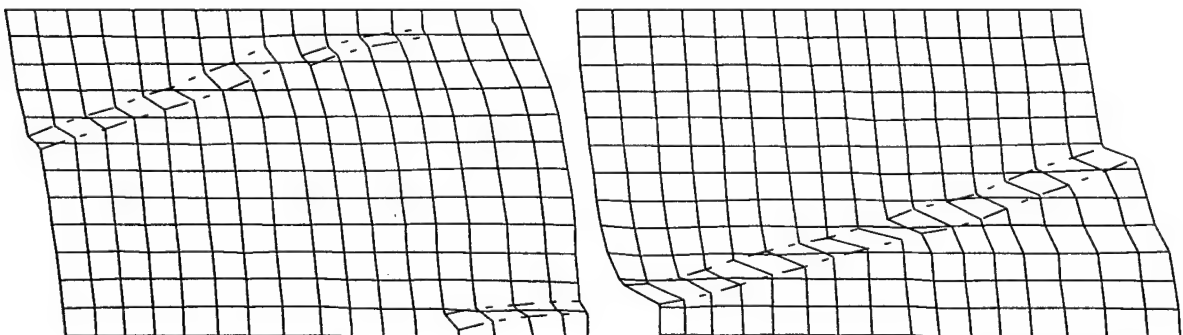


Figure 3.10 Initial Grid and Deformed Grid After Horizontal Correction

Typically, of the seven times in which images were taken, only four were necessary to accurately determine the data pertinent to the onset and inclination of the shear band. These images were usually the first, third, fifth and last ones taken. Since there were four cameras, a total of sixteen images were digitized per test. To determine the inclination of the shear band, a combined average angle of all four images was used. Figure 3.11 shows the appearance of these images when combined together. Due to time constraints of this lengthy process, only three tests were digitized. These tests were #77, #78a and #79. All other shear band inclinations were determined by careful observation and are summarized in Chapter Five.

Test #78a; 8/14/97; Pure Torsion; ECP=50 psi; Loire

(1) $t=0000$ sec.(2) $t=1500$ sec.(3) $t=2500$ sec.(4) $t=3400$ sec.**Figure 3.11 Digitized Images at Various Time Intervals After Corrections**

3.5 Accuracy of Digitization Method

The digitization process generates a great deal of information about shear bands. This data can give a new insight in the shear banding phenomenon. In order to fully understand the quality of this new process, the accuracy must be evaluated. This was accomplished by comparing the results produced from digitization to the data collected from the various testing gauges. It was found that these two methods resulted in information which was in excellent agreement with each other prior to the formation of the dominant shear band (Saada, 1998).

The issue of how accurately a grid could be digitally reproduced was also a concern. Each grid line was approximately 0.04 inches (0.10 cm) or 3 to 4 pixels wide. It was noticed that these ink lines were darker in the middle and lighter near the edges. When these lines were digitized, either the second or third pixel was chosen. This leads to a possible error of 4 percent. By incorporating the use of a polynomial fitting curve, this error was reduced to 2 percent which was considered more than adequate for this study (Saada, 1998). Figure 3.12 demonstrates the above.

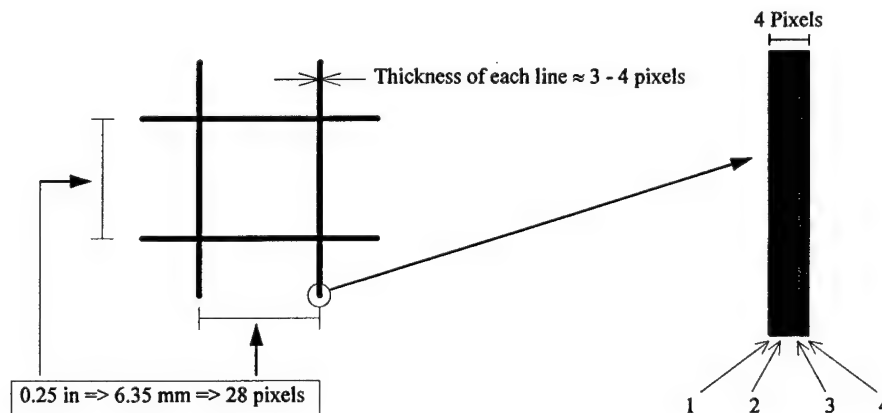


Figure 3.12 Estimation of the Error Associated with the Digitization Process (Saada, 1998)

Chapter Four

Results

4.1 Introduction

The majority of the data used in this experiment was taken from the data acquisition program. However, in order to use this information in full confidence, there must be no doubt of the accuracy of this data. To guarantee this, the information was checked against manually collected results and expected behavior. For this section, three specific tests are examined in great detail to ascertain their precision and validity.

This investigation will also give a better understanding of the behavior of the sand used and of non-cohesive, granular materials in general. A tabulation of the results along with the parameters used in the several theories is presented in this section.

4.2 Evaluation of Acquired Data

4.2.1 Explanation of Tests Evaluated

With the experiments performed on the Loire sand being the last portion of the overall research, the expected behavior was relatively predictable. This made the evaluation of the results much easier and poor experiments could be spotted and repeated. Three tests are discussed in depth as a representation of the general research. These tests are: Test #77 (GL22TF), Test #78a (GL24TF), and Test #79 (GL26TF). All of these experiments were conducted at 50 psi (345 kPa) and 50% initial relative density. Each test was also generalized and the specimens had a dogbone shape with complete saturation. The major differences in these tests were the stress paths. The first test (Test #77), was a torsion-compression test ($\beta=30^\circ$), the second (Test #78a), was a pure torsion

test ($\beta=45^\circ$), and the last (Test #79), was a torsion-extension test ($\beta=60^\circ$). The last two tests in this series (Tests #76a and #80) were pure compression and pure extension tests respectively. However, these types of tests do not always develop clear shear bands and, therefore, will not be discussed.

4.2.2 Description of Plotted Data

Five types of plots are presented in this section. As previously mentioned, there is a separate plot for each of the three tests being analyzed. Figures 4.1 a,b,c plot the changes in torque, cell pressure and axial force versus the change in the angle of rotation. These figures show that these tests were indeed generalized since the cell pressure increased for a decrease in axial load. An important note to make is that the axial force has units of Newton's (force) while cell pressure has units of kilopascals (pressure). Therefore, in order to complete the comparison, the cross sectional area of the sample needed to be introduced. However, the feedback program automatically accounted for this and the mean stress remained the same.

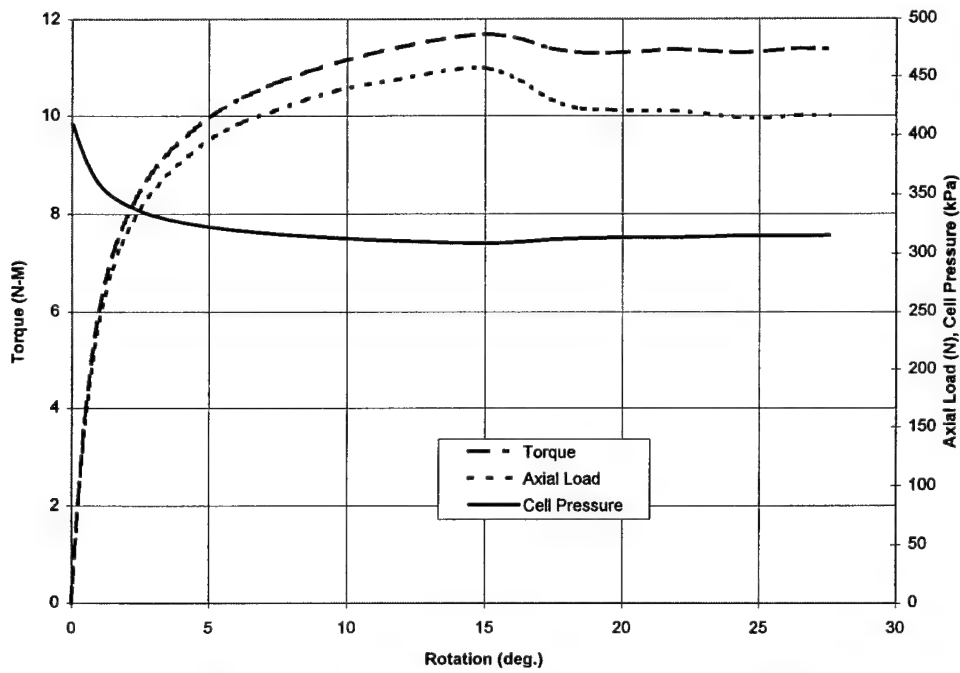
Figures 4.2 a,b,c compare the axial force to the axial displacement up to and even beyond the failure. Note that for all tests, at the maximum or minimum axial force (depending on the type of test), the axial displacement underwent a change of inflection. This was usually indicative of the formation of the shear band. In Figure 4.2 b, the axial force and displacements were almost nonexistent since this test was a pure torsion test.

Figures 4.3 a,b,c further illustrate the concept of generalized tests. These plots show the three principal stresses and how they changed. The stresses shown were all effective stresses due to the constant 10 psi (69 kPa) back pressure. They are similar to

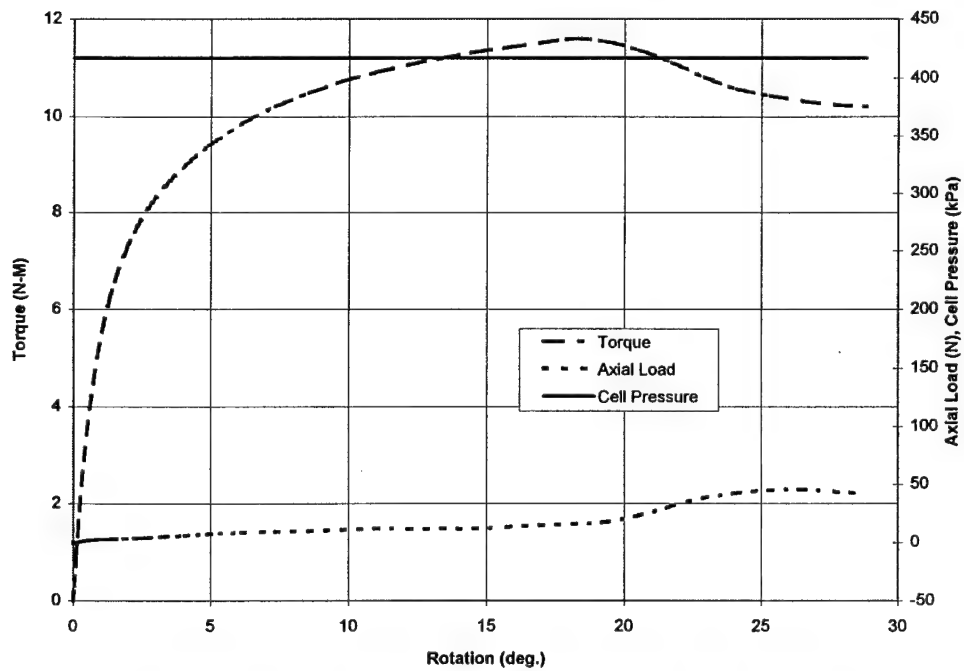
figures 4.1 a,b,c but they have converted the axial force to a stress. Also, the mean of all three stresses is plotted. This effective mean stress remained constant throughout the duration of the test at a value of approximately 50 psi (345 kPa). This number was the initial confining pressure minus the back pressure of all three tests.

Figures 4.4 a,b,c plot the volume changes of each test versus the angle of rotation. As is typical of loose samples (50% initial relative density), an initial decrease in volume happened due to the motion of the particles. After this decrease, the volume tended to increase for the remainder of the test up to failure. Once a shear band was fully formed, the volume remained constant. This occurrence was often used as an indication of the tests completion.

Figures 4.5 a,b,c show how the principal strains change. This was necessary to obtain the maximum rate of change of $((\epsilon_1 / \epsilon_3)_{\max})$ for calculating the angle of dilation (ψ) for plain strain.



**Figure 4.1a Torque, Axial Load and Cell Pressure
GL22TF, Test #77 (Torsion-Compression)**



**Figure 4.1a Torque, Axial Load and Cell Pressure
GL22TF, Test #78a (Pure-Torsion)**

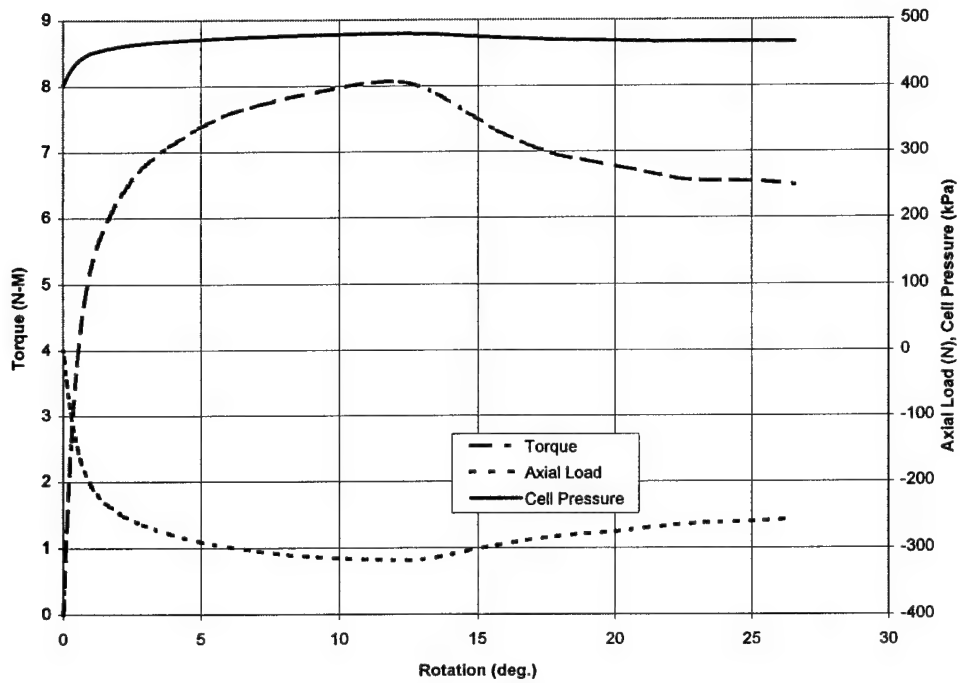


Figure 4.1a Torque, Axial Load and Cell Pressure
GL22TF, Test #78a (Pure-Torsion)

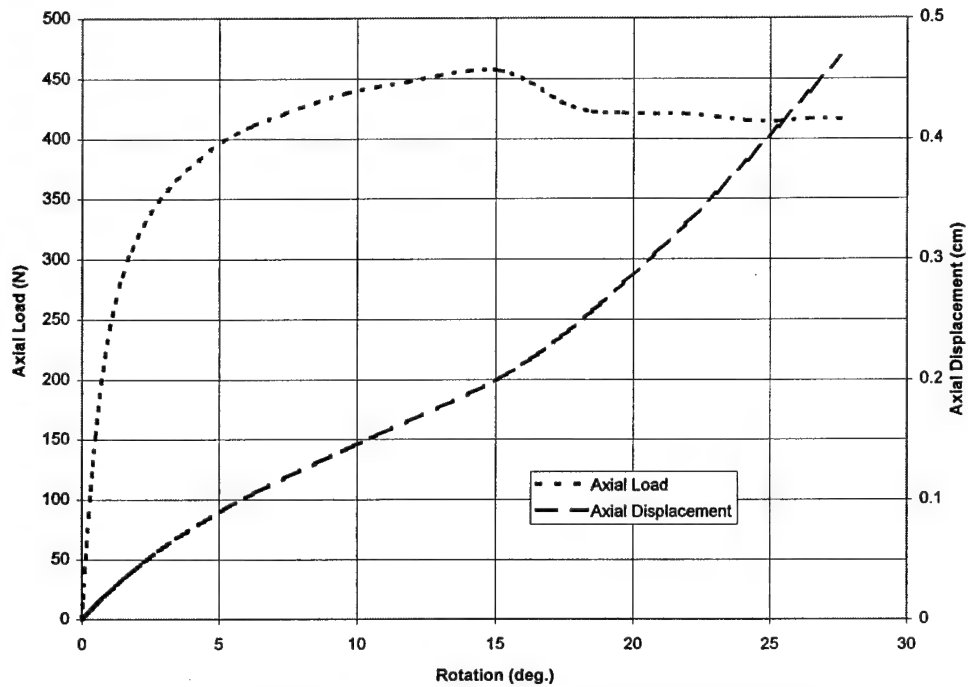


Figure 4.2a Axial Load and Displacement
GL22TF, Test #77 (Torsion-Compression)

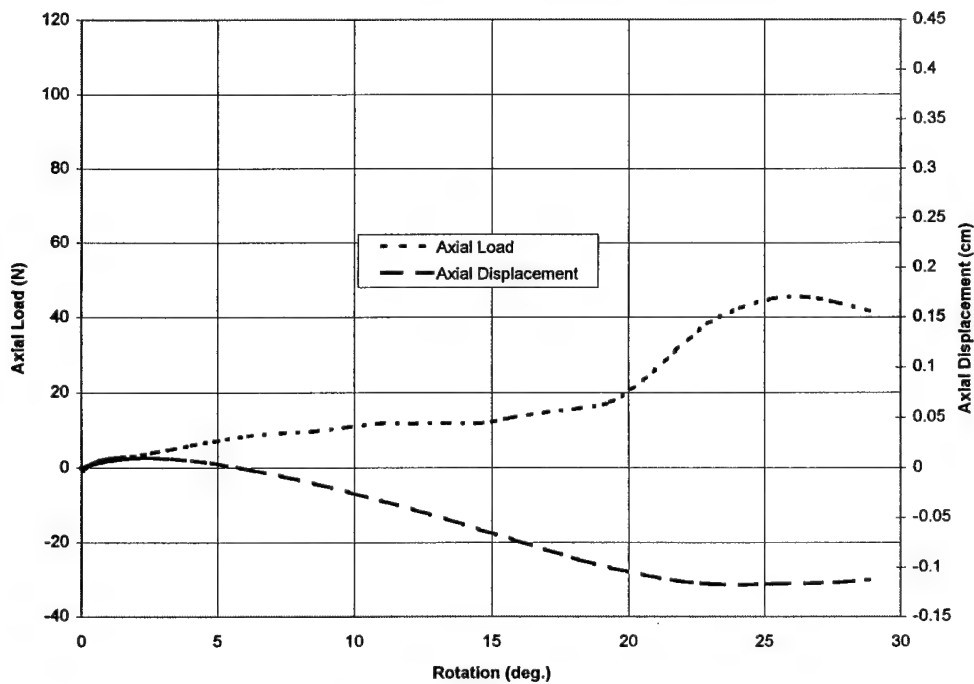


Figure 4.2b Axial Load and Displacement
GL24TF, Test #78a (Pure-Torsion)

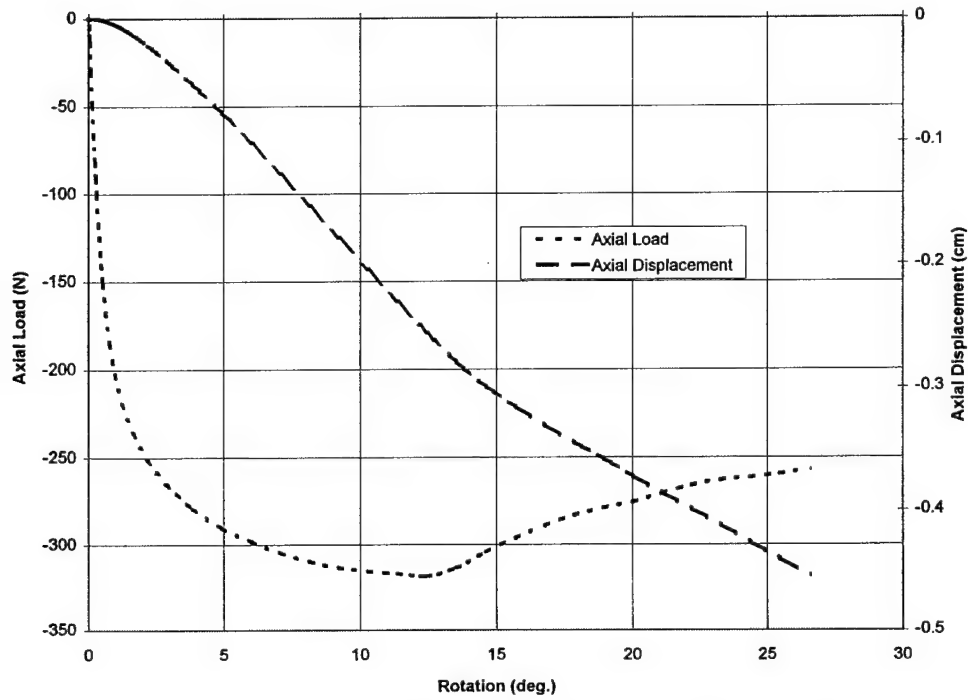


Figure 4.2c Axial Load and Displacement
GL26TF, Test #79 (Torsion-Extension)

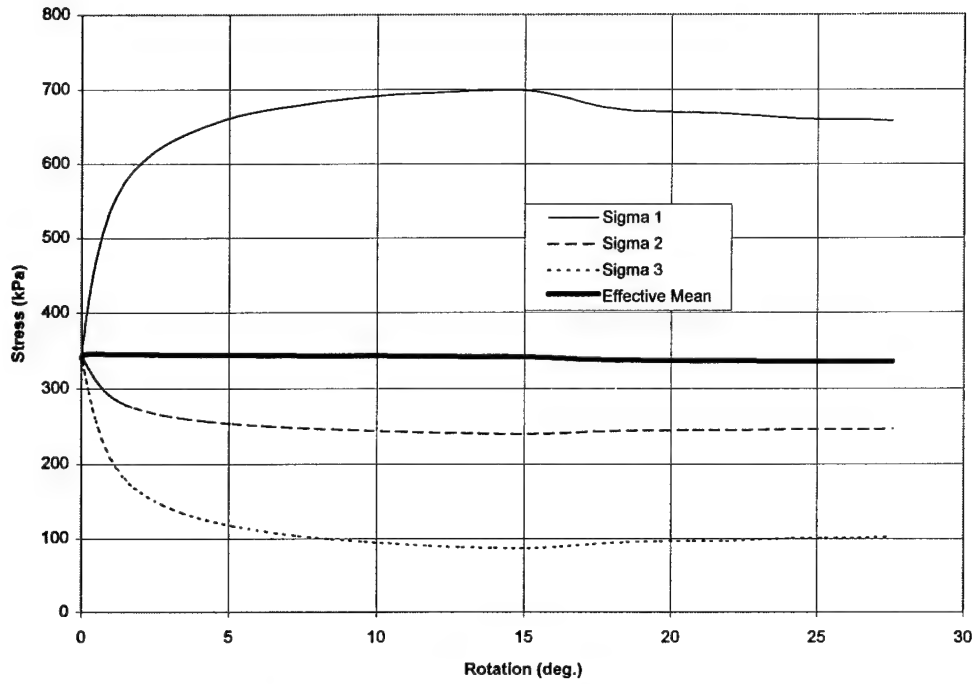


Figure 4.3a Effective Principal Stresses
GL22TF, Test #77 (Torsion-Compression)

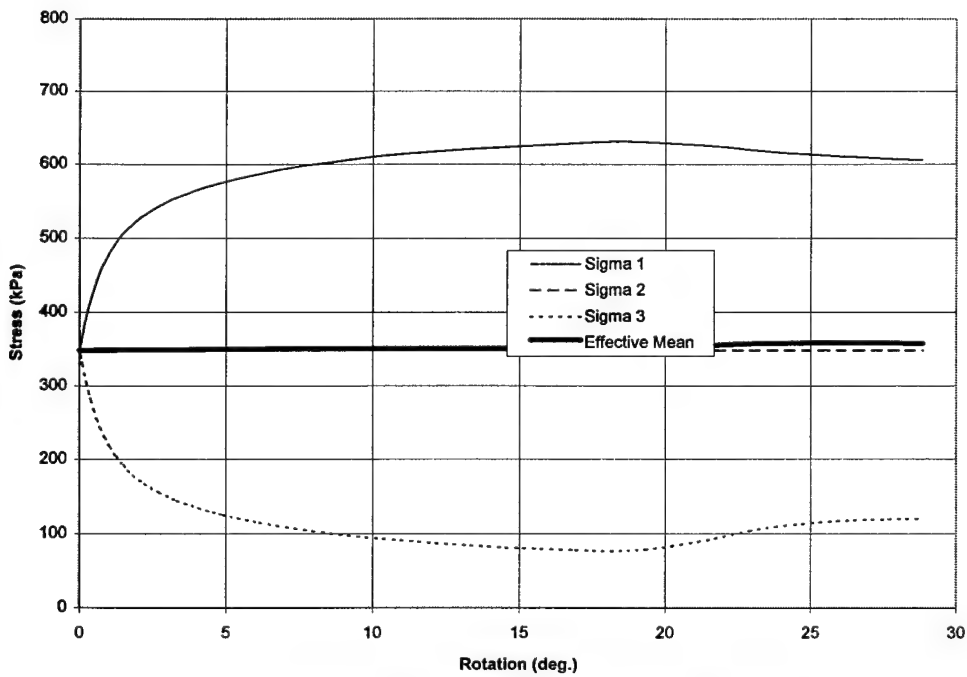


Figure 4.3b Effective Principal Stresses
GL24TF, Test #78a (Pure-Torsion)

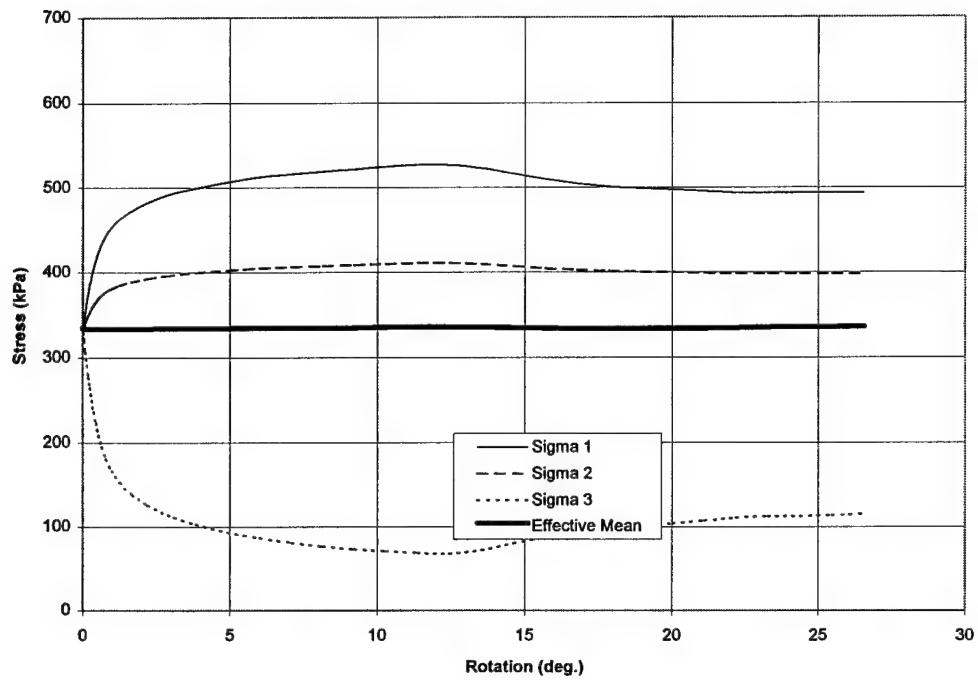


Figure 4.3c Effective Principal Stresses
GL26TF, Test #79 (Torsion-Extension)

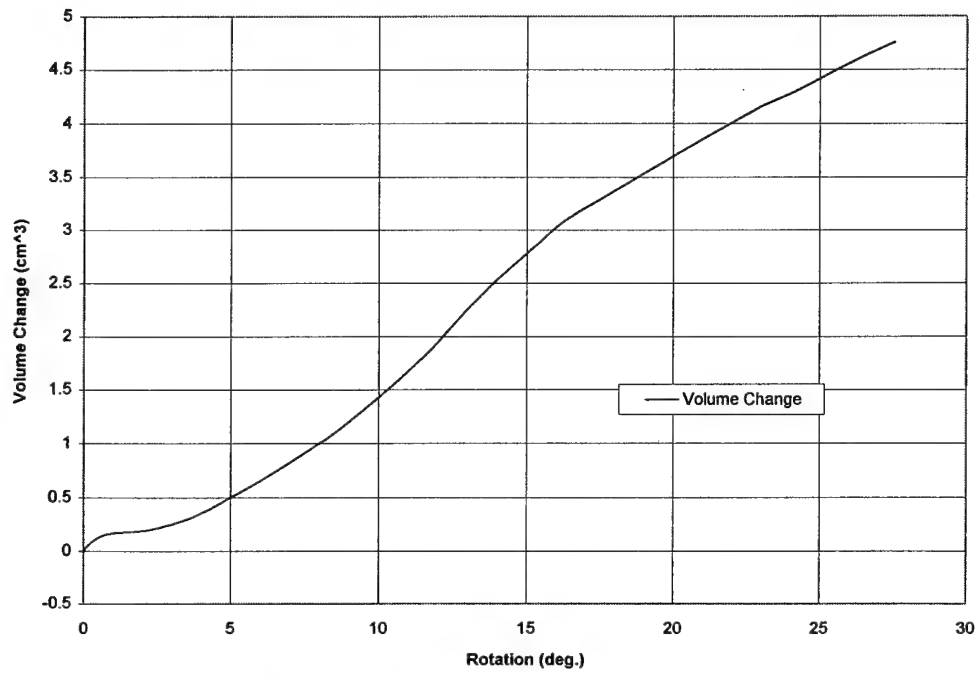


Figure 4.4a Volume of Specimen
GL22TF, Test #77 (Torsion-Compression)

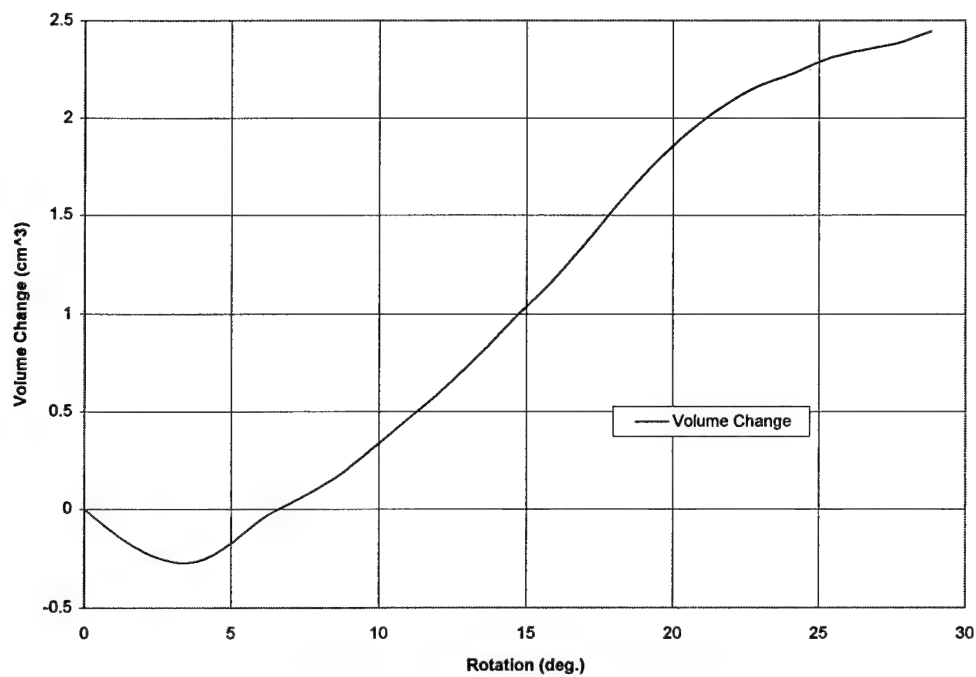


Figure 4.4b Volume of Specimen
GL24TF, Test #78a (Pure-Torsion)

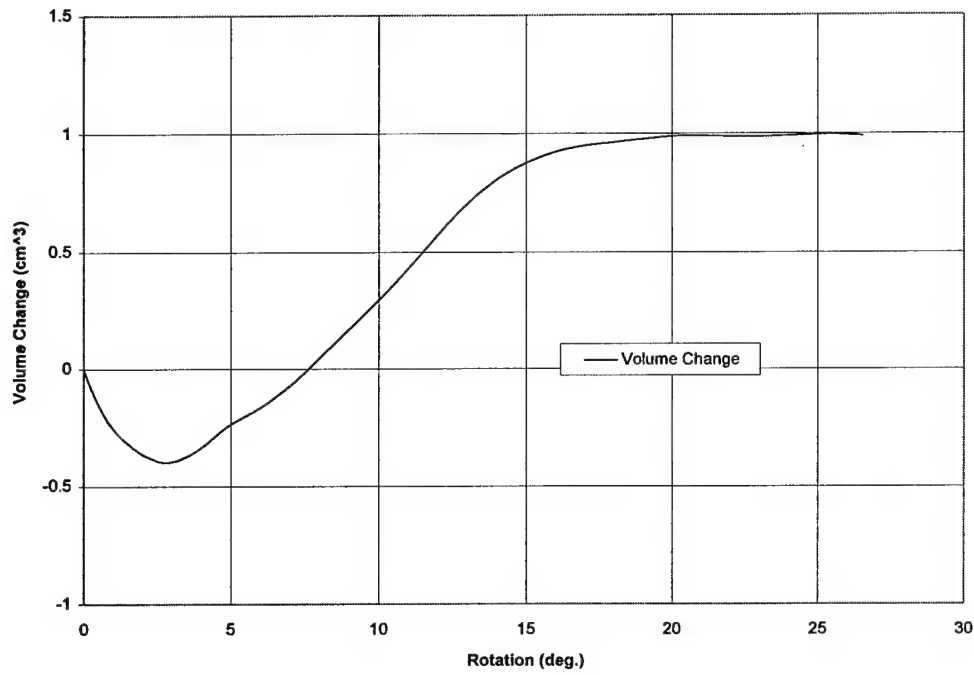


Figure 4.4c Volume of Specimen
GL26TF, Test #79 (Torsion-Extension)

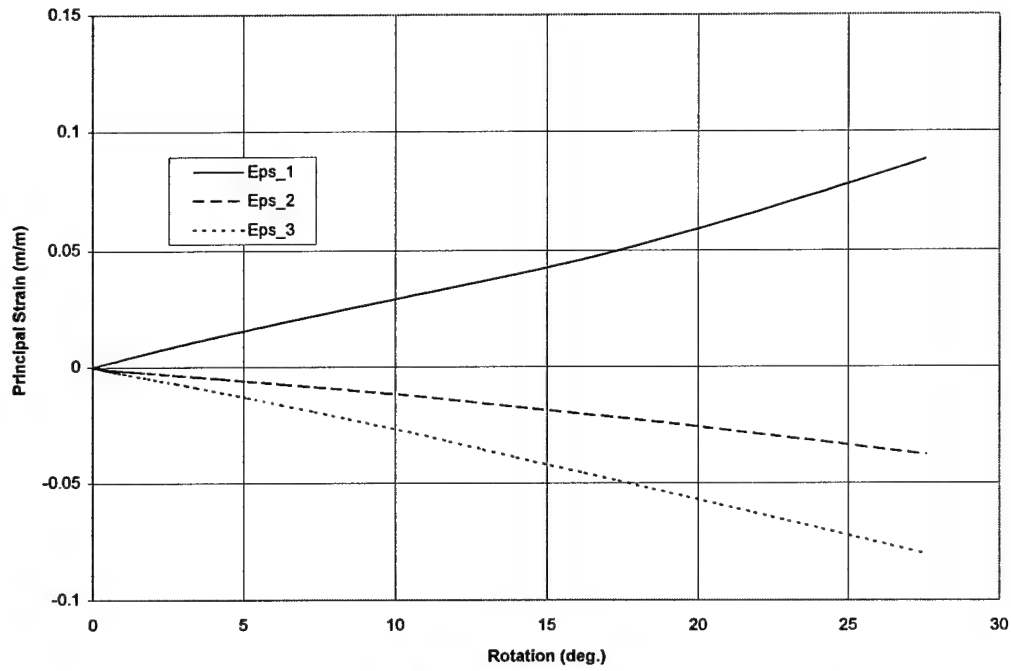


Figure 4.5a Displacement Principal Strain
GL22TF, Test #77 (Torsion-Compression)

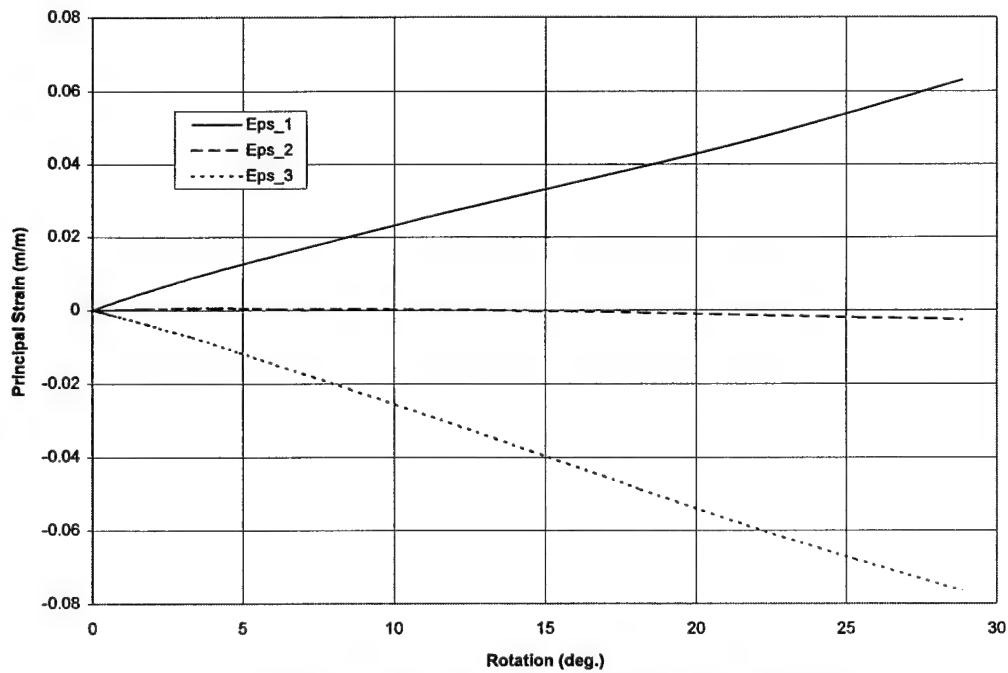


Figure 4.5b Displacement Principal Strain
GL24TF, Test #78a (Pure-Torsion)

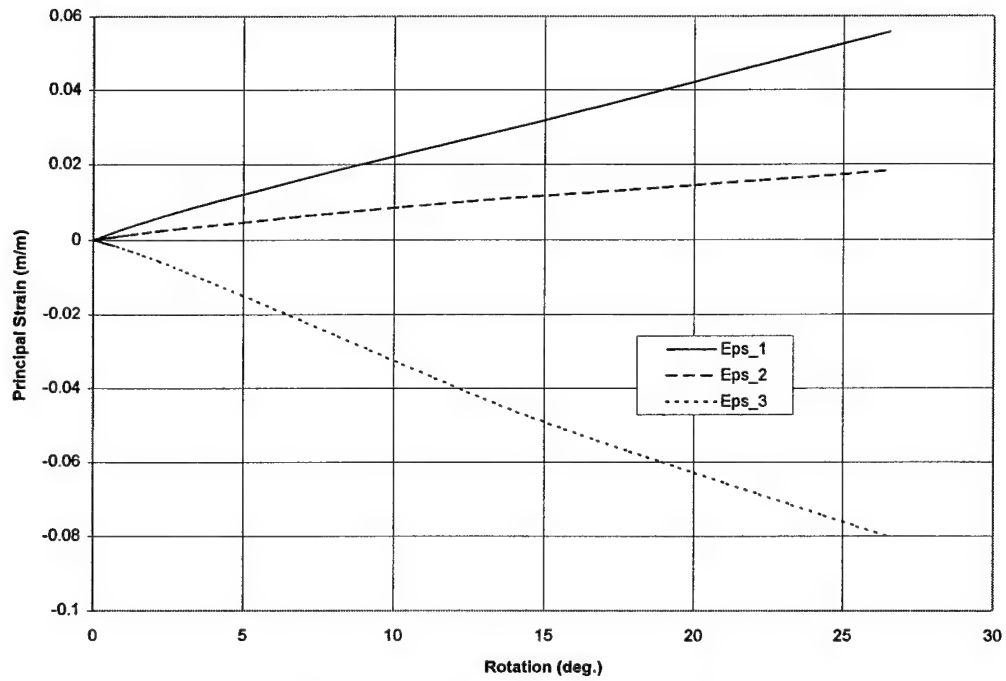


Figure 4.5c Displacement Principal Strain
GL26TF, Test #79 (Torsion-Extension)

4.3 Calculation of the Effective Angle of Friction (ϕ')

The effective angle of friction was determined using the standard Mohr's circle approach. For this method, a tangent line was drawn from the origin to the Mohr's circle, which was found by using the effective major and minor principle stresses throughout the duration of the test. Figure 4.6a illustrates the described method.

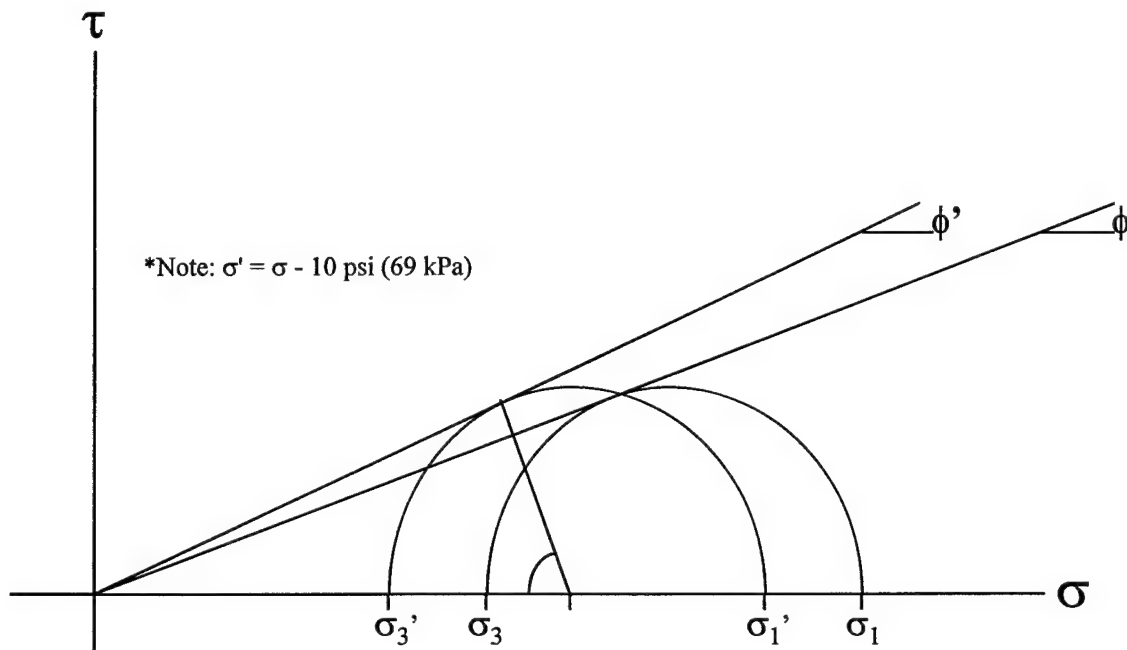


Figure 4.6a
Use of Mohr's Circle to Determine ϕ'

The angle formed by the intersection of this line and the horizontal axis gives the angle of obliquity. The maximum angle of obliquity is better known as the effective friction angle. This parameter can be found mathematically using equation 4.1, assuming the soil is non-cohesive.

$$\sin \phi'_{\max} = \left[\frac{(\sigma_1'/\sigma_3')_{\max} - 1}{(\sigma_1'/\sigma_3')_{\max} + 1} \right] \quad (4.1)$$

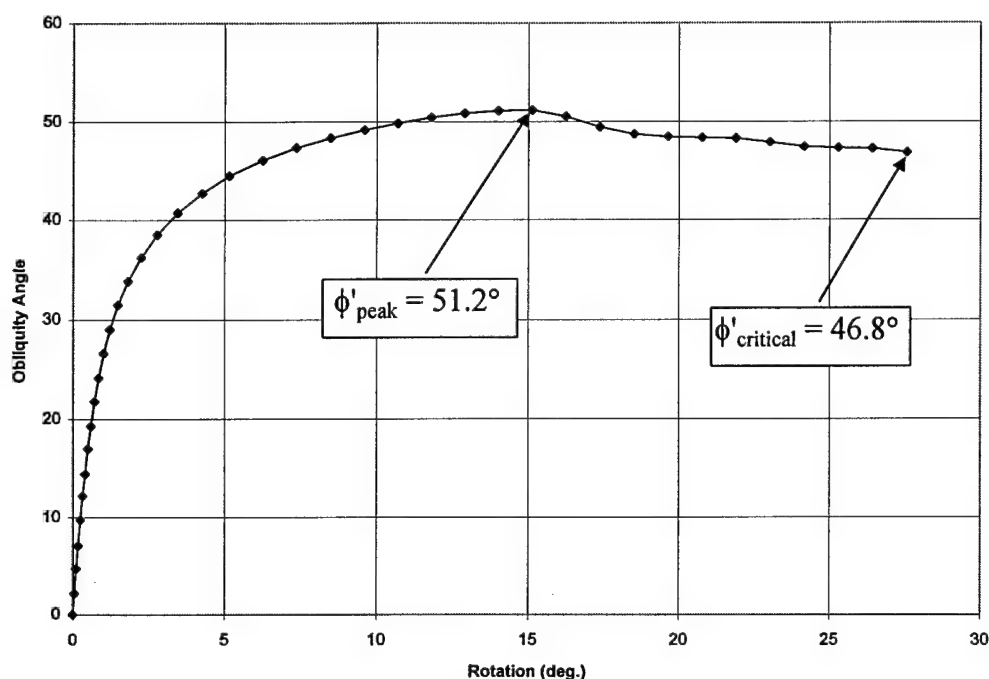


Figure 4.6b Change in Obliquity Angle
GL22TF, Test #77 (Torsion-Compression)

Figure 4.6b demonstrates the determination of this key parameter for Test #77. For this particular test, the peak friction angle was 51.2° , and the ultimate friction angle, close to the critical state, was 46.8° .

Pure compression tests were also used to determine the critical friction angle for each set (Saada et. al., 1994). Table 4.1, found later in this chapter, summarizes the peak and critical friction angles as found for each test.

4.4 Determination of the Angle of Dilation (ψ)

As described in chapter 1.3, there were several methods for finding the angle of dilation. Bolton's (1986) method (see equation 1.1c) used the term $(d\varepsilon_1/d\varepsilon_3)_{\max}$ which was easily found from a plot of the rate of dilation versus rotation. Figures 4.7 a,b,c demonstrate how this quantity was found for Tests #77, #78a, and #79 respectively. In

addition to the maximum rate of dilation, these figures also plot shear stress (τ_{oct}) versus rotation to demonstrate where the maximum value of dilation rate occurred in reference to maximum value of shear stress. Notice that the two peak values occurred at approximately the same rotation. Bolton's theory exploited the concept of plane strain which the hollow cylinder tests closely resembled in pure torsion. This was especially true once the dominant shear band fully formed (from discussion with University of Grenoble).

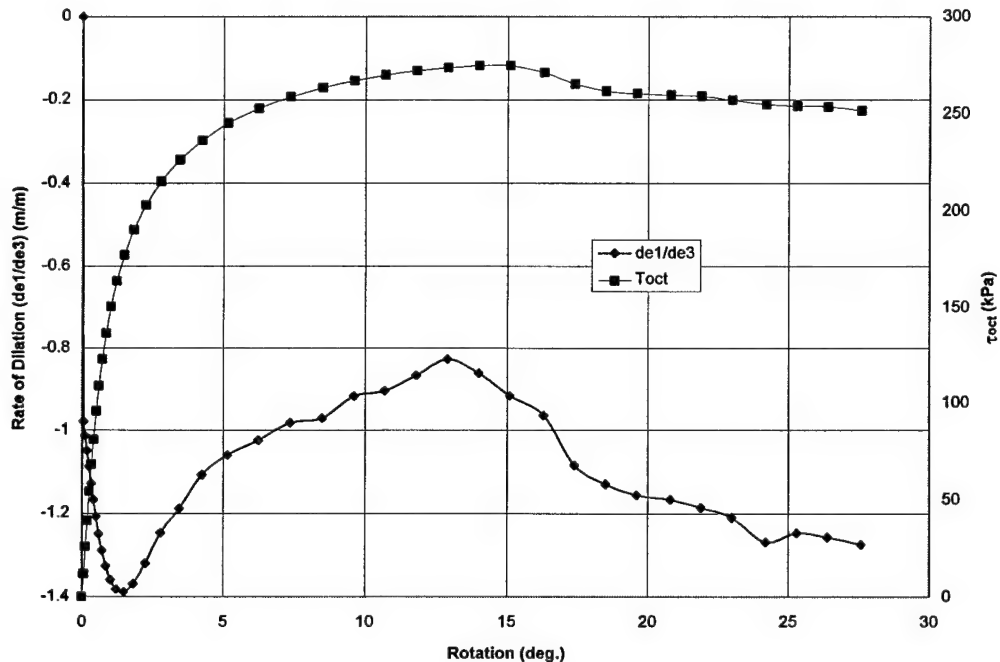


Figure 4.7a Maximum Rate of Dilation
GL22TF, Test #77 (Torsion-Compression)

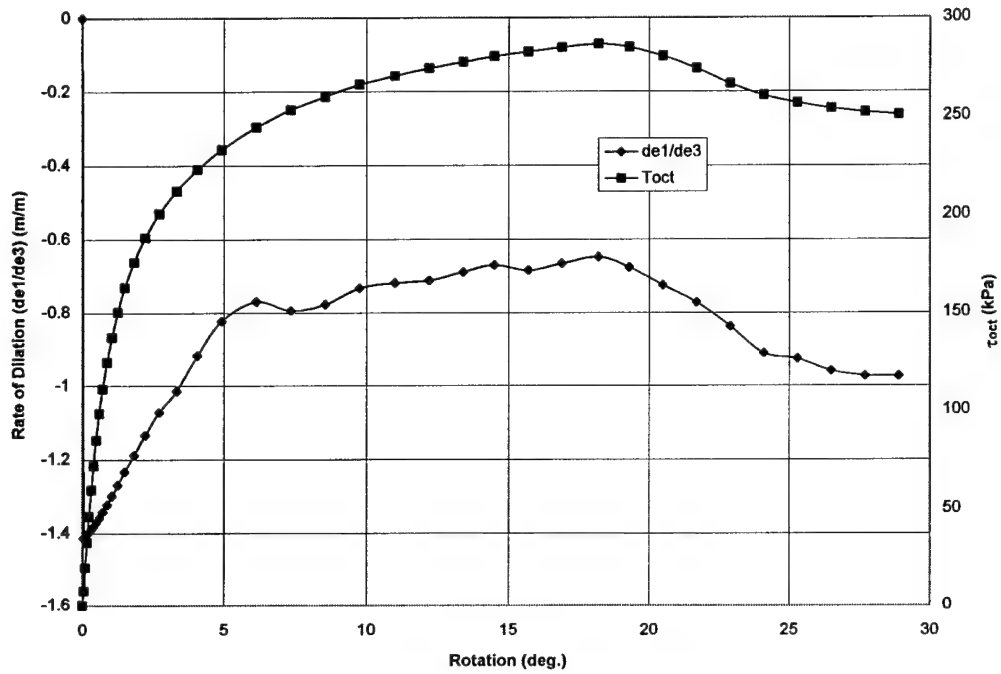


Figure 4.7b Maximum Rate of Dilation
GL24TF, Test #78a (Pure-Torsion)

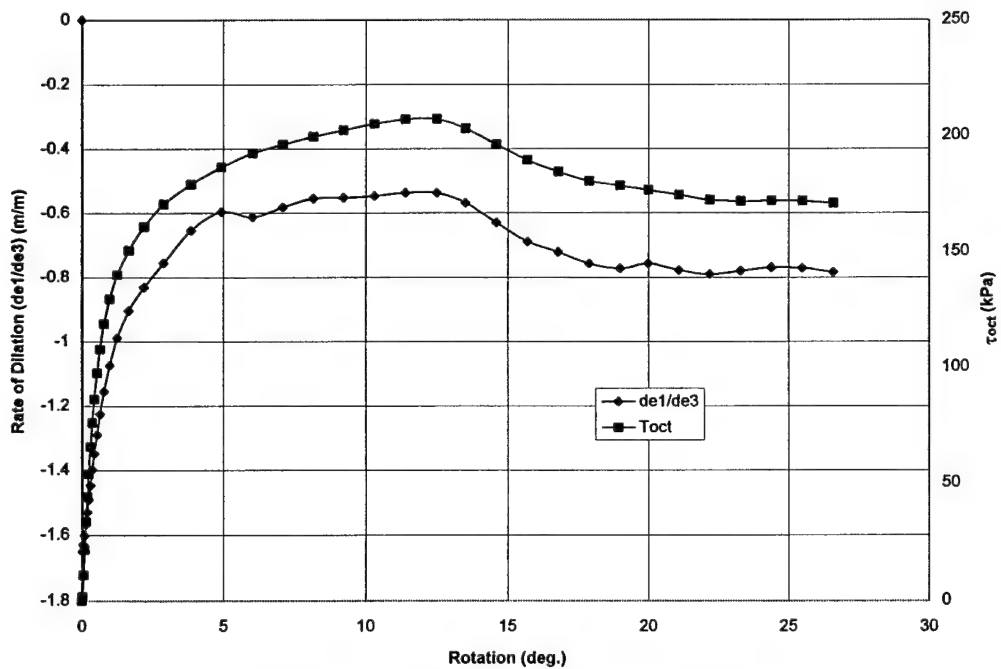


Figure 4.7c Maximum Rate of Dilation
GL26TF, Test #79 (Torsion-Extension)

The second method for finding ψ , as suggested by Zitouni (see equation 1.3), incorporated the angle θ . Figures 4.8 a,b,c show this method for Test #77, #78a, and #79, as well as plot the shear stress (τ_{oct}) versus strain (ϵ_1) for ease of comparison. The line from which θ was found is tangent to the ϵ_3 versus ϵ_1 curve. Also, notice that this tangency stops at around the maximum shear stress. Both methods used for calculating ψ should give approximately the same value.

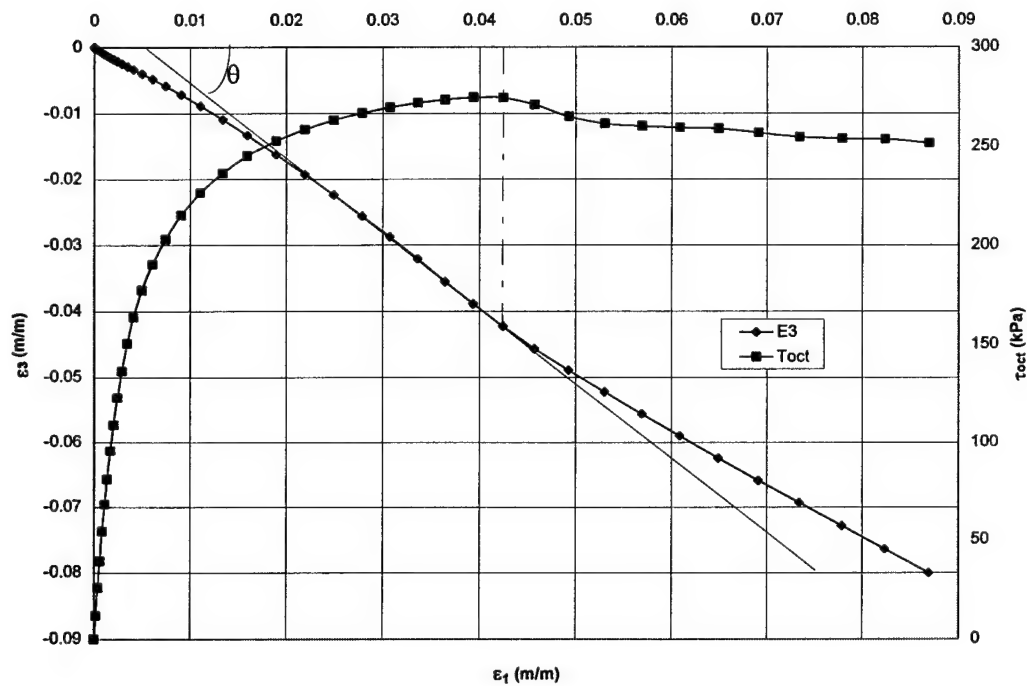


Figure 4.8a Zitouni's Method for Determining Ψ
GL22TF, Test #77 (Torsion-Compression)

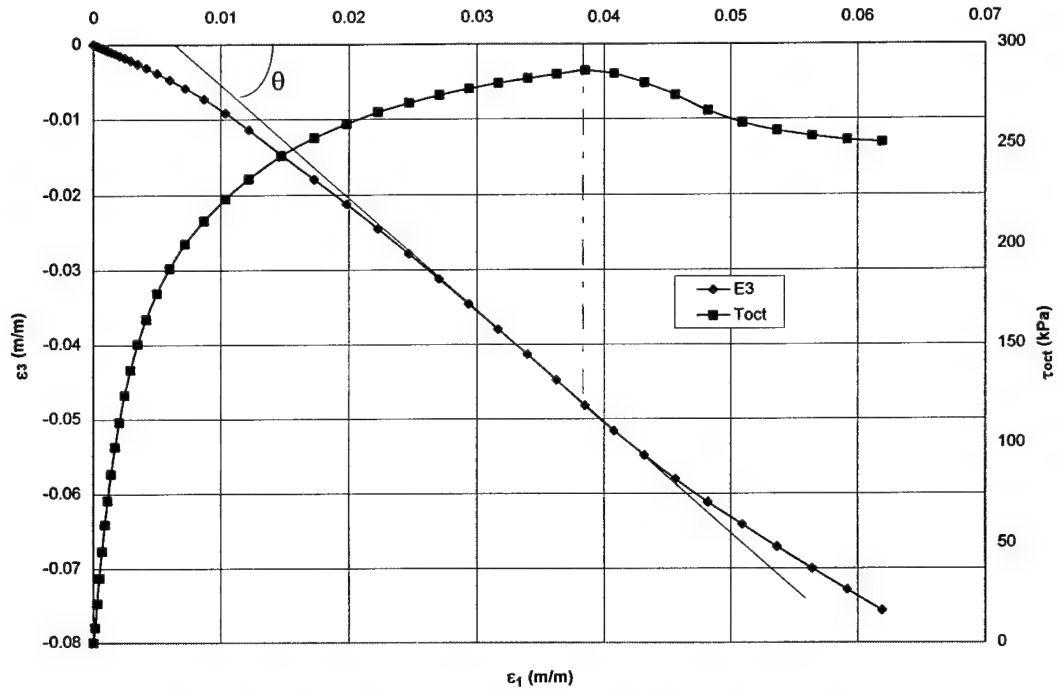


Figure 4.8b Zitouni's Method for Determining Ψ
GL24TF, Test #78a (Pure Torsion)

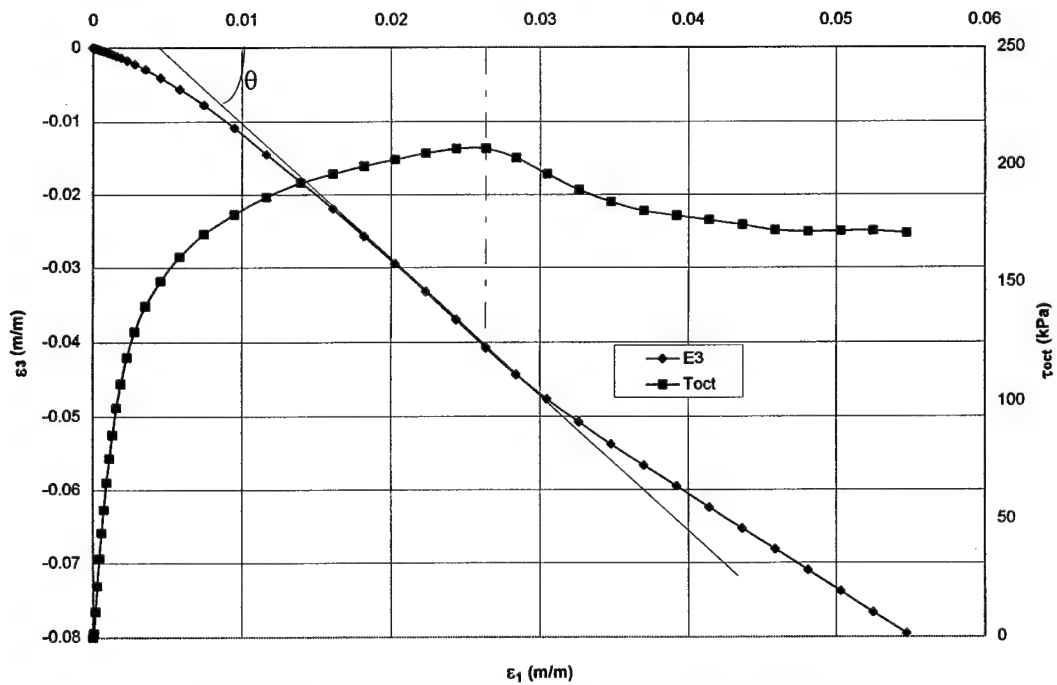


Figure 4.8c Zitouni's Method for Determining Ψ
GL26TF, Test #79 (Torsion-Extension)

Table 4.1 summarizes the resultant friction and dilation angles as found for each test. Both computed values of Ψ are listed here. Notice that these two dilation angles are very close to one another.

Table 4.1 Summary of the Angles of Friction and Dilation

Confining Pressure	Initial Relative Density	Test Number	β	ϕ' (Peak)	ϕ' (Critical)	ψ (Zitouni)	ψ (Plane Strain)
30 psi	50%	71	0	42.8	31.6	---	---
30 psi	50%	72	30	54.1	50.3	6.0	6.9
30 psi	50%	73	45	53.0	46.4	14.4	16.5
30 psi	50%	74b	60	55.6	45.9	19.8	21.3
30 psi	50%	75	90	41.2	26.4	---	---
50 psi	50%	76a	0	39.9	32.1	---	---
50 psi	50%	77	30	51.2	46.8	2.9	5.4
50 psi	50%	78a	45	51.6	42.0	11.0	12.4
50 psi	50%	79	60	50.5	38.4	16.3	17.5
50 psi	50%	80	90	41.9	20.0	---	---
70 psi	50%	81b	0	41.9	36.2	---	---
70 psi	50%	82	30	51.8	46.2	2.2	3.7
70 psi	50%	83a	45	49.1	40.0	10.2	9.1
70 psi	50%	84a	60	48.1	35.0	15.3	17.1
70 psi	50%	85	90	39.8	15.7	---	---
30 psi	80%	86a	0	43.3	37.1	---	---
30 psi	80%	87a	30	54.1	50.3	5.8	6.1
30 psi	80%	88	45	53.0	46.4	14.5	15.3
30 psi	80%	89	60	66.0	47.8	25.7	27.6
30 psi	80%	90	90	48.3	26.4	---	---
50 psi	80%	91a	0	44.3	37.5	---	---
50 psi	80%	92	30	55.4	50.5	4.2	5.7
50 psi	80%	93a	45	63.1	46.8	16.5	18.4
50 psi	80%	94d	60	48.4	34.0	19.5	20.7
50 psi	80%	95	90	33.3	10.4	---	---

70 psi	80%	96a	0	43.2	34.0	---	---
70 psi	80%	97a	30	53.6	46.5	5.5	14.2
70 psi	80%	98	45	59.5	46.6	5.9	14.2
70 psi	80%	99c	60	44.2	32.1	22.8	26.1
70 psi	80%	100a	90	48.5	20.0	---	---

4.5 Summary and Conclusions

The results of the testing schedule can be seen by analyzing figures 4.1 a,b,c through figures 4.5 a,b,c. Tests #77, #78a, and #79 demonstrated typical behavior of torsion-compression, pure torsion, and torsion-extension tests. Chapter Five will give further detail on the effect of the different parameters studied. However, several conclusions can be drawn from how the different parameters effect the angles of friction and dilation. Based on the results listed in table 4.1, the following observations were made.

- The angle of friction did appear to be slightly affected by confining pressure and relative density. However, these differences were slight and no trends could be established. It was noticed that the inclination of the major principal stress (β) did affect the friction angle. Pure compression and extension tests yielded lower angles of friction.
- The angle of dilation was not considerably affected by either confining pressure or relative density. The stress path, on the other hand, had a noticeable impact on the angle Ψ . As was expected, the greater the angle β , the higher the resultant angle of dilation turned out to be.

Chapter Five

Analysis

5.1 Introduction

For this chapter, the results of the various tests will be analyzed. The two key topics discussed will be the validity of the equations predicting the angle of shear banding (as presented in Chapter One) and the effect of the different testing conditions. Also, a comparison will be made to analyze the similarities and differences between the Loire sand and the LSI-30 sand. Specifically, the effect of grain size will be discussed to investigate the validity of theory presented by Koender et al. (1990).

5.2 Analysis of Shear Band Equations

The three theories investigated in this chapter are as follows:

- Coulomb's Theory $\Rightarrow (45 - \phi'/2)$
- Roscoe's Theory $\Rightarrow (45 - \psi/2)$
- Arthur-Vardoulakis's Theory $\Rightarrow (45 - (\psi + \phi')/4)$

These theories predict the angle of the shear band with respect to the major principal axis. However, there were several different methods to determine the angles of friction (ϕ') and dilation (ψ) as presented in Chapter Four. For this study, there were three methods used to find the angle of friction and two formulas were used to obtain

the angle of dilation. The three values of ϕ' used were: the angle of friction measured at the peak for a pure compression test, the angle of friction measured at the peak for the particular test being investigated, and the angle of friction measured at the critical state for the particular test being investigated. The two values of Ψ used were: the angle of dilation as calculated from a plain strain formula, and the angle of dilation as calculated by Zitouni's formula. This gave many different predictions using the above formulas. Figures 5.1 a,b to 5.6 a,b graphically compare the precision of those theories to the observed angle of shear banding. The plots were set up to show the accuracy of Coulomb's and Roscoe's theories on the first chart and Arthur-Vardoulakis' theory below on the second chart. In each of those plots, the angles were corrected to account for the different beta angles for ease of comparison. Essentially, the shear band angle with respect to the horizontal is added to the angle beta. Notice that the charts presenting the Arthur-Vardoulakis theories have a total of seven predicted lines. Six of these are the different combinations of ϕ' and ψ , while the one, entitled Art-Vard (best), was the most accurate theory discovered by Saada et al. in the paper "Bifurcation and Shear Band Propagation in Sands" (1997). This particular theory suggested the use of the angle of friction obtained at the peak value for pure torsion in combination with the angle of dilation found from the equation 1.1c for plane strain. This variation of the Arthur-Vardoulakis theory still appears to give accurate results, however, it does not appear to outweigh the others in precision for the Loire sand.

Figures 5.1 a,b to 5.6 a,b plot the actual shear band inclination along with the several inclinations predicted by the various theories. Inspection of these figures reveals that the Arthur-Vardoulakis theory is much more accurate than either Coulomb's or Roscoe's. In general, Coulomb's theory tended to overestimate the angle of shear banding while, in contrast, Roscoe's theory underestimated the angle. since the Arthur-Vardoulakis theory is a direct average of those two predictions, this theory gives more accurate results.

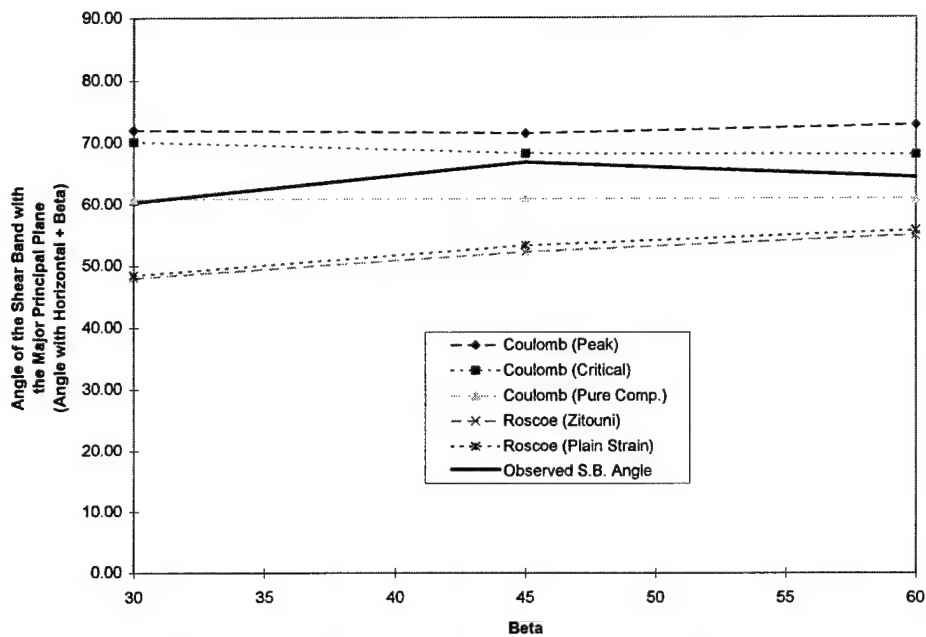


Figure 5.1a Predicted Inclinations with Respect to the Major Principal Plane (Coulomb & Roscoe)
Tests #72, #73 & #74a

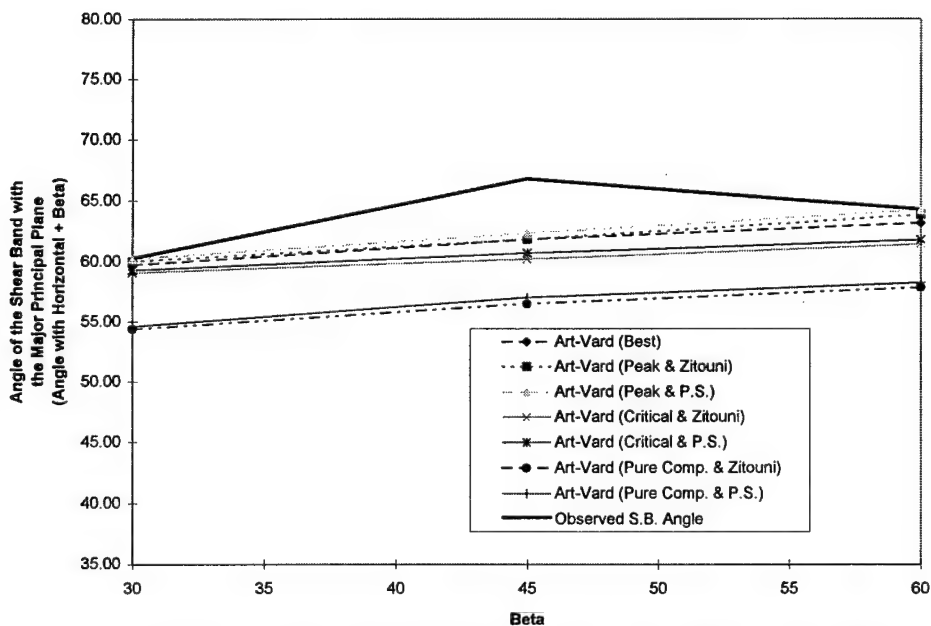


Figure 5.1b Predicted Inclinations with Respect to the Major Principal Plane (Arthur-Vardoulakis)
Tests #72, #73 & #74a

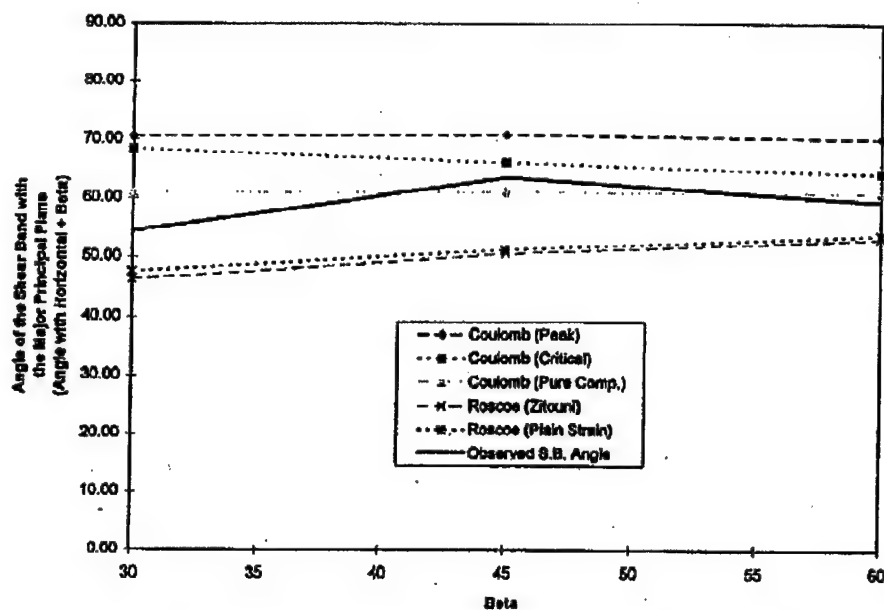


Figure 5.2a Predicted Inclinations with Respect to the Major Principal Plane (Coulomb & Roscoe)
Tests #77, #78a & #79

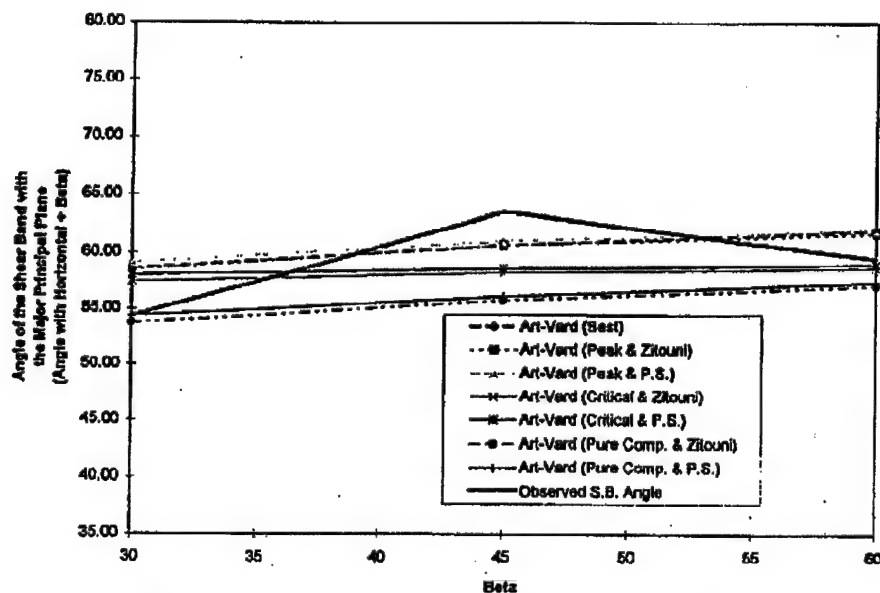


Figure 5.2b Predicted Inclinations with Respect to the Major Principal Plane (Arthur-Vardoulakis)
Tests #77, #78a & #79

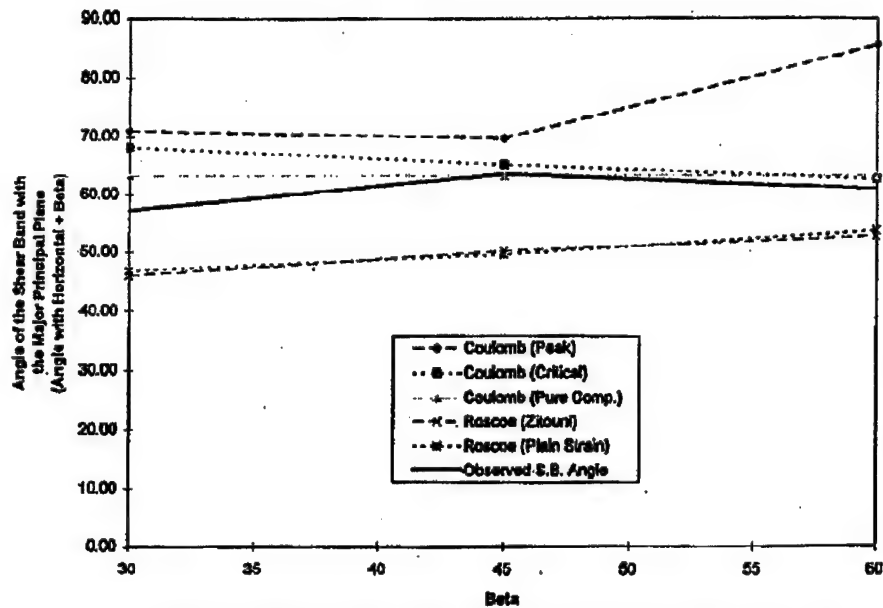


Figure 5.3a Predicted Inclinations with Respect to the Major Principal Plane (Coulomb & Roscoe)
Tests #82, #83a & #84a

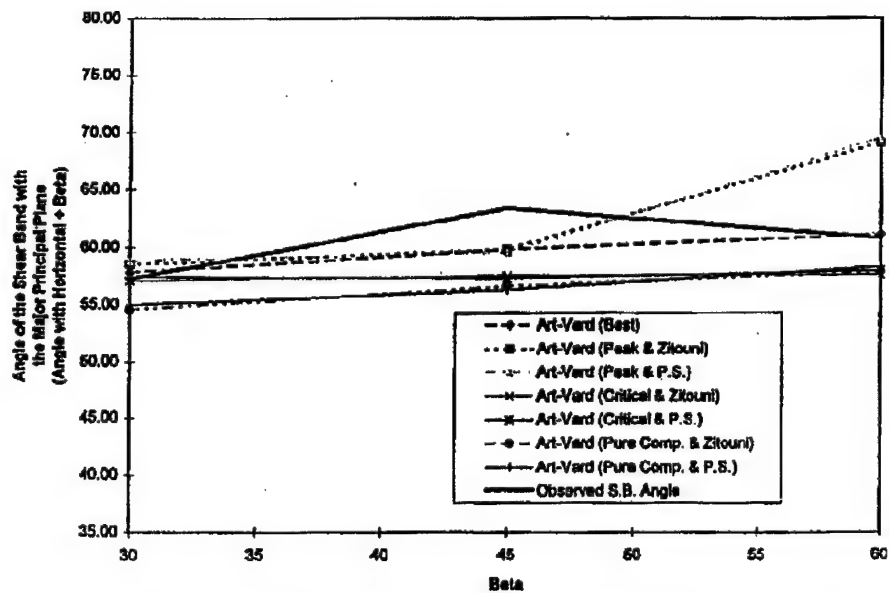


Figure 5.3b Predicted Inclinations with Respect to the Major Principal Plane (Arthur-Vardoulakis)
Tests #82, #83a & #84a

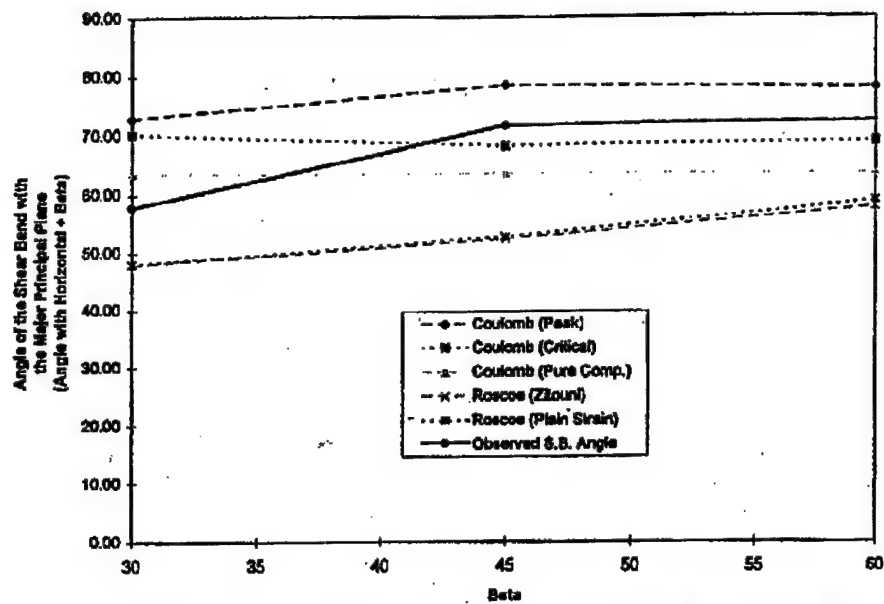


Figure 5.4a Predicted Inclinations with Respect to the Major Principal Plane (Coulomb & Roscoe)
Tests #87a, #88 & #89

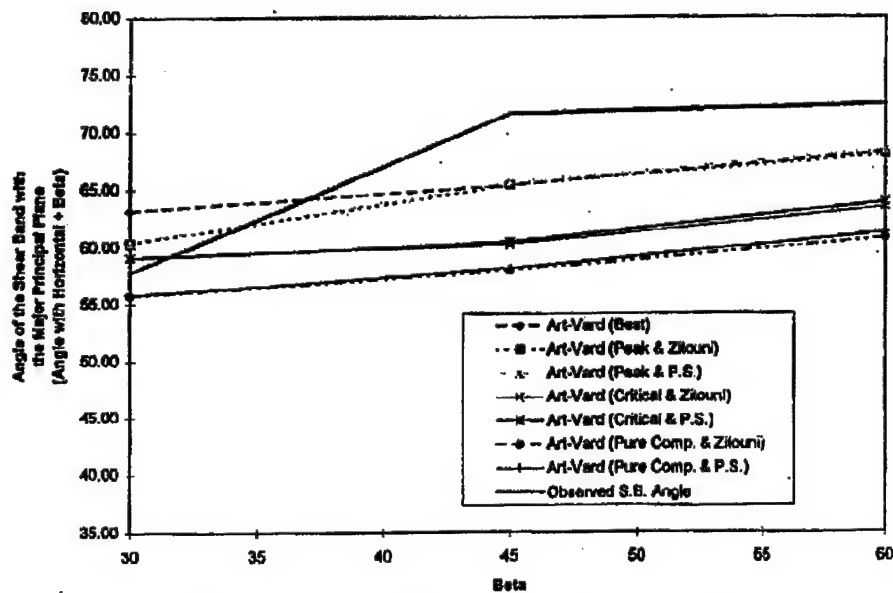


Figure 5.4b Predicted Inclinations with Respect to the Major Principal Plane (Arthur-Vardoulakis)
Tests #87a, #88 & #89

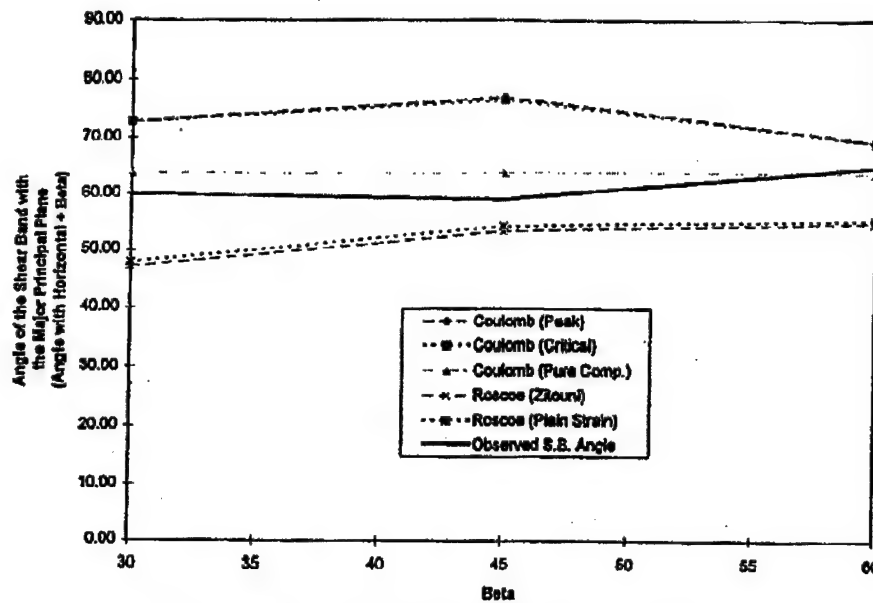


Figure 5.5a Predicted Inclinations with Respect to the Major Principal Plane (Coulomb & Roscoe) Tests #92, #93a & #94d

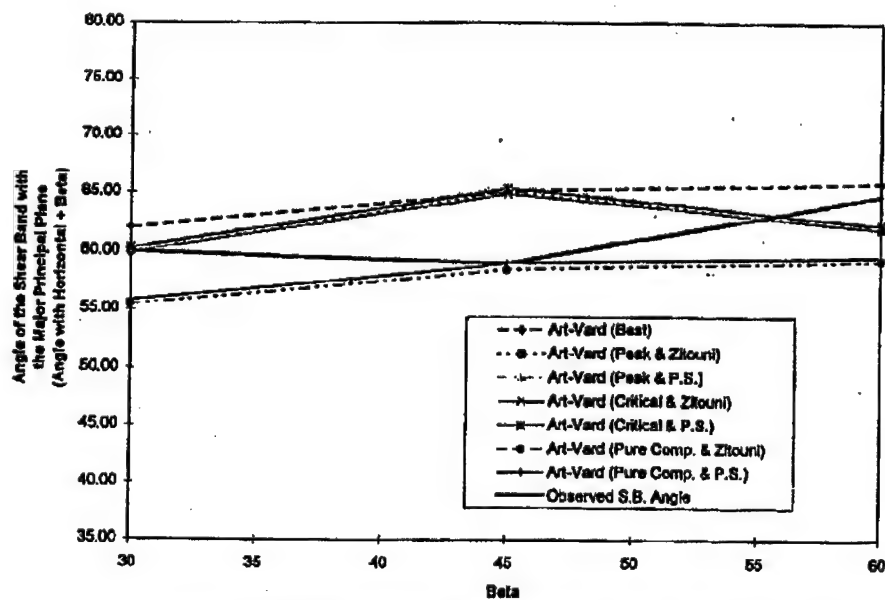


Figure 5.5b Predicted Inclinations with Respect to the Major Principal Plane (Arthur-Vardoulakis) Tests #92, #93a & #94d

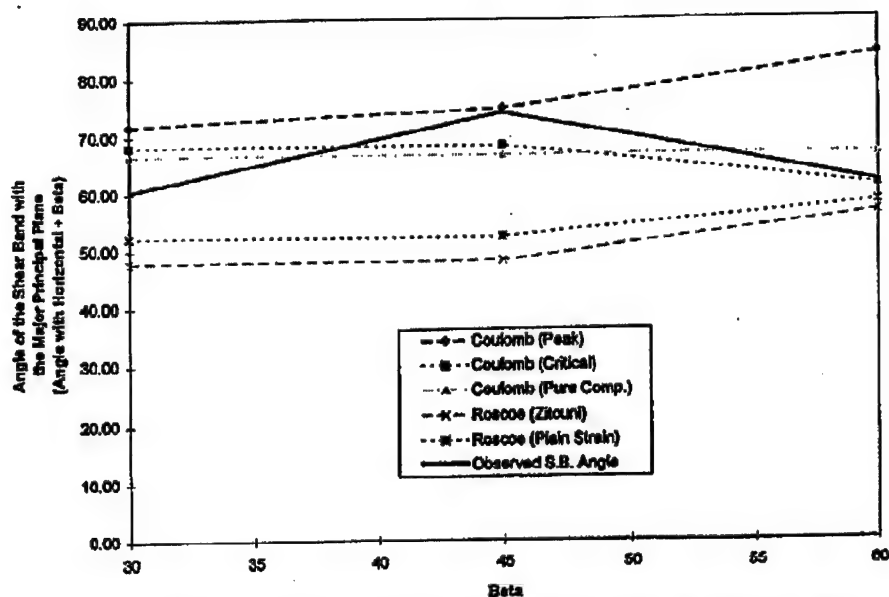


Figure 5.6a Predicted Inclinations with Respect to the Major Principal Plane (Coulomb & Roscoe)
Tests #97a, #98 & #99c

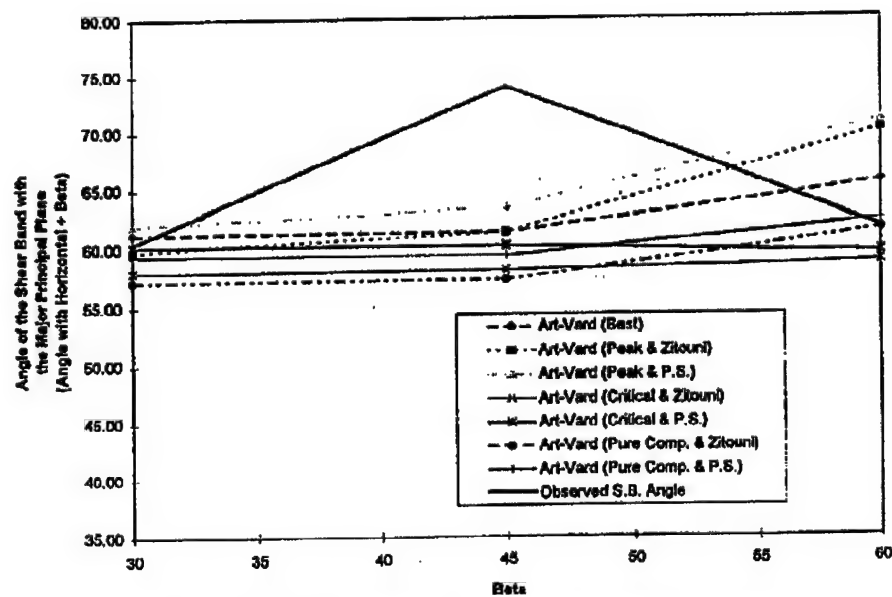


Figure 5.6b Predicted Inclinations with Respect to the Major Principal Plane (Arthur-Vardoulakis)
Tests #97a, #98 & #99c

5.3 Test Results

Chapter Four presented the results from the 35 different tests run on the Loire sand. This information, as summarized in table 4.1, listed the various angles of dilation and friction. Tables 5.1a and 5.1b used the collected information to calculate the predicted angles of the shear bands. As previously stated, it was apparent that Coulomb's theory, in general, seemed to over predict this angle. An exception to this generalization was when the angle of friction was calculated from a pure compression test. The angle of friction was found to vary depending on the type of test run and a pure compression test resulted in a noticeable smaller friction angle. For this reason, the predictions of the shear band angle when using a friction angle found from a pure compression test (Table 5.1a, Column #3) appeared to give moderately accurate results. Roscoe's theory, on the other hand, invariably under predicted the actual shear band angle. From this information, this theory by itself did not give accurate predictions. By analyzing the Arthur-Vardoulakis predictions in Table 5.1b, there did not appear to be one dominant combination that outweighed the others. It was noted that when the angle of friction found from a pure compression test was used (Table 5.1b, Columns 6 & 7), this combination seemed to give the least accurate results. In general, however, the Arthur-Vardoulakis theory did indeed tend to give much more accurate estimates than the Coulomb and Roscoe theories.

**Table 5.1a Predicted Shear Band Inclinations with the Horizontal
(Coulomb & Roscoe)**

Conf. Press.	Density	Beta (β)	Test	Predictions based on:					Actual
				Coul. (ϕ'_{pk})	Coul. (ϕ'_{cr})	Coul. (ϕ'_{pc})	Roscoe (ψ_{zt})	Roscoe (ψ_{ps})	
				1	2	3	4	5	
30 psi	50%	30	72	42.1	40.2	30.8	18.0	18.4	30.3
30 psi	50%	45	73	26.5	23.2	15.8	7.2	8.2	21.8
30 psi	50%	60	74b	12.8	8.0	0.8	-5.1	-4.4	4.3
50 psi	50%	30	77	40.6	38.4	31.1	16.5	17.7	31.0
50 psi	50%	45	78a	25.8	21.0	16.1	5.5	6.2	21.8
50 psi	50%	60	79	10.3	4.2	1.1	-6.9	-6.2	-1.7
70 psi	50%	30	82	40.9	38.1	33.1	16.1	16.9	27.3
70 psi	50%	45	83a	24.6	20.0	18.1	5.1	4.6	18.4
70 psi	50%	60	84a	25.5	2.5	3.1	-7.4	-6.5	0.9
30 psi	80%	30	87a	42.9	40.2	33.6	17.9	18.1	27.8
30 psi	80%	45	88	33.5	23.2	18.6	7.3	7.7	26.6
30 psi	80%	60	89	18.0	8.9	3.6	-2.2	-1.2	12.3
50 psi	80%	30	92	42.7	42.7	33.8	17.1	17.9	30.0
50 psi	80%	45	93a	32.0	31.6	18.8	8.3	9.2	14.0
50 psi	80%	60	94d	9.3	9.2	3.8	-5.3	-4.6	4.8
70 psi	80%	30	97a	41.9	38.3	36.6	17.7	22.1	30.4
70 psi	80%	45	98	29.8	23.3	21.6	3.0	7.1	29.0
70 psi	80%	60	99c	23.9	1.1	6.6	-3.6	-2.0	1.6

Note: Most accurate prediction(s) are in shaded box

**Table 5.1b Predicted Shear Band Inclinations with the Horizontal
(Arthur-Vardoulakis)**

				Predictions based on:							
Conf. Press.	Density	Beta (β)	Test	A-V Best	A-V ϕ'_{pk} ψ_{zi}	A-V ϕ'_{pk} ψ_{ps}	A-V ϕ'_{cr} ψ_{zi}	A-V ϕ'_{cr} ψ_{ps}	A-V ϕ'_{pc} ψ_{zi}	A-V ϕ'_{pc} ψ_{ps}	Actual
				1	2	3	4	5	6	7	
30 psi	50%	30	72	29.7	30.0	30.2	29.1	29.3	24.4	24.6	30.3
30 psi	50%	45	73	16.9	16.9	17.4	15.2	15.7	11.5	12.0	21.8
30 psi	50%	60	74b	3.2	3.8	4.2	1.4	1.8	-2.1	-1.8	4.3
50 psi	50%	30	77	28.6	28.5	29.2	27.4	28.1	23.8	24.4	31.0
50 psi	50%	45	78a	15.6	15.6	16.0	13.3	13.6	10.8	11.1	21.8
50 psi	50%	60	79	2.0	1.7	2.0	-1.3	-1.0	-2.9	-2.6	-1.7
70 psi	50%	30	82	27.8	28.5	28.9	27.1	27.5	24.6	25.0	27.3
70 psi	50%	45	83a	14.9	14.9	14.6	12.6	12.3	11.6	11.3	18.4
70 psi	50%	60	84a	1.1	9.1	9.5	-2.4	-2.0	-2.1	-1.7	0.9
30 psi	80%	30	87a	33.2	30.4	30.5	29.0	29.1	25.7	25.8	27.8
30 psi	80%	45	88	20.4	20.4	20.6	15.2	15.4	12.9	13.1	26.6
30 psi	80%	45	89	8.2	7.9	8.4	3.4	3.9	0.7	1.2	12.3
50 psi	80%	30	92	32.1	29.9	30.3	29.9	30.3	25.4	25.8	30.0
50 psi	80%	45	93a	20.1	20.1	20.6	19.9	20.4	13.5	14.0	14.0
50 psi	80%	60	94d	5.9	2.0	2.3	2.0	2.3	-0.8	-0.4	4.8
70 psi	80%	30	97a	31.3	29.8	32.0	28.0	28.2	27.2	29.4	30.4
70 psi	80%	45	98	16.4	16.4	18.4	13.1	15.2	12.3	14.4	29.0
70 psi	80%	60	99c	5.6	10.1	11.0	-1.3	-0.5	-1.5	2.3	1.6

Note: Most accurate prediction(s) are in shaded box

5.4 Influence of Testing Parameters

5.4.1 Confining Pressure

The three initial confining pressures selected for use in the testing program were at 40, 60, and 80 psi (276, 414, and 552 kPa). With the inclusion of the 10 psi (69 kPa) back pressure, this yielded the three initial effective confining pressures of 30, 50, and 70 psi (207, 345, and 483 kPa) respectively. To examine the effects of these different starting pressures, Figures 5.7a and 5.7b were used. Each of the tests considered were conducted under generalized conditions, in which the effective mean stress was kept constant throughout the duration of the test. The first plot, 5.7a, compares the different shear band angles for the three different pressures at an initial relative density of 50%. These graphs for loose samples do not appear to show any significant pressure effects. Figure 5.7b, compares the same three pressures only this time the samples were all at 80% initial relative density. This plot shows more deviation than the first but this also points to the conclusion that there was no influence of confining pressure on the resultant shear band angle. There were no consistent trends which might indicate a significant effect of confining pressure.

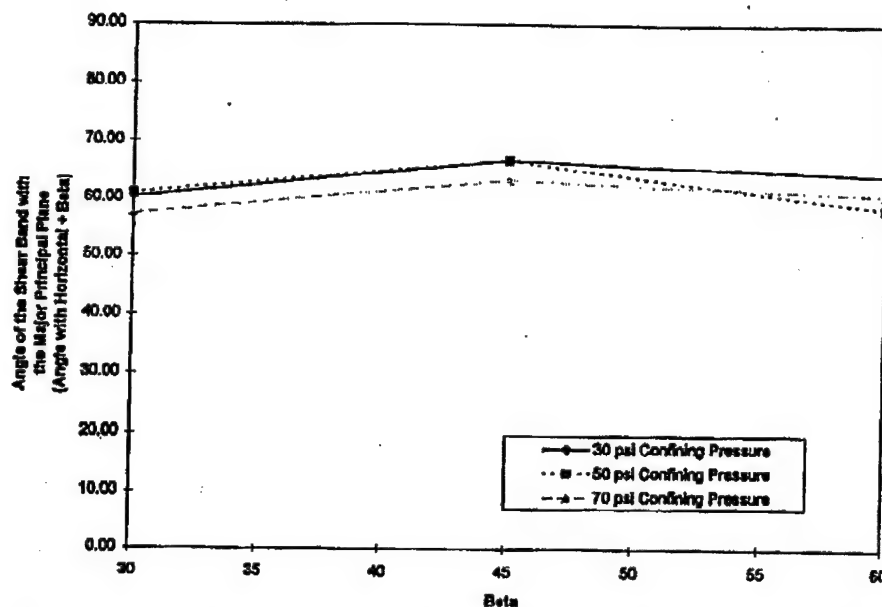


Figure 5.7a Effect of Confining Pressure on Shear Band Inclination
Tests #72-74b, #77-79 & #82-84a
(Loose Samples)

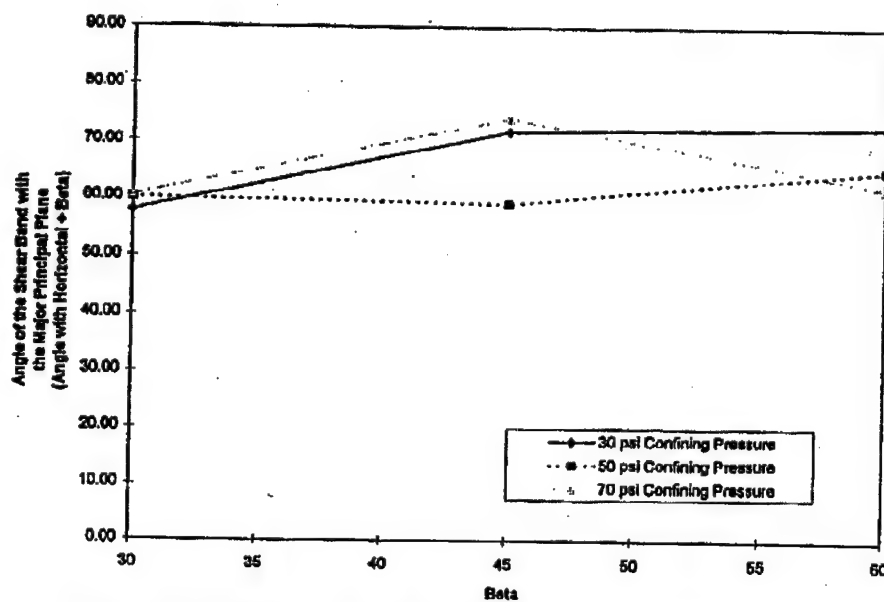


Figure 5.7a Effect of Confining Pressure on Shear Band Inclination
Tests #87a-89, #92-94d & #97a-99c
(Dense Samples)

5.4.2 Generalized Versus Direct Tests

The majority of the tests conducted for this research were generalized tests. However, a series of tests were conducted to determine if direct testing would produce similar results. For these tests, the cell pressure remained the same as at the start of the test. Figure 5.8 compares three series of tests to see any differences between the two testing styles. Each of the three series were run at an initial confining pressure of 30 psi (207 kPa) for sake of comparison. Based on this plot, the mean stress does not appear to have an obvious linear influence on the inclination of the shear band. A greater number of samples should be tested and compared before any definitive conclusions can be reached on this parameter.

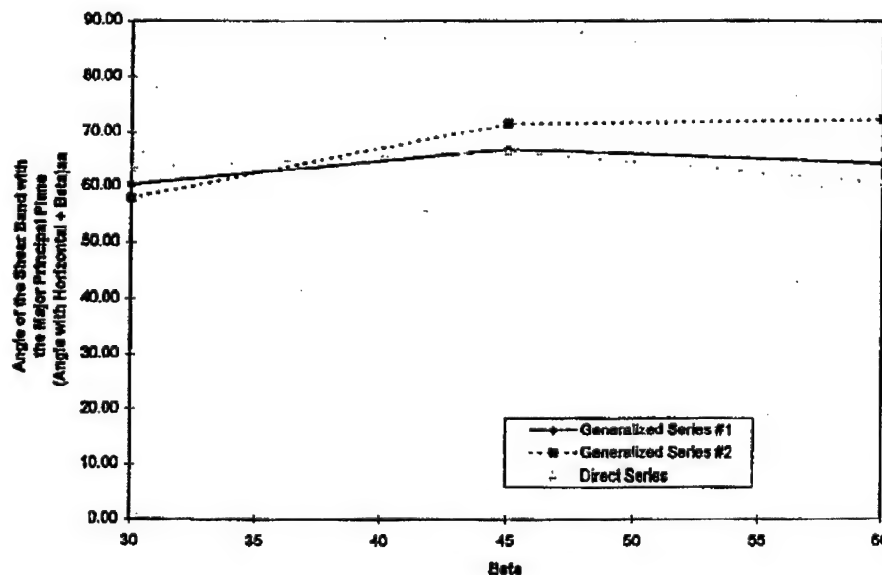


Figure 5.8 Effect of Generalized vs. Direct Testing on Shear Band Inclination
Tests #72-74b, #87a-89 & #102-104
(30 Psi Effective Confining Pressure)

5.4.3 Relative Density

In general, the relative density of a given soil is an extremely important parameter. To investigate the effect of relative density, dense and loose samples were tested. The dense samples were chosen to be at a nominal relative density of 80% and the loose samples were at 50%. Figure 5.9a plots the results of the six series of generalized tests. Three of these were loose samples and the other three were dense samples. Inspection of this plot indicates that the initial relative density did not appear to significantly effect the inclination of the shear band. Notice, however, that the relative density changes at the application of the confining cell pressure as well as during the test.

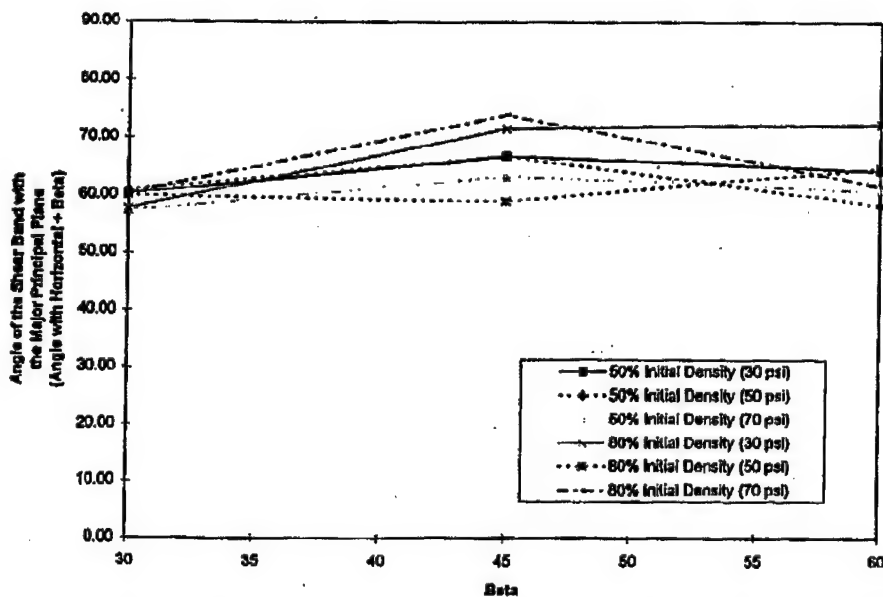


Figure 5.9a Effect of Relative Density on Shear Band Inclination
Tests #72-74b, #77-79, #82-84a, #87a-89, #92-94d & 97a-99c

A closer inspection might indicate that the relative density had a minor effect on the shear band inclination. Figure 5.9b averaged the angles found for each density. In other words, the shear band angles observed from the three generalized tests at 50% initial density were averaged and compared to the corresponding average angles at 80%. By visual inspection of this graph, there is a small variation indicating that the angles of the dense sample are slightly greater than the loose samples. Notice that there are counteracting effects that tend to act in favor of the Arthur-Vardoulakis equation; some factors that lead to an increase in ϕ' might lead to a decrease in ψ .

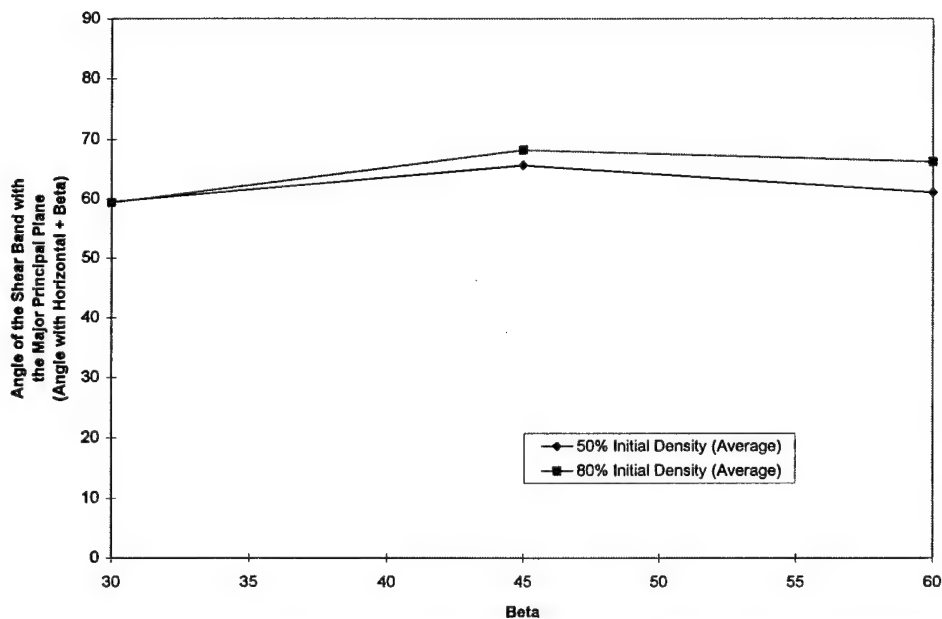


Figure 5.9b Effect of Relative Density on Shear Band Inclination
Averaged Values

5.5 Comparison Between LSI-30 and Loire Sand

5.5.1 Overview

Many predictions and generalizations can be developed using the results from the various tests conducted for this research. A potential problem might arise, however, when applying the same conclusions to another sand. For this reason, a systematic comparison between the Loire and LSI-30 sand was needed. To make this analysis, a summary of the LSI-30 information was required. The thesis by C. Tucker Cope (1997) contained this information which is presented in this section for comparison. The physical properties of the two sands (the resultant friction and dilation angles) and the prediction theories for each sand are compared.

5.5.2 Physical Properties

Some of the differences between the two studied sands were discussed earlier in Chapter Two. The general finding was that the Loire sand closely imitated the LSI-30 sand in type and grain size distribution. By consulting figure 2.1, it is clear that each of the grain size distribution curves are essentially parallel to one another. The main difference between these two media was obviously the actual particle sizes. On average, the Loire sand was approximately 50% larger than the LSI-30. Subtle differences between the sands exist in the specific gravity and void ratio characteristics but these were not as important as the average grain size.

5.5.3 Angles of Friction and Dilation Comparison

Chapter Four summarized the various angles of friction and dilation from the various tests. Table 5.2 presents the corresponding table as found by Cope for the LSI-30 sand. Half of the tests run on the finer sand did not measure the volume change so this summary has only four sets of tests. The angles of dilation were measured in two different fashions. The first is the same method as used for the Loire sand, this being the plane strain assumption (equation 1.1c). The second one uses the triaxial formula (equation 1.2). Notice that the angles of friction and dilation for the Loire sand were, on average, about five degrees greater than the LSI-30.

Table 5.2 Summary of the Angles of Friction and Dilation
(LSI-30 sand, generalized tests)
(Cope, 1997)

Confining Pressure	Initial Relative Density	Test Number	β	ϕ' (Peak)	ϕ' (Critical)	ψ (Plane Strain)	ψ (Triaxial)
30 psi	50%	21	0	38.6	24.5	---	---
30 psi	50%	22	30	50.1	49.2	1.12	11.17
30 psi	50%	23	45	47.1	45.1	9.36	11.58
30 psi	50%	24	60	44.6	42.0	14.49	8.84
30 psi	50%	25	90	42.8	25.4	---	---
50 psi	50%	26	0	38.9	24.1	---	---
50 psi	50%	27	30	45.4	43.1	-0.26	8.92
50 psi	50%	28	45	47	43.5	7.92	9.48
50 psi	50%	29a	60	42.9	34.2	17.05	12.42
50 psi	50%	30	90	41.7	19.5	---	---
70 psi	50%	31	0	37.9	21.8	---	---
70 psi	50%	32	30	44.4	40.9	-1.23	7.64
70 psi	50%	33	45	48.9	41.3	7.24	8.53
70 psi	50%	34	60	43	31.3	14.66	8.14
70 psi	50%	35	90	42	20.1	---	---

From this observation, the assumption was made that the actual inclinations of the shear bands for the Loire sand should be approximately two to three degrees greater than the LSI-30. Table 5.3 lists the observed angles of shear banding for the two sands to see if the Loire sand did indeed have the slightly sharper angles.

Table 5.3 Summary of the Actual Shear Band Inclinations
(LSI-30 & Loire sand)

Eff. Con. Pres.	Initial Relative Density	Beta (β)	Test (LSI-30)	Test (Loire)	Actual (LSI-30)	Actual (Loire)
30 psi	50%	30	22	72	26.0	30.3
30 psi	50%	45	23	73	15.8	21.8
30 psi	50%	60	24	74b	0.7	4.3
50 psi	50%	30	27	77	29.6	31.0
50 psi	50%	45	28	78a	15.5	21.8
50 psi	50%	60	29a	79	4.7	-1.7
70 psi	50%	30	32	82	29.4	27.3
70 psi	50%	45	33	83a	15.3	18.4
70 psi	50%	60	34	84a	0.9	0.9
30 psi	80%	30	37	87a	28.1	27.8
30 psi	80%	45	38	88	20.6	26.6
30 psi	80%	45	39	89	1.2	12.3
50 psi	80%	30	42	92	32.0	30.0
50 psi	80%	45	43	93a	19.0	14.0
50 psi	80%	60	44	94d	0.0	4.8
70 psi	80%	30	47	97a	29.5	30.4
70 psi	80%	45	48	98	18.9	29.0
70 psi	80%	60	49	99c	0.0	1.6

In general, it does appear that the Loire sand has the greater shear band angles, but there does not seem to be enough evidence to strongly argue this point. It was the finding of Cope that the Arthur-Vardoulakis theory produced the most accurate angle predictions. Specifically, the peak angle of friction in combination with the angle of dilation found using the plane strain formula (same combination as Table 5.1b, Column 3), and the combination of plane strain dilation angle with the angle of friction from the pure torsion test (same combination as Table 5.1b, Column 1) gave the best results. These conclusions agree with the ones using the Loire sand.

5.6 Summary and Conclusions

The analysis of the three theories predicting the failure angle (Coulomb, Roscoe, and Arthur-Vardoulakis) reinforced the findings of Cope. Coulomb's theory had the tendency to over estimate the actual inclination of the shear band and, in a similar fashion, Roscoe's theory would under estimate the angle. The theory suggested by Arthur and Vardoulakis takes an average of the first two. This gave the best prediction of the shear band inclination. As mentioned previously, specific combinations of each formula might yield slightly more accurate results. The two best predictions were different combinations of the Arthur-Vardoulakis theory. Each of these predictions used the angle of dilation as found by using the plane strain formula. The angle of friction used was either the general peak friction angle or the angle of friction found from a pure torsion test. For the most part, the peak angles of

friction for the torsion related tests ($\beta=30^\circ$, 45° , & 60°) gave the same angles of friction. This explains the relative similarity between the two theories.

The findings on the influence of the various parameters investigated in this research also agreed very well with Cope. The confining pressure, generalized versus direct testing, and relative density were all shown to have minimal effects on the inclination of the shear band.

Another important variable that this research studied was the effect of grain size on the failure angle. Koenders et. al. (1990) (Table 1.1) suggested that the average grain size would determine which of the three proposed theories would be the most accurate. The combined research of this project disagrees with that proposal. According to Koenders, Coulomb's theory should give the best predictions for both the LSI-30 and the Loire sands, since the average grain size (D_{50}) of each is smaller than 0.65 mm. In both cases, the Arthur-Vardoulakis theory yielded the most accurate prediction.

Chapter Six

Conclusions

6.1 Summary

The research done for this thesis conducted a total of 35 different tests to study the factors influencing the inclination of shear banding in non-cohesive, coarse-grain sands. The testing was done using a hollow cylinder torsional triaxial device. The capabilities of this set up were such that tests could be conducted while the mean stress remained constant. The majority of the tests were conducted under these conditions. Other parameters that were examined were the relative density, confining pressure and stress path. Samples were tested at two different relative densities, namely 50% and 80%. Three initial effective confining pressures were chosen of 30, 50, and 70 psi (207, 345, and 483 kPa). Finally, the specimens were subjected to five different stress paths. These tests had the principle stress applied at angles of 0, 30, 45, 60, and 90 degrees from the vertical axis. All the tests were drained to measure the volume change in the specimen. The volume change was necessary to calculate the angle of dilation, a crucial variable in several prediction theories. The testing program was modeled after the research done by C. Tucker Cope (1997) to investigate the effect of particle size on shear banding.

6.2 Results and Conclusions

Three theories predicting the angle of failure were studied to determine the most accurate one. This was the primary focus of this thesis. Based on the results, it was clear that the Arthur-Vardoulakis theory gave the best results. However, the quantities needed to calculate the angle could be found using different methods. For this reason, there were

friction (ϕ') obtained from the peak stress and the angle of dilation using the plane strain formula (ψ_{ps}) were used. This combination proved to be the most accurate in nearly half of all the tests conducted where a shear band formed. This finding matched the conclusion as noted by Cope.

The second goal of this research was to determine the effect of various testing variables on the shear band. Of the various parameters studied, only the stress path influenced the angle of shear banding. The angle beta, or the angle of principle stress in relation to the vertical axis, was the only variable that clearly affected the inclination of the shear band. All others parameters were observed to have only minimal effects.

Finally, the last objective was to study the influence of grain size on the shear band angle. The results of the tests on both the LSI-30 and Loire sands led to the same conclusions. Each one indicated that the Arthur-Vardoulakis theory was the most accurate, despite the noticeable difference in the average grain size. This points to the conclusion that, at least within reasonable limits, the grain size will not effect the shear band angle.

6.3 Suggestions for Future Research

While great care was taken to keep strict control over various factors, a program of testing might be recommended to try and reproduce the results as found from the existing data. Sand is anisotropic by nature and by running several tests with the same parameters might help to observe the accuracy of this research. As can be seen by consulting the summary of tests, it was common to rerun a test. This was done to guarantee that no mistakes were made.

Another suggestion to improve on the conclusions might be to test samples under a larger variety of stress paths. For this thesis, only three different useful beta angles ($\beta = 30^\circ, 45^\circ \text{ \& } 60^\circ$) were studied. Perhaps a better understanding would arise from testing samples at angles of 15° and 75° . This would give a total of five points from which to draw conclusions from instead of three.

The variation of the medium used might help to broaden the results as found with the LSI-30 and Loire sands. Perhaps an extremely fine sand and a very coarse sand (sands finer than LSI-30 and coarser than Loire) should be studied to analyze if indeed there is a trend that depends on grain size. In general, it would help to draw conclusions with more than just two sets of data.

Finally, the results from the digitization process should be studied in greater detail. Appendix B of this thesis contains the results of the digital imaging procedure for Tests # 77, 78a & 79. This information details the shear band inclinations, the strains in and around the shear band and also the width of the shear band. Eventually a model can be developed from this information to accurately simulate the genesis and propagation of a shear band.

Appendix A

References

- Arthur, J.R.F. and Dunstan T. (1982) Rupture Layers in Granular Media. Proc. IUTAM *Conference Deformation and Failure of Granular Materials*, Delft, 453-459.
- Arthur, J.R.F., Dunstan T., Al-Ani Q.A.J.L. & Assadi A. (1977) "Plastic Deformation and Failure in Granular Media," *Geotechnique*, 27, No.1, 53-74.
- Balasubramaniam, A.S. (1976) "Local Strains and Displacement Patterns in Triaxial Specimens of Saturated Clay," *Soil Foundations*, 16, No. 1, 101-114.
- Bolton, M. D. (1986) "The Strength and Dilatancy of Sands," *Geotechnique*, 36, No.1, 65-78.
- Cope, C. Tucker (1997) *Shear Banding In Sand Under Combined Stress Paths*, Masters Thesis, Department of Civil Engineering, Case Western Reserve University, Cleveland, Ohio.
- Houlsby, G.T. and Wroth, C.P. (1980) "Strain and Displacement Discontinuities in Soils," *Journal of Engineering Mechanics Division of American Society of Civil Engineers*, 117, EMA, Aug., 753-772.
- Koenders, M.A., Arthur, J.R.F., and Dunstan, T. (1990) "The Behaviour of Granular Materials at Peak Stress," *Yielding, Damage, and Failure of Anisotropic Solids*, J.P. Boehler, Ed., London, Mechanical Engineering Publications. pg. 805-818.
- Lade, P.V., Yamamuro, J.A., and Skyers, B.D., "*Effects of Shear Band Formation in Triaxial Extension Tests*," *Geotechnical Testing Journal*, GTJODJ, Vol. 19, No.4, December 1996, 398-410.
- Liang, L. (1995) *Development of an Energy Method for Evaluating the Liquefaction Potential of a Soil Deposit*, Ph.D. Thesis, Department of Civil Engineering, Case Western Reserve University, Cleveland, Ohio.
- Liang, L., Saada, A.S., Figueroa, J.L., Cope, C.T. (1996) *The Use of Digital Image Processing in Monitoring Shear Band Development*, Department of Civil Engineering, Case Western Reserve University, Cleveland, Ohio.

- Schantz, T. and Vermeer, P.A. (1996) "Angles of Friction and Dilatancy of Sand," *Geotechnique*, Vol. 46, No.1, 145-151.
- Vardoulakis, I. (1980) "Shear Band Inclination and Shear Modulus of Sand in Biaxial Tests," *International Journal of Numerical and Analytical Methods in Geomechanics*, Vol. 4, 103-119.
- Veemer, P.A. (1990) "The Orientation of Shear Bands in Biaxial Tests," *Geotechnique*, Vol. 40, No. , 223-236.
- Yoshida, T., Tatsuoka, F., Siddiquee, M.S.A., Kamegai, Y. & Park C.S. (1994) "Shear Banding in Sands Observed in Plane Strain Compression," *Localization and Bifurcation Theory for Soils and Rocks*, Chambon, Desrues, Vardoulakis, 165-178.

Appendix B

Digitization Results

B.1 Explanation of Appendix Graphs

Upon completion of the digitization process, several graphs were created. These plots summarize the various strains found using this new procedure. Three tests were completely digitized and the graphs from digitization are included in this appendix. The three test were Test #77 (Torsion-Compression), Test #78a (Pure Torsion) and Test #79 (Torsion-Extension). Each of these tests were conducted at 50 psi (345 kPa) initial effective confining pressure and 50% initial relative density. For each of the three tests, four images were digitized per camera. By analyzing this digitized data, the MATLAB™ software was able to create seven plots for each camera. A total of 28 plots for each test were generated, because four cameras were needed to completely capture the entire surface of the specimen.

The digitization process assigns coordinates to each grid intersection point. By knowing the coordinates at the initial and subsequent times, the strains of a rectangle composed of four of these points could be found. Figure A demonstrates this method.

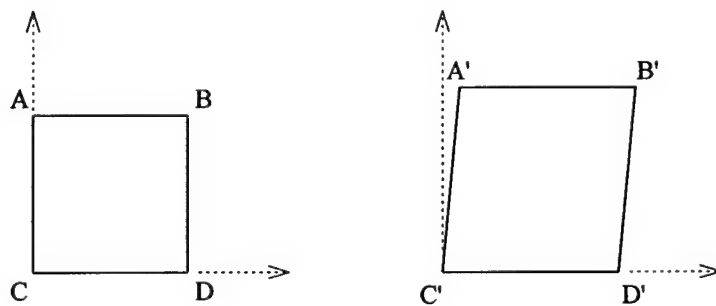


Figure A

The rectangle on the left (which initially begins as a square) is created when connecting lines between points A through D. At some subsequent time, the rectangle on the right can be created by connecting lines between points A' through D'. The actual coordinates are not as important as the length of the line segments connecting two points, since the strain is computed by dividing the change in length over the original length. Each of the seven plots are explained in greater detail below.

Figure 1: This figure contains four separate graphs.

- **Top left plot (τ_{oct} vs. time):** Shows the shear stress (Tau Octahedral) verses time along with the four times images were taken and digitized. Typically, the first two times were taken before failure (peak of the τ_{oct} vs. time) and the last two were taken after failure.
- **Top right plot (γ vs. time):** Shows the average shear strains of elements in various locations. These locations are at the top of the grid, at the bottom and the average of these two. Referring to Figure A, the shear strain is found by determining the angle between the vertical axis and line A'C' or B'D'. These two angles are averaged for each element and then averaged over the number of elements used. Typically, this is done for two or three rows of elements to obtain a more accurate measurement. In addition, a global shear strain curve is included to show the strain found using the rotation of sample as measured with the RVDT. This line is included for the sake of comparison. In the case where a shear band is at the top or bottom of a grid the results may appear to be inaccurate. This is due

to the fact that in areas near the shear band, larger deformations have occurred. When a shear band is at the upper or lower limits of the grid, only one row of elements is available to use for an average. This line indicating the strains at the top or bottom of the grid are typically inaccurate under these conditions.

- **Bottom left plot ($\epsilon_{\text{vert.}}$ vs. time):** This plot demonstrates the vertical strains of elements in several locations (same as previous graph). To calculate the vertical strain, the height change of the element is divided by the original height; where the height change is taken as the average height change between the two horizontal lines (segments A'B' and C'D' in Figure A). The global vertical strain is also included.
- **Bottom right plot ($\epsilon_{\text{horiz.}}$ vs. time):** This graph is very similar to the vertical strain plot. In this plot however, the horizontal strains are shown. They are determined by finding the average horizontal change between two vertical lines (A'C' and B'D' in Figure A) and dividing this quantity by the original width of the element. As with the previous two graphs, a global strain is also shown.

Figure 2: This figure contains four separate graphs. These four plots are identical to the ones seen in Figure 1. However, in addition to the four curves for the strain plots, a fifth line is also plotted. This line is the average strains (shear, vertical, and horizontal) of just those elements within the shear band. These strains are typically much larger than those calculated outside the shear band and therefore the scale is adjusted accordingly.

Figure 3: This figure contains four separate graphs. These plots present data similar to Figure 2 except a rotation of axis is incorporated. The axis were rotated to be along and normal to the shear band. This figure is useful when making comparisons.

Figure 4: This figure shows three separate plots. These three graphs show the various strains (shear, vertical, and horizontal) as calculated for each row of elements. In other words, the strains are shown along the height of the specimen. Each plot has three curves which represent the strains as calculated at the second, third, and fourth times. For this figure, the strains are calculated at the nodes.

Figure 5: This figure shows three separate plots. For this figure, the same information from Figure 4 is calculated except for this plot the strains are calculated at the center of each element.

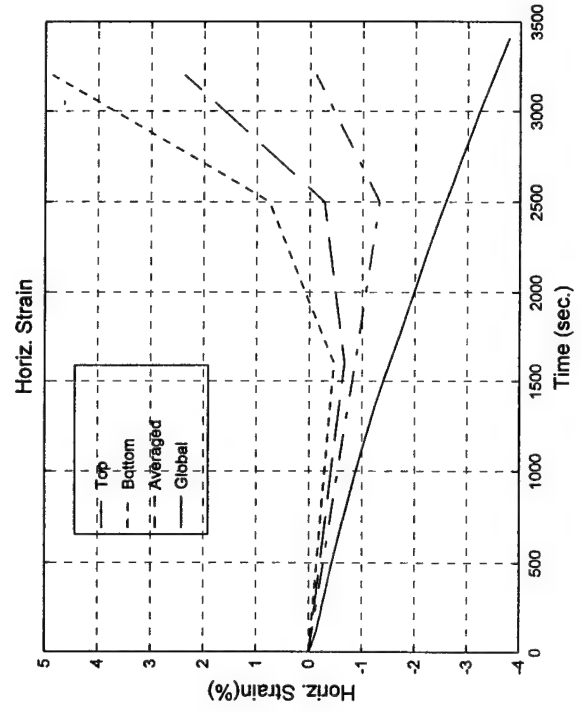
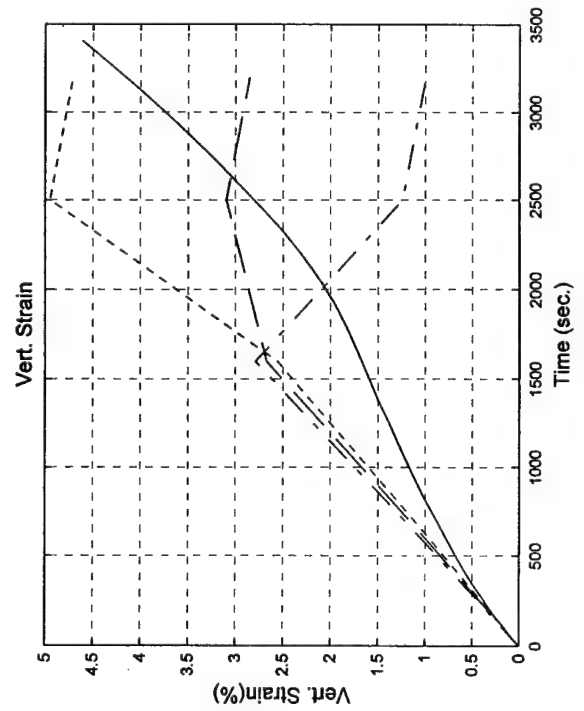
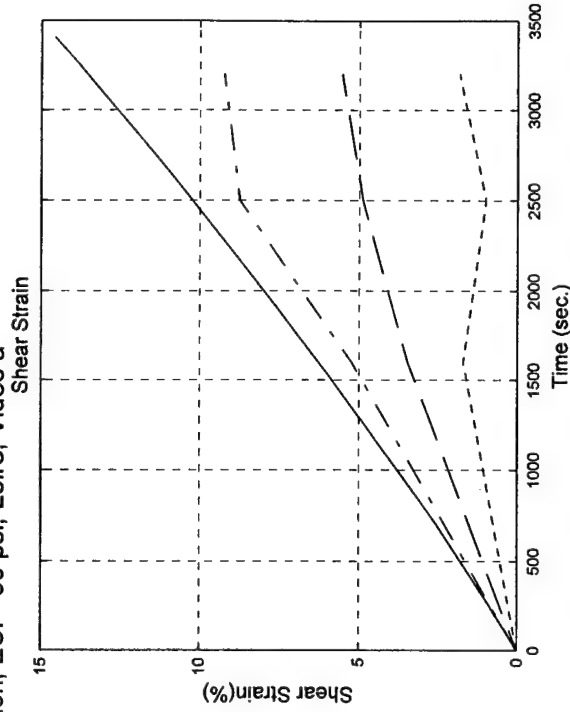
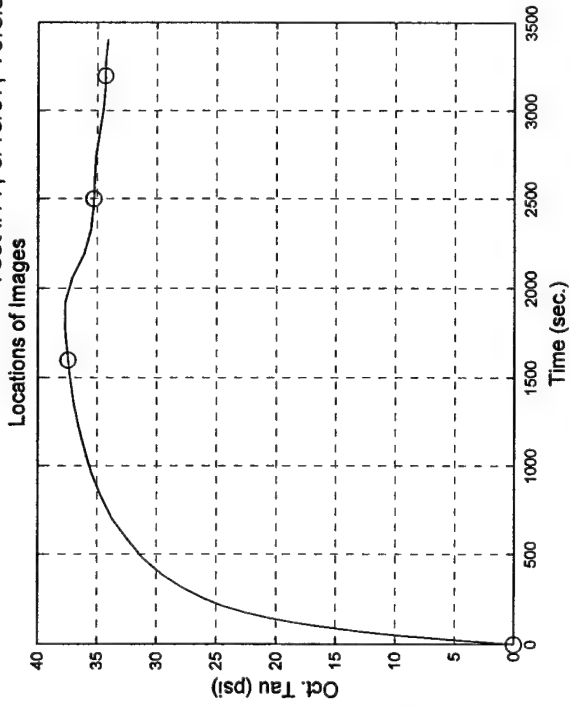
Figure 6: This figure shows three separate plots. The various curves from Figures 4 and 5 are superimposed here. The lines are from Figure 4 while the points are from Figure 5.

Figure 7: This figure shows three separate plots. This figure joins the various points from Figure 6 and creates a combination of the two curves.

B.2 Test #77

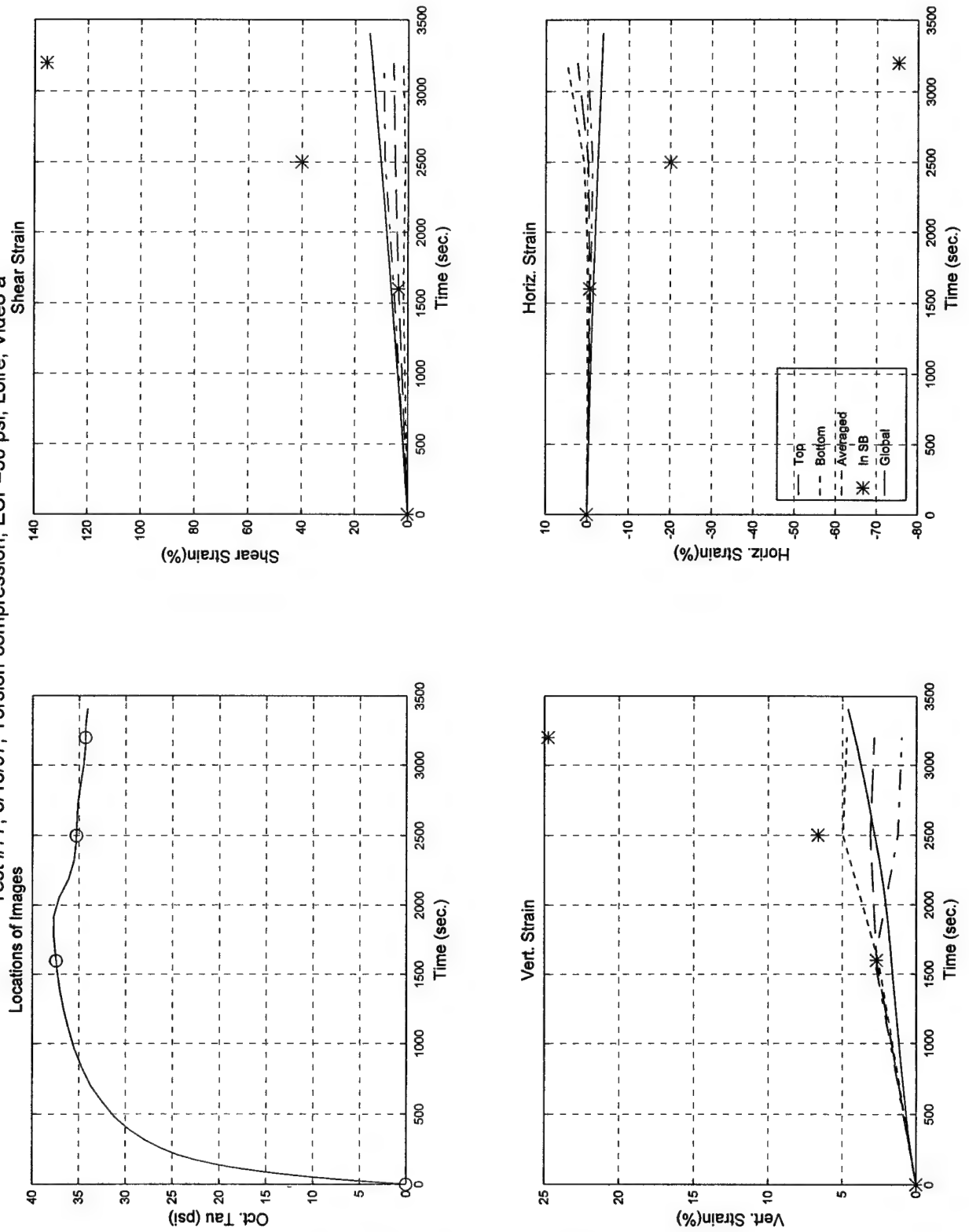
- **Torsion-Compression ($\beta = 30^\circ$)**
- **Effective Confining Pressure = 50 psi (345 kPa)**
- **50% Initial Relative Density**
- **Generalized Test**
- **Digitized Times Intervals: 0000, 1600, 2500 & 3200 sec.**

Test #77; 3/18/97; Torsion-compression; ECP=50 psi; Loire, Video a

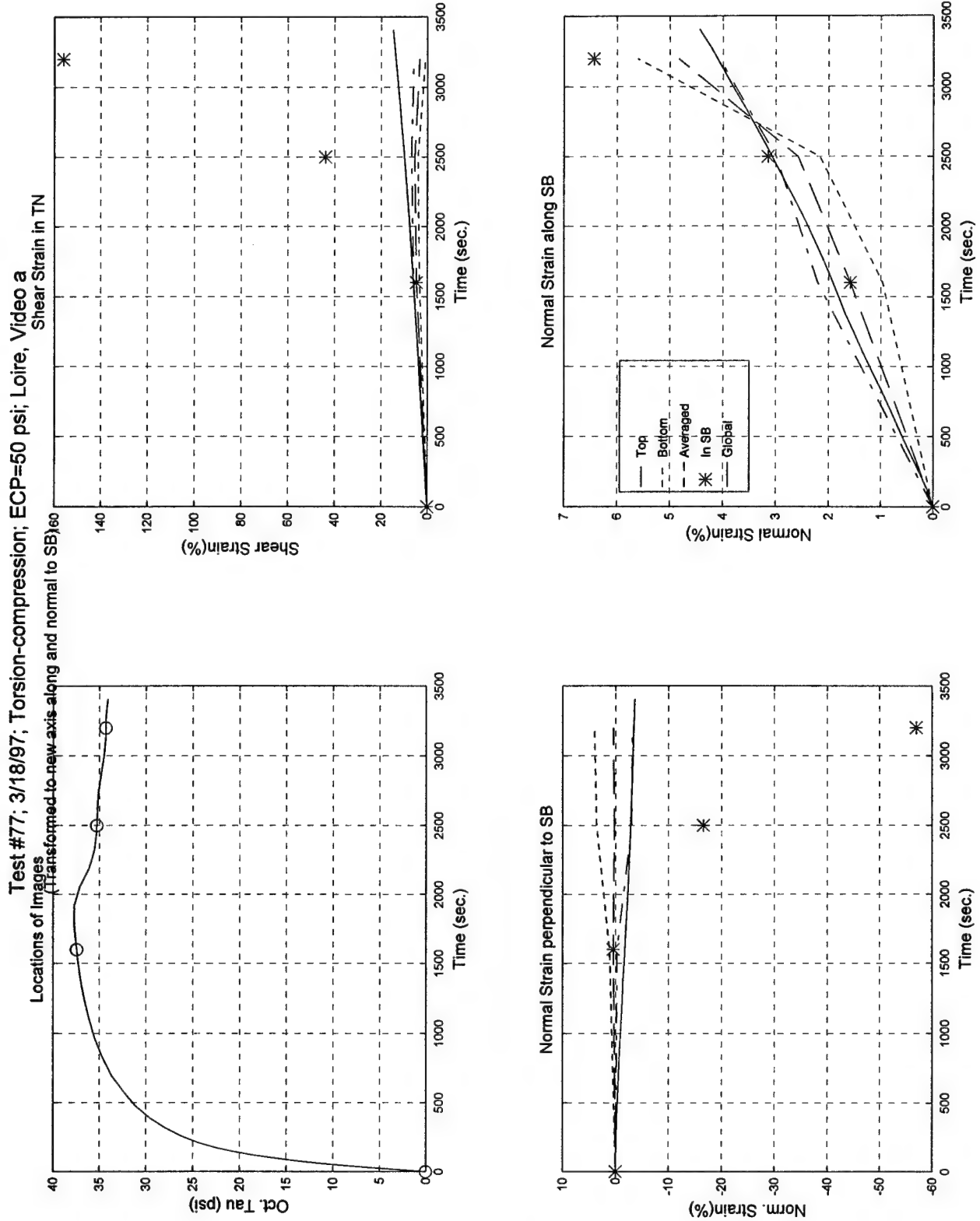


Test #77, Camera #A, Figure 1

Test #77; 3/18/97; Torsion-compression; ECP=50 psi; Loire, Video a

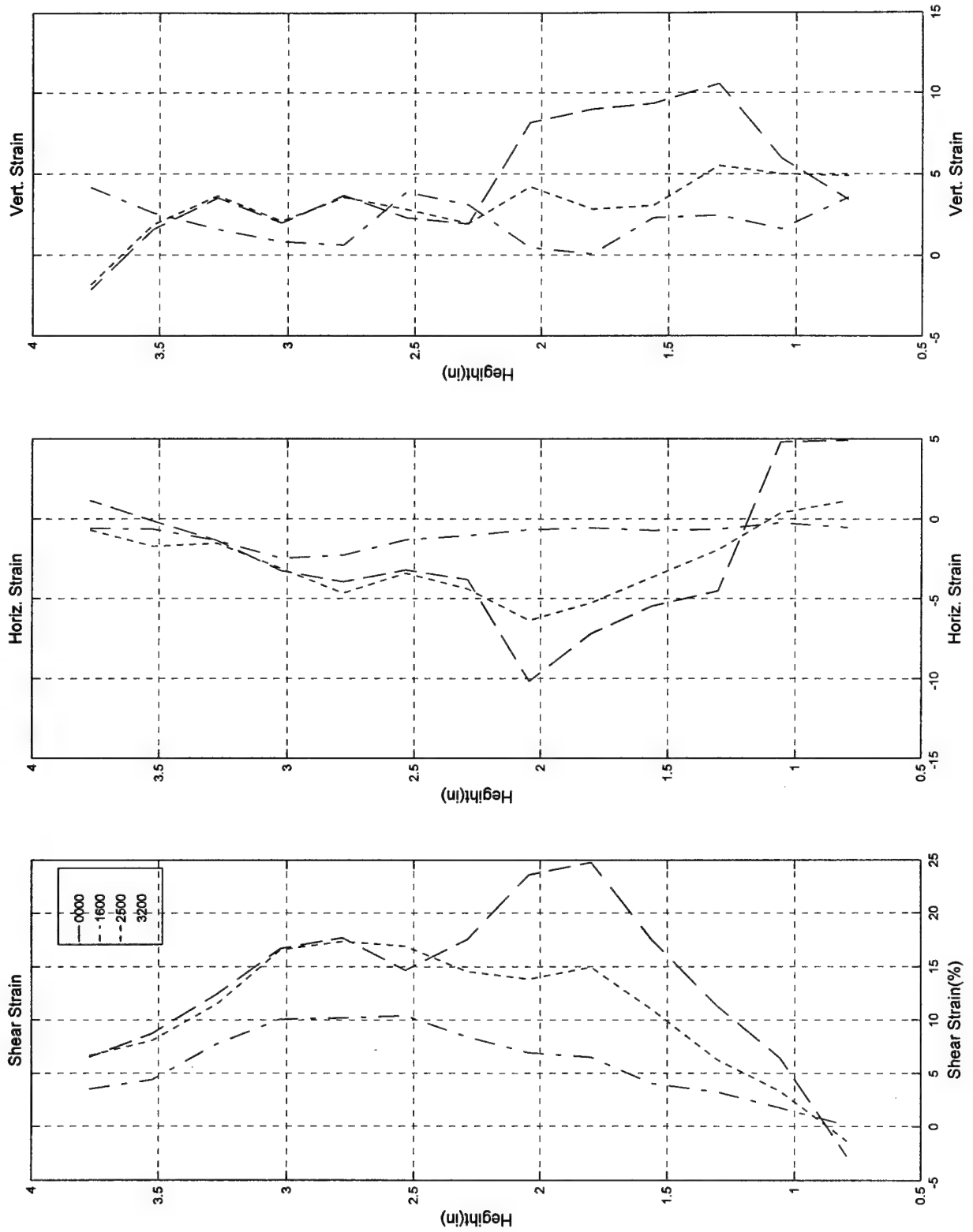


Test #77, Camera #A, Figure 2



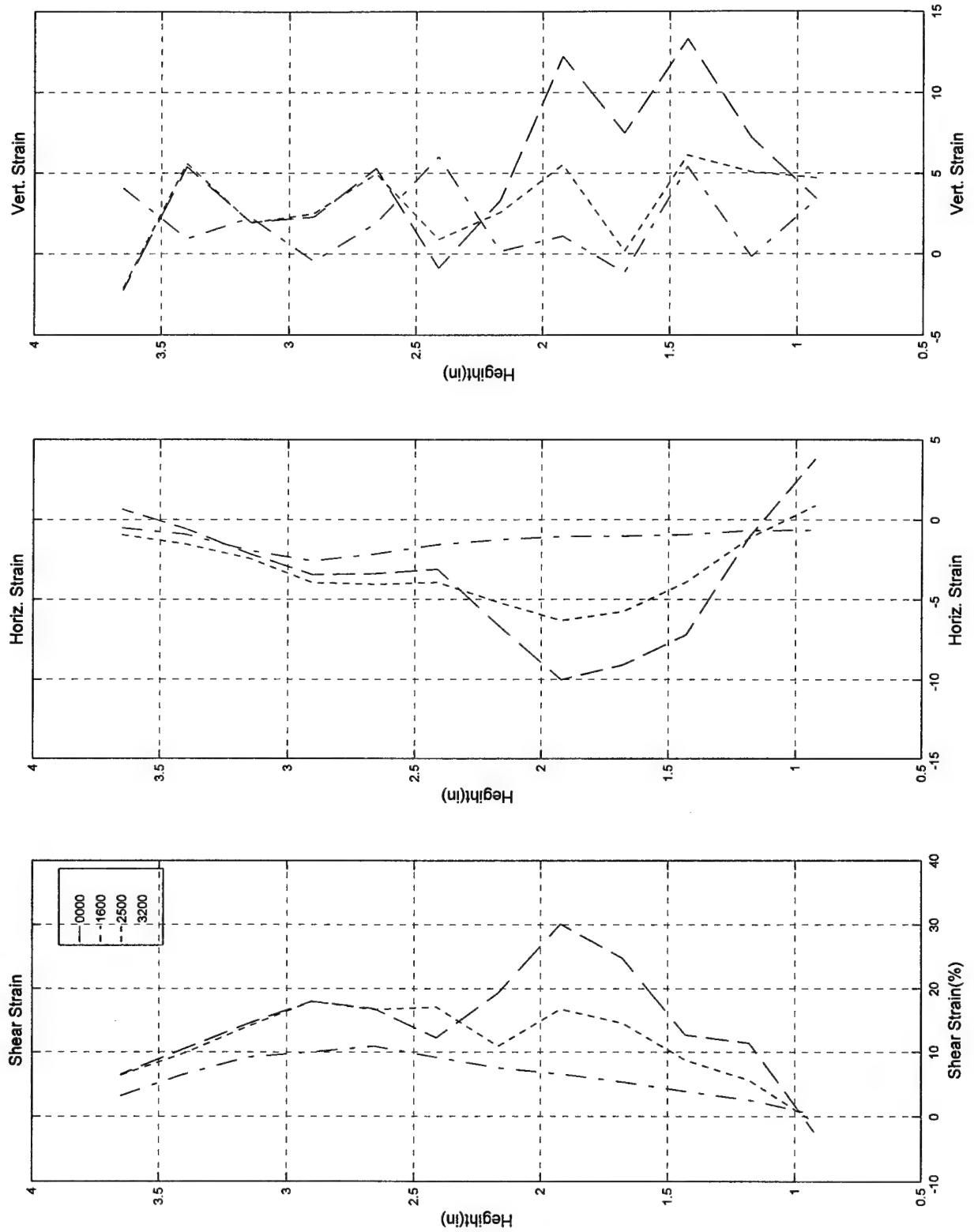
Test #77, Camera #A, Figure 3

Test #77; 3/18/97; Torsion-compression; ECP=50 psi; Loire, Video a



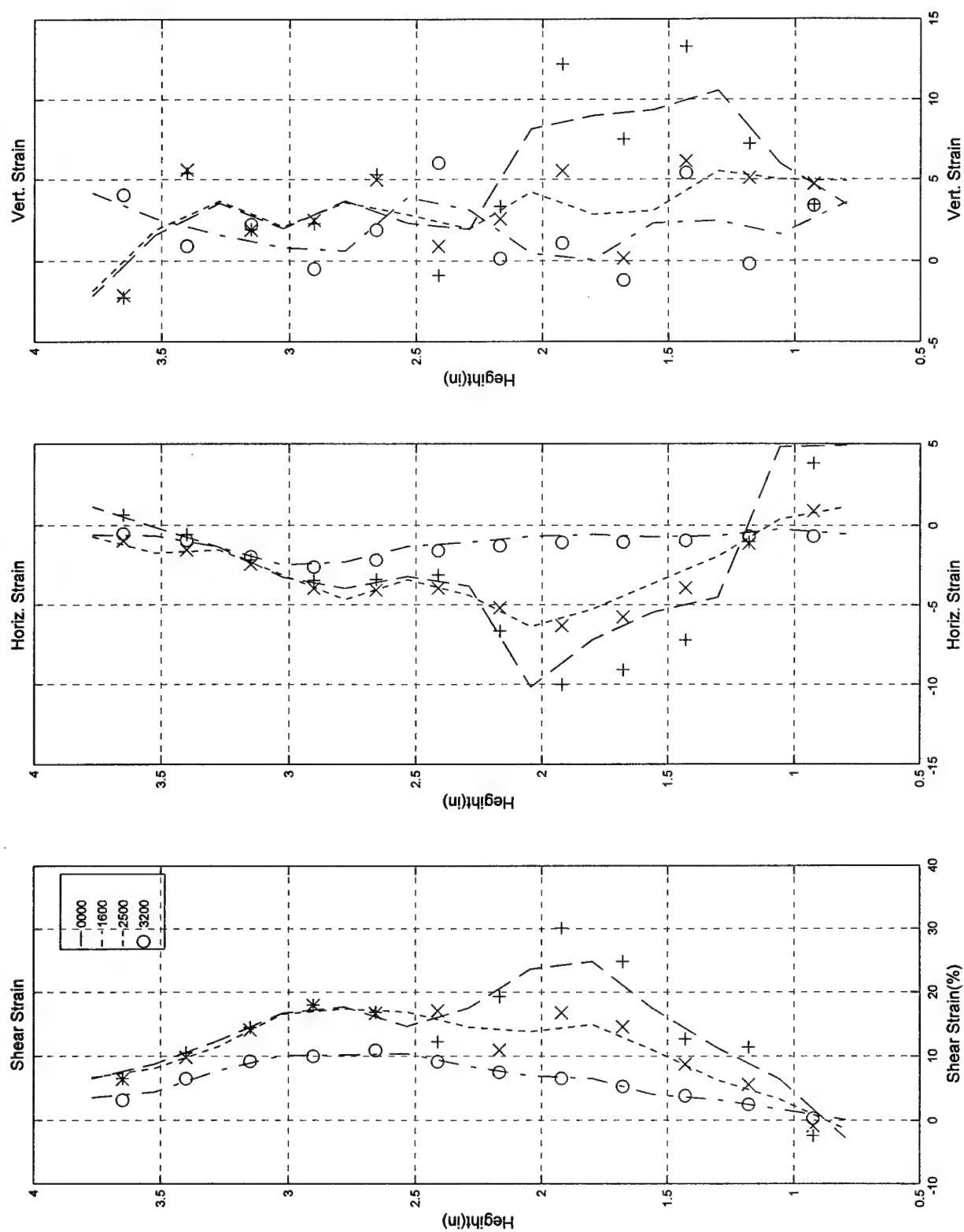
Test #77, Camera #A, Figure 4

Test #77; 3/18/97; Torsion-compression; ECP=50 psi; Loire, Video a



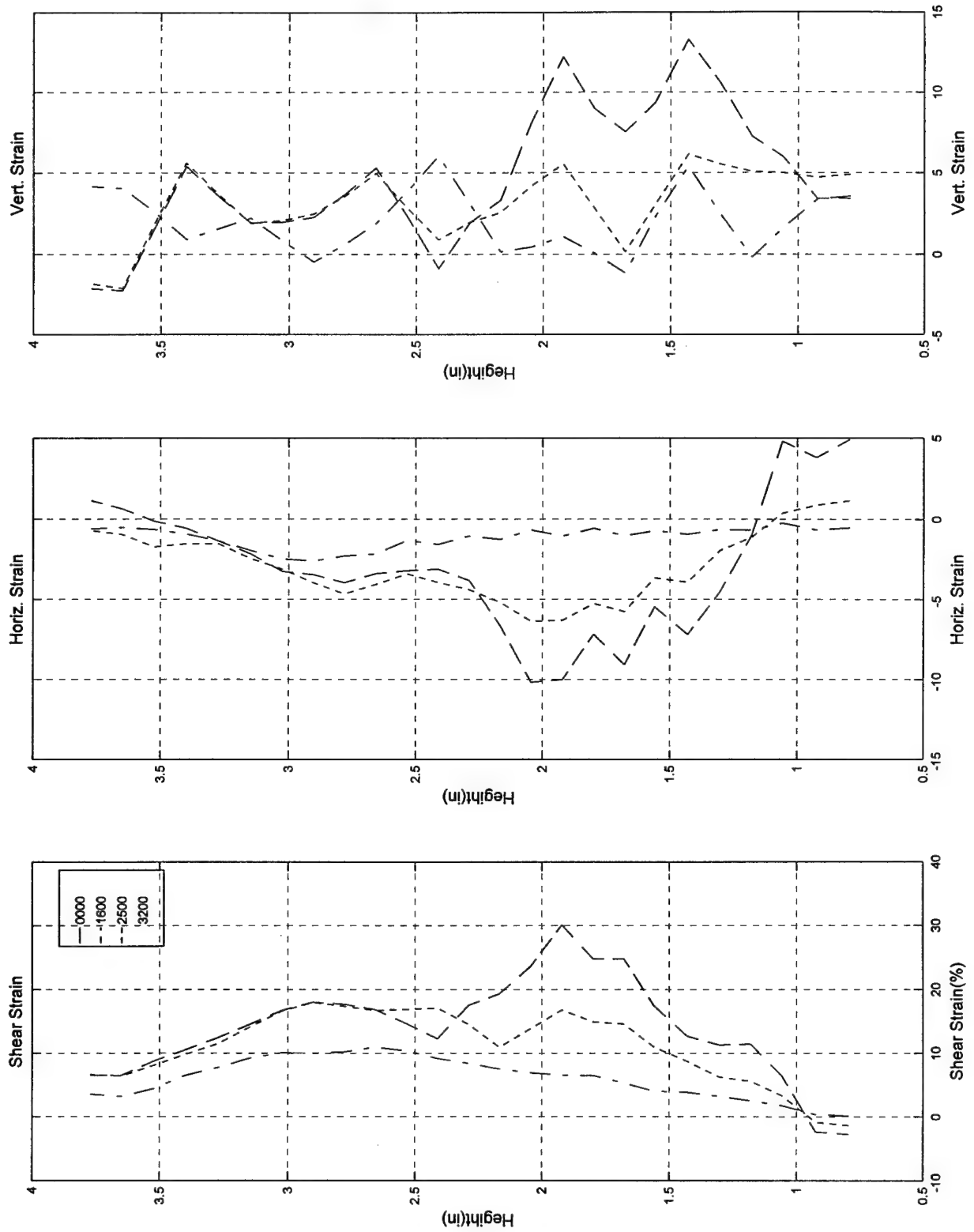
Test #77, Camera #A, Figure 5

Test #77; 3/18/97; Torsion-compression; ECP=50 psi; Loire, Video a



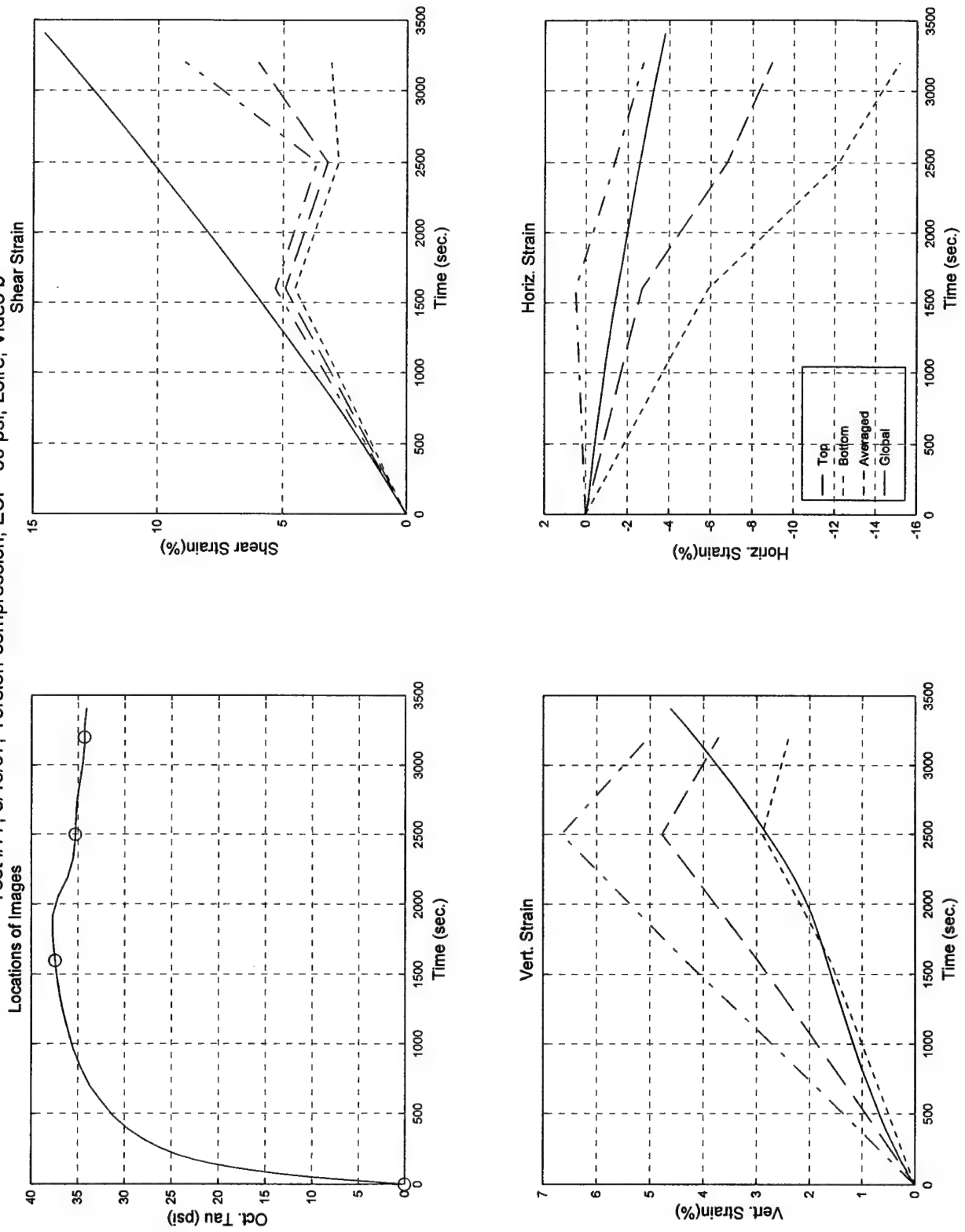
Test #77, Camera #A, Figure 6

Test #77; 3/18/97; Torsion-compression; ECP=50 psi; Loire, Video a



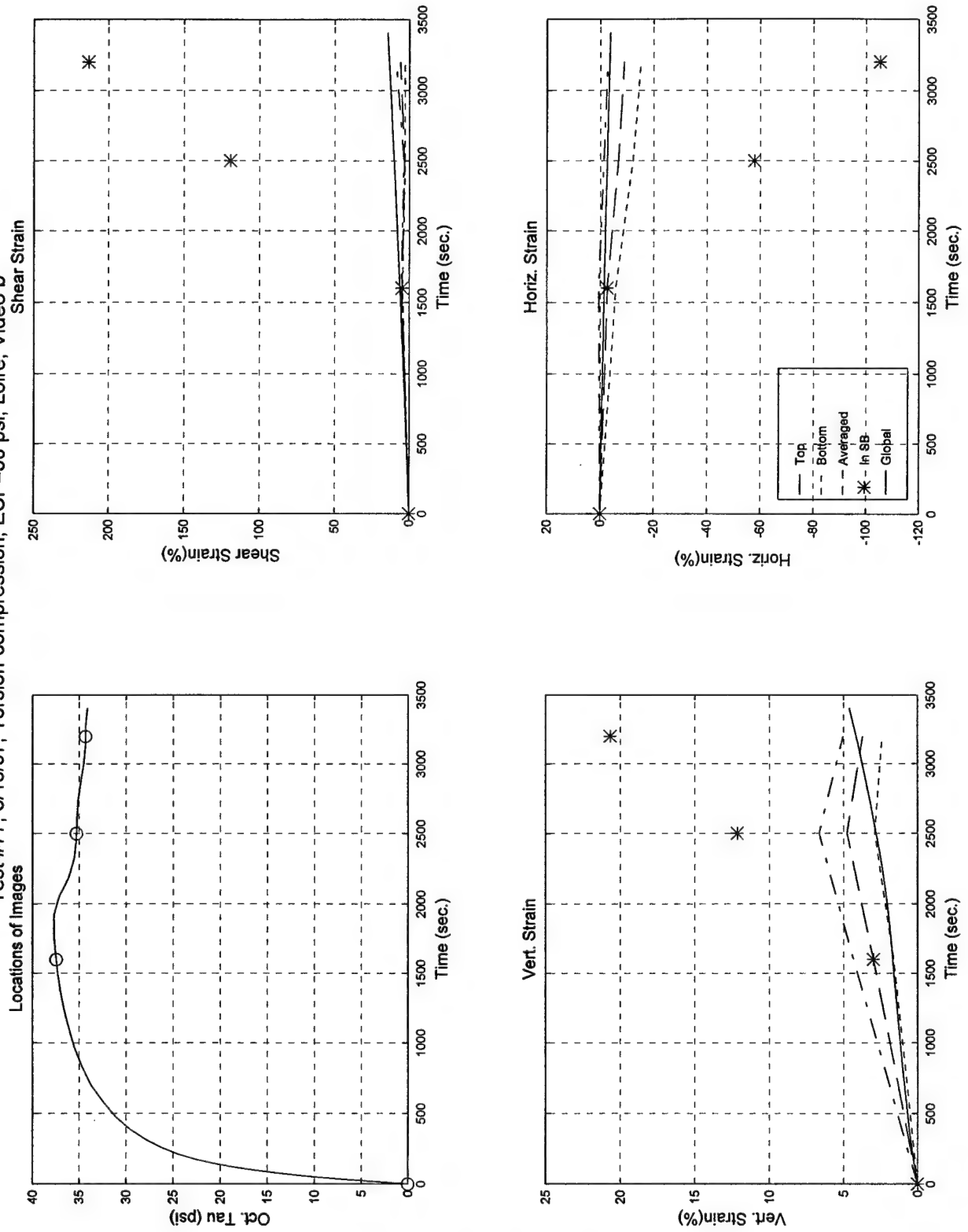
Test #77, Camera #A, Figure 7

Test #77; 3/18/97; Torsion-compression; ECP=50 psi; Loire, Video b

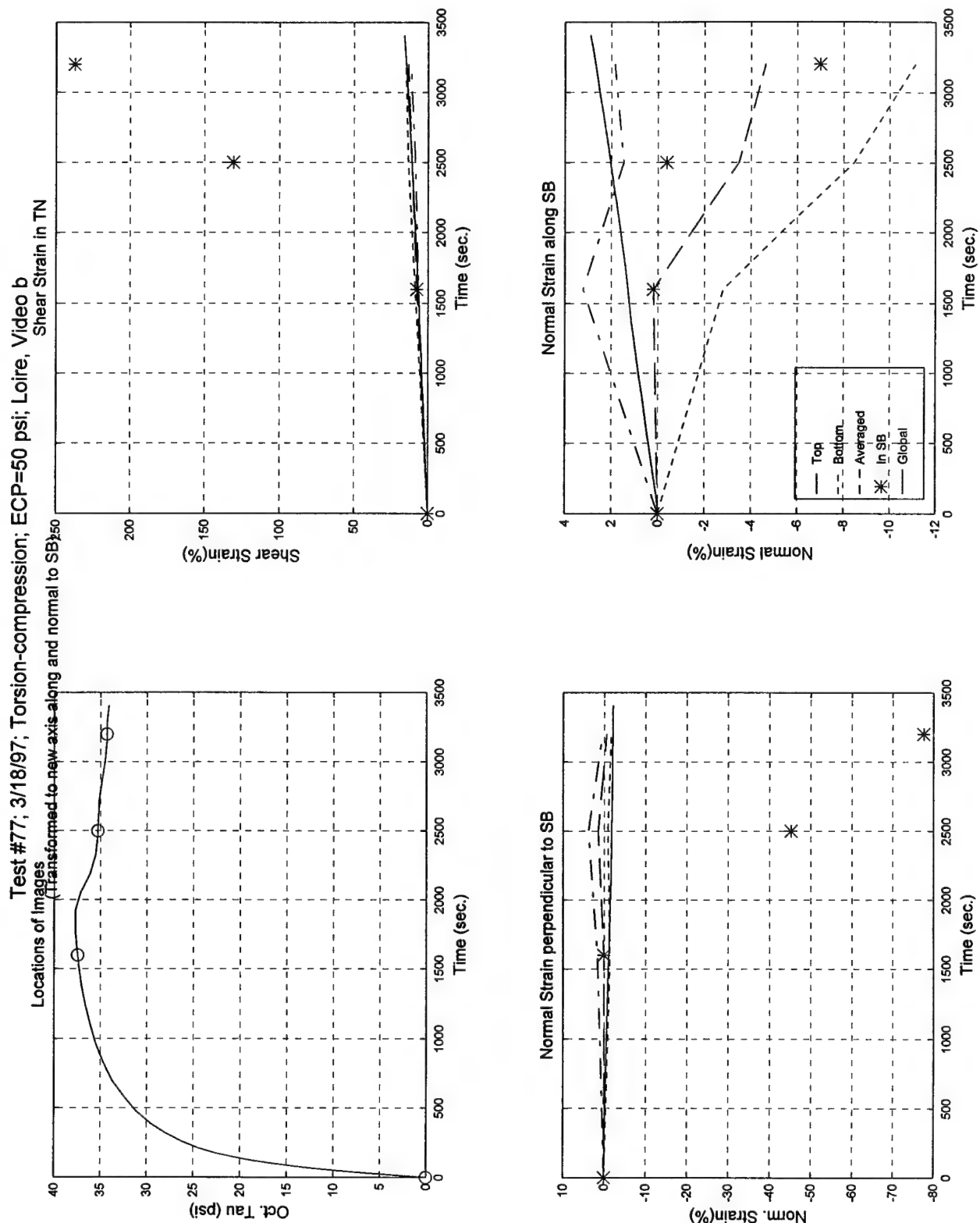


Test #77, Camera #B, Figure 1

Test #77; 3/18/97; Torsion-compression; ECP=50 psi; Loire, Video b

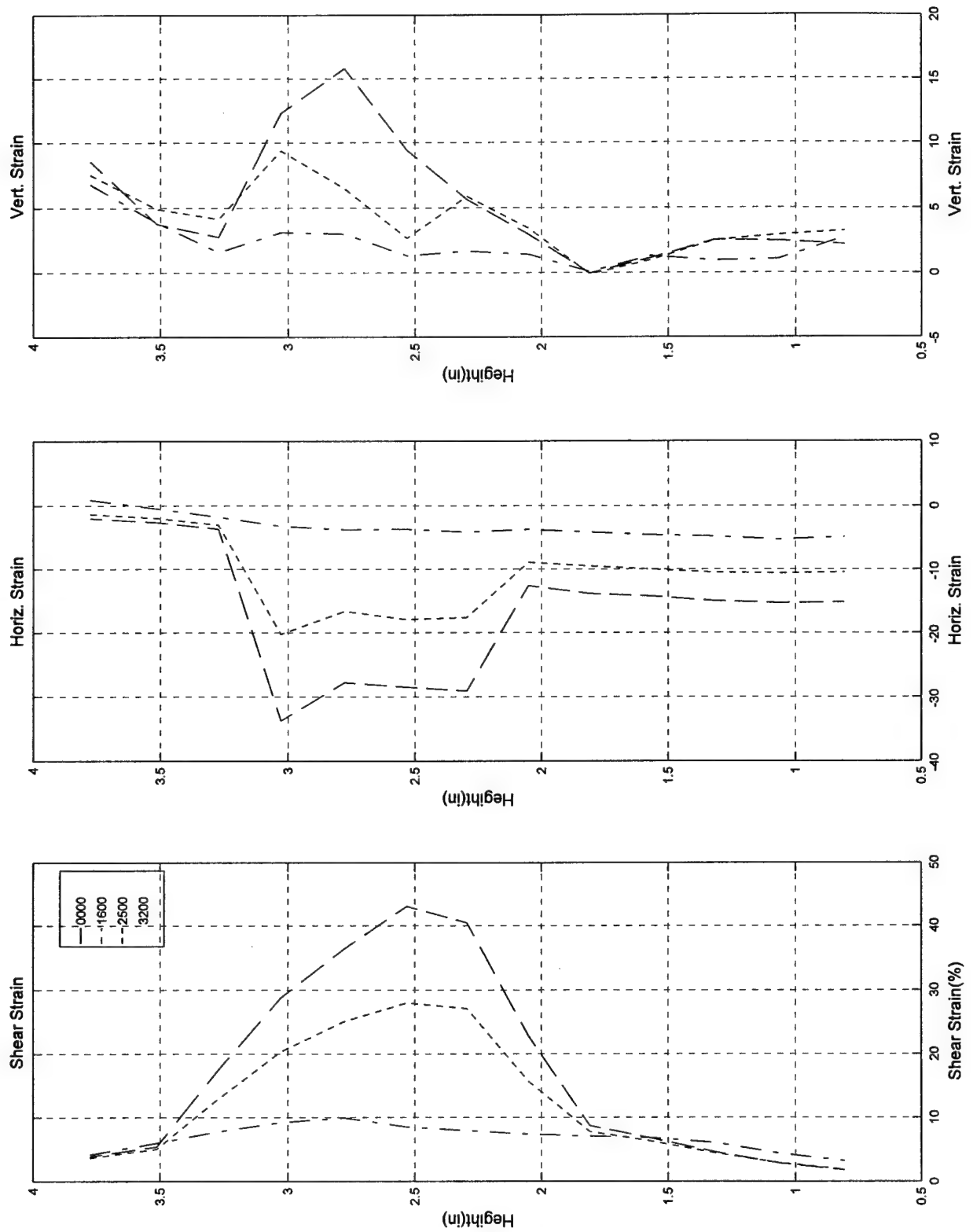


Test #77, Camera #B, Figure 2



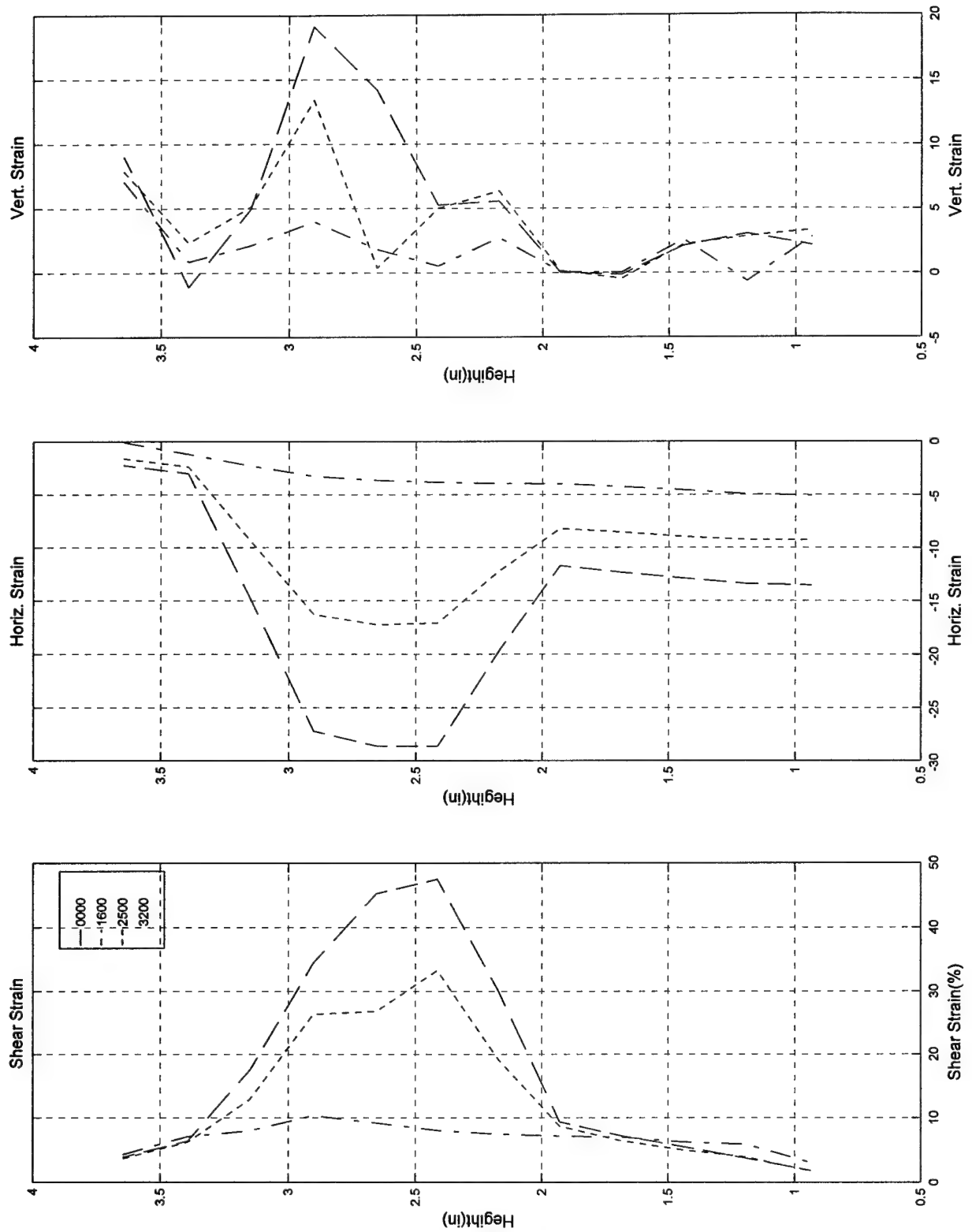
Test #77, Camera #B, Figure 3

Test #77; 3/18/97; Torsion-compression; ECP=50 psi; Loire, Video b



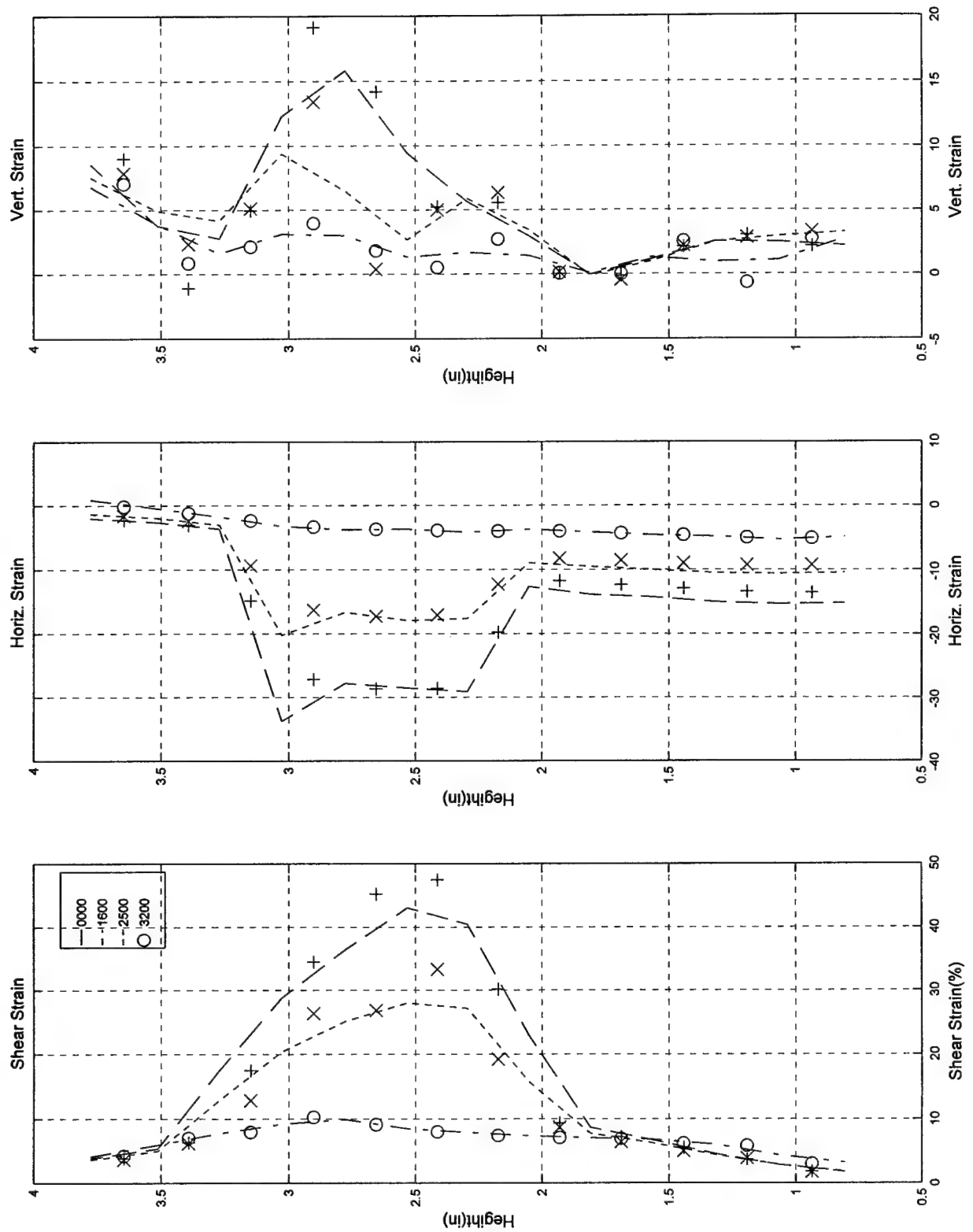
Test #77, Camera #B, Figure 4

Test #77; 3/18/97; Torsion-compression; ECP=50 psi; Loire, Video b



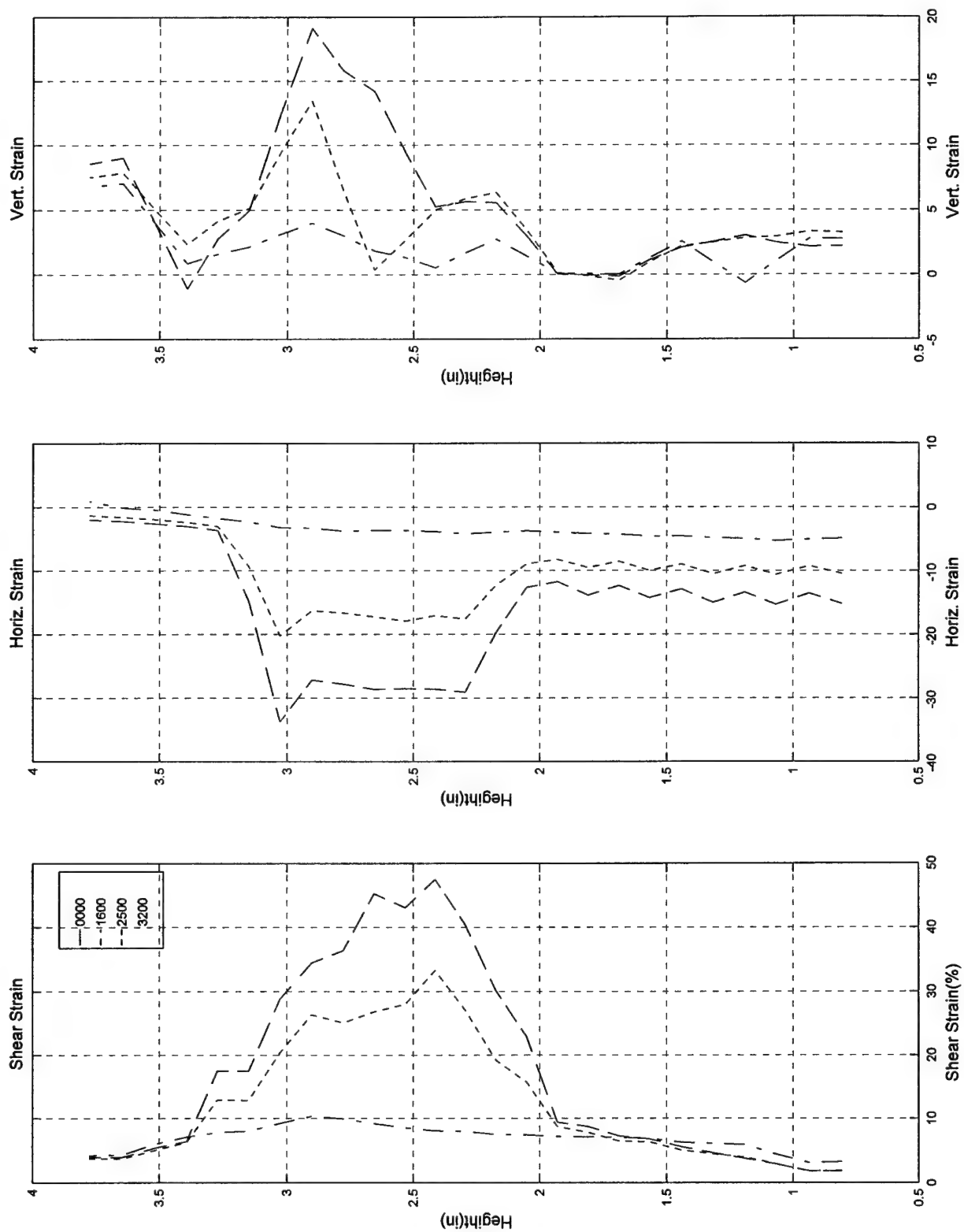
Test #77, Camera #B, Figure 5

Test #77; 3/18/97; Torsion-compression; ECP=50 psi; Loire, Video b



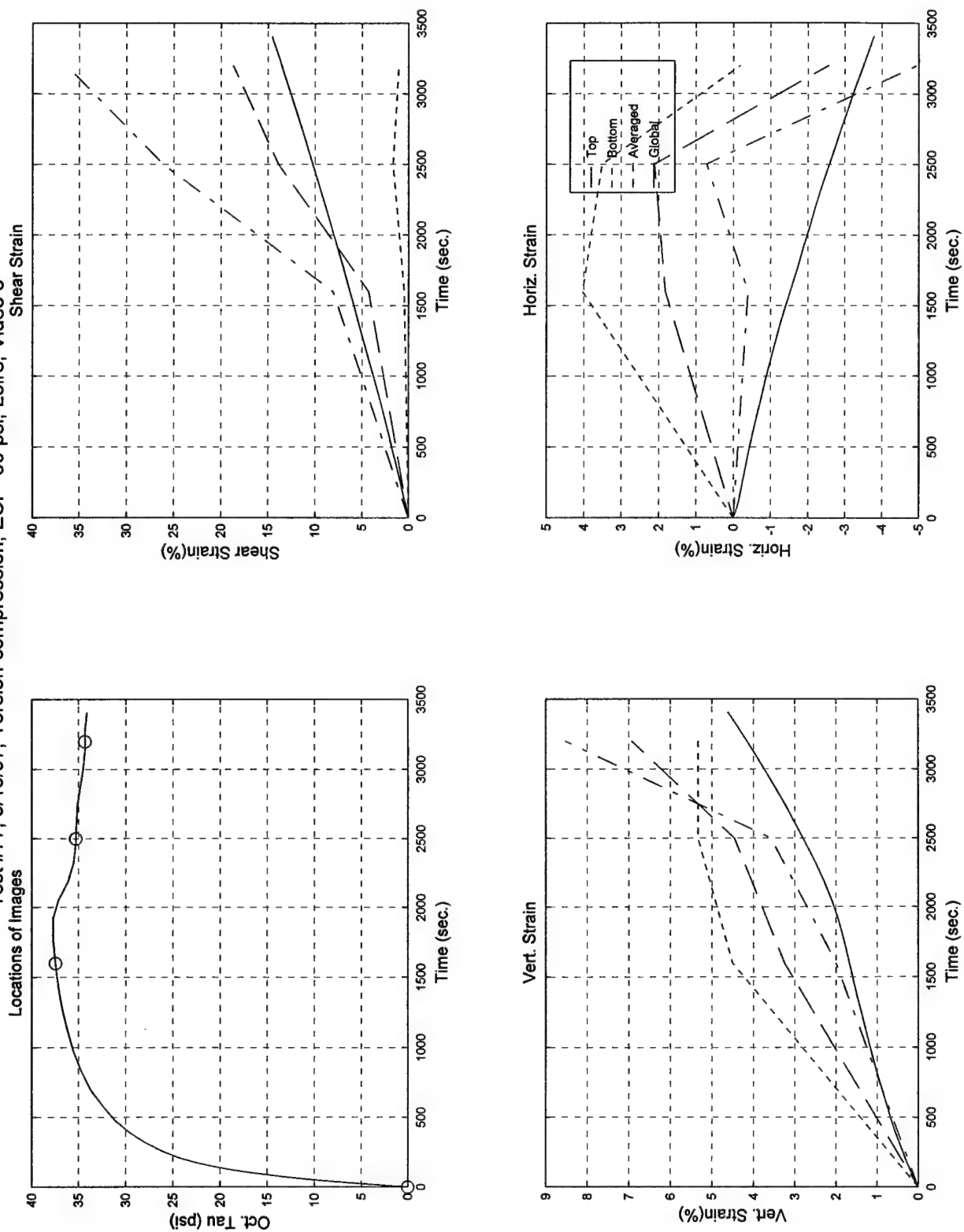
Test #77, Camera #B, Figure 6

Test #77; 3/18/97; Torsion-compression; ECP=50 psi; Loire, Video b



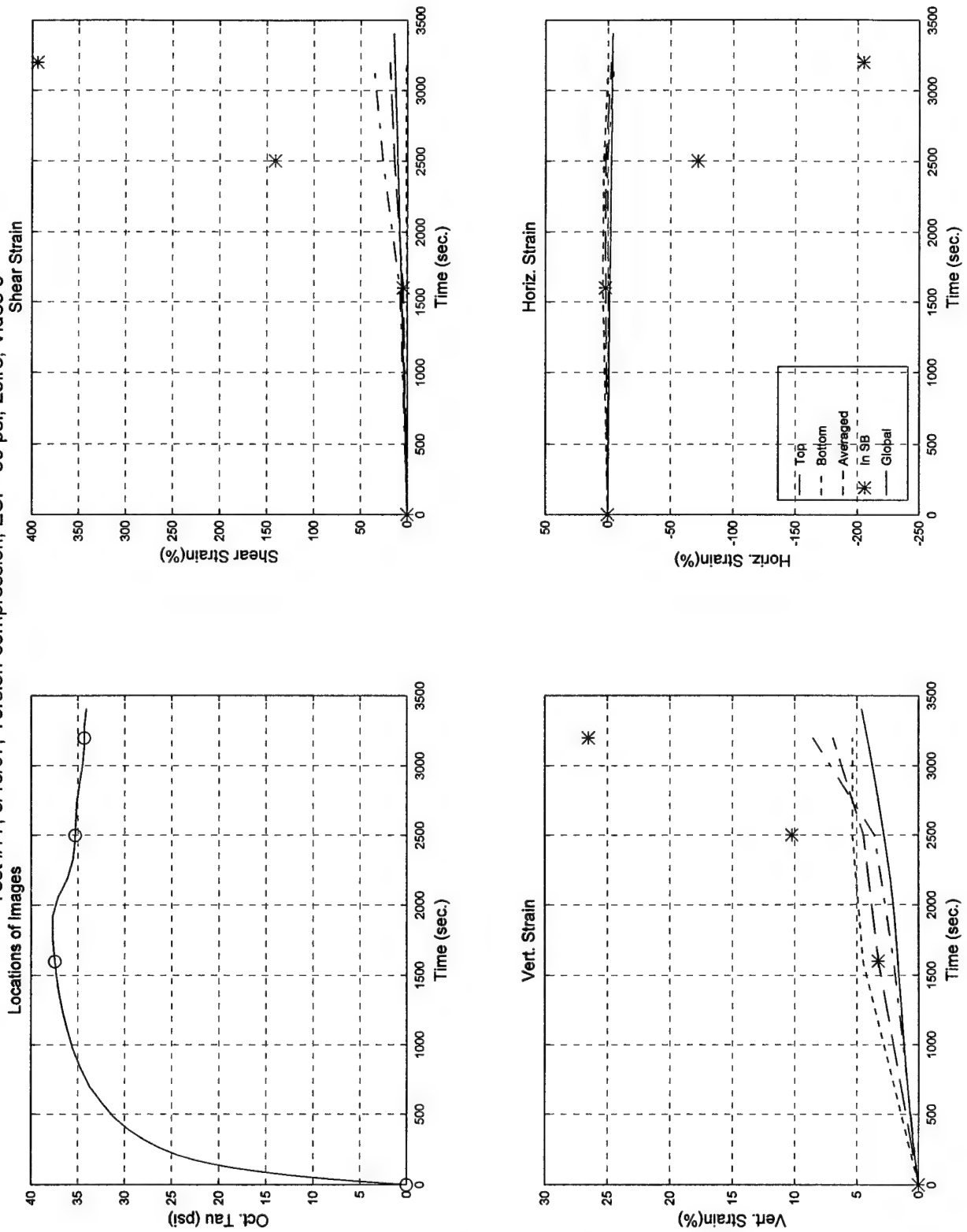
Test #77, Camera #B, Figure 7

Test #77; 3/18/97; Torsion-compression; ECP=50 psi; Loire, Video c

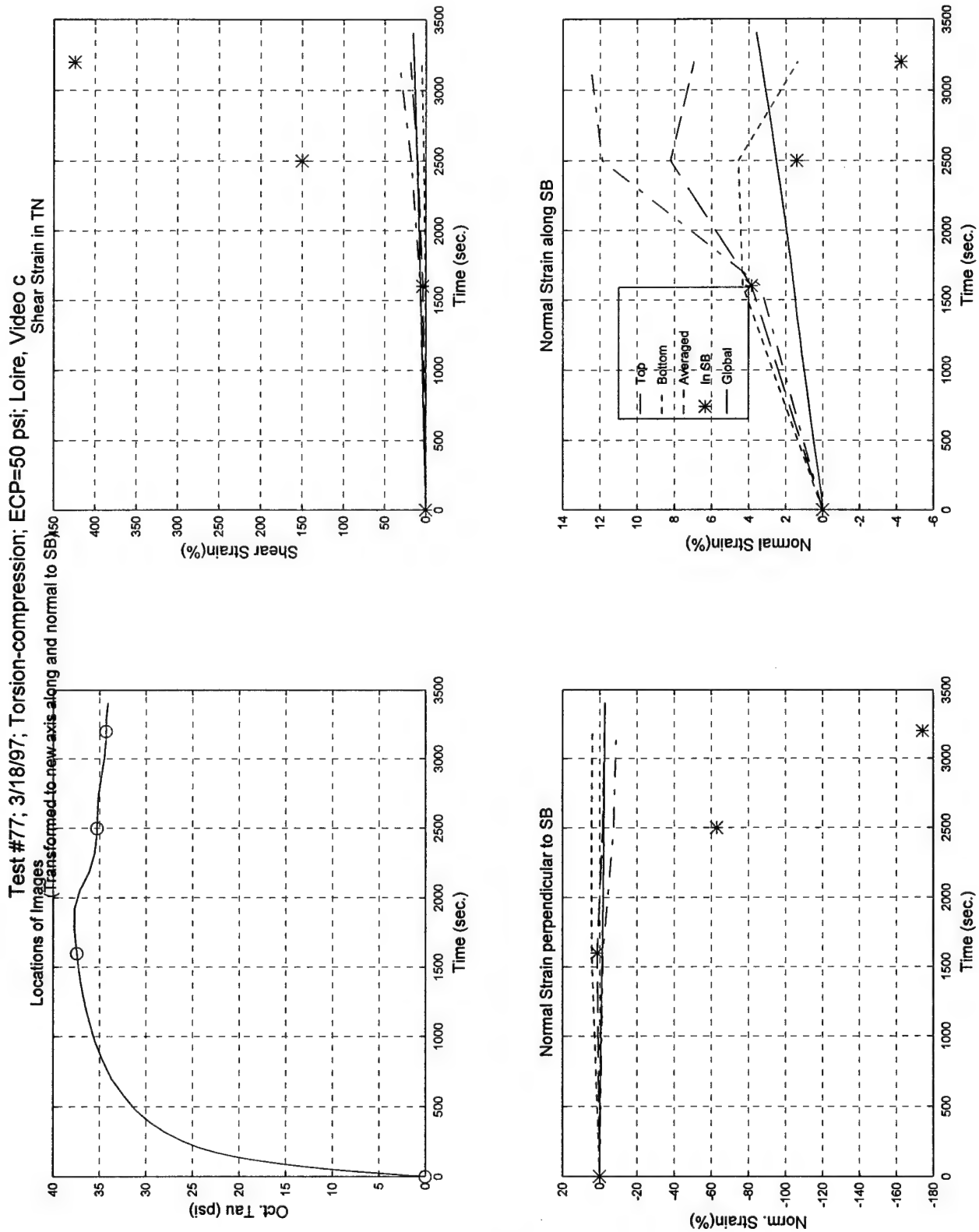


Test #77, Camera #C, Figure 1

Test #77; 3/18/97; Torsion-compression; ECP=50 psi; Loire, Video c

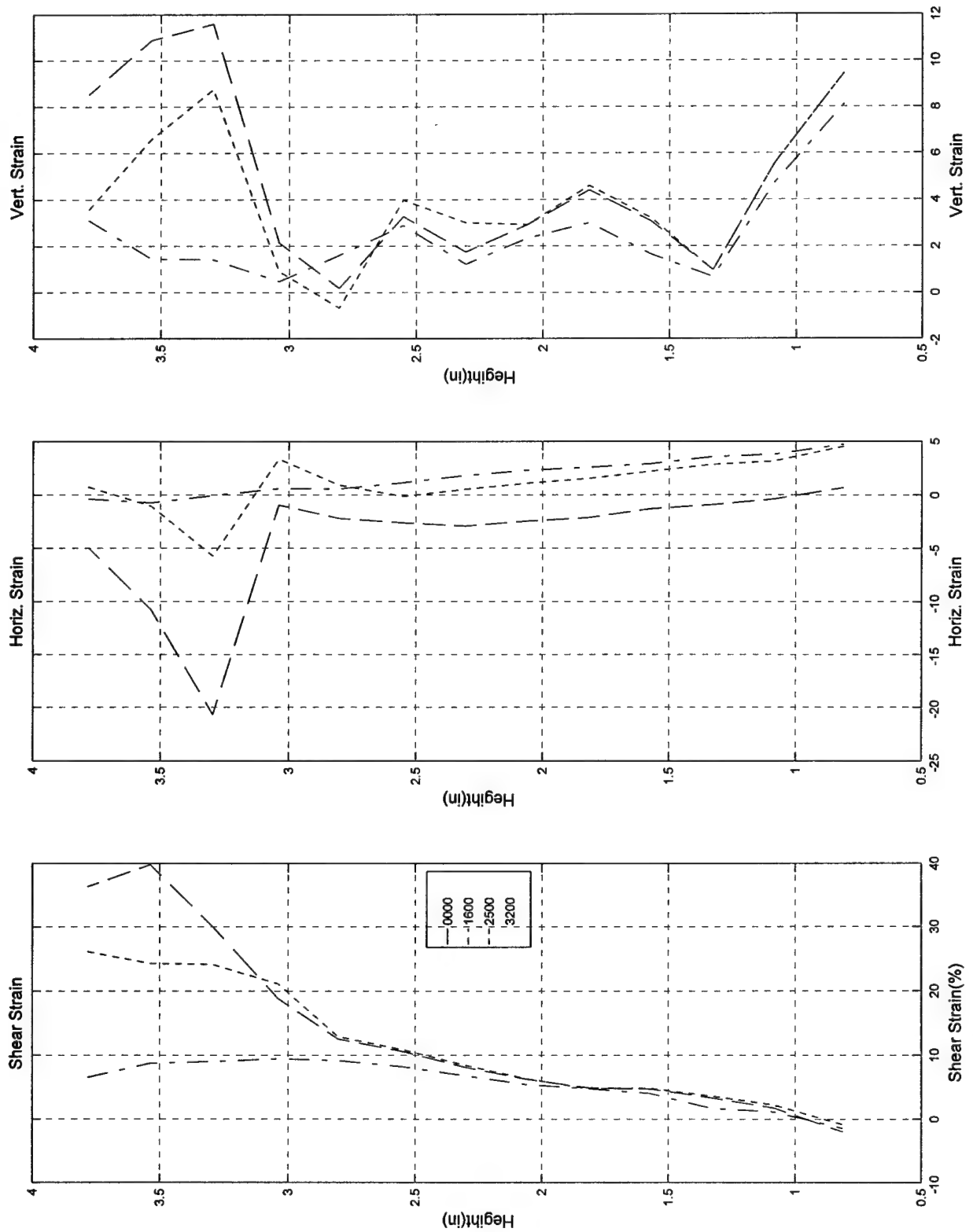


Test #77, Camera #C, Figure 2



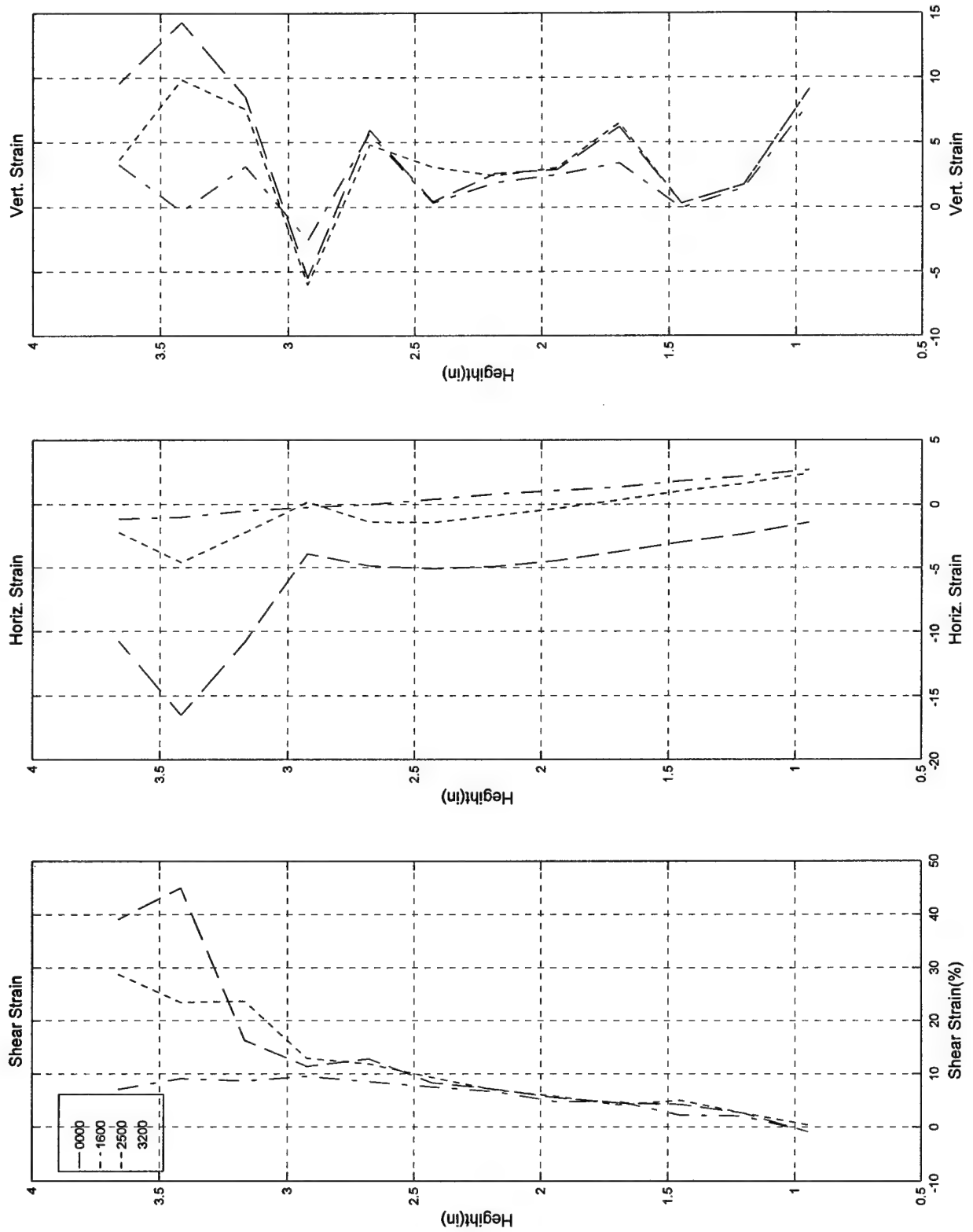
Test #77, Camera #C, Figure 3

Test #77; 3/18/97; Torsion-compression; ECP=50 psi; Loire, Video c



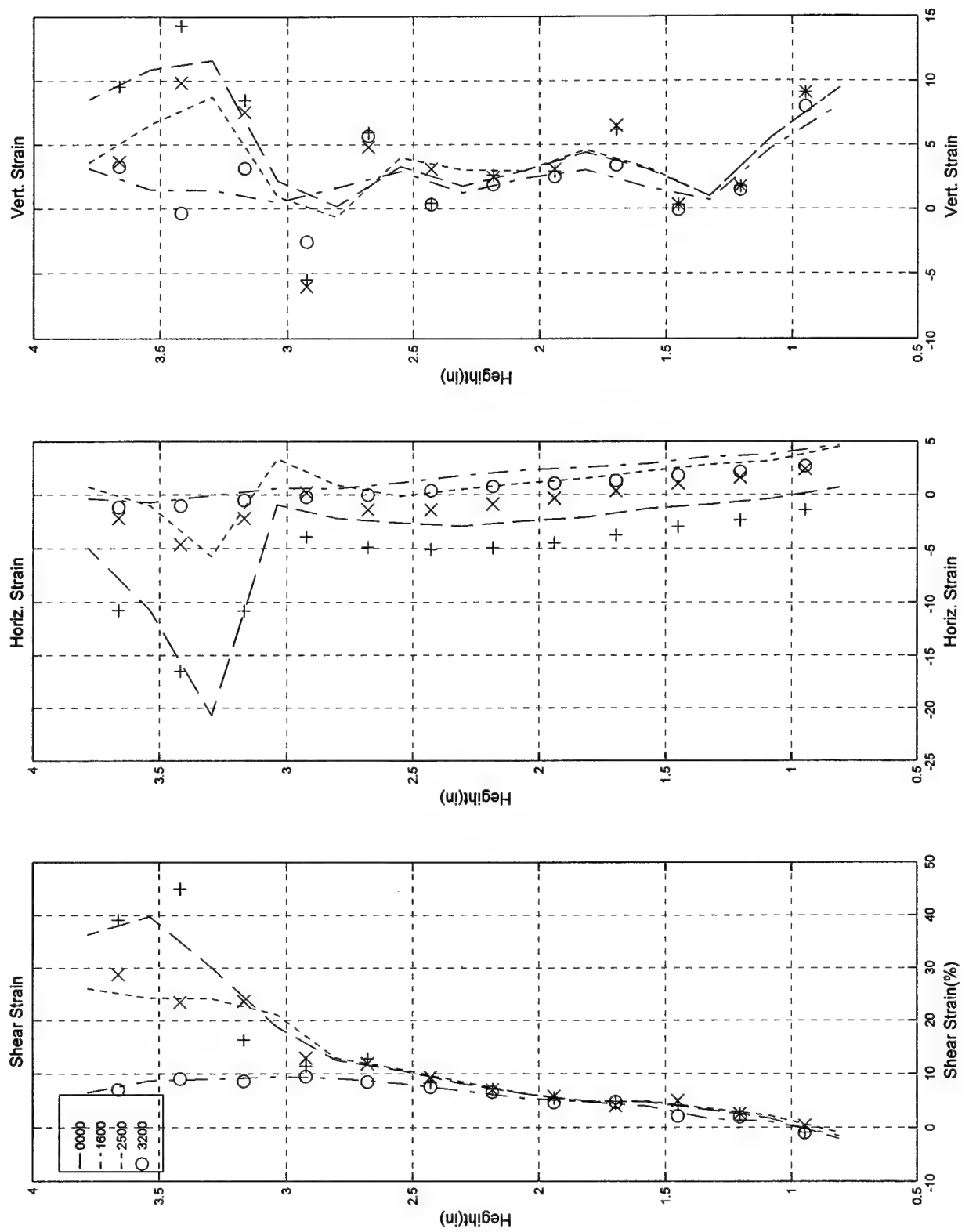
Test #77, Camera #C, Figure 4

Test #77; 3/18/97; Torsion-compression; ECP=50 psi; Loire, Video c



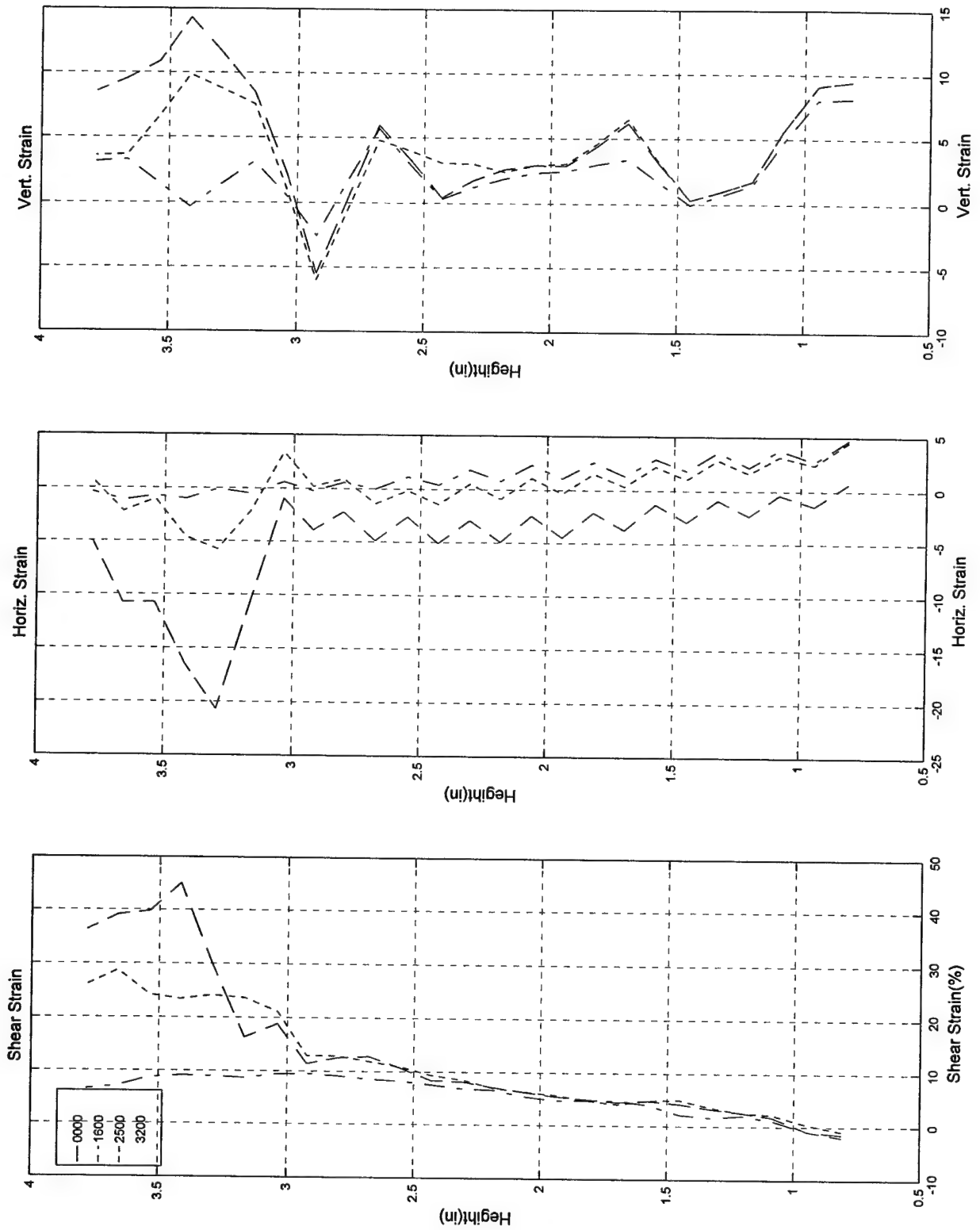
Test #77, Camera #C, Figure 5

Test #77; 3/18/97; Torsion-compression; ECP=50 psi; Loire, Video c



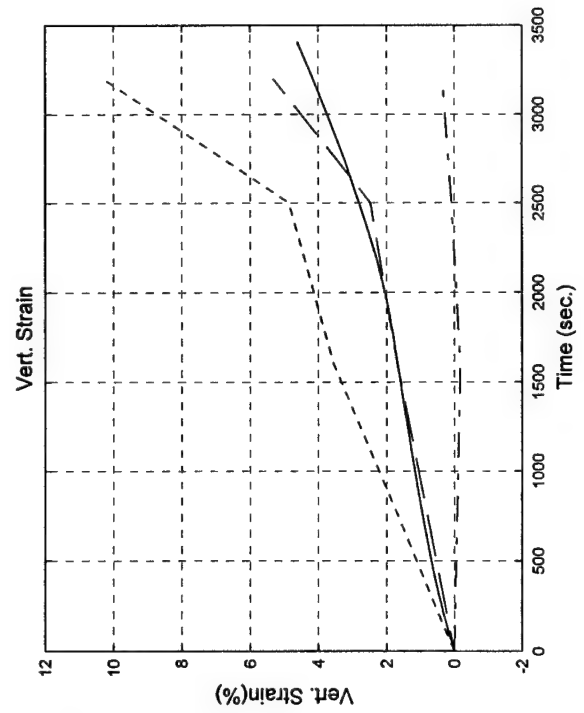
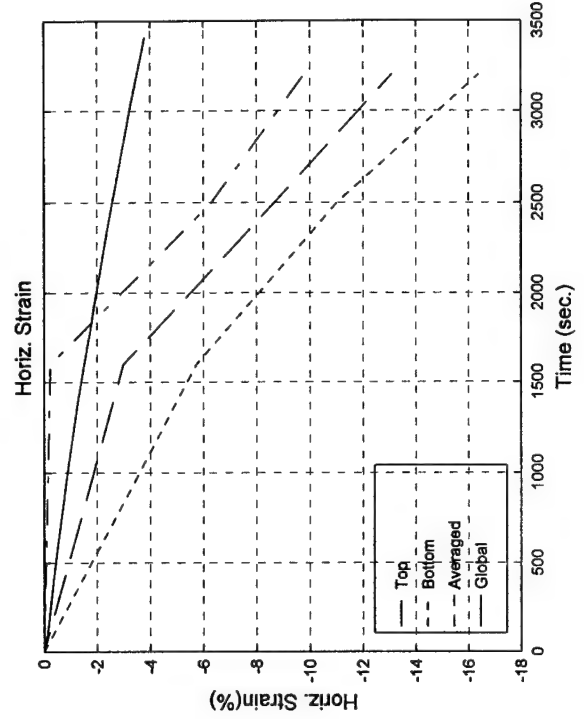
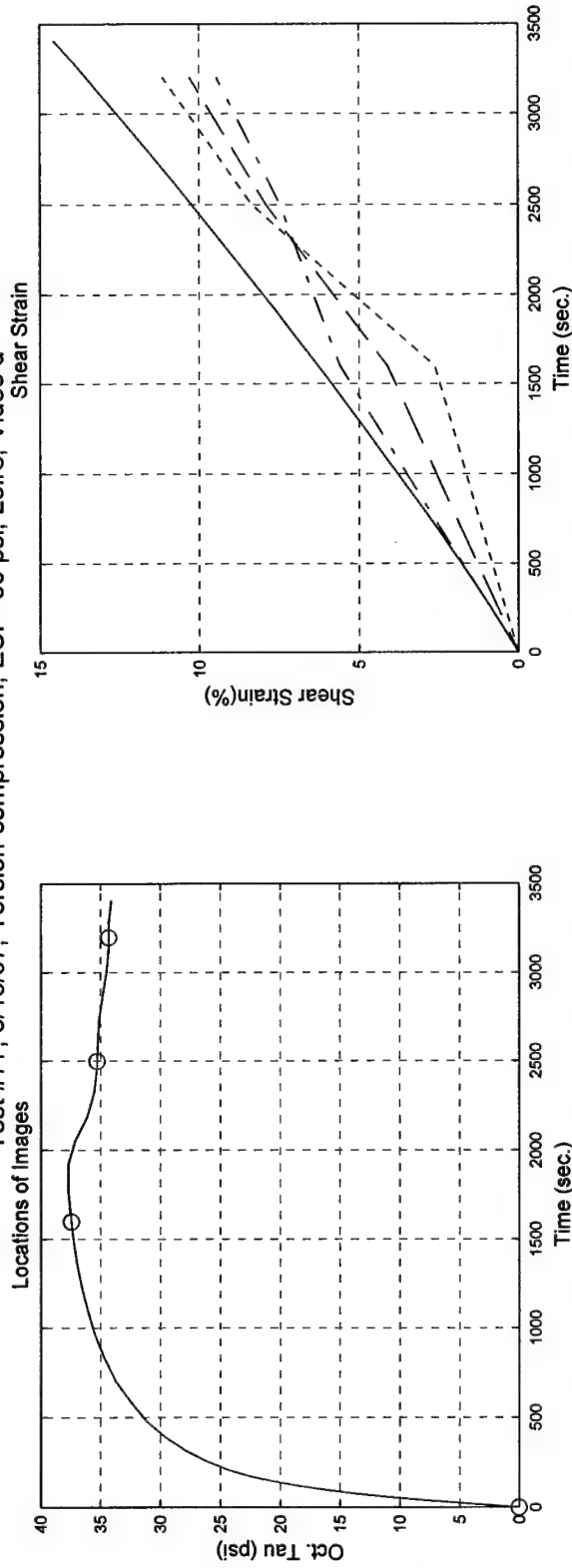
Test #77, Camera #C, Figure 6

Test #77; 3/18/97; Torsion-compression; ECP=50 psi; Loire, Video c



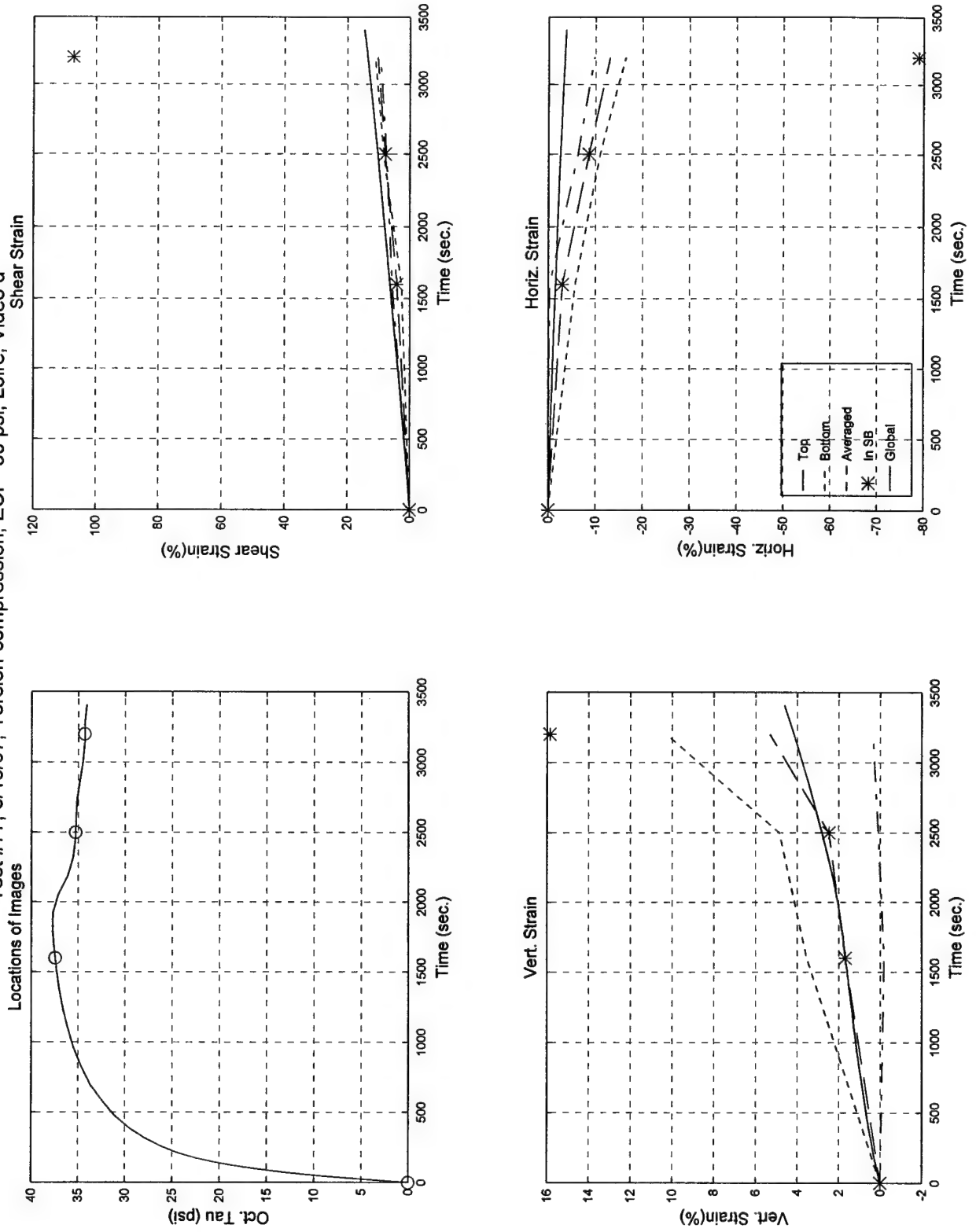
Test #77, Camera #C, Figure 7

Test #77; 3/18/97; Torsion-compression; ECP=50 psi; Loire, Video d

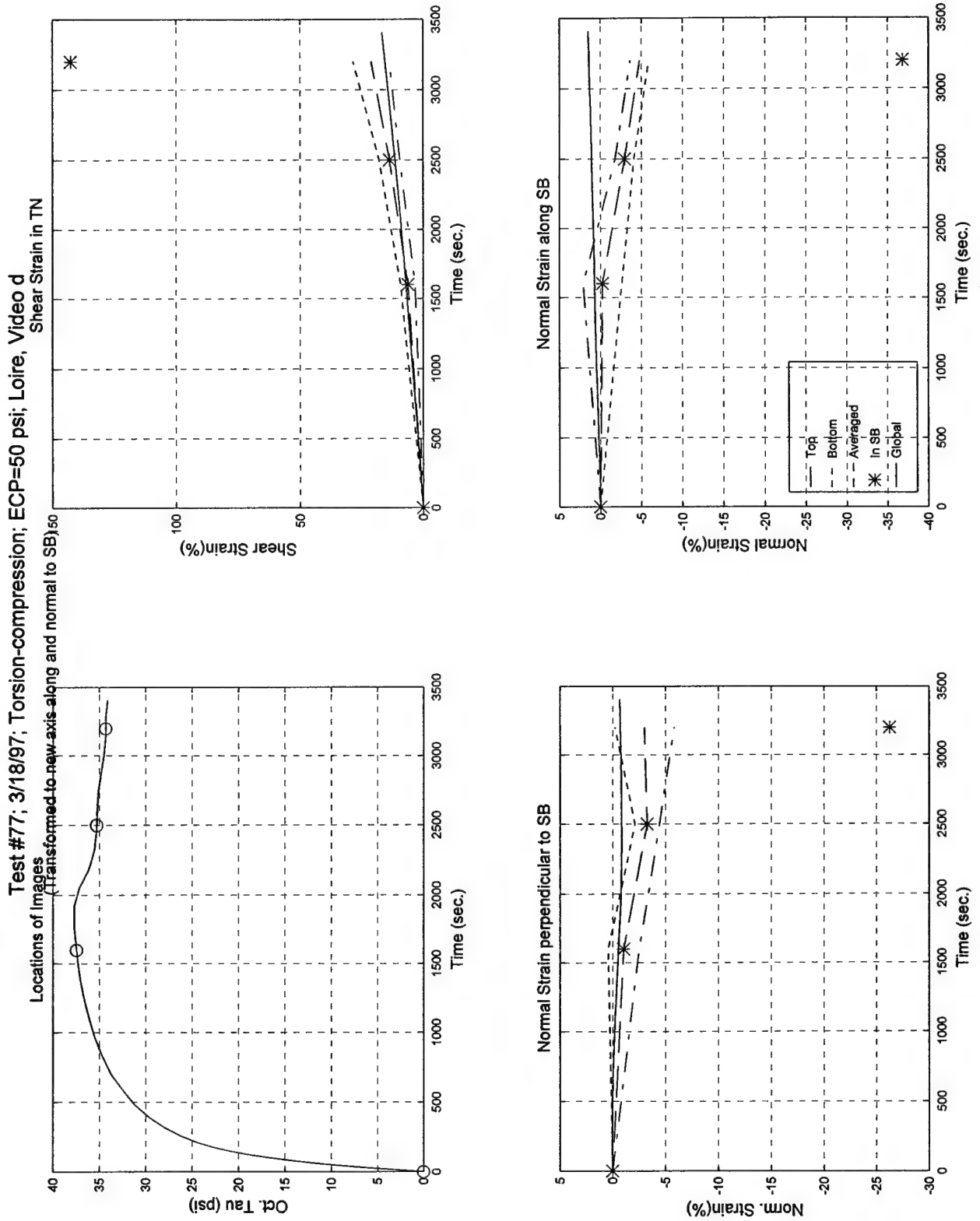


Test #77, Camera #D, Figure 1

Test #77; 3/18/97; Torsion-compression; ECP=50 psi; Loire, Video d

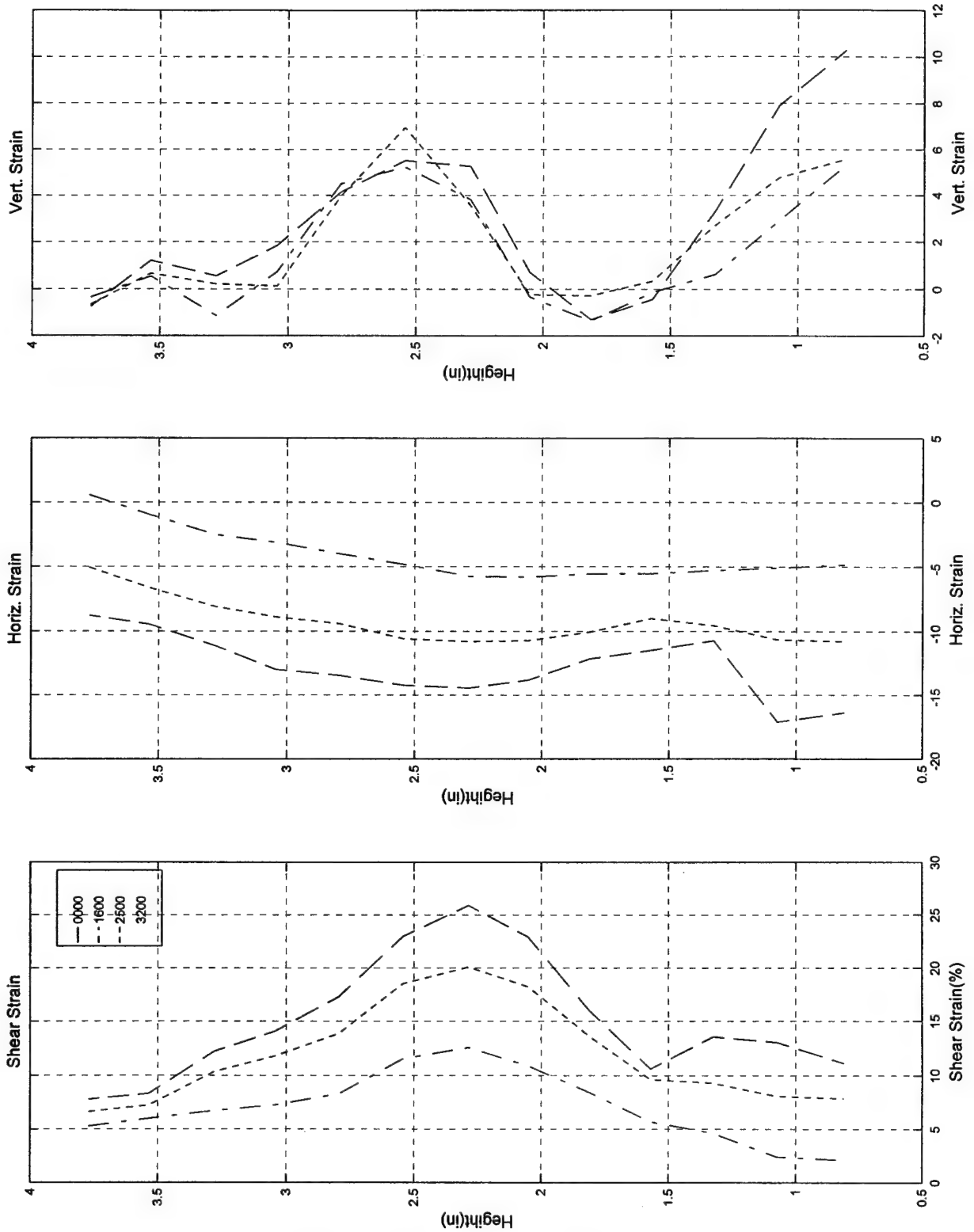


Test #77, Camera #D, Figure 2



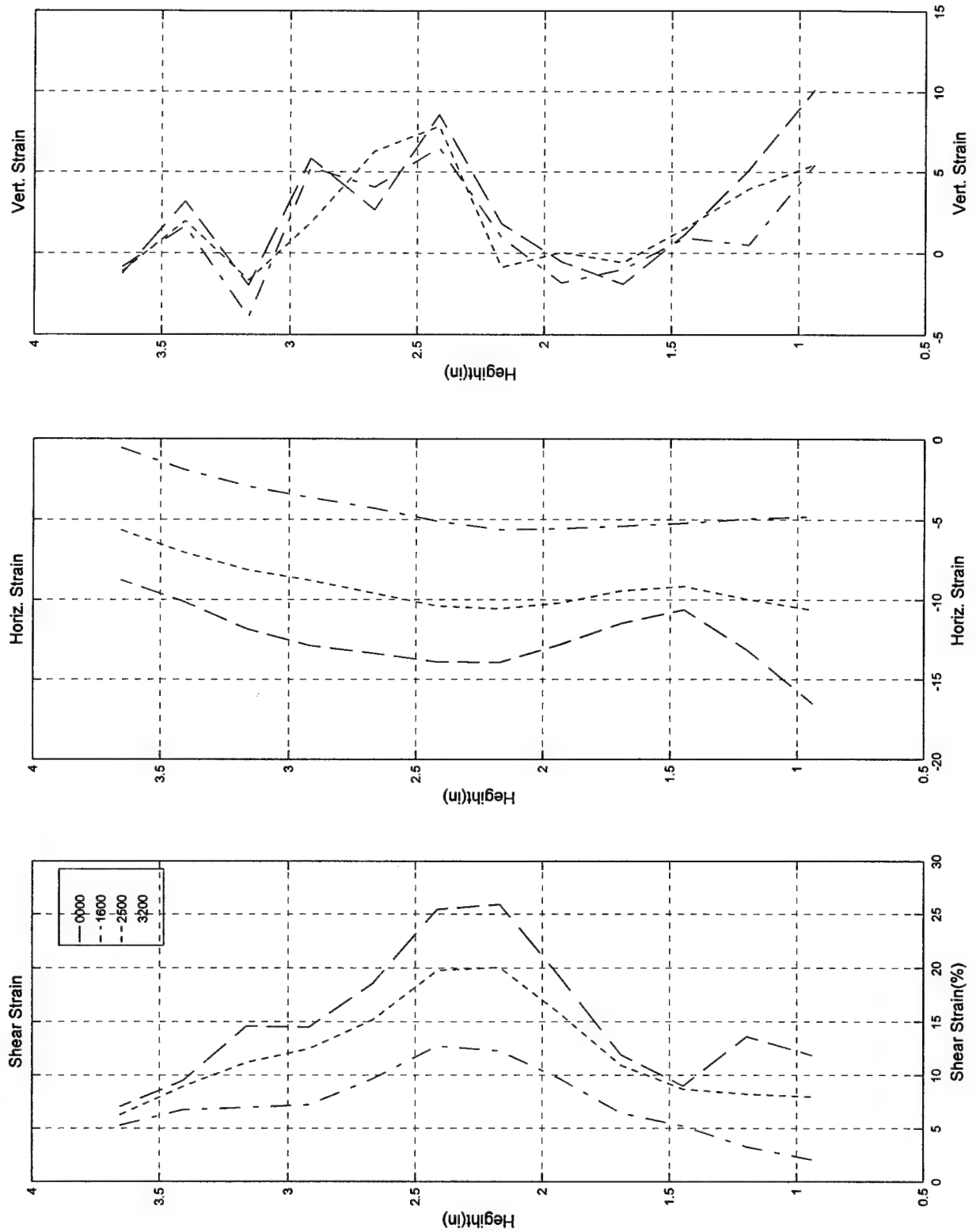
Test #77, Camera #D, Figure 3

Test #77; 3/18/97; Torsion-compression; ECP=50 psi; Loire, Video d



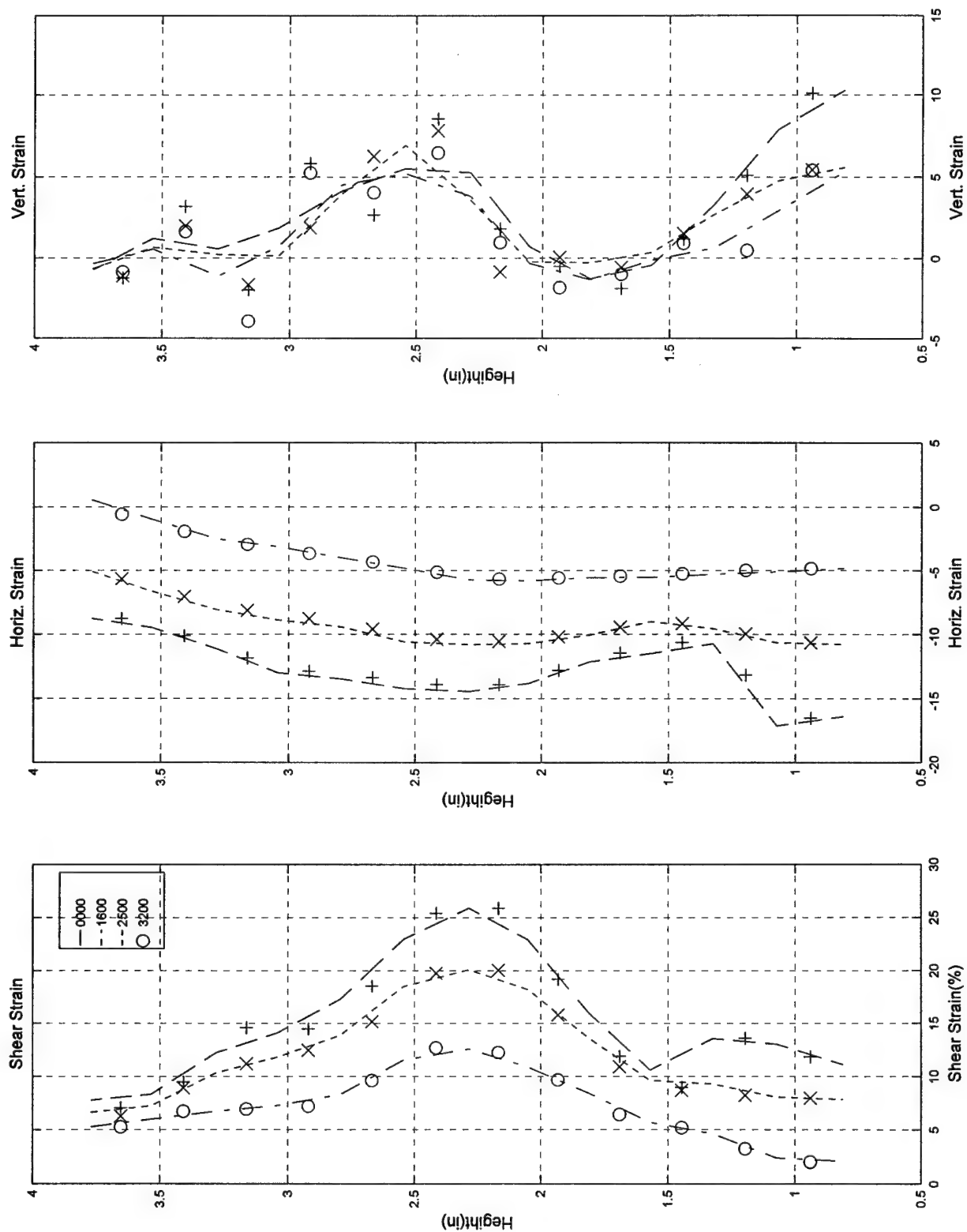
Test #77, Camera #D, Figure 4

Test #77; 3/18/97; Torsion-compression; ECP=50 psi; Loire, Video d



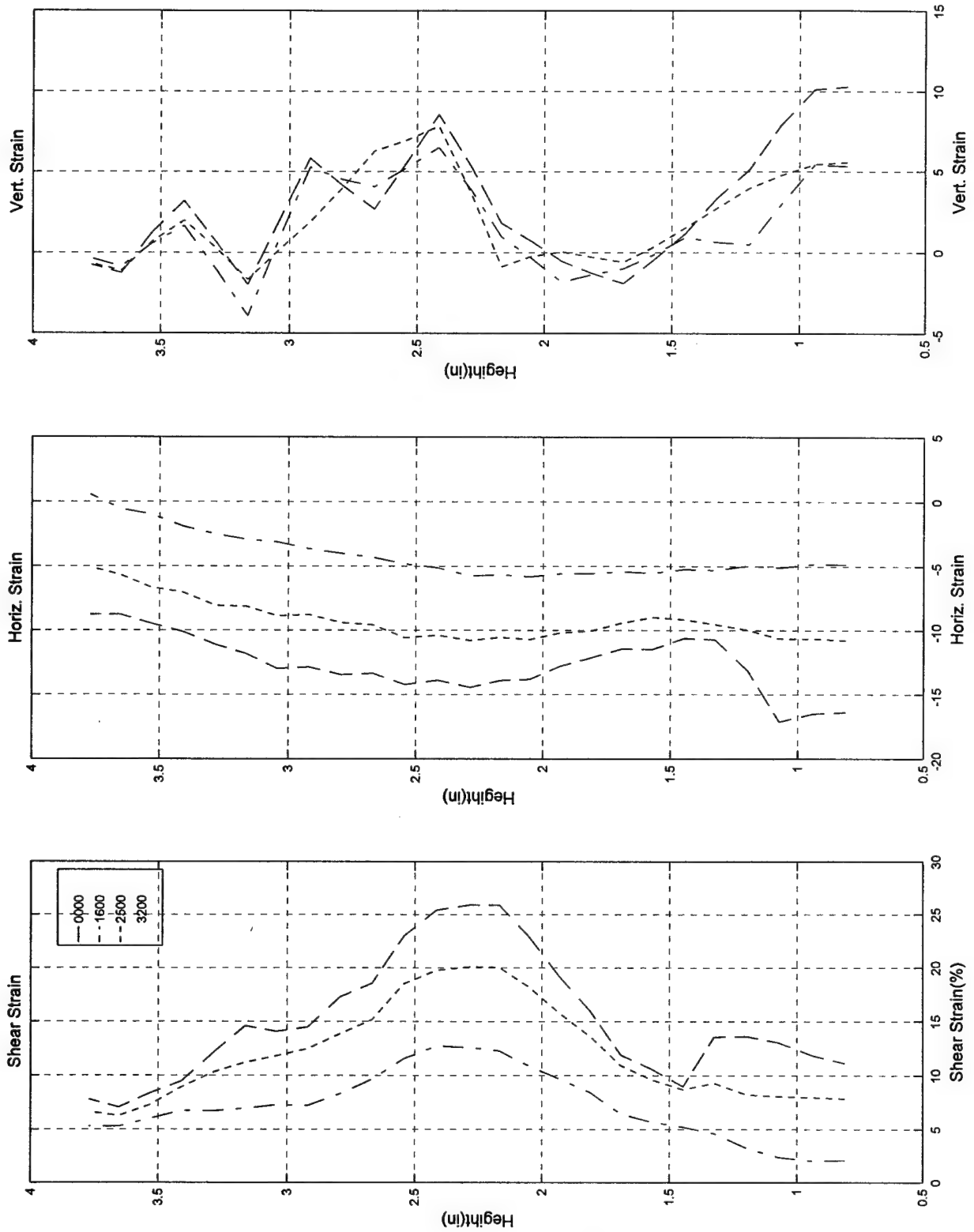
Test #77, Camera #D, Figure 5

Test #77; 3/18/97; Torsion-compression; ECP=50 psi; Loire, Video d



Test #77, Camera #D, Figure 6

Test #77, 3/18/97; Torsion-compression; ECP=50 psi; Loire, Video d

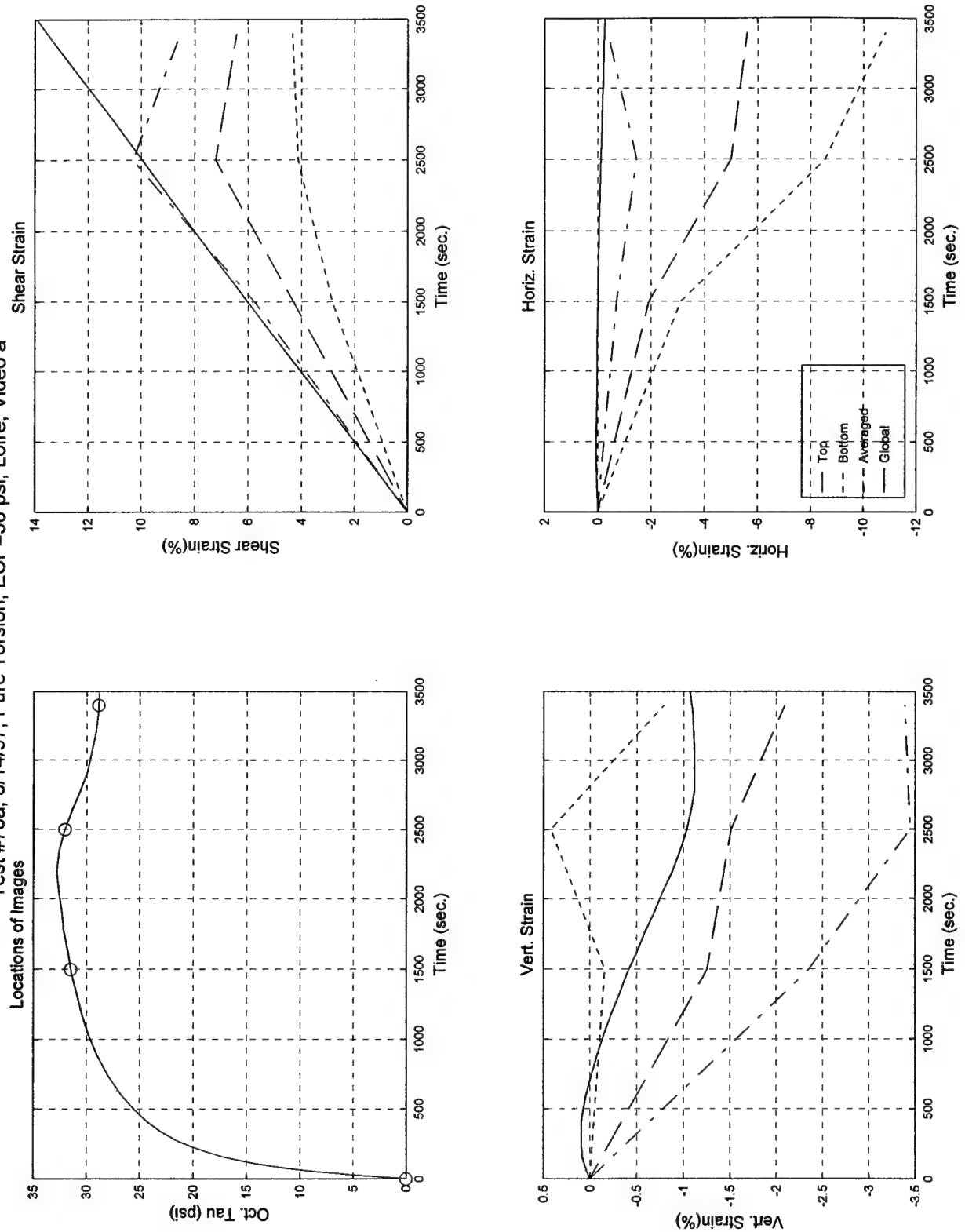


Test #77, Camera #D, Figure 7

B.3 Test #78a

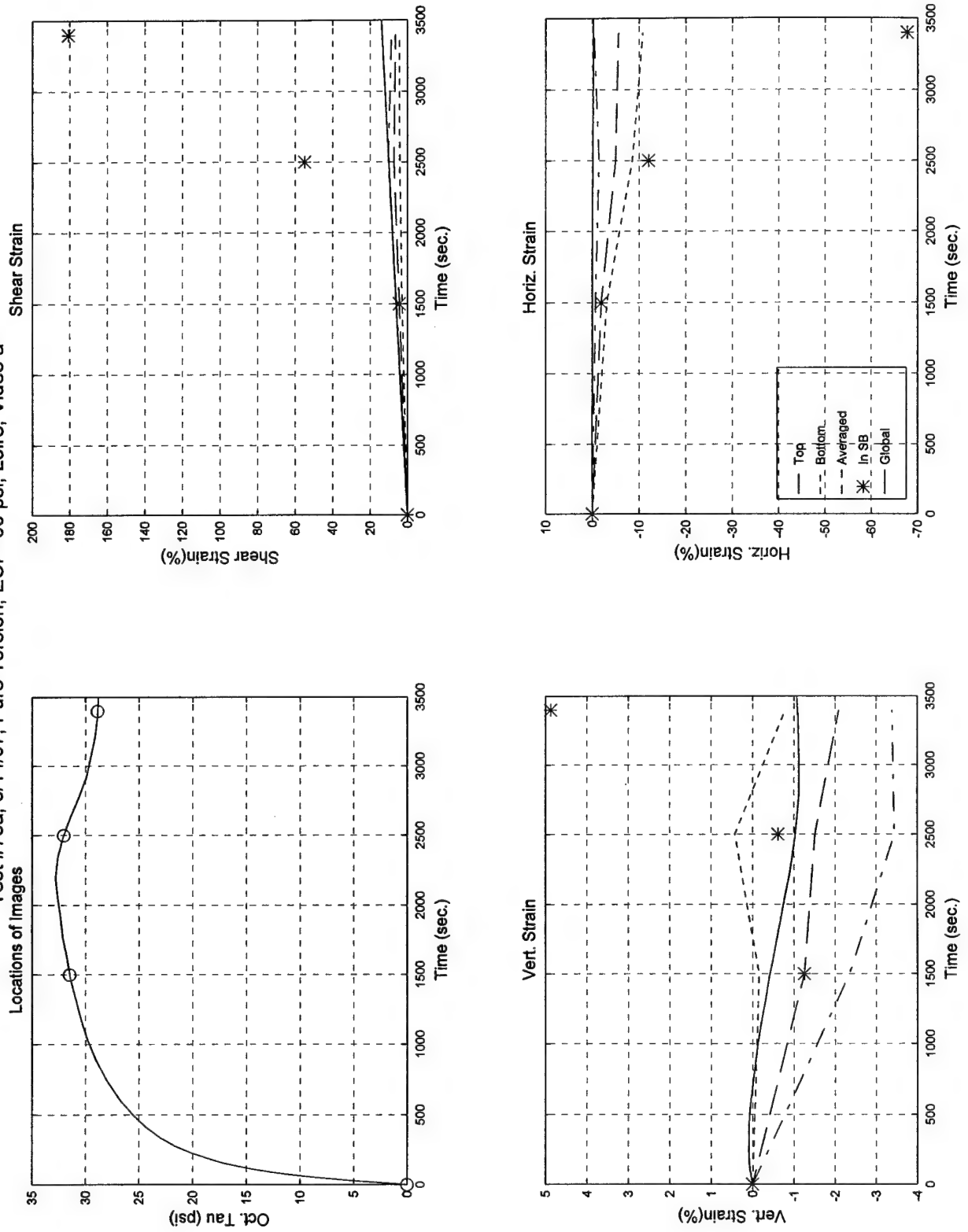
- **Pure Torsion ($\beta = 45^\circ$)**
- **Effective Confining Pressure = 50 psi (345 kPa)**
- **50% Initial Relative Density**
- **Generalized Test**
- **Digitized Times Intervals: 0000, 1500, 2500 & 3400 sec.**

Test #78a; 8/14/97; Pure Torsion; ECP=50 psi; Loire, Video a



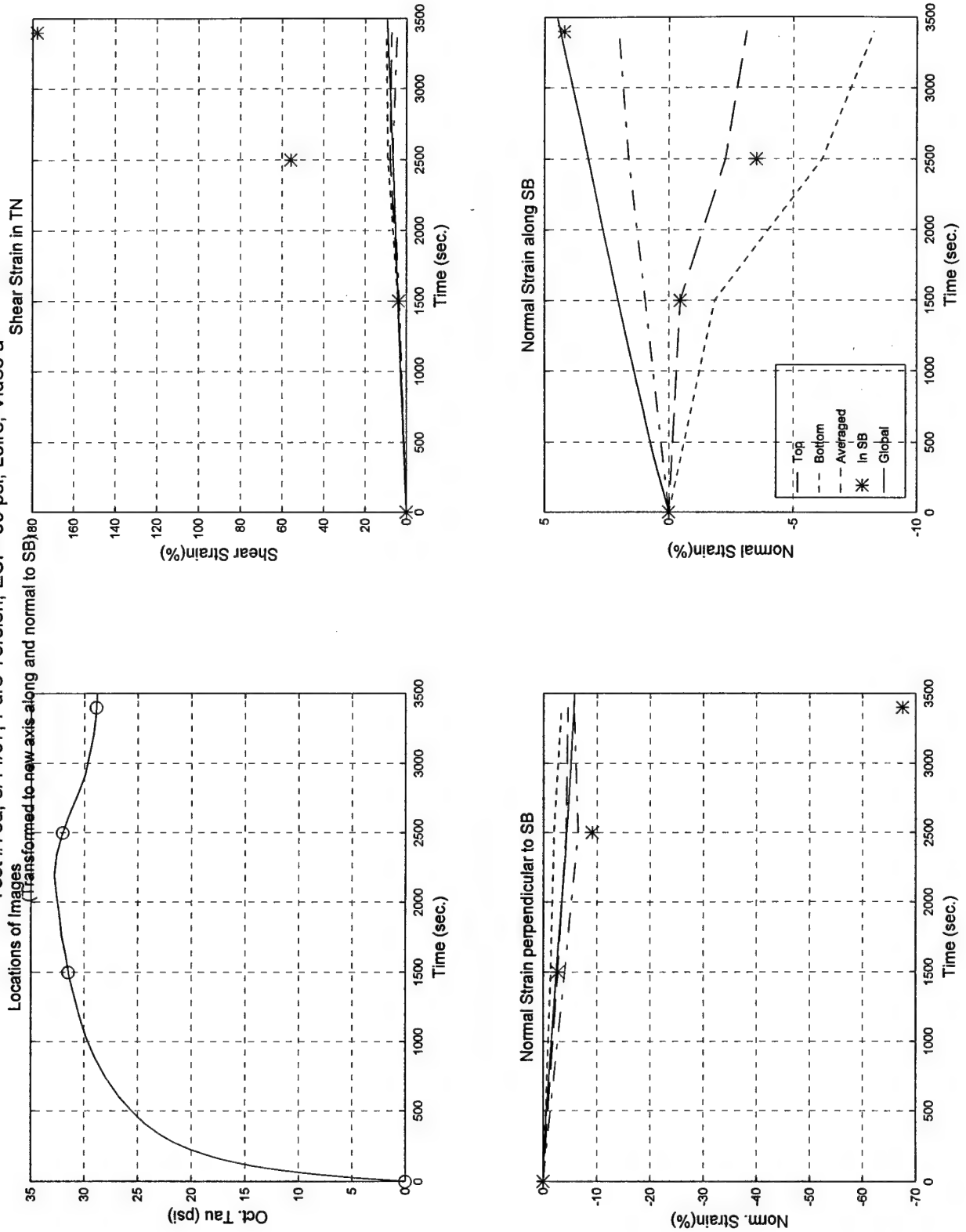
Test #78a, Camera #A, Figure 1

Test #78a; 8/14/97; Pure Torsion; ECP=50 psi; Loire, Video a



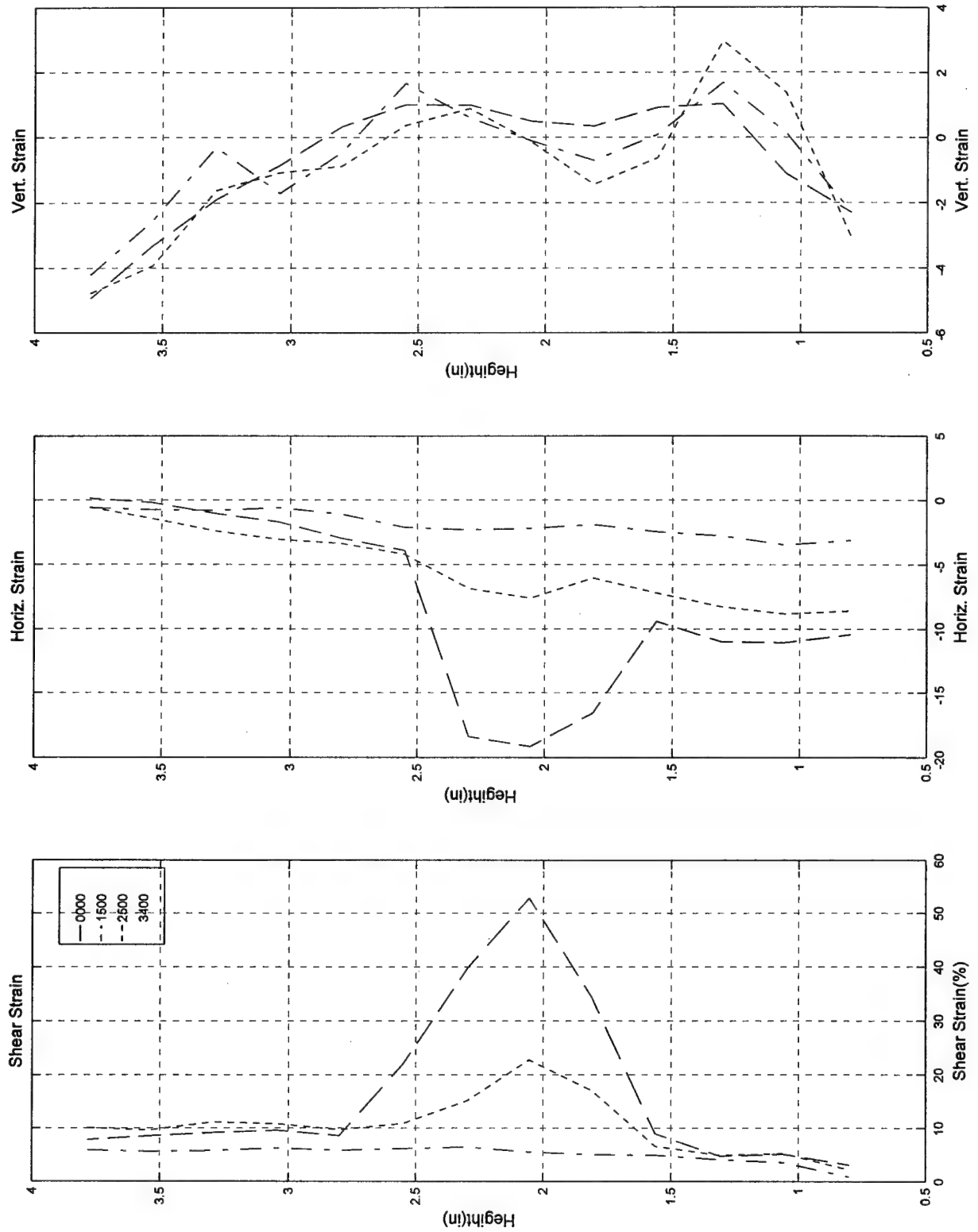
Test #78a, Camera #A, Figure 2

Test #78a; 8/14/97; Pure Torsion; ECP=50 psi; Loire, Video a



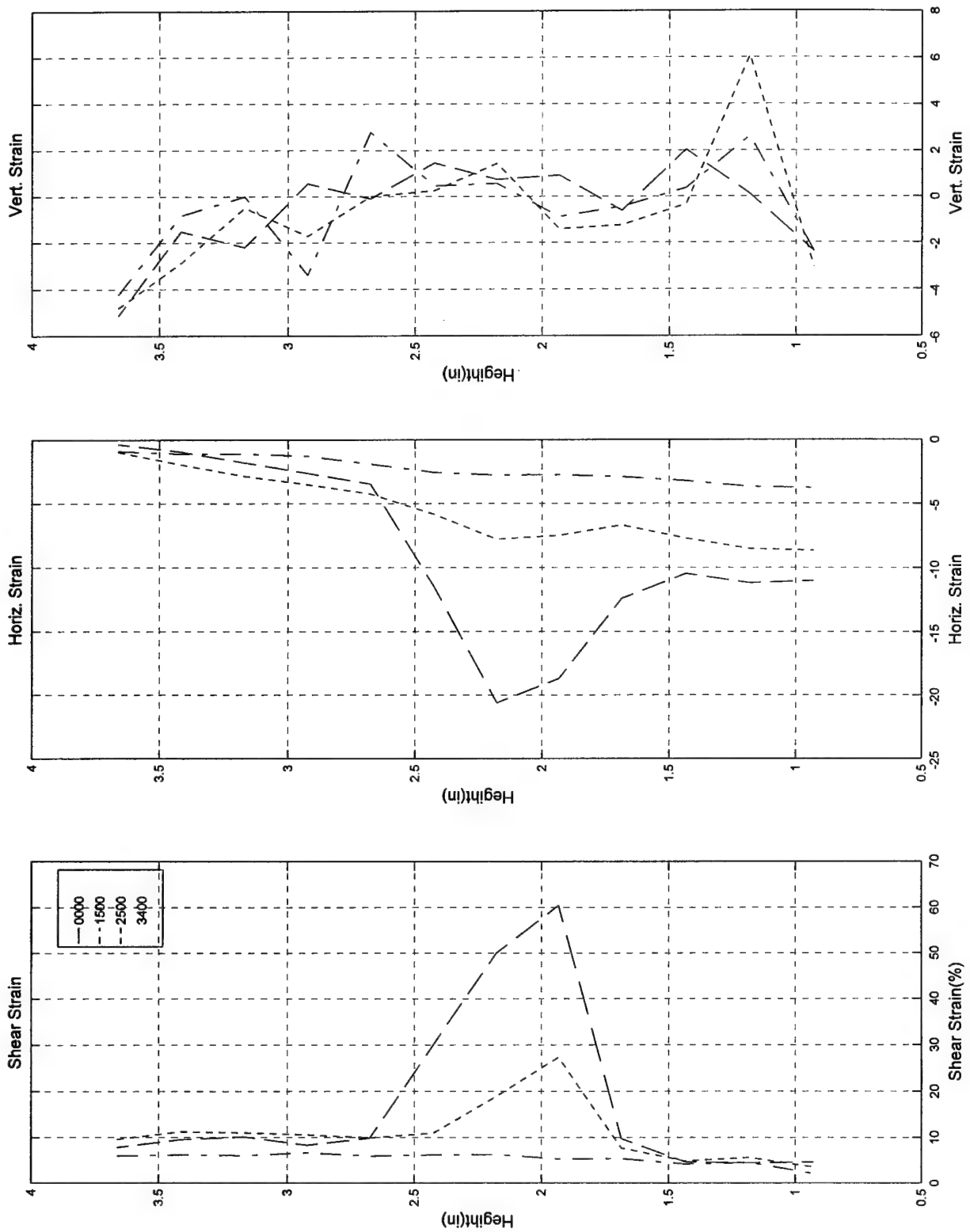
Test #78a, Camera #A, Figure 3

Test #78a; 8/14/97; Pure Torsion; ECP=50 psi; Loire, Video a



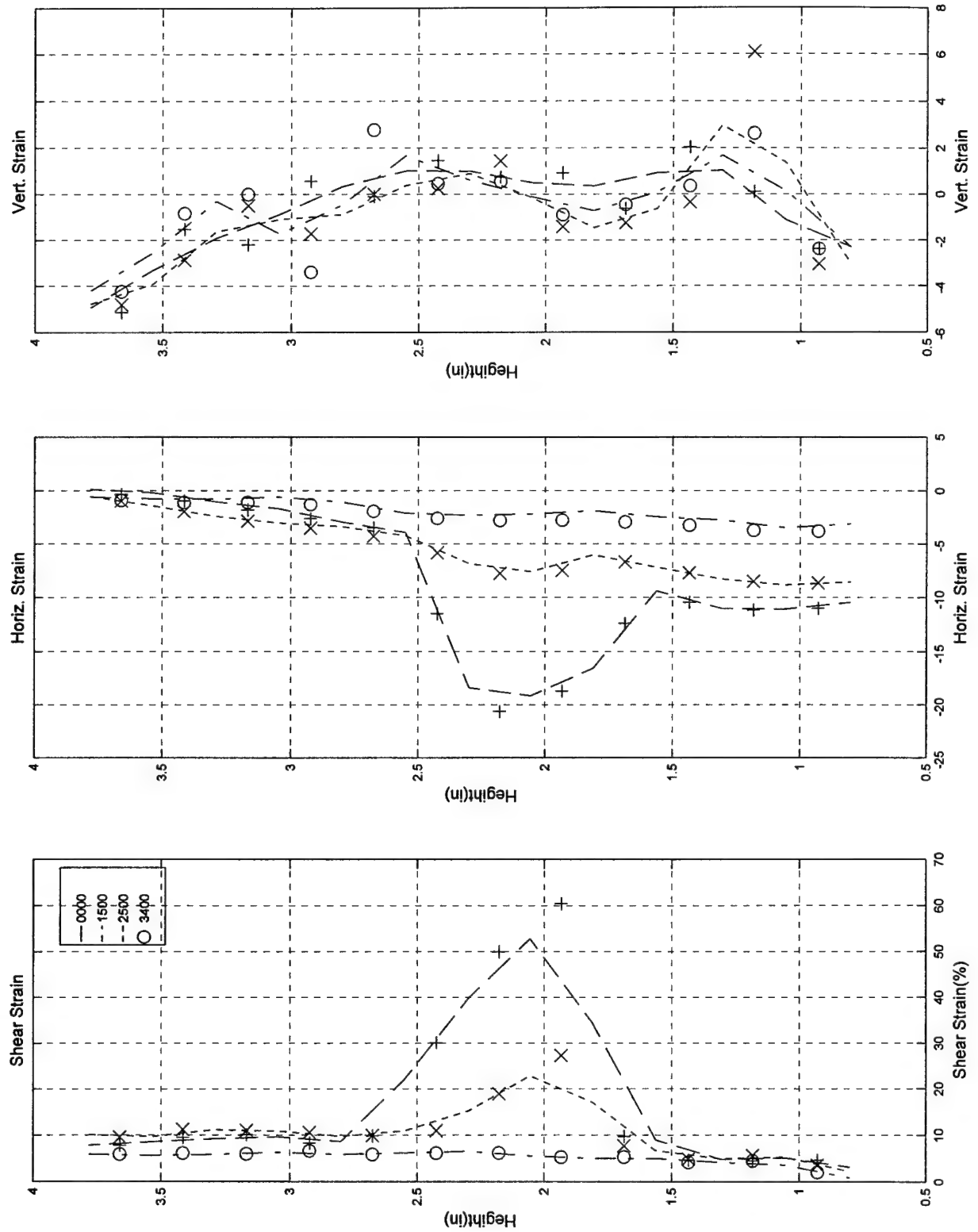
Test #78a, Camera #A, Figure 4

Test #78a; 8/14/97; Pure Torsion; ECP=50 psi; Loire, Video a



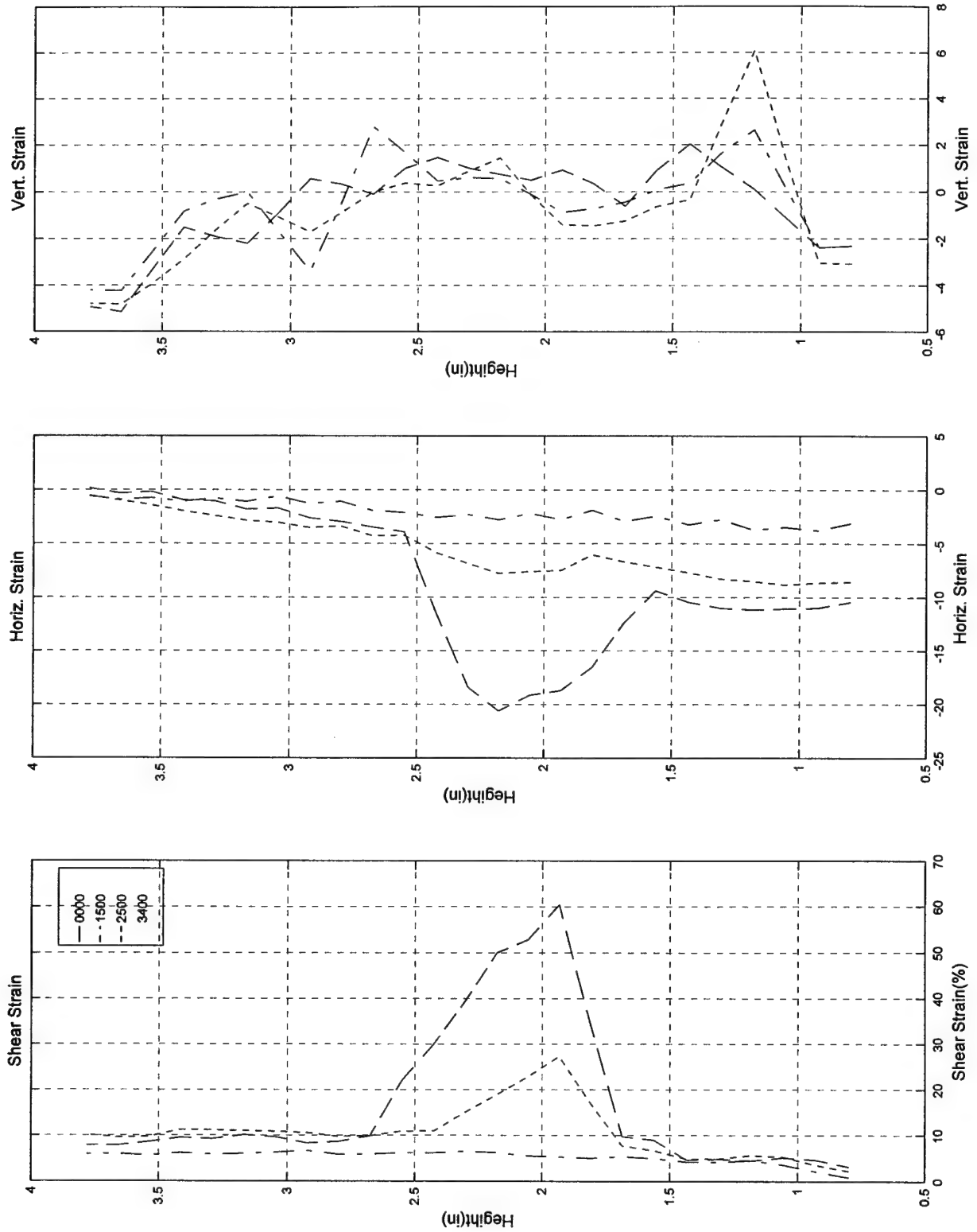
Test #78a, Camera #A, Figure 5

Test #78a; 8/14/97; Pure Torsion; ECP=50 psi; Loire, Video a



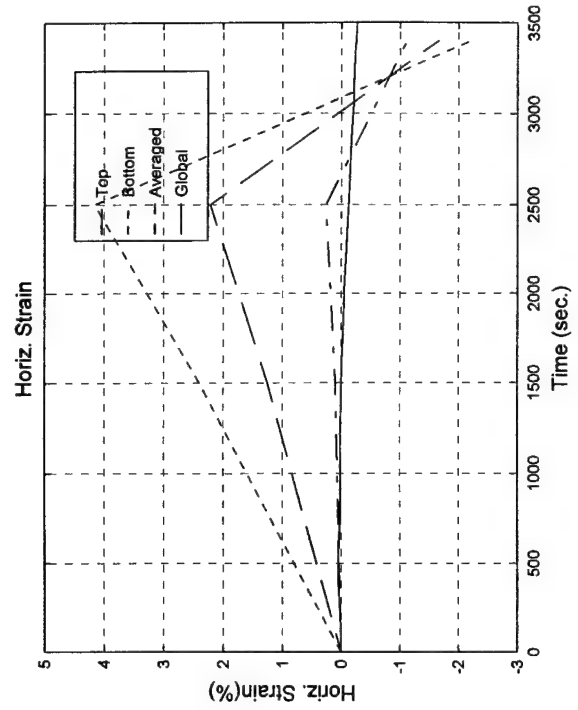
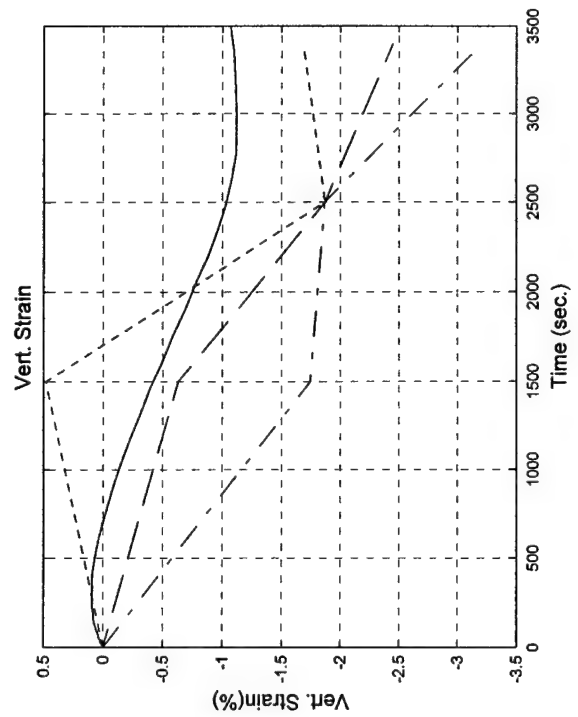
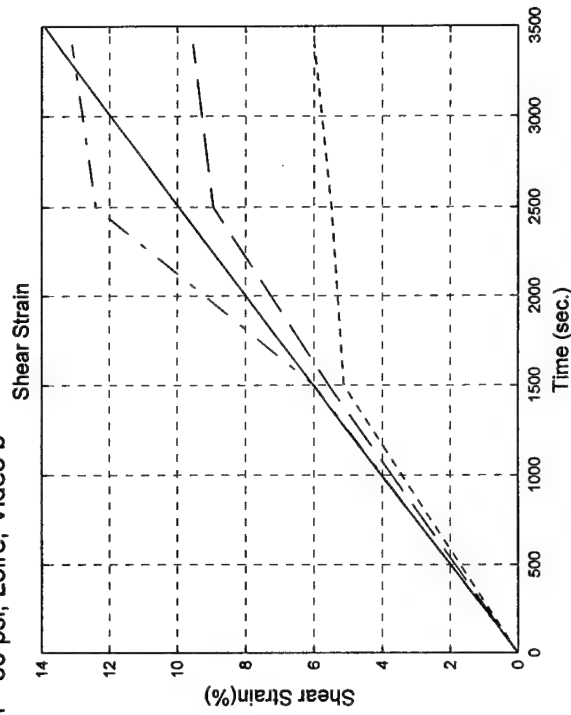
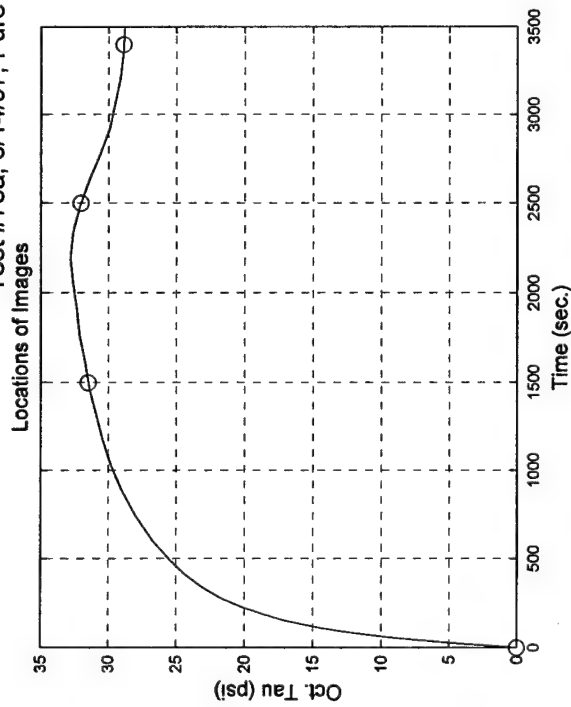
Test #78a, Camera #A, Figure 6

Test #78a; 8/14/97; Pure Torsion; ECP=50 psi; Loire, Video a



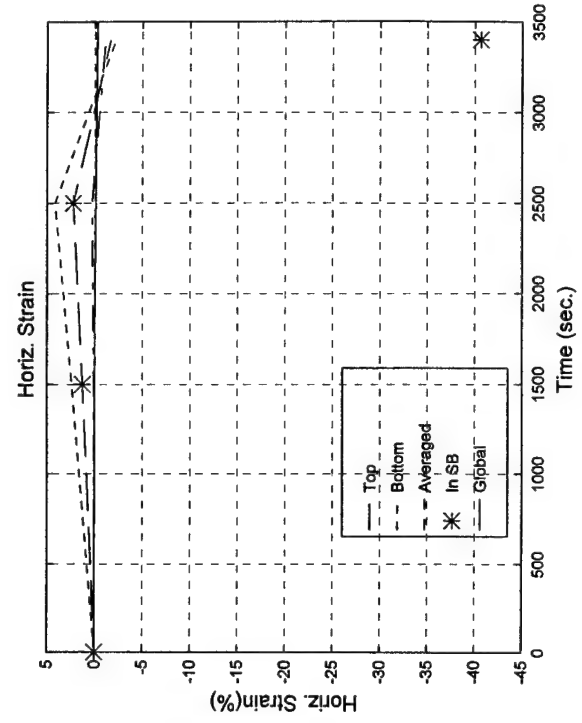
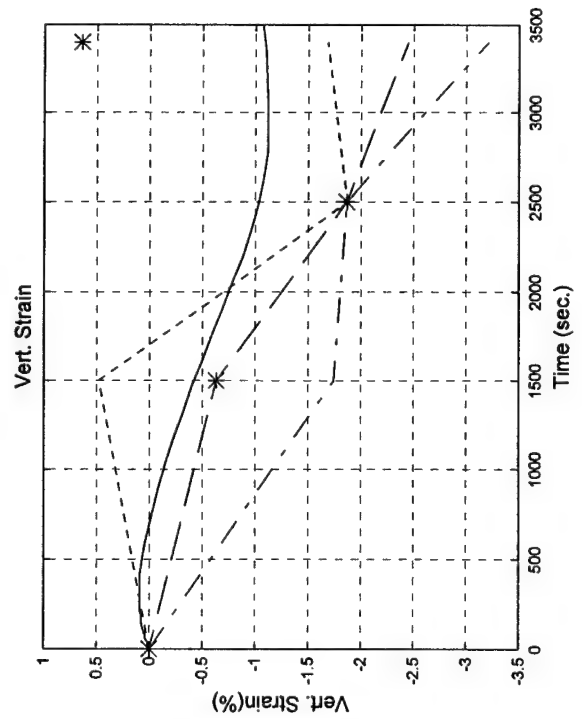
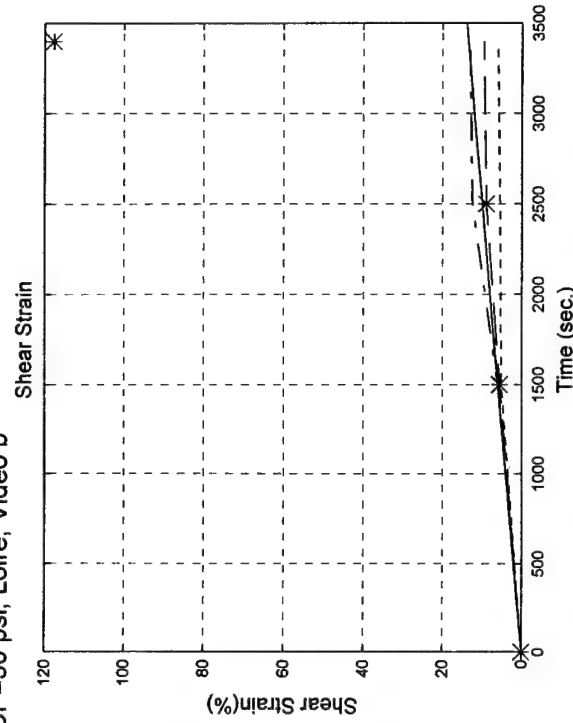
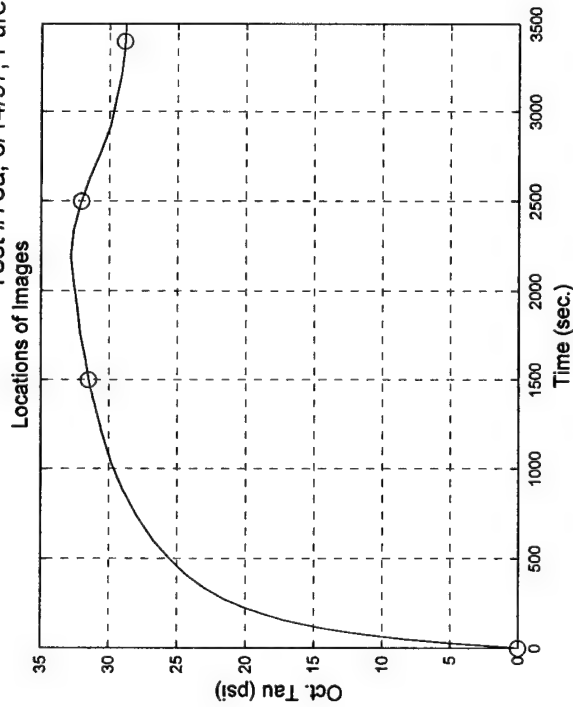
Test #78a, Camera #A, Figure 7

Test #78a; 8/14/97; Pure Torsion; ECP=50 psi; Loire, Video b



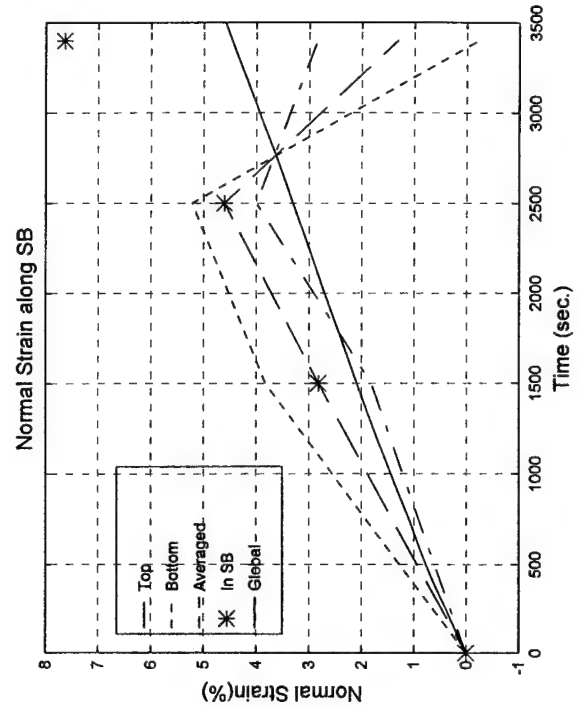
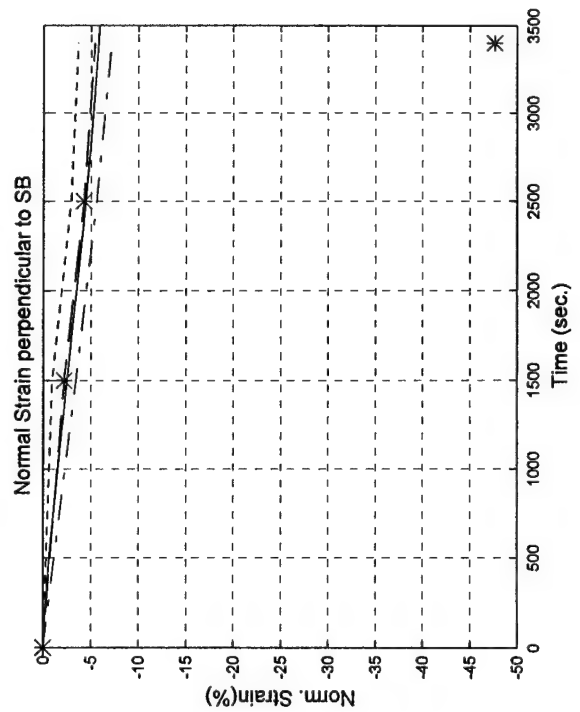
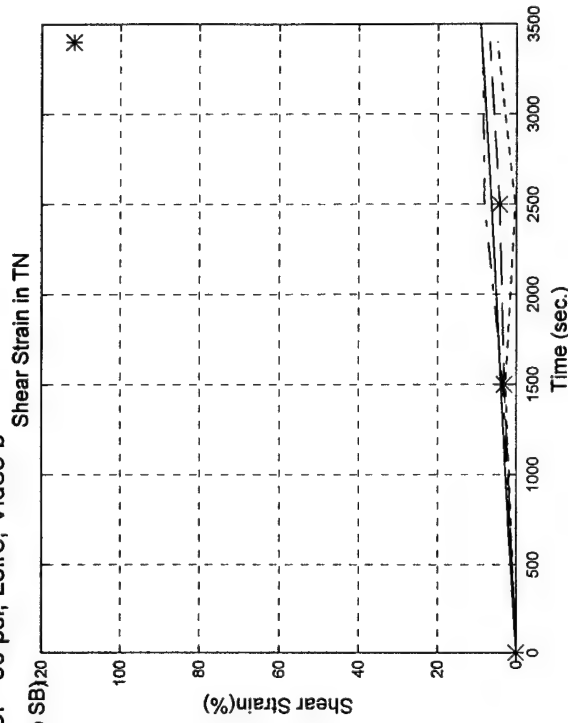
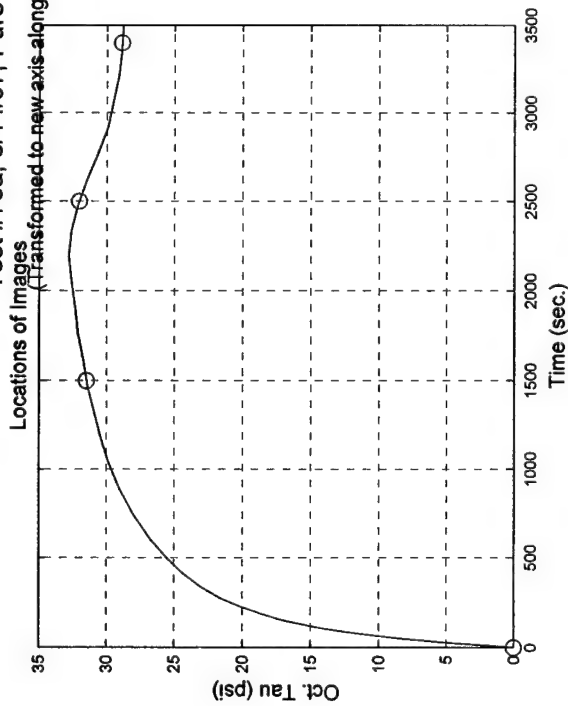
Test #78a, Camera #B, Figure 1

Test #78a; 8/14/97; Pure Torsion; ECP=50 psi; Loire, Video b



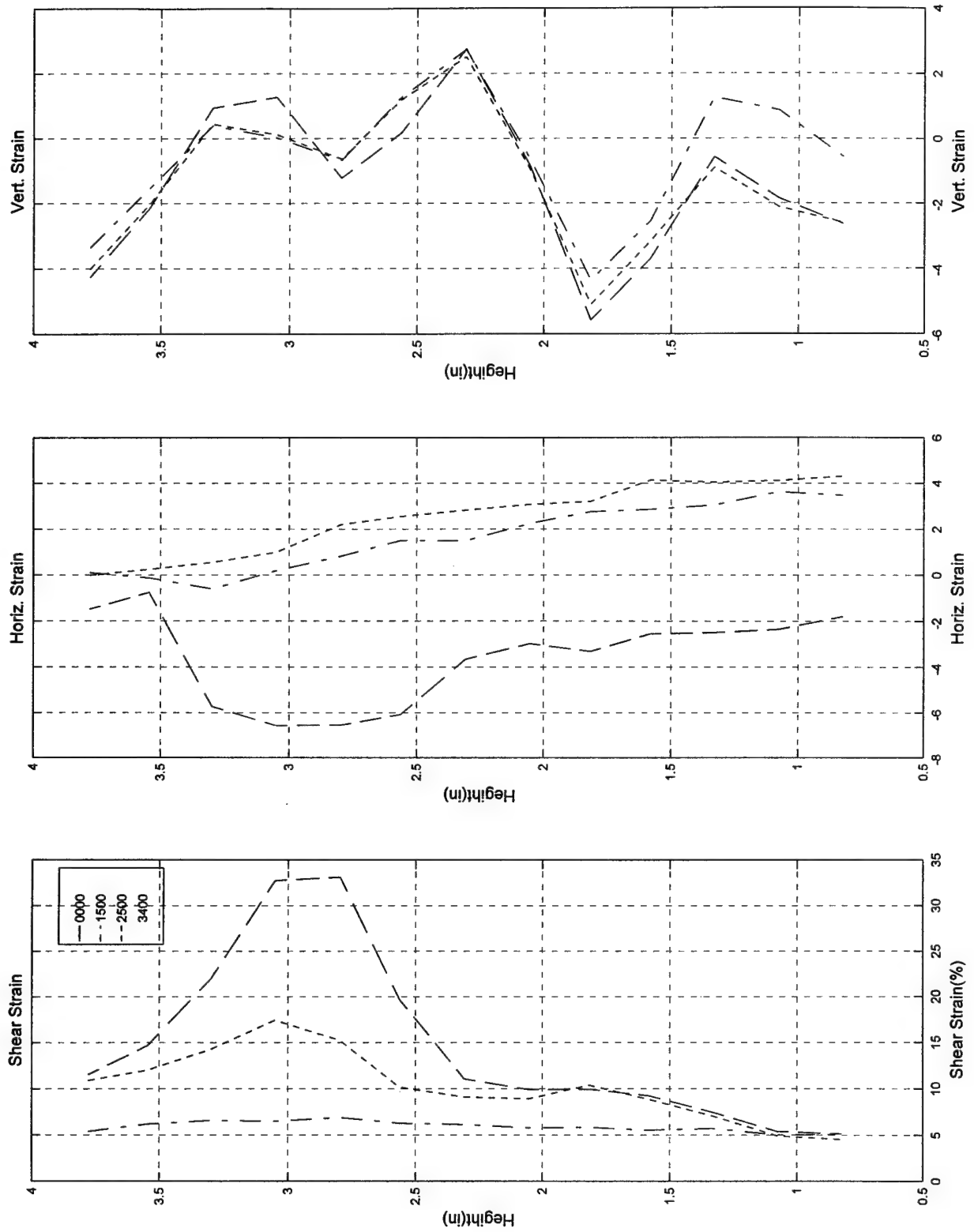
Test #78a, Camera #B, Figure 2

Test #78a: 8/14/97; Pure Torsion; ECP=50 psi; Loire, Video b
 Locations of Images
 (Transformed to new axis along and normal to SB)₂₀



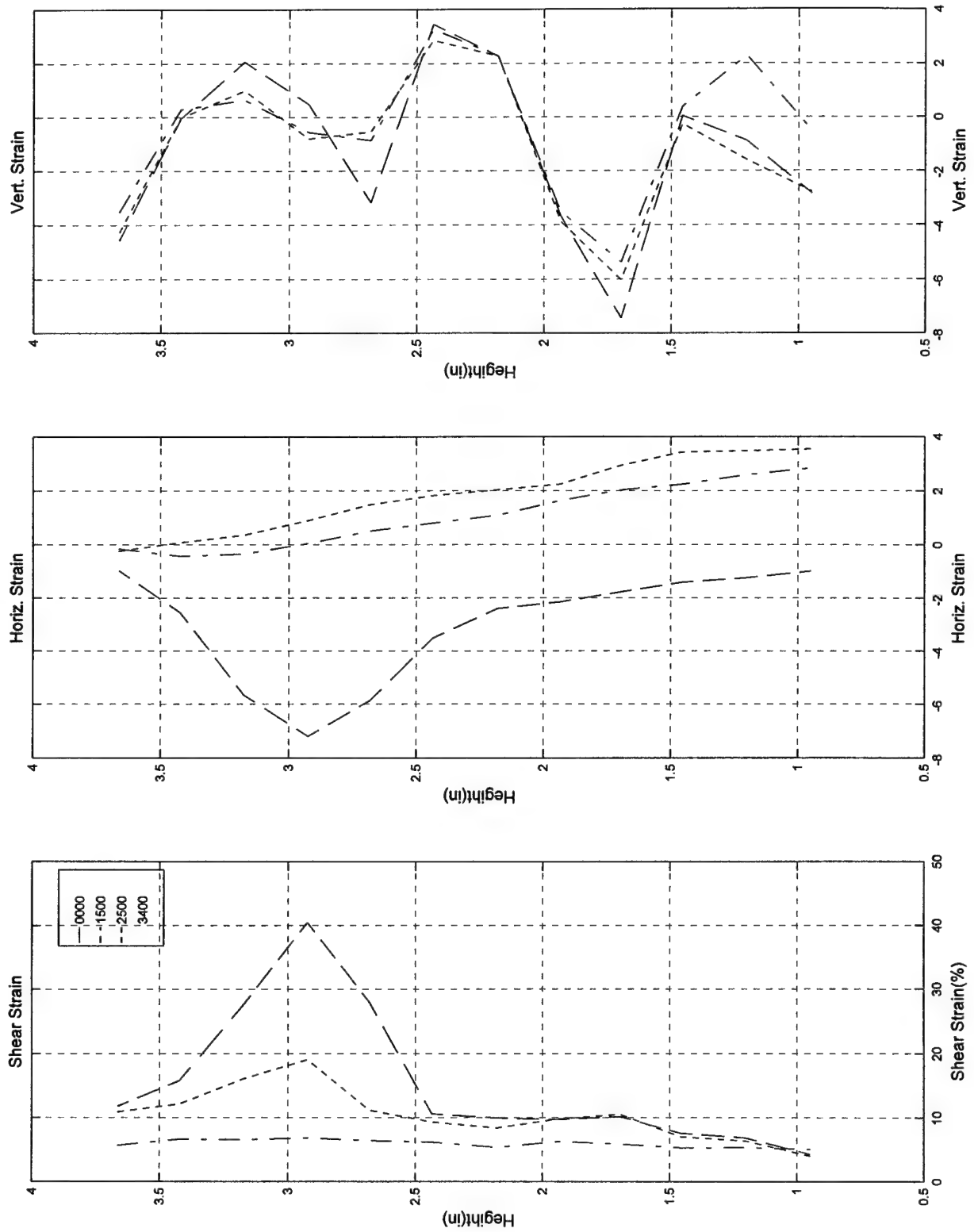
Test #78a, Camera #B, Figure 3

Test #78a; 8/14/97; Pure Torsion; ECP=50 psi; Loire, Video b



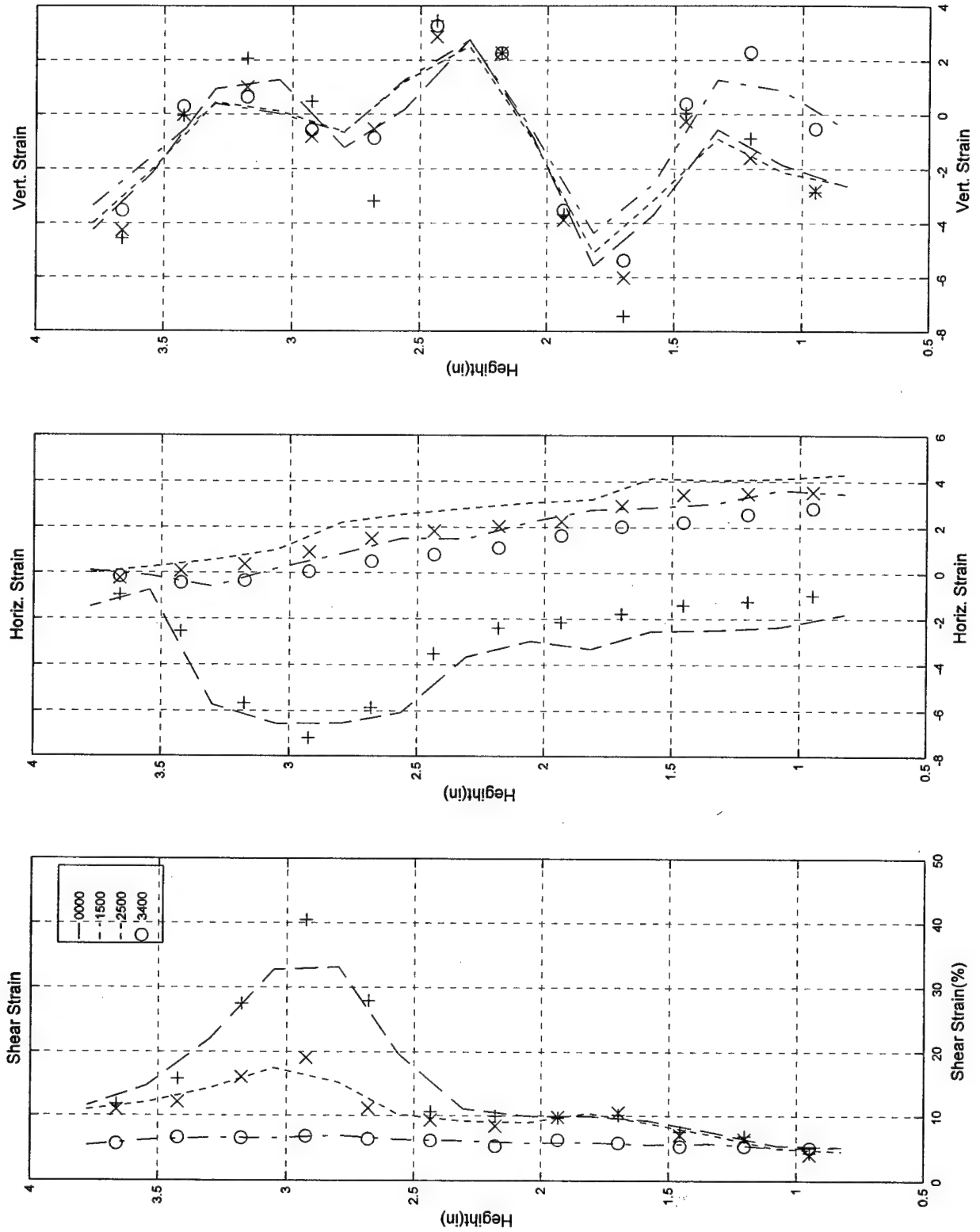
Test #78a, Camera #B, Figure 4

Test #78a; 8/14/97; Pure Torsion; ECP=50 psi; Loire, Video b



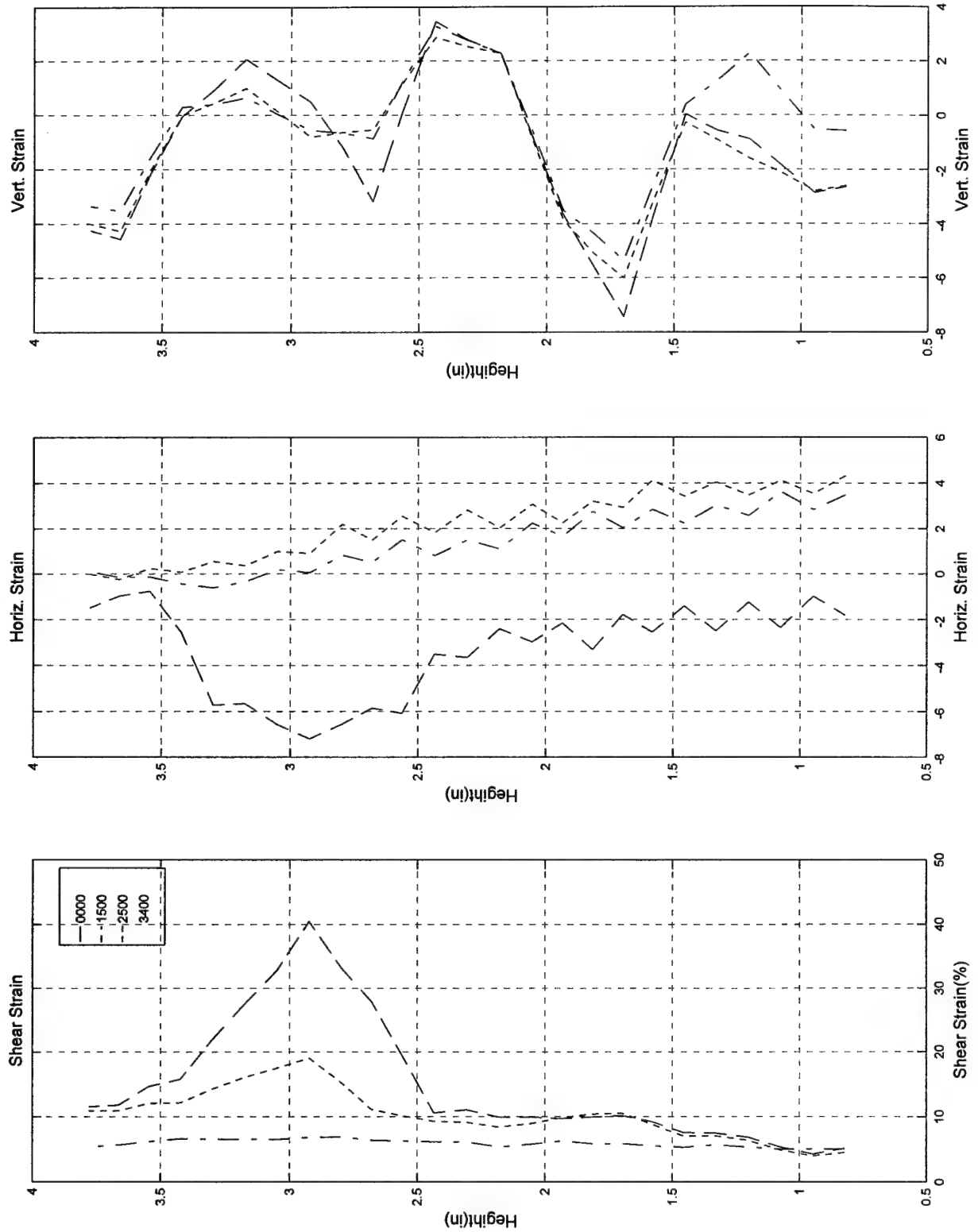
Test #78a, Camera #B, Figure 5

Test #78a; 8/14/97; Pure Torsion; ECP=50 psi; Loire, Video b



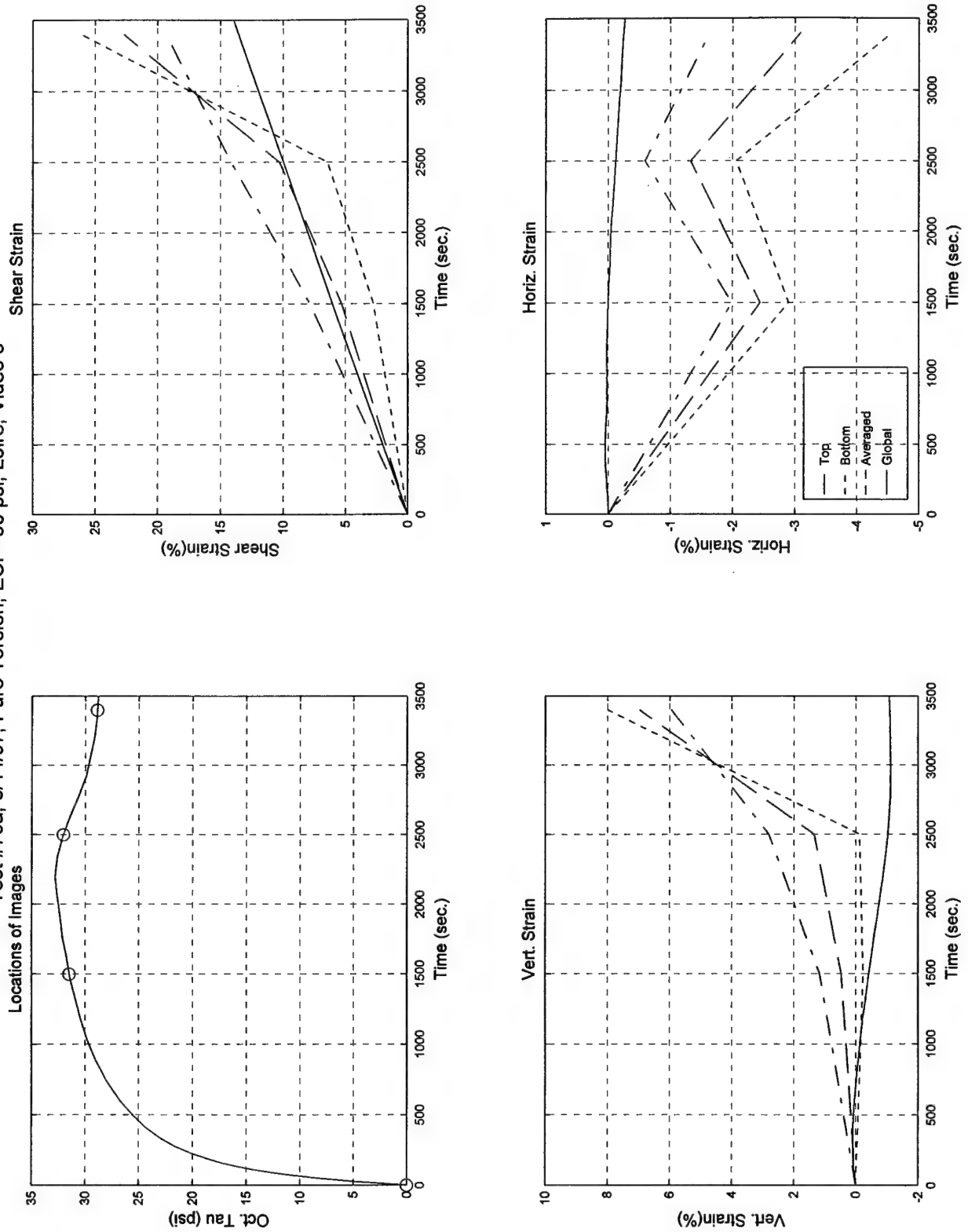
Test #78a, Camera #B, Figure 6

Test #78a; 8/14/97; Pure Torsion; ECP=50 psi; Loire, Video b



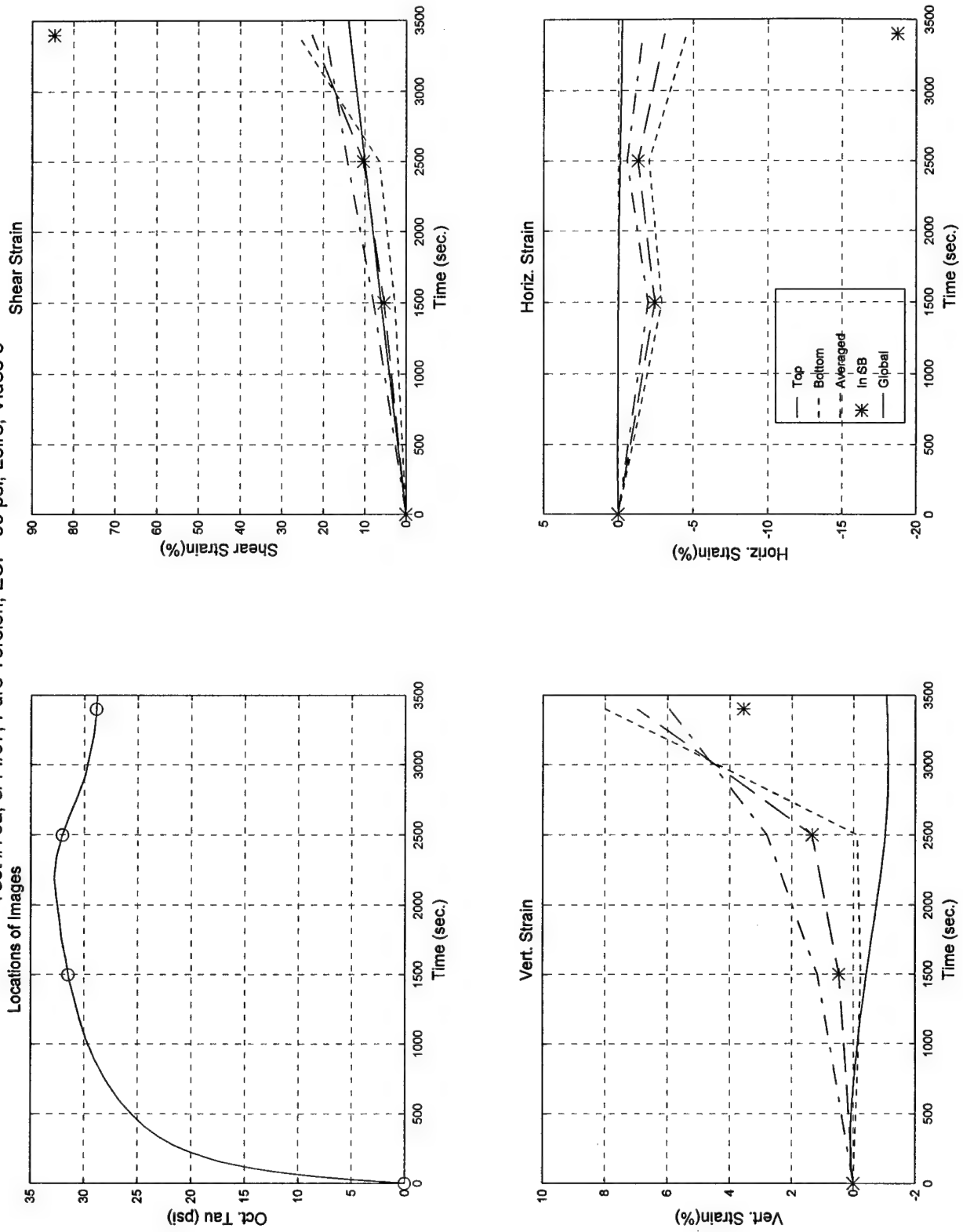
Test #78a, Camera #B, Figure 7

Test #78a; 8/14/97; Pure Torsion; ECP=50 psi; Loire, Video c



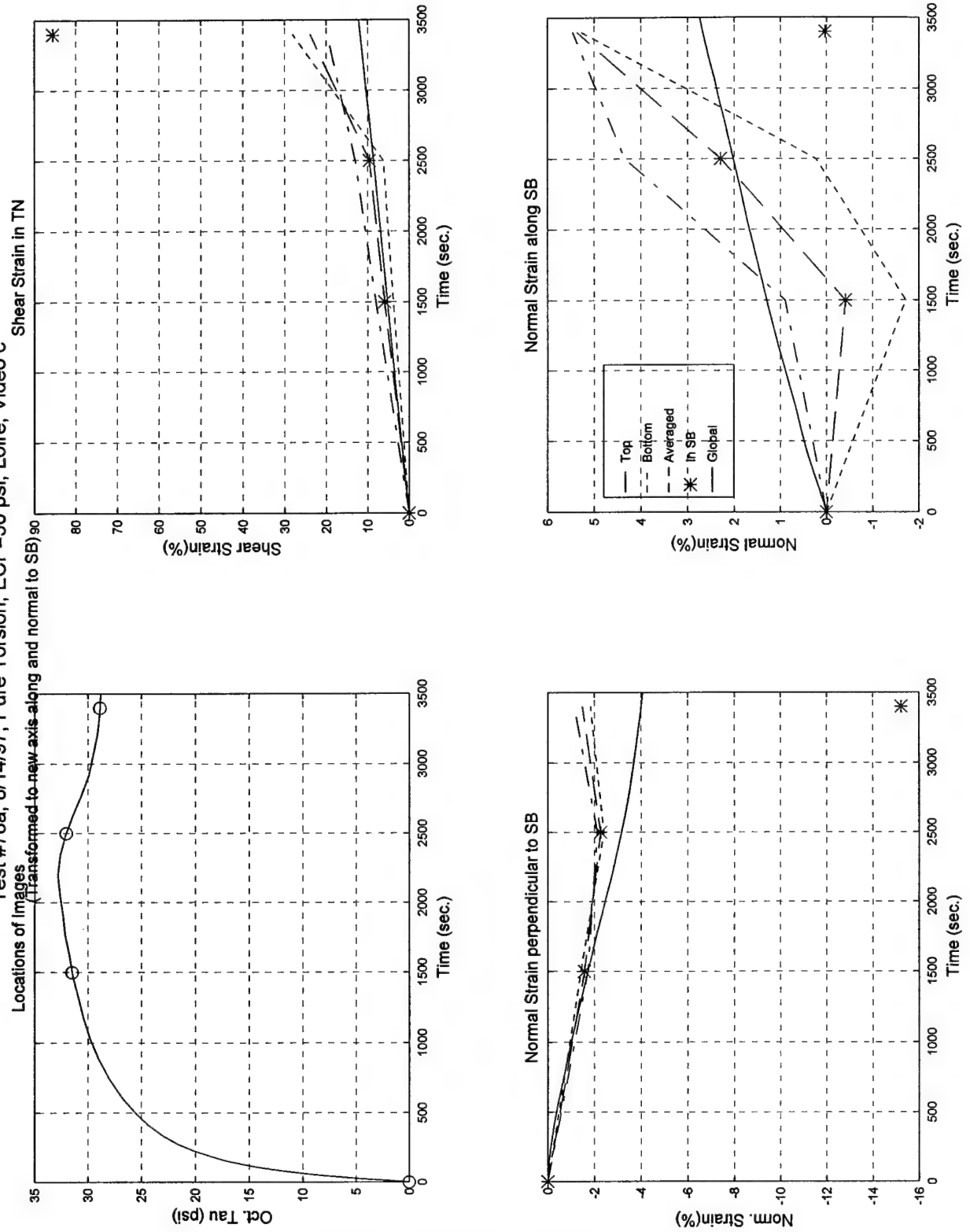
Test #78a, Camera #C, Figure 1

Test #78a; 8/14/97; Pure Torsion; ECP=50 psi; Loire, Video c



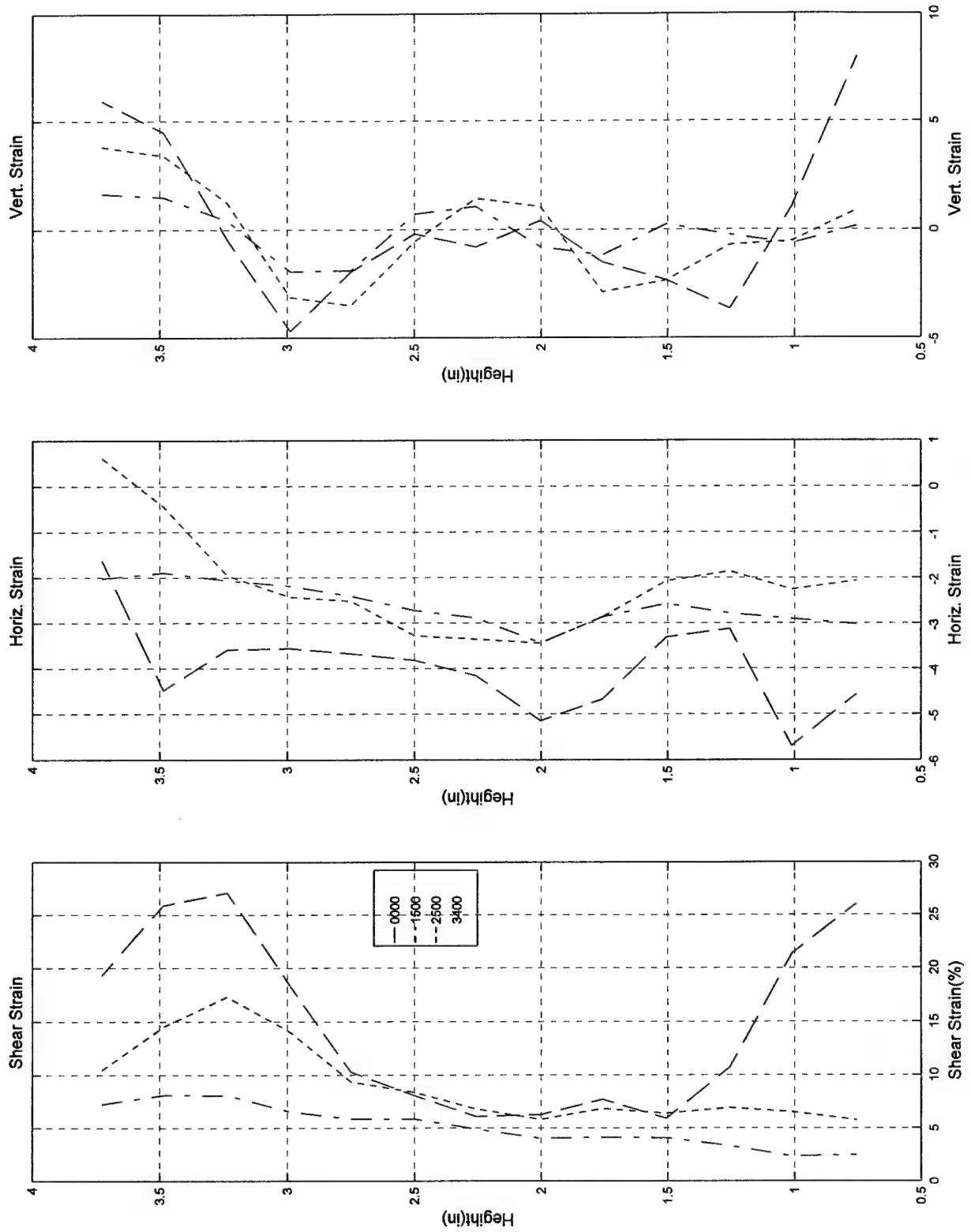
Test #78a, Camera #C, Figure 2

Test #78a; 8/14/97; Pure Torsion; ECP=50 psi; Loire, Video c



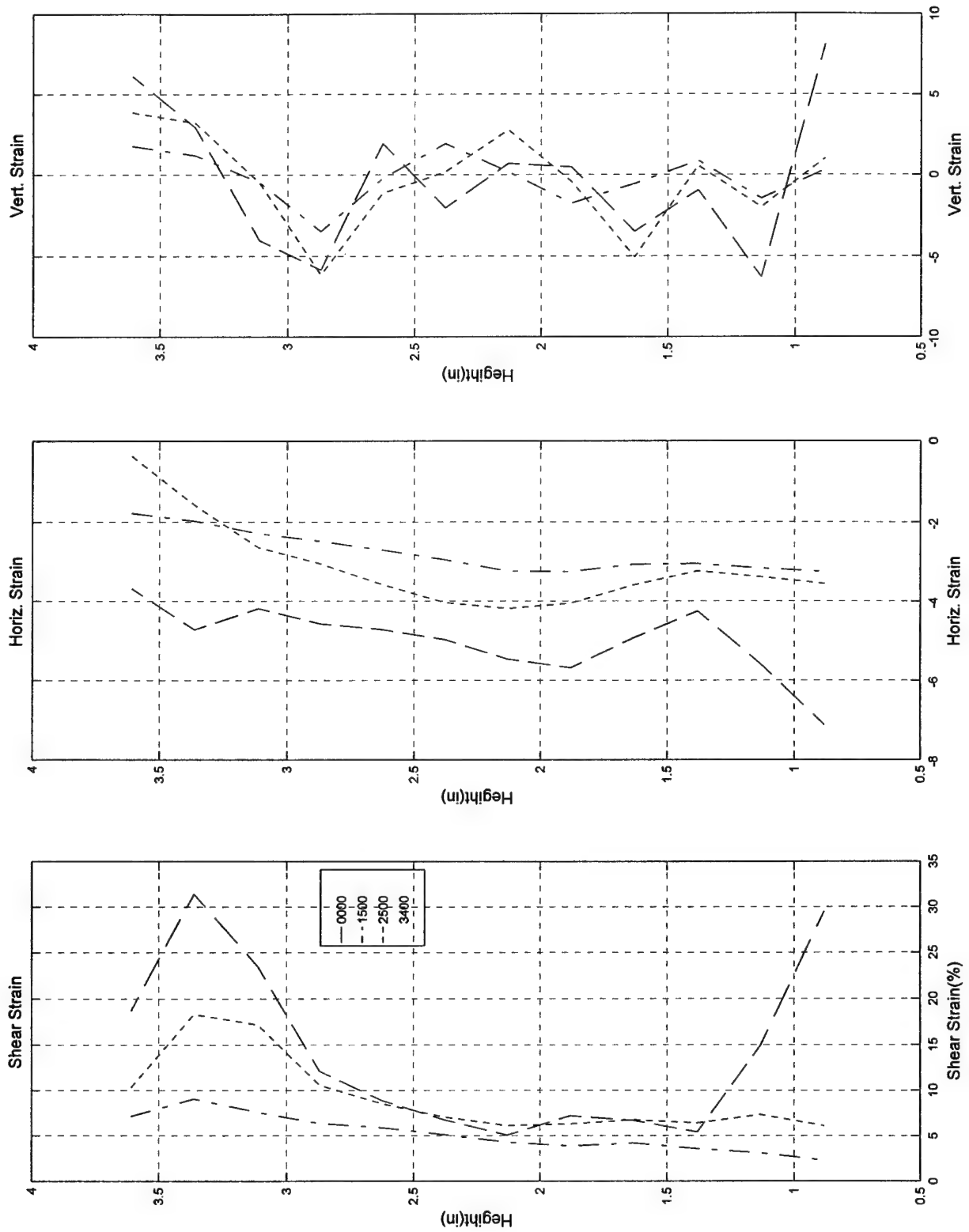
Test #78a, Camera #C, Figure 3

Test #78a; 8/14/97; Pure Torsion; ECP=50 psi; Loire, Video c



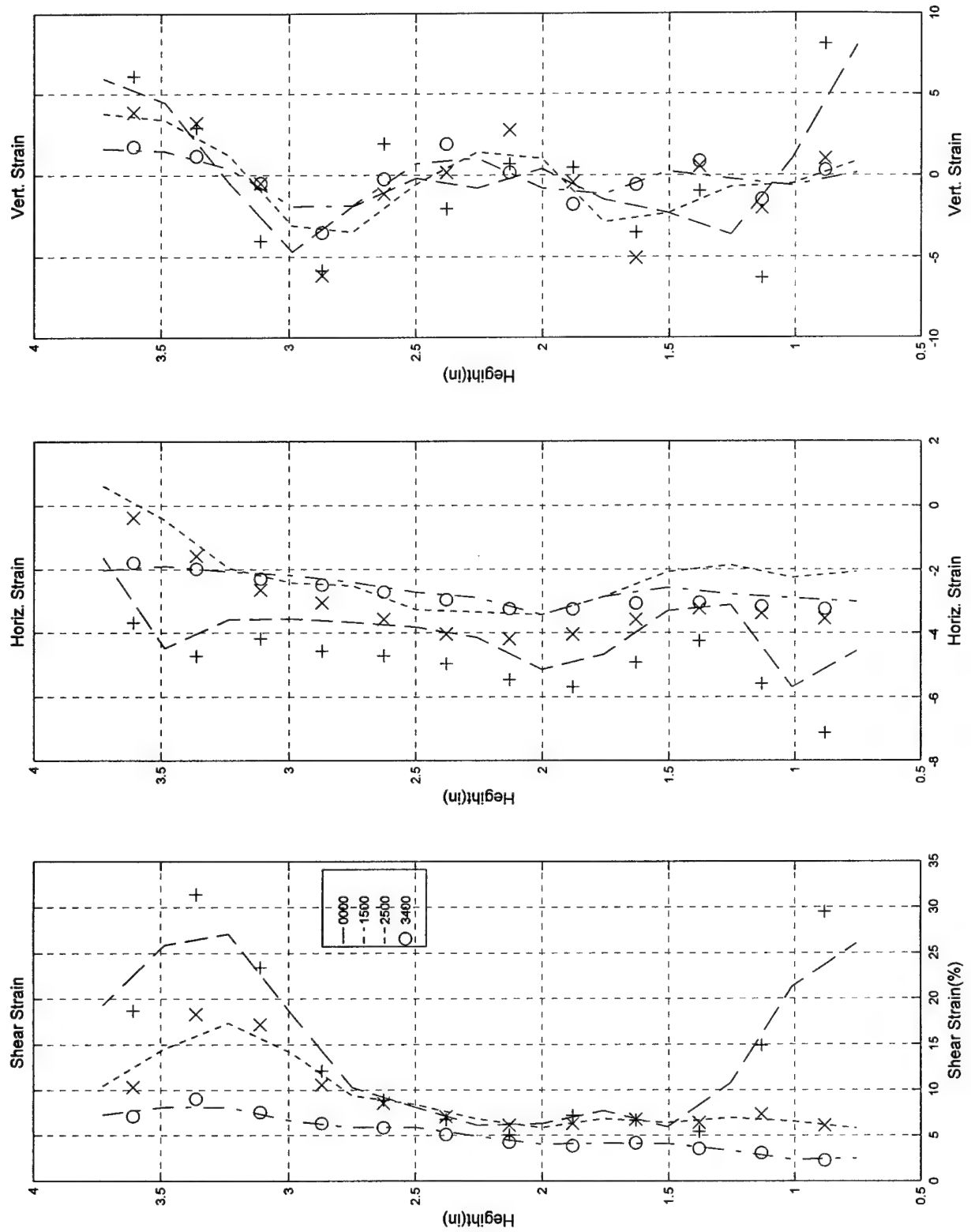
Test #78a, Camera #C, Figure 4

Test #78a; 8/14/97; Pure Torsion; ECP=50 psi; Loire, Video c



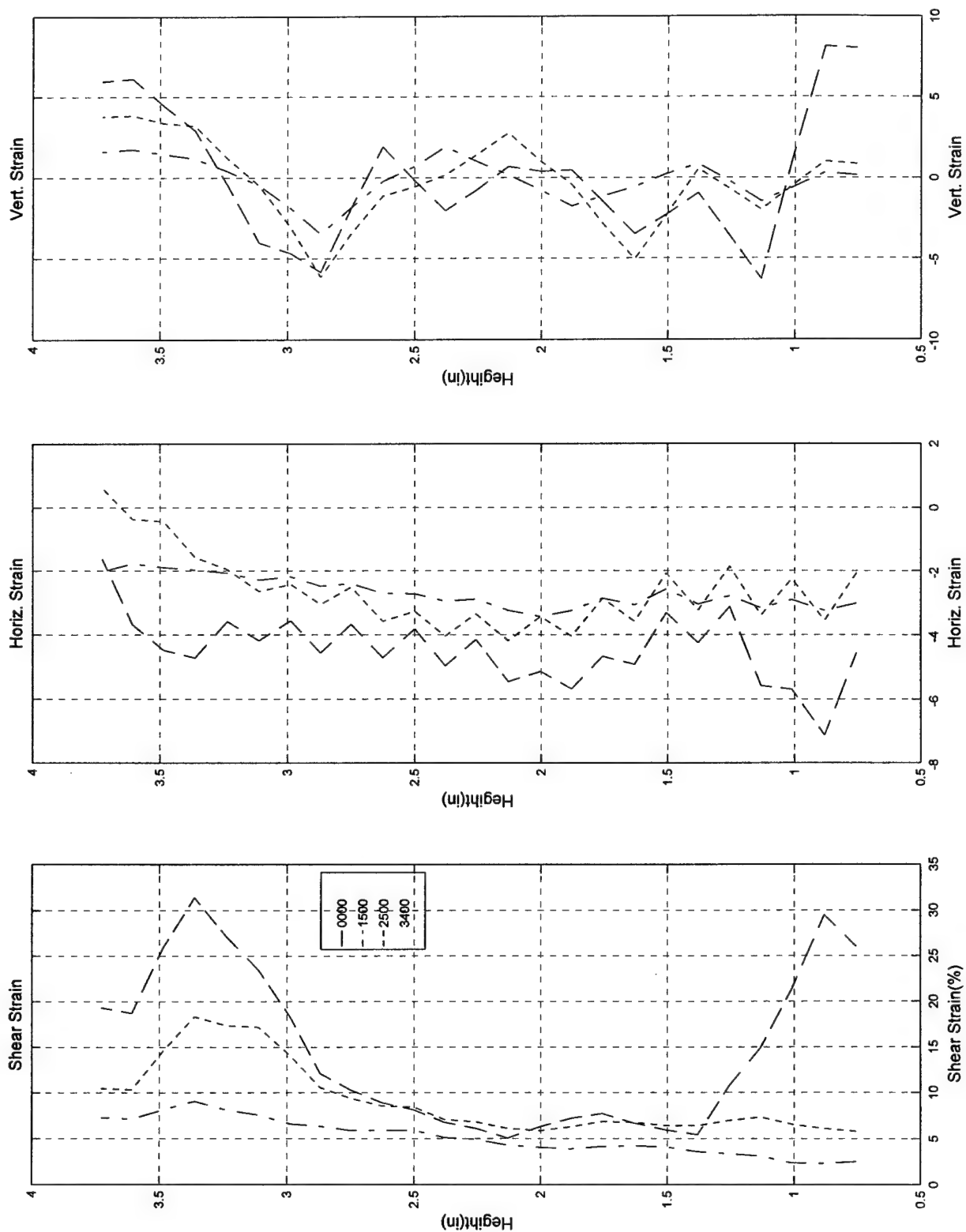
Test #78a, Camera #C, Figure 5

Test #78a; 8/14/97; Pure Torsion; ECP=50 psi; Loire, Video c



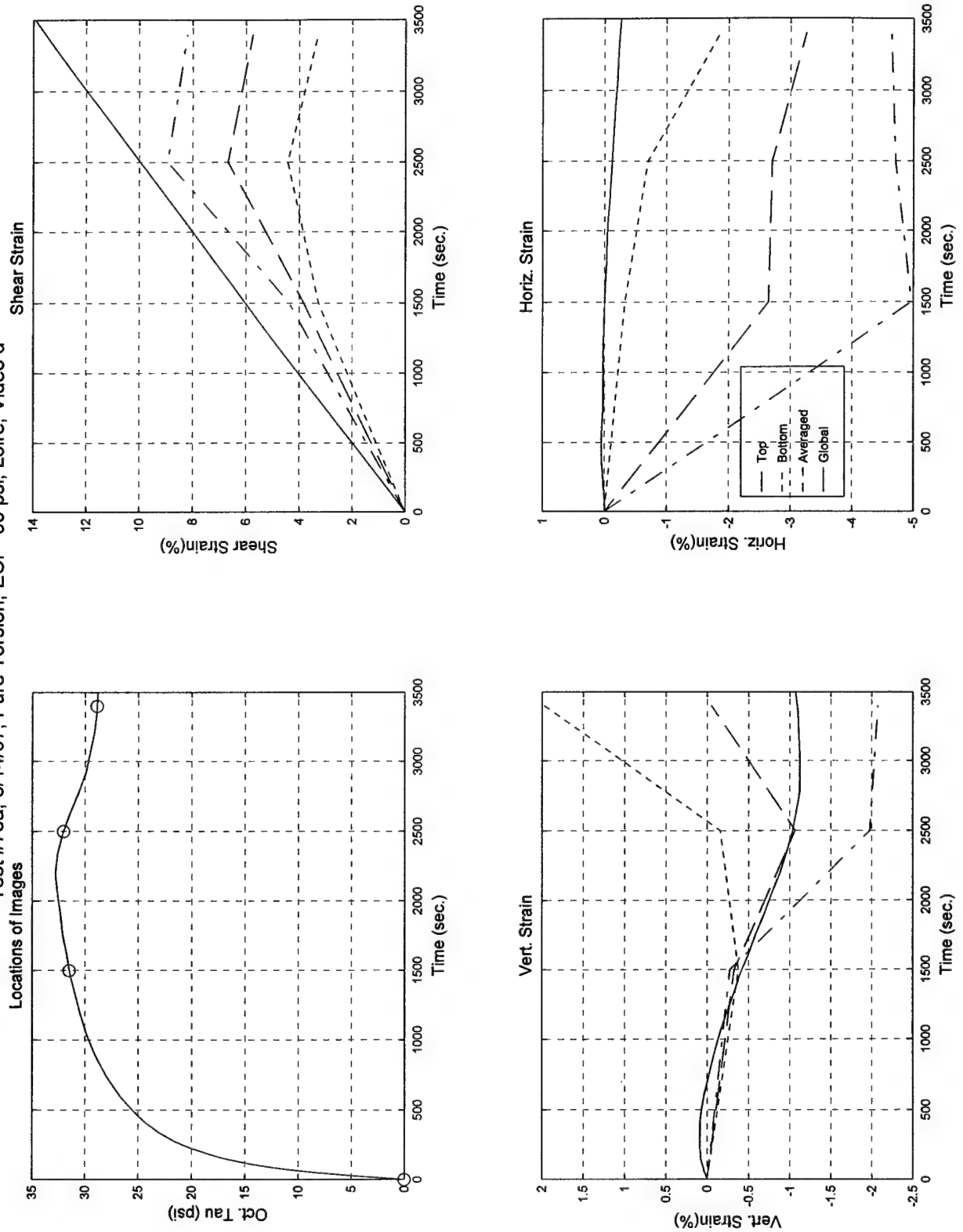
Test #78a, Camera #C, Figure 6

Test #78a; 8/14/97; Pure Torsion; ECP=50 psi; Loire, Video c



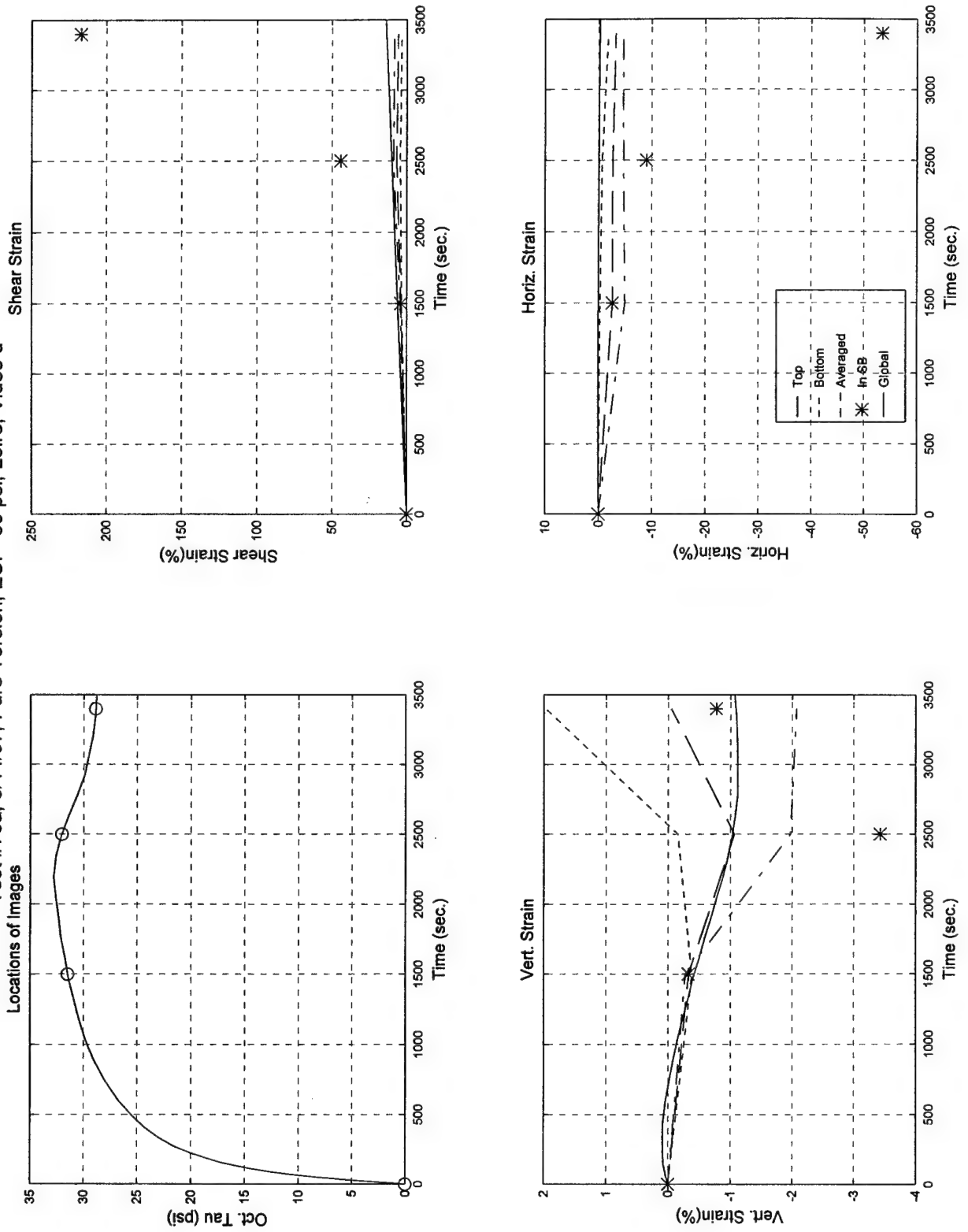
Test #78a, Camera #C, Figure 7

Test #78a; 8/14/97; Pure Torsion; ECP=50 psi; Loire, Video d



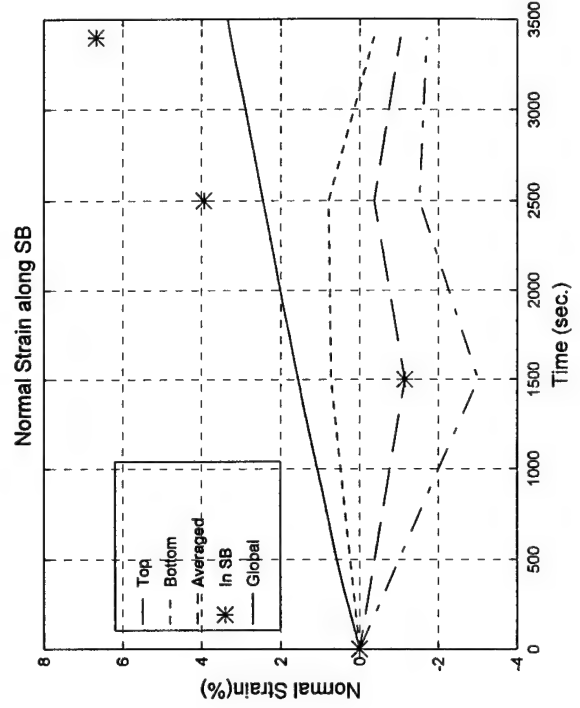
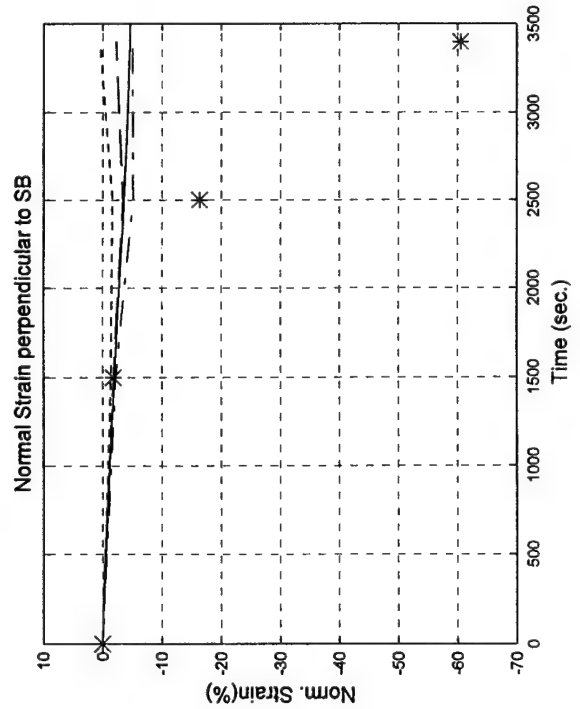
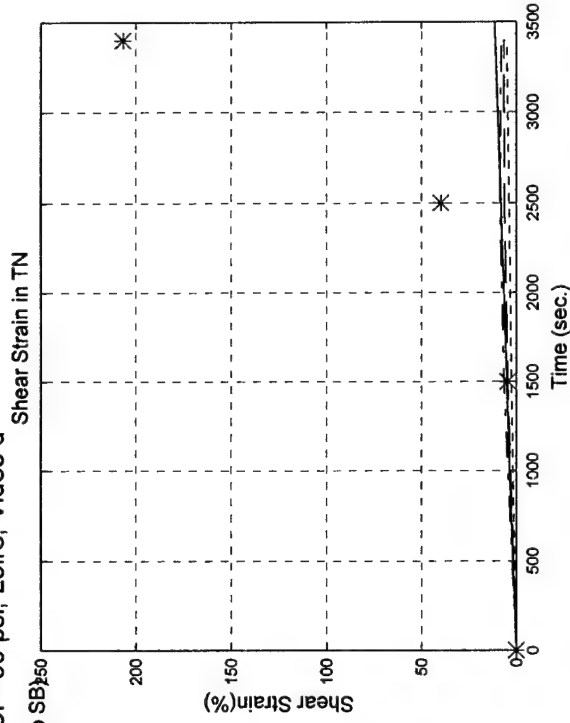
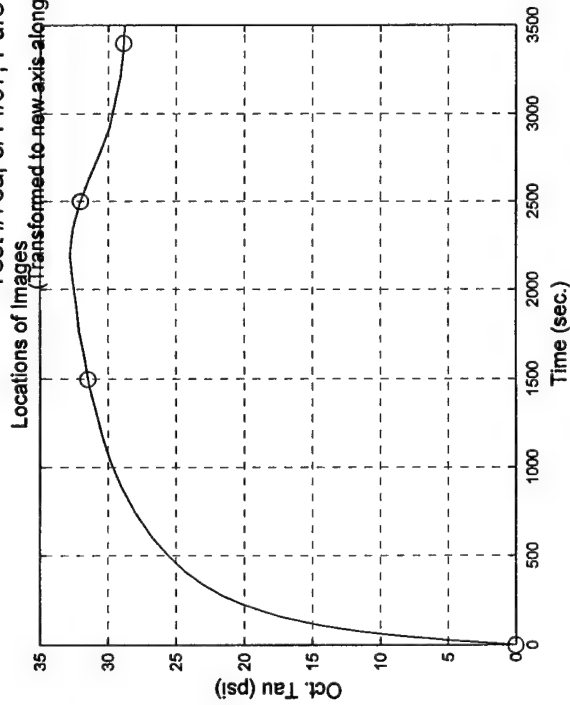
Test #78a, Camera #D, Figure 1

Test #78a; 8/14/97; Pure Torsion; ECP=50 psi; Loire, Video d



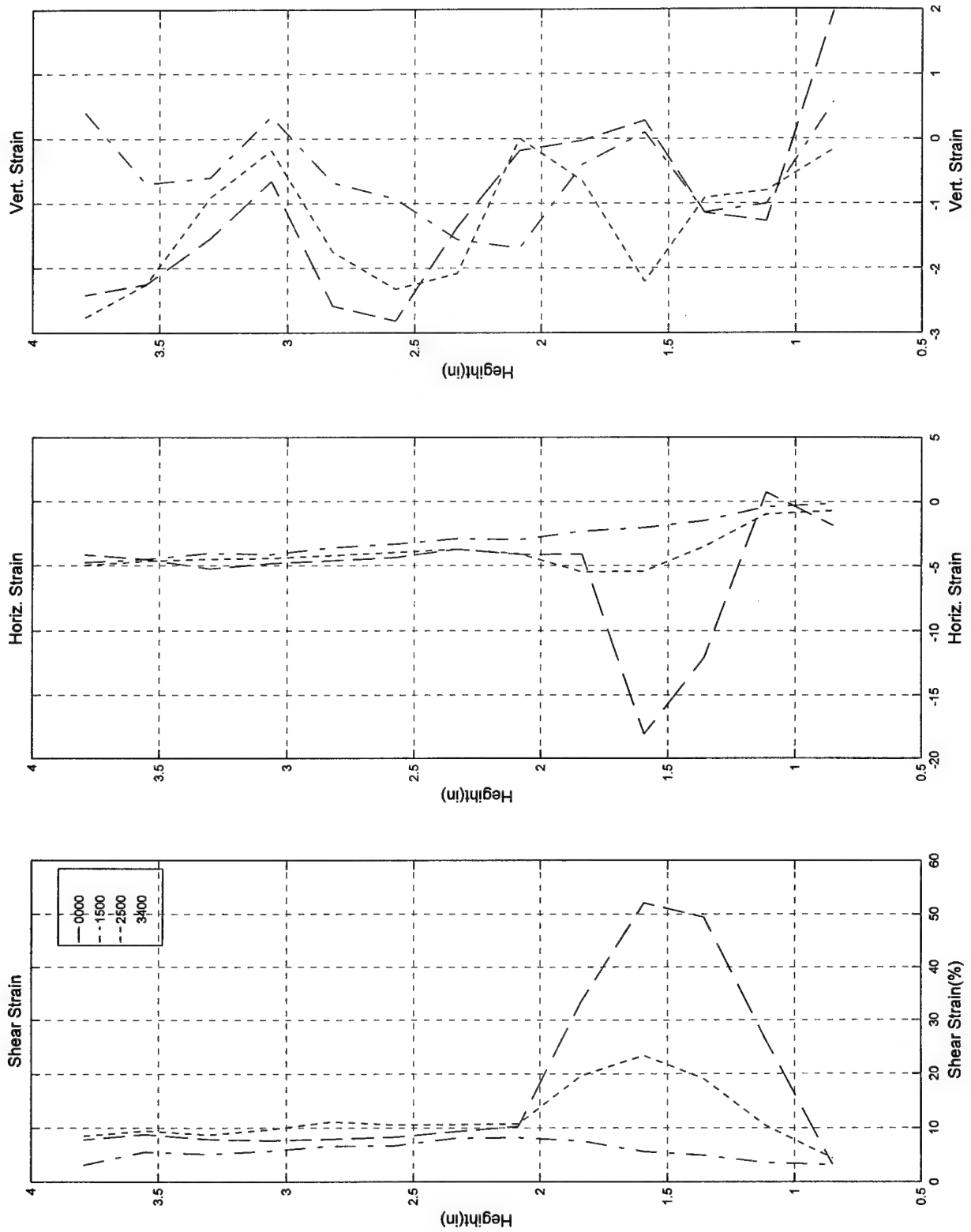
Test #78a, Camera #D, Figure 2

Test #78a; 8/14/97; Pure Torsion; ECP=50 psi; Loire, Video d



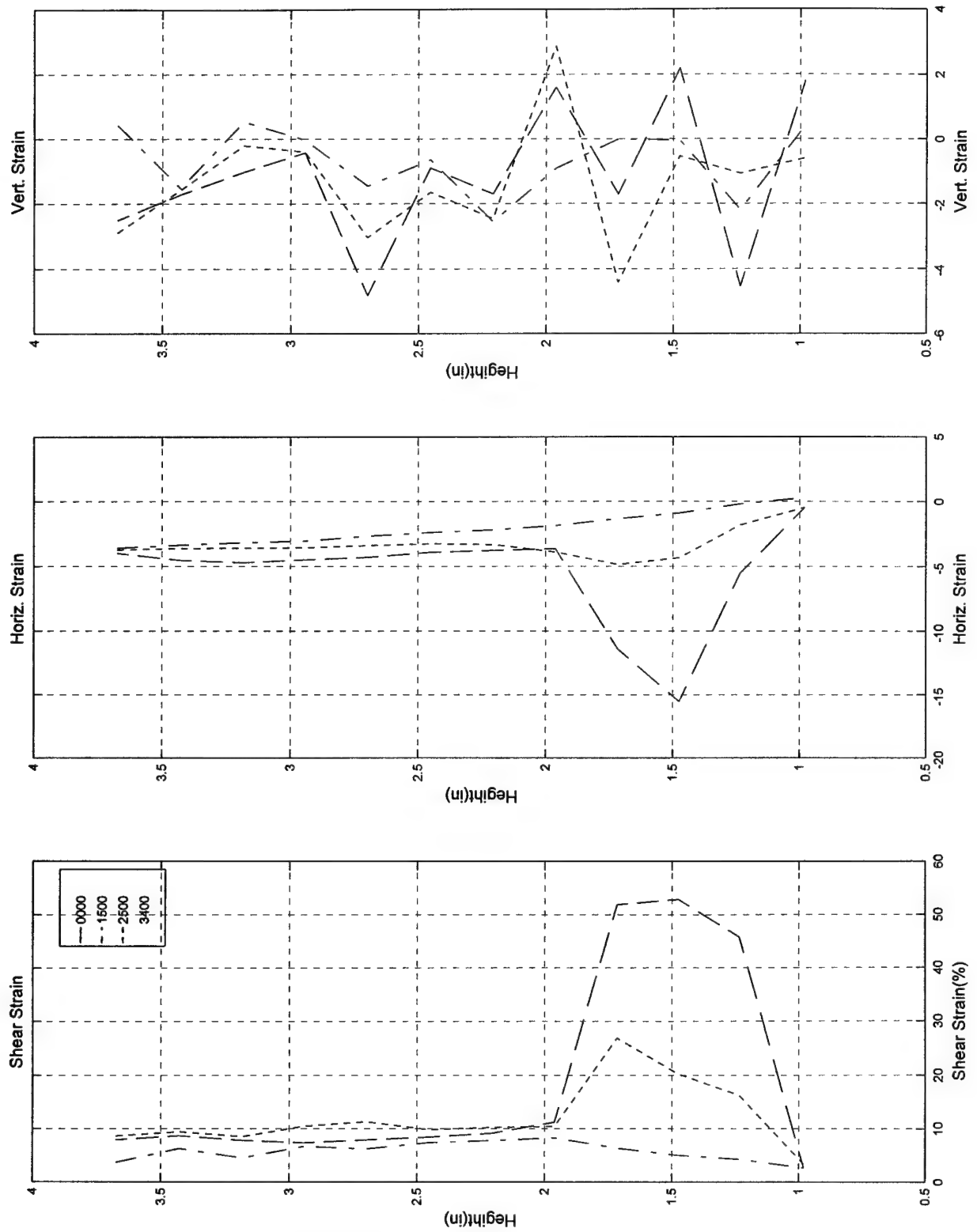
Test #78a, Camera #D, Figure 3

Test #78a; 8/14/97; Pure Torsion; ECP=50 psi; Loire, Video d



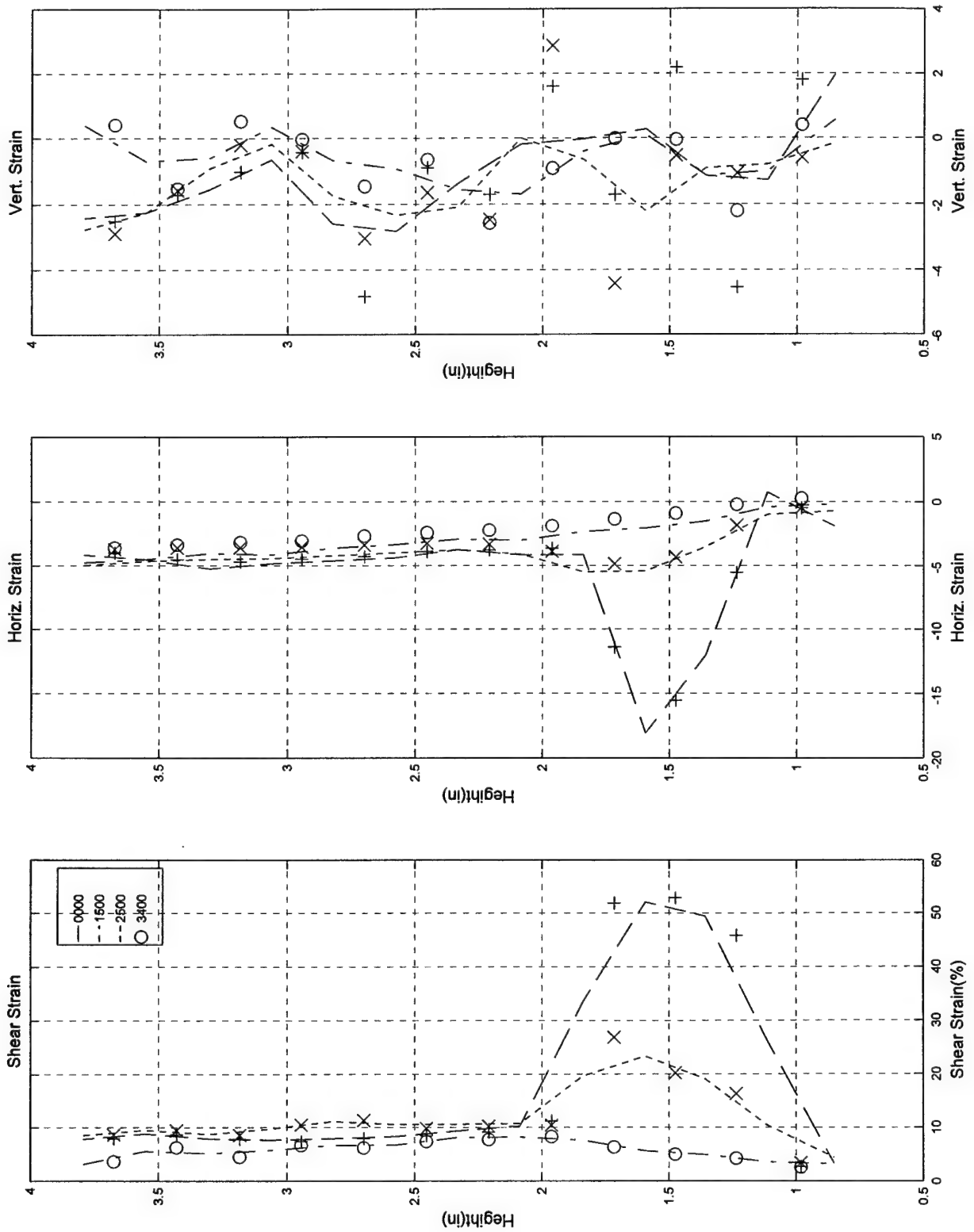
Test #78a, Camera #D, Figure 4

Test #78a; 8/14/97; Pure Torsion; ECP=50 psi; Loire, Video d



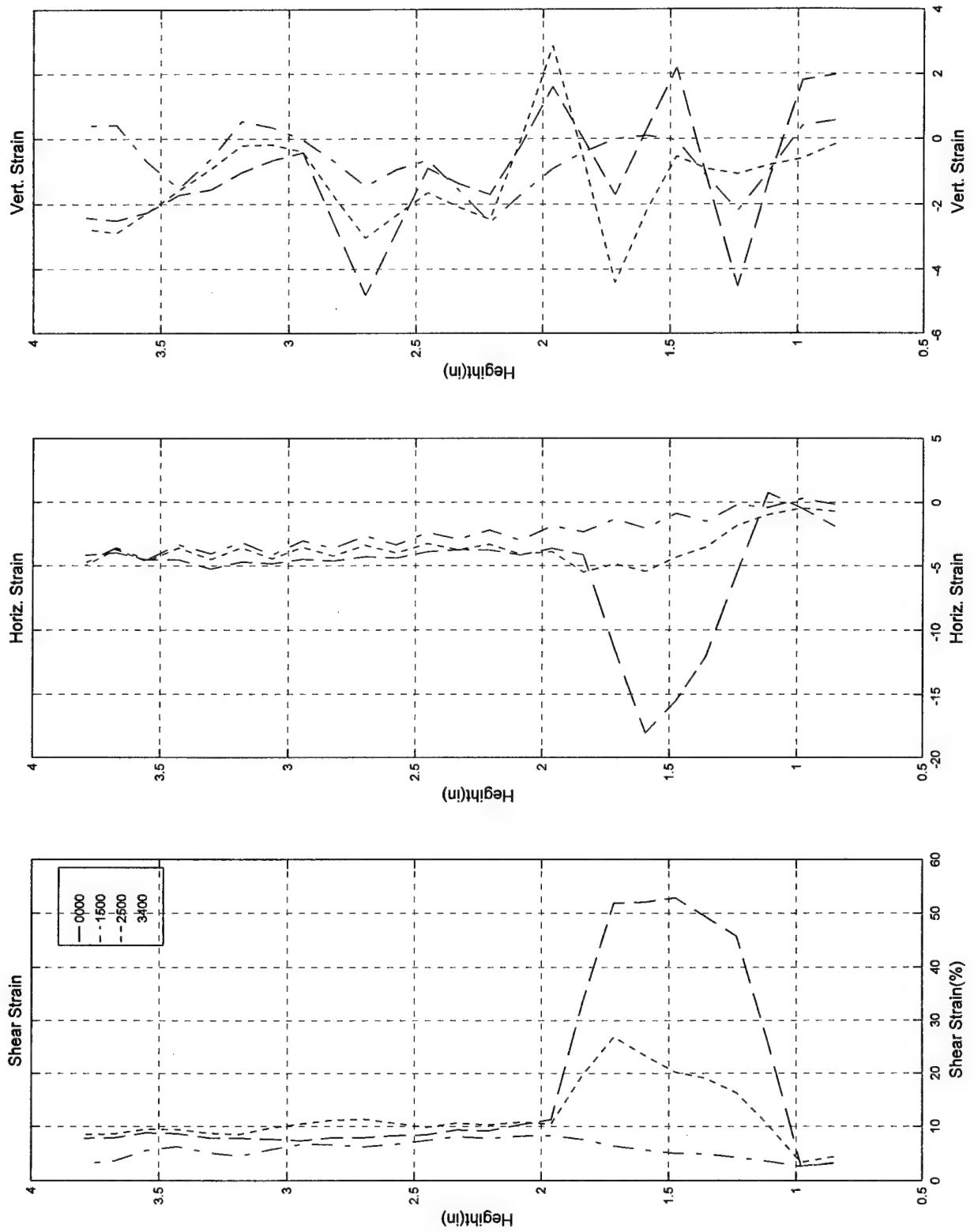
Test #78a, Camera #D, Figure 5

Test #78a; 8/14/97; Pure Torsion; ECP=50 psi; Loire, Video d



Test #78a, Camera #D, Figure 6

Test #78a; 8/14/97; Pure Torsion; ECP=50 psi; Loire, Video d

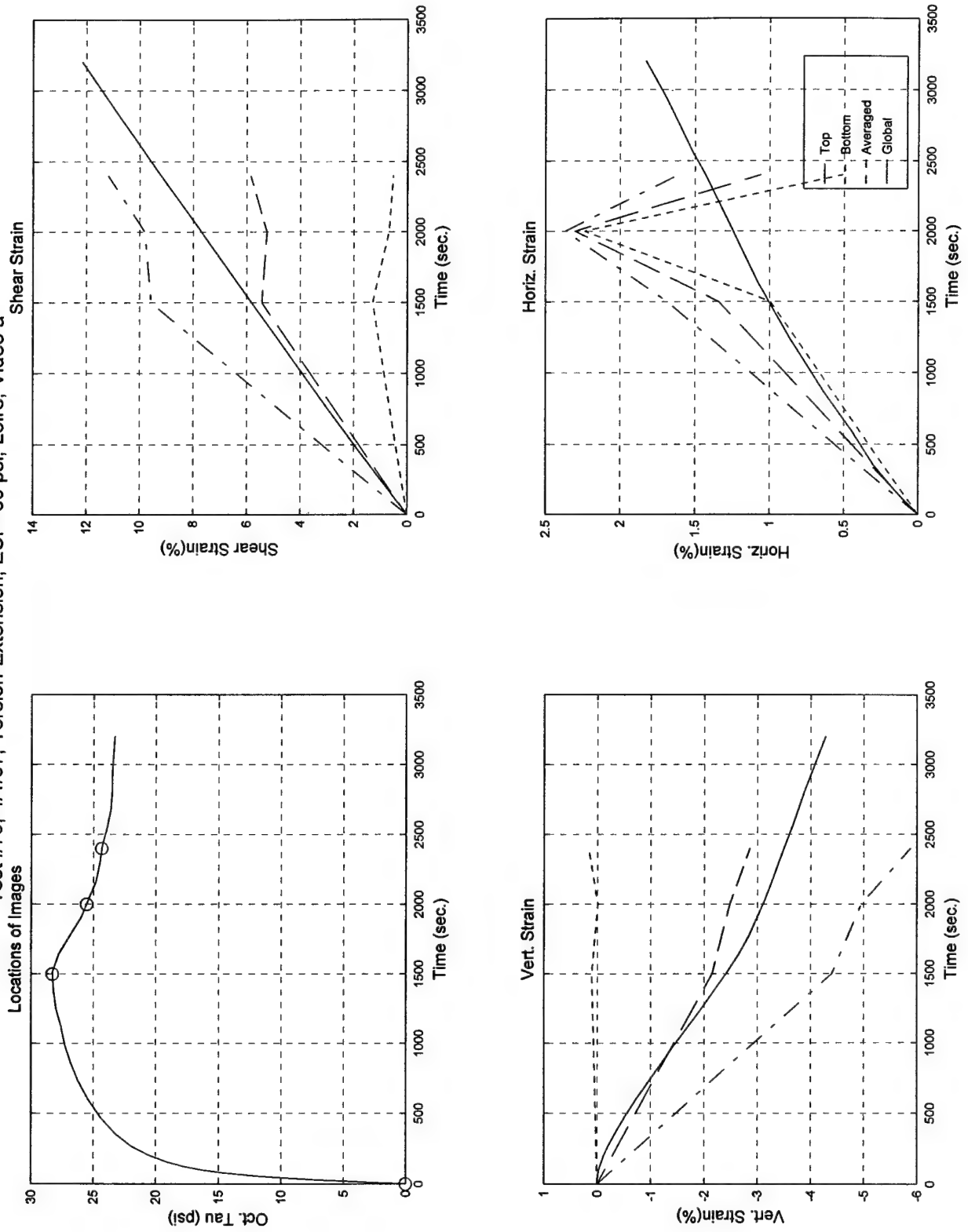


Test #78a, Camera #D, Figure 7

B.4 Test #79

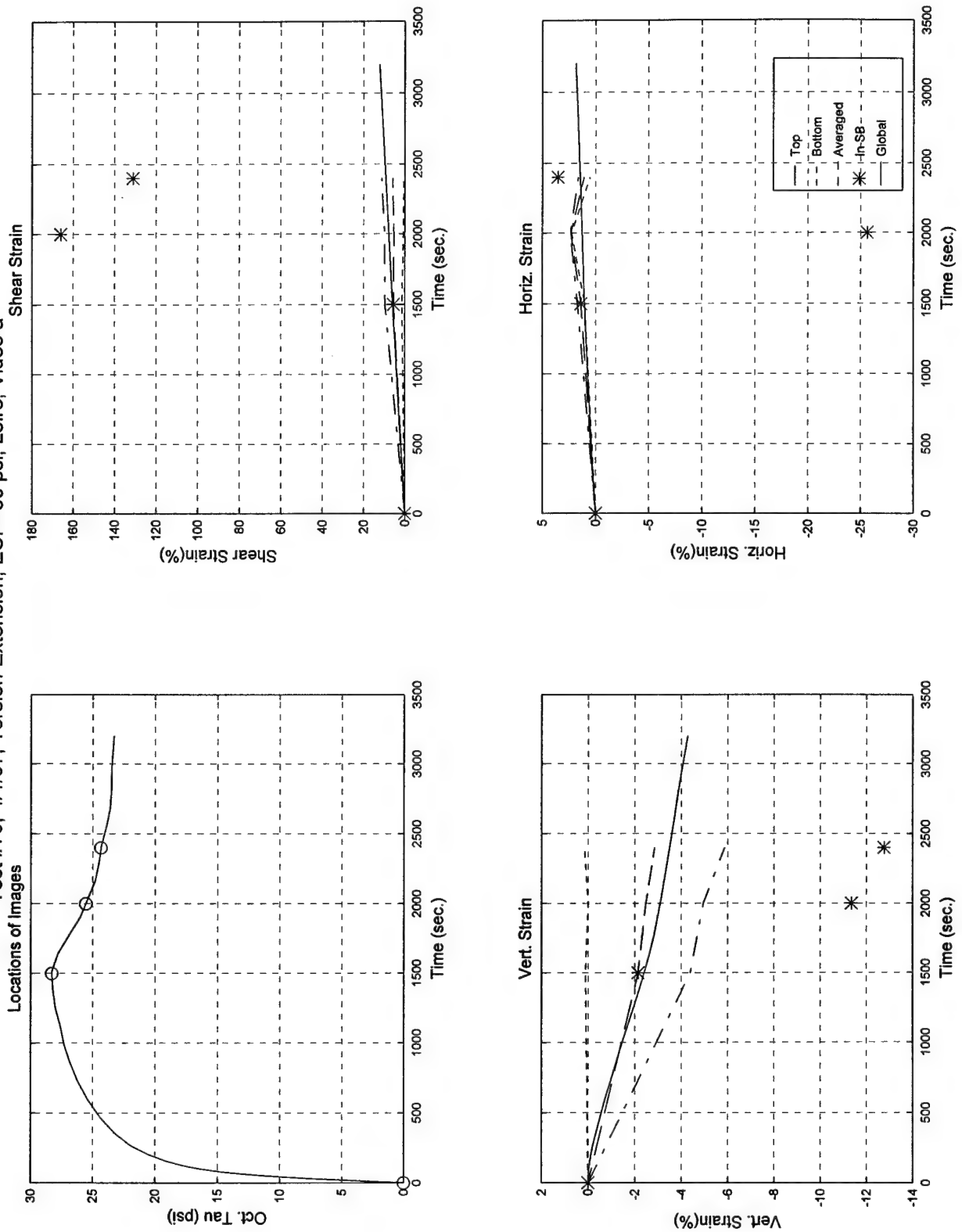
- **Torsion-Extension ($\beta = 60^\circ$)**
- **Effective Confining Pressure = 50 psi (345 kPa)**
- **50% Initial Relative Density**
- **Generalized Test**
- **Digitized Times Intervals: 0000, 1500, 2000 & 2400 sec.**

Test #79; 4/1/97; Torsion-Extension; ECP=50 psi; Loire, Video a



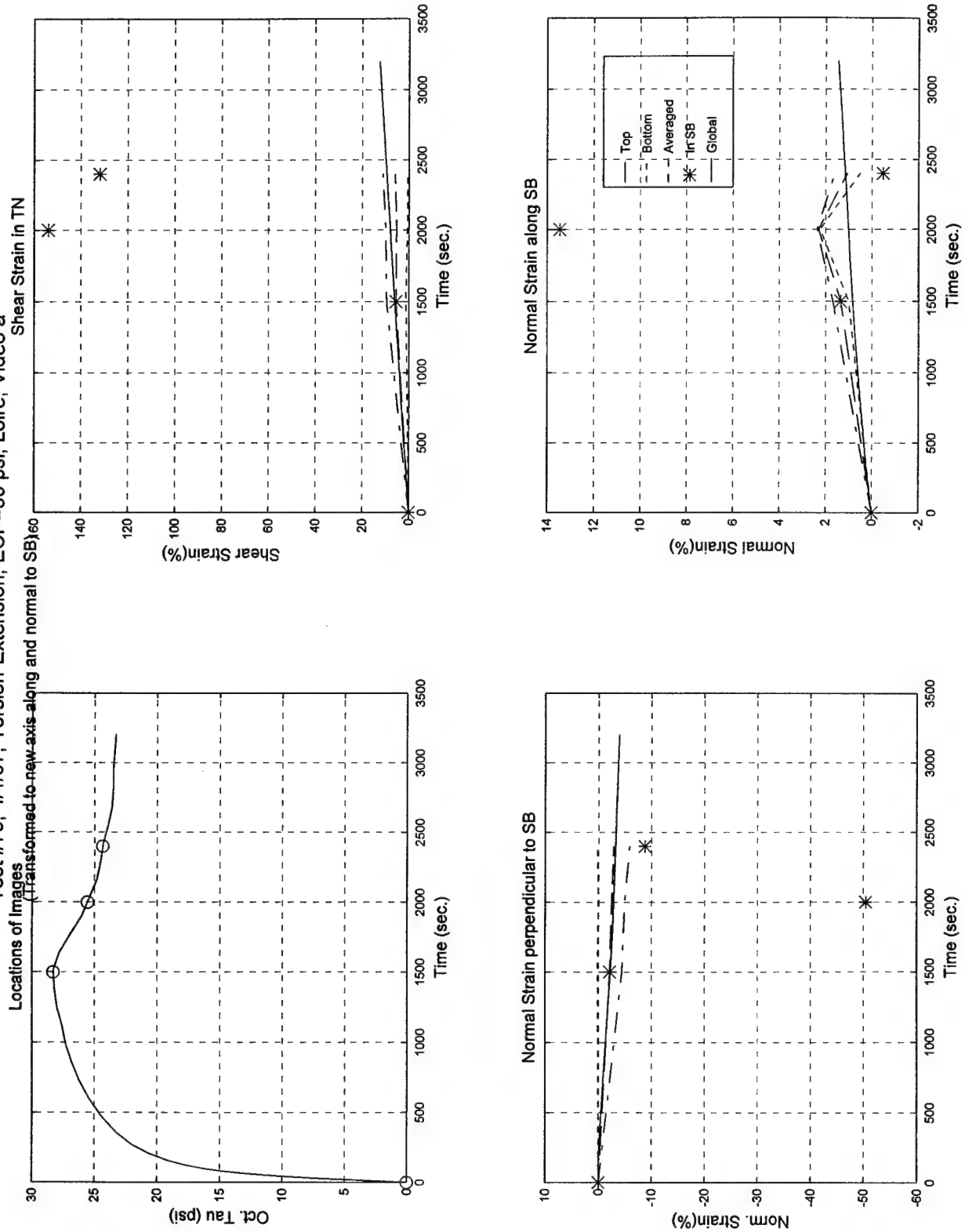
Test #79, Camera #A, Figure 1

Test #79; 4/1/97; Torsion-Extension; ECP=50 psi; Loire, Video a



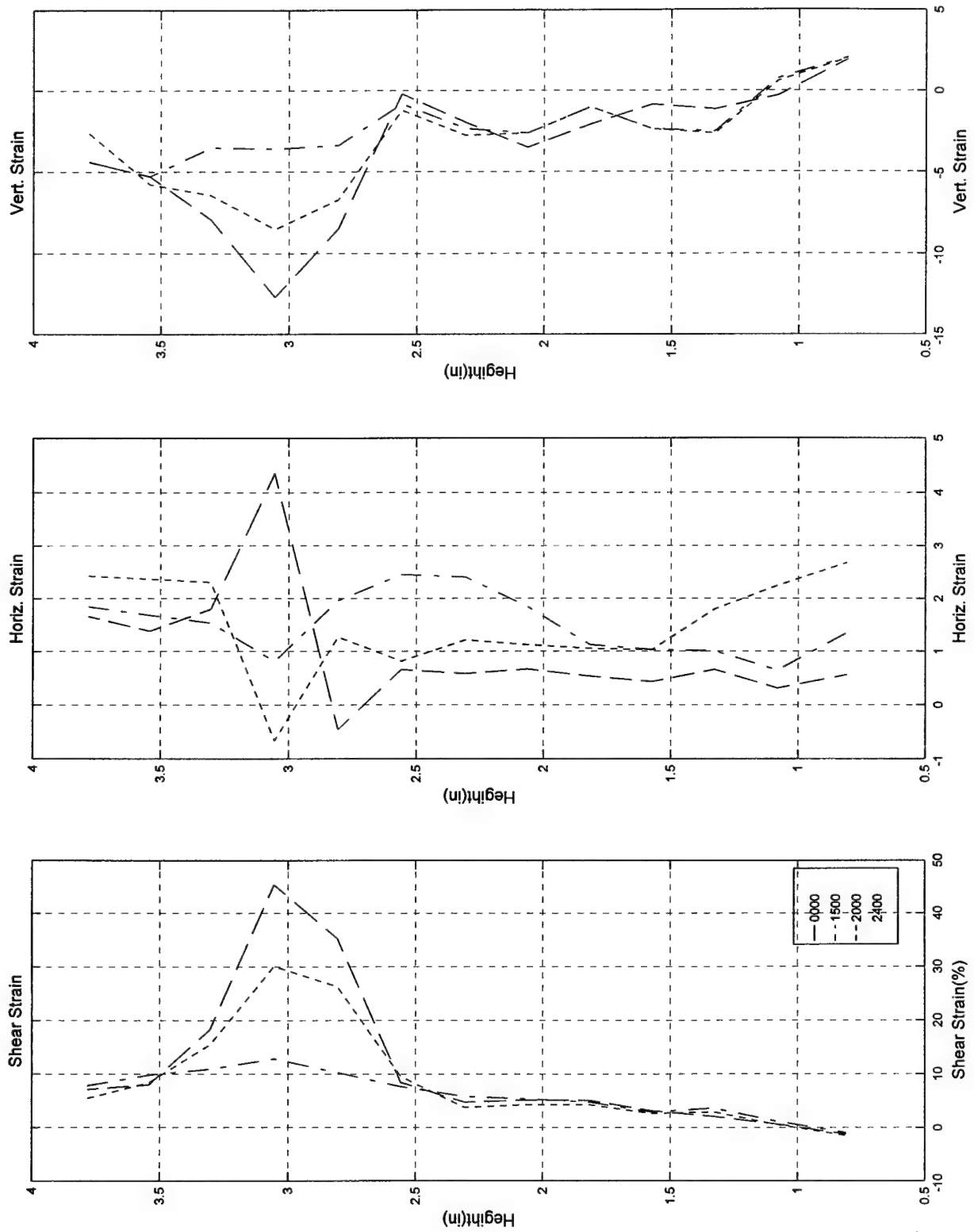
Test #79, Camera #A, Figure 2

Test #79; 4/1/97; Torsion-Extension; ECP=50 psi; Loire, Video a



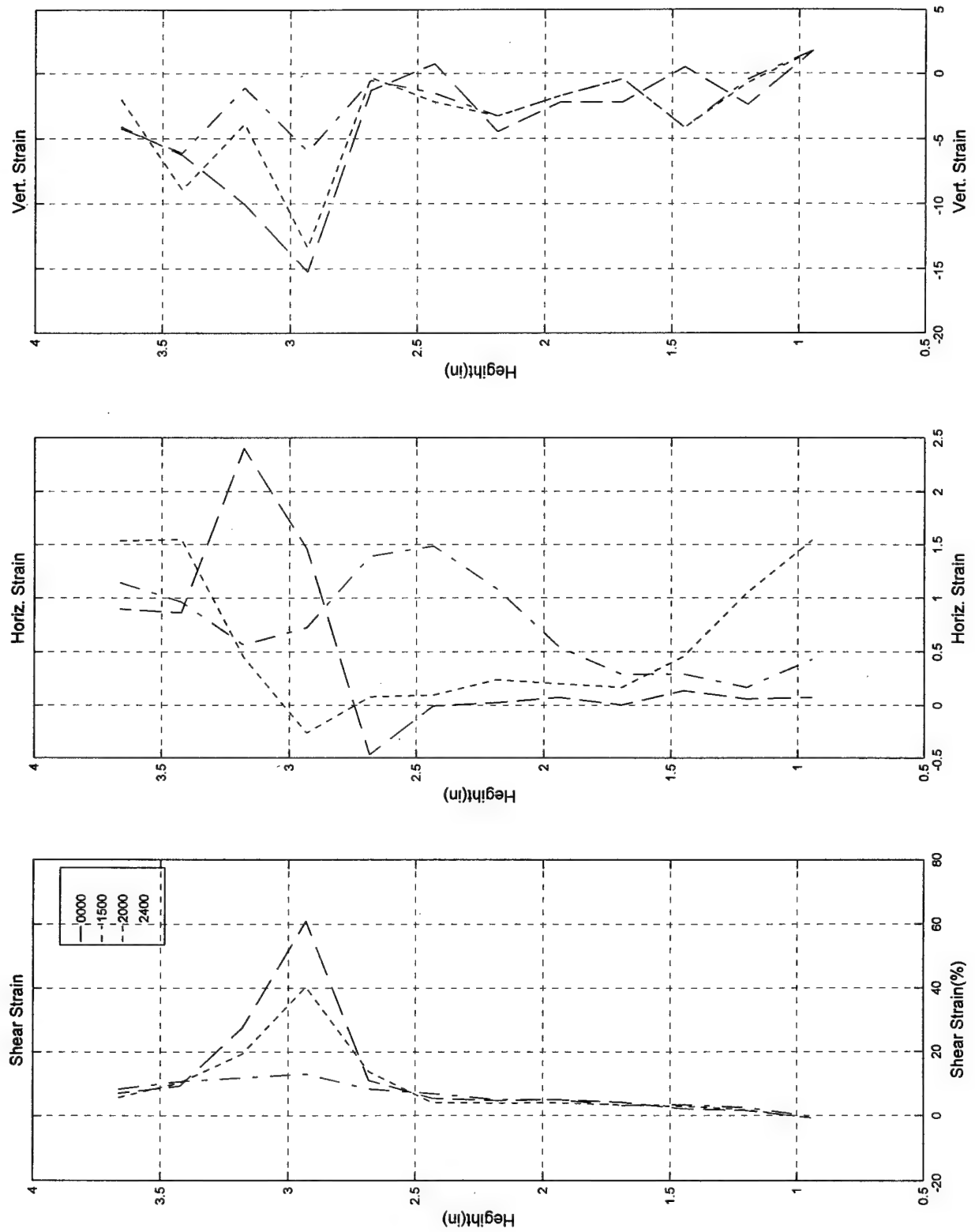
Test #79, Camera #A, Figure 3

Test #79; 4/1/97; Torsion-Extension; ECP=50 psi; Loire, Video a



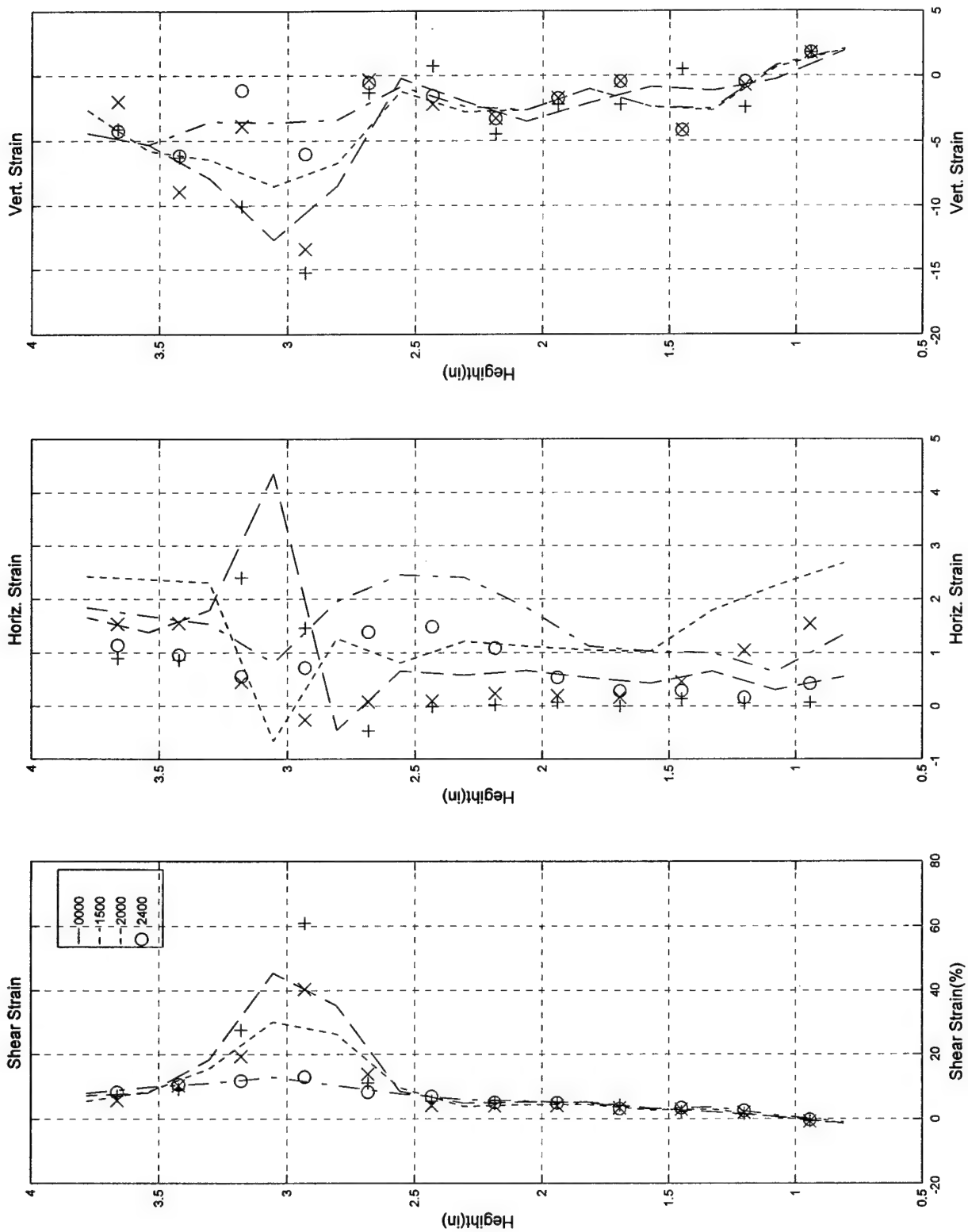
Test #79, Camera #A, Figure 4

Test #79; 4/1/97; Torsion-Extension; ECP=50 psi; Loire, Video a



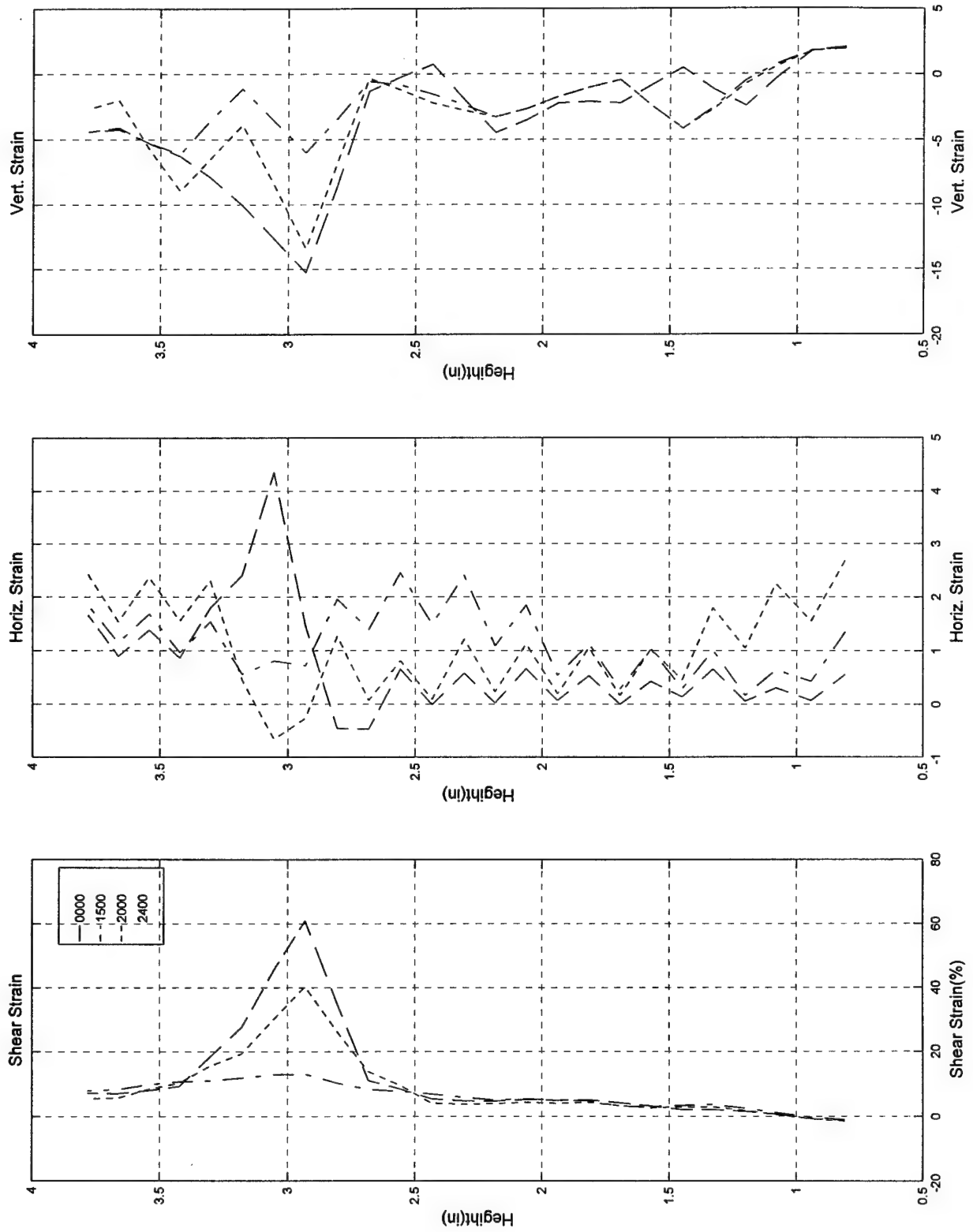
Test #79, Camera #A, Figure 5

Test #79; 4/1/97; Torsion-Extension; ECP=50 psi; Loire, Video a



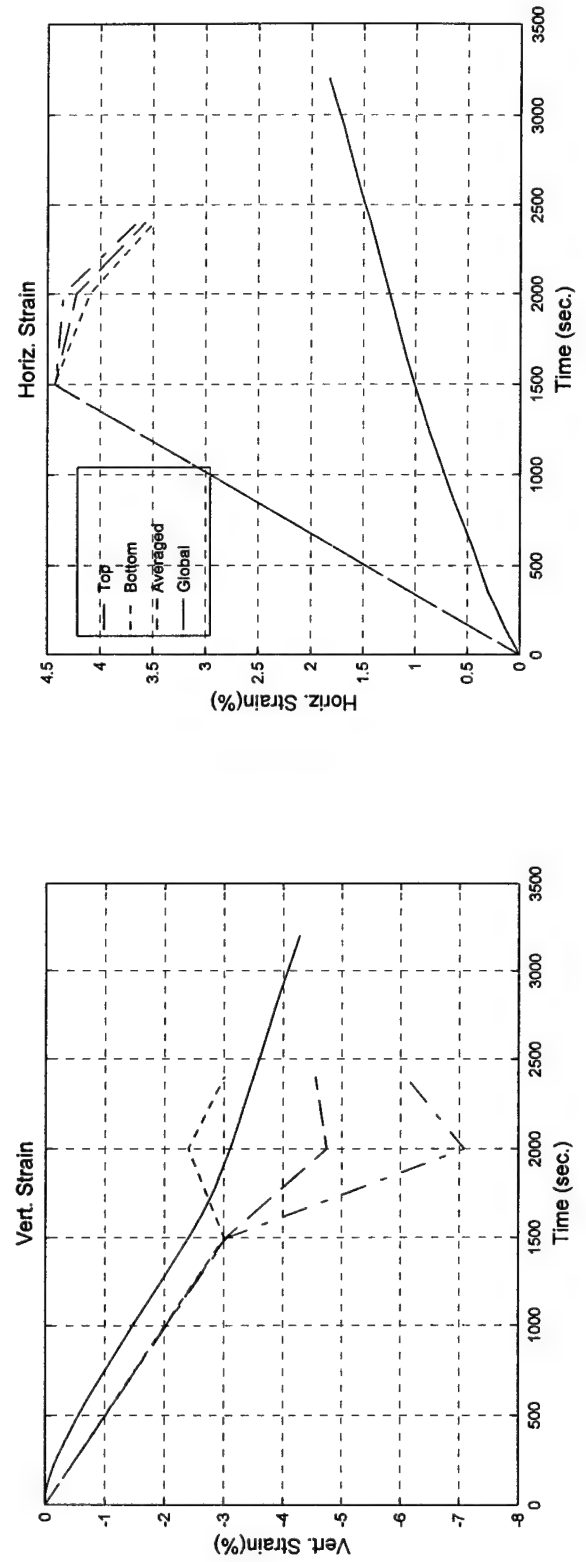
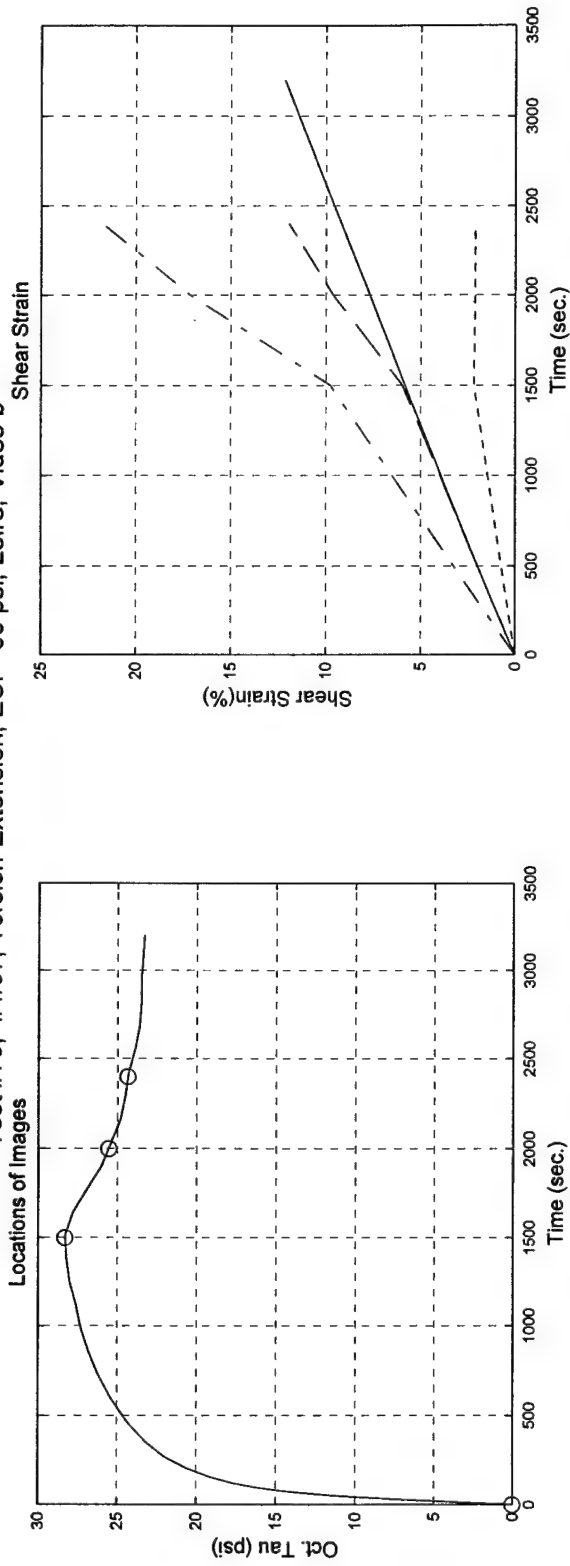
Test #79, Camera #A, Figure 6

Test #79; 4/1/97; Torsion-Extension; ECP=50 psi; Loire, Video a



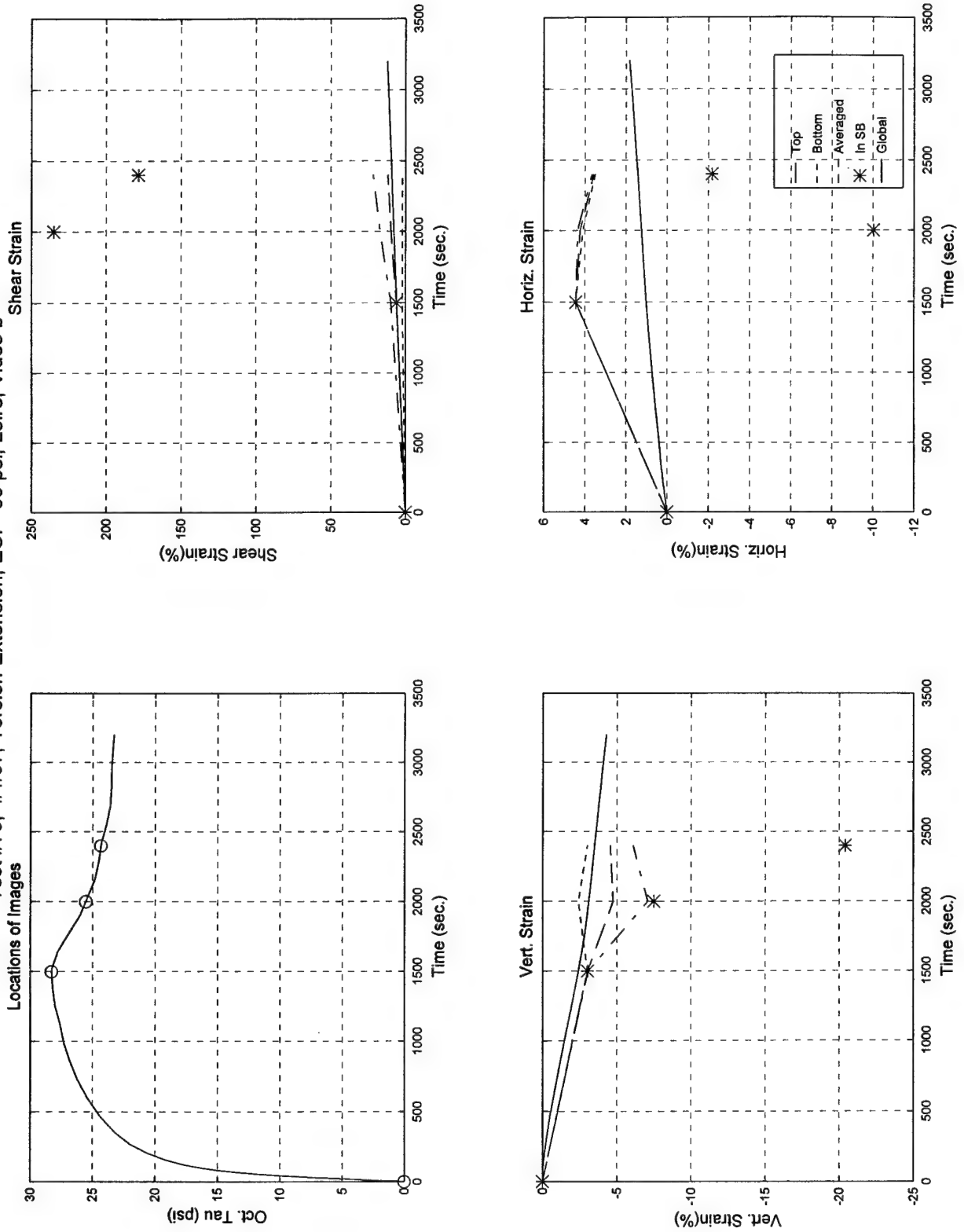
Test #79, Camera #A, Figure 7

Test #79; 4/1/97; Torsion-Extension; ECP=50 psi; Loire, Video b



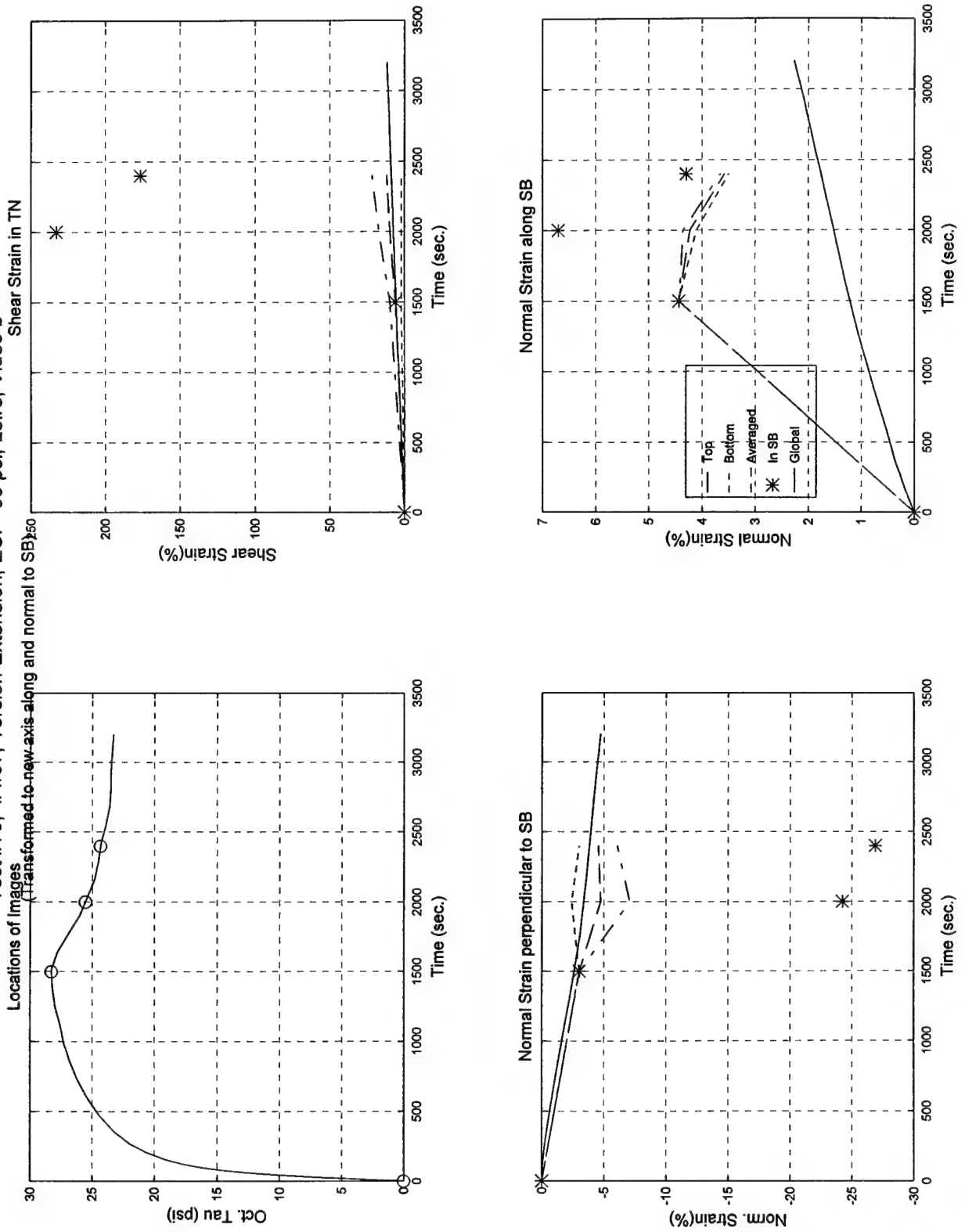
Test #79, Camera #B, Figure 1

Test #79; 4/1/97; Torsion-Extension; ECP=50 psi; Loire, Video b



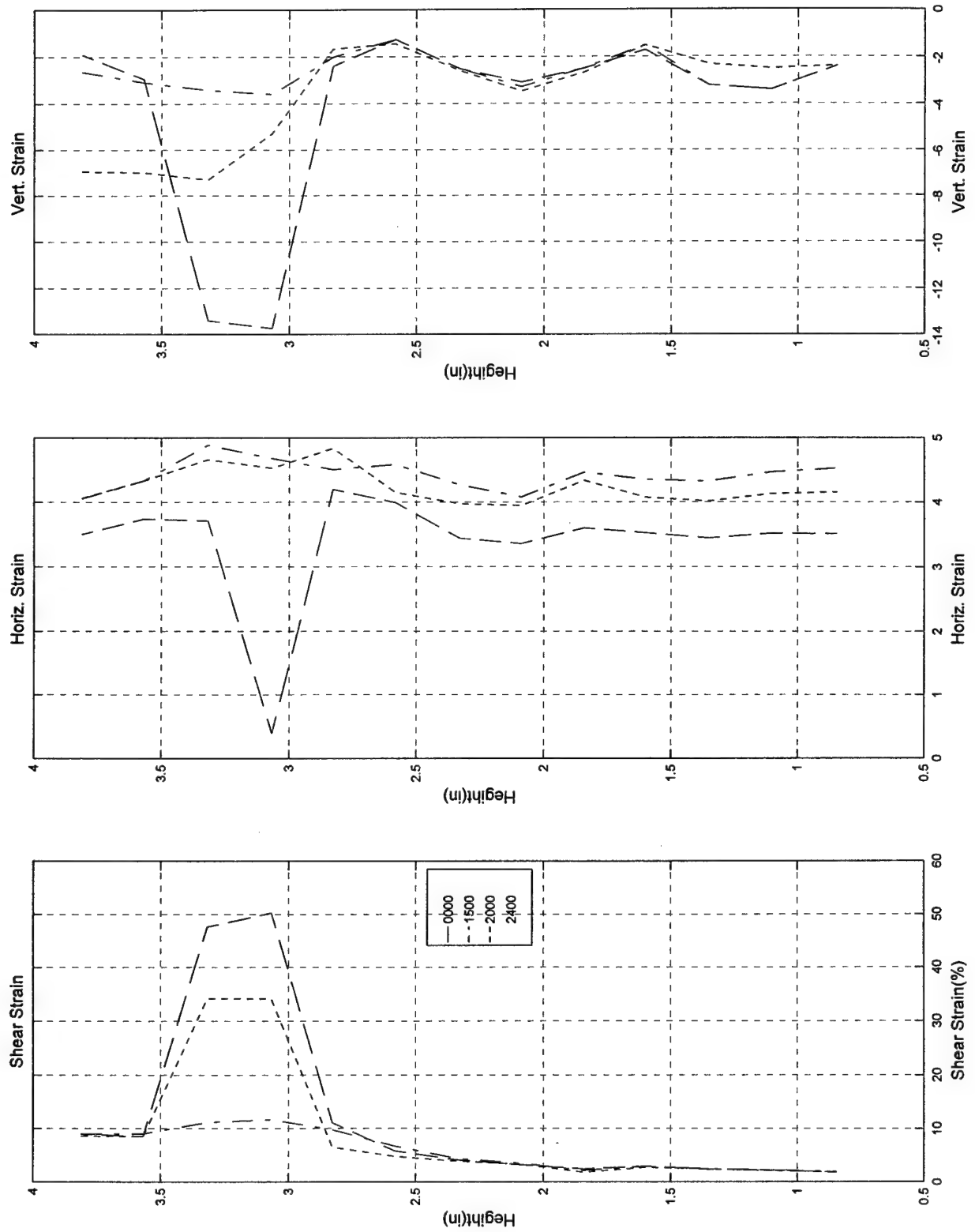
Test #79, Camera #B, Figure 2

Test #79; 4/1/97; Torsion-Extension; ECP=50 psi; Loire, Video b



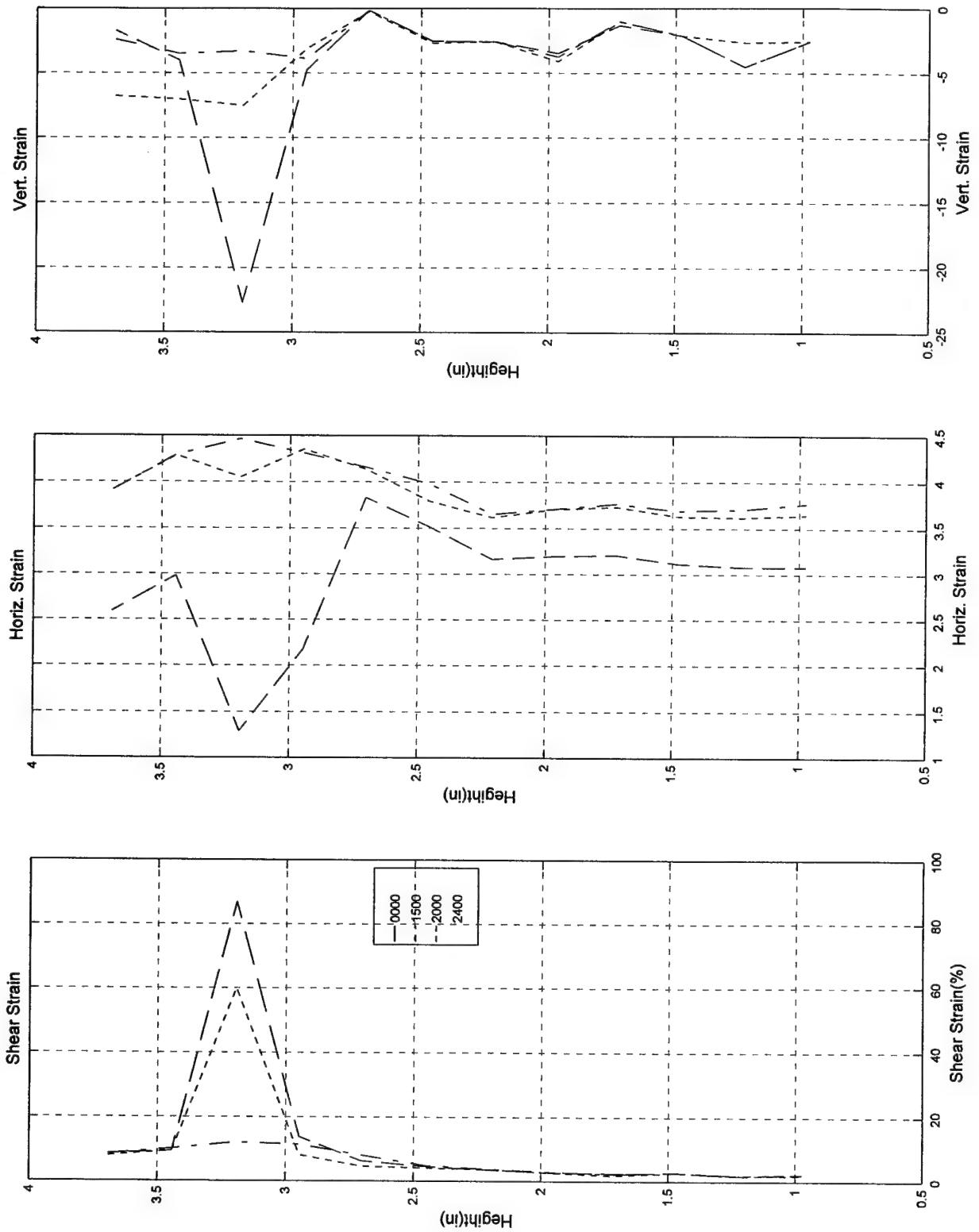
Test #79, Camera #B, Figure 3

Test #79; 4/1/97; Torsion-Extension; ECP=50 psi; Loire, Video b



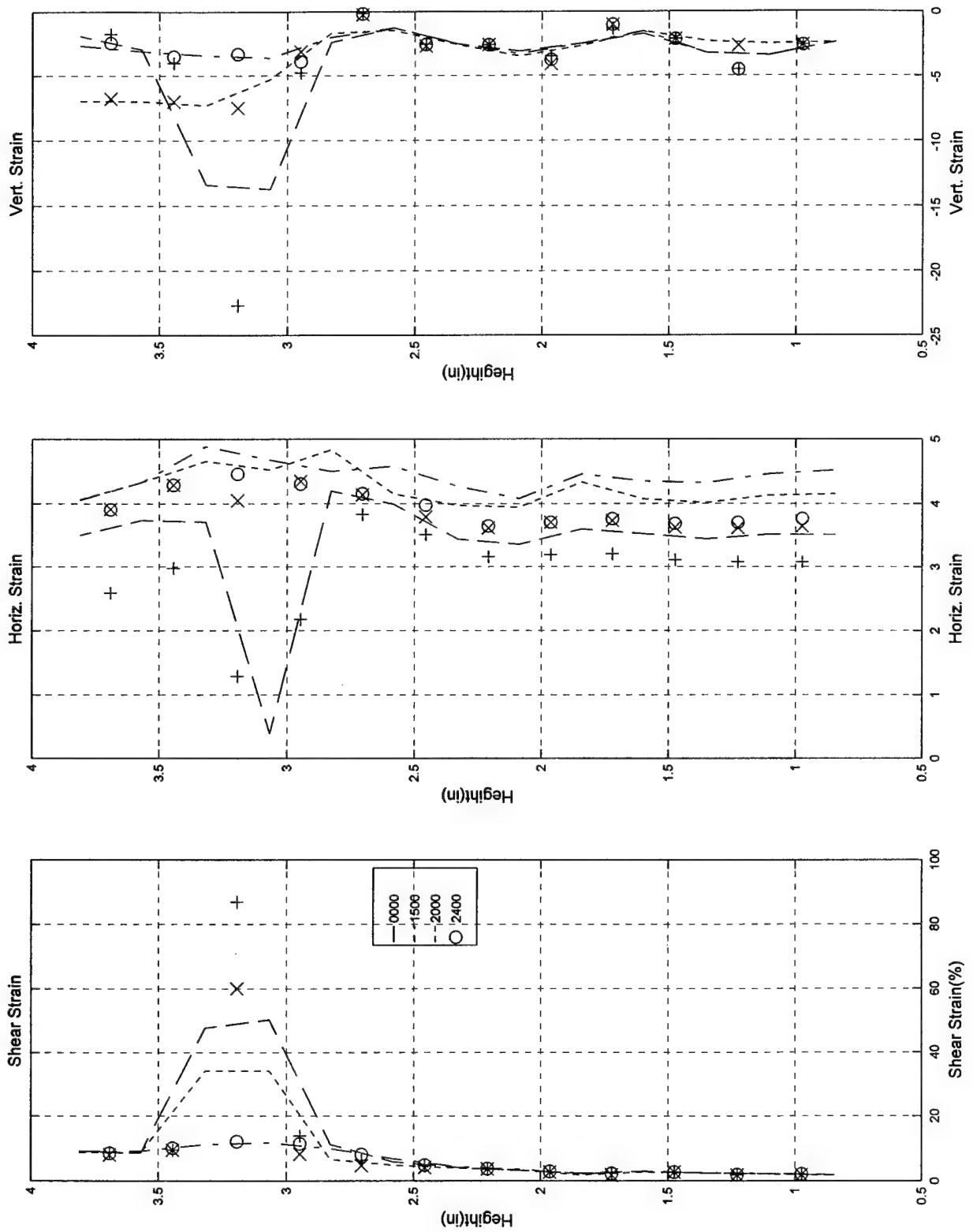
Test #79, Camera #B, Figure 4

Test #79; 4/1/97; Torsion-Extension; ECP=50 psi; Loire, Video b



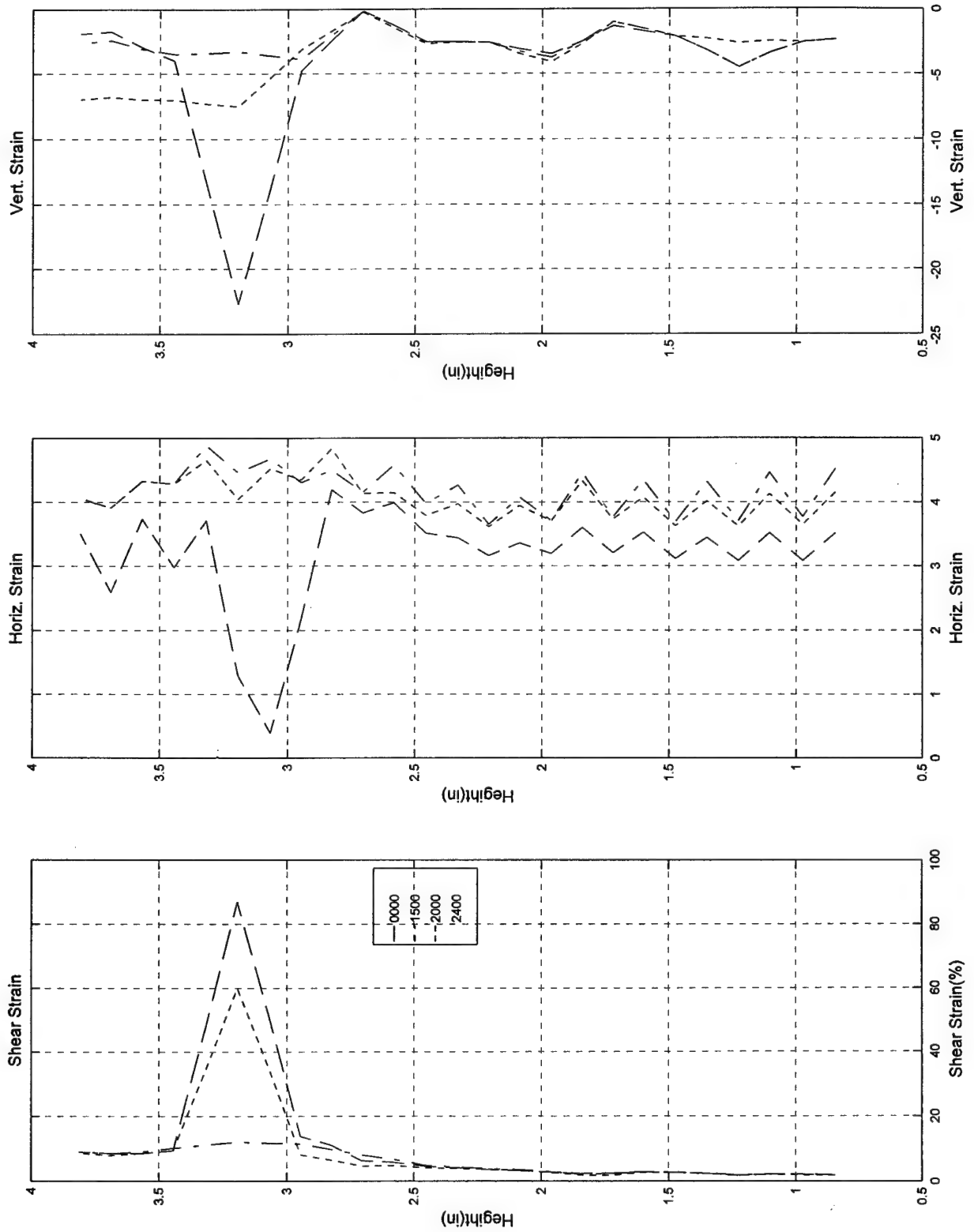
Test #79, Camera #B, Figure 5

Test #79; 4/1/97; Torsion-Extension; ECP=50 psi; Loire, Video b



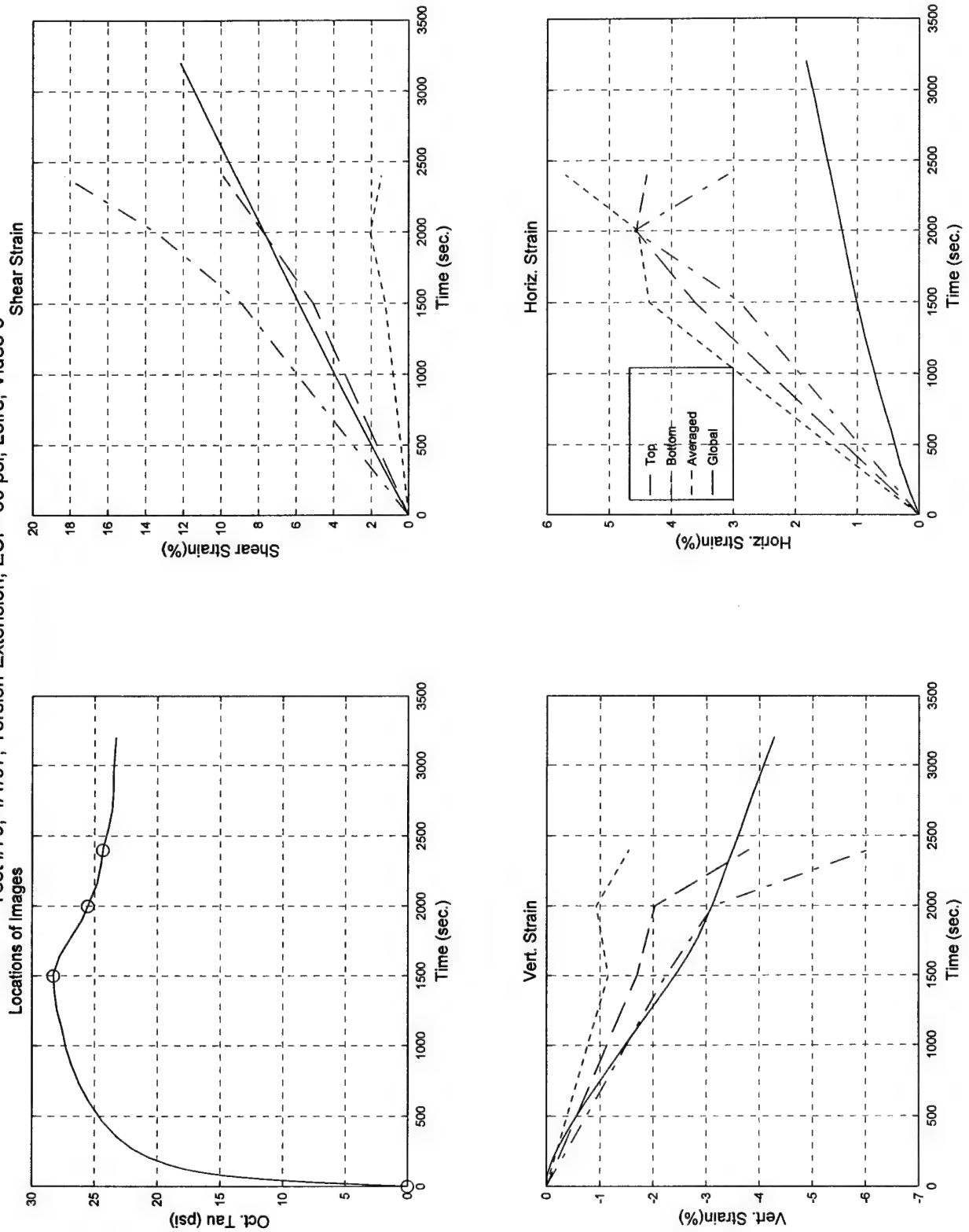
Test #79, Camera #B, Figure 6

Test #79; 4/1/97; Torsion-Extension; ECP=50 psi; Loire, Video b



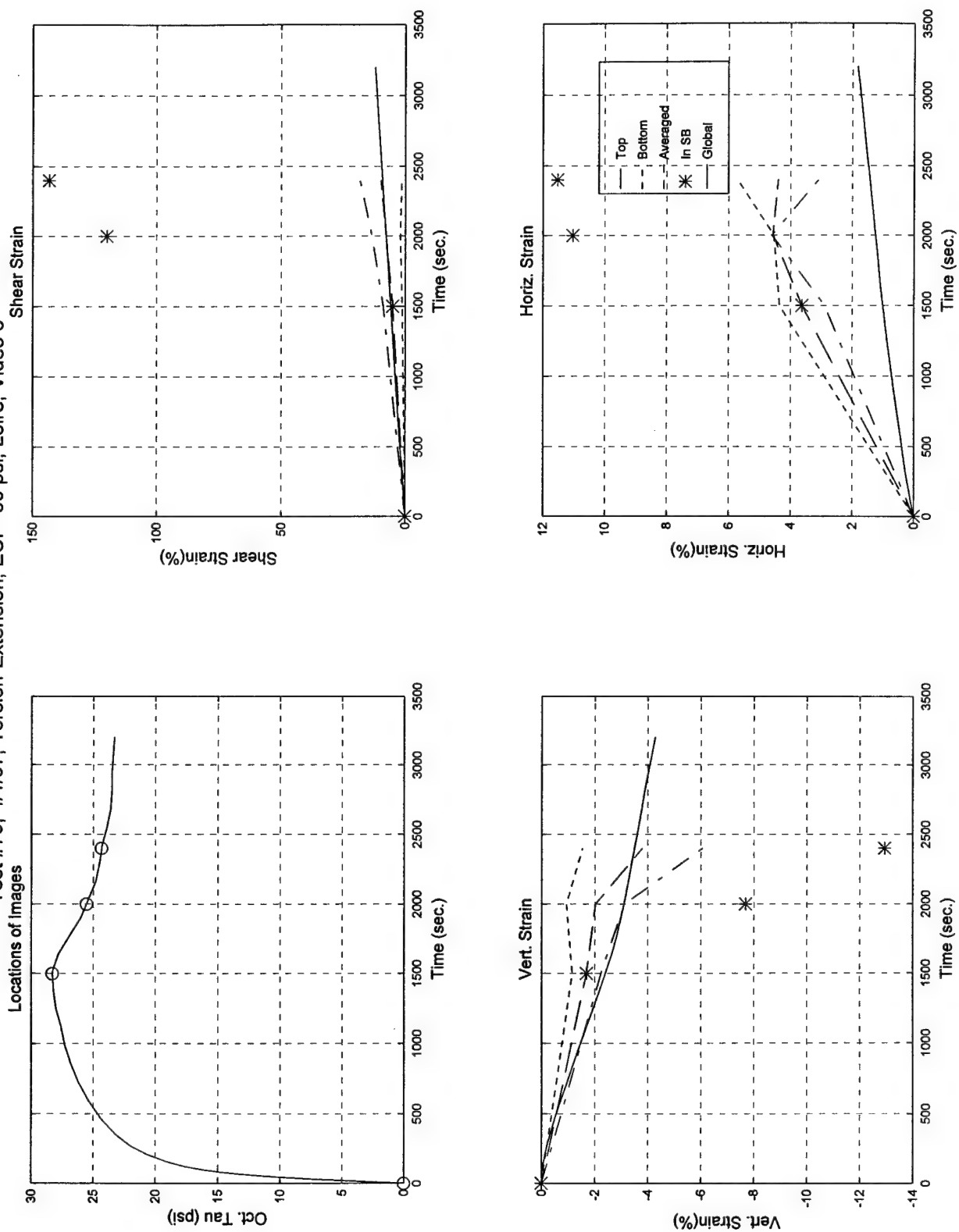
Test #79, Camera #B, Figure 7

Test #79; 4/1/97; Torsion-Extension; ECP=50 psi; Loire, Video c



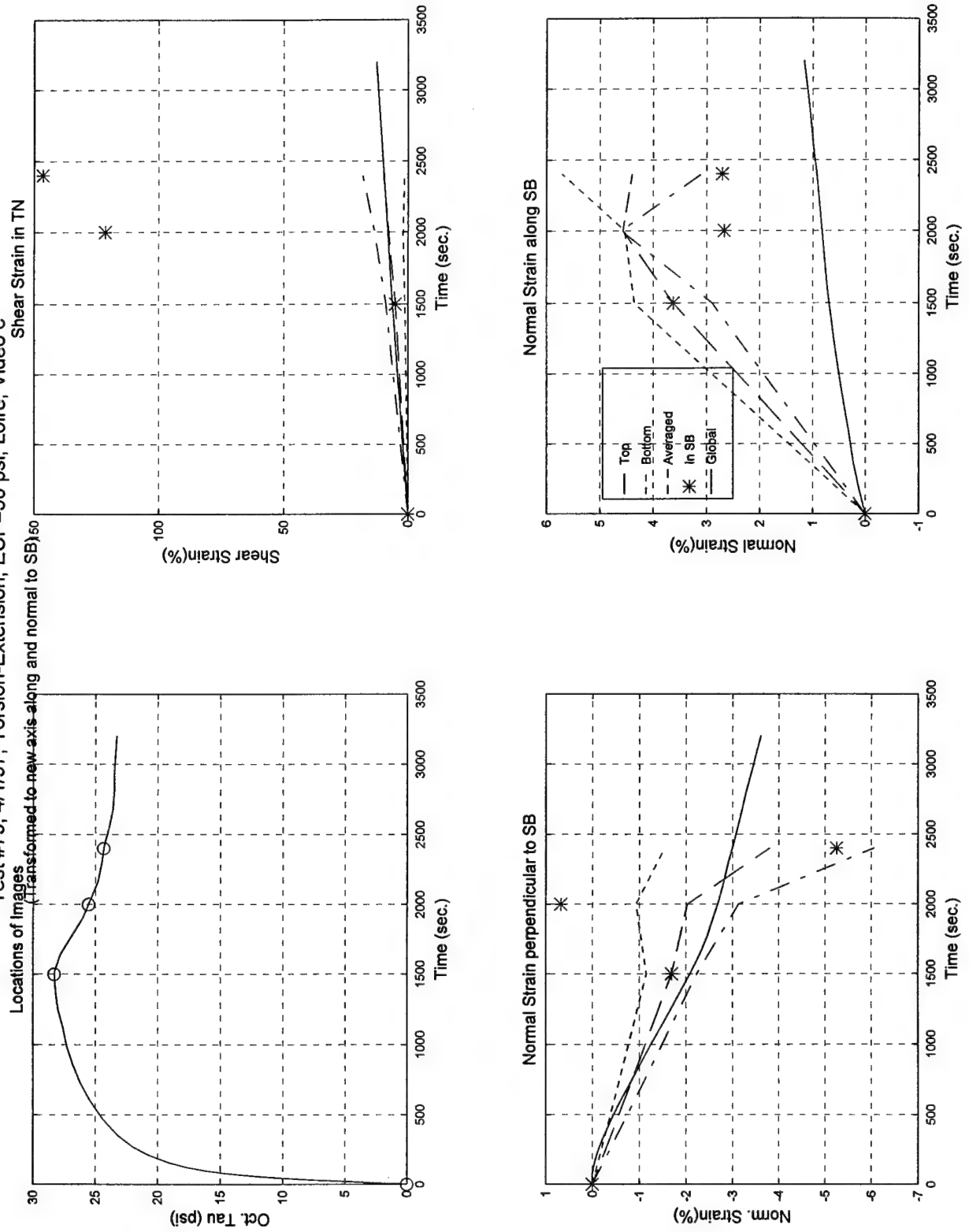
Test #79, Camera #C, Figure 1

Test #79; 4/1/97; Torsion-Extension; ECP=50 psi; Loire, Video c



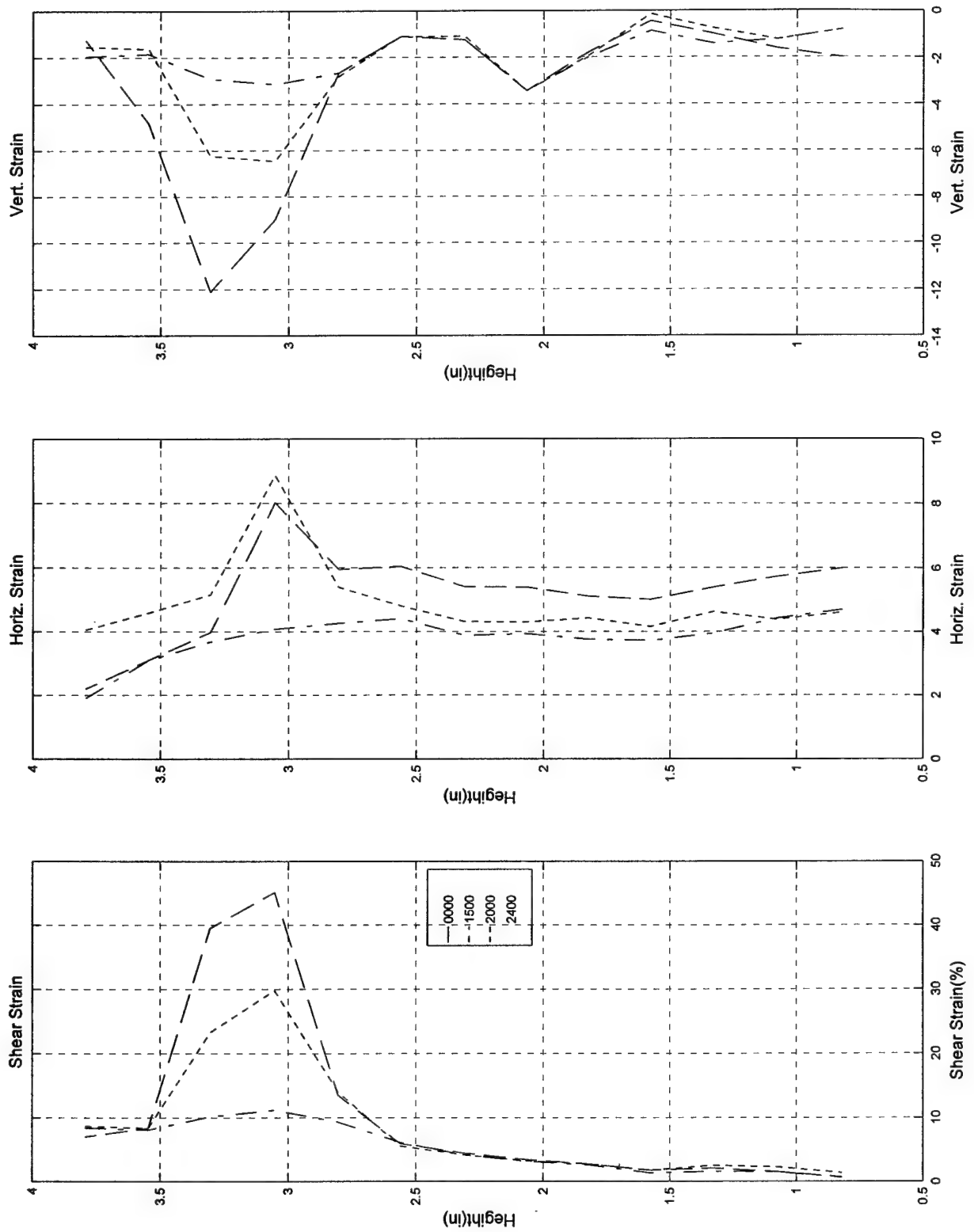
Test #79, Camera #C, Figure 2

Test #79; 4/1/97; Torsion-Extension; ECP=50 psi; Loire, Video c



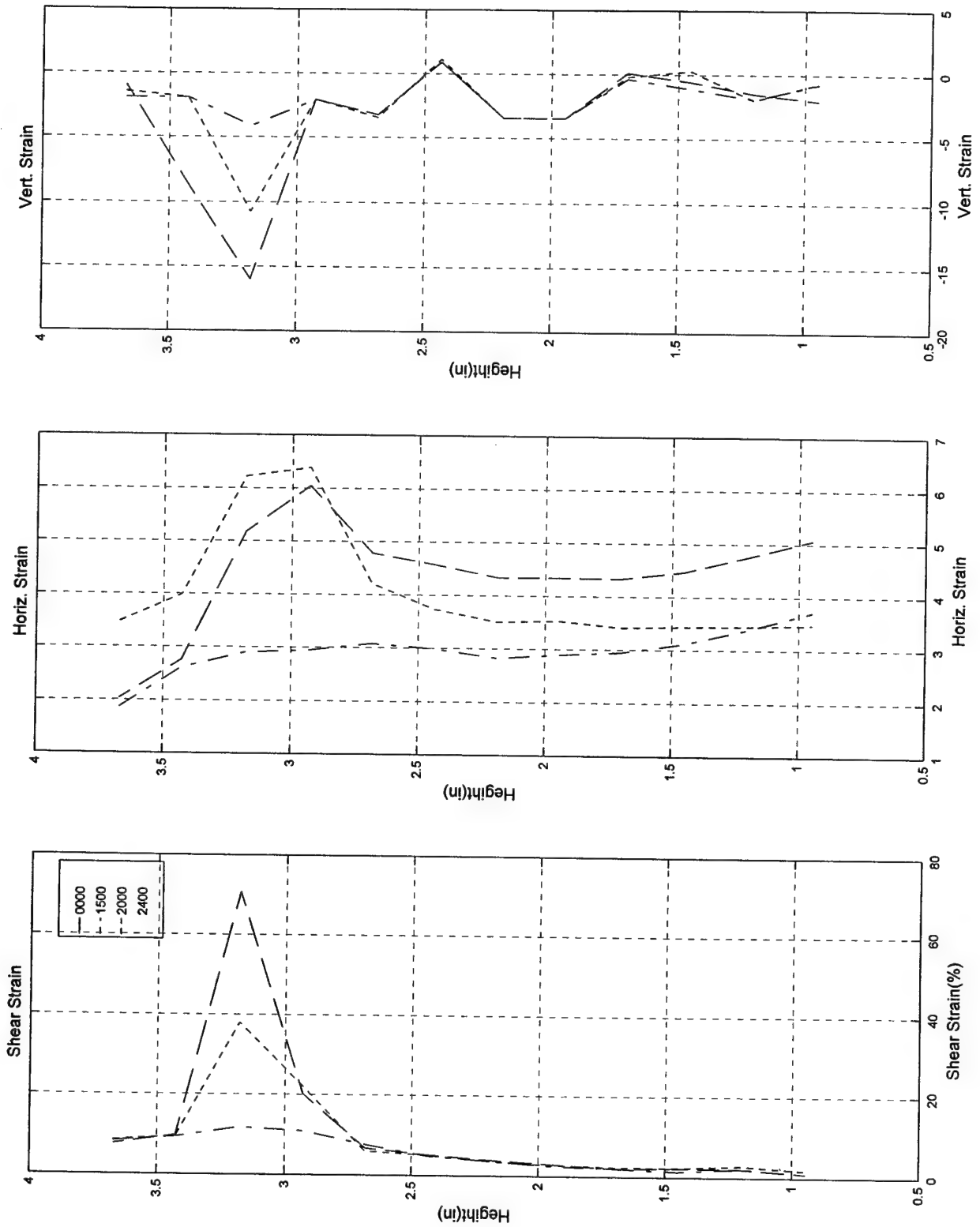
Test #79, Camera #C, Figure 3

Test #79; 4/1/97; Torsion-Extension; ECP=50 psi; Loire, Video c



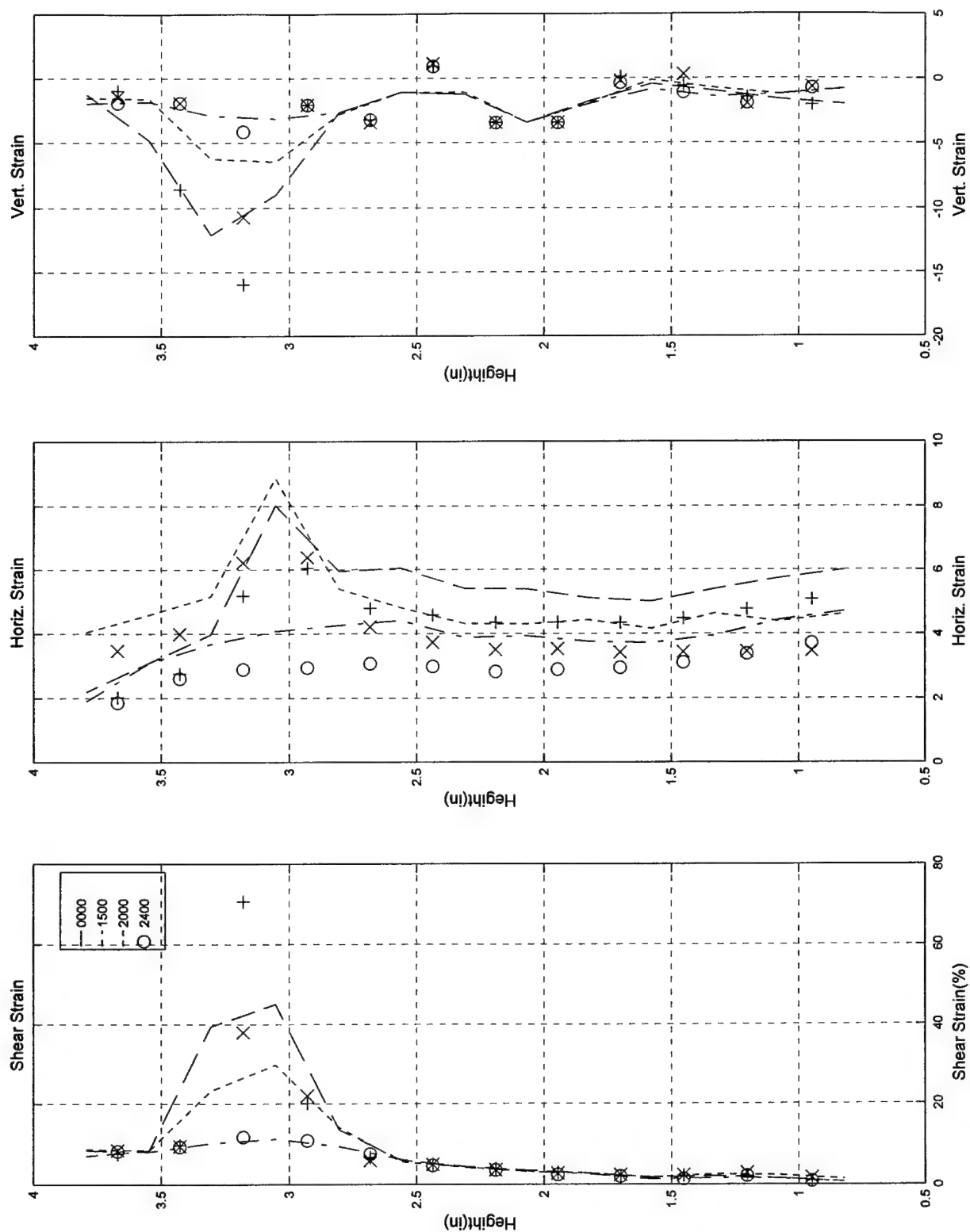
Test #79, Camera #C, Figure 4

Test #79; 4/1/97; Torsion-Extension; ECP=50 psi; Loire, Video c



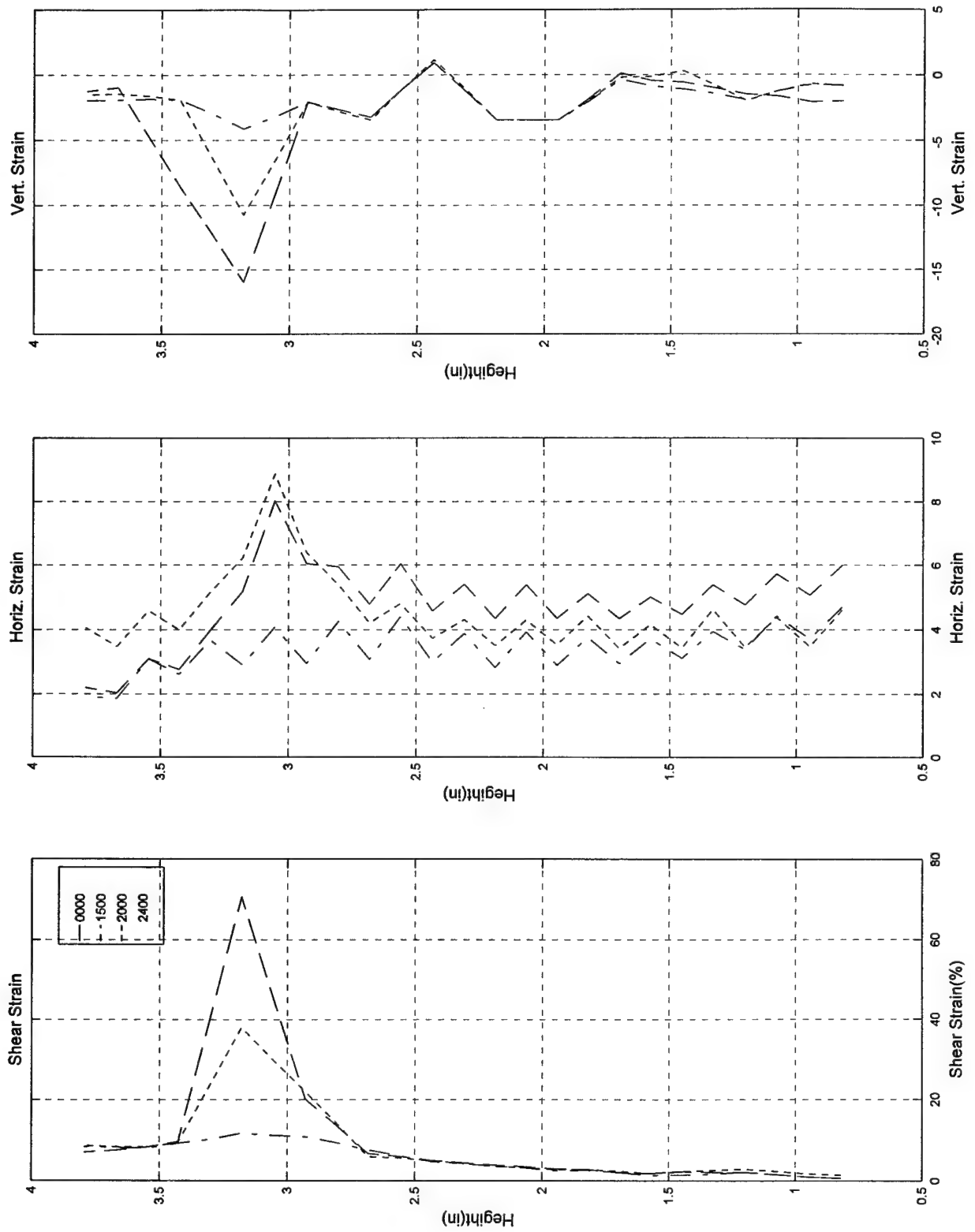
Test #79, Camera #C, Figure 5

Test #79; 4/1/97; Torsion-Extension; ECP=50 psi; Loire, Video c



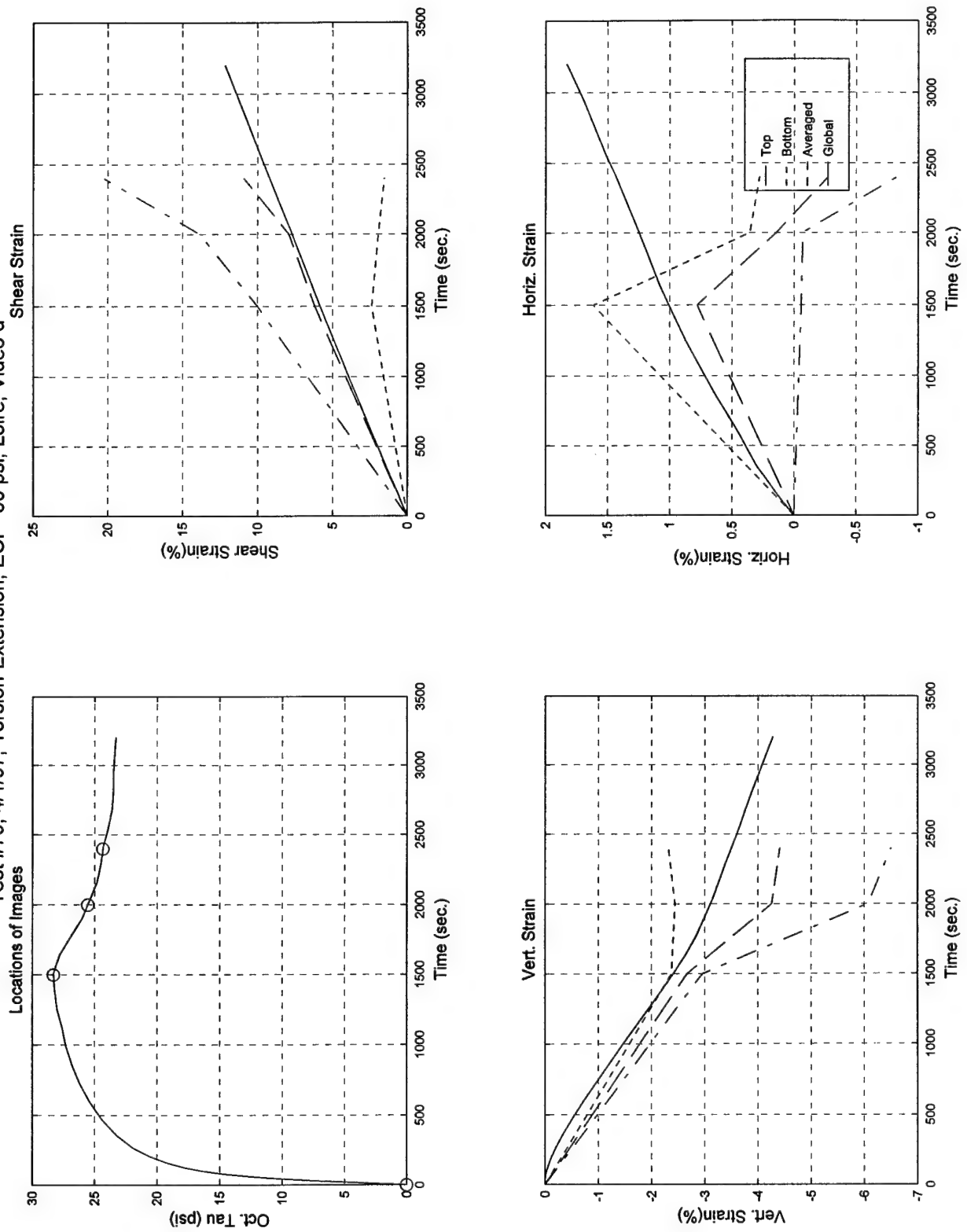
Test #79, Camera #C, Figure 6

Test #79; 4/1/97; Torsion-Extension; ECP=50 psi; Loire, Video c



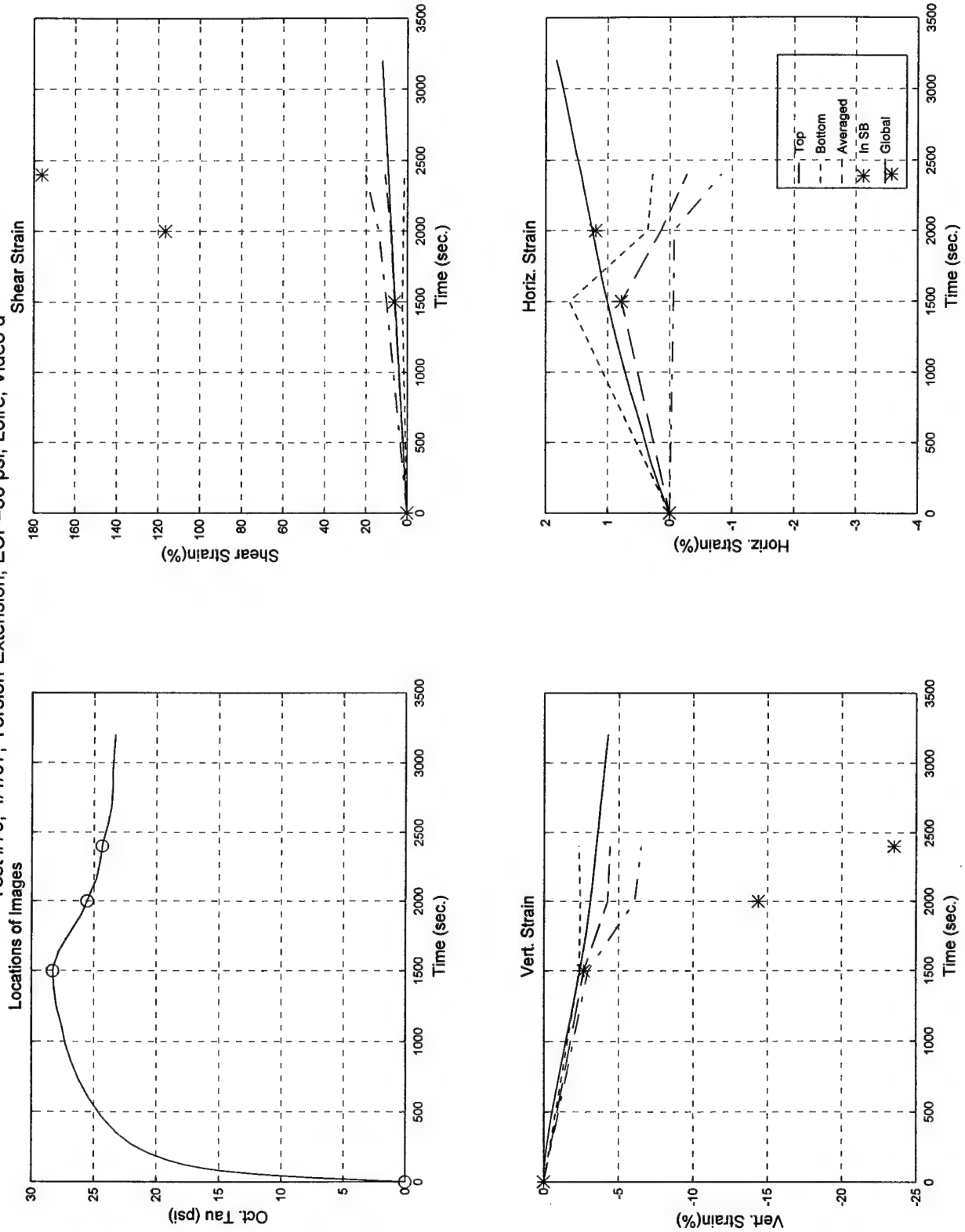
Test #79, Camera #C, Figure 7

Test #79; 4/1/97; Torsion-Extension; ECP=50 psi; Loire, Video d



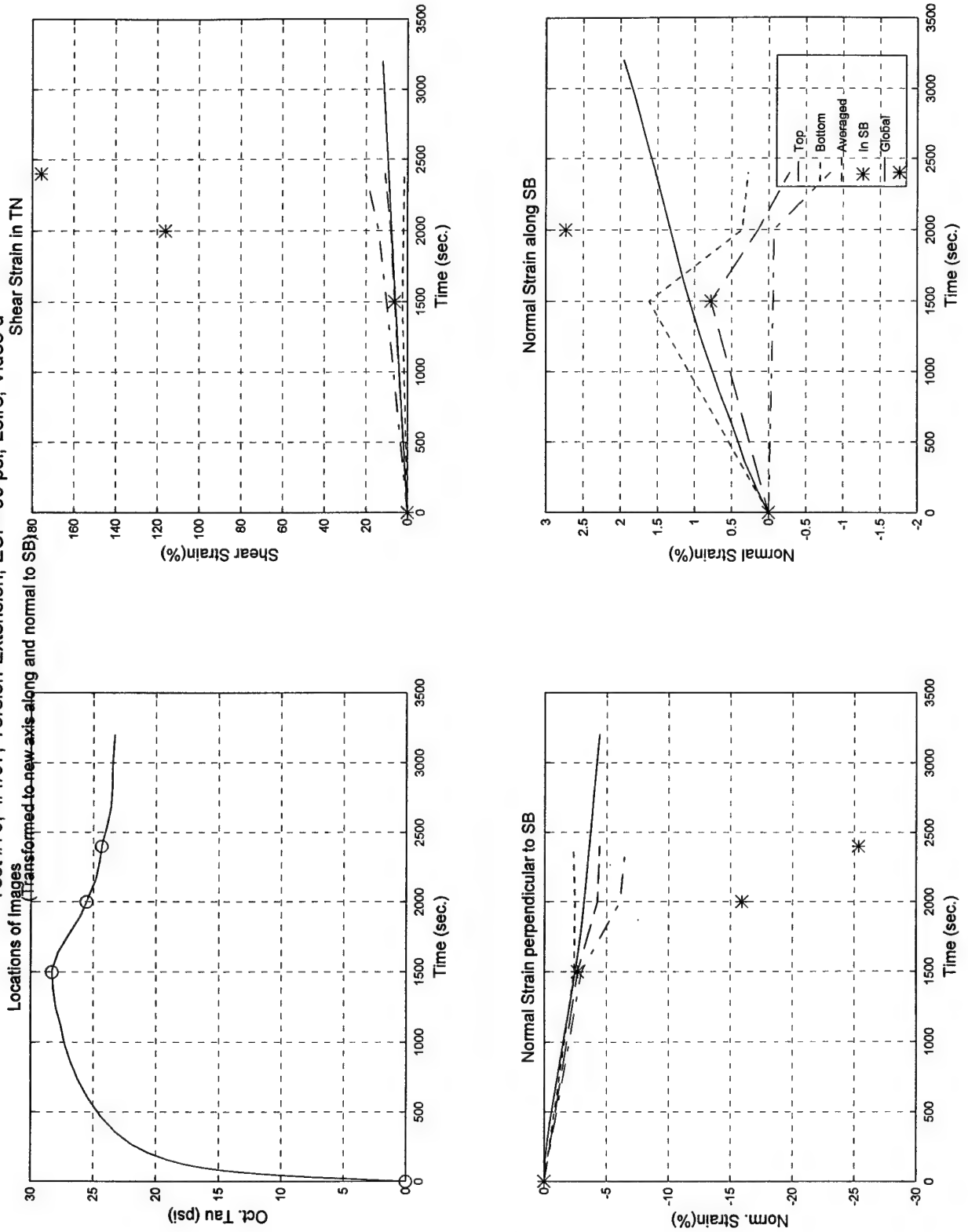
Test #79, Camera #D, Figure 1

Test #79; 4/1/97; Torsion-Extension; ECP=50 psi; Loire, Video d



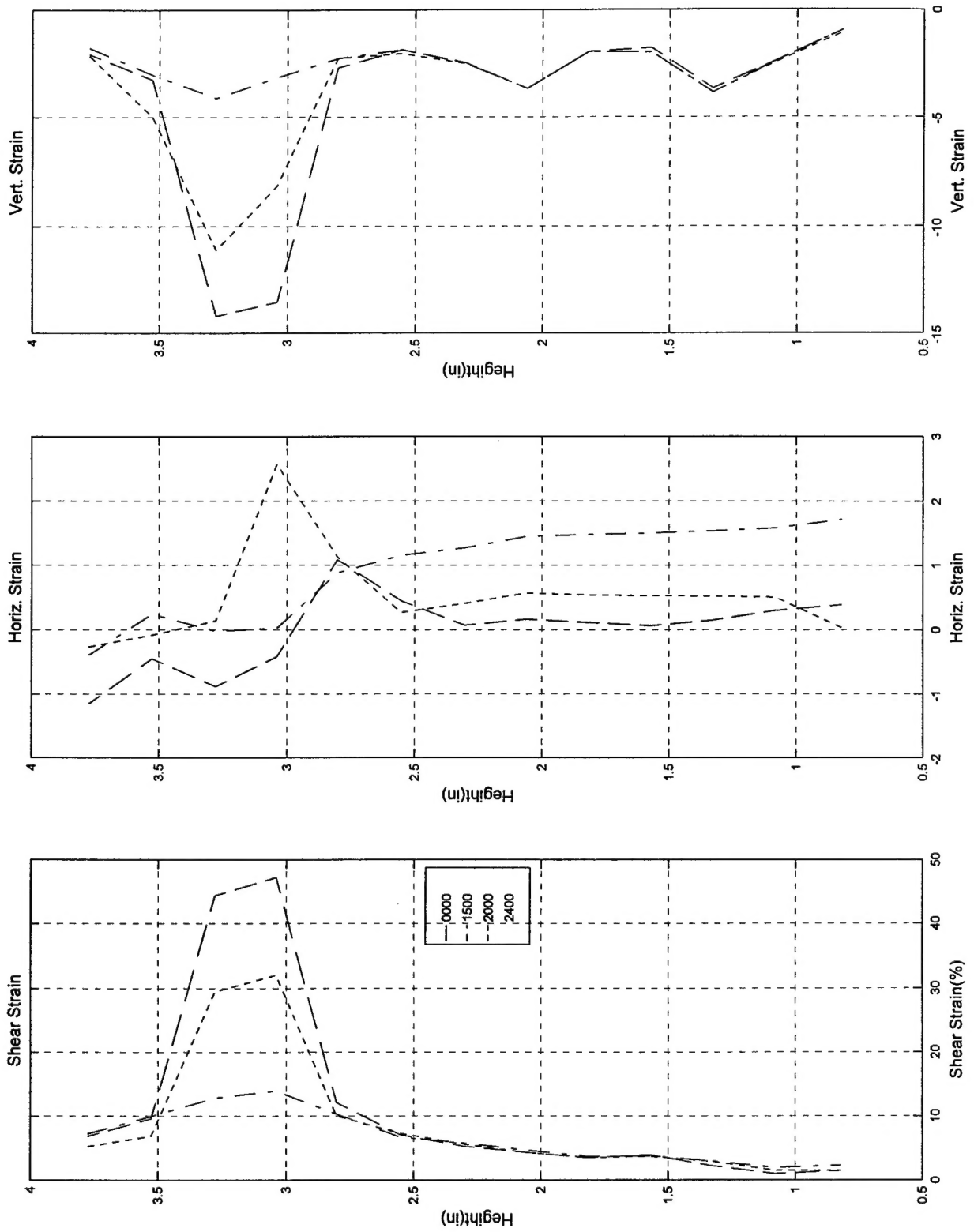
Test #79, Camera #D, Figure 2

Test #79; 4/1/97; Torsion-Extension; ECP=50 psi; Loire, Video d



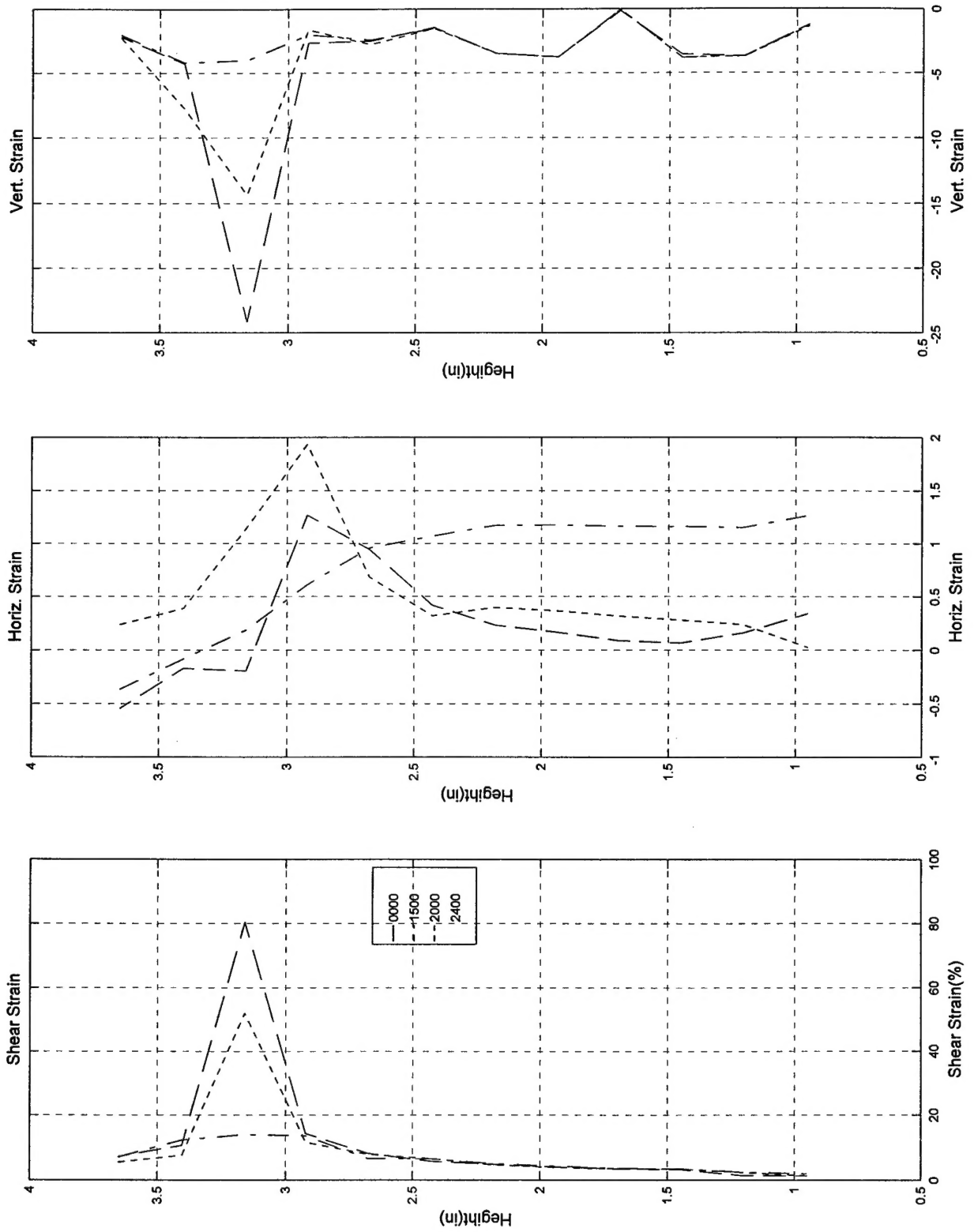
Test #79, Camera #D, Figure 3

Test #79; 4/1/97; Torsion-Extension; ECP=50 psi; Loire, Video d



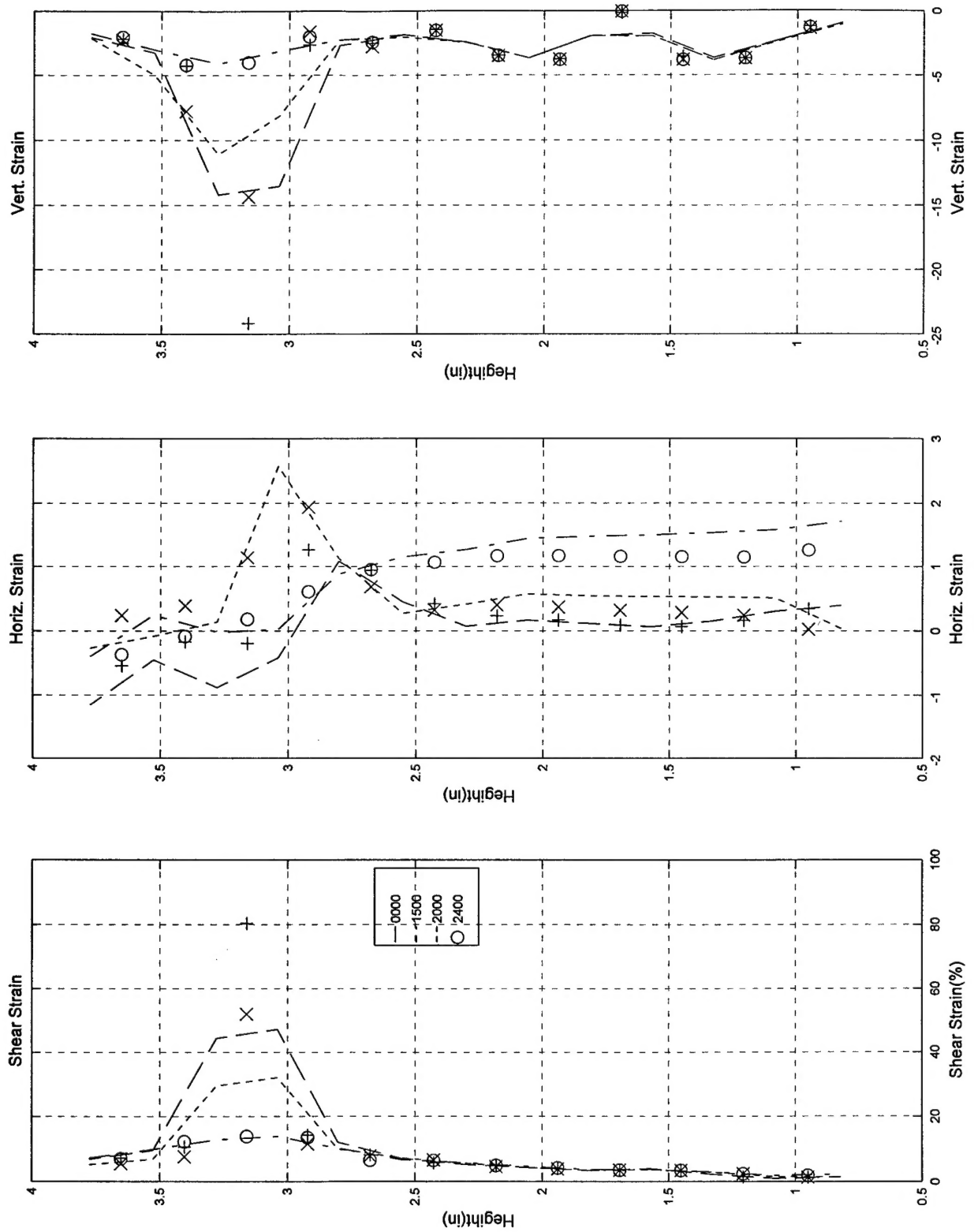
Test #79, Camera #D, Figure 4

Test #79; 4/1/97; Torsion-Extension; ECP=50 psi; Loire, Video d



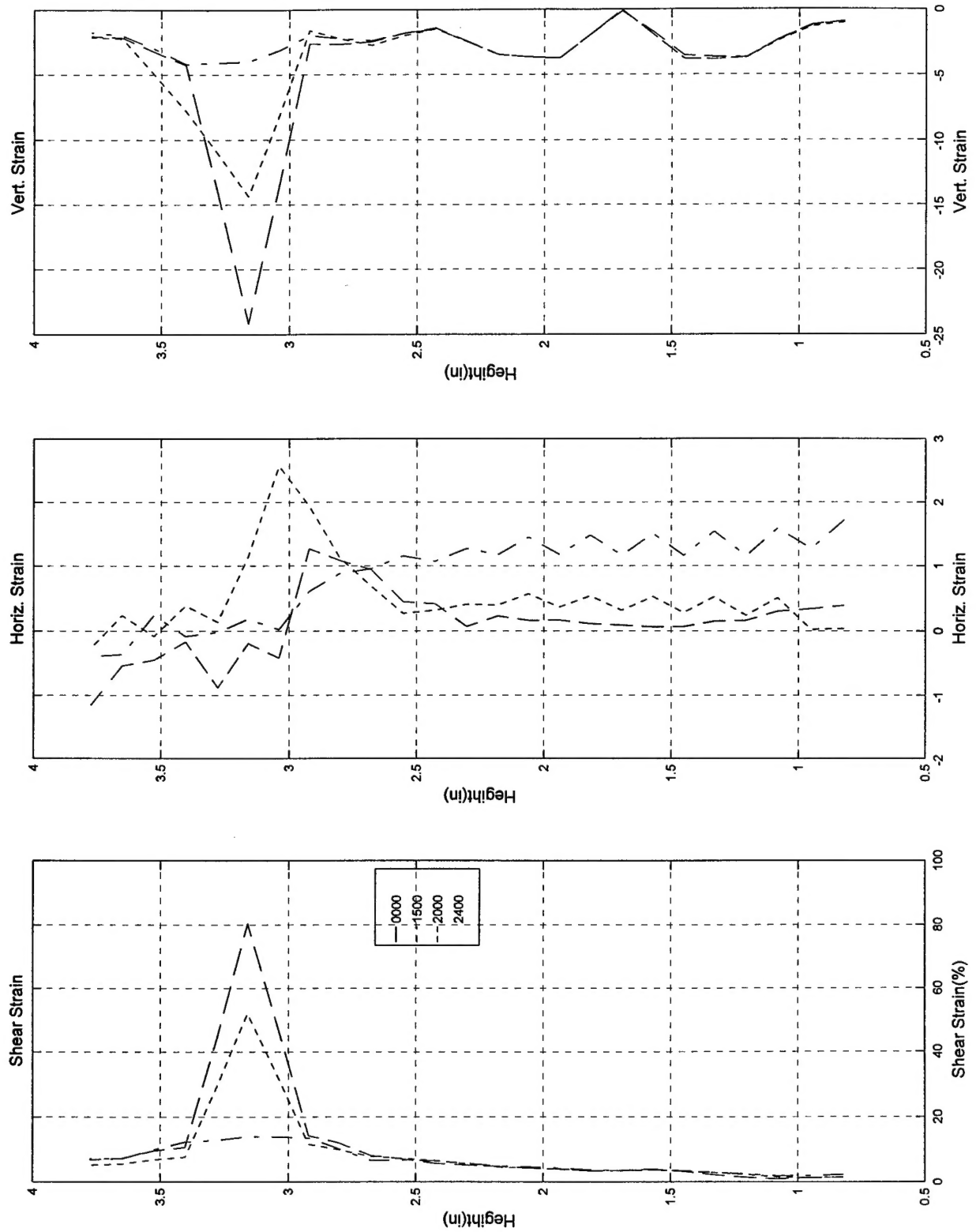
Test #77, Camera #D, Figure 5

Test #79; 4/1/97; Torsion-Extension; ECP=50 psi; Loire, Video d



Test #79, Camera #D, Figure 6

Test #79; 4/1/97; Torsion-Extension; ECP=50 psi; Loire, Video d



Test #79, Camera #D, Figure 7